Lecture Notes in Mechanical Engineering

Harish Kumar
Prashant K. Jain *Editors*

Recent Advances in Mechanical Engineering

Select Proceedings of NCAME 2019

Springer

Lecture Notes in Mechanical Engineering

Lecture Notes in Mechanical Engineering (LNME) publishes the latest developments in Mechanical Engineering - quickly, informally and with high quality. Original research reported in proceedings and post-proceedings represents the core of LNME. Volumes published in LNME embrace all aspects, subfields and new challenges of mechanical engineering. Topics in the series include:

- Engineering Design
- Machinery and Machine Elements
- Mechanical Structures and Stress Analysis
- Automotive Engineering
- Engine Technology
- Aerospace Technology and Astronautics
- Nanotechnology and Microengineering
- Control, Robotics, Mechatronics
- MEMS
- Theoretical and Applied Mechanics
- Dynamical Systems, Control
- Fluid Mechanics
- Engineering Thermodynamics, Heat and Mass Transfer
- Manufacturing
- Precision Engineering, Instrumentation, Measurement
- Materials Engineering
- Tribology and Surface Technology

To submit a proposal or request further information, please contact the Springer Editor in your country:

China: Li Shen at li.shen@springer.com
India: Dr. Akash Chakraborty at akash.chakraborty@springernature.com
Rest of Asia, Australia, New Zealand: Swati Meherishi at swati.meherishi@springer.com
All other countries: Dr. Leontina Di Cecco at Leontina.dicecco@springer.com

To submit a proposal for a monograph, please check our Springer Tracts in Mechanical Engineering at http://www.springer.com/series/11693 or contact Leontina.dicecco@springer.com

Indexed by SCOPUS. The books of the series are submitted for indexing to Web of Science.

More information about this series at http://www.springer.com/series/11236

Harish Kumar · Prashant K. Jain
Editors

Recent Advances in Mechanical Engineering

Select Proceedings of NCAME 2019

Springer

Editors
Harish Kumar
Department of Mechanical Engineering
National Institute of Technology Delhi
Delhi, India

Prashant K. Jain
Department of Mechanical Engineering
Indian Institute of Information Technology
Design and Manufacturing
Jabalpur, India

ISSN 2195-4356 ISSN 2195-4364 (electronic)
Lecture Notes in Mechanical Engineering
ISBN 978-981-15-1070-0 ISBN 978-981-15-1071-7 (eBook)
https://doi.org/10.1007/978-981-15-1071-7

This Springer imprint is published by the registered company Springer Nature Singapore Pte Ltd.
The registered company address is: 152 Beach Road, #21-01/04 Gateway East, Singapore 189721, Singapore

Preface

The 1st National Conference on Advances in Mechanical Engineering (NCAME)–2019 has been the first conference of its series organized by Department of Mechanical Engineering of National Institute of Technology Delhi, India. It was considered as a forum to bring together scientists, university professors, graduate students, and mechanical engineers, presenting new science, technology, and engineering ideas and achievements.

The motive of this conference is of great importance. The time and location of the conference were quite excellent. The month of March in Delhi is very pleasant with the advantage of Delhi as the capital of the country with excellent connectivity by road, train, and air. The conference attracted many participants working in various fields of engineering: design, mechanics, materials, etc. The success of the conference inspired the organizers to turn the conference into an annual event.

More than 140 papers were presented at NCAME–2019. They covered topics ranging from the mechanics of machines, material engineering, structural strength, and tribological behavior to transport technologies, machinery quality, and innovations, in addition to dynamics of machines, walking mechanisms, and computational methods. However, for this book, only 54 peer-reviewed papers, authored by research groups representing various universities and institutes, were selected for inclusion.

Furthermore, I thank the staff and management of the institute for their cooperation and support, especially Prof. Praveen Kumar, Hon. Director, National Institute of Technology Delhi and all members of the program committee and the organizing committee for their work in preparing and organizing the conference. Last but not least, I thank Springer for its professional assistance and particularly Dr. Akash Chakraborty who supported this publication.

Delhi, India — Harish Kumar
Jabalpur, India — Prashant K. Jain

Contents

Recent Development in Virtual Cellular Manufacturing System 1
P. K. Arora, Abid Haleem, Harish Kumar and Shahroz A. Khan

IoT Integration in Industry—A Literature Review 9
Bhavesh Chandrayan and Ravinder Kumar

Defect Reduction in Manufacturing Industry Using Lean Six Sigma Approach 19
Narottam, K. Mathiyazhagan and Vikas Sharma

Modeling the Interrelationship of Critical Success Factors Adoption of Sustainable Lean Manufacturing Using DEMATEL Approach 31
Naveen Kumar and K. Mathiyazhagan

Green Supply Chain Management: Evolution of the Concept, Practices and Trends 47
J. Martínez and K. Mathiyazhagan

Human Upper Limb Joint Torque Minimization Using Genetic Algorithm 57
Anil Kumar Gillawat and Hemant Jayantilal Nagarsheth

A Low-Cost Cold Chain Suggestion for Indian Fruit and Vegetable 71
Vardan Parashar, Abid Haleem and J. A. Usmani

Optimization of Cutting Parameters of Machinability Aspects During Dry Turning 79
Anurag Sharma, R. C. Singh and Ranganath M. Singari

Total Interpretive Structural Modelling of Critical Factors of Sustainable-Oriented Innovation for Indian Manufacturing MSMEs 95
Sonal Khurana, Bisma Mannan and Abid Haleem

Cloud Computing in Industries: A Review 107
Zareef Askary and Ravinder Kumar

Evaluation of High Temperature Tribological Behaviour of Nickel Coating Using LRT 117
S. Chaudhary, R. C. Singh, Rajiv Chaudhary and Sonia

Numerical and Experimental Investigations on Film Cooling Performance of Trench Model Embedded with Compound Angle Film Hole Jets 127
V. G. Krishna Anand and K. M. Parammasivam

Identifying and Modelling of Constructs for Innovation Management of MSMEs: An ISM Approach 135
Bisma Mannan, Sonal Khurana and Abid Haleem

Investigation of Drivers Towards Adoption of Circular Economy: A DEMATEL Approach 147
Annayath Maqbool, Shahbaz Khan, Abid Haleem and Mohd Imran Khan

Simulation-Based Analysis of Performance Parameters of Thrust Pad Bearing Under Thin Film Lubrication with Chamfered Inlet 161
Poonam Kumari and Mohammad Sikandar Azam

Workplace Safety Improvement Through Quality Control Circle Approach in Heavy Engineering Industry 175
D. Dinagaran, K. R. Balasubramanian, S. P. Sivapirakasam and Kuruva Gopanna

A Bio-inspired Climbing Robot: Dynamic Modelling and Prototype Development 191
Asesh Patra, Meet Patel, Priyabrata Chattopadhyay, Anubhab Majumder and Sanjoy Kumar Ghoshal

Effect of Electrochemical Micromachining Process Parameters on Surface Roughness and Dimensional Deviation of Ti6Al4V by Tungsten Electrode 211
Venkatasreenivasula Reddy Perla, Subbarama Kousik Suraparaju, K. J. RathanRaj and A. Sreenivasulu Reddy

Transmissibility Along Human Segments When Exposed to Vibration 227
Arvinder Singh, Harkirat Singh, Ishbir Singh and Sachin Kalsi

A Comprehensive Review on Microfluidics Technology and its Applications 235
Su. Venkatesan, J. Jerald, P. Asokan and R. Prabakaran

Drilling Process Improvements in EN31 Steel Under Different Environments 247
Manoj Kumar Sinha, Jamil Ahmad, Harish Kumar and Ranganath M. Singari

A New 3D Benchmarking Artifact to Evaluate Dimensional Accuracy and Geometric Tolerancing of Additive Manufacturing Technique 261
Md Qamar Tanveer, Mohd Suhaib and Abid Haleem

Effect of 3D-Printed Ankle Foot Orthosis During Walking of Foot Deformities Patients 275
Harish Kumar Banga, Parveen Kalra, Rajendra M. Belokar and Rajesh Kumar

Robust Taguchi Based Optimization of Surface Finish During Hard Turning EN 31 with Carbon Nanotubes-Based Nano-Coated Tip 289
Navriti Gupta, R. S. Walia and A. K. Agrawal

Convection of Viscoplastic Fluid in U-Tube Bends 299
N. H. Khan, M. K. Paswan and M. A. Hassan

Performance Analysis of Temperature and MRR Using High-Speed Micro-Drilling on Incoloy 800 Superalloy 313
T. Venkatesan, J. Jerald and P. Asokan

Design and Development of Zirconia-Dolerite Ball Plate for Error Mapping of Probe-Type Coordinate Measuring Machine 321
Vinay A. Kulkarni and B. B. Ahuja

Application of Industrial Internet of Things for Online Monitoring of Bearings 333
Saroj Kumar, Parminder Singh, Shankar Sehgal, Harmesh Kumar, Naveen Aggarwal, Sarbjeet Singh and Deepam Goyal

Acquisition of Jugular Venous Pulse Waveform by a Non-invasive Technique 343
S. Bagyaraj, M. Ragumathulla and D. Vaithiyanathan

Condition Monitoring of Induction Motor Using Internet of Things (IoT) 353
Anurag Choudhary, Shefali Jamwal, Deepam Goyal, Rajeev Kumar Dang and Shankar Sehgal

Development of Aluminium-Yttrium Oxide Metal Matrix Composite Foam Through FSP 367
Sachin Rathore, Ratnesh Kumar Raj Singh and K. L. A. Khan

Model-Based Adaptive Prognosis of a Hydraulic System 375
Sawan Kumar, Sumanta Kumar Dutta, Sanjoy Kumar Ghoshal and J. Das

Effect of Intercritical Heat Treatment and Volume Fraction on the Morphological Properties, Mechanical Properties, and Work Hardening Behaviour of Dual-Phase Steel 393
Shubham Sharma, Jujhar Singh, N. Jayarambabu, Chander Prakash, Sunpreet Singh, Abhinav Sharma and Harish Kumar

Rheological Characterization and Finishing Performance Evaluation of Vegetable Oil-Based Bi-dispersed Magnetorheological Finishing Fluid 407
Vikas Kumar, Rajesh Kumar and Harmesh Kumar

Experimental Investigation of Microstructure and Mechanical Properties of Brass–Iron Joined by TIG Welding Process 417
J. Nithin Kumar, M. Devaiah, P. Sandeep kumar and P. Sudheer Rao

Finite Element Modeling and Simulation of Projectile Impact on Ductile Target 429
Sanan H. Khan, Servesh K. Agnihotri, Ateeb A. Khan and Afsar Husain

Characterization and Mechanical Properties of 2024/Y_2O_3 Composite Developed by Stir Rheocasting 439
Semegn Cheneke Lemessa and D. Benny Karunakar

Conversion and Utilization of Gravitational Potential Energy for Hydraulic Excavator 455
Tushar Kanti Saha, Abhinav Kr. Singh, Mohit Bhola, Sumanta Kumar Dutta and Sanjoy Kumar Ghoshal

Microstructure and Wear Study of Al 7075-T6/Eggshell/SiC/Al_2O_3 Hybrid Composites 471
Girija Moona, Vikas Rastogi, R. S. Walia and Rina Sharma

Determination of the Degradation Pattern of Pump Using Two-Phase Diagnostic Bond Graph 483
Sumanta Kumar Dutta, Sawan Kumar, Tushar Kanti Saha and Sanjoy Kumar Ghoshal

Ballistic Performance of Thin Aluminium Cylindrical and Hemispherical Shells 501
Nikhil Khaire and G. Tiwari

Experimental Study on PCM-Based External Wall Cladding for Energy Efficient Buildings 513
Kolli Sravani, R. Parameshwaran and V. Vinayaka Ram

The Machining Characteristics of the Al7075-B_4C Nanocomposites Developed Using Ultrasonic Liquid Processor 527
Surender Kumar and P. K. Sood

Influence of Alloying Compositions on the Properties of Nickel-Based Superalloys: A Review 537
Dileep Kumar Ganji and G. Rajyalakshmi

Patient Pulse Rate Monitoring System Using LabVIEW 557
A. R. Krishnan, S. Jayanth and R. Janani

War Field Spy and Fighter Robot 565
Manisha Bharti and Ayush Kumar Agrawal

Erosive Wear Study of Nitrogen-Containing 23-8-N Austenitic Stainless Steel and Bead on Plate Weld Using ER2209 Stainless Steel Filler Wire 575
Naveen Kumar, Navneet Arora and S. K. Goel

Calcium Fluoride a Potential Solid Lubricant for Green Tribology and Sustainability 587
Sanjay Mohan, Ankush Anand, Mir Irfan Ul Haq, Ankush Raina and Rajiv Kumar

Friction and Wear Behaviour of AA2024/ZrO_2 Composites: Effect of Graphite 597
Smridh Slathia, Rahul Anand, Mir Irfan Ul Haq, Ankush Raina, Sanjay Mohan, Rajiv Kumar and Ankush Anand

A Fractographic Study of PE, PP Self-reinforced Composites in Quasi-static Loading Conditions 603
M. Sharan Chandran and K. Padmanabhan

Analysis of a Double-Stage Thermoelectric Refrigerator 619
Sudhanshu Sharma and Vijay Kumar Dwivedi

A Review on Solar Energy-Based Smart Greenhouse 629
Padma Wangmo, Vinay Kumar Jadoun and Anshul Agarwal

Analysis of Firm-Level Innovativeness Indicators 635
Sanjay Kumar, Abid Haleem, Sushil and Mohd. Asim Qadri

Comparative Study of Basin Type Double Slope Active Solar Stills Based on Energy Metrics 643
Abhishek Sharma, Vijay Kumar Dwivedi and Desh Bandhu Singh

About the Editors

Dr. Harish Kumar is currently Assistant Professor at Department of Mechanical Engineering, National Institute of Technology Delhi. He obtained his B. Tech. (Mechanical & Automation Engineering) and Ph.D. from GGS Indraprastha University, Delhi. His major research interests include mechanical measurement and metrology and composites. He has more than 35 publications to his credit, published in international peer reviewed journals. He has served as Scientist in CSIR-National Physical Laboratory, New Delhi during 2007-2017 and as a guest researcher at National Institute of Standards and Technology, USA in 2016. He has been serving as editor of several peer reviewed journals.

Dr. Prashant K. Jain is currently Associate Professor at Department of Mechanical Engineering, Indian Institute of Information Technology, Design and Manufacturing, Jabalpur. He obtained his B. E. (Mechanical Engineering) from Dr. H. S. Gour University, Sagar, M. E. (Advanced Production Systems) from SATI, Vidisha and Ph. D. from Indian Institute of Technology Delhi, Delhi. He also has served at IIT Delhi as Project Scientist and at Delhi College of Engineering, Delhi (now Delhi Technological University, Delhi) as Lecturer. His major research interests include rapid prototyping / additive manufacturing, geometric modelling, CAD/CAM integration, computational geometry, rapid prototyping and tooling. He has more than 85 publications to his credit, published in international peer reviewed journals, national and international conferences in India and abroad.

Recent Development in Virtual Cellular Manufacturing System

P. K. Arora, Abid Haleem, Harish Kumar and Shahroz A. Khan

Abstract Virtual cellular manufacturing has been known to a way to overcome the difficulties of both cellular manufacturing system and functional layout system. With virtual cellular manufacturing system, groups of resources are dedicated to the manufacturing of a part family, but these cells are not real in the manufacturing system. In virtual cellular manufacturing system, machines remain in their original layout, and the machine cells are instead formed in the planning and control system and remain virtual in nature. In the present work, different models for the formation of virtual cell have been discussed. Factors that may affect the efficiency of manufacturing system have also been discussed.

Keywords Group technology · Machine cell · Part family · Manufacturing system · Cellular manufacturing system

1 Introduction

Production is a process of transferring the materials into useful articles. If supporting activities like quality control and production planning are introduced along with production, it is known as manufacturing. Manufacturing is a systematic activity, so each manufacturing system has a specific objective. The useful output is transformed from the various inputs.

P. K. Arora (✉) · S. A. Khan
Galgotias College of Engineering and Technology, Greater Noida, UP, India
e-mail: pawanar@rediffmail.com

A. Haleem
Jamia Millia Islamia, New Delhi 110025, India

H. Kumar
National Institute of Technology Delhi, New Delhi, Delhi 110040, India

H. Kumar and P. K. Jain (eds.), *Recent Advances in Mechanical Engineering*,
Lecture Notes in Mechanical Engineering,
https://doi.org/10.1007/978-981-15-1071-7_1

The objective of manufacturing system is to get high efficiency and flexibility. Manufacturer has to solve a number of problems at the manufacturing floor. Traditional manufacturing system is not capable of satisfying the requirements of manufacturing system where quick response to the product design change is required. In today's era, manufacturing industry is under a continuous pressure to control the cost of its product. Competition is increasing day by day. A variety of products need different operation and machines. The concept of innovative manufacturing is being developed by management of manufacturing industries in order to minimize the production cost. It is possible by increasing the utilization of resources. Cellular manufacturing is termed as an application of group technology. Group technology is generally a selection and coding of machine cells for part families. In group technology and cellular manufacturing system (CMS), machine cell and part families are formed independently. Different researchers have developed different models to optimize the CMS. The main disadvantage of this CMS is that it fix the machine cell for specific part family. Machine cells are not fully utilized in many of the cases. Virtual cellular manufacturing systems (VCMS) are the most appropriate to overcome this problem. In VCMS, machine cells are not fixed. They are virtual in nature and the position of machine is not physically changed. The advantage of forming machine cell is to improve the utilization of resources. Different researchers have proposed different models to form a virtual cell. In VCMS, there is no need to move the machine, instead machine will remain in their original position. The virtual cell may result decrease in setup time, change in machine usage and decrease in material handling time. The points of interest may be to incorporate enhanced execution, higher system effectiveness, improved product generation control and better product quality.

Various designs and production tools are used in VCMS. Design tools may include computer-aided design for assembly and manufacturing. Production tools may include computer-integrated manufacturing, just in time, material requirement planning and manufacturing resources planning. VCMS depends upon utilization of the cellular manufacturing systems (CMS) and job shop manufacturing. It is furnished by making virtual gathering of the machine cell and part family incidentally in the creation and arranging the product in control system. Some of the machines may be accessible in more than one cell for the increased utilization of resources. The effectiveness of any manufacturing system may be enhanced by the maximum utilization of virtual cells. The objective is to find the similarity index among the part families and reduce the setup time. It was found that the virtual cellular manufacturing system is more valuable than other manufacturing system when product variety and demand variability are high [1] (Fig. 1).

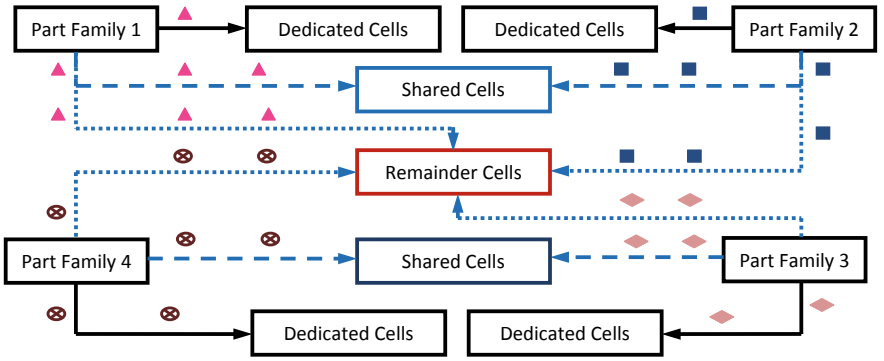

Fig. 1 Virtual cellular manufacturing system

2 Development of Virtual Cellular Manufacturing System

The cellular manufacturing system has been emerged as a technique to optimize the manufacturing system. A numerical model is proposed in which logical group of cells is formed. This model was efficiently responding with change in demand and technological changes. The proposed model was able to maximize the product output and reduce the setup time. The suggested model was tested with randomly generated changes and other self-generated changes in demands. It was found that the proposed model is working efficiently as compared to cellular manufacturing system and functional layout systems [1]. A model of axiomatic design theory was proposed [2]. It is based on waste elimination theory and the objective is to minimize system cost and improve system efficiency. A model was planned in which coding is in LINGO programming and is kept running over utilitarian and disseminated courses of action of similar machines [3]. Mak et al. [4] build up a hereditary planning technique to investigate the manufacturing cell arrangement and genetic algorithm for VCMS. A new scheduling model has been developed using genetic algorithm. The objective of the proposed model is to minimize the total material movement. This may increase the overall efficiency of the manufacturing system. Slomp et al. [19] has build up a technique of creating VCMS by taking the original thought of group generation. Virtual cells are formed by taking multi-objectives in real time based on the demand. Labor grouping is also considered in addition to machine cell. Worker movement in inter-cell is also taken into account. Long [5] focused on research on virtual supply chain networks by combining agent technology and computational experiment. A bilateral model was proposed for dynamic VCMS and Supply chain management [6]. This covers multi-facility, multi-plants and market demands completely. This mathematical model was nonlinear and efforts were made to optimize this model. Transportation cost related to the distribution of finished products from each plant to markets is calculated. Exceptional elements and number of labor movements between active plants were also calculated.

A scientific model which intends to limit the average manufacturing cost with workforce requirements was developed [7]. A hybrid model using constraint programming and discrete particle swarm programming was introduced to solve the manufacturing problem. The proposed model was demonstrated with randomly generated data. Mak et al. [4] introduced a mathematical model to describe the characteristics of VCMS. A genetic algorithm model was developed to optimize the scheduling in the manufacturing system. The proposed model was compared with traditional manufacturing and cellular manufacturing system. It was found that result was comparatively more superior. Virtual manufacturing systems have problem because of dynamic environment and nonlinear nature of the problem. Sarker and Li [8] found this solution by developing heuristic solution which is found to be more realistic and responsive. It is observed that the virtual cell scheduling is more complicated due to overlapping among the cells and the multiplicity of possible virtual cell. A specific model is proposed for CMS that combines the setup efficiency obtained by traditional CMS with the flexibility of a job shop [9]. Efficiency with temporary allocation of machine to the part family rather than fixed allocation of machine to part family was compared.

Zamani [10] developed a model for producing capability-based CMS (CBVCMS). The objective function of the proposed model is to minimize the dissimilarities among the parts. The validity of the model was checked with examples available in the literature. The virtual cell gives the better results as compared to functional layout. Mak et al. [4] proposed a scheduling model for the manufacturing system. The objective of this model is to minimize the total distance travelled by all the parts. The performance with age-based genetic algorithm was compared with traditional genetic algorithm. Erenay et al. [11] concentrated on centers around stochastic cell-producing outline. A mathematical model was developed to create dedicated and remainder cells. It is also proposed to minimize the count of cells. Calculation for expected cells in utilization was done.

Ko and Egbelu [12] created two calculations to produce VCMS. The primary calculation was utilized to test directing information and produce sets of machines that show up every now and again. These VCMS are then broke down to utilizing the second calculation which indicates the last VCMS setup. A machine can appear in various VCMS (machine sharing) and a VCMS can serve numerous parts. Mak et al. [17] introduced a strategy to tackle the assembling cell arrangement and the issues for development of VCMS. The goal is to limit the average materials and segments voyaging separation acquired. Moodie et al. [13] proposed a structure for employments booking by utilizing VCMS. Each activity is allotted to an arrangement of workstations. This issue is fathomed by a straight programming where the goal is to limit both travel separations. Hamedi et al. [3] introduced a technique to pick a reasonable design that can enhance the execution of VCMS, particularly limiting the material stream between machines required by each family gathering. It is also presented in selecting a layout that may increase the efficiency of virtual manufacturing systems by lowering the flow of material in between the machines. A multi-objective programming is developed to form VCMS based on resource element.

Routing similarities are mainly discussed in design-oriented papers, whereas processing similarities are mainly discussed in operation-oriented studies. Babu et al. [14] evaluated the importance of enterprise modeler (EM), cell design manager (CDM), cell operation manager (COM), simulator (SIM), performance evaluator (PE) and report generator (REP). Mak and Ma [15] proposed a numerical model which is utilized for creating ideal generation plans for VCMS working under a multi-period fabricating situation. Thomalla [16] recommended the arrangement of issues yet with the goal of limiting delay. In this work, Lagrangian unwinding approach is utilized. An alternate approach is recommended by Mak and Wang [17], who tried a hereditary calculation to get arrangement of issues with the aim of limiting aggregate travel separations. There are many optimization techniques like genetic algorithm (GA) and simulating annealing (SA). These are already suggested by researchers to have better solution of cell formation problems. The use of information technology in Enterprise resource planning (ERP) is also increasing day by day. This may lead to the availability of data for VCMS. The available details on different manufacturing system like tooling, allowance of fixtures and tolerances are mapped with the manufacturing system. We can therefore conclude that VCMS design may enhance efficiency of manufacturing system using data from ERP systems. The cell formation under random product demands is a new avenue for research. In an innovation manufacturing system, cloud-based design and manufacturing has emerged as a new development in the manufacturing system. The proposed model and existing model were also discussed. The proposed model indicates that VCMS has emerged from the interaction of fuzzy machine agents with fuzzy agent attractor [18]. It may improve the overall efficiency of the manufacturing system. Mahadevi [19] presented an arithmetic model for planning a dynamic VCMS with possibilities of change of workers and machines. To verify the model, LINGO software was used.

3 Discussion

The evolution of manufacturing system from production flow analysis to virtual manufacturing system has been occurred. Production flow analysis was developed by Burbidge. The previous demand was stable but now it has been changed to unstable and dynamic in nature. The continuous change in demand forced to change the manufacturing system employed. Thereafter group technology and cellular manufacturing system came in existence. These systems also have their own limitations. Researchers have proposed various models to optimize the cellular manufacturing system. Various authors have also addressed the limitations and improvements in the cellular manufacturing system. This may include under-utilization of machines and high setup time. Virtual cellular manufacturing can be effectively executed to meet the challenges from the change of location of machine cell. Different researchers have proposed different models to form virtual cell. Extensive work on designing of cellular manufacturing system have been undertaken for minimizing mean flow time

of parts and also maximizing the production. This has been done for different conditions. The simulation tools were also used in simulating potential cellular designs before making the decisions for selection. Economic justification and managerial issues were also addressed in group forming of part and machine cells. Various techniques and methodologies have been designed and developed by researchers for various functional areas of CMS and VCMS. But it is felt that most of the studies were being concentrated upon the clustering of the machines into machine cells and parts into part families with various techniques.

4 Conclusion

After going through the systematic review of the work done in the development of virtual manufacturing system, design may be done in various methods. These methods may include machine-component group analysis, genetic algorithm based approach, fuzzy clustering approach, graph partitioning approach and artificial intelligence approach. Virtual cellular manufacturing builds on the notion that a manufacturing system should have a physical and a logical design. Virtual manufacturing system in industry is implemented to decrease setup time, decrease in work in advance, decrease in lead time, improve in quality that can be accomplished by execution of CMS. VCMS is executed without physically revamping existing manufacturing formats. Therefore, VCMS can be actualized to fulfill the changed needs of clients with no cost of manufacturing plant design change. Some arrangement can be utilized for planning the groups of parts with a specific end goal to effectively actualize VCMS. It has been observed that less work has been addressed in the area of combinational complexity of VCMS design problem. In any case, consolidating different research could fundamentally upgrade the quality and effectiveness of the system considered. The incorporation of observational investigation into either plan or operational examinations could upgrade the authenticity of the system, particularly as parameter ranges, informational indexes and asset types. Research on the development in manufacturing system and the development of efficient tools is going on to achieve good solutions in reasonable processing time.

References

1. Khilwani N, Ulutas B, Islier A, Tiwari M (2009) A methodology to design virtual cellular manufacturing systems. J Intell Manuf 22(4):533–544
2. Han W, Zhao J, Chen Y (2012) A virtual cellular manufacturing system design model based on axiomatic design theory. Appl Mech Mater 271–272:1478–1484
3. Hamedi H, Ismail N, Esmaeilian G, Ariffin M (2012) Virtual cellular manufacturing system based on resource element approach and analyzing its performance over different basic layouts. Int J Ind Eng Computations 3(2):265–276

4. Mak K, Lau J, Wang X (2005) A genetic scheduling methodology for virtual cellular manufacturing systems: an industrial application. Int J Prod Res 43:2423–2450
5. Long Q (2014) An agent-based distributed computational experiment framework for virtual supply chain network development. Expert Syst Appl 41(9):4094–4112
6. Aalaei A, Davoudpour H (2016) Revised multi-choice goal programming for incorporated dynamic virtual cellular manufacturing into supply chain management: a case study. Eng Appl Artif Intell 47:3–15
7. Mak K-L, Ma J, Su W (2010) Production scheduling for virtual cellular manufacturing systems with workforce constraints using a hybrid algorithm. In: 2010 sixth international conference on natural computation (ICNC 2010), pp 4445–4449
8. Sarker B, Li Z (2001) Job routing and operations scheduling: a network-based virtual cell formation approach. J Oper Res Soc 52:673–681
9. Kannan VR, Ghosh S (1996) Cellular manufacturing using virtual cells. Int J Oper Prod Manag 16(5):99–112
10. Zamani MR (2017) Dependency of capability-based virtual cellular manufacturing systems performance on basic layouts. Int J Eng Tech Res 7:183–189
11. Erenay B, Suer G, Huang J, Maddisetty S (2015) Comparison of layered cellular manufacturing system design approaches. Comput Ind Eng 85:346–358
12. Ko KC, Egbelu PJ (2003) Virtual cell formation. Int J Prod Res 41(11):2365–2389
13. Moodie CL, Drolet J, Ho YC, Warren GMH (1994) Cell design strategies for efficient material handling. In: Tanchoco JMA (ed) Material flow systems in manufacturing (Chap. 3). Chapman & Hall, New York, NY, pp 76–101
14. Subash Babu A, Nandurkar K, Thomas A (2000) Development of virtual cellular manufacturing systems for SMEs. Logistics Inf Manag 13(4):228–242
15. Mak KL, Ma J (2011) A novel hybrid algorithm for multi-period production scheduling of jobs in virtual cellular manufacturing systems. In: Proceedings of the World Congress on engineering WCE 2011, London, UK
16. Thomalla CS (2000) Formation of virtual cells in manufacturing systems. In: Proceedings of group technology/cellular manufacturing world symposium, San Juan, Puerto Rico, 13–16
17. Mak K, Wang X (2002) Production scheduling and cell formation for virtual cellular manufacturing systems. Int J Adv Manuf Technol 20:144–152
18. Slomp J, Chowdary BV, Suresh NC (2005) Design and operation of virtual manufacturing cells: a mathematical programming approach. Robot Comput Integr Manuf 21(3):273–288
19. Mahdavi I, Aalaei A, Paydar MM, Solimanpur M (2009) Production planning and cell formation in dynamic virtual cellular manufacturing systems with worker flexibility. In: IEEE proceedings—computational intelligence for modeling, control, and automation, pp 663–667

IoT Integration in Industry—A Literature Review

Bhavesh Chandrayan and Ravinder Kumar

Abstract The paper attempts to enlighten the managerial perspective of the Internet collaborative framework called as Internet of Things (IoT) which interlinks the fundamental concept of cyber computing to the available advanced manufacturing methods for an agile and truly wireless communication to carry out operations in the industrial sector. The correlation between developing a wireless domain framework to facilitate smart manufacturing is outlined in the paper with a channelized concentration on the latest innovation in the same pool along with the barriers and possible evolution of Supply Chain Management (SCM) in the future which will unite the manufacturing methods with a framework developed to facilitate the processes in real time along with a greater equipment control over the existing devices. The paper showcases the findings of various research authors in the field of IoT, and it propagates to the fundamentals of Industry Internet of Things (IIoT) and also collaborative manufacturing. The research also highlights the nature of the evolution and the vision for the future development of the IoT services which could seamlessly control the industrial operations with fluidity and minimum latency by integrating the elements of IoT into the elements of SCM.

Keywords IoT · Supply chain management · Cyber computing · Smart manufacturing · Industry Internet of Things (IIoT) · Industry 4.0

1 Introduction

In the recent years, the global competition in the manufacturing sector has put industries in great pressure to push out the products and services with respect to the market's fluctuating demand. The need for quicker transaction processes and better product life has accentuated the need for an integrated service which can facilitate the global variations with ease and minimal time loss. With the advancement of the applications of Internet, the concept of interlinking industrial services with it came

B. Chandrayan (✉) · R. Kumar
Amity University, Noida Campus, Noida, Uttar Pradesh 201303, India
e-mail: chandrayanbhavesh@gmail.com

H. Kumar and P. K. Jain (eds.), *Recent Advances in Mechanical Engineering*,
Lecture Notes in Mechanical Engineering,
https://doi.org/10.1007/978-981-15-1071-7_2

into light and since then, a lot of research has been done in the field to generate a framework to manage the global demands using Internet.

IoT is a wide and dense web of devices and appliances that are embedded with sensors, electronics and connectivity to the cloud computing, enabling them to transfer real-time data. The purpose of this interlinking is to evolve a mesh of information to transfer over the Internet which can control the devices and applications as per the user's control without being physically present near the device. This direct integration is proposed to optimize the time loss, improve efficiency and economic profits and to minimize physical interaction with the devices.

Utilization of this service to control and develop the manufacturing sector has been thought upon for a long time with research being done to achieve this level of agility with no loss in the productivity. This advancement has bought the Fourth Revolution in the industry closer, and hence, the name Industry 4.0. Various manufacturing equipment and processes are controlled remotely using IoT to adapt to the dynamic customer demands and for the continuous optimization of the ongoing processes with ease. All the manual configurations are expected to be automated under IIoT which is expected to benefit the industry and create a dense network of smart manufacturing processes. This proposed model where the Internet is integrated into the devices using software and sensors can actuate the desired changes in the physical world without manual intervention across the globe. This concept opens the gateway to vast applications of this integration along with critical barriers which can hinder the expected fluidity of the whole framework, the reason why researchers have been digging deep to identify the issues and target them for solutions.

To understand the cyber network connectivity and its influence on the industrial sector, multiple research articles are reviewed which will help generate a concise outlook to how successful this technology can inculcate the automation process in the industry. The research papers bring about a detailed analysis of the IoT as a part of the Industrial Revolution and helps generalize this concept with a peek into the future prospect of IIoT and automation.

The paper bifurcates the basic framework of IoT and SCM into four and eight elements, respectively, which can help educate the fundamental concept of integration of one of the pillars (i.e. IoT) of Industry 4.0 into SCM (Figs. 1 and 2).

2 Literature Review

The literature review narrows down various researches on the topic to 20 relevant and latest researches which could help assess the challenges, limitations, barriers and practices of the IoT implementation in SCM which could help channelize and construct an intricate review and conclusion to justify the aim of the research paper. The various researches incorporating all the important keywords related to the research topic are briefed below (in descending order of their publishing year).

Birkel and Hartmann [1]. The paper showcases detailed introduction to the risks and challenges associated with the integration of IoT in SCM and helps model a

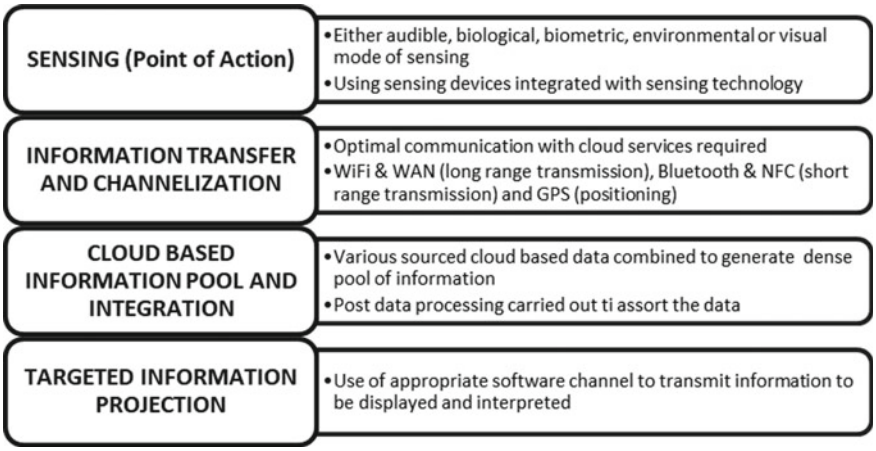

Fig. 1 Various elements of Information of Things (IoT)

holistic review framework for differentiating and understanding the literature incorporated so as to bring about the knowledge to practice and research on the deduced gaps.

Anandhi et al. [2]. The paper highlights the benefits of IoT integration SCM by using RFID tag tracking methodology to boost the real-time positioning and information pulse updates to avoid anti-counterfeiting by the application of cloud storage and Internet-based online information and data tracking architecture.

Tao et al. [3]. The paper reports the use of IIoT for smart manufacturing (SM). SM needs smart interconnection among the several attributes of manufacturing. This issue can be solved using IIoT; it compromises access hub (A-Hub), customized access module (CA-Module) and local service pool (LSP).

Yang et al. [4]. In this era of globalization, competitions are growing worldwide, and the need of customized products is increasing. To acknowledge this type of challenges, and to meet the customer demand, it requires new technologies. The paper talks to transform manufacturing sector using IoT which has an enormous potential connecting all the resources required for the production, based highly on integrated smart cyber-physical system (CPS).

Abdel-Basset et al. [5]. The literature demonstrates and suggests the construction of an intelligent and smart framework for SCM by applying IoT in the various steps of supply chain processes so as to collaborate big information data, products, process tracking, etc., which could upscale the infrastructure towards smart and efficient tradition.

Chamekh et al. [6]. The paper proposes a secured framework for information sharing and data tracking in the SCM by using Merkel tree architecture which claims to replace the peer-to-peer bases information transfer with additional security and scalable management scheme.

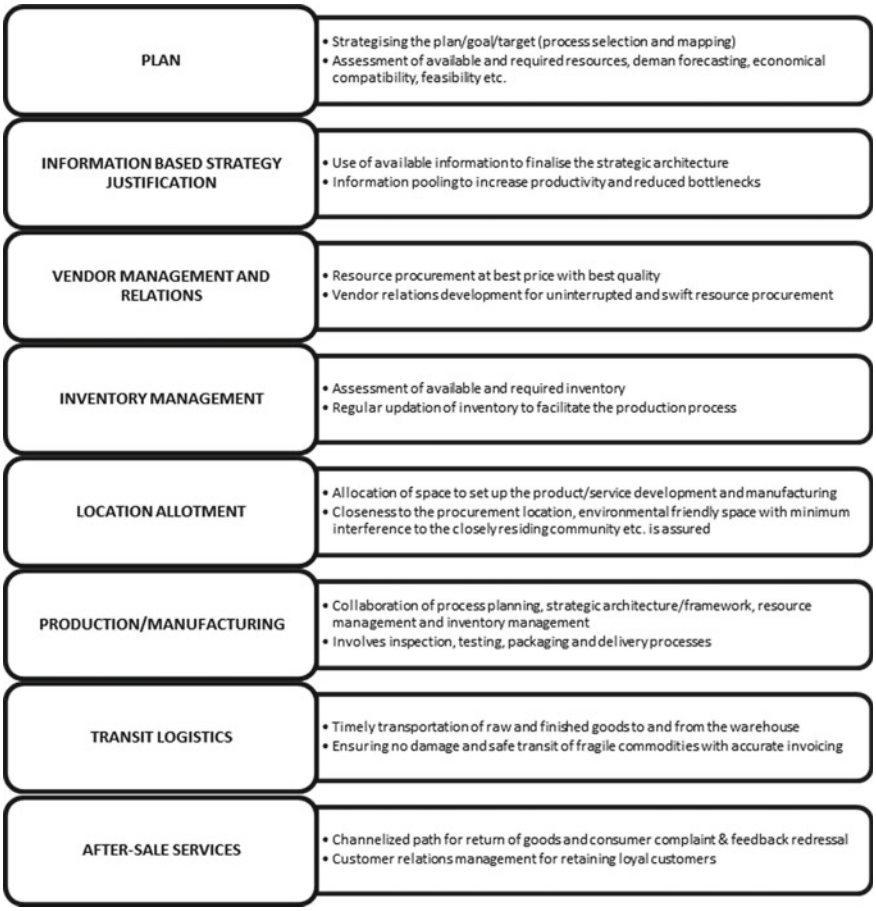

Fig. 2 Various elements of Supply Chain Management (SCM)

Wollschlaeger et al. [7]. This paper focuses on the industrial automation, with introduction of IoT, CPS and discusses the evaluation of industrial communication. And also, review is done on the effect of implementation of IoT and CPS on industrial automation with relation to Industry 4.0.

Lade et al. [8]. This article is the case study executed at one of the Bosch's large-scale manufacturing facilities to analyse the manufacturing and IoT. This paper reports the view on the future development of the IoT.

Chen [9]. Introduction of IoT was first carried out by Kelvin Ashton in 1999 to manage supply chain at Oil of Olay. This paper highlights the IoT devices and their application with limitation along with the assessment of the successful potential of the technology in future with respect to privacy and security.

Ben-Daya et al. [10]. The paper presents a bibliometric analysis while exploring the impacts and enablers for IoT in the processes of SCM to determine the limiting

factors or barriers which hinder the narrowing of research gap while suggesting solutions to future scope of study.

Haddud et al. [11]. The paper describes and aims to identify all possible challenges and limitations of the implication of IoT in SCM in an organization along with the literature-based benefits by conducting an online survey among academic sector researchers. The paper provides knowledge regarding the barriers to the implementation and significantly ranks them to assess the priority and criticality.

Caputo et al. [12]. This paper presents the theoretical discussion and analysis of IoT with its element from managerial point of view and trying to develop the dynamic conceptual framework, integrating the concept from the innovation and management, for manufacturing industries. This developed framework is applied in the case of additive manufacturing.

Bi et al. [13]. Important application of IoT is WSNs technology, a modelling and simulation approach for complete design process of WSN. Next generation manufacturing can be well supported by IoT infrastructure. It provides sophisticated channel to share data among manufacturing resources at anytime, anywhere.

Lu and Cecil [14]. This paper highlights the combined framework which gives a foundation for advance manufacturing domains and CPS. The architectural design of this framework is based on cloud computing and on focus of fairly recent initiatives in Europe, the USA and many other countries.

Bi et al. [15] Manufacturing enterprises operation and design require several different levels of decision making, and hence, the IT infrastructure for data acquisition and sharing has an impact on the performance of the enterprise in a broader sense. The paper objectifies at finding out the impact and correlation of the evolving IoT on the enterprises aiming towards modern manufacturing methods.

Tao et al. [16]. In pursuit of accomplishment of intelligent perception and various manufacturing resources, the investigation of IoT technologies in CMFG is being showcased in the paper.

Butala et al. [17]. This paper discusses a case study for the application of the IoT into the manufacturing sector. The paper outlines the IoT, its role in manufacturing and new possibilities which it will access for distributed manufacturing systems—i.e. employment of localized resources for the development of product and production via manufacturing systems.

Dutton [18]. The Internet is playing a significant role for social and economic development in the UK and worldwide. This paper provides a new vision for IoT, which will help to connect number of objects—'things' like sensors, monitors and RFID devices—to the Internet, and also it has social and economic implication which need to short-out.

Houyou et al. [19]. The paper elaborates the probable potential effect of the IoT methodologies and architecture infrastructure on the automation of the factory. Facilitation of reconfiguration in the proposed way serves as an enabler for flexible and agile manufacturing, similar to Lemgo Model Factory in this case. The delineation resulting in a reverse engineering approach facilitates the IoT focussed architecture in terms of working and component involved.

Liu et al. [20]. After Web 2.0, cloud computing and IoT are the new revolutions that are popular among the industrialists. The incubation of cloud manufacturing under the presence of cloud computing and IoT proves to be a paradigm shift in the manufacturing sector. Utilization and sharing of manufacturing resources are made flexible and effective with the use of cloud manufacturing as the latest mythology to organize activities associated to manufacturing.

3 Conclusion and Future Prospects

The paper collaborates the detailed explanations and scientific researchers from various authors to limelight the uses of IoT in the manufacturing sector, keeping in mind the limitations and ways to tackle the limitations. The penetration of Internet in the manufacturing and service sector has facilitated a smooth flow of work with seamless synchronization with the concerned devices and machines leading to a dense intricate network of devices interconnected and ready to be used in a click. The availability of wireless connectivity promotes this cloud-based technology to survive and develops into a productive tool to control electronic devices and with time and proper management can be used to configure the whole plant using a single smart screen.

It was clearly concluded that this cloud service can be put to maximum benefit if the mechanized devices can be automated to interlink them. The automation is the probable cause of slow development as machines require complex and delicate sensors to achieve wireless information transfer, and if this challenge can be tackled and implemented, the utilization of IoT can be optimized with ease.

The literature review also clarifies the difference in the theoretical conclusion of the various researches which identity the integration as a beneficial step for the organization yet the failed practical outlook which is due to various barriers affecting the overall management style of the supply chain. Each element or pillar of Industry 4.0 can be integrated to the supply chain with positive outcome provided the constricting factors or boundary conditions of the organizational management style is not conflicted, which would be a fair solution to maximize the technological advantage of the overhauling. Due to the dynamic organizational goals and prospects, variety of hindrances in the implementation causes the slow growth and limited benefits for this type of management automation.

The future research can be focused on deeper integration of this technology with artificial intelligence collaboration to fully automate the manufacturing sector with minimum human interaction which could boost the production rate and highly minimize the human error and factory waste. IIoT can influence the CPS to achieve remote device access over the globe which can remove the human proximity constraints by providing the resources to operate the device over the Internet. A strategic architecture is proposed which can simplify the elemental integration of IoT in the SCM to bring it closer to an ideal model for various industries (Fig. 3).

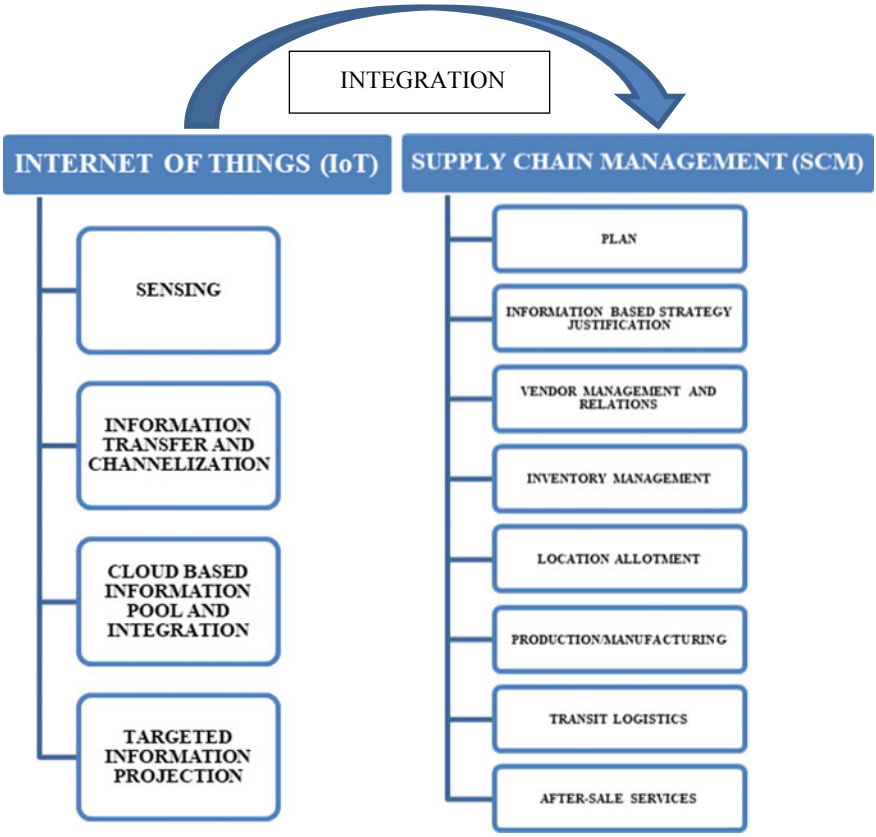

Fig. 3 IoT integration architecture for enhanced supply chain management

The effective integration of IoT in SCM can ensure the primary requirement of a successful manufacturing domain, i.e. ensuring the balance between demand and supply with agility and dynamic response to consumer's feedback and requirements. A step by step integration can help eliminate the elements of distress, and hence, boost the SCM in the long run. The framework suggests deeper study regarding the integration of individual elements of IoT and SCM to improve efficiency of SCM which could facilitate the transformation of Industry 3.0 to 4.0.

4 Research Gap

After compiling the literature review of various research papers, conference proceedings and published articles, it is clear to conclude that the implementation of IoT in the SCM has a noticeable differentiation in terms of real scenario practical demonstration of the proposed benefits to that of the theorized and study-based outcomes.

The three main factors of these barriers are domain based on technology, finances and politics, in terms of their area of hindrance and need more case studies to find solutions to them. The lack of case studies leaves this research topic with great scope of investigation and solution to the proposed issues with the implementation.

Developing nations find a great deal of issues with this implementation due to lack of technology, connectivity, cloud access, economic instability and inability to invest in a robust management which could aid the implementation and reap the benefits, rather an old traditional practice is more often noticed due to the lack of knowledge of the proposed architecture discussed in this paper, and hence, the research gap in terms of chronological advances in practice and automation is not recorded or presented. This calls for all research scholars to include their researches on this pillar of Industry 4.0 which can revolutionize the industrial sector globally.

References

1. Birkel HS, Hartmann E (2019) Impact of IoT challenges and risks for SCM. Supply Chain Manag Int J
2. Anandhi S, Anitha R, Sureshkumar V (2019) IoT enabled RFID authentication and secure object tracking system for smart logistics. Wirel Pers Commun 104(2)
3. Tao F, Cheng J, Qi Q (2018) IIHub: an industrial Internet-of-Things hub toward smart manufacturing based on cyber-physical system. IEEE Trans Ind Inform 14(5):2271–2280
4. Yang C, Shen W, Wang X (2018) The Internet of Things in manufacturing: key issues and potential applications. IEEE Syst Man cybern Mag 4(1):6–15
5. Abdel-Basset M, Manogaran G, Mohamed M (2018) Internet of Things (IoT) and its impact on supply chain: A framework for building smart, secure and efficient systems. Future Gener Comput Syst
6. Chamekh M, Hamdi M, El AS, Kim TH (2018) Secured distributed IoT based supply chain architecture. In: 2018 IEEE 27th international conference on enabling technologies: infrastructure for collaborative enterprises (WETICE), IEEE, pp 199–202
7. Wollschlaeger M, Sauter T, Jasperneite J (2017) The future of industrial communication: automation networks in the era of the internet of things and industry 4.0. IEEE Indus Electron Mag 11(1):17–27
8. Lade P, Ghosh R, Srinivasan S (2017) Manufacturing analytics and industrial Internet of Things. IEEE Intell Syst 32(3):74–79
9. Chen ET (2017) The Internet of Things: opportunities, issues, and challenges. Internet Things Mod Business Environ, 167–187
10. Ben-Daya M, Hassini E, Bahroun Z (2017) Internet of Things and supply chain management: a literature review. Int J Prod Res, 1–24
11. Haddud A, DeSouza A, Khare A, Lee H (2017) Examining potential benefits and challenges associated with the Internet of Things integration in supply chains. J Manuf Technol Manag 28(8):1055–1085
12. Caputo A, Marzi G, Pellegrini MM (2016) The Internet of Things in manufacturing innovation processes: development and application of a conceptual framework. Business Process Manag J 22(2):383–402
13. Bi Z, Wang G, Xu LD (2016) A visualization platform for Internet of Things in manufacturing applications. Internet Res 26(2):377–401
14. Lu Y, Cecil J (2016) An Internet of Things (IoT)-based collaborative framework for advanced manufacturing. Int J Adv Manuf Technol 84(5–8):1141–1152

15. Bi Z, Xu LD, Wang C (2014) Internet of Things for enterprise systems of modern manufacturing. IEEE Trans Ind Inf 10(2):1537–1546
16. Tao F, Zuo Y, Xu LD, Zhang L (2014) IoT-based intelligent perception and access of manufacturing resource toward cloud manufacturing. IEEE Trans Ind Inform 10(2):1547–1557
17. Butala P, Vrabič R, Oosthuizen G (2013) Distributed manufacturing systems and the internet of things: a case study
18. Dutton WH (2013) The Internet of Things
19. Houyou AM, Huth HP, Kloukinas C, Trsek H, Rotondi D (2012) Agile manufacturing: general challenges and an IoT@ work perspective. In: IEEE 17th conference on emerging technologies and factory automation (ETFA), IEEE, pp 1–7
20. Liu Q, Gao L, Lou P (2011) Resource management based on multi-agent technology for cloud manufacturing. In: International conference on electronics, communications an (ICECC), IEEE, pp 2821–2824

Defect Reduction in Manufacturing Industry Using Lean Six Sigma Approach

Narottam, K. Mathiyazhagan and Vikas Sharma

Abstract In today's competitive environment, customer's requirement is zero defect. This threatens each supplier to reduce nonconformance, maintain market share, and improve profitability. This paper aims to deploy the Lean Six Sigma methodology for reducing defects and improving profitability and bottom-line results of an automotive glass manufacturing industry. Lean Six Sigma methodology is widely used in industries as compared to other management practices and process improvement approaches. It is a data-driven, fact-based philosophy which improves quality and reduces variation in the process with the help of statistics. It also helps to find out the root causes of quality issues and controlling the process parameters. The define–measure–analyze–improve–control (DMAIC) approach used to reduce the defects in the glass bending process by optimizing the process parameters and finding the root cause of the problem. The process yield increased to 99.10 from 97.33% in six months by using this approach. This study begins with the identification of causes through cause and effect diagram (C and E diagram) and root cause analysis of defective products. This objective of this paper is to present a solution development methodology for improving the process in an automotive glass manufacturing industry in India by using the Lean Six Sigma approach.

Keywords Case study · Glass manufacturing · Defect reduction · Lean Six Sigma

Narottam · V. Sharma
The NorthCap University, Sec 23A, Gurugram, Haryana, India
e-mail: narottam428@gmail.com

V. Sharma
e-mail: vikassharma@ncuindia.edu

K. Mathiyazhagan (✉)
Mechanical Engineering, Amity School of Engineering & Technology, Amity University, Sec 125, Noida, UP, India
e-mail: kmathiyazhagan@amity.edu

H. Kumar and P. K. Jain (eds.), *Recent Advances in Mechanical Engineering*,
Lecture Notes in Mechanical Engineering,
https://doi.org/10.1007/978-981-15-1071-7_3

1 Introduction

This paper presents a case study in a glass manufacturing industry for defect reduction in India. The increase in demand from different customers and the quality concerns on customer line are the major changes happening on a daily basis. Different quality improvement initiatives and cycle time reduction activities happened to increase good pieces. Capacity planning and demand forecasting suggest adding new production lines at the factory. The number of defects on the shop floor is not well controlled, especially in the new production line. One has carried out preventive measures to prevent the occurrence of defects such as checking the process parameters, raw material quality, and man management at the end of the production line.

Usually, for the automotive industry, the policy is conducted with the development of staff, reduces non value added activities, fast response to meet customers' requirements and to give timely feedback, optimizing process parameters, and better waste management. It is considered that the LSS methodology is used to improve the quality, profitability and reduces waste. Customer satisfaction and zero defect are the concerning points of every customer. The organizations have to improve and sustain quality to keep customers because now, they are the key elements to drive the economy. Different methodologies, techniques, and tools may be used to maintain a good quality level and help in continuous improvement in the company [11].

Six Sigma is defined as "a strategic initiative to increase market share, profitability, and customer satisfaction through statistical tools and techniques that lead to breakthrough improvement in quality" [6]. Statistical measurement, management strategy, and quality culture are three paradigms of management. Lean Six Sigma methodology consists of two approaches: define–measure–analyze–improve–control (DMAIC) and define–measure–analyze–design–verify (DMADV). Define–measure–analyze–improve–control (DMAIC) is used in the existing process for improvement. Each phase of the methodology is interlinked to find the root cause of the problem. DMADV is used to find the potential of the new or existing process. The process improvement focuses on measuring, analyzing, and improving the process. It includes improving quality, reducing wastes, and sustaining the improvements attained in the process.

This present study was developed in a glass manufacturing company in India. The main objective of the study was to improve the process yield by reducing the defect in the process. There are a few papers available in the literature related to a case study in the glass manufacturing industry. The purpose of the study is to apply Lean Six Sigma in an automotive glass manufacturing process to reduce defects and variation in the process.

2 Literature Review

LSS is essential for the Indian industry as the customer demand is zero defect. It is a philosophy and business strategy based on data and facts. It improves profitability and market share. It consists of two methodologies for the organization perspective. The DMAIC is used to improve the existing processes. DMAIC identifies the major steps within the methodology namely define, measure, analyze, improve, control. LSS can be successfully applied in the healthcare sector, thermal power plants, transactional services, retail industry, and manufacturing sector [5, 8, 9, 10]. The design for Six Sigma (DFSS) is used for designing a new process or product or when the existing processes are not able to achieve desired metrics such as profitability, customer satisfaction, defects [2]. DFSS methodology consists of five phases, i.e., define, measure, analyze, design, and verify (DMADV) [3]. DFSS consists of an approach to optimize new products from the design stage and processes at an optimum cost and easy to implement. DFSS is used to designing new processes to minimize variation and improving performance [4] to improve bottom-line results [1, 7]. DFSS strongly derive customer needs into products or processes. It is more focused and integrated on the design of the product or product development process. Lean Six Sigma (DMAIC) and new product development (DFSS) are more beneficial in improving bottom-line results.

Sharma et al. applied LSS in an automobile component manufacturing industry and to improve sigma value from 2.67 sigma to 4.11 sigma with a gain of 12% in the process yield. Meena et al. applied the LSS methodology in a pump manufacturing process and to reduce 76.4% of waste from the process. It improves the production process and saves 39lakh Indian rupees per annum from the assembly process.

3 Problem Description

This Lean Six Sigma case study applied in an automotive glass manufacturing industry whose process yield of model A was 97.33% against the target of 99.10% for the bending process of laminated windshield glass of the car. This process consists of different subprocesses in the bending of the glass. When we analyzed the contribution of the process, distortion(SDS), breakage, and slip have a major contribution to the rejection percentage.

3.1 Define Phase

In the define phase, problem statement, project scope, project goal, and timeline of the completion must be undertaken. The purpose is to prepare SIPOC analysis, customer requirements, and the flow chart of the process. The project team is decided

including black belt, production supervisor, quality supervisor, and the maintenance person.

3.1.1 Problem Statement

The average yield of model A from June 16 to August 16 was 97.33% against the target of 99.10%. Bending process is a major contributor and having 1.85% rejection. Defects include in the Pareto chart are spot distortion, breakage, and slippage. Spot distortion contributes 0.57%, breakage 0.54%, slippage 0.22% of overall rejection.

Historical Pareto of bending defects is shown in Fig. 1. Spot distortion on the glass has a maximum contribution but due to the dusty environment and different make of glass, chances of defect on glass increases. We can reduce it to a certain limit, but we cannot eliminate it. Breakage of glass occurs during loading or unloading from the mold and during the heating process.

Figure 2 having a process flow of the bending process. Cut glass is received from preprocessing in the form of inner and outer glass. Outer glass is 1 mm wider than inner glass. After print on the inner glass, pairing of glass takes place by interleaving powder in between two glasses. Pair of glass loading on the mold as per the customer specification. Inspection of glass takes place for appearance defects and functional defects as per customer requirement and dispatch to the customer.

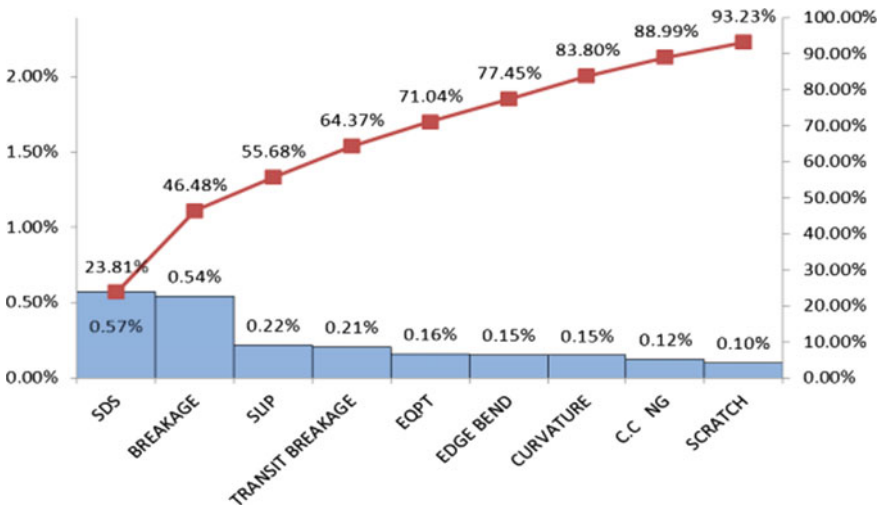

Fig. 1 Pareto chart of the bending process of side-door glass (June 16 to August 16)

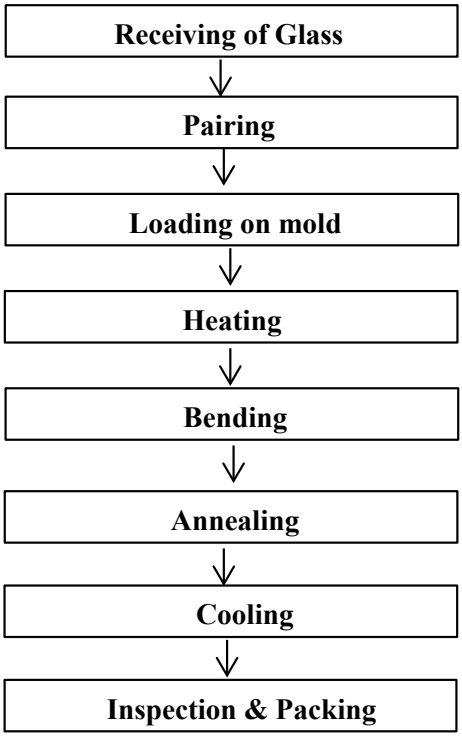

Fig. 2 Process flow diagram of bending of laminated glass

3.2 Measure Phase

In the second phase of DMAIC, we collect data for measuring the process performance. Data collection plan was drafted to measure the performance of the bending process parameters. We have collected 5400 glasses data in the controlled condition to measure the first time yield and rolled throughput yield. Process capability of end temperature is shown in Fig. 3. It is measured regarding the capability index (Cp). The purpose of this index is to measure whether the process parameters can meet the customer specification or requirements.

3.3 Analyze Phase

In the analyze phase, root cause analysis done through C and E diagram and failure mode and effect analysis (FMEA). C and E diagram for breakage of the glass is shown in Fig. 4. First, all the possible causes collected by the team members and then the nominal group technique used to select the potential causes of breakage.

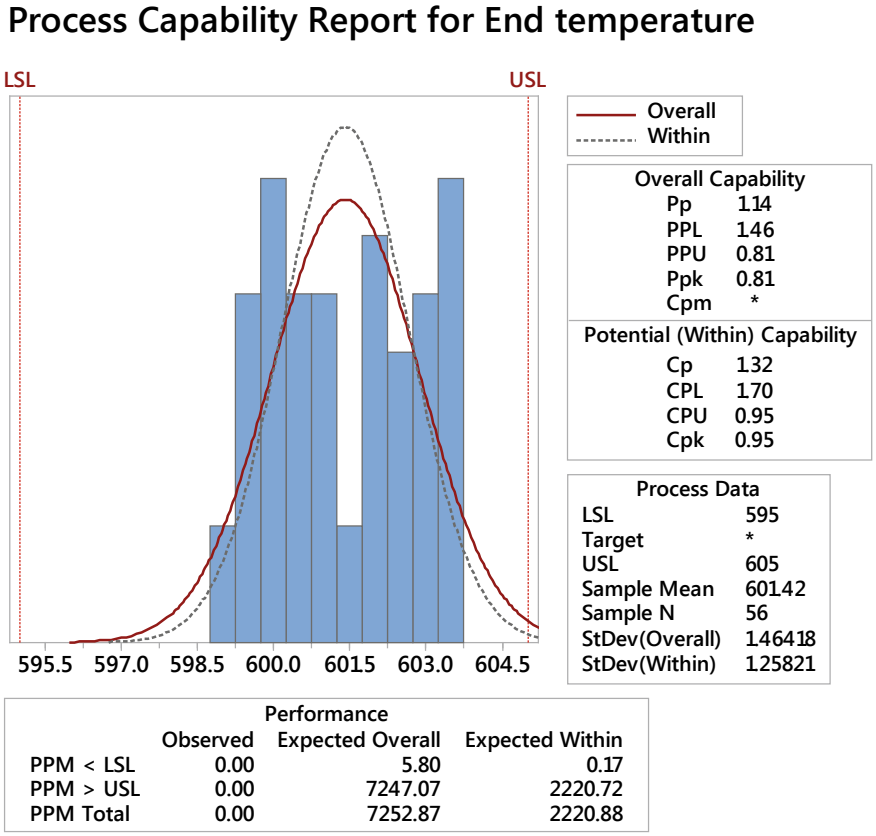

Fig. 3 Process capability of end temperature of glass during bending

Mold cloth torn off, mold condition NG, grinding chips in glass, and less powdering are the probable causes for breakage.

Validation of causes done to find the root causes and trails taken after rectification. Similarly, the cause and effect diagram made for spot distortion and slippage of glass to find the root causes. For slippage of glass, one cause found potential, i.e., jerk during wagon movement through the heating zones. After the solution development, the position of the carbon stopper changed from top to the bottom of the mold ring. Three potential causes found for spot distortion in the glass. These are glass dusty, make mix and imbalance of ceiling and floor heating condition. Hypothesis testing used to select potential causes and solution development.

In one proportion test shown in Fig. 5, of all mold condition verification before job change for breakage on the bending process, found significant as the P-value is less than 0.05. Similarly, one proportion test is done for carbon stopper position change to reduce slippage of glass and heating condition modification to reduce spot distortion. These factors found significant for the changes and the trial was successful.

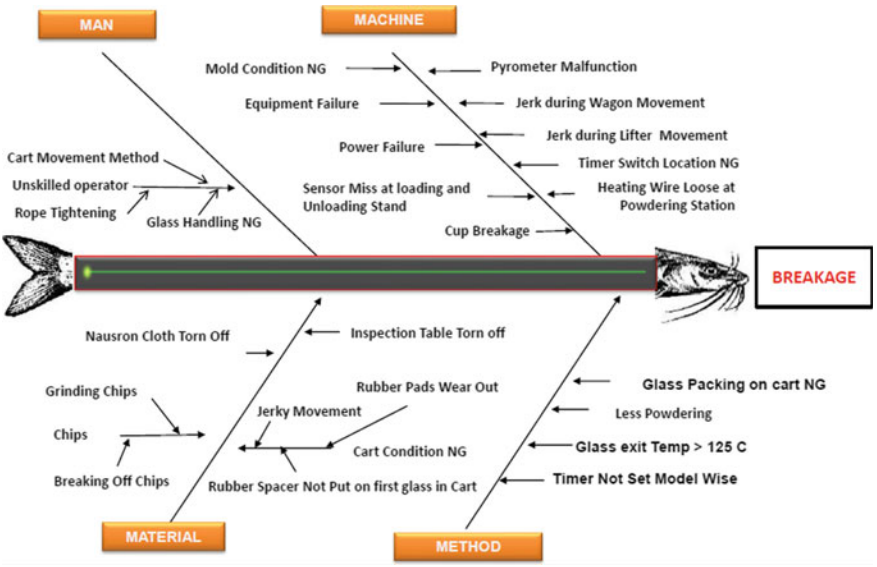

Fig. 4 Cause and effect diagram for breakage of the glass

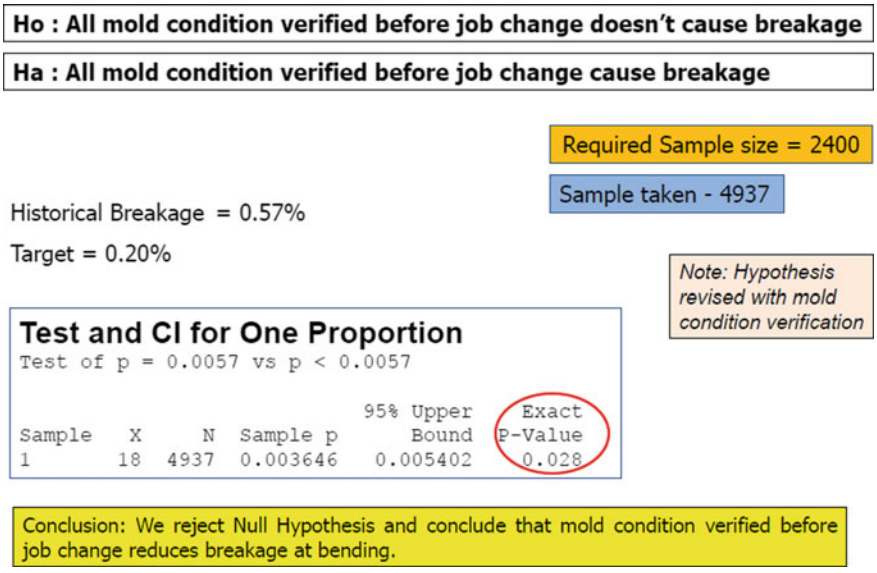

Fig. 5 Hypothesis testing for breakage of glass

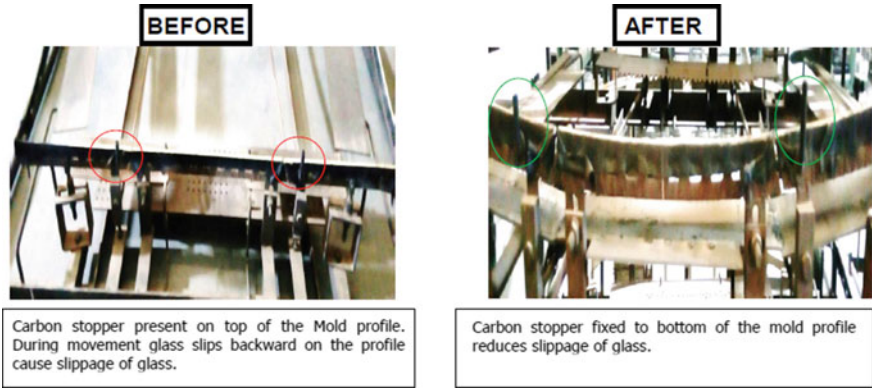

Fig. 6 Kaizen for carbon stopper modification to slippage of the glass

3.4 Improve Phase

In improve phase of DMAIC, based on proposed improvements, different kaizens were planned for causes and trial taken after the modification and found successful (Fig. 6).

Process capability of end temperature collected after the heating condition optimization and found value of Cp greater than 1.33. It shows that the bending process is capable of meeting customer requirements and specifications.

Process yield also improved from 97.33 to 90.05% and the defect-reduced as per target is taken in the define phase.

3.5 Control Phase

In the control phase, control chart is used to verify the process control and quality control parameters. It is more focused on the needs and requirements of the customers. In the bending process, zone-wise temperature monitored to control the process specification within required limits. X-bar and R chart are shown in Fig. 7 for overall zone temperature against the specification limits. A control plan also developed to monitor the process parameters, and it should be exactly defined to the supervisors. If any nonconformance is observed, information regarding needed action also added to the control plan (Fig. 8).

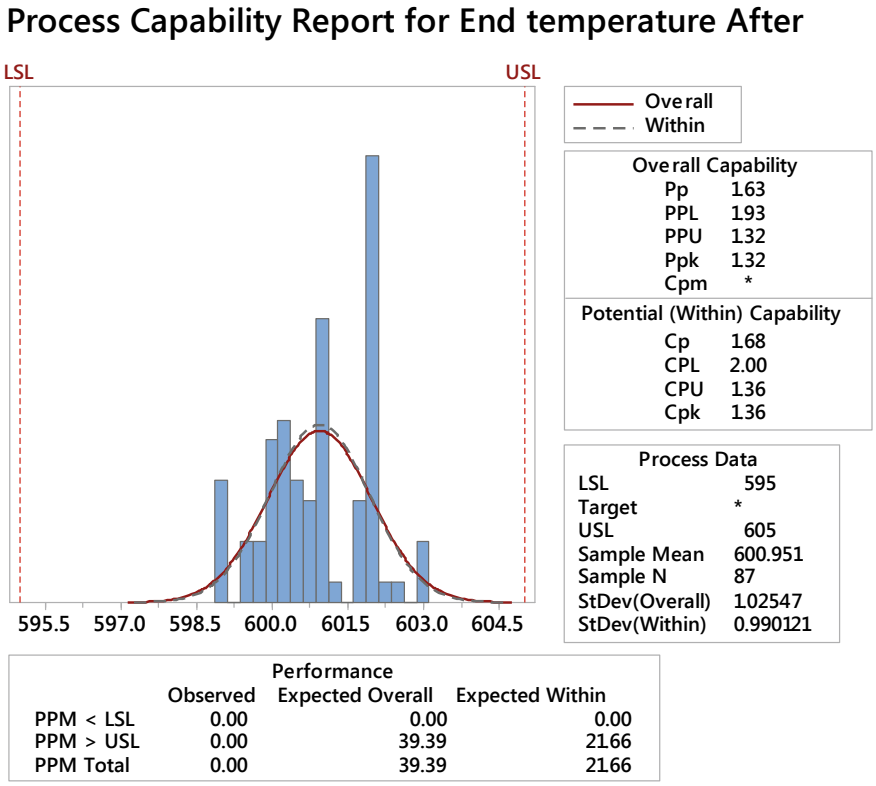

Fig. 7 Process capability after the modification in heating zone temperature

4 Results and Discussions

In the define phase, supplier, input, process, output, and customers (SIPOC), problem statement, Pareto chart, and graphs are used. In the measure phase, process capability, input–output sheet, a process flow diagram, and flow cart are used. In analyze phase C and E diagram, nominal group technique, FMEA, statistical testing, and Pareto chart are used. In the improve phase, the design of experiments, bar chart, kaizen, and regression are used. In the control phase, the control chart and control plan are used to complete the project. Lean Six Sigma played a decisive role in the achievement of the targets and ensuring that there is a disciplined approach to the issues through the DMAIC cycle.

Lean Six Sigma is getting popular in Indian industries and other organizations. In this study, bending yield improved from 97.33 to 99.10% by reducing the defects and variation in the process. It was achieved through the Lean Six Sigma methodology, as well as its associated tools.

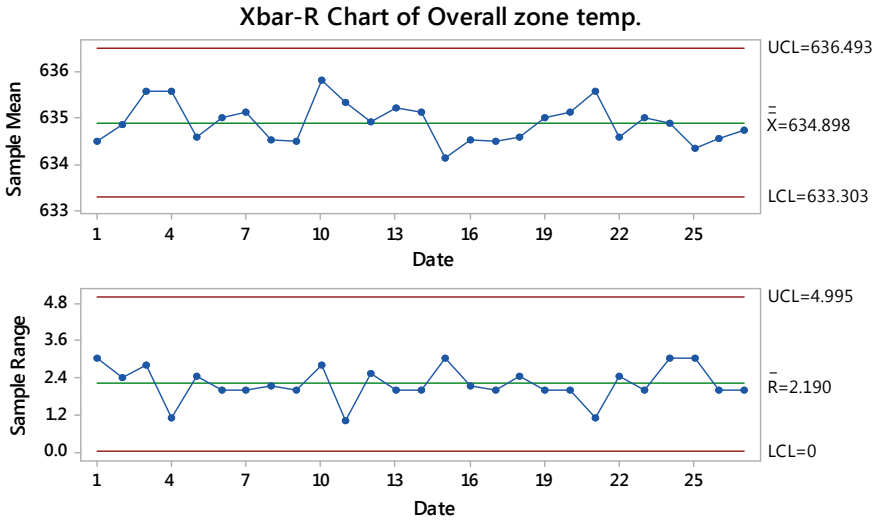

Fig. 8 X-bar and R chart for overall zone temperature of the bending process

The action implemented contributed to a significant reduction in spot distortion from 0.58 to 0.32%, breakage from 0.55 to 0.13%, and slippage from 0.22 to 0.07% in the project duration of six months.

The results achieved are shown in Fig. 9 in the form of bar graphs. This reduced the cost of poor quality (COPQ) and improved the efficiency of the resources. It improves productivity and reduction in rework percentage. DMAIC approach shows that the performance of the company increased leads to customer satisfaction and the target of zero defect. Process capability improves from 0.84 to 1.36 and also helps in better control of process parameters.

5 Conclusions and Recommendation

This case study provided an approach of prioritizing process improvement project in manufacturing industries through LSS methodology. This paper is the first attempt in glass manufacturing industries in India. Results from the case study showed that the LSS methodology used in manufacturing industries for defect reduction and process improvement. Teamwork and management commitment are critical factors for the successful implementation of any improvement activity. The proposed approach can be implemented in different industrial backgrounds and a variety of processes and products.

Top management guiding principles and leadership are the critical success factors along with middle management commitment and dedication. These factors result in faster completion of the project with good financial results and learning of team

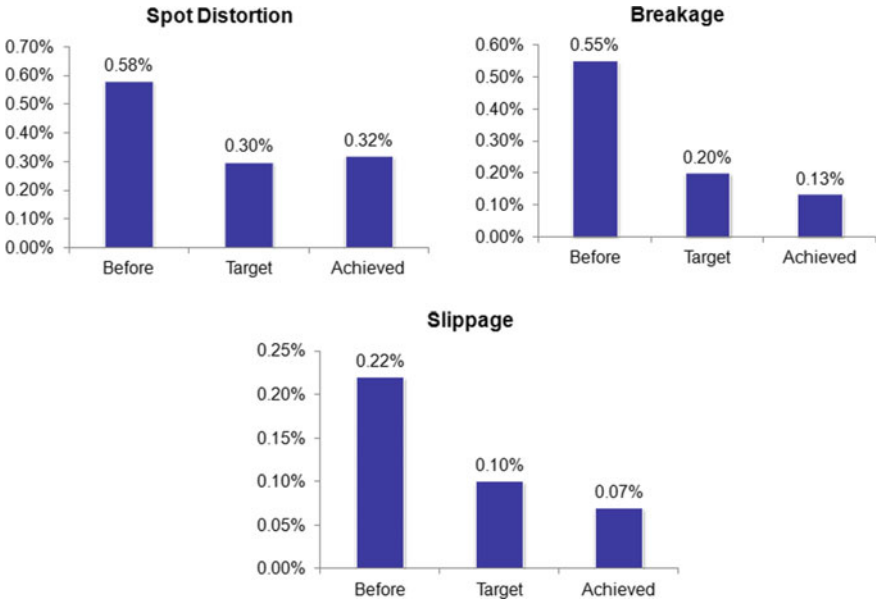

Fig. 9 Defect-wise target and achieved results

members. This case study can be horizontally deployed in other processes or plants throughout the location.

6 Implications

LSS projects can be effectively implemented by dedication, recognition, and process communication from a selection of the project to the achievement. The tools and techniques used in this study were used in a glass manufacturing process.

References

1. Aboelmaged MG (2010) Six Sigma quality: a structured review and implications for future research. Int J Qual Reliab Manag 27(3):268–317
2. Andersson R et al (2006) Similarities and differences between TQM, Six Sigma and Lean. TQM Mag 18(3):282–296
3. Banuelas R, Antony J (2003) Going from Six Sigma to design for Six Sigma: an exploratory study using analytic hierarchy process. TQM Mag 15(5):334–344
4. Chung et al (2008) An empirical study on the correlation between critical DFSS success factors, DFSS implementation activity levels and business competitive advantages in Taiwan's high-tech manufacturers. Total Qual Manag Bus Excell 19(6):595–607
5. Dreachslin J, Lee P (2007) Applying Six Sigma and DMAIC to diversity initiatives. J Healthc Manag 52(6):361–367

6. Harry MJ (1998) Six Sigma: a breakthrough strategy for profitability. Qual Prog 31(5):60–64
7. Johnson J et al (2006) Designing new housing at the University of Miami: a 'Six Sigma' DMADV/DFSS case study. Qual Eng 18(3):299–323
8. Kaushik P et al (2008) A Case study application of Six Sigma methodology in a small and medium-sized manufacturing enterprise. TQM J 24(1):4–16
9. Kumar UD et al (2008) On the optimal selection of process alternatives in a Six Sigma implementation. Int J Produc Econ 111(2):456–467
10. Tong J, Tsung F, Yen B (2004) A DMAIC approach to printed circuit board quality improvement. Int J Adv Manuf Technol 23(7–8):523–531
11. Zu X et al (2008) The evolving theory of quality management : the role of Six Sigma. J Oper Manag 26(5):630–650

Modeling the Interrelationship of Critical Success Factors Adoption of Sustainable Lean Manufacturing Using DEMATEL Approach

Naveen Kumar and K. Mathiyazhagan

Abstract The aim of the study was to modeling the interrelation of critical success factors (CSFs) for sustainable lean manufacturing in Indian small and medium-scale enterprises. In the competitive era, small and medium-scale industries have partial resources and façade huge competition. Based on literature review, 10 critical success factors were extracted which suggested by experts. Same was followed by interviewing the ground leaders, and key managers have expertise in sustainable lean manufacturing. The decision-making trial and evaluation laboratory (DEMATEL) method was used to analyze the interrelationship of critical success factors for sustainable lean manufacturing adoption in Indian industries. CSFs' interrelationship has been identified and expended in industries through experts. This study proposes the key interrelationship of critical success factors to challenge obstacles in sustainable lean implementation in Indian industries. For sustainable lean manufacturing implementation, effectiveness, innovative technology usage, management review, agile manufacturing processes, teamwork, govt. regulations and follow-ups considered as critical success factors. Innovations are considered as input for sustainability and performance measured in economic, operational, environmental and CSR activities. Researcher focused on goal setting through bench marking in identical clusters. The findings may be helpful for industries' consultants and manager facing difficulties in implementing sustainable lean manufacturing in Indian industries. The study also suggests qualitative approach for improvement action to develop loss-making small and medium-scale enterprises in a reputed industry. This may help managers to prioritize resources allocation toward sustainability in process and organization's systems. The importance of presenting interrelationship of CSFs might helpful for new business practitioner to survive in competitive scenario.

N. Kumar
Department of Mechanical Engineering, The NorthCap University, Gurugram 122017, Haryana, India
e-mail: Naveenkumar42906@gmail.com

K. Mathiyazhagan (✉)
Department of Mechanical Engineering, Amity School of Engineering & Technology, Amity University, Sec 125, Noida 201313, Uttar Pradesh, India
e-mail: Kmathiyazhagan@amity.edu

H. Kumar and P. K. Jain (eds.), *Recent Advances in Mechanical Engineering*,
Lecture Notes in Mechanical Engineering,
https://doi.org/10.1007/978-981-15-1071-7_4

Keywords Benchmarking · Sustainable lean manufacturing · Innovation

1 Introduction

Small and medium-sized industries (SMEs) are contributing regularly to the Indian gross domestic product in Indian manufacturing sector. As it already stated that SMEs have a major role in the economic growth of any nation and equally participated in the green environment collectively [1]. Global pollution contributed around 70% by SMEs and accountable for more than 50% of industrialized contamination in the Asia-Pacific region. Whitehead clearly explained the examples of SMEs contribution to environmental damages and emissions. By energy-efficient measures' implementation, 30% of consumption could reduce which is more energy than Japan and Korea consumption per year. India's manufacturing output served 45% by SMEs contribution and created 40% employment of workforce available in India [2]. Today's concern in industries is wanted to be remaining sustainable throughout the product life cycle. In SMEs, sustainability could be achieved by the continuous review among all three aspects: economic, environment and social [3, 4]. Challenges in the SMEs business process from both demand and supply. On one side, original equipment manufacturers (OEMs) are very challenging in demand, and on another side, a number of competitors in the market feed them. In continuation of supply side, a number of regulations and procurement are difficult to complete. Hence, most of the SMEs focused on economic aspects only without showing interest in environmental and social aspects unless there is rigorous regulation from government and major cost-saving projects. Researchers also explained that social and environmental practices are leading by customers' needs and government regulations [5]. Now, sustainability has become a necessity for industries to move business growth in the current scenario just because of old manufacturing practices and regulation implemented by authorities. For meeting the demands of customers effectively, SMEs need to adopt various improvement techniques like sustainable manufacturing, innovative technology, benchmarking processes, flexible manufacturing systems, etc. In this study, ten CSFs have been considered from literature review as shown in Table 1.

It would be very interactive for both researchers and experts to get involved in various approached for implementing sustainable manufacturing systems. Individual SMEs have to identify their weak aspects and work continuously to get their sustainable model [20]. In addition to above, all three aspects (economic, environmental and social) need to consider across the end-to-end processes including supply chain partners to the ultimate customer. By implementing lean in through process, all wastes out from operations and effective cost benefits are shown in the system which motivates the SMEs to move toward the sustainable lean manufacturing [21]. Innovation needed in the newly designed process and product to get efficient output with minimum resources utilization.

Table 1 CSFs of SLM implementation in Indian SMEs

S. No.	Critical success factors adoption of SLM	References
1	Management review	Baumgartner [6], Aboelmaged [7], Sangwan et al. [8]
2	Teamwork	Lannelongue et al. [9], Taubitz [10], Vinodh et al. [11]
3	Govt. regulation follow-ups and reviews	Ghazilla et al. [5], Mittal and Sangwan [12]
4	Innovative technology adoption	Sangwan et al. [8], Dora et al. [13]
5	Flexible/agile manufacturing processes	Engert et al. [14]
6	Goal setting through benchmarking	Aboelmaged [7], Ghazilla et al. [5] [57]
7	Employee focus	Martínez-Jurado and Moyano-Fuentes [15]
8	IT system robustness	Sangwan et al. [8], Panizzolo et al. [16]
9	Machine conditions	Singh et al. [17], Rose et al. [18]
10	Prevention of pollution	Jabbour et al. [19]

Sustainability helps in growing business and manufacturing processes in a competitive era. In a literature review, sustainability directly relates to the environment, a social and economic subset of growth. Some researchers identified lean and green relation toward effective utilization of energy and reduction in pollution through waste optimization [22, 23]. Bergmiller and McCright [44] explained the positive relationship between lean and green operation with significant results. Today's SMEs (small and medium-sized enterprises) need to understand a product's life cycle considering base as increasing customer demands and global competition [24]. Sustainable manufacturing helps to achieve market share by improving the environmental efficiency of manufacturing SMEs, which need both technical and financial assistance.

Though lean is swiftly and attractive tool to reduce waste, companies may experience difficulties to sustain long-term success. Sustainable lean needs attention for performance improvement and capability development. Though still evolving the context to add theory and practice by relating developmental stages which help in lean capability development and sustainability, lean manufacturing (LM) is a decision-making method aimed at refining methods created on a difficult scheme of organized social and technical practices. Lean manufacturing practices are frequently used in growing industries and focusing on employee involvement techniques like small group activity, pieces of training, supplier development. The strategy for sustainability system will be driven by customer requirements and environmental conditions. Many researchers gave a lean model in which cost is given by customers, and as a manufacturer, we have to deliver a final product with respect to fit, form and function. In past decades, lot of research evolved for lean and sustainable manufacturing, but no

clear directions toward sustainability in manufacturing come across. Sustainability considering new manufacturing systems to understand the requirements of the manufacturing sector in large scale to identify bottlenecks and limitations. Management should focus on waste elimination, in the direction of profitability by lean implementation in their small-scale/medium-scale/large-scale organizations [25]. According to Ahmed et al. [42], inventory reduction, just in time, kanban, poka-yoke, helps to reduce cost occurred due to seven wastes. In human resource management practices, lean includes communication of objectives, employee training progress, kaizen and suggestions, relationship development, rewards and recognition, and employee safety and health [26]. Customers and suppliers linkage create a healthy working environment in plant and increase delivery success rate [43]. With reliable delivery, customer may adopt different supply chain activity like a focused factory, uniform workload and group technology. Flexible manufacturing needs to be driven by customer orders, to achieve market demand and increase production, in the journey of lean production [27]. Flexible manufacturing is an effective tool of lean manufacturing which affects total manufacturing cost and reduces market selling price [25].

2 Review Background

For sustainable growth that chances current desires without compromising the facility of the upcoming group toward encounter, current demand, innovation and social action should be aligned to escort further business practices. For sustainable operations, goal setting through benchmarking also focused on all aspects: pollution, economic growth and social equality [28, 29] on a long-term assignment. In surroundings, there are certain conditions; due to that, many human beings are not able to get adequate access to environmental services to maintain support to life cycle [30]. Sustainable lean manufacturing decides to create practices and techniques for converting raw material into finished goods by less use of resources like energy, manpower, toxic materials, emissions and defects [31]. Many industries are taking initiative by focusing on corporate social actions at operational level [28]. For sustainable process development, an interrelation between different areas with integration of business aspects is required [50]. Adoption of lean manufacturing creates synergy to support environmental management and improve environment performance [19]. An environment standard also helps to identify and reduce environment waste and focus on environment performance. Value stream mapping also maps the environmental waste as it covered complete supply chain from supplier to customer [11]. EMS mixing with lean manufacturing may lead growing industry and better subject understanding [32]. Jabbour et al. [19] explained that integration of lean and EMS

resulting in prevention of pollution and waste generation which directly impacts on cost [15].

It is important for an organization to produce more marginal profit value and contribute in social activities. Sustainable lean manufacturing concerns about the role of people, their development, efforts for solutions against their problems, rewarding for innovative ideas and rewarding them [15]. Researchers explained the key results of lean manufacturing implementation with social aspects like improved housekeeping, material handling, kaizen reduced several accidents, security risks and ergonomics [33]. Sustainable lean considers both worth and resource protection through initial pilots and salvos. Azevedo et al. [46] ruminate on lean reaction with expansive sustainability concerns further than being eco-friendly and considers a vice, supplier selection (top management interference), and supply chain issues come in front. We have to further explore barriers in sustainable lean manufacturing and how lean captures sustainability with confirmatory performance.

2.1 Review Result

There is a fundamental relation between lean and sustainable manufacturing. Industries that have lean manufacturing always upgrade toward sustainable manufacturing. Sustainable manufacturing is focus to reduce the wastes in the organization with the help of sustainable practices. Waste reduction is a common focus in both lean and sustainable manufacturing, in addition long-term focus on profit, people and planet. Tools used for sustainable lean manufacturing are SMED (single minute exchange of die), VSM (value stream mapping), TQM (total quality management), TPM (total productive maintenance) and continuous improvement through quality circles. Focus areas of sustainable lean manufacturing are resource utilization to get maximum output in natural conditions, clear progression plan for lean capabilities, team building among employees and workshops on lean culture. By acting on the above focus areas, industries may achieve actual growth with improved processes, improvement in manufacturing capacity and capabilities and reduce overall unit cost.

The reason for identifying interrelationship of critical success factors of sustainable lean manufacturing are:

– to develop an understanding of factors to produce more with fewer resources and
– meeting customer demand efficiently.

Stonebraker et al. [47] stated that an effective and sustainable supply chain helps in improving the performance of an organization. The operational strategy can change the normal environment into a sustainable one in organizations. Lean helps in building potential for organizations to develop and achieve actual growth, improving manufacturing capacity and capability and lowering unit cost.

3 Problem Description

SMEs have a major role in the growth of Indian economy from last one decade. There is drastic increment seen in the last six years. This makes additional opportunity to create jobs at various levels. According to CII reports, 80% growth in employment generated through small and medium-scale industries from rural and urban areas in India. SMEs have 8% of total contribution in the country's gross domestic product. Now, researchers have special attention toward Indian SMEs which are preparing for sustainable manufacturing processes [34–36]. It is difficult to find the relationship in CSFs of SLM implementation in SMEs. The listed critical success factors of SLM are tabulated in Table 1.

4 Determination Approach

The procedure for CSFs' interrelationship is started with researchers' findings for sustainable lean manufacturing in Indian industries and briefly explained in Sect. 2. From summary research, gap and problem identified for implement DEMATEL methodology. A workshop was conducted with experts and researchers working with Indian SMEs. After data collection, DEMATEL methodology derived and interrelationship identified. Then finally, results are discussed and conclusion is explained in the last step.

4.1 DEMATEL

The DEMATEL methodology used globally by many researchers and are interested to use the same to get solutions. It helps in capturing interrelationship strength and contextual relations between the critical success factors [37]. The methodology derived to identify cause and effect relations [51]. DEMATEL proposed by researchers to prioritize a portfolio of investment firm [38]. Researchers practice DEMATEL approach in automobiles industries to categorize indicators toward sustainable supply chain [49]. From the above research summary, we appreciate the DEMATEL and found

STEPS OF DEMATEL METHODOLOGY	1- Collect experts rating and execute average matrix Z
	2 -Initial direct relationship matrix D
	3- Derived total relation matrix T
	4-Determine the sum of matrix column and row of matrix T
	5-Set thresold value (a)
	6-Build a cause and effect relationship diagram
	Step 7-Is relationship diagram acceptable ? if yes; then casue and effect interrealtionship of factors, if no; then review step 5 again.

Fig. 1 Steps of DEMATEL approach for CSFs interrelationship (established from researchers' study [39, 40])

appropriate approach for evaluating interrelationship of listed CSFs. The various steps for DEMATEL method are shown in Fig. 1:

Step 1 (Initial Average matrix)—Through a paired comparison degree of effect calculated between two CSFs by experts' rating between (0 and 4) as shown in Table 2.
Step 2 (Initial Influence matrix)—Normalizing average matrix and get normalized initial direct- relation. As shown in Table 3.
Step 3 (Full direct/indirect matrix)—In this step, matrix T shows a interrelationship of CSFs and can transferred into visual display by diagraph mapping.
Step 4 (Total influence matrix T)—Total matrix T is completed and defined by $T = X(\mathrm{I} - X)^1$ where I is identical matrix. Respectively,

$$T = X + X^2 + \cdots + X^h = X(IX)^1$$

5 Results and Discussions

The results derived from DEMATEL study have been shown in Fig. 2. As relative vectors are listed in two different sets, i.e., cause set and effect set [41], four CSFs acquired in cause set are management review (P1), flexible/agile manufacturing processes (P5), goal setting through benchmarking (P6) and teamwork (P2).

Table 2 Average relationship matrix

Critical success factors	P1	P2	P3	P4	P5	P6	P7	P8	P9	P10
Management review (P1)	0	3	3	0	1	2	1	2	2	2
Teamwork (P2)	3	0	2	2	2	1	3	2	1	3
Govt. regulation follow-ups and reviews (P3)	1	1	0	1	3	2	2	1	0	2
Innovative technology adoption (P4)	2	2	3	0	3	3	3	3	3	0
Flexible/agile manufacturing processes (P5)	2	1	2	0	0	2	0	0	0	2
Goal setting through benchmarking (P6)	3	2	2	2	3	0	2	3	3	0
Employee focus (P7)	0	0	1	0	1	0	0	0	1	1
IT system robustness (P8)	2	2	2	0	3	1	1	0	0	0
Machine conditions (P9)	1	1	1	1	1	0	1	1	0	2
Prevention of pollution (P10)	0	2	2	2	1	0	1	1	3	0

Table 3 Direct influence matrix

Critical success factors	P1	P2	P3	P4	P5	P6	P7	P8	P9	P10
Management review (P1)	0.12	0.24	0.27	0.08	0.19	0.17	0.16	0.19	0.18	0.20
Teamwork (P2)	0.25	0.13	0.25	0.16	0.25	0.15	0.25	0.20	0.16	0.25
Govt. regulation follow-ups and reviews (P3)	0.14	0.13	0.12	0.10	0.24	0.16	0.17	0.12	0.08	0.17
Innovative technology adoption (P4)	0.24	0.23	0.31	0.08	0.32	0.25	0.27	0.26	0.25	0.15
Flexible/agile manufacturing processes (P5)	0.16	0.12	0.18	0.05	0.09	0.15	0.07	0.07	0.07	0.16
Goal setting through benchmarking (P6)	0.27	0.22	0.26	0.16	0.30	0.12	0.22	0.25	0.24	0.14
Employee focus (P7)	0.02	0.02	0.07	0.02	0.07	0.02	0.02	0.02	0.06	0.07
IT system robustness (P8)	0.17	0.16	0.19	0.04	0.23	0.12	0.12	0.07	0.06	0.09
Machine conditions (P9)	0.10	0.11	0.13	0.08	0.12	0.05	0.11	0.10	0.06	0.15
Prevention of pollution (P10)	0.09	0.16	0.19	0.14	0.15	0.07	0.13	0.12	0.20	0.09

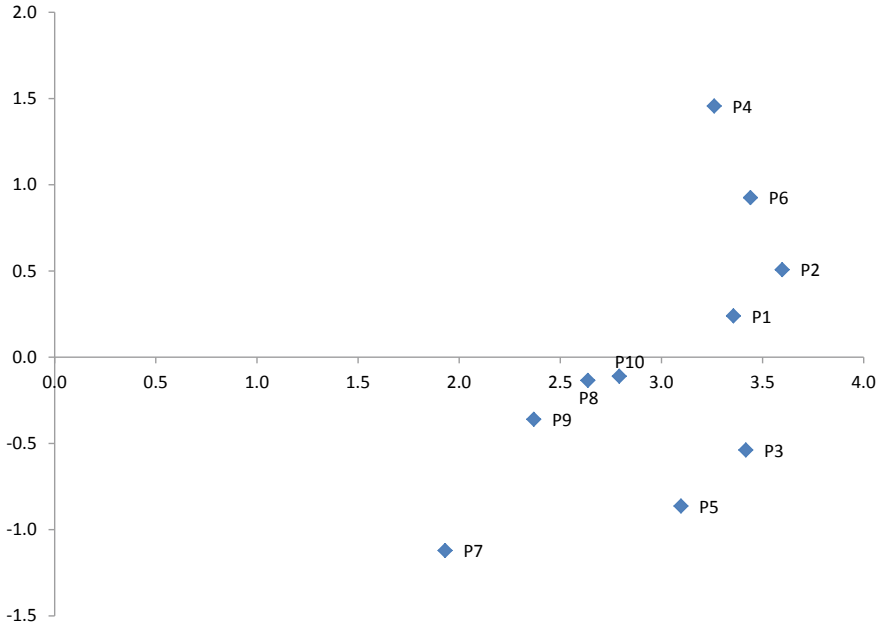

Fig. 2 Diagraph of CSFs (casual diagram)

Six CSFs are like employee focus (P7), IT system robustness (P8), machine condition (P9), govt. regulation follow-ups and reviews (P3), innovative technology adoption (P4) and prevention of pollution (P10) are evaluated in effect group. Management review (P1) plays effective role CSFs for SLM implementation in Indian SMEs. As researcher [6–8] clearly stated that management review is important and considered as critical factor of SLM and becomes distinct care between professionals also. The relative importance of CSFs is shown in Table 3 ($D + R$ values). The outcomes are tabulated in Tables 4, 5, 6. Henceforth, CSFs with greater values are considered. From the prominence vector calculation, four factors are in the top priorities such as teamwork (P2), goal setting through benchmarking (P6), govt. regulation follow-ups and reviews (P3) and management review (P1). Prevention of pollution (P10), IT system robustness (P8), machine condition (P9) and employee focus (P7) get least priority in ten CSFs.

6 Conclusions and Recommendations

Now, sustainable manufacturing contributing significantly is the growth of the industry economically by reducing defects, wastes. Through process management, a manufacturing model has been carried out for sustainable lean manufacturing. Sustainable lean manufacturing geared process toward improvement by a set of tools, concepts,

Table 4 Sum of rating received from experts for CSFs

	D Sum	R sum	$D + R$	$D - R$
Management review (P1)	1.80	1.56	3.36	0.24
Teamwork (P2)	2.05	1.55	3.60	0.51
Govt. regulation follow-ups and reviews (P3)	1.44	1.98	3.42	−0.54
Innovative technology adoption (P4)	2.36	0.90	3.26	1.46
Flexible/agile manufacturing processes (P5)	1.12	1.98	3.10	−0.86
Goal setting through benchmarking (P6)	2.18	1.26	3.44	0.93
Employee focus (P7)	0.40	1.53	1.93	−1.12
IT system robustness (P8)	1.25	1.39	2.64	−0.13
Machine conditions (P9)	1.00	1.36	2.37	−0.36
Prevention of pollution (P10)	1.34	1.45	2.79	−0.11

Table 5 Prominence vector ($D + R$)

Rank	CSFs	$D + R$
1	Team work (P2)	3.60
2	Goal setting through benchmarking (P6)	3.44
3	Govt. regulation follow-ups and reviews (P3)	3.42
4	Management review (P1)	3.36
5	Innovative technology adoption (P4)	3.26
6	Flexible/agile manufacturing processes (P5)	3.10
7	Prevention of pollution (P10)	2.79
8	IT system robustness (P8)	2.64
9	Machine conditions (P9)	2.37
10	Employee focus (P7)	1.93

Table 6 Relative vector ri-si ($D - R$)

Rank	Cause group—CSFs	$D - R$
1	Management review (P1)	1.456695
2	Flexible/agile manufacturing processes (P5)	0.925045
3	Goal setting through benchmarking (P6)	0.507141
4	Teamwork (P2)	0.239408
	Effect group—CSFs	
1	Employee focus (P7)	−0.11071
2	IT system robustness (P8)	−0.1347
3	Machine conditions (P9)	−0.35999
4	Govt. regulation follow-ups and reviews (P3)	−0.53842
5	Innovative technology adoption (P4)	−0.86305
6	Prevention of pollution (P10)	−1.12142

principles and systems [55]. Value stream mapping provides a graphical view of manufacturing processes and has been one of the tested techniques in the world lean application in industries [56]. In industries, inventory levels, non-value-added activities and productivity improvement controlled through value stream mapping [54]. Value stream is also tested in the medical sector to reduce the waiting time of patients [53].

In sustainable manufacturing, social aspects are related to operator safety, working environment, ergonomics and operator fatigue. The efficiency of manufacturing processes is monitored by the consumption of raw material versus output, water, energy, and machine breakdowns. To fulfill the present moment without affecting to future capacity, a set of actions required considered as sustainability [48, 52]. Sustainable lean manufacturing has ability to maintain growth as expected by stakeholders without compromising with environment and society [45].

Altogether, nations are aiming on decreasing the use of harmful material in their regular processes. SMES acted on implementation of sustainable lean manufacturing and govt. regulations enforcing to maintain environmental social action. Generally, identifying interrelationship of CSFs is challenging and their effect on SLM implementation. In this study, DEMETAL identifies the interrelationship of 10 critical success factors. The management review, teamwork and goal setting through benchmarking have direct relationships with SLM implementation in SMEs.

6.1 Research Suggestion and Limitation

This review helps the executives and researchers to guide SLM implementation in Indian SMEs by identifying highly impacted critical success factors. In the current competitive scenario, SMEs need SLM implementation for creating a difference in terms of cost, quality and delivery. For initial start-ups, it may be helpful for getting desired results by considering critical factors assignment in right direction. This study considers only Indian SMEs for SLM implementation; for original equipment manufacturers, more critical success factors may be identified and evaluated through other techniques.

References

1. Speier C, Mollenkopf D, Stank TP (2008) The role of information integration in facilitating 21st century supply chains: a theory-based perspective. Transp J 21–38 (2008)
2. Dubal JK (2016) A pivotal role of SMEs in India. Glob J Res Anal 4 (5). Retrieved from https://worldwidejournals.in/ojs/index.php/gjra/article/view/9882
3. Tajbakhsh A, Hassini E (2015) A data envelopment analysis approach to evaluate sustainability in supply chain networks. J Cleaner Prod 105:74–85
4. Piercy N, Rich N (2015) The relationship between lean operations and sustainable operations. Int J Oper Prod Manag 35(2):282–315

5. Ghazilla RAR, Sakundarini N, Abdul-Rashid SH, Ayub NS, Olugu EU, Musa SN (2015) Drivers and barriers analysis for green manufacturing practices in malaysian SMEs: a preliminary findings. Procedia CIRP 26:658–663
6. Baumgartner RJ (2014) Managing corporate sustainability and CSR: a conceptual framework combining values, strategies and instruments contributing to sustainable development. Corp Soc Responsib Environ Manag 21:258–271. https://doi.org/10.1002/csr.1336
7. Aboelmaged M (2018) The drivers of sustainable manufacturing practices in Egyptian SMEs and their impact on competitive capabilities: a PLS-SEM model. J Cleaner Prod 175:207–221
8. Sangwan KS, Bhamu J, Mehta D (2014) Development of lean manufacturing implementation drivers for Indian ceramic industry. Int J Prod Perform Manag 63(5):569–587
9. Lannelongue G, Gonzalez-Benito J, Quiroz I (2017) Environmental management and labour productivity: the moderating role of capital intensity. J Environ Manag 190:158–169. https://doi.org/10.1016/j.jenvman.2016.11.051
10. Taubitz MA (2010) Lean, green & safe: integrating safety into the lean, green and sustainability movement. Prof Saf 55:39–46
11. Vinodh S, Arvind KR, Somanaathan M (2011) Tools and techniques for enabling sustainability through lean initiatives. Clean Technol Environ Policy 13:469–479. https://doi.org/10.1007/s10098-010-0329-x
12. Mittal VK, Sangwan KS (2014) Prioritizing drivers for green manufacturing: environmental, social and economic perspectives. Procedia CIRP 15:135–140
13. Dora M, Van Goubergen D, Kumar M, Molnar A, Gellynck X (2013) Application of lean practices in small and medium-sized food enterprises. Br Food J 116(1):125–141
14. Engert S, Rauter R, Baumgartner RJ (2015) Exploring the integration of corporate sustainability into strategic management: a literature review. J Clean Prod 112:2833–2850. https://doi.org/10.1016/j.jclepro.2015.08.031
15. Martínez-Jurado PJ, Moyano-Fuentes J (2014) Lean management, supply chain management and sustainability: a literature review. J Clean Prod 85:134–150. https://doi.org/10.1016/j.jclepro.2013.09.042
16. Panizzolo R, Garengo P, Sharma MK, Gore A (2012) Lean manufacturing in developing countries: evidence from Indian SMEs. Prod Plann Control 23(10–11):769–788
17. Singh B, Garg SK, Sharma SK (2010) Scope for lean implementation: a survey of 127 Indian industries. Int J Rapid Manuf 1(3):323–333
18. Rose AMN, Deros BM, Rahman MA (2010) Development of a framework for lean manufacturing implementation in SMEs. In: The 11th Asia Pacific industrial engineering and management systems conference, Melaka, Malaysia, Dec 2010
19. Jabbour CJC, de Sousa Jabbour ABL, Govindan K, Teixeira AA, de Sousa Freitas WR (2013) Environmental management and operational performance in automotive companies in Brazil: the role of human resource management and lean manufacturing. J Cleaner Prod 47:129–140
20. Hsu C-H, Chang A-Y, Luo W (2017) Identifying key performance factors for sustainability development of SMEs–integrating QFD and fuzzy MADM methods. J Clean Prod 161:629–645
21. Machado VC, Leitner U (2010) Lean tools and lean transformation process in health care. Int J Manag Sci Eng Manag 5(5):383–392
22. Achanga P, Shehab E, Roy R, Nelder G (2006) Critical success factors for lean implementation within SMEs. J Manuf Technol Manag 17(4):460–471
23. Agan Y, Acar MF, Borodin A (2013) Drivers of environmental processes and their impact on performance: a study of Turkish SMEs. J Clean Prod 51:23–33
24. Bey N, Hauschild MZ, McAloone TC (2013) Drivers and barriers for implementation of environmental strategies in manufacturing companies. CIRP Ann Manuf Technol 62(1):43–46
25. Caldera HTS et al (2017) Exploring the role of lean thinking in sustainable business practice: a systematic literature review. J Cleaner Prod 1–20. http://dx.doi.org/10.1016/j.jclepro.2017.05.126
26. Djassemi M (2014) Lean adoption in small manufacturing shops: attributes and challenges. J Technol Manag Appl Eng 30(1):2–10

27. Dowlatshahi S, Taham F (2009) The development of a conceptual framework for just-in-time implementation in SMEs. Prod Plann Control 20(7):611–621
28. Fisher J, Bonn I (2011) Business sustainability and undergraduate management education: an Australian study. High Educ 62:563–571. https://doi.org/10.1007/s10734-010-9405-8
29. Gutowski TG (2011) Manufacturing and the science of sustainability. The MIT faculty has made this article openly available. Please share how this access benefits you. Your story matters, p 18
30. Milne MJ, Gray R (2013) W(h)ither ecology? The triple bottom line, the global reporting initiative, and corporate sustainability reporting. J Bus Ethics 118:13–29. https://doi.org/10.1007/s10551-012-1543-8
31. Bhanot N, Rao PV, Deshmukh SG (2016) An integrated approach for analysing the enablers and barriers of sustainable manufacturing. J Clean Prod 142:4412–4439. https://doi.org/10.1016/j.jclepro.2016.11.123
32. Kurdve M, Zackrisson M, Wiktorsson M, Harlin U (2014) Lean and green integration into production system models—experiences from Swedish industry. J Clean Prod 85:180–190. https://doi.org/10.1016/j.jclepro.2014.04.013
33. James J, Ikuma LH, Nahmens I, Aghazadeh F (2013) The impact of Kaizen on safety in modular home manufacturing. Int J Adv Manuf Technol 70:725–734. https://doi.org/10.1007/s00170-013-5315-0
34. Dheeraj N, Vishal N (2012) An overview of green supply chain management in India. Res J Recent Sci 1:77–82
35. Govindan K, Kaliyan M, Kannan D, Haq AN (2014) Barriers analysis for green supply chain management implementation in Indian industries using analytic hierarchy process. Int J Prod Econ 147:555–568
36. Carvalho H, Govindan K, Azevedo SG, Cruz-Machado V (2017) Modelling green and lean supply chains: an eco-efficiency perspective. Resour Conserv Recycl 120:75–87
37. Gandhi S, Mangla SK, Kumar P, Kumar D (2015) Evaluating factors in implementation of successful green supply chain management using DEMATEL: a case study. Int Strateg Manag Rev 3(1):96–109
38. Altuntas S, Dereli T (2015) A novel approach based on DEMATEL method and patent citation analysis for prioritizing a portfolio of investment projects. Expert Syst Appl 42(3):1003–1012
39. Hidayanto AN, Abednego N, Aminah S, Sucahyo YG (2015) Analysis of cloud adoption determinants by using BOCR analysis and DEMATEL. Int J Bus Inf Syst 18(2):221–248
40. Wang Z, Mathiyazhagan K, Xu L, Diabat A (2016) A decision making trial and evaluation laboratory approach to analyze the barriers to green supply chain management adoption in a food packaging company. J Clean Prod 117:19–28
41. Fu X, Zhu Q, Sarkis J (2012) Evaluating green supplier development programs at a telecommunications systems provider. Int J Prod Econ 140(1):357–367
42. Ahmed A, Page J, Olsen J (2015) Adoption lean six sigma to any logic simulation in a manufacturing environment. In: 21st International congress on Modelling and simulation, Gold Coast, Australia, (29 November to 04 December, 2015), pp 29–35
43. Andrew S, Halcomb EJ (2012) Mixed method research. In: Borbasi S, Jackson, D (eds) Navigating the maze of research: enhancing nursing & midwifery practice 3rd ed. Marrickville, New South Wales, Elsevier
44. Bergmiller G, McCright P (2009) Are lean and green programs synergistic. Proc Ind. 1–6
45. Faulkner W, Badurdeen F (December, 2014) Sustainable value stream mapping (Sus- VSM): a methodology to visualize and assess manufacturing sustainability performance. J Cleaner Prod 85:1–11
46. Azevedo S, Carvalho H, Duarte S, Cruz-Machado V (2012) Influence of green and lean upstream supply chain management practices. IEEE Trans Eng Manag 59(4):753–765
47. Stonebraker PW, Goldhar J, Nassos G (2009) Weak links in the supply chain: measuring fragility and sustainability. J Manuf Technol Manag 20(2):61–177
48. Brundtland Commission (1987) Report of the world commission on environment and development. United Nation. http://www.undocuments.net/wced-ocf.htm. (Accessed November 2018)

49. Li Y, Mathiyazhagan K (2018) Application of DEMATEL approach to identify the influential indicators towards sustainable supply chain adoption in the auto components manufacturing sector. J Cleaner Prod 172:2931–2941
50. Jørgensen TH (2008) Towards more sustainable management systems: through life-cycle management and integration. J Cleaner Prod 16(10):1071–1080
51. Lin CW, Chen SH, Tzeng, GH (2009) Constructing a cognition map of alternative fuel vehicles using the DEMATEL method. J Multilevel Criteria Decis Anal 16(1–2):5–19
52. Clancy G, Froling M, Svanström M (2013) Changing from petroleum to wood based materials: critical review of how product sustainability characteristics can be assessed and compared. J Cleaner Prod 39:372–385. https://doi.org/10.1016/j.jclepro.2012.07.027
53. Lummus RR, Vokurka RJ, Rodeghierro B (October 2006) Improving quality through value stream mapping: a case study of a physician's clinic. Total Qual Manag 17(8):1063–1075
54. Seth D, Gupta V (2005) Application of value stream mapping for lean operations and cycle time reduction: an Indian case study. Prod Plann Control 16(1):44–59. https://doi.org/10.1080/09537280512331325281
55. Eatock J, Dixon D, Young T (2009) An exploratory survey of current practice in the medical device industry. J Manuf Technol Manag 20(2):218–234, Emerald Group Publishing Limited 1741 038X. https://doi.org/10.1108/17410380910929637
56. Lasa IS, Laburu CO, de Vila RC (2008) An evaluation of the value stream mapping tool. Bus Process Manag J 14(1):39–52
57. Sangwan KS, Mittal VK (June, 2015) A bibliometric analysis of green manufacturing and similar frameworks. Manag Environ Qual Int J 26(4):566–587

Green Supply Chain Management: Evolution of the Concept, Practices and Trends

J. Martínez and K. Mathiyazhagan

Abstract Companies are increasingly addressed toward sustainability, due to internal agents as senior management and employees and external stakeholders, such as national and international regulations, society and the market, to mitigate and/or eliminate impacts to the environment. To do this, companies establishing control strategies and mitigation of environmental impact and cleaner production, as green procurement or green supply chain management. The latter is a management approach that integrates the design stages, manufacturing, purchasing, distribution and logistics through practices that involve the entire supply chain, seeking to achieve the TBL (triple bottom line) to maximize the environmental, economic and social benefit. A literature review was proposed in Scopus bibliographic manager and Springer Link, from Boolean operators to analyze the evolution of the concept, practices that compose and trends on the field. It was found that even the concept of GSCM is under construction and there are altogether 231 articles that raise various trends and approaches GSCM, most of them focused on the automotive and construction.

Keywords Green supply chain management · Trends · Concept · Practices · Bibliometric analysis

1 Introduction

In this environment of globalization, companies have been integrated in stages based on a single set of products and/or services, increasing the system reliability, decreasing the delivery time and additional costs for the end customer are eliminated. The integration of these stages is known as supply chain. According to the Council of

J. Martínez
EAM University Institution, Armenia, Colombia
e-mail: jpmartinez@eam.edu.co

K. Mathiyazhagan (✉)
Department of Mechanical Engineering, Amity School of Engineering & Technology, Amity University, Sector 125, Noida, Uttar Pradesh, India
e-mail: madii1984@yahoo.com

H. Kumar and P. K. Jain (eds.), *Recent Advances in Mechanical Engineering*,
Lecture Notes in Mechanical Engineering,
https://doi.org/10.1007/978-981-15-1071-7_5

Supply Chain Management [1], a supply chain integrates many companies, starting with the acquisition of raw materials, followed by the manufacturing process and ending with the final distribution to the consumer, including the intermediate stages as transport and warehouse [2].

All providers of goods and services and all clients are interconnected by the consumer demand for finished products as well as materials and the logistics process, from procurement of raw materials to delivery of finished products to the end user [3]. However, supply chains even with their new environmental efforts continue to generate environmental problems such as pollution, emissions and discharges. These emissions have a high cost to the supply chain as well as an impact on the welfare of society and, at the same time, increase the loss in productivity and propose a bad image for the organizations [3].

To increase the competitiveness of supply chains and to minimize the impact on health and the environment, several mitigation mechanisms emerge as the list of ISO 14000 standards, TQEM (Total Quality and Environment Management), industrial ecology, green engineering, cleaner production and closed supply chain and among others [3]. Among all these trends, green supply chain management (GSCM) has been achieved attention between entrepreneurs and researchers [4].

Martinez Giraldo says the GSCM approach emerges as a way of integrating environmental management in organizations and respond to internal and external pressures, as well as part of the adoption of policies of corporate social responsibility [4]. The GSCM approach includes environmental considerations in all stages of the supply chain, from product design, purchasing processes to manufacturing operations, distribution, system information, sales and product management after completing its life cycle [5].

The goal of this article was to analyze research trends in green supply chain management, in order to determine how it has been developing this concept, the practices that include GSCM and potential fields of work.

2 Review Background

Delivery, quality, service, innovation, flexibility are used as strategies to achieve to draw attention to their customers. These strategies are seen as competing priorities [6]. Sarache et al. [7] define competitive priorities as the dimensions of business competition, which involves giving special treatment to this dimension on the other.

The competitive market and emerging priorities are relative. In the last decade, given the changing market requirements and pressure from the government, other requirements of internal and external customers have emerged. Thus, they have arisen the environment and after-sales service as new competitive priorities [8]. Showing that, customers increasingly consider the environment as a decision variable at the time of purchase, resulting in increased pressure on organizations.

In order to meet these customer needs, companies ensure a good relationship with suppliers, achieving national and international standards, devise strategies recirculation water, waste recovery and packaging from recycled material and a reverse logistics to return the material once its life cycle ends. To meet all requirements, companies have implemented practices reagent type, such as mitigation and waste treatment, recycling programs, reuse [9]. Also, there are proactive strategies that seek to control emissions and waste from the source establishing strategies such as green design or industrial ecology.

2.1 Review Result

Green Supply Chain Management Concept Definition

Green supply chain management (GSCM) is defined as the integration of environment thinking through the supply chain, including design, selection of raw materials, manufacturing processes, product delivery and product handling after its life cycle [10]. Another concept is proposed by Sarkis [11] in which the GSCM is a strategic approach aimed at increased environmental measures to the entire supply chain. Thus, GSCM is transverse to the supply chain and includes all stakeholders, the internal and external clients, the government and all the society.

Currently, there is no consensus on the GSCM concept. On the contrary, it was found that this varies depending on the approach of each researcher [12]. Some of the definitions detected in the state of the art that each author has incorporated over time within the scope of the GSCM concept are summarized in Table 1.

Table 1 Evolution of the GSCM concept

Author	Definition
Green et al. [42]	Integration between innovation and shopping can be considered to the environmental context
Min and Galle [43]	Build a product environmentally sustainable, developing reusable packaging, energy conservation, waste reduction, recycling and the creation of an environmentally sensitive organizational culture
[44]	Handling material and information flows as well as the cooperation of companies along the supply chain, aiming at sustainable, economic and social development
Sarkiset al. [45]	Integrating green practices throughout the supply chain, including functional areas such as purchasing, production and sales, from strategic, tactical and operational
Andic et al. [40]	Eliminating or mitigating the negative effects of the supply chain on the environment

Table 2 Equations search for bibliographic analysis

Keyword	Operator	Keyword
Green supply	AND	Definition
Green supply	AND	Concept
Green supply	AND	Innovation
Green supply	AND	Practices
Green supply	AND	Trends

3 Problem Description

For the literature review, keywords were established in UNESCO thesauri. After the keywords have obtained, the search with structure equations was conducted. They are presented in Table 2.

These equations were validated in search databases internationally renowned: Science Direct, JSTOR and Emerald. Scopus was employed as bibliographic gestor. The relevance of this manager and tools is based on the impact factor of the journals that comprise [13].

4 Solution Approach

The total papers obtained according to the keywords are presented in Tables 3 and 4. Preliminary work as presented by Ahí and Searcy (2014), they state that there is a correlation between the concepts of GSCM and sustainable supply chain management (SSCM). SSCM is defined as the involvement of the planning and management of supply activities, acquisition, conversion and logistics involved during the phases of pre-fabrication, manufacture, use and post-use in the life cycle in closed loop through multiple life cycleswith perfect shared information about the entire product life cycles between companies explicitly considering the social and environmental implications to achieve a shared vision. Meanwhile, Wolf [14] raises a related definition of mitigation strategies, i.e., the ability of the company to plan, mitigate, detect, respond to and recover from potential global risks. These risks involve substantial considerations of

Table 3 Results obtained with equations search

Keyword	Keyword	Articles
Green supply	Definition	142
Green supply	Concept	49
Green supply	Innovation	6
Green supply	Practices	32
Green supply	Trends	2
Total		231

Table 4 Evolution of GSCM practices

Source	Practices detected
Green et al. [42]	Shopping regulation compliance for profit, encourage excellence among suppliers, collaborative process substitution
Sheu [16]	Design of reusable products, customer–company collaboration for the return of the product, integration of reverse logistics in the supply chain
Srivastrava [17]	Adoption of the 6 Rs (reuse, reuse, recycle, refurbished, remanufacture, reverse logistics). Source reduction, pollution control, planning to reduce overproduction, environmentally sustainable design, disassembly process scheduling
Parmigiani et al. [46]	Carbon footprint reduction, pollution prevention, ISO 14001 environmentally safe manufacturing, disposal of hazardous materials, substitution of raw materials, life cycle assessment, effective partnerships
Büyüközkan et al. [47]	Social responsibility as a criterion for selecting suppliers, green image as a marketing strategy, use of environmentally friendly technologies and materials, compliance with environmental policies, participation in environmental projects, environmental certifications, pollution control

Source Compiled from Martinez (2015) and Fahimnia et al. [48]

marketing and supply chain as product development, channel selection, market decisions, sourcing, manufacturing complexity, transportation, government and industry regulation, availability of resources, talent management platforms, alternative energy and security.

As shown in Table 3, the biggest trend of GSCM research, still it is based on the concept as proposed to define the approach. Also, when a concept arises, the need arises to establish its components; hence, the practices are the second set of keywords.

Even Table 3 shows 231 papers as a result of the search, only 61 were read, because some of them are in two or three categories as green supply chain definition and also are included in green supply chain concept.

5 Results and Discussions

Among the definitions referred to excel proposed by Liu and Chang [15], who argue that the management GSCM is an important strategy for companies to improve their environmental and economic performance at the same time by reducing environmental risks and increasing their ecological efficiency. However, although proactive organizations such as Dell, HP and Sony have adopted initiatives, GSCM in its operational process [16] is still a new concept and has not been widely adopted,

particularly by small and medium-sized enterprises [17]. For example, global manufacturers of manufactured products, most manufacturing enterprises in China [18] appear to be still in the first stage of learning environmental practices (Martinez 2015). Even the early adopters under GSCM practices are merely in the initial stages of implementation [7]. They propose that a connection between the closed cycle and strategic orientation based on the processes and implementation practices GSCM is necessary.

Weather research GSCM in the period between 1990 and 2019 states the first publications whereas it relates to the supply chain, given in 2000 with four items, reaching its maximum output of 339 items in 2018. These contributions are mainly due to author's review documents such as Sarkis 61 where GSCM methodology relates to strategies decreased carbon footprint [7, 14, 19–22], resilience strategies [15, 18, 23–25], circular economy [26–28], all items have in common that the relationship that wins between the environment and economic developments is confirmed. Researchers also excel as Zhu, Govindan, Jabbour and Cruz Machado, who are among the five most cited and are part of the trends presented.

5.1 Processes Compose GSCM

Regarding the practices that make up the GSCM, Al-Aomar et al. propose a list of practices GSCM as relations with suppliers of material, reuse, recycling, implementation of HACCP standards, reducing water and energy, either sunlight or LED, among others that apply in the hospitality sector [29] These practices are minimization of materials and include worker safety, but few minimization strategies from design.

Another set of practices are proposed by Rosangela et al., who validate the hypothesis that adopting GSCM practices has a positive impact on the operating, economic and environmental performance of suppliers of Brazilian automotive supply chain [30]. They also state that the main pressures that influence the performance of companies are declaring companies, advances provider in developing products that respect the environment, the environmental partnership with suppliers and the cost of ecological packaging. As for the relationship between these practices and performance, the results show that adoption has a positive effect only in the economic and environmental performance of the companies studied [31].

Noor et al. [27] discussed the relationship between the GSCM concept and the concept of innovation [32]. This article validates the hypothesis that although several empirical studies described in the literature implicit GSCM has a significant bearing on green innovation, it is not provided the sufficient evidence to support that relationship in the development of new green product. All GSCM practices should be considered when investigating its relation to eco-innovation. Then, it is believed that manufacturers quite see how these practices may involve GSCM green innovation together in the process of product life cycle management.

The GSCM does not have processes that make it a standard. And, the concept is relatively new practices that make up the GSCM, obey the focus of research styles search and what it considers as relevant.

Green design focuses on creating products with (non-toxic materials and simultaneously meets the modular design [33]. On the other hand, industrial ecology proposes an analogy between natural ecological systems and the "community" of industrial plants. At the same way in a biological ecosystem, the industrial ecosystem should be viewed as an interrelated part of a larger system where the outcome of one of the organizations becomes an important raw material for another [34]. Industrial ecology explores new possibilities for interaction between companies, as a result of a rethinking of industrial activities, changing the waste concept and completing the understanding of its environmental impacts and its interrelation [35].

Other practices detected include remanufacturing, which plays a central role in efforts ecological efficiency, responsibility extended to the producer and the environment [36]. Recent days, researchers are focused to integrate the traditional manufacturing with green manufacturing [37]. Others are focused in terms of waste, refurbished, reuse, remanufacturing, as well as the use of energy [38]. Kristianto and Helo [25] are investigating the integration between: (i) product design and manufacturing processes and ecology and social principles, life cycle assessment, extension of product life cycle management and reuseand (ii) the design of supply chain networks and programming production lines and products.

According to Govindan et al., green thinking is important role for supplier selection [39]. Zhu et al. [31] establish the importance of measuring the performance of GSCM practices that have been developed for the use of performance indicators. These trends are also related to the proposals by Giraldo and Paulin [40, 41], who identifies the creation of new practices such as human resources management and green innovation as starting points for integrating more links in the supply chain.

6 Conclusions and Recommendations

The main quantity of papers related to green supply chain management is focused on building its concept, with a total of 142 articles. These papers have in common the inclusion of green practices on each stage of the supply chain, including all the hierarchical levels since the top management with the inclusion until the minor operational level. Also, these GSCM concept papers are based on the presentation and delimitation of this management approach. Thus, the integration of GSCM concept with other concepts are better and ensure the more sustainable environment.

As it was defined in Table 1, the innovations and trends in GSCM are a new research topic with just eight papers that contain these words into the title. However, several papers apply the concept and include practices and trends of GSCM. Some of these found in the literature are: the economic implications of the GSCM, implementation of GSCM in economic sectors such as automotive, the inclusion of the GSCM

in senior management, the development of new products with environmental considerations the positioning of the corporate environmental image, the reuse of waste and the creation of closed production cycles and the use of cleaner technologies such as LED panels.

Finally, after this review some questions associated with GSCM have emerged. Some questions are related with the appropriate way to measure green practices impacts, by building environmental performance indicators, as well as validation and relationship with other green trends emerged. Others are associated with the role among internal and external clients to implement GSCM.

6.1 Research Implication and Limitation

This study helps to identify the evolution of GSCM concept and several trends in the field. This review paper shows that the green supply chain is still under construction and the boundary definition has changed to include other emerged theories as cleaner production, closed supply chain, sustainable supply chain among others. The GSCM concept will be continue evolving to incorporate some practices that led communicate the supply chain stages. The principal limitation of this study was the quantity of paper analyzed in comparison with other review papers; this situation is due to access different sources of papers and bibliographic gestors.

References

1. Council of Supply Chain Management (2019). Obtained from: http://www.cscmpspain.org/ recovered 26 May
2. Mentzer JT, DeWitt W, Keebler JS, Min S, Nix NW, Smith CD, Zacharia ZG (2001) Defining supply chain management. J Bus Logist 22(2):1–25
3. Li S, Ragu-Nathan B, Ragu-Nathan TS, Rao SS (2006) The impact of supply chain management practices on competitive advantage and organizational performance. Omega 34(2):107–124
4. Hervani AA, Helms MM, Sarkis J (2005) Performance measurement for green supply chain management. Benchmarking: An Int J 12(4):330–353
5. Sarache-Castro WA, Costa-Salas YJ, Martínez-Giraldo JP (2015) Environmental performance evaluation under a green supply chain approach. Dyna 82(189):207–215
6. Giraldo JM, Castro WAS (2012) Green supply chains: conceptual bases and trends. Appl Agroind
7. Sarache Castro WA, Cardenas Aguirre DM, Giraldo García JA, Sánchez Parra JH (2007). Procedure for evaluating the manufacturing strategy: applications in the metalworking industry. Notebooks Administration, 20(33)
8. Burgos Jimenez J (1999) An approach to the environmental integrity target address operations. J Econ Bus 4:259–284

9. Epstein, MJ (2000) Environmental performance in company practices to fund and manage a strategy for environmental protection. Ecoe
10. Mackenzie D, Moss L, Engelhardt J, Martyn R (1991) Green design: Design for the Environment. London: Laurence King
11. Sarkis J (2003) A strategic decision framework for green supply chain management. J Clean Prod 11(4):397–409
12. Vachon S, Klassen RD (2006) Extending green practices across the supply chain: the impact of upstream and downstream integration. Int J Oper Prod Manag 26(7):795–821
13. Andic E, Yurt Ö, Baltacioglu T (2012) Green supply chains: efforts and potential applications for the Turkish market. Resour Conserv Recycl 58:50–68
14. Wolf J (2011) Sustainable supply chain management integration: a qualitative analysis of the German manufacturing industry. J Bus Ethics 102(2):221–235
15. Liu S, Chang YT (2017) Manufacturers' closed-loop orientation for green supply chain management. Sustainability 9(2):222
16. Sheu JB (2008) Green supply chain management, logistics and nuclear power reverse generation. Transp Res Part E: Logist Transp Rev 44(1):19–46
17. Srivastava SK (2007) Green supply-chain management: a state-of-the-art literature review. Int J Manag Rev 9(1):53–80
18. Zhu Q, Sarkis J, Geng Y (2005) Green supply chain management in China: pressures, practices and performance. Int J Oper Prod Manag 25:449–468
19. There P, Searcy C (2013) A comparative analysis of literature definitions for green and sustainable supply chain management. J Clean Prod 52:329–341
20. Chu SH, Yang H, Lee M, Park S (2017) The impact of institutional pressures on green supply chain management and firm performance: top management roles and social capital. Sustainability 9(5):764
21. Testa F, Iraldo F (2010) Shadows and lights of GSCM (green supply chain management): determinants and effects of these practices based on a multi-national study. J Clean Prod 18:953–962
22. Lai K, Wong CW (2012) Green logistics management and performance: some empirical evidence from Chineses manufacturing exporters. Omega 40:267–282
23. Zhu Q, Sarkis J, Lai K (2012) Green supply chain management innovation diffusion and its relationship to organizational improvement: an ecological perspective modernization. J Eng Technol Manag 168–185
24. Agi MA, Nishant R (2017) Understanding influential factors on Implementing green supply chain management practices: an interpretive structural modeling analysis. J Environ Manage 188:351–363
25. Kristianto Y, Helo P (2015) Reprint of "product architecture modularity Implications for operations economy of green supply chains". Transp Res Part E: Logist Transp Rev 74(February):63–80. ISSN 1366-5545
26. Dubey R, Gunasekaran A, Ali SS (2015). Exploring the relationship between leadership, operational practices, institutional pressures and environmental performance: a framework for green supply chain. Int J Prod Econ
27. Seman NAA, Zakuan N, Jusoh A, Arif MSM, Saman MZM (2012) The relationship of green supply chain management and green innovation concept. Came—Soc Behav Sci 57:453–457
28. Gunasekaran A, Subramanian N, Rahman S (2015) Green supply chain collaboration and incentives: current trends and future directions. Transp Res Part E: Logist Transp Rev 74(February):1–10, ISSN 1366-5545
29. Chen P-C, Hung S-W (2014) Collaborative green innovation in emerging countries: a social perspective capital. Int J oper Prod Manage 34(3):347–363
30. Govindan K, Kadziński M, Sivakumar R (2017) Application of a novel PROMETHEE -based method for construction of a group ranking to compromise prioritization of green suppliers in food supply chain. Omega, 71(September):129–145. ISSN 0305-0483
31. Zhu Q, Sarkis J, Lai KH (2008) Confirmation of a measurement for green supply chain management practices implementation. Int J Prod Econ 111:261–267

32. Tuzkaya G, Ozgen A, Ozgen D, Tuzkaya UR (2009) Environmental performance evaluation of suppliers: a hybrid approach fuzzy multi-criteria decision. Int J Environ Sci Technol 6(3):477–490
33. Liu J, Feng Y, Zhu Q, Sarkis J (2018) Green supply chain management and the circular economy: reviewing theory for advancement of both fields. Int J Phys Distrib Logist Manag 48(8):794–817. https://doi.org/10.1108/IJPDLM-01-2017-0049
34. Sarkis J (2018) Sustainable and green supply chains: advancement through resources, conservation and recycling. Resour Conserv Recycl 134:A1–A3. https://doi.org/10.1016/j.resconrec.2017.12.022
35. Shah P, Zhu Q, Sarkis J (2017) Product deletion and the supply chain: a Greening perspective. Paper presented at the 2017 IEEE technology and engineering management society conference, TEMSCON 2017, 324–328. https://doi.org/10.1109/temscon.2017.7998397 Retrieved from www.scopus.com
36. Li X, Zhu Q (2017) Evaluating the practice of green food service supply chain management based on fuzzy DEMATEL-ANP model. Paper presented at the proceedings of SPIE—the international society for optical engineering, 10322. https://doi.org/10.1117/12.2265152 Retrieved from www.scopus.com
37. Liu Y, Zhu Q, Seuring S (2017) Linking capabilities to green operations strategies: the moderating role of corporate environmental proactivity. Int J Prod Econ 187:182–195. https://doi.org/10.1016/j.ijpe.2017.03.007
38. Wang Z, Mathiyazhagan K, Xu L, Diabat A (2016) A decision making trial and evaluation laboratory approach to analyze the barriers to green supply chain management in a food packaging adoption company. J Clean Prod 117:19–28. https://doi.org/10.1016/j.jclepro.2015.09.142
39. Diabat A, Al-Salem M (2015) An integrated supply chain Problem with environmental considerations. Int J Prod Econ 164:330–338. https://doi.org/10.1016/j.ijpe.2014.12.004
40. Giraldo M, Paulin J (2015a) Green management practices in the manufacturing sector Caldas. Master's thesis, Universidad Nacional de Colombia - Sede Manizales
41. Giraldo M, Paulin J (2015b) Practice green management in manufacturing Caldas. Master's thesis, Universidad Nacional de Colombia - Sede Manizales
42. Green KW Jr, Zelbst PJ, Meacham J, Bhadauria VS (2012) Green supply chain management practices: impact on performance. Supply Chain Manag: An Int J 17(3):290–305
43. Min H, Galle WP (1997) Green purchasing strategies: trends and Implications. J Supply Chain Manag 33(3):10
44. Seuring SA (2011) Green supply chain costing: joint cost management in the supply chain polyester linings. Greener Manag Int 71–81
45. Sarkis J, Zhu Q, Lai KH (2011) An organizational theoretic review of green supply chain management literature. Int J Prod Econ 130(1):1–15
46. Parmigiani A, Klassen RD, Russo MV (2011) Efficiency meets accountability: performance Implications of supply chain configuration, control, and capabilities. J Oper Manag 29(3):212–223
47. Büyüközkan G, Cifci G (2011) Evaluation of the green supply chain management practices: a fuzzy ANP approach. Prod Plan Control 23(6):405–418
48. Fahimnia B, Jabbarzadeh A, Sarkis J (2018) Greening versus resilience: a supply chain design perspective. Transp Res Part E: Logist Transp Rev 119:129–148. https://doi.org/10.1016/j.tre.2018.09.005

Human Upper Limb Joint Torque Minimization Using Genetic Algorithm

Anil Kumar Gillawat and Hemant Jayantilal Nagarsheth

Abstract Minimization of joint torque has been a keen interest of researchers to predict the trajectory to achieve the desired position. Dynamic equations are used to define objective function and range of motions of human upper limb joints are set as constraints. MATLAB genetic algorithm (GA) toolbox is used to minimize the joint torques. Desired position is defined as a nonlinear constraint. Optimization problem consists of eleven objectives and thirty-one variables. Torques at joints are fed as objective function such that the magnitude of the torque is minimized. Variables used may be broadly classified into four groups: angular displacements, angular velocities, and angular accelerations comprising 10 sets each. One more variable is added as time of rotation. GA parameters are required to be predicted for the developed objective function. Analytic hierarchy process (AHP) approach is used to determine the GA parameters. The results obtained are satisfactory.

Keywords Joint torques · Human upper limb · Genetic Algorithm · Optimisation parameters

Abbreviations

AHP Analytic Hierarchy Process
DoF Degree of Freedom
GA Genetic Algorithm
RoM Range of Motion

A. K. Gillawat (✉) · H. J. Nagarsheth
Mechanical Engineering Department, Sardar Vallabhbhai National Institute of Technology, Ichchhanath, Surat 395007, India
e-mail: anilkumargillawat@gmail.com

H. Kumar and P. K. Jain (eds.), *Recent Advances in Mechanical Engineering*,
Lecture Notes in Mechanical Engineering,
https://doi.org/10.1007/978-981-15-1071-7_6

1 Introduction

Growing interest toward humanoid robots and their application in industries and biomechanics, anthropomorphism and dexterity of human limbs has attracted many researchers. Developments in anthropomorphic robotic parts by increasing the level of dexterity and agility and imitating human motion have attracted scientific interest. The torques required by joint actuators of a humanoid robot while walking should be controlled appropriately by optimizing motion parameters. This will result in improved working capability and/or increased working space and/or increased overall working force. Therefore, research toward the development of humanoid parts mimicking human has been most challenging and attractive research area for researchers since the 1980s. The researchers have worked on minimizing joint motions [1], robot trajectories [2–7], minimizing positioning error [8–10], and avoiding obstacle [11–13]. This research has attracted researchers from the field of pattern recognition, artificial intelligence, control systems, electronic circuit devices, and biological applications. Genetic algorithm has played a big role in simplifying the problem of identification of different parameters required in kinematic [14–16] and dynamic analysis [17, 18]. Genetic algorithm is also modified [16] Learning Robot Behaviors Using Genetic Algorithms and/or combined with other intelligent systems [17, 19, 20] for increased accuracy and reduced processing time. Some of the researchers have also worked on defining the parameters of Genetic Algorithm. However, different optimization techniques such as genetic algorithm, neural networks, fuzzy systems, and many new and combination of the existing optimization techniques were explored by different researchers, but Genetic Algorithm was found to have certain advantages over other existing algorithms and hence Genetic Algorithm is preferred for finding optimum trajectory with minimum joint torques within specified range of motions.

Chaiyarataiia and Zalzala [21] reviewed developments in GA and GA applications in pattern recognition, robotics, artificial life, expert system, electronic circuit design, cellular automata, and biological applications. The main themes studied include genetic algorithm techniques, genetic operator technique, niching techniques, genetic drift, and method of benchmarking genetic algorithm performances, measurement of difficulty level of a test-bed function, population genetics, and developmental mechanism in genetic algorithms. Parker [22] used a binary-coded GA with multi-criteria with minimum joint displacement for positioning robotic arm at the target location. Davidor [11] and Schultz [13] applied GA for optimizing robot trajectories in obstacle avoidance problem. Khoogar and Parker [23] and Nearchou and Aspragathos [12] used errors as fitness function in GA for robot motion to avoid obstacles and minimize number of moves to reach desired position. A task-based manipulator was designed by Kim and Khosla [24] using multipopulation genetic algorithm (MPGA) and maintaining constant complexity. Doyle and Jones [25] proposed a GA-based path-planning scheme with optimum path for a manipulator. Kubota et al. [26] used virus theory of evolution-based GA (VEGA) with

reverse transcription operator for trajectory planning of a cellular manipulator system. VEGA was capable of generating collision-free trajectory. Yun and Xi [18] used improved GA for optimum motion planning in joint space (OMPJS) with optimum path planning and optimum trajectory planning for robots with kinematics, dynamics, and control constraints. Nearchou [16] formulated the inverse kinematic problem for redundant robot manipulators with obstacle and used modified GA and showed that the accuracy of the mGA solution is substantially better than Pseudoinverse method and simple GA. Thomaz et al. [27] proposed chromosome attitudes structure evolution-based GA path-planning approach for controlling a simulated mobile robot to reach a defined position by performing collision-free straight motion. Pires et al. [4, 28–30] proposed gas [14, 15] and MOGA to manipulate collision-free trajectories with minimum space/time ripple in the trajectory in the workspace with any number of obstacles. Cernic et al. [31] used GA for neural network-based robot navigation controller optimization. Calafiore et al. [32] developed GA-based optimal joint trajectories for two-link SCARA robot within the frequency bandwidth constraints and defined range of values for joint position, velocity, and acceleration by minimizing either the number of conditions for regression matrix or the logarithmic determinant of the Fisher information matrix.

This paper presents a study of optimizing trajectory of 21-DOF human upper limb by minimizing both individual and total joint torques of human upper limb by applying genetic algorithm to dynamic equation derived.

2 Material and Methodology

Mathematical model is developed for kinematic and dynamic analysis of human upper limb for defined structure for given range of motions, velocities, and accelerations. These mathematical models are used to generate MATLAB code which is used as input for optimizing the joint torques and finding the optimum values of variables, i.e., individual angular displacement, angular velocities, and angular acceleration. These optimum values are used as input for the joint motors so that minimum joint torque is used at individual motors to reach the end-effector at desired position (Fig. 1).

2.1 Problem Definition

Multi-objective function for joint torques is prepared in MATLAB as a function of angular displacements, angular velocities, angular accelerations and time of rotation. Range of motion (RoM) of the joints is considered as constraints for the angular displacements. Required position of joint is given as input and considered as one more constraint. Limitations of singular velocities and angular velocities are

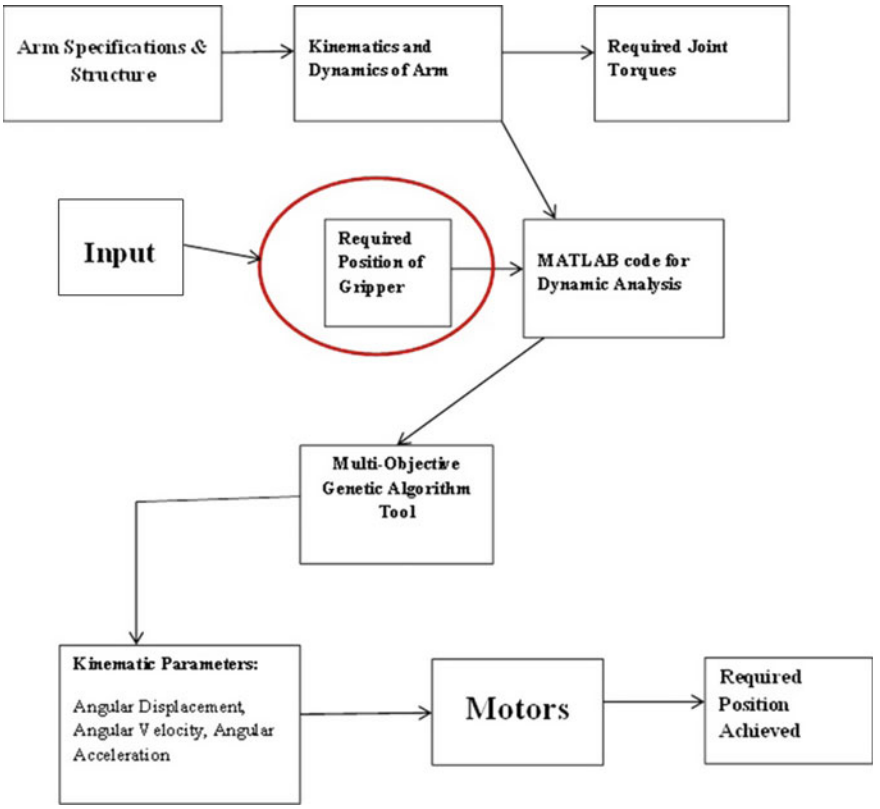

Fig. 1 Application of genetic algorithm

selected within reasonable range. Total time for rotation of joints is selected for study. Ten joints are considered for study; hence, we have ten objective functions to be minimized with ten each joint angular velocities and joint angular accelerations. Therefore, the optimization problem here considered is multi-objective–multi-variable optimization problem with ten objective functions and thirty-one variables. The objective function problem is defined as:

Minimize joint torques

$$|\tau_i| = I(\theta)\ddot{\theta} + C(\theta, \dot{\theta}) + G(\theta) \quad \text{for } i = 10$$

Subjected to

$$\begin{gathered}\text{Lower Bound} \leq \theta_i \leq \text{Upper Bounds} \\ \text{Lower Bound} \leq \dot{\theta}_i \leq \text{Upper Bounds} \\ \text{Lower Bound} \leq \ddot{\theta}_i \leq \text{Upper Bounds} \\ 0 < \text{Time} \leq T \\ P_{\text{required}} = (P_x, P_y, P_z)\end{gathered}$$

where

$I(\theta)$ $n \times n$ inertial acceleration-related symmetric matrix
C $n \times 1$ nonlinear Coriolis and centrifugal force vector
G $n \times 1$ gravity loading force vector.

3 Genetic Algorithm Implementation

Genetic algorithm is implemented in two processes. The first process is selection of individuals to produce next generation followed by the second process to use these selected individuals to form children (next generation) by crossover and mutation techniques. Extensive computation is carried out for finding optimum GA parameters for the dynamic model.

Population Selection: Population size selection is considered very important in finding an optimum solution using GA as small population size results in poor solution, whereas large population size makes an algorithm to take more computation time for finding optimal solution [33]. The population size of 400 is selected as optimum population size for the problem after extensive trial runs.

Selection Function: The selection of individuals is very important as fitter individuals are capable of producing offsprings with even better fitness. Hence, the selection mechanism decides which and how many individuals are selected for mating and how many offsprings are produced by each individual. The basic principle for selection strategy is "the better is an individual; the higher is its chance of being parent" [34]. It is observed that tournament selection function with size 6 has the minimum normalized torque value. Hence, tournament selection function with size 6 is selected as selection function for GA study of our function.

Crossover Fraction: Crossover fraction identifies the fraction of each population available for crossover. If all children are crossover children, 1 value for crossover fraction is assigned whereas 0 value is assigned if all children are mutation children [35]. An assessment for different values of crossover fractions ranging from 0 to 1 with 0.1 steps is done and 0.9 crossover fraction is selected as selection function for GA study of our function.

Table 1 GA parameter selection

S. no.	Genetic parameter	Selection parameter	Values
1	Population size	Double vector type	400
2	Selection function	Tournament selection	6
3	Crossover fraction	–	0.9
4	Crossover function	Scattered	–
5	Elite function	–	0.05 of population size
6	Mutation function	Constraint dependent	–
7	Migration	Forward	0.2
8	Fitness function	Serial	–
9	Stall generation	–	50
10	Function tolerance	–	–

Crossover Function: In current study, seven different crossover functions are verified on GA model to give diversity. Scattered crossover function has the minimum normalized torque value for the determined selection parameters. Hence, scattered crossover function is selected as selection function for GA study of our function. Different genetic parameters selected are listed in Table 1.

4 Result and Discussion

Figure 3 shows uniform and diverse average spread and hence the solution obtained is not stucked in the local minima. In Fig. 4, linear and concentrated Pareto front shows the effectiveness of the selection of optimization parameters. The graph shows that the solution is non-dominating. Rank histogram (Fig. 5) shows that rank 1 dominates all remaining ranks whereas rank 4 is dominated by all other ranks (i.e., rank 1, rank 2, and rank 3). Rank 1 gives the best solution. Figure 8 shows that the stopping criteria are met and Fig. 10 shows the best and mean fitness value of the function. The fitness function decreases with the generation and the mean and best fitness are very near to each other, which show the effectiveness of the algorithm (Figs. 2, 6, 7 and 9).

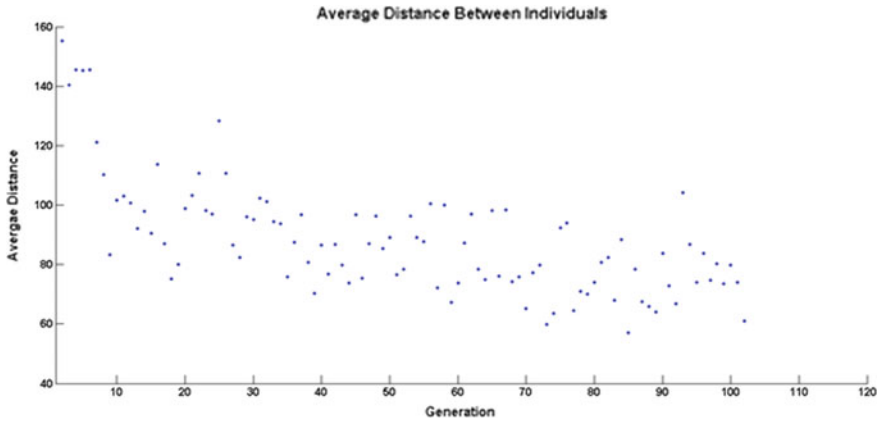

Fig. 2 Average distance between individuals

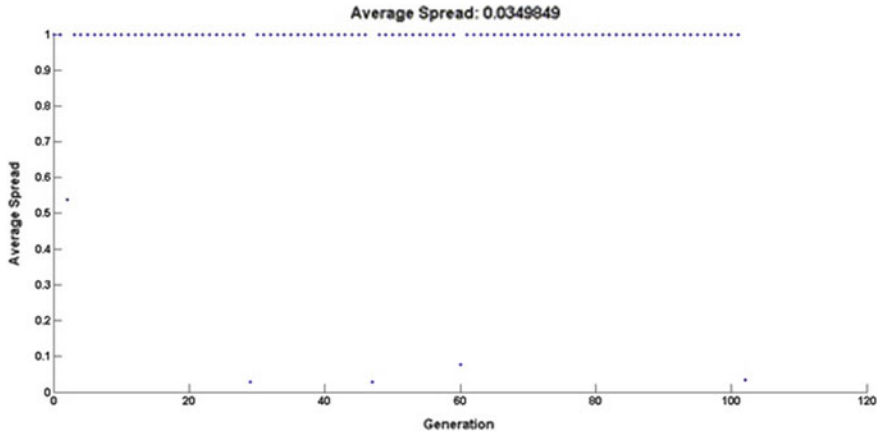

Fig. 3 Average speed

4.1 Analysis of the Objective Functions for the Selected Parameters

Selected GA parameters and values discussed in Sect. 3 and the default functions were used to analyze the optimization problem using the developed function. Required position of last link of the developed model is set at *P* (10, 23, 30) in limited time of 35 s. The population size was kept 200 for more than five variables for the double vector population type. The reproduction elite count was kept 5% of population size (i.e., 10). The optimized solution for the different parameters is listed in Table 1. Different plots were plotted for analyzing the optimization function.

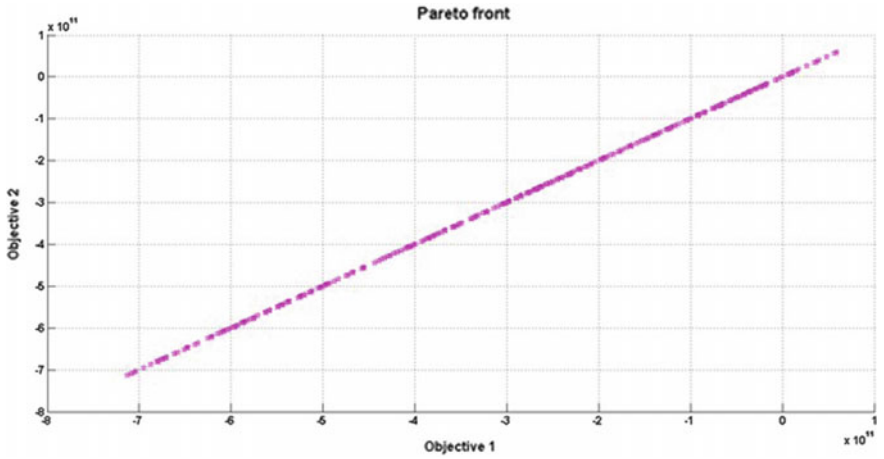

Fig. 4 Pareto front

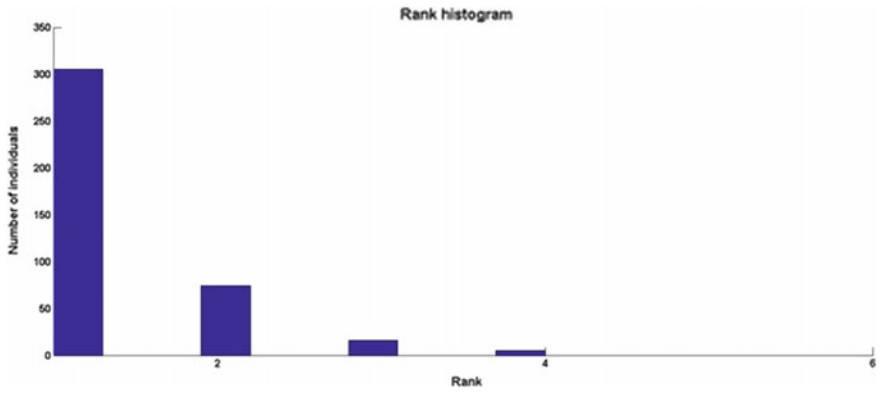

Fig. 5 Rank history

Table 3 shows the *f*-count and fitness variation. Figure 11 shows that the total torque required decreases with an increase in number of iteration. The stopping criteria are reached in 11 iterations only (Table 2).

5 Conclusion

This paper aims to use MATLAB GA toolbox for optimizing the parameters for joint torque minimization. The parameter selection is made for the prepared code for joint analysis of human upper limb. The GA parameters are used as input for GA analysis to get the optimum joint torque. However, selection of population size is important

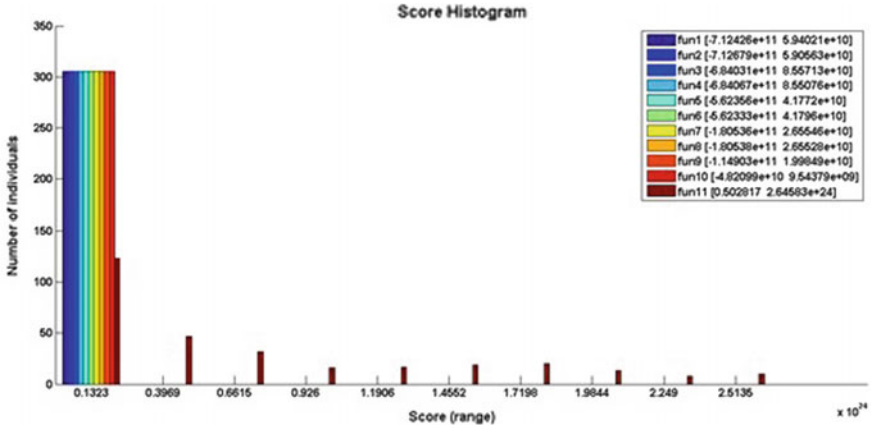

Fig. 6 Score histogram

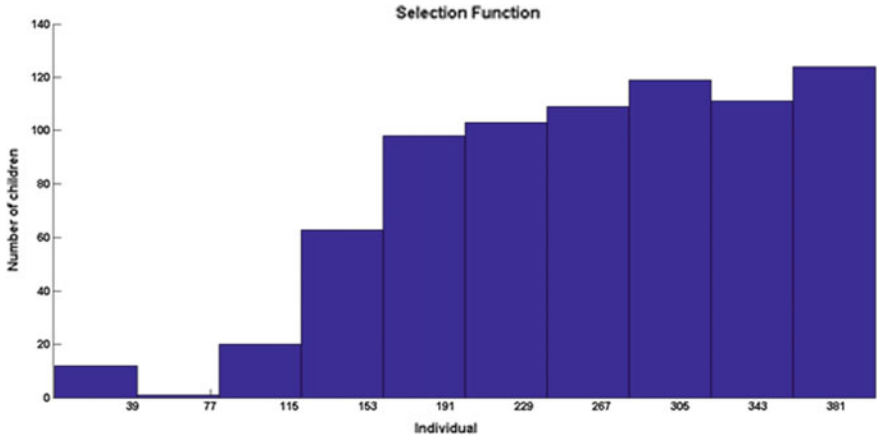

Fig. 7 Selection function

for finding optimum solution in optimum run-time, but crossover fraction does not affect the quality of solution. The result shows that the proposed GA parameters were capable of finding optimum solutions with better quality in optimum run-time.

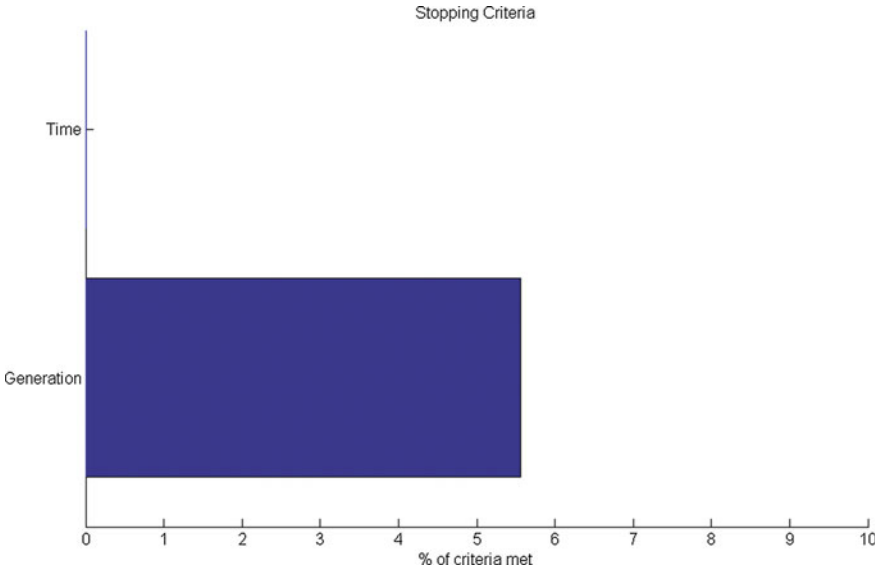

Fig. 8 Stopping criteria

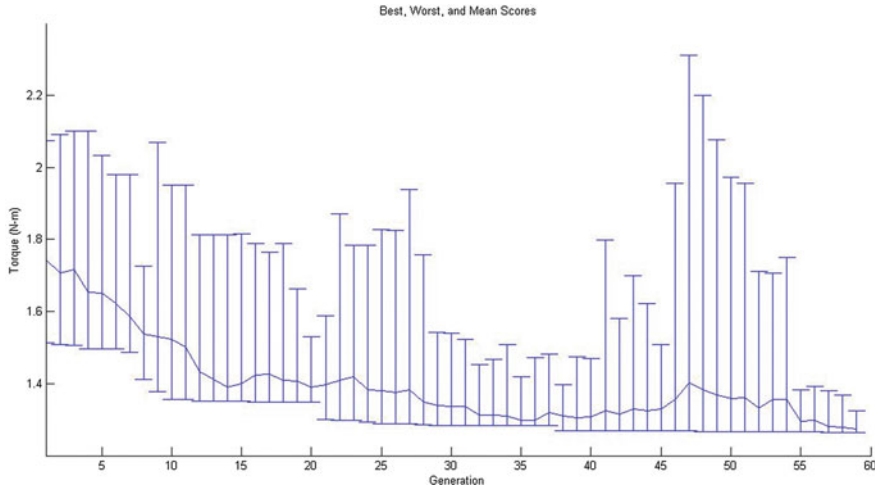

Fig. 9 Range function

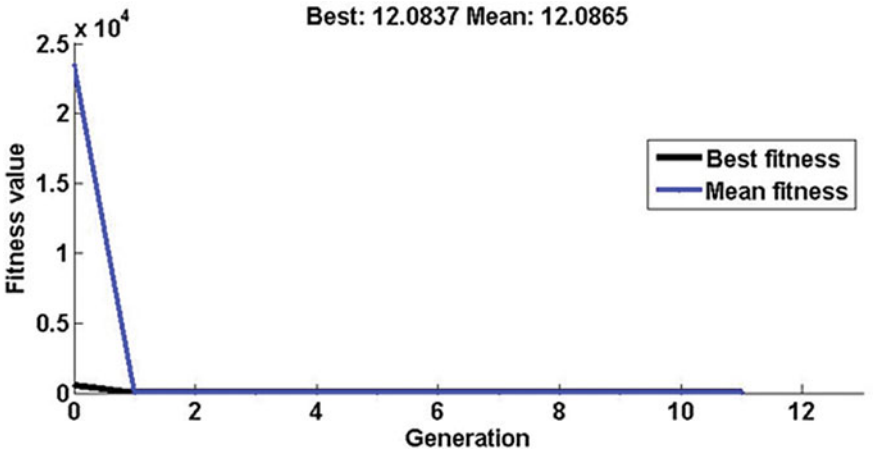

Fig. 10 Fitness function

Table 2 Optimized parameters for minimized torque

Joint no.	Angular displacement (°)	Angular velocities (rad/s)	Angular acceleration (rad/s^2)	Time (s)	Torques (N-m)
1	0.867527	−0.29094	−0.23721		0.19448
2	0.375	−0.35422	−0.50476		−0.01872
3	10.31595	0.312572	0.169414		0.100115
4	0.802879	0.315417	−0.11577		−0.03054
5	6.498761	−0.97359	0.218346	3.766646	0.241311
6	24.2627	0.493939	0.187353		−0.62851
7	24.53314	−0.22274	−0.24416		0.006304
8	54.71407	0.840316	−0.14706		0.019761
9	46.30327	−0.87329	−0.44119		0.002885
10	8.090477	0.826411	0.439089		0.000319

Table 3 Function variables

Best max stall generation	Function count	$f(x)$ = Total torque (N-m)	Constraint
1	10,600	12.3049	0.05901
2	21,000	12.2656	0.0572
3	31,400	12.2195	0.03367
4	50,000	12.0899	0.04271
5	60,400	12.1056	0.0003427
6	86,400	12.1026	0.0005718
7	286,600	12.0868	0.0004051
8	297,000	12.0869	1.153e−05
9	497,200	12.0867	8.142e−06
10	697,400	12.0865	3.667e−06
11	707,800	12.0865	2.477e−07

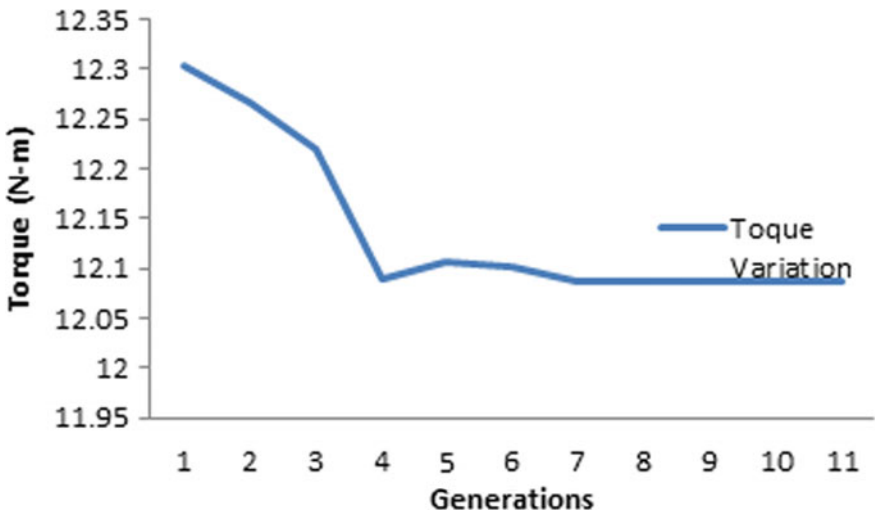

Fig. 11 Torque variation as a function of iterations

Authors' Contributions Anil Kumar Gillawat has designed and written the manuscript of the paper which is a part of Ph.D. work. Hemant Jayantilal Nagarsheth is Ph.D. supervisor and has approved of this research for the paper. The final manuscript was proof read and approved by both authors.

References

1. Yahsi S, Ozgoren K (1984) Minimal joint motion optimization of manipulators with extra degrees of freedom. Mech Mach Theory 19(3):325–330
2. Garg DP, Kumar M (2002) Optimization techniques applied to multiple manipulators for path planning and torque minimization. Eng Appl Artif Intell 15(3):241–252
3. Marcos MG, Machado JAT, Perdicoulis TPA (2009) Trajectory planning of redundant manipulators using genetic algorithms. Commun Nonlinear Sci Numer Simul 14:2858–2869
4. Pires SEJ, de Moura Oliveira PB, Machado JAT (2007) Manipulator trajectory planning using a MOEA. Appl Soft Comput 7(3):659–667
5. Saramagoa SFP, Steffen VJ (1998) Optimization of the trajectory planning of robot manipulators taking into account the dynamics of the system. Mech Mach Theory 33(7):883–894
6. Števo S, Dekan ISM (2014) Optimization of robotic arm trajectory using genetic algorithm. IFAC Proc Volumes 47(3):1748–1753
7. Wu J, Wu H, Song Y, Cheng Y, Zhao W, Wang Y (2016) Genetic algorithm trajectory plan optimization for EAMA: EAST articulated maintenance arm. Fusion Eng Des 109(111):700–706
8. Ata AA, Myo TR (2005) Optimal point-to-point trajectory tracking of redundant manipulators using generalized pattern search. Int J Adv Rob Syst 2(3):239–244
9. Barati M, Khoogar A, Nasirian M (2011) Estimation and calibration of robot link parameters with intelligent techniques. Iran J Electr Electron Eng 7(4):225–234
10. Liu Y, Liang B, Qiang W, Yan-Shu J (2006) Improvement on robots positioning accuracy based on genetic algorithm. In: IMACS multiconference on computational engineering in systems applications (CESA), Beijing, China
11. Davidor Y (1990) Robot programming with a genetic algorithm. In: Proceedings of 1990 IEEE international conference computer systems software engineering (CompEuro '90). IEEE, pp 186–191
12. Nearchou A, Aspragathos N (1996) Application of genetic algorithms to point-to-point motion of redundant manipulators. Mech Mach Theory 31(3):261–270
13. Schultz A (1994) Learning robot behaviors using genetic algorithms. In: Proceedings of the fifth international symposium on robotics and manufacturing: research, education, and applications (ISRAM '94). ASME, pp 14–18
14. Abo-Hammour ZS, Mirza NM, Mirza SM, Arif M (2002) Cartesian path generation of robot manipulators using continuous genetic algorithms. Robot Auton Syst 41(4):179–223
15. Khawaja A, Rahman M, Wagner M (1998) Inverse kinematics of arbitrary robotic manipulators using genetic algorithms. Adv Rob Kinematics Anal Control 375–382
16. Nearchou AC (1998) Solving the inverse kinematics problem of redundant robots operating in complex environments via a modified genetic algorithm. Mech Mach Theory 33(3):273–292
17. Kamali K, Mahmoodinia P, Akbarzadeh TA (2008) A GA optimized bi-level tuning fuzzy controller for a planar 3-RRR parallel manipulator. In: 16th annual (international) conference on mechanical engineering-ISME2008, Kerman, Iran
18. Yun WM, Xi YG (1996) Optimum motion planning in joint space for robots using genetic algorithms. Robot Auton Syst 18(4):373–393
19. Köker R (2011) A neuro-genetic approach to the inverse kinematics solution of robotic manipulators. Sci Res Essays 6(13):2784–2794
20. Roy S, Pratihar DK (2003) A genetic-fuzzy approach for optimal path-planning of a robotic manipulator among static obstacles. J Inst Eng (India) 84:15–22
21. Chaiyarataiia N, Zalzala A (1997) Recent developments in evolutionary and genetic algorithms: theory and applications. In: 2nd international conference on genetic algorithms in engineering systems: innovations and applications, Glasgow, UK
22. Parkar J, Khoogar A, Goldberg D (1989) Inverse kinematics of redundant robots using genetic algorithms. In: IEEE international conference on robotics and automation, pp 271–276
23. Khoogar A, Parker J (1991) Obstacle avoidance of redundant manipulators using genetic algorithm. In: Proceedings of IEEE Southeastcon, pp 317–320

24. Kim JO, Khosla PK (1992) A multi-population genetic algorithm and its application to design of manipulators. In: Proceeding of IEEE/RSJ international workshop on intelligent robots and systems (IROS 92)
25. Doyle A, Jones D (1996) Robot path planning with genetic algorithms. In: 2nd Portuguese conference on automatic control, Porto, Portugal, pp 312–318
26. Kubota N, Fukuda T, Shimojima K (1996) Trajectory planning of cellular manipulator system using virus-evolutionary genetic algorithm. Robot Auton Syst 19:85–94
27. Thomaz CE, Pacheco MAC, Vellasco MMBR (1999) Mobile robot path planning using genetic algorithms. Lecture notes in computer science 1606, pp 671–679
28. Pires SEJ, Machado JAT (1999) A trajectory planner for manipulators using genetic algorithms. In: Proceedings of the 1999 IEEE international symposium on assembly and task planning, 1999, ISATP '99, Porto. IEEE, pp 163–168
29. Pires SEJ, Machado JAT, Oliveira M (2001) An evolutionary approach to robot structure and trajectory optimization. In: ICAR'01-10th international conference on advanced robotics, Budapest, Hungary, pp 333–338
30. Pires SEJ, Oliveira M, Machado PBJAT (2004) Multi-objective genetic manipulator trajectory planner. Applications of evolutionary computing. In: EvoWorkshops 2004. Lecture notes in computer science 3005, pp 219–229
31. Cernic S, Jezierski E, Britos P, Rossi B, Martínez RG (1999) Genetic algorithms applied to robot navigation controller optimization. In: Proceedings of the international conference on intelligent systems and control, Páginas, Santa Bárbara, California, pp 230–234
32. Calafiore G, Indri M, Bona B (2001) Robot dynamic calibration: optimal excitation trajectories and experimental parameter estimation. J Robotic Syst 18(2):55–68
33. Roeva O, Fidanova S, Paprzycki M (2013) Influence of the population size on the genetic algorithm performance in case of cultivation process modelling. In: Federated conference on computer science and information systems, Poland, pp 371–376
34. Razali NM, Geraghty J (2011) Genetic algorithm performance with different selection strategies in solving TSP. In: World Congress on engineering, London, UK, IAENG, pp 1134–1139
35. Ayad A, Awad H, Yassin A (2013) Parametric analysis for genetic algorithms handling parameters. Alexandria Eng J 52(1):99–111

A Low-Cost Cold Chain Suggestion for Indian Fruit and Vegetable

Vardan Parashar, Abid Haleem and J. A. Usmani

Abstract India produces a massive amount of fruit and vegetables. However, the contemporary fruit and vegetable cold chain are not as per the requirements, which lead to a high decay rate and significant constraint for the fruit and vegetable industry. Fruit and vegetables cold chain are a special supply chain, must keep the appropriate low temperature during the processing, storage, transportation, distribution and retail for maintaining the quality and reduce the loss as far as possible. Temperature management is an essential factor to improve the shelf life of perishable products. This paper tries to study the issues faced by the Indian cold chain of fruits and vegetables and further gives low-cost solutions to maintain the low temperature at different stages of the cold chain. The paper discusses different low-cost techniques for controlling the temperature like pre-cooling, ice cooling and free cooling techniques. These are the methods applied to maintain the temperature of food lower than ambient to improve the shelf life.

Keywords Cold chain control · Fruits and vegetables · Shelf life · Temperature control

1 Introduction

After harvesting, the most important thing is to maintain food products at desirable controlled temperature environment during storage and transportation. A substantial loss of shelf life happens during loading and unloading during transportation and warehousing. So, it is imperative to reduce the harvest losses and transportation losses during entire cold supply chain. In India, more than 40% of the total production of food becomes waste from harvesting to the eating plate, and this is mainly just because of the weak cold chain.

Due to lack of cold chain after harvesting and during storage and handling of agriculture crops, occurring high losses are big challenge for small farmers. More

V. Parashar (✉) · A. Haleem · J. A. Usmani
Jamia Millia Islamia, New Delhi, India
e-mail: vardan.parashar@gmail.com

H. Kumar and P. K. Jain (eds.), *Recent Advances in Mechanical Engineering*,
Lecture Notes in Mechanical Engineering,
https://doi.org/10.1007/978-981-15-1071-7_7

than 30% fruits and vegetables wastage become a burden for this community. Result of that retailers struggles to maintain the quality without disturbing the finance of agribusiness in Indian scenario.

Cold chain is an integrated approach, and throughout the distribution network, the important issue is of quality assurance from the point of origin to the point of consumption along with the maintenance of predetermined ambient parameter. The planning, execution, traceability, controls and monitoring play an important role towards maintaining the quality and integrity of the products. The food industry in a developing country like India faces enormous challenges during a cold chain, precisely due to the operational difficulty like economic challenges for refrigeration, and energetic changes of customer need new rules and lower life cycles.

To control the temperature, fruits should be away from out of the sunlight and away from any source of heat, properly ventilated and maintain humidity. During loading, unloading, handling and storage of costly food items, a skill labour requires reducing the wastage. A sustainable cold chain consists of distribution marketing strategy, inventory control, network planning, outsourcing and distribution planning to retain the quality in market.

Due to the limited shelf life of food product, its cold supply chain becomes more difficult as compared to the supply chain of perishable items. There is a need to develop low-cost cold chain logistics in India. A better cold chain provides new method to temperature control along with food quality improvement. Foods stuff are dependent on time and temperature, and they need to be adequately taken care of concerning storing, preparation, packaging, transportation and handling during the cold chain [1]. Fruits in India have a poor cold chain, especially in the local market just because of not only the desired temperature condition but also the lack of awareness of the quality and potency of products. Here fruits and vegetables can be easily visually inspected and sorted by quality appearance.

Adopting suitable low-cost cold chain in Indian scenario has certain issue as lack of infrastructure of transport medium, roads and continuous electric power supply in rural areas. Even farmers are not able to maintain cold chain parameter after having high rates of borrowed money for producing the agriculture crops.

The temperature rise of fruits directly affects its quality, because of the increased microbial growth during respiration and transpiration. It decreases the fruit quality, increases spoilage and the increase of the risk of food poisoning [2]. Loss and damage to perishable goods during storage and transportation are a substantial global issue which can be further reduced by managing the temperature of agriculture products during the supply chain to improve shelf life. Most of the fruits increase in shelf life to provide refrigeration effect, and the same can achieve by some simple tradition techniques as free open-air cooling, ice cooling, cooling by Peltier effect, etc.

2 Need for Cold Chain Logistics

In order to have quality food product with maintain organic parameter, every cold chain parameter must keep in mind from source to consumption point. By receiving and emitting heat, a mass moves from one place to another connected with airflow in the refrigerator system. A significant issue for maintaining the proper cold chain is not only the high cost but also the lack of awareness of desired temperature range during storing, transportation, loading and unloading the fruits in cold chain logistics in India. During transportation, the orientation of food also has high significance for maintaining the desired temperature. To maintain the freshness of food temperature control and time management is also a primary task during the cold chain.

Refrigerated transportation is almost non-existent in rural India. The farmers mostly use open trucks to transport their product, and this leads to a high percentage loss. Indian retail sector has a market of about $180 billion, but the organised sector represents only a 2% share of this market [3, 4]. Temperature and humidity monitoring data play a vital role in identifying product quality risks in the cold supply chain. Understanding the environmental conditions and the product's susceptibility to heat, cold and humidity is required to maintain product quality throughout the cold chain [5].

More than 20% of food gets wasted due to lack of effective cold chain, and this amount is more than the food subsidies provided by the Indian Government. Only post-harvest losses exceed 10% of total food production which is equal to Australia's annual food production. India produces a wide range of fruits and vegetables, but 25% of these wastes is due to wrong handling of these products and does not maintain a desired temperature throughout the entire cold supply chain. As per the IIR, 2009 report, worldwide global food losses are more than 25%. The losses of fruit and vegetable losses exceed 40% in developing country due to lack of refrigeration, infect developed country and maintain the loss of fruits and vegetables up to 15%. To fill this considerable difference, a proper and low-cost logistics cold chain is to be developing in India. Table 1 relates to the technical investment and economically based opportunities during the cold chain of a perishable item. Critical part of food chain includes handling, storing, distribution to cold storage, transport and temperature control warehousing, retail marketing and food service operations are to be processed and monitored. The cold chain is to plan, execute and manage the desired temperature of products to reduce the waste by proper handling and storing [6].

A temperature maintain supply chain (cold chain) is to be used for decrease the losses after harvesting of fruits and vegetables. The improved cold chain can be developed by identifying the issue and challenges during storing, transport, retailing and final consumption. Strategies required for planning and implementation develop an economic, improved and develop a practical, low-cost cold chain for domestic users. Essential to building a fresh system, farmers can afford and operate in an area far away from the city, processing fruits and vegetables at low temperature after harvest. In order to follow the transportation of domestic fruits and vegetables, the need is to speed up the researchers in the new direction of application of energy and

Table 1 Predicted shelf life of perishable at optimum temperature

Food product	Storage potential			
	At an optimum cold temperature	Optimum temperature + 10 °C	Optimum temperature + 10 °C	Optimum temperature + 10 °C
Fresh green vegetables	1 Month at 0 °C	Two weeks at 10 °C	One week at 20 °C	Less than two days at 30 °C
Potatoes	5–10 months at 4–12 °C	Less than two months at 22 °C	Less than one month at 32 °C	Less than two weeks at 42 °C
Mangoes	2–3 weeks at 13 °C	One week at 23 °C	Four days at 33 °C	Two days at 43 °C
Apples	3–6 months at 1 °C	Two months at 10 °C	One month at 20 °C	A few weeks at 30 °C

Source DGCIS Annual Export [7]

develop user-friendly and low-cost refrigerated technology. The government should provide support in policies and develop a better cold chain of fruits and vegetables.

3 Temperature Management in Food Cold Chain

As same to control the temperature of food products for having the improved shelf life, management and monitoring also play an essential role for the better cold supply chain. Lack of maintaining the recommended proper temperature is the cause for rusting and crumbling of fresh fruits. Strongly recommend maintaining the proper temperature for fresh fruits having potency and maintaining freshness also [8]. The preferable condition for storage of food items varies concern temperature requirement of different foods. Even temperature variation for a short period affects the shelf life and decreases the quality. For avoiding such condition, management of temperature range is done carefully after harvesting, storing and transportation [9].

Temperature management is an important factor for supply of fruits and vegetables because color, taste and potency of fruits and vegetables are depends on it [10]. Different products during cold chain after harvesting to final consumption have different preferable temperature range. Table 2 shows predetermined temperature environment during storage and transportation for fruits and vegetables.

All the types of perishable food with different temperature control should be maintained from the point of supply to the point of consumption, through the process of storage and distribution. The freshness and safety of food must be maintained by the value and quality to make happy to customers. Table 2 shows preferable temperature condition for vegetables and fruits. Thus, it is necessary to have suitable storage temperature in the cold chain.

Different temperature standard levels to endure the quality during the cold chain are “cool” (13 °C), “chill” (2 °C), “frozen” (−18 °C) and “deep frozen” (−29 °C),

Table 2 Preferable temperature condition for vegetables and fruits

1–4 °C	5–9 °C	More than 10 °C
Apple	Bean (French)	Lemon
Berry fruits	Black grapes	Fruit mango
Cheery	Capsicum	Pineapple
Grape	Cucumber	Potato, tomato
Broccoli	Mandarin, orange	Banana
Mushroom	Potato	Pumpkin

Source Zhang [3]. Cold chain management

each related to specific product groups. Any diversity will cause high damage; product result loses market value or utility [11].

4 Methods to Develop a Low-Cost Cold Chain

To develop an improved cold chain, following methods can help the farmer, retailer and the consumer to improve and sustain the shelf life of food with the help of cold chain so to improve the potency and quality. By pre-cooling, a farmer can choose the simple method for agriculture crops to reducing temperature such as using direct ice or flow the cool air from an open chamber, wash the crops by running water time to time (If recommended), by forced air flow, hydro-cooling and vacuum cooling. Few more advanced techniques for refrigeration effect can produce by a chamber for the free cooling process to control the temperature and humidity through Peltier effect and any other methods. For storage and transport, options are small cold room and large-scale commercial refrigerator warehouse. They are most commonly used for costly products but are not able to use for products having meagre cost like fruits and vegetables. Some low-cost conditioning techniques can use for small cooling units with the help of chillers, blast freezing, dry ice, gel packs, eutectic plates, etc.

Cold chain logistics can use information management system to ensure the quality, increase costumer satisfaction and improve integrity and transportation of products in the right direction. Relevant information about control temperature leads to initiate new researcher to develop the low-cost technology of cold chain logistics. Radio-frequency identification (RFID) technology is a monitoring system for cold chain logistics to trace the vehicle during transportation of perishable products. This system is developed and implemented to identify all location of the moving vehicle of interest and continue the supply without a break. Supportive policies in finance and taxation need to be introduced and effective implementation be supported. Local government should plan the rules and see that the technique is appropriate for the particular type of fruit or vegetable. Demand, supply and market order can be developing on the same platform to have transmissibility in the cold chain by local government.

5 Providing Temperature Controlled Environments

The success of the cold chain depends on the methods adopted for temperature control during transportation and storing. Temperature requirements in cold chain vary from −10 °C to 12 °C for different types of fruits (and vegetables) to maintain the improved shelf life. The integrity of the product also plays an important role to maintain the potency of fruits. The integrity of fruits should also be maintained during the packaging of food.

Dry ice (solid carbon dioxide) has a temperature of about −80 °C and used for freezing the food environment for extended periods of storing especially for storing pharmaceuticals items. The phase change of products during transportation can maintain the required temperature by gel packs that maintain the temperature between 2 °C and 8 °C. Refrigeration effect produces for a short period by Eutectic plates.

Liquid nitrogen is used at about −196 °C, to keep package store frozen for long period of time. The cell is storing products for an extended period at a liquid nitrogen environment. During summer and winter, insulated pieces are placed to maintain the temperature constant. To maintain the proper air circulation, a 15 cm clearance must be provided between the fruit palates. Convection heat by fruits also causes an increase in temperature of cargo. Solar energy and another ambient parameter may also increase the temperature of cargo. So, proper cold air circulation should be maintained to reduce the heat generation inside the cargo during transportation of fruits and other food stuff.

6 Results and Discussion and Future Course of Action

Farmers and small mandi retailers are the major part of Indian population deals with agriculture product, and they cannot afford the traditional cooling method to maintain the suitable cold chain. They are only dependent on the low-cost cold chain methods like evaporative coolers, cool chambers, cooling by phase change materials and economically developed temperature controlling methods. If these temperature control low-cost cold chain techniques will be adopted by the major rural population, then it will affect to reduce the rate of waste agriculture products and support the farmers and small retailers to stable financially also [12, 13].

In this paper, we have identified the present scenario of the cold chain for food stuff in India. We identified that high loss of agriculture product is because of not maintaining the desirable temperature environment. Losses can somewhat be contained by using low-cost temperature control techniques and educating the domestic retailer and user towards the maintenance of desired temperature range during storing, packaging and transportation throughout the cold chain. As traditional techniques (AC/Refrigirator/Deep Frizer) cannot be used by local retailers so they need a low cost technique for cooling of their agriculture products.

7 Conclusion

India is having a long cold chain in food export in world. The export of fruit and vegetable in India and consumption in India are also on a vast level. As discussed in previous literature that very high losses of fruits and vegetables have in India due to lack of cold chain so it is essential to improve the cold chain for Indian economic development. This paper discusses the benefits of maintaining the better cold chain especially temperature range to reduce the wastage and improve the shelf life of fruits and vegetables. It is necessary to maintain a better cold chain to increase export volume, quality of fruits and increase shelf life from source to origin to consumption.

Thus, it is tough to develop low-cost and appropriate cold chain to reduce the losses and improve efficiency. We are proposing controlling the losses of fruits and vegetables by applying the different low-cost techniques for temperature control and refrigeration. This reduction in the loss of food products helps the agricultural economy of India and supports the fruit and vegetable industry.

References

1. Myo Min Aung (2014) Temperature management for the quality assurance of a perishable food supply chain. Food Control 40:198–207
2. Carullo A, Corbellini S, Parvis M, Reyneri LL, Vallan A (2009) A wireless sensor network for cold-chain monitoring. IEEE Trans Instrum Meas 58(5):1405–1411 (Vancouver, Canada)
3. Zhang L (2007) Cold chain management. Master's thesis. Cranfield University, Cranfield
4. Likar K, Jevsnik M (2006) Cold chain maintaining in food trade. Food Control 17:108
5. Kohli P (2010) Future of cold chain—India
6. Alimentarius C (1999) Code of hygienic practice for refrigerated packaged foods with extended shelf life. CAC/RCP 46:1999
7. DGCIS Annual Export (2017–2018) APEDA agri exchange—annual report
8. Abad E, Palacio F, Nuin M, Zárate GD, Juarros A, Gómez JM et al (2009) RFID smart tag for traceability and cold chain monitoring of foods: demonstration in an intercontinental fresh fish logistic chain. J Food Eng 93(4):394–399
9. Jobling J (2000) Temperature management is essential for maintaining product quality. Good Fruit Veg Mag 10(10):30–31
10. Jedermann R, Edmond JP, Lang W (2007) Shelf life prediction by intelligent RFID. In: Haasis HD, Kreowski HJ, Scholz-Reiter B (eds) Dynamics in logistics. First international conference, LDIC 2007 Bremen, Germany. Springer, Berlin, pp 231–238
11. Rodrigue J-P, Notteboom T (1998–2016) The cold chain and its logistics. Department of Global Study and Geography, Hofstra University, New York
12. Rais M, Sheoran A (2015) Scope of supply chain management in fruits and vegetables in India. J Food Process Technol 6:427
13. Shukla M, Jharkharia S (2013) Agri-fresh produce supply chain management: a state-of-the-artliterature review. Int J Oper Produc Manag 33(2):114–158

Optimization of Cutting Parameters of Machinability Aspects During Dry Turning

Anurag Sharma, R. C. Singh and Ranganath M. Singari

Abstract New research and development in the field of difficult to machine materials and high speed machining for less time manufacturing require optimization. The presented study deals with an application of Taguchi parameter and regression analysis for optimizing machining parameters during turning of AISI D3 steel alloy. L9[OA] orthogonal array with three parameters (speed, feed and depth of cut) has been used during performing experiments in dry machining condition. Machinability aspects like coefficient of friction, machining time and cutting temperature have been evaluated for optimization on *S*/*N* ratio as lower the better characteristic. Analysis of variance ANOVA is used for determining the effect of contribution in terms of percentage regarding each machining parameter with error. Predicted values have been verified by performing confirmation experimental run. The values evaluated are within error limits. Chip thickness has been measured for calculating chip compression ratio. The chips have been found continuous, long and coiled.

Keywords Dry turning · Optimization · ANOVA · Cutting inserts

1 Introduction

Hard turning is designated in the category of turning materials with hardness in the range of 45–65 HRC and usually performed during dry condition without any application of coolant or cutting fluid [1]. This is eco-friendly and cost-effective. The chips created are free from oil or any subsequent material of cutting fluids. This can be readily used as safe scrape for remelting formation of workpiece material [1, 2]. High chromium tool steel alloy AISI D3 with HRC 60 is used in manufacturing blanking and forming dies, forming tools, press tools, punches, bushes and wear-resistant moulds. It is categorized as difficult to machine materials. Machining parameters to be followed are cutting speed 30–260 m/min, feed 0.05–0.15 mm/rev and depth of cut

A. Sharma (✉) · R. C. Singh · R. M. Singari
Department of Mechanical Engineering, Delhi Technological University, New Delhi, Delhi 110042, India
e-mail: mtechanurag@gmail.com

H. Kumar and P. K. Jain (eds.), *Recent Advances in Mechanical Engineering*,
Lecture Notes in Mechanical Engineering,
https://doi.org/10.1007/978-981-15-1071-7_8

0.2–0.5 mm [2]. In 1970, polycrystalline cubic boron nitride (c-BN) was introduced in the category of cutting tool material. Presently coated with TiN is favourable in machining hardened steel alloys. The coating on cutting tool material extends to life and increases material removal rate [3].

1.1 Optimization

Machining process consists of various cutting parameters for a definite combination of cutting tool and workpiece. Taguchi technique was discovered in 1950 by Genichi Taguchi. It is based on (*S*/*N*) ratio signal-to-noise. It minimizes the practice of hit and trial for selecting the best combination of controlled factors (cutting parameters in machining) for the better conditional output of machining properties. It is one of the reliable approach for optimization practised by researchers and presented in various collected literature work [3–5]. Dureja et al. [3] used Taguchi *S*/*N* ratio for determining optimized levels of machining parameters in hard turning of AISI D3 cold working tool steel alloy for surface roughness and tool wear. Chips show machining condition and an indication of cutting parameters. Segmented chips are created at a low cutting speed, feed and depth of cut while on increasing cutting parameters the chips become continuous, long and coiled in dry turning [4]. Gupta et al. [5] used optimization for finding out cutting parameters having combined joint 50% contribution of (R_a) surface roughness and 50% contribution of (F_c) cutting forces in turning of steel alloy of AISI 4 340. Mandal et al. [6, 7] made ceramic material cutting inserts of zirconia toughened alumina in the dry turning of AISI 4340 steel alloy for finding out optimized cutting parameters of surface roughness and tool wear and developed regression model. Durkbasa et al. [8] found out optimized cutting parameters using Taguchi *S*/*N* ratio for hot working hardened steel AISI H13. Further supported by ANOVA analysis of variance to calculate significant value and percentage of contribution of cutting parameter and error in the model. High-alloy white cast iron and different types of steel alloy (EN 19, AISI 304 and AISIP20) have been optimized by researchers to find out optimum level of cutting parameters to save power, economy and wastage of time in trying hit and trial method to achieve better results in limited resource and time period [9–12]. Viswanathan et al. [13] used optimization process for achieving cutting parameters for magnesium alloy for surface roughness, cutting forces, tool wear and cutting temperature using grey analysis. Long continuous chips, especially of ductile materials created during turning may damage surface finish by rubbing or passing over the workpiece. Chip breaker was designed by Bahattin Yilmaz et al. to solve the problem of long chips by breaking at short length. This improved surface finish and cutting temperature. Optimization of machining parameters was performed with chip breaker and without chip breaker [14].

Review of research work shows lot of scope and future work with optimization of cutting parameters with different types of machinability aspects, workpiece material, tool material and machining conditions. In presented research investigations,

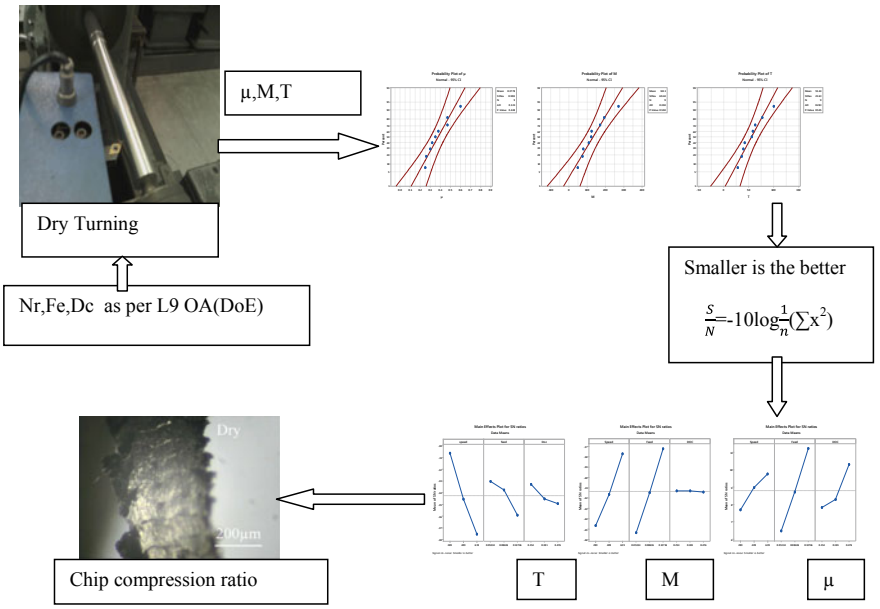

Fig. 1 Workflow diagram under dry turning. μ—Coefficient of friction, M—Machining time, s, T—Cutting temperature, °C, N_r—Cutting speed, rpm, F_e—Feed, mm/rev, D_c—Depth of cut, mm, R_a—Surface roughness, F_c—Cutting force

an attempt has been made to measure the coefficient of friction, machining time and cutting temperature in dry turning of (AISI D3) cold worked steel alloy with titanium nitrate-coated tungsten carbide cutting inserts. Optimization of machining parameters has been performed with the regression model and confirmatory tests (Fig. 1).

2 Experimentation

2.1 Workpiece and Cutting Inserts Material

AISI D_3 material has been used in the shape of circular bar of dimensions 28 mm (diameter) and 300 mm (length). The composition of material was according to the specified range of percentage of elements examined through chemical testing of a sample as shown in Table 1.

Cutting inserts have been used in the shape of diamond of tungsten carbide coated with titanium nitride of thickness 4 mm, end relief angle 11°, front rake angle 0°, nose radius 8 mm of specification as DCMT11T308HQ grade PV 20 with left-hand cutting tool holder of a square face of 12 mm and length 80 mm. The sample of

Table 1 Chemical composition of $AISID_3$ steel

C	Si	Mn	S	P	Cr	Ni	Mo	Co	Nb	V	W	Fe
2.02	0.259	0.430	0.029	0.020	11.00	0.074	<0.10	0.011	0.023	0.038	0.087	85.909

Table 2 Chemical composition of cutting inserts

C	Co	Mn	V	Nb	Ni	W	Mo	Ti
7.10	16.25	0.30	2.05	5.23	4.95	15.88	0.69	47.55

cutting tool insert was examined chemically for checking for the composition of percentage of elements as shown in Table 2.

2.2 Design of Experiments (DOE)

Taguchi approach was used in the design of experiments (DOE). L9 array was made for calculating optimum surface roughness, machining time and coefficient of friction in dry turning. It used the signal-to-noise (*S*/*N*) ratio as the function for three categories, higher is better, lower is better, nominal is better, and smaller is better. Finally, smaller is better has been used during analysis.

3 Experimental Results and Discussion

3.1 Probability Analysis

Experiments were performed as per DOE. Cutting parameters with controlled three levels were selected as shown in Table 3 for dry turning. The experimental results were plotted in the probability distribution graph as shown in Fig. 2 for responses of (a) coefficient of friction, (b) machining time and (c) temperature at the interface of cutting insert and workpiece at the confidence level of 95%. Each plot shows mean value of the response, standard deviation (StDev), the number of experiments (*N*), Anderson–Darling value (AD) and *P*-value [15]. Figure 2 shows that response experimental values are approximately aligned with the intermediate straight line, *P*-value is more than 0.01 and value of (AD) is low. They evidently show and comprehensively prove that data are normally distributed. This is applied for the usage in further analysis and interpretation.

Table 3 Machining parameters with different levels of value

Levels	Machining parameters		
	N_r	F_e	D_c
Level 1	289	0.05334	0.254
Level 2	409	0.08636	0.381
Level 3	639	0.13716	0.476

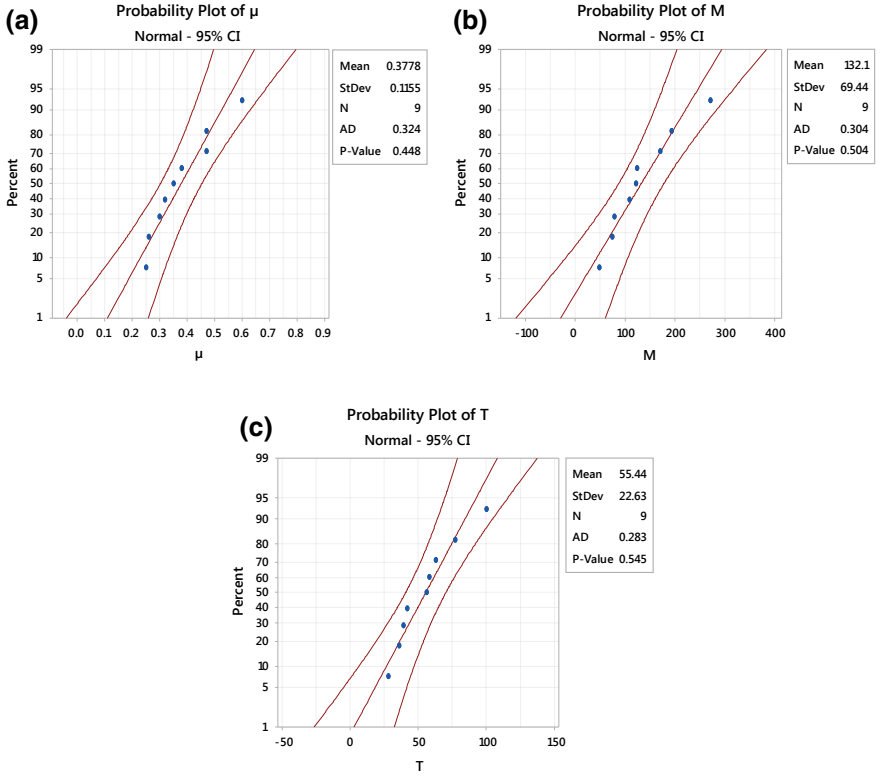

Fig. 2 Probability plot for **a** coefficient of friction, **b** machining time and **c** temperature at interface of cutting insert and workpiece in dry turning

3.2 Optimization Based on Taguchi S/N

The optimization based on Taguchi *S*/*N* (ratio) involves reduction in variability and alignment of mean value to target value [15]. In any process, variability may arise due to factors having no control are termed as uncontrollable factor or noise. The expected value of the response is termed as target or signal. *S*/*N* is the ratio of expected target values to unexpected noise [5, 15].

Smaller is the better characteristic,

$$\frac{S}{N} = -10 \log \frac{1}{n} (\Sigma x^2) \tag{1}$$

is further supported by ANOVA table has a sum of square parameters, *F*-values, *P*-value and percentage of contribution. The *P*-value is defined for a significance level of five percentage {i.e. the confidence interval of 95% for all responses}. Symbolic and unsymbolic values of factors have been shown in Table 4 according to L9

Table 4 L9 Taguchi orthogonal array

Run	Symbolic values factors (conventional)			Unsymbolic values factors (experimental)		
	N_r	F_e	D_c	N_r	F_e	D_c
1	1	1	1	289	0.05334	0.254
2	1	2	2	289	0.08636	0.381
3	1	3	3	289	0.13716	0.476
4	2	1	2	409	0.05334	0.381
5	2	2	3	409	0.08636	0.476
6	2	3	1	409	0.13716	0.254
7	3	1	3	639	0.05334	0.476
8	3	2	1	639	0.08636	0.254
9	3	3	2	639	0.13716	0.381

Table 5 Signal-to-noise ratios for investigated parameters

Run	Responses			*S*/*N* (dB) values of responses		
	μ_1	M_1	T_1	μ_1	M_1	T_1
1	0.60	271.10	28	4.437	−48.662	−28.943
2	0.47	170.65	36	6.558	−44.608	−31.126
3	0.25	108.52	39	12.041	−40.668	−38.821
4	0.47	192.78	42	6.558	−45.666	−32.465
5	0.30	123.96	58	10.458	−41.865	−35.269
6	0.32	73.85	63	9.897	−37.367	−35.987
7	0.38	121.45	77	8.404	−41.68	−37.73
8	0.35	78.75	56	9.119	−37.925	−34.964
9	0.26	47.78	100	11.701	−33.584	−40.000

orthogonal array (design of experiments). The responses with calculated *S*/*N* values are depicted in Table 5.

3.3 Coefficient of Friction

Friction exhibits tool life and surface integrity of the machined workpiece. The increasing coefficient of friction during turning shows the corresponding increment of cutting forces and temperature at the interface of cutting insert and workpiece. This is a vital combination affecting surface topography and tool behaviour [16].

$$\text{Coefficient of friction } (\mu) = \frac{F_c \sin\alpha + F_t \cos\alpha}{F_c \cos\alpha - F_t \sin\alpha} \tag{2}$$

where α is orthogonal rake angle, F_c is the main cutting force, and F_t represents the thrust forces. F_t is calculated with Eq. (5)

$$F_t = \sqrt{F_r^2 + F_f^2} \tag{3}$$

where F_r and F_t represent the radial and feed force.

Figure 3 shows the mean effects plot for the mean of *S*/*N* ratios for coefficient friction μ for cryogenic turning, respectively, with speed, feed and depth of cut. On incrementing speed, feed and depth of cut, mean of *S*/*N* ratio values of coefficient of friction has been correspondingly rising. Cutting parameters optimized at highest values of *S*/*N* ratio at (level 3, speed 639 rpm), (level 3, feed 0.13716 mm/rev) and (level 3 depth of cut 0.476 mm) for the coefficient of friction are shown in Table 6. Delta shows the difference between the maximum and minimum response of *S*/*N* ratio for each cutting parameters. Rank shows the order of priority between the

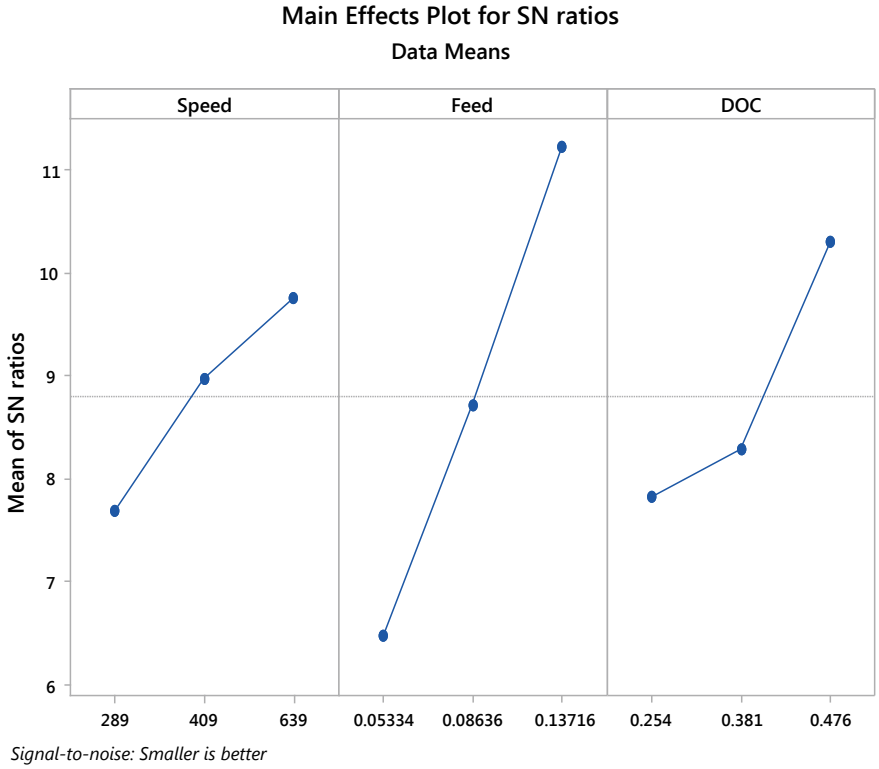

Fig. 3 Main effects plot for mean *S*/*N* ratios for the coefficient of friction (μ)

Table 6 Response table for coefficient of friction (μ), machining time (M) and cutting time (T) for S/N ratio

Response	Level	N_r	F_e	D_c
μ	1	7.679	6.466	7.818
	2	8.971	8.711	8.272
	3	**9.741**	**11.213**	**10.301**
	Delta	2.062	4.746	2.483
	Rank	3	1	2
M	1	−44.67	−45.35	−41.32
	2	−41.64	−41.48	**−41.31**
	3	**−37.73**	**−37.22**	−41.42
	Delta	6.94	8.13	0.11
	Rank	2	1	3
T	1	**−30.63**	**−33.05**	**−33.30**
	2	−34.57	−33.79	−34.53
	3	−37.56	−35.94	−34.94
	Delta	6.93	2.89	1.64
	Rank	1	2	3

parameters [7]. The smallest coefficient of friction and its S/N ratio can be calculated by using Eqs. (4) and (5). The predicted coefficient of friction and S/N ratio has been obtained as 0.21 and 13.661, respectively. In these equations, d_p is the average S/N ratios of all variables, d_p is the calculated response, N_o is the average S/N ratio when variable N (speed) is at optimum level, F_o is the average S/N ratio when variable F (feed) is at optimum level, and D_o is the average S/N ratio when variable D (depth of cut) is at optimum level, A_p is predicted responses (i.e. coefficient of friction, machining time and cutting temperature). ANOVA Table 7 shows that P-value is insignificant for values of coefficient of friction at speed, feed and depth of cut. P-value is significant if it is less than 0.05 at 95% level of confidence. F-value shows the level of importance of parameters. Feed shows the maximum value of 24.45. The percentage of contribution has been calculated, feed has maximum percentage of contribution at 64.78%, next higher percentage of contribution is at depth of cut 23.65% and next higher percentage of speed at 12.47%.

$$d_p = \overline{d_p} + (\overline{N_o} - \overline{d_p}) + (\overline{F_o} - \overline{d_p}) + (\overline{D_o} - \overline{d_p}) \tag{4}$$

$$A_p = 10^{-d_p/20} \tag{5}$$

Table 7 Analysis of variance for means of coefficient of friction (μ), machining time (M) and cutting time (T) for S/N ratio

Response	Source	DF	Adj SS	Adj MS	F-value	P-value	% Cont.
μ	N_r	2	6.518	3.2591	04.71	0.175	12.47
	F_e	2	33.829	16.9145	24.45	0.039	**64.78**
	D_c	2	10.489	05.2446	07.58	0.117	20.65
	Error	2	1.383	0.6917	–	–	2.65
	Total	8	52.220	–	–	–	100.00
M	N_r	2	72.099	36.0494	1118.94	0.001	42.05
	F_e	2	99.269	49.6346	1540.61	0.001	**57.90**
	D_c	2	0.023	0.0117	0.36	0.733	0.01
	Error	2	0.064	0.0322	–	–	0.04
	Total	8	171.456	–	–	–	100.00
T	N_r	2	32.712	16.3558	45.08	0.022	30.80
	F_e	2	47.929	23.9643	66.05	0.015	**45.13**
	D_c	2	24.846	12.4230	34.24	0.028	23.39
	Error	2	0.726	0.3628	–	–	0.68
	Total	8	106.213	–	–	–	100.00

3.4 Machining Time

Machining time has been calculated in seconds as time measured between the start of cut and end of cut for every cutting parameter. Figure 4 depicts the main effects plot for mean S/N ratios for machining time. On increasing, speed and feed S/N ratio have been raised but with increasing depth of cut S/N ratio has been declined marginally. From Table 7, machining time has been optimized at highest level of S/N ratio at (level 3, speed 639 rpm), (level 3, feed 0.13716 mm/rev) and (level 2, depth of cut 0.381 mm). Depth of cut has been given less importance. By using Eqs. (4) and (5), S/N ratio of predicted response machining time at optimized level is 1.6793 and predicted response value is 47.86 s. ANOVA Table 7 shows P-value is significant if less than 0.05. Speed and feed are significant at P-value 0.001, respectively. F-value shows the importance of cutting parameters with maximum value for feed. The percentage of contribution has been calculated for each cutting parameter. Feed has the maximum percentage of contribution at 57.90%, next higher percentage of contribution is at speed 42.05%, and next higher contribution is at depth of cut at 0.01%.

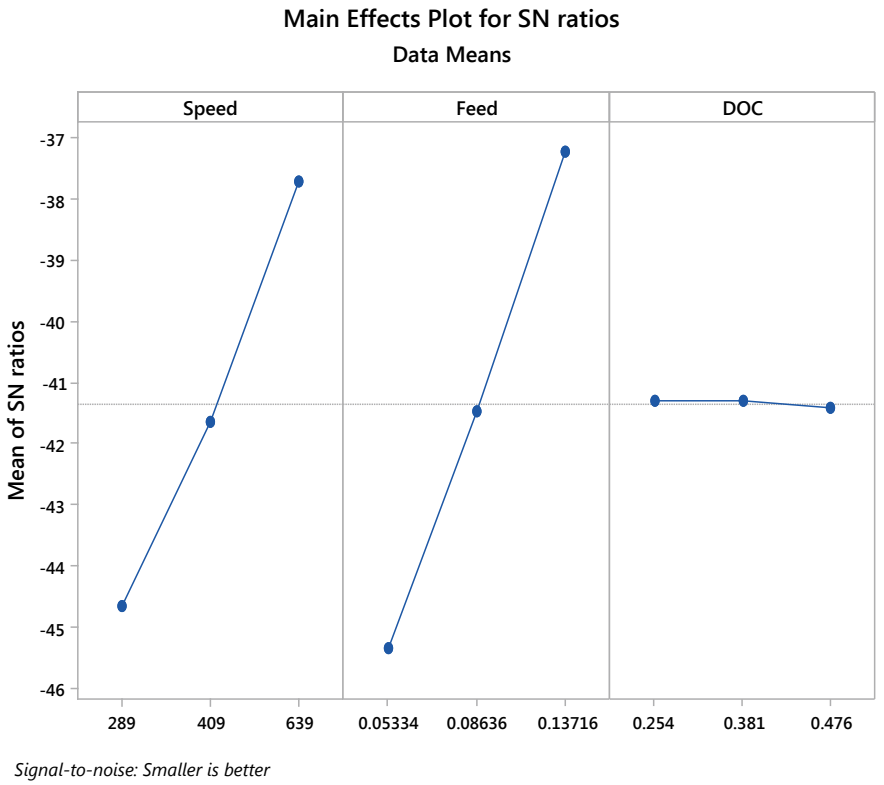

Fig. 4 Main effects plot for mean *S*/*N* ratios *M*

3.5 Cutting Temperature

Cutting temperature has been measured in degree celsius at the end of turning operation of each experiment as per L9 DoE. Figure 5 shows the main effects plot for mean *S*/*N* ratios of temperature. It is evident that with an increment of levels of cutting parameters (speed, feed and depth of cut), mean *S*/*N* ratio of temperature declined. From Table 6, it has been shown that cutting parameters optimized at (level 1, speed 289 rpm), (level 1, feed 0.05334 mm/rev) and (level 1, depth of cut 0.254 mm). Depth of cut shows less rank as per the order of priority. By using Eqs. (4) and (5), the *S*/*N* ratio of predicted response cutting temperature at optimized level 1.35 and predicted response value is 25.12 °C. ANOVA Table 7 shows that *P*-value is significant for speed and feed and depth of cut. *F*-value is maximum for feed. The percentage of contribution of percentage has been calculated and found that feed has maximum contribution at 45.13%, next higher contribution of speed at 30.80% and next higher contribution of depth of cut at 23.39%.

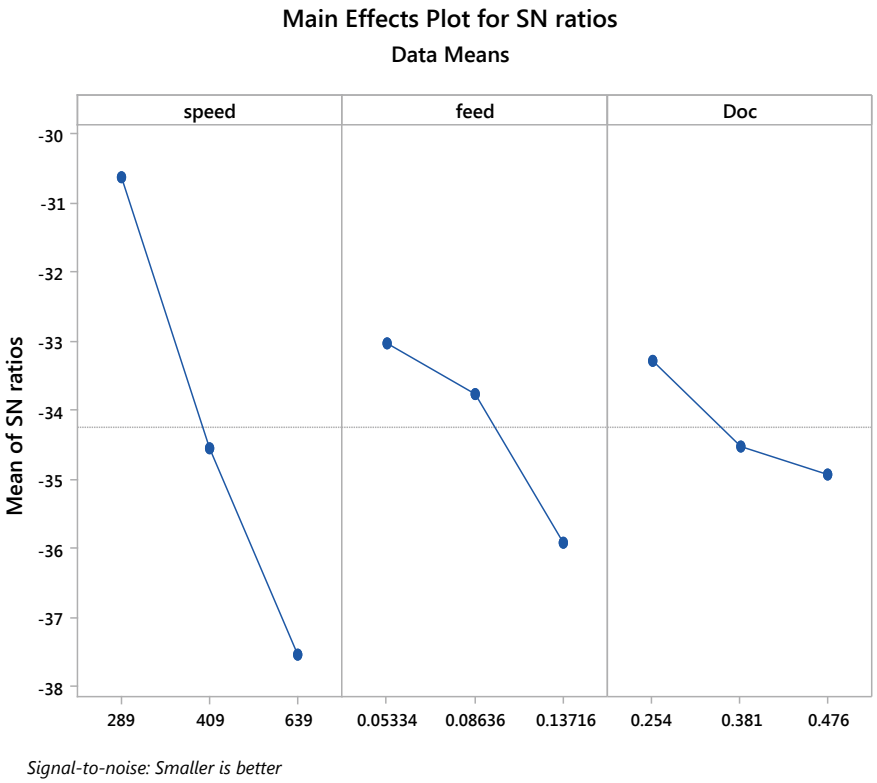

Fig. 5 Main effects plot for mean *S*/*N* ratios *T*

3.6 Confirmation Experiment

Optimized level of cutting parameters for each response has been performed on the machine, and the experimental value has been recorded. The values are in good agreement within in the range of error limit. Table 8 shows the predicted value of the coefficient of friction as 0.21 and experimental value as 0.20 at optimum level of (level 3, speed 639 rpm), (level 3 feed 0.13716 mm/rev) and (level 3 depth of cut

Table 8 Comparison between predicted optimum responses and experimental confirmatory values

Response	Control factors in dry turning			Predicted value	Confirmation test value	Range of % error
	N_r	F_e	D_c			
μ	639	0.13716	0.476	0.21	0.20	2.65
M	639	0.13716	0.381	47.86 s	47.85 s	0.04
T	289	0.05334	0.254	25.12 °C	25.00 °C	0.68

Table 9 .

	Regression models	*R*-Sq (%)
	Dry turning	
μ	0.9134 − 0.00029222 × (Speed) − 2.418 × (Feed) − 0.493 × (Depth of cut)	90.64
M	419.6 − 0.2771 × (Speed) − 1373 × (Feed) − 100.8 × (Depth of cut)	91.98
T	−35.4 + 0.1208 × (Speed) + 229 × (Feed) + 42.8 × (Depth of cut)	84.67

0.476 mm). The percentage of error by the ANOVA model is 2.65%. The predicted value of machining time is 47.86 s and experimental value is 47.85 s at optimum level of (level 3 speed 639 rpm), (level 3, feed 0.13716 mm/rev) and (level 2 depth of cut 0.381 mm). The percentage of error calculated by ANOVA model is 0.04%. Predicted value of response of cutting temperature is 25.12 °C and experimental value is 25.00 °C at optimum level (level 1 speed 289 rpm), (level 1 feed 0.05334 mm/rev) and (level 1 depth of cut 0.254 mm). The percentage of error calculated by ANOVA model is 0.68%.

3.7 Development of Regression Models

Regression models have been made for each response, i.e. coefficient of friction, machining time and cutting temperature. The value of *R*-square is 90.64% for coefficient of friction, 91.98% for machining time and 84.67% for cutting temperature as shown in Table 9. The models are having efficiency from more than 84–92% which are in good agreement with predicted and experimental values.

3.8 Chip Compression Ratio

Deformed chip thickness ratio to undeformed chip thickness is defined as chip compression ratio by utilizing Eq. (6).

$$\text{Chip compression ratio (CR)} = \frac{t_\text{d}}{t_\text{u}} \tag{6}$$

The undeformed chip thickness was calculated by using Eq. (7).

$$t_\text{u} = F_\text{e} \sin \phi \tag{7}$$

where ϕ is the angle of approach angle of the cutting tool, and F_e is the feed measured in mm/rev.

The chips have been collected during dry turning measured by an optical microscope for a particular chip at five distinct locations, and the average has been calculated for a final reported value of chip thickness. From Fig. 6, chip compression ratio is above one and between 2.1 and 2.8 for the experimental run in turning as per L9 DoE. It shows adhesion between the cutting tool and chip. Chip compression ratio exhibits tool wear and friction between the cutting tool and workpiece [1]. Generally, the chip compression ratio declined with increment in cutting speed at constant feed and depth of cut [17–19]. From Fig. 7a Optical images of chip at speed in 289 rpm, feed 0.05334 mm/rev and depth of cut 0.254 mm and (b) speed 639 rpm, feed 0.13716 mm/rev and depth of cut 0.381 mm. Chips created are continuous and

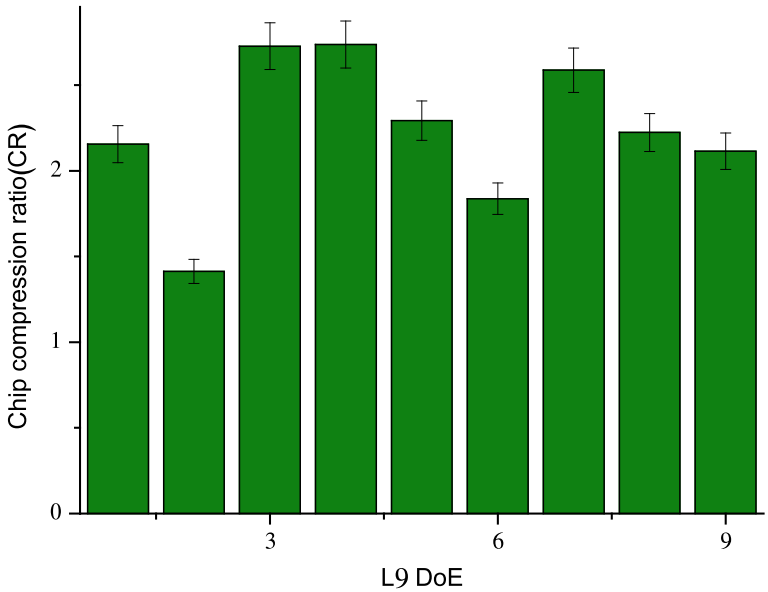

Fig. 6 Chip compression ratio (CR)

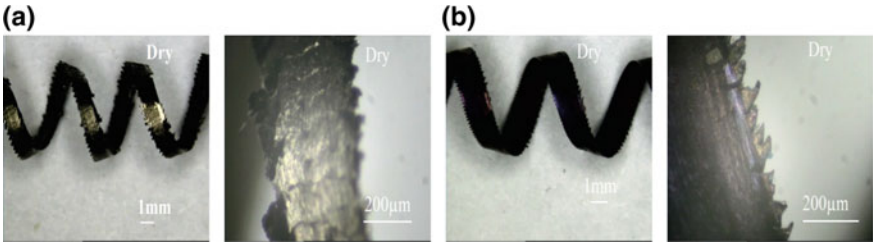

Fig. 7 **a** Optical images of the chip at speed in 289 rpm, feed 0.05334 mm/rev and depth of cut 0.254 mm and **b** speed 639 rpm, feed 0.13716 mm/rev and depth of cut 0.381 mm

coiled. On incrementing cutting parameters, chips have increased in thickness and colour of chips changed to dark violet due to tempering. This may be due to the rise in cutting temperature in dry turning.

4 Conclusions

Optimization of machinability aspects (coefficient of friction, machining time and cutting temperature) has been done by using Taguchi-based *S*/*N* ratio. The workpiece material was AISI D3 and TiN-coated cutting inserts. The experiment was performed in dry machining condition. Probability distribution was checked for each machinability aspect before any further analysis. ANOVA was used for measuring percentage of contribution of cutting parameter and error. Regression model was developed. Confirmation tests were conducted for checking predicted values of responses at optimum cutting parameters. Concluding remarks based on mentioned work are as follows:

1. Optimization of cutting parameters for coefficient of friction is at (level 3, speed 639 rpm), (level 3, feed 0.13716 mm/rev), (level 3, depth of cut 0.476 mm), machining time is at (level 3, speed 639 rpm), (level 3, feed 0.13716 mm/rev), (level 2, depth of cut) and cutting time (level 1, speed 289 rpm), (level 1, 0.05334 mm/rev), (level 1, depth of cut 0.254 mm) for minimum respective value.
2. Predicted response value of coefficient of friction is 0.20, machining time is 47.86 s, and cutting time is 25.12 °C.
3. ANOVA models have shown that feed rate has maximum percentage of contribution as compared to speed and depth of cut in determining optimum response values of coefficient of friction, machining time and cutting temperature.
4. Regression models developed for prediction of coefficient of friction, machining time and cutting temperature have high *R*-square values more than 84–92%, and predicted values are very close to the experimental values of confirmation tests.

Acknowledgements Authors are highly thankful to workshop and laboratory facilities shared by Delhi Technological University and Indian Institute of Technology, Delhi (India).

References

1. Ei Hakim MA, Abad MD, Abdelhameed MM, Shalaby MA, Veldhuis SC (2011) Wear behaviour of some tool materials in hard turning of HSS. Tribol Int 44:1174–1181
2. Liew PJ, Shaaroni A, Sidik NAC, Yan J (2017) An overview of current status of cutting fluids and cooling techniques of turning hard steel. Int J Heat Mass Transf 114:380–394
3. Dureja JS, Singh R, Bhatti MS (2014) Optimization flank wear and surface roughness during hard turning of AISI D3 steel by Taguchi and RSM methods. Prod Manuf Res 2:767–783

4. Rath D, Panda S, Pal K (2018) Prediction of surface quality using chip morphology with nodal temperature signatures in hard turning of AISI D3. Mater Today (5):12368–12375
5. Gupta MK, Sood PK (2016) Optimizing multi-characteristics in machining of AISI 4340 steel using Taguchi's approach and utility concept. J Inst Eng (India) Ser C 97(1):63–69
6. Mandal N, Doloi B, Mondal B (2016) Surface roughness predication model using zirconia toughened alumina (ZTA): Taguchi method and regression analysis. J Inst Eng (India) Ser C 97(1):77–84
7. Mandal N, Doloi B, Mondal B, Das R (2011) Optimization of flank wear using zirconia toughened alumina (ZTA) cutting tool: Taguchi method and regression analysis. Measurement 44:2129–2155
8. Durakbasa MN, Akdogan A, Vanil AS, Bulutsuz AG (2015) Optimization of end milling parameters and determination of the effects of edge profile for high surface quality of AISI H13 steel by using precise and fast measurements. Measurement (68):92–99
9. Gunay M, Yucel E (2013) Application of Taguchi method for determining optimum surface roughness in turning of high-alloy white cast iron. Measurement 46:913–919
10. Kumar V, Kumar BJK, Rudresha N (2018) Optimization of machining parameters in CNC turning of stainless steel (EN19) by Taguchi's orthogonal array experiments. Mater Today Proc (5):11395–11407
11. Aggarwal A, Singh H, Kumar P, Singh M (2008) Optimization of multiple quality characteristics for CNC turning under cryogenic cutting environment using desirability function. J Mater Process Technol 205:42–50
12. Xavior MA, Adithan M (2009) Determining the influence of cutting fluids on tool wear and surface roughness during turning of AISI 304 austenitic stainless steel. J Mater Process Technol 209:900–909
13. Viswanathan R, Ramesh S, Subburam V (2018) Measurement and optimization of performance characteristics in turning of Mg alloy under dry and MQL conditions. Measurement 120:107–113
14. Yilmaz B, Karabulut S, Gullu A (2018) Performance of analysis of new chip breaker for efficient machining of Inconel 718 and optimization of the cutting parameters. J Manuf Process 32:553–563
15. Mia M, Dey PR, Hossain MS, Arafat MdT, Asaduzzaman Md, Ullah MdS, Zobaer SMT (2018) Taguchi S/N based optimization of machining parameters for surface roughness, too wear, and material removal rate in hard turning under MQL cutting condition. Measurement 122:380–191
16. Khan A, Maity K (2017) Comparative study of some machinability aspects in turning of pure titanium with untreated and cryogenically treated carbide inserts. J Manuf Process 28:272–284
17. Dhar N, Ahmed M, Islam S (2007) An experimental investigation on effect of minimum quantity lubrication in machining AISI 1040 steel. Int J Mach Tools Manuf 47(5):748–753
18. Varadarajan A, Philip P, Ramamoorthy B (2002) Investigations on hard turning with minimal cutting fluid application (HTMF) and its comparisons with dry and wet turning. Int J Mach Tools Manuf 42(2):193–200
19. Wang C, Xie Y, Zheng L, Qin Z, Tang D, Song Y (2014) Research on chip formation mechanism during the high-speed milling of hardened steel. Int J Mach Tools Manuf 79:31–48
20. Hasclik A, Caydas U (2008) Optimization of turning parameters for surface roughness and tool life based on Taguchi method. Int J Adv Manuf Technol 38:896–903
21. Zebia W, Kowlczyk R (2015) Estimating the effect of cutting data on surface roughness and cutting force during WC-CO turning with PCD tool using Taguchi design and ANOVA analysis. Int J Adv Manuf Technol 77:2241–2256

Total Interpretive Structural Modelling of Critical Factors of Sustainable-Oriented Innovation for Indian Manufacturing MSMEs

Sonal Khurana, Bisma Mannan and Abid Haleem

Abstract The global integration of markets, rapid changes in technology and reduced lifecycles for product and technology have made the Micro, Small and Medium Enterprises (MSMEs) to focus on sustainability measures while considering innovation as an essential aspect to attain benefit in sustainable competition. Thus, the present study contributes to the empirical literature by finding out relationships between the critical factors which enhance the sustainable-oriented innovation for Indian manufacturing MSMEs. To this end, an exhaustive review of the literature and the opinion of the experts is taken, and a model is prepared using TISM technique to find the relationship between the factors. The outcome of the present study after applying total interpretive structural modelling technique is a framework which depicts the relationship between the factors influencing sustainable-oriented innovation for Indian manufacturing MSMEs.

Keywords Collaboration · Open innovation · Stakeholders · Total interpretive structural modelling

1 Introduction

The new understanding of innovation proposes that Micro, Small and Medium Enterprises (MSMEs) have an essential function in innovation [14]. The potential of MSMEs to provide employment in developing countries is very large. The proportion of MSMEs in Organisation for Economic Cooperation and Development (OECD) exports is about 25% and in exports from Asia is about 35% [26]. Innovation drives the competitiveness of a nation [8]. However, a more complex task is to maintain

S. Khurana (✉) · B. Mannan · A. Haleem
Department of Mechanical Engineering, Jamia Millia Islamia, New Delhi 110025, India
e-mail: sonal.khurana@gmail.com

B. Mannan
e-mail: bismamannan@gmail.com

A. Haleem
e-mail: haleem.abid@gmail.com

H. Kumar and P. K. Jain (eds.), *Recent Advances in Mechanical Engineering*,
Lecture Notes in Mechanical Engineering,
https://doi.org/10.1007/978-981-15-1071-7_9

competitiveness as these firms are more vulnerable due to a variety of issues. These issues are more relevant for developing countries like India which to some extent is at a very low rank on the global competitive index (rank 40 amongst 137 participating nations) [32]. Keeping this in mind, present study targets at making a model to give structure to the factors that affect implementation of sustainable innovated practices for Indian manufacturing MSMEs as these firms contribution to the manufacturing output of the economy is more than 50% [9]. This is done using the TISM approach. The present study is carried out in the framework of the economy of a developing country like India. The northern part of India, i.e. Delhi NCR region is selected for the study as previous researches have focussed on the southern part of India. Various researchers [13, 25] have carried out the research limiting their research to identifying the critical factors focussing on Karnataka. Thus, the present study assumes significance as the focus is on Delhi NCR region.

In the present study, the definition of MSMEs is given with the focus on their aim in investing in plant and machinery only. Therefore, MSMEs comprise firms in the manufacturing sector and include those in automobile, electrical and machine tool enterprises which have a target of investing in plant and machinery which range from up to Rs. one hundred million as of 2006/07. It is in accordance with the statement of Micro, Small and Medium Enterprises Development Act, 2006 of the Government of India [10].

Innovation in present study mentions to technological innovation only. Technological product innovation is the application of a product with enhanced performance attributes in sustainability like as to give better services to the customer. Technological process innovation is the application of novel or enhanced producing or supply methods which is sustainable. It can cause modifications in facilities, personnel, working techniques or a blend of any two [20].

The present study thus aims to fill the gap in the literature on sustainable-oriented innovation for Indian manufacturing MSMEs by constructing a model of the factors influencing sustainable practices in Indian MSMEs. The remaining part of the paper advances in the following way: the next section contains a systematic study of the literature of the critical factors that helps in achieving sustainable-oriented innovation for Indian manufacturing MSMEs. A model is constructed using TISM technique. The results are examined along with managerial/practical implications of work. Finally, outcomes are derived, and limitations provided for future research.

2 Literature Review

A detailed systematic review of the literature is carried out to find out the critical factors which would influence the Indian manufacturing MSMEs in implementing sustainable-oriented innovation practices. Systematic literature review helps to get an overview of the existing work done by researchers in the field of sustainable-oriented innovation in MSMEs.

2.1 Integrating Stakeholders

Tyl et al. [30] in their paper have investigated the need for integrating the stakeholders in the green innovation process. A stakeholder is a human being or any organisation(s) that gets influenced by the process of the firm in either direct or indirect way. They are at a level where they can take the benefit from the 'value' and the 'goodness' from the product.

Various researchers [4, 31] in their studies have reported that giving value on the relations of the stakeholder is one of the essential components of organisation's strategy in moving towards sustainability.

2.2 Collaboration with Customer

Bhanot et al. [1] and Gupta and Barua [9] have studied the impact of interaction with the outside customer and the support given by them on enterprise innovation and concluded that networks which are strong create a positive influence on innovations and growth of the enterprise.

Subrahmanya [25] in his paper has emphasised that those organisations that do or do not have sufficient in-house resources can help them available external to the organisation.

2.3 Relationship with Suppliers

Subrahmanya [25] has suggested that the organisations that are having or not having sufficient in-house assets can add them with outside help and cooperation. This cooperation can take place concerning products or processes either occasionally or continuously with the help of suppliers or help from the consultants. De Marchi [6] has emphasised that in today's scenario, good relationship with the supplier has received greater importance. Collaboration with suppliers can be beneficial in reducing the overall environmental influence and ensuring eco-friendly attributes of inputs. De Marchi [6] acknowledges the relevance of the effect of networks of cooperation abilities amongst the determinants of environment-friendly technologies. In this aspect, a few studies ratify that cooperation of suppliers is vital driver of green innovation [6, 7, 9, 11, 12, 16, 25].

2.4 Open Innovation

Sag et al. [24] have pointed out that it has been found by the research that open innovation is useful for MSMEs to enhance their innovative activity, to satisfy the needs of the consumer quickly and to achieve environmental benefits.

A growing number of enterprises, especially MSMEs, rely more on outside knowledge and association done for research for carrying out innovation and gaining competitive advantages [5, 15, 17–19, 21].

2.5 Governance

Government initiatives are significant to implement sustainable-oriented innovation practices. The famous *Porter-hypothesis* [22] states that supportive Government for green initiatives can cause a win-win situation which can lead to reducing the pollution level and increasing the profit level.

Carrillo-Hermosilla et al. [3] report that innovations which are green are difficult to achieve as the Government, many times, can act as a barrier in the creating and adapting new system. Thus, benefits consisting of subsidies should be given by the Government for the growth of environmentally friendly activities.

Tang and Tang [29] point out that the enterprises should give acknowledgement to Governmental schemes. Efforts in the direction of sustainability should be seen as the long-term efforts because they require huge initial investment and yield profits in the long run [2, 16, 28].

2.6 Network with Universities

Network with the universities helps in academic–industrial collaboration. This helps the industries to incorporate new technologies, this provides the universities with the new topics of research, and they can also see the implementation of new technologies [33].

2.7 Help from Consultants

Consultants provide the firms with the expertise to carry out the research. They have expertise in particular fields which can be used by the firms in the implementation of new technologies [23].

2.8 Support from Technology Resource Centre

Support from the technology resource centre acts as a catalyst in incorporating new technologies as they provide suitable training on the usage of new technology. They also provide support in terms of maintenance of new machines incorporated by the firms.

3 Solution Methodology

After the factors are identified, a model is constructed of the factors using the total interpretative structural modelling technique.

3.1 Total Interpretative Modelling Technique

TISM is used as a tool of qualitative research which is used in the preliminary stages of problem solving to make a model of the factors [27]. This is done before applying statistical techniques, and the same can be applied to validate the model obtained through TISM technique. The steps to apply TISM are as follows:

(1) Identifying components: Identify components amongst which relationships are to be derived.
(2) Defining contextual relation: A very essential step is to define the contextual relation among the components. The same is shown in Table 1.
(3) Interpreting the relation: This is where the difference lies between the ISM and the TISM technique. TISM explains the relation between the two components. The same is depicted in Table 2.
(4) Interpretative Logic of Pair-wise Comparison: TISM technique allows giving reason behind the relationship between two components. If, for each paired comparison, the answer is 'Y', the reason is given.
(5) Reachability Matrix and checking of Transitivity: The comparisons made by pairing the contextual relations in the interpretive logic knowledge base are converted into reachability matrix by entering 1 in i-j cell, and if the equivalent entry in the knowledge base is 'Y' and in other case, write 0 in the entry.
(6) Level Partitioning on Reachability Matrix: It is carried out for placing the components level-wise.
(7) Develop Diagraph: The levels obtained are shown diagrammatically by making a model (Tables 3, 4, 5, 6 and 7).

Table 1 Structural self-interaction matrix (SSIM) of critical factors

Variable	C8	C7	C6	C5	C4	C3	C2
C1	A	X	V	V	X	A	V
C2	A	A	V	X	A	O	
C3	A	O	A	O	A		
C4	A	X	V	V			
C5	A	A	V				
C6	A	A					
C7	A						
C8							

C1: Network with Universities; C2: Relationship with Suppliers; C3: Collaboration with Customer; C4: Help from Consultants; C5: Integrating Stakeholders; C6: Open Innovation; C7: Governance; C8: Support from Technology Resource Centre
V: Association in the direction of component i to component j and not vice versa
A: Association in the direction of component j to component i but not vice versa
X: Association in both the directions; component i to j and j to i
0 (zero), when the association among the components does not emerge to be accurate

Table 2 Interpretive logic knowledge base

S. No.	Element number	Y/N	In what way
C1: Network with universities			
1.	C1–C2	Y	This helps the suppliers to give their best quality raw material
2.	C2–C1	N	–
3.	C1–C3	Y	Transitive
4.	C3–C1	Y	Collaboration with customer enhances network with universities
5.	C1–C4	Y	Network with universities enhances help from the consultants
6.	C4–C1	Y	Help from the consultants increases when the firm has a good network with universities
7.	C1–C5	Y	It gives confidence to the stakeholder to take an active part in the decisions of the firm
8.	C5–C1	N	–
9.	C1–C6	Y	It has a positive influence on open innovation
10.	C6–C1	N	Open innovation can be carried out if the firm has a network with universities
11.	C1–C7	Y	It enhances support from technology resource centre
12.	C7–C1	Y	It encourages the support centre to give aid to the firm in the development of eco-friendly products

(continued)

Table 2 (continued)

S. No.	Element number	Y/N	In what way
C2: Relationship with suppliers			
13.	C2–C3	Y	Transitive
14.	C3–C2	N	–
15.	C2–C4	N	–
16.	C4–C2	Y	It will improve the relationship with the suppliers
17.	C2–C5	Y	This relationship improves as the stakeholders will get confidence for investing in the firm
18.	C5–C2	Y	This relationship encourages the suppliers, and they work hard to give their best in terms of quality to the firm
19.	C2–C6	Y	This will positively influence open innovation
20.	C6–C2	N	–
21.	C2–C7	N	–
22.	C7–C2	Y	This support will influence the relationship with the suppliers
C3: Collaboration with customers			
23.	C3–C4	N	–
24.	C4–C3	Y	This help will aid in fulfilling the expectations of the customer
25.	C3–C5	N	–
26.	C5–C3	Y	Transitive
27.	C3–C6	Y	Transitive
28.	C6–C3	Y	Open innovation will help in meeting the expectations of the customer
29.	C3–C7	N	–
30.	C7–C3	Y	Transitive
C4: Help from consultants			
31.	C4–C5	Y	This will give confidence to the stakeholder
32.	C5–C4	N	–
33.	C4–C6	Y	It is a part of open innovation and hence will influence the same
34.	C6–C4	N	–
35.	C4–C7	Y	Help from the consultants will increase the support from technology resource centre
36.	C7–C4	Y	Help from support centres will also increase the help from consultants
C5: Integrating stakeholders			
37.	C5–C6	Y	Integrating stakeholders will enhance open innovation
38.	C6–C5	N	–

(continued)

Table 2 (continued)

S. No.	Element number	Y/N	In what way
39.	C5–C7	N	–
40.	C7–C5	Y	This will give confidence to the stakeholders for investing in the firm
C6: Open innovation			
41.	C6–C7	N	–
42.	C7–C6	Y	Support from technology resource centre will enhance open innovation

C7: Governance; C8: Support from Technology Resource Centre

Table 3 Initial reachability matrix

	C1	C2	C3	C4	C5	C6	C7	C8
C1	1	1	0	1	1	1	1	0
C2	0	1	0	0	1	1	0	0
C3	1	0	1	0	0	0	0	0
C4	1	1	1	1	1	1	1	0
C5	0	1	0	0	1	1	0	0
C6	0	0	1	0	0	1	0	0
C7	1	1	0	1	1	1	1	0
C8	1	1	1	1	1	1	1	1

Table 4 Final reachability matrix

	C1	C2	C3	C4	C5	C6	C7	C8
C1	1	1	1	1	1	1	1	0
C2	0	1	1	0	1	1	0	0
C3	1	1	1	1	1	1	1	0
C4	1	1	1	1	1	1	1	0
C5	0	1	1	0	1	1	0	0
C6	1	0	1	0	0	1	0	0
C7	1	1	1	1	1	1	1	0
C8	1	1	1	1	1	1	1	1

3.2 Analysis of TISM

From Fig. 1, it can be interpreted that good governance enhances the network with the universities as proper government initiatives promote academic–industrial collaboration. Good governance also promotes help from consultants and technology resource centres as they are being recognised by the government as change agents

Table 5 Level partitioning level 1

S. No.	Reachability set	Antecedent set	Intersection set	Level
1.	1, 2, 3, 4, 5, 6, 7	1, 3, 4, 6, 7, 8	1, 3, 4, 6, 7	
2.	2, 3, 5, 6	1, 2, 3, 4, 5, 7, 8	2, 3, 5	
3.	1, 2, 3, 4, 5, 6, 7	1, 2, 3, 4, 5, 6, 7, 8	1, 2, 3, 4, 5, 6, 7	One
4.	1, 2, 3, 4, 5, 6, 7	1, 3, 4, 7, 8	1, 3, 4, 7	
5.	2, 3, 5, 6	1, 2, 3, 4, 5, 7, 8	2, 3, 5	
6.	1, 3, 6	1, 2, 3, 4, 5, 6, 7, 8	1, 3, 6	One
7.	1, 2, 3, 4, 5, 6, 7	1, 3, 4, 7, 8	1, 3, 4, 7	
8.	1, 2, 3, 4, 5, 6, 7, 8	8	8	

Table 6 Level partitioning level 2

S. No.	Reachability set	Antecedent set	Intersection set	Level
1.	2, 4, 5, 7	4, 7, 8	4, 7	
2.	2, 5	2, 4, 5, 7, 8	2, 5	Second
4.	2, 4, 5, 7	4, 7, 8	4, 7	
5.	2, 5	2, 4, 5, 7, 8	2, 5	Second
7.	2, 4, 5, 7	4, 7, 8	4, 7	
8.	2, 4, 5, 7, 8	8	8	

Table 7 Level partitioning level 3

S. No.	Reachability set	Antecedent set	Intersection set	Level
1.	4, 7	4, 7	4, 7	Third
4.	4, 7	4, 7	4, 7	Third
7.	4, 7	4, 7	4, 7	Third
8.	8	8	8	Fourth

in the implementation of sustainable-oriented innovation in Indian MSMEs. Network with universities, help from consultants and support from technology resource centres drive the relationship with suppliers and stakeholders. This helps to achieve open innovation and enhances the collaboration with customer. Innovation which is carried out by the exchange of ideas and by interacting with the customer influences sustainable-oriented innovation in manufacturing MSMEs.

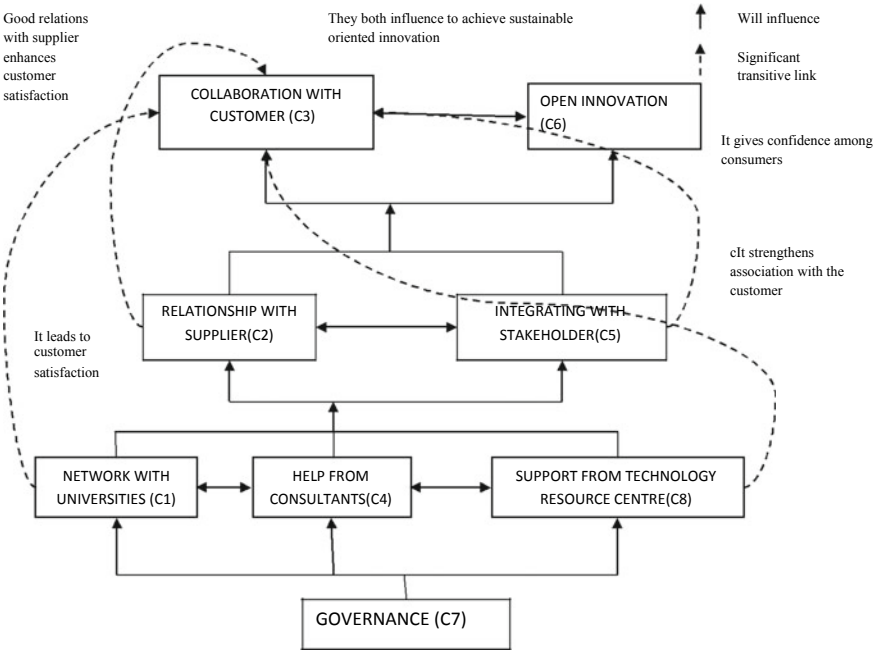

Fig. 1 Total interpretive structural model

4 Results and Discussion

The present study aims at constructing a model between the critical factors affecting the sustainable-oriented innovation in Indian manufacturing MSMEs. The model is made using the TISM technique. The viewpoint of the experts is taken to make structural self-interaction matrix. The result of the technique is the model representing a structure of factors which influence the sustainable-oriented innovation in Indian manufacturing MSMEs.

5 Managerial Implications

This will help those MSMEs which are trying to move in the direction of sustainable-oriented innovation to recognise the parameters which need to be given more weight as they drive the other factors. The outcome of the present study can act as a catalyst in the drive towards sustainable-oriented innovation for the Indian manufacturing industries. The results can also be useful for organisations to identify the gaps and movement of information and resources among the industry professionals and the researchers and can work jointly on areas where the gap can be reduced in sustainability implementation.

6 Limitations of Study and Conclusions

This research attempts to explore the relationship between the critical factors that influence the implementation of sustainable innovated practices for Indian manufacturing meshes by constructing a model. A systematic study of the literature was conducted across various journals to find out the set of variables which influences in moving in the direction of sustainable-oriented innovation. After this, a model is made using TISM technique.

A major problem encountered was in identifying what can be included in the ambit of sustainable-oriented innovation for MSMEs considering the Indian perspective. Although an extensive review of the literature was performed to extract the variables, still many scopes exist for further refinement. Also, TISM has the constraint that it is a qualitative technique and it captures inaccuracy and ambiguity linked with the judgement of the experts.

References

1. Bhanot N, Rao PV, Deshmukh SG (2017) An integrated approach for analysing the enablers and barriers of sustainable manufacturing. J Clean Prod 142:4412–4439
2. Boons F, Montalvo C, Quist J, Wagner M (2013) Sustainable innovation, business models and economic performance: an overview. J Cleaner Prod 45:1–8
3. Carrillo-Hermosilla J, Del Río P, Könnölä T (2010) Diversity of eco-innovations: reflections from selected case studies. J Clean Prod 18(10–11):1073–1083
4. Cuerva MC, Triguero-Cano Á, Córcoles D (2014) Drivers of green and non-green innovation: empirical evidence in low-tech SMEs. J Clean Prod 68:104–113
5. Dahlander L, Gann DM (2010) How open is innovation? Res Policy 39(6):699–709
6. De Marchi V (2012) Environmental innovation and R&D cooperation: empirical evidence from Spanish manufacturing firms. Res Policy 41(3):614–623
7. Fernández-Olmos M, Ramírez-Alesón M (2017) How internal and external factors influence the dynamics of SME technology collaboration networks over time. Technovation 64:16–27
8. Freel MS (2000) Do small innovating firms outperform non-innovators? Small Bus Econ 14(3):195–210
9. Gupta H, Barua MK (2016) Identifying enablers of technological innovation for Indian MSMEs using best-worst multi-criteria decision-making method. Technol Forecast Soc Change 107:69–79
10. https://msme.gov.in/know-about-msme. Accessed on 26th July 2018
11. Khurana S, Mannan B, Haleem A (2018) A comparative study of practices for integration of sustainability with innovation for micro, small & medium scale manufacturing enterprises (MSMEs) in India and in England. In: IOP conference series: materials science and engineering, vol 404, no 1. IOP Publishing, UK, p 012023
12. Khurana S, Khan J, Mannan B (2012) Enablers and barriers for implementing technology transfer projects: a study of SMEs in India. Emerging paradigms in marketing, pp 303–311
13. Krishnaswamy KN, Mathirajan M, Subrahmanya MB (2014) Technological innovations and its influence on the growth of auto component SMEs of Bangalore: a case study approach. Technol Soc 38:18–31
14. Lee VH, Foo ATL, Leong LY, Ooi KB (2016) Can competitive advantage be achieved through knowledge management? A case study on SMEs. Expert Syst Appl 65:136–151

15. Lee S, Park G, Yoon B, Park J (2010) Open innovation in SMEs—an intermediated network model. Res Policy 39(2):290–300
16. Luthra S, Garg D, Haleem A (2015) An analysis of interactions among critical success factors to implement green supply chain management towards sustainability: an Indian perspective. Resour Policy 46:37–50
17. Mannan B, Khurana S, Haleem A (2016) Modeling of critical factors for integrating sustainability with innovation for Indian small-and medium-scale manufacturing enterprises: an ISM and MICMAC approach. Cogent Bus Manag 3(1):1140318
18. Mannan B, Khurana S, Haleem A (2015) Technological innovation challenges and opportunities in India and the developing countries. In: 2015 annual IEEE India conference (INDICON). IEEE, pp 1–6
19. Mannan B, Khurana S (2012) Enablers and barriers for introduction of robotics as an AMT in the Indian industries (case of SME's). Int J Comput Appl 19–24
20. Organisation for Economic Co-operation and Development (Paris) (2009) Eco-innovation in industry: enabling green growth. OECD, Promoting entrepreneurship and innovative SMEs in a global economy: towards a more responsible and inclusive globalisation. OECD
21. Popa S, Soto-Acosta P, Martinez-Conesa I (2017) Antecedents, moderators, and outcomes of innovation climate and open innovation: an empirical study in SMEs. Technol Forecast Soc Change 118:134–142
22. Porter ME, Van der Linde C (1995) Toward a new conception of the environment-competitiveness relationship. J Econ Perspect 9(4):97–118
23. Rahman NA, Yaacob Z, Radzi RM (2016) An overview of technological innovation on SME survival: a conceptual paper. Procedia-Soc Behav Sci 224:508–515
24. Sağ S, Sezen B, Güzel M (2016) Factors that motivate or prevent adoption of open innovation by SMEs in developing countries and policy suggestions. Procedia-Soc Behav Sci 235:756–763
25. Subrahmanya MB (2015) Innovation and growth of engineering SMEs in Bangalore: why do only some innovate and only some grow faster? J Eng Tech Manage 36:24–40
26. Subrahmanya MB (2005) Pattern of technological innovations in small enterprises: a comparative perspective of Bangalore (India) and Northeast England (UK). Technovation 25(3):269–280
27. Sushil S (2012) Interpreting the interpretive structural model. Global J Flex Syst Manage 13(2):87–106
28. Talebi K, Ghavamipour M, Ir A (2012) Innovation in Iran's small and medium-size enterprises (SMEs): prioritize influence factors affecting innovation of SMEs, using analytic network process (ANP) method. Afr J Bus Manage 6(43):10775–10785
29. Tang Z, Tang J (2012) Stakeholder–firm power difference, stakeholders' CSR orientation, and SMEs' environmental performance in China. J Bus Ventur 27(4):436–455
30. Tyl B, Vallet F, Bocken NM, Real M (2015) The integration of a stakeholder perspective into the front end of eco-innovation: a practical approach. J Clean Prod 108:543–557
31. Wagner M (2015) The link of environmental and economic performance: drivers and limitations of sustainability integration. J Bus Res 68(6):1306–1317
32. World Economic Forum (2018) The global competitiveness report. World Economic Forum
33. Xie X, Zeng S, Peng Y, Tam C (2013) What affects the innovation performance of small and medium-sized enterprises in China? Innovation 153271286

Cloud Computing in Industries: A Review

Zareef Askary and Ravinder Kumar

Abstract Cloud computing is a new paradigm with a lot of promise. This paper provides a glimpse of how far this technology has come in implementation in industries and what the future holds. The basic concepts of cloud computing and its features have been explained here. A wide variety of industries have been considered. With everything being connected, industries are not far behind. This paper attempts to answer the question whether cloud computing can make industries more interconnected. A survey of 29 papers was carried out with focus on implementation in industries. Some aspects of computer science have also been discussed.

Keywords Cloud computing · Industry 4.0 · Compatibility · Frameworks

1 Introduction

The birth of the industrial revolution was due to the advancement of non-human powered machines. Then came the concept of mass production of goods and services in every sector. Later with the development of computer technology, computer-controlled machines were created improving efficiency even further. Production was becoming more interdisciplinary. Different fields of science and engineering were conceived to help operators work efficiently. As technologies developed in other fields, this also led to the growth of industries and vice versa. Industries are in the brink of a new revolution. A new generation of paradigms called Industry 4.0. With the advancement of computer and electro-mechanical technology, new ways of managing production have developed. Previously, networking could only be used via a local area network, but cloud computing allows resources to be controlled or monitored via the Internet. Cloud computing is classified into models based on the type of service [1]. They are namely Infrastructure as a Service (IaaS), Platform as a Service (PaaS) and Software as a Service (SaaS).

Z. Askary (✉) · R. Kumar
Amity University, Noida, Uttar Pradesh 201303, India
e-mail: zareefaskary@hotmail.com

H. Kumar and P. K. Jain (eds.), *Recent Advances in Mechanical Engineering*,
Lecture Notes in Mechanical Engineering,
https://doi.org/10.1007/978-981-15-1071-7_10

IaaS: It is the base level of cloud computing generally used by system admins. Raw computing power is provided by the IaaS services. Examples are Rackspace.com, Amazon EC2, GoGrid.

PaaS: It is layer above IaaS generally used by developers. It is a platform which provides services such as operating systems, programming language execution environment, database, web server, etc. Examples are Google App Engine, Windows Azure, Heroku, force.com.

SaaS: It is the top layer of cloud computing generally used by end customers. The name might seem misleading, but the installation of software is always not necessary. It can be accessed through a web browser directly. Examples are Google Drive, Microsoft Office 365, salesforce.com.

2 Literature Review

Ramachandra et al. [2] have shown the key issues in cloud computing. The review has been done by taking into account parameters which are cloud architecture, deployment and delivery models. The vulnerabilities of the parameters have been identified, and countermeasures have also been proposed. The vulnerabilities need to be identified, and the concerned stakeholders need to take necessary steps and mitigate them. The implementation of cloud computing requires members from a third party with many layers. As the number of layers increases the points of attacks tend to increase, so security measures are needed to be taken in all the layers.

Alsmadi et al. [3] determine the gap between literature and industrial reports of cloud computing services (CCS) adoption. Six factors were identified from the literature which are performance expectancy (PE), effort expectancy (EE), peers influence (PI), facilitating conditions (FC), perceived security (PS) and perceived privacy (PP). PE, EE, PI, FC correlation was also done with respect to age. After analysis was done, the researchers found that PI was the most important factor, while PE, EE, FC, PS and PP had negligible effect on the adoption of CCS.

Pedone et al. [4] have highlighted the compatibility of Industrial Internet Reference Architecture (IIRC) and Reference Architectural Model Industrie (RAMI 4.0) frameworks. The frameworks were chosen as they are considered as the major standardization frameworks. They have also shown that the implementation of the above frameworks shows similarity to the Open Connectivity Unified Architecture. With the understanding of the aforementioned, an architecture of a prototype smart factory was made. In the cloud computing, space interoperability is important for its implementation in large scale. They concluded that better frameworks need to be devised for better compatibility of frameworks.

Wang et al. [5] have highlighted how the implementation of IoT and cloud computing decongests the bottlenecks in the enterprise systems (ES). This paper deals with the problems faced while generating assembly plans. The problems are expected to be mitigated by the use of IT. In conclusion, the architecture devised should be

modular, flexible which facilitates the reuse of old components, and the assembly planning should be done with the help of relational matrices.

As the growth of IT in industries grows, the interaction between man and machine, machine and machine, man and man has become more efficient. Tao et al. [6] have proposed a cloud computing and IoT-based manufacturing system CCIoT-CMfg and analysed their relationship. In conclusion they have the applications of IoT and CC in different levels of an organization, their advantages, the technological infrastructure needed for implementing these new technologies and the challenges faced while implementing these systems.

Yu et al. [7] have shown the emergence of cloud computing and information and communication technology (ICT) in China. In developing nations, ICT can be used to upgrade their old infrastructure. The adoption of these new technologies depends on a number of factors such as government support and business interest which by looking after their own interests increases the rate of adoption. The researchers highlight the need of having a consensus of what the government and the business want to achieve in order to work towards adoption of new technologies.

Dinita et al. [8] describe the various attributes of an autonomous virtual management system from the perspective of cloud computing. The researchers created a prototype where the following objectives were achieved to know the limitations of the network infrastructure, develop a strategy by which the entire system can manage the workload, show the systems benefits by develop metrics which measures carbon foot print, create an application that detects threats and other vulnerabilities and accordingly reacts. The main conclusion shown here is the less consumption of power of an autonomous virtual management system in cloud computing.

Botta et al. [9] focus on the unification of cloud computing and IoT. The CloudIoT paradigm has been studied in detail. The drivers of these technologies are accessibility, parts, processing capabilities, storage and big data. With the integration of cloud and IoT where the cloud fails, IoT compensates and vice versa. The CloudIoT paradigm can be used to benefit healthcare, make cities and communities smart, make homes smart and improve surveillance, intelligent transport systems. The challenges have also been shown namely security, performance, reliability, legal aspects and massive data processing. Fog computing seems to be next generation of cloud computing technologies which integrates IoT.

Du et al. [10] aim to combine robots and cloud computing. It was achieved by designing a robot cloud stack and the use of service-oriented architecture (SOA). Finally, simulation of the system was done. Three conclusions were drawn from the simulations. Robot cloud computing is a feasible technology, it can improve profits, and it is better to have one large robot controlling centre rather than having multiple robot centres managing small areas.

Fahmideh et al. [11] have proposed a framework for migrating legacy systems to cloud computing systems. The framework is based on evidence-based software engineering and goal-oriented modelling. An evidential repository of obstacles was used to test the system. The framework was corroborated by the use of Pivotal Cloud Foundry and Microsoft Azure cloud platform. The researchers stipulate that the repository used can be further improved by incorporating practical obstacles

faced while migrating. The framework can be used to test legacy systems whether migration is possible, is it cost effective, secure and are the performance goals met. Furthermore, the framework can be used for obstacles faced in future.

Givehchi et al. [12] give an overview of the industrial automation concepts through cloud computing. The present scenario and future scope have been highlighted. The researchers have hypothesized a framework with the help of literature survey. They point out that there is further need of integration of IT services, the need of a well-defined repository, a detailed investigation of the connected devices. This could be accomplished with the integration of cloud services.

Hofmann et al. [13] show the present state of cloud computing implementation. Cloud computing is the next paradigm shift of the technology in industries. Presently, it is easy for small start-ups to adopt clouding computing due to lack of complexity. As cloud computing is a new field where its implementation is not widespread there are a lot of unknowns these include technical limitations as well as competition from other IT services such as ERP. ERP is already a well-established service which has widespread use. This hinders the adoption of cloud services.

Marston et al. [14] have shown two perspectives, one for the information systems researchers and the other for the stakeholders. The advantages have been listed out, and as well as SWOT analysis has been carried out. The roles of the stakeholders, enablers, service providers and regulatory bodies have also been shown. Also, how should an organization approach the adoption of cloud computing be carried out has been highlighted.

Mezgár and Rauschecker [15] have shown what the future holds after cloud computing integration into industries. Manufacturing companies need to continuously evolve their system architectures of network enterprises (NE) for the changing demands of the market. Cloud computing seems to be the offers an insight of the problems faced by NEs. Also, a new scheme of classification has been proposed by taking into account interoperability and standardization issues. Based on the classifications, four use cases have been shown. A new approach has been devised, namely Manufacturing as a Service (MaaS) which increases network flexibility and helps in managing manufacturing services through a proprietary cloud connector with a few modifications. The researchers hypothesize based on their own work and present the literature connecting virtual enterprise (VE) and cloud computing show a lot of promise. Also, for this integration to be possible, the interoperability and portability issues need to be mitigated.

Nieuwenhuis et al. [16] have shown how all the parties of the business environment are affected by the adoption of cloud computing technologies. The change in the network of old enterprise model has also been shown here. Taking into consideration three case studies, literature and consulting experts, they have created a new network of enterprise model after integration of cloud. The conclusions that were drawn are the complexity involved for the customer is shifted to the vendor, as the complexity decreases, a standardized software emerges, customization of the software becomes limited, and new value-added services are needed to be developed instead.

Ooi et al. [17] have shown how variables such as performance expectancy (PE), effort expectancy (EE), firm size (FS), top management support (MS) and absorptive

capacity (AC) of cloud computing technology can lead to innovativeness (IN) and firm performance (FP) among the manufacturing firms of Malaysia. It is also shown how the implementation of cloud computing increases IN and FP. Comparison of their data with available literature was done. With the help of tools such as partial least squares-structural equation modelling-artificial neural network (PLS-SEM-ANN), a conceptual framework was developed. It was concluded that PE predicts IN, EE predicts PE, MS is important for EE, FS is vital for IN and EE. AC is the most important for the development of IN.

Shu et al. [18] have tried to enable technologies for Complex Industrial Applications (CIA) by combining Cyber-Physical Systems (CPS) with cloud computing. They have formed an architecture called cloud-integrated CPS (CCPS). They have also summarized the technologies that drive cloud computing adoption. Three problems were analysed, namely virtualized resource management techniques, scheduling of cloud resources for CIA and life cycle management (LCM), and suggestions were given to mitigate these problems.

Trigueros-Preciado et al. [19] focus on the gap between adoption and literature of cloud computing in Small and medium-sized enterprises (SMEs). The main focus is to identify the barriers and effects of the adoption of cloud computing in SMEs. Ignorance of the technology of cloud computing was identified as the main barrier, followed by security issues, distrust in transferring data to third parties, the managers not knowing how to measure the effect of cloud computing adoption, compliance with the laws and regulations. The effects of adoption of cloud computing include cost reduction for software, systems and IT specialists, pliability and expandable nature, and also, these SMEs cannot use other technologies that cloud computing provides.

Varghese and Buyya [20] highlight the latest developments of cloud computing technology. It seems that computer power is being decentralized. The processing power as well as the software seems to be heading to a decentralized architecture as it can be seen in the case of VM ware. This makes it easier for devices as well as people to be better connected by utilizing the IoT paradigm. Eventually leading to the emergence of new fields to the paradigm of cloud computing which is being led by both academia and industries.

Xu [21] has highlighted the facets of cloud computing, organizations that use cloud computing and cloud computing service providers. Two models have been suggested in manufacturing industries, namely cloud manufacturing with absolute adoption of cloud computing technologies and cloud manufacturing. The author speculates that the pay by use model will revolutionize the manufacturing. Production-oriented manufacturing and service-oriented manufacturing have been discussed in detail.

Singh et al. [22] propose a model which distributes the customer data into different cloud service providers and which is economically feasible. Distributing data has one major advantage that is there is no single point of failure. If one server is compromised, then all the data is not lost. The model was subjected to two scenarios, one where there were no budgetary constraints and the other where the budget was fixed. Both these cases can be used depending on the situation of the customer.

Alshamaila et al. [23] propose an adoption model for cloud computing which is based on the technological organizational and environmental (TOE) framework. This model was made by surveying SMEs in the north east of England. Various factors which played a significant role in adopting cloud computing were identified. The factors have been divided into three categories. Technological-relative benefit, unpredictability of results, closeness to the existing technology, degree of complexity, degree of experimentation; Organizational-scale, higher management support, ingenuity, experience; Environmental-competitiveness, sector, scope of the operations, supplier support. Cloud computing firms need to bring awareness to their technologies so that adoption occurs in a wide scale. Security does not seem to be an issue for adoption of cloud computing.

Oliveira et al. [24] identified the factors which influence the adoption of cloud computing in industries. This was accomplished by creating a research model which incorporated diffusion of innovation (DOI) theory and TOE framework. Data was collected from various firms in Portugal to test the hypothesis. The factors are relative benefit, closeness to the existing technology, higher management support and scale of the organization. Other factors found with DOI theory are better quality of business functions, quicker completion of tasks, higher productivity and emergence of new commercial opportunities.

Gangwar et al. [25] identified the factors which influence the adoption of cloud computing in industries. This was accomplished by creating a research model which incorporated technology acceptance model (TAM) and TOE framework. Data was collected from various IT, manufacturing and finance firms in India. The factors are relative benefit, closeness to the existing technology, degree of complexity, higher management support and experience.

With the advent of IoT, the amount of data to be processed increases exponentially. Jiang et al. [26] propose a model for the storage and management of the data generated from IoT devices. Generally, older technologies without IoT integration would store its data on local servers without access to the Internet. This model allows data from the IoT devices to store data whether it is structured or unstructured data.

Hsu et al. [27] have done a TOE analysis with incorporation of diffusion theory to find the factors which influence an organizations willingness to adopt cloud computing technology. The results were verified with firms in Taiwan. Cloud adoption mainly depends on recognizable benefits, IT potential and business effect. Recognizable benefits is the strongest factor among the three. It was found that the size of the firm does not matter, but IT potential matters. Pricing mechanism also depends on IT potential.

Gupta et al. [28] have found the factors which affect adoption of cloud computing in SMEs and SMBs. Advantages offered by cloud computing services have also been identified. Cloud computing is user friendly and convenient which are the factors which carry the most weightage. Privacy and security are the second most important factor. It is safer to store data in a remote location which is operated by a third party whose sole job is to safeguard the data of its customers. Protecting data is not the responsibility of the SME or SMB. The aforementioned factors have an effect on the cost of operations that is it reduces cost substantially.

Wu et al. [29] highlight the drivers which push firms to support their supply chain with cloud computing. The research has been done by the use of diffusion information theory. An empirical study and regression analysis were done to examine the model. It was concluded that factors such as the firms business process complexity and compatibility with the existing information systems determine the degree of ease by which cloud computing can be adopted (Table 1 and Fig. 1).

Table 1 Overview of the papers reviewed

Summary	Authors
Parameters, vulnerabilities	Ramachandra et al. [2]
Six factors identified concerned with adoption	Alsmadi et al. [3]
Compatibility of frameworks	Pedone et al. [4]
Cloud and IoT integration	Wang et al. [5]
IoT-based manufacturing system CCIoT-CMfg	Tao et al. [6]
Development of ICT in China, adoption factors	Yu et al. [7]
Autonomous virtual management system	Dinita et al. [8]
CloudIoT paradigm application, fog computing	Botta et al. [9]
Integration of cloud computing and robots	Du et al. [10]
Framework for migrating legacy systems to cloud computing systems	Fahmideh et al. [11]
Hypothesis of framework based on literature	Givehchi et al. [12]
Present scenario and competition from ERP	Hofmann et al. [13]
Role of concerned parties, method of adoption	Marston et al. [14]
Interoperability and standardization issues	Mezgár and Rauschecker [15]
Creation of network enterprise model	Nieuwenhuis et al. [16]
Ranking of factors which lead to cloud adoption in Malaysia	Ooi et al. [17]
Formation of cloud-integrated CPS (CCPS), drivers of cloud adoption	Shu et al. [18]
Identify barriers and effects of adoption of cloud computing in SMEs	Trigueros-Preciado et al. [19]
Latest trend of cloud computing technology, decentralization of processing power	Varghese and Buyya [20]
Models of cloud computing in manufacturing industries	Xu [21]
Distribution of data into different cloud providers	Singh et al. [22]
TOE analysis in SMEs of north east England	Alshamaila et al. [23]
TOE and DOI analysis of firms in Portugal	Oliveira et al. [24]
TAM and TOE model for firms in India	Gangwar et al. [25]
Model where data from IoT devices stored in the cloud	Jiang et al. [26]
TOE and DOI analysis of firms in Taiwan	Hsu et al. [27]
Factors affecting cloud adoption in SMEs and SMBs	Gupta et al. [28]
Supply chain and cloud computing integration	Wu et al. [29]

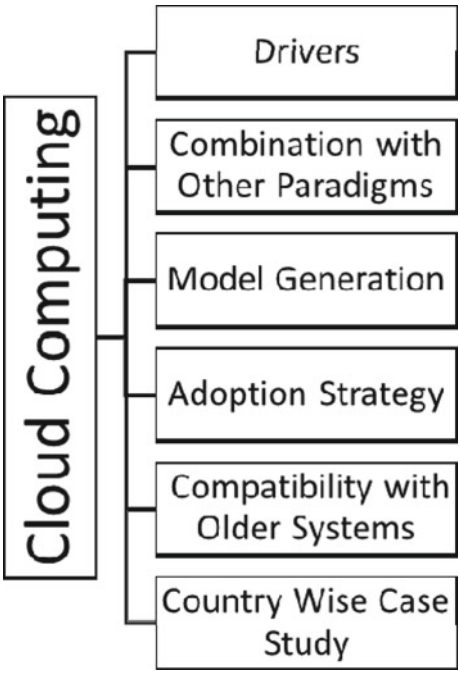

Fig. 1 Factors discussed in the paper

3 Conclusion and Research Gaps

Cloud computing is still in its early stages, and experimentation is still underway to find the best suited process for its implementation. The term cloud computing was first used in an internal document of Compaq in 1996. The present state of cloud computing in industries can be attributed to the various drivers and barriers in which analysis has also been done. Framework models have been created to find the optimum model which satisfies the criteria that the organization is looking for. The frameworks need to be created as one framework cannot be used in all applications. Models have been made by incorporating TOE framework with other theories and approaches like TAM and DOI. The distribution of data into multiple cloud servers has also been shown to have benefits. Cloud computing offers a way to mitigate the issues of older systems like ERP. Various combinations of technology such as CPS, IoT with cloud computing show great promise in increasing efficiency in industries. The integration of IoT and cloud computing is known as fog computing. This is the next stage of cloud computing which incorporates the use of edge devices. As the cloud is decentralized, it can provide processing power for large calculations otherwise impossible without the cloud. The data from robots can be processed with the cloud alone. Cloud computing has been widely adopted in SMEs due to lack of complexity and scale. Cloud computing is being adopted in all aspects of everyday life starting from a city's infrastructure to household appliances. In industries,

cloud computing is a new paradigm which provides lots of opportunities for the organizations to capitalize in this new technology.

As far as research gaps are concerned, the implementation of cloud computing in developing countries is negligible, and this is due to poor infrastructure, unwillingness to adopt new technologies and the justification of spending a lot of capital to adopt cloud computing. Due to these reasons, research of cloud computing in developing countries is limited. Most networking systems used in industries use primitive technology like LAN and private databases migrating to cloud computing systems require new hardware to run which requires capital. This investment may not show immediate benefits but may show long-term benefits. There is no research on long-term benefits of cloud computing adoption, so it is difficult for industries to know whether their investment is profitable. Furthermore, industry-wide adoption is required to actually reap the benefits of cloud computing.

References

1. Mell P, Grance T (2011) The NIST definition of cloud computing (Technical report). National Institute of Standards and Technology, U.S. Department of Commerce
2. Ramachandra G, Iftikhar M, Khan FA (2017) A comprehensive survey on security in cloud computing. Procedia Comput Sci 110:465–472
3. Alsmadi D, Prybutok V (2018) Sharing and storage behavior via cloud computing: security and privacy in research and practice. Comput Hum Behav 85:218–226
4. Pedone G, Mezgár I (2018) Model similarity evidence and interoperability affinity in cloud-ready Industry 4.0 technologies. Comput Ind 100:278–286
5. Wang C, Bi Z, Da Xu L (2014) IoT and cloud computing in automation of assembly modeling systems. IEEE Trans Ind Inform 10(2):1426–1434
6. Tao F, Cheng Y, Da Xu L, Zhang L, Li BH (2014) CCIoT-CMfg: cloud computing and internet of things-based cloud manufacturing service system. IEEE Trans Ind Inform 10(2):1435–1442
7. Yu J, Xiao X, Zhang Y (2015) From concept to implementation: the development of the emerging cloud computing industry in China. Telecommun Policy 40(2–3):130–146
8. Dinita RI, Wilson G, Winckles A, Cirstea M, Jones A (2013) Hardware loads and power consumption in cloud computing environments. In: 2013 IEEE international conference on industrial technology (ICIT). IEEE, pp 1291–1296
9. Botta A, De Donato W, Persico V, Pescapé A (2015) Integration of cloud computing and internet of things: a survey. Future Gener Comput Syst 56:684–700
10. Du Z, He L, Chen Y, Xiao Y, Gao P, Wang T (2016) Robot cloud: bridging the power of robotics and cloud computing. Future Gener Comput Syst 74:337–348
11. Fahmideh M, Beydoun G (2017) Reusing empirical knowledge during cloud computing adoption. J Syst Softw 138:124–157
12. Givehchi O, Trsek H, Jasperneite J (2013) Cloud computing for industrial automation systems—a comprehensive overview. In: 2013 IEEE 18th conference on emerging technologies and factory automation (ETFA). IEEE, pp 1–4
13. Hofmann P (2010) The limits of public clouds for business applications–an overly simplistic reliance on the utility model risks blinding us to the real opportunities and challenges of cloud computing. In: Proceedings of the 1st international conference on E-Business intelligence (ICEBI2010). Atlantis Press
14. Marston S, Li Z, Bandyopadhyay S, Zhang J, Ghalsasi A (2011) Cloud computing—the business perspective. Decis Support Syst 51(1):176–189

15. Mezgár I, Rauschecker U (2014) The challenge of networked enterprises for cloud computing interoperability. Comput Ind 65(4):657–674
16. Nieuwenhuis LJ, Ehrenhard ML, Prause L (2017) The shift to cloud computing: the impact of disruptive technology on the enterprise software business ecosystem. Technol Forecast Soc Change 129:308–313
17. Ooi KB, Lee VH, Tan GWH, Hew TS, Hew JJ (2017) Cloud computing in manufacturing: the next industrial revolution in Malaysia? Expert Syst Appl 93:376–394
18. Shu Z, Wan J, Zhang D, Li D (2015) Cloud-integrated cyber-physical systems for complex industrial applications. Mob Netw Appl 21(5):865–878
19. Trigueros-Preciado S, Pérez-González D, Solana-González P (2013) Cloud computing in industrial SMEs: identification of the barriers to its adoption and effects of its application. Electron Mark 23(2):105–114
20. Varghese B, Buyya R (2017) Next generation cloud computing: new trends and research directions. Future Gener Comput Syst 79:849–861
21. Xu X (2012) From cloud computing to cloud manufacturing. Robot Comput-Integr Manuf 28(1):75–86
22. Singh Y, Kandah F, Zhang W (2011) A secured cost-effective multi-cloud storage in cloud computing. In: 2011 IEEE conference on computer communications workshops (INFOCOM WKSHPS). IEEE, pp 619–624
23. Alshamaila Y, Papagiannidis S, Li F (2013) Cloud computing adoption by SMEs in the north east of England: a multi-perspective framework. J Enterp Inf Manag 26(3):250–275
24. Oliveira T, Thomas M, Espadanal M (2014) Assessing the determinants of cloud computing adoption: an analysis of the manufacturing and services sectors. Inf Manag 51(5):497–510
25. Gangwar H, Date H, Ramaswamy R (2015) Understanding determinants of cloud computing adoption using an integrated TAM-TOE model. J Enterp Inf Manag 28(1):107–130
26. Jiang L, Da Xu L, Cai H, Jiang Z, Bu F, Xu B (2014) An IoT-oriented data storage framework in cloud computing platform. IEEE Trans Ind Inform 10(2):1443–1451
27. Hsu PF, Ray S, Li-Hsieh YY (2014) Examining cloud computing adoption intention, pricing mechanism, and deployment model. Int J Inf Manag 34(4):474–488
28. Gupta P, Seetharaman A, Raj JR (2013) The usage and adoption of cloud computing by small and medium businesses. Int J Inf Manag 33(5):861–874
29. Wu Y, Cegielski CG, Hazen BT, Hall DJ (2013) Cloud computing in support of supply chain information system infrastructure: understanding when to go to the cloud. J Supply Chain Manag 49(3):25–41

Evaluation of High Temperature Tribological Behaviour of Nickel Coating Using LRT

S. Chaudhary, R. C. Singh, Rajiv Chaudhary and Sonia

Abstract This study aimed to investigate the effects of temperature, load and frequency on the wear and friction behaviour of the cast iron and nickel-coated tribosurface on mild steel. The experiments were performed at three different levels of loads (10, 20, 30 N), frequency (24, 30, 36 Strokes/s) and temperature (40, 80, 120 °C) using a linear reciprocating tribometer. An L9 orthogonal array as per the Taguchi technique was used to analyze the specific wear rate (SWR) and coefficient of friction (COF). The coated surface showed better tribological behaviour as compared to cast iron. The temperature had maximum influence on the tribological behaviour followed by load and frequency.

Keywords Nickel coating · Taguchi analysis · Friction · Wear

1 Introduction

The effective tribological design increases the life of material in various mechanical devices by reducing wear and friction. Tribology has very wide application in metal machining as it affects the tool life, forces required to shape a piece, tolerance and accuracy. Coating has emerged as an economical and efficient way to improve the tribology in machining technology. The phenomenon of formation of metallic or composite layer on metal surface to protect it from corrosion and to enhance the mechanical properties of the metallic substrate by improving its hardness or decreasing the coefficient of friction on its surface is called coating. The CrN coatings showed better anti-wear characteristic under high load and elevated temperature [1]. Chromium nitride (CrN) deposited by RF magnetron sputtering improved hardness and moderated residual stress [2]. Coating of CrN by physical vapour deposition showed better stability and mechanical properties than chromium (Cr) and titanium

S. Chaudhary (✉) · R. C. Singh · R. Chaudhary
Department of Mechanical Engineering, Delhi Technological University, Delhi, India
e-mail: mait.sumit@gmail.com

Sonia
Department of Mechanical Engineering, CBSGI, Jhajjar, India

H. Kumar and P. K. Jain (eds.), *Recent Advances in Mechanical Engineering*,
Lecture Notes in Mechanical Engineering,
https://doi.org/10.1007/978-981-15-1071-7_11

nitride (TiN) [3]. DLC-coated graphite carbon structures for Ti–6Al–4V alloy and aluminium–bronze 630 tribopair worked as a solid lubricant to prevent the wear [4]. Combination of TiN and CrN was used as a coating over ferrous substrate. CrN showed better adhesion with the substrate resulting in thicker layer of coating, and TiN was stable up to 700 °C temperature [5]. The glass fibre reinforced (GFR), and bronze- and carbon (C)-filled PTFE polymers showed better tribological behaviour by reducing friction coefficient up to 17% [6]. The theoretical and experimental analysis in the piston ring and cylinder liner tribopair showed enhanced tribological performance for the coated surfaces by reducing the power consumption indicating lower friction coefficient [7–9]. The coatings had a wide application for several industrial and medical applications to serve various functions such as thermal conductors, antimicrobial materials [10, 11] and antifriction and wear-resistant materials in bearing applications [12–14].

The coating showed a promising and effective mode for improving tribology than the conventional material. The coating of hard material like nickel has been done and investigated for the tribological behaviour on linear reciprocating tribometer.

2 Experimental Setup

The coating of nickel had been done by physical vapour deposition method. The microhardness of the coated and uncoated material was measured. The tribological behaviour of the coated specimen was investigated at various temperatures on linear reciprocating tribometer.

2.1 Linear Reciprocation Tribometer (LRT)

The linear reciprocating tribometer shown in Fig. 1 having load range of 5–50 N, frequency 1–50 Hz, stroke range 1–20 mm, consisted of a reciprocating drive motor attached to the pin holder block, a lever-actuated arm device to connect the motor drive and the pin holder block and other attachments to allow the pin specimen to be pressed against the stationary plate specimen with a controlled static load. The wear track on the plate was a straight line, resulted due to multiple wear passes on the same track. The temperature of the plate could be controlled according to the test conditions. Static load was applied to the pin holder. The coefficient of friction measured by load cell had been shown on the online monitor. The tribological investigation was carried out according to ASTM G133.

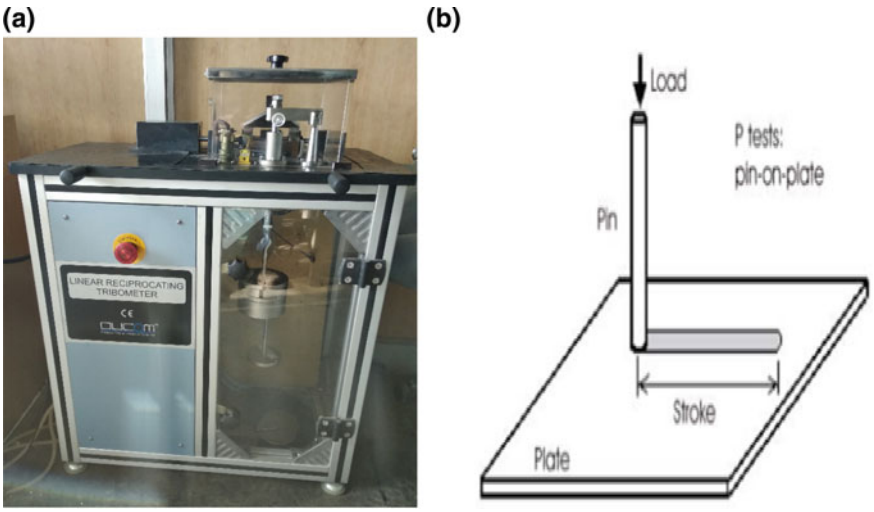

Fig. 1 Linear reciprocating tribometer

2.2 Test Specimens and Specimen Preparation

The pins were preparing by turning and grinding operation. A casted rod of cast iron was machined and turned to a diameter of 6 mm on a conventional lathe machine. Turning was followed by parting operation, at the required length of 15 mm, which was performed on the conventional lathe machine. The pins were then grinded, to ensure a smooth flat circular surface at both ends of the pins. The prepared pins were then coated with nickel by physical vapour deposition.

Mild steel plates were machined using wire electrical discharge machine or wire-EDM. A sheet of mild steel, having a thickness of 6 mm, was casted and sent for grinding operation for smooth flat surface, reducing the thickness to 5 mm. These plates were then processed and cut into squares of 20×20 mm^2 dimensions, using a wire-EDM, for high-dimensional accuracy.

3 Design of Experiment

The experiment was performed under different conditions of load, frequency and temperature given in Table 1 for coated and uncoated pin.

To optimize the minimum number of trails, Taguchi L9 orthogonal array was selected. The combination of different parameters according to L9 orthogonal array is given in Table 2.

The output parameters for the experimentation were coefficient of friction and wear of material. The coefficient of friction and wear should be minimum for

Table 1 Test conditions

S. No.	Parameter	Range
1	Load	10 N, 20 N, 30 N
2	Frequency	24, 30, 36 Strokes/s
3	Temperature	40 °C, 80 °C,120 °C

Table 2 Taguchi L9 orthogonal array

Experiment set	Load (*N*)	Frequency (Strokes/s)	Temperature (°C)
A	10	24	40
B	30	30	40
C	20	36	40
D	20	24	80
E	30	36	80
F	10	30	80
G	30	24	120
H	20	30	120
I	10	36	120

improved tribology. The coated and uncoated pins were tested against mild steel plate for tribological investigation.

4 Result and Discussions

4.1 Hardness Testing

The microhardness of the tribopairs of mild steel as plate and cast iron and nickel-coated pins was determined using Vickers's hardness; Fig. 2 represents the depth of indentation of the indenter in the specimen, and the corresponding microhardness has been calculated as given in Table 3. The microhardness of nickel-coated pin was 240% more than the cast iron pin, moreover, nickel coating would also provide protecting shield from the environmental attack.

4.2 Tribological Testing

The coefficient of friction was measured by the online monitor connected to the tribometer; the specific wear rate was measured by the weight loss technique. The specific wear rate was calculated as given in Eq. 1.

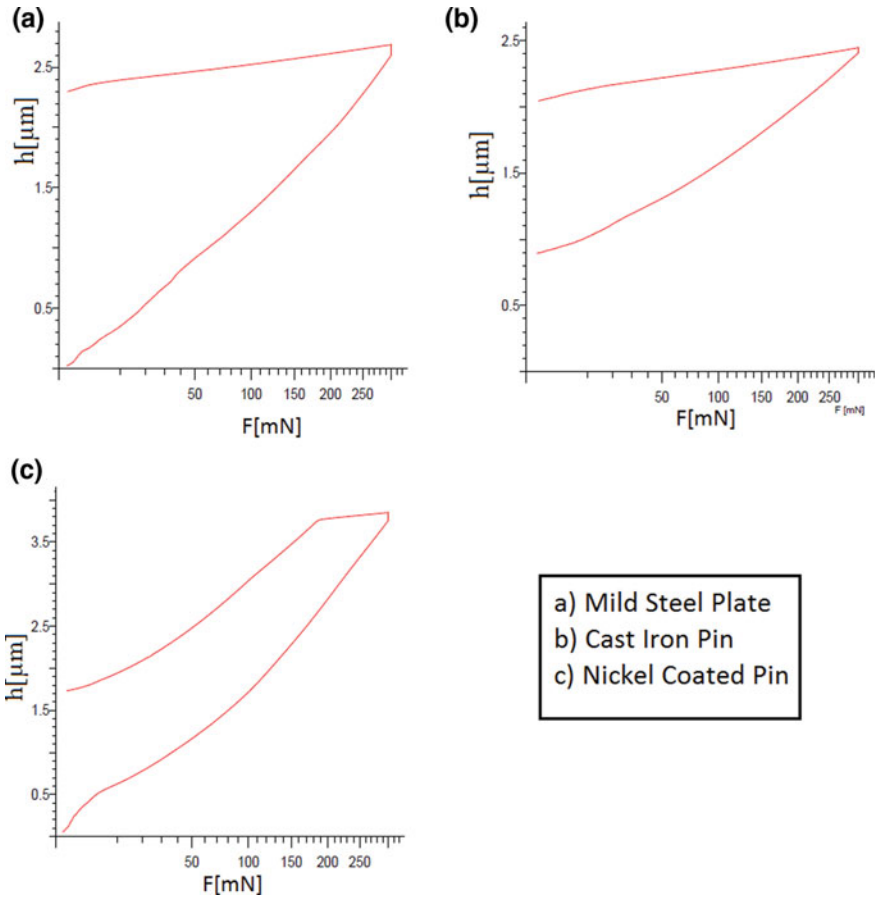

Fig. 2 Depth of indentation versus applied load

Table 3 Vickers hardness value of different materials

S. NO.	Material	HV value
1	Mild steel plates	177.12
2	Nickel-coated pins	518.69
3	Pure cast iron pins	215.87

$$\mathrm{Sw} = \mathrm{Vw}/(P * D) \tag{1}$$

Where,

Sw Specific wear rate, mm^3/N-m
Vw Volume of wear loss, in mm^3

P Applied load in Newton, N
D Sliding Distance in meters, m

Table 4 shows the coefficient of friction and specific wear rate for the different test conditions for cast iron pin and mild steel disc. The coefficient of friction and specific wear rate showed increment with the increase in temperature and load. Table 5 shows the coefficient of friction and specific wear rate for the different test conditions for nickel-coated pin and mild steel disc. The coefficient of friction in case of coated pin was little less than the cast iron pin, but the specific wear rate at higher temperatures was very less in case of coated pin due to higher hardness of the pin material.

Table 4 Experimental results for tribological investigation for cast iron pin versus mild steel plate

Experimental set	Load (N)	Frequency (Strokes/s)	Temperature (°C)	Coefficient of friction	Wear (mm^3/N-m)
A	10	24	40	0.39	0.124
B	30	30	40	0.38	0.131
C	20	36	40	0.45	0.137
D	20	24	80	0.53	0.138
E	30	36	80	0.48	0.120
F	10	30	80	0.50	0.095
G	30	24	120	0.44	0.274
H	20	30	120	0.51	0.241
I	10	36	120	0.64	0.283

Table 5 Experimental results for tribological investigation for nickel-coated pin versus mild steel plate

Experimental set	Load (N)	Frequency (Strokes/s)	Temperature (°C)	Coefficient of friction	Wear (mm^3/N-m)
A	10	24	40	0.41	0.108
B	30	30	40	0.37	0.098
C	20	36	40	0.40	0.129
D	20	24	80	0.51	0.118
E	30	36	80	0.39	0.089
F	10	30	80	0.51	0.125
G	30	24	120	0.42	0.159
H	20	30	120	0.46	0.163
I	10	36	120	0.57	0.169

4.3 Taguchi Analysis

Taguchi methodology has been utilized to find the importance of each parameter, and it also provides the optimum set of parameters which results in lower and lower specific wear rate as well. The values of coefficient of friction and specific wear rate between the tribopairs were observed and recorded for L9 orthogonal array. The results were analyzed for 'smaller is better', and S/N ratio was obtained. S/N ratio value is used to optimize the process parameters.

Figure 3 shows the S/N ratio by considering smaller is better for the cast iron versus mild steel specimen by considering coefficient of friction and specific wear rate. The corresponding delta value and rank for the tribopair show that temperature was the most dominating factor followed by load for coefficient of friction and specific wear rate shown by Tables 6 and 7. Figure 4 shows the S/N ratio by considering smaller is better for nickel-coated versus mild steel specimen by considering coefficient of friction and specific wear rate. The corresponding delta value and rank for the tribopair shows that temperature was the most dominating factor followed by load for specific wear rate shown in Table 7, and load was the most dominating factor followed by temperature for coefficient of friction as shown in Tables 8 and 9.

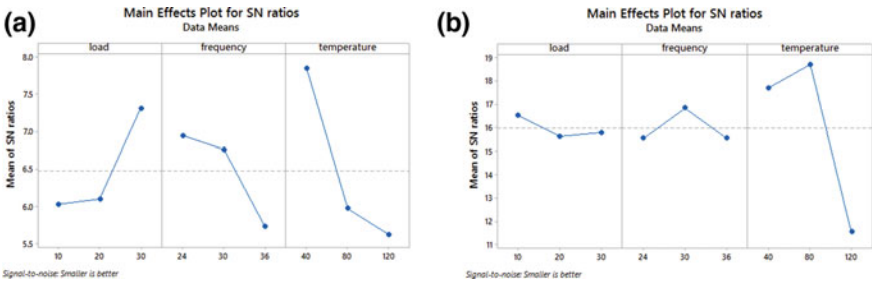

Fig. 3 S/N ratio for cast iron versus mild steel considering smaller is better **a** COF and **b** SWR

Table 6 Response table for S/N ratio of COF considering smaller is better for cast iron versus mild steel

Level	Load	Frequency	Temperature
1	6.025	6.941	7.840
2	6.100	6.75 8	5.970
3	7.303	5.729	5.619
Delta	1.278	1.212	2.221
Rank	2	3	1

Table 7 Response table for S/N ratio of SWR considering smaller is better for cast iron versus mild steel

Smaller is better			
Level	Load	Frequency	Temperature
1	16.51	15.53	17.68
2	15.61	16.82	18.69
3	15.77	15.55	11.52
Delta	0.90	1.29	7.17
Rank	3	2	1

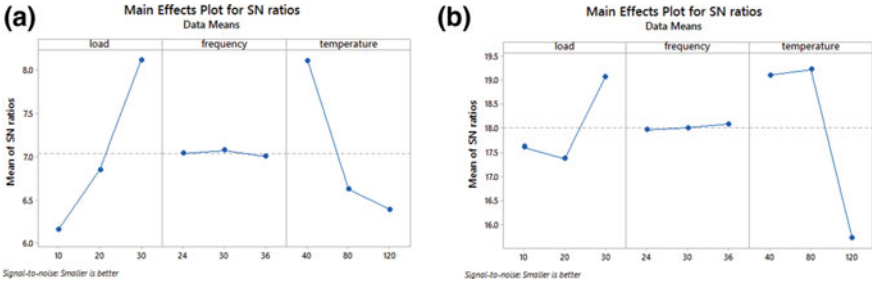

Fig. 4 S/N ratio for nickel coating versus mild steel considering smaller is better **a** COF and **b** SWR

Table 8 Response table for S/N ratio of COF considering smaller is better for nickel coating versus mild steel

Smaller is better			
Level	Load	Frequency	Temperature
1	6.153	7.043	8.113
2	6.851	7,076	6.625
3	8.117	7.007	6.387
Delta	1.958	0.070	1.726
Rank	1	3	2

Table 9 Response table for S/N ratio of SWR considering smaller is better for nickel coating versus mild steel

Smaller is better			
Level	Load	Frequency	Temperature
1	17,61	17.96	19.10
2	17.37	18.00	19.21
3	19.05	18.08	15.72
Delta	1.68	0.13	3.49
Rank	2	3	1

5 Conclusions

The coated pin was tested for tribological investigation and to know the contribution of different factors Taguchi analysis was used.

- The hardness of the nickel-coated pin was 240% more than the cast iron pin.
- At 40 °C and high speed, the nickel-coated pin showed better tribological properties than cast iron pins.
- At elevated temperature and high speed, the coated pin showed significant improvement in the tribological properties.
- Taguchi analysis shows that temperature was the most dominating factor followed by load which affects the tribological properties, but in the case of COF for nickel-coated pin, load was the most dominating factor followed by temperature. Frequency had a very little effect.

Acknowledgements Author (Sumit Chaudhary) is SRF of CSIR and is receiving financial support from CSIR under HRDG sanction letter number 08/133/(0013)/2015-EMR-1.

References

1. Podgornik B, Mandrino D et al (2016) Performance of CrN coatings under boundary lubrication. Tribol Int 96:247–257
2. Friedrich C et al (1997) PVD CrN coatings for tribological application on piston rings. Surf Coat Technol 97(1–3):661–668
3. Broszeit E et al (1999) Deposition, properties and applications of PVD CrN coatings. Surf Coat Technol 115(1):9–16
4. Costa MYP et al (2010) An investigation on sliding wear behavior of PVD coatings. Tribol Int 43(11):2196–2202
5. Navinšek B, Panjan P, Milošev I (1997) Industrial applications of CrN (PVD) coatings, deposited at high and low temperatures. Surf Coat Technol 97(1–3):182–191
6. Unal H, Mimaroglu A, Kadroglu U, Ekiz H (2004) Sliding friction and wear behaviour of polytetrafluoroethylene and its composites under dry conditions. Mater Des 25(3):239–245 (2004)
7. Moosavian A et al (2016) Piston scuffing fault and its identification in an IC engine by vibration analysis. Appl Acoust 102:40–48
8. Mishra PC (2014) A review of piston compression ring tribology. Tribol Ind 36(5):269–280
9. Shah AS, Bhatt DV (2014) Experimental study to measure piston ring assembly friction of multi cylinder I.C. Engine on motorized engine test rig: a case study. In: International conference on advances in tribology and engineering systems, Springer, New Delhi, pp 60–63 (2014)
10. Grass G, Rensing C, Solioz M (2011) Mini reviews metallic copper as an antimicrobial surface. Appl Environ Microbiol 77(5):541–1547
11. Sharifahmadian O, Salimijazi HR, Fathi MH, Mostaghimi J, Pershin L (2013) Relationship between surface properties and antibacterial behavior of wire arc spray copper coatings. Surf Coat Technol 233:74–79
12. He J, Zhang F, Mi P, Qin Y, Chen K, Yang Y, Zhang J, Yin F (2016) Microstructure and wear behavior of nano C-rich TiCN coatings fabricated by reactive plasma spraying with Ti-graphite powders. Surf Coat Technol 305:215–222

13. Jin X, Gao L, Liu E, Yu F, Shu X, Wang H (2015) Microstructure, corrosion and tribological and antibacterial properties of Ti-Cu coated stainless steel. J Mech Behav Biomed Mater 50:23–32
14. Kumar D, Murtaza Q, Singh RC (2016) Sliding wear behavior of aluminum alloy coating prepared by two-wire electric arc spray process. Int J Adv Manuf Technol 85:237–252

Numerical and Experimental Investigations on Film Cooling Performance of Trench Model Embedded with Compound Angle Film Hole Jets

V. G. Krishna Anand and K. M. Parammasivam

Abstract The Trench film cooling is a cooling technique where film cooling holes are embedded within a cut slot made on the surface with the application of thermal barrier coatings. The goal of the present investigation is to compare the cooling effectiveness of trench model embedded with compound angled film hole viz. 45°, 90°, 135° through numerical and experimental investigation at two different blowing ratios. The width and depth of trench are maintained at 2D and 0.7D, respectively, with *D* as the hole diameter. Results of the study show that trench model embedded with 90° compound angled film hole delivered highest cooling effectiveness for two tested ratios of blowing between coolant and mainstream flows. Experimental results on film cooling effectiveness produced good agreement with computational results.

Keywords Compound hole jets · Trench model · Cooling effectiveness

1 Introduction

Film cooling is a widely employed cooling technique for aircraft gas turbines, rocket nozzle, thrust chamber, marine and industrial gas turbine components. The downsides of flat model cooling are injectant jump off at higher BR, less lateral spreading of injected coolant. In trench film cooling, the film holes are embedded within cut slot made on the film cooling surface with the application of thermal barrier coatings. Dorrington et al. [1] performed an experimental study on various trench configurations. Their results concluded that height of trench of 0.75 times the film hole size offered higher cooling effectiveness and width of trench 2D and 3D provided a comparable film cooling performance, and they also reported that film effectiveness provided with trench is higher than shaped holes at high blowing ratios. Kross and Pfitzner [2] carried out an experimental and numerical study on trench configuration at high blowing ratios with tetrahedral obstructions placed at leading-edge regions of trench. They concluded that trench configuration provided better performance even at high

V. G. Krishna Anand (✉) · K. M. Parammasivam
Department of Aerospace Engineering, MIT Campus, Anna University, Chennai 600044, India
e-mail: kakrishnaanand@gmail.com

H. Kumar and P. K. Jain (eds.), *Recent Advances in Mechanical Engineering*,
Lecture Notes in Mechanical Engineering,
https://doi.org/10.1007/978-981-15-1071-7_12

blowing ratios and also additional tetrahedral obstruction provides further improved cooling performance. Goldstein and Jin [3] performed investigations to determine the behavior of cylindrical film hole with compound angles. They reveal that lateral averaged effectiveness offered with compound angle is higher than streamwise film hole injection because of better span side spreading. Taslim and Khanicheh [4] conducted experimental investigation with compound angling on round and expanded shaped hole models to study the impact of FCE. They conclude as diffuser shaped compound hole provides better cooling effects due to wide span side coverage with low momentum and increased film coolant concentration at hole exit. Chandran et al. [5] carried out studies to understand the behavior of different hole shapes on FCE. The study reported as the shaped and trenched models offered better film coverage than other configurations and also trench shaped film hole offered higher effectiveness only for increased BR of injected coolant. Anand and Parammasivam [6] performed optimization studies on trench film cooling parameters to optimize and identify the significant trench film cooling parameters. They conclude that the height of trench, film hole compound angle and BR have significant influence on trench FCE and the study also optimized these significant parameters.

Lu et al. [7] conducted an experimental study of FCE on various trench width of 2D and 3D with trench depth kept constant at 0.75D also incorporating some modification on trench trailing edge. They reported that the trenched film hole offered better film effectiveness compared with cylindrical film hole non-trench case, and downstream trailing edge modification of trench provided a very small performance improvement. Oguntade et al. [8] performed numerical investigation with modified trailing edge shape of trench and conclude that fillet shaped trench outlet offered highest effectiveness compared with other trench outlet tested configurations. Computational results predicted on trench film cooling model with realizable k-ε model with EWT produced close results with experimental data. Mcgovern and Leylek [9] performed computational study with compound oriented film holes on flat plate model.

Lot of studies performed on trench model utilized streamwise oriented film cooling holes embedded in trenches. The studies [3, 4] reported on film cooling surface without trench and embedded with compound angled film hole reported higher FCE. Hence, the present investigation aimed to compare the cooling performance of trench model embedded with compound angled film hole viz. 45°, 90°, 135° through numerical and experimental investigation at two different BR of 1.2 and 2.

2 Numerical Investigations

Numerical investigation is performed through a series of steps viz. computational domain modeling, model mesh generation, numerical solution, post process of results. The computational model used in present study is based on experimental domain dimension. The domain used in computation is shown in Fig. 1. It consists

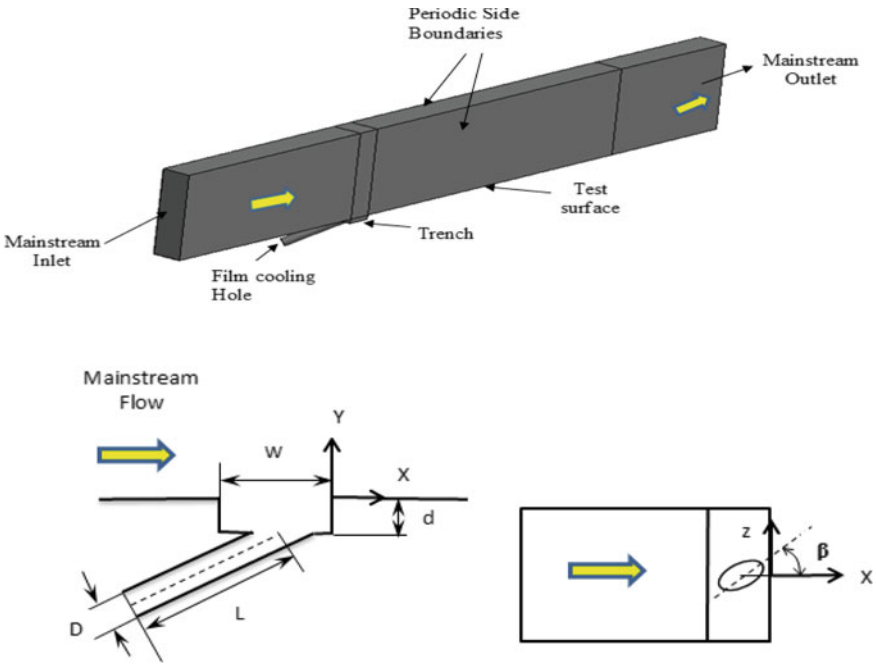

Fig. 1 Details of computational domain with trench and film hole compound angle (β)

of mainstream region, trench region and film hole region. The vertical lateral boundaries are specified with periodic boundary condition. The co-ordinate system origin of the computational domain is at the end of the trench side. The details for trench and compound angle are shown in Fig. 1. The width and depth of trench are maintained at 2D and 0.7D, respectively, with *D* of 4 mm for cooling hole. The modeling of computational domain is followed by mesh generation. Hybrid mesh system was employed for the computational domain.

The surface close to the wall was the change in temperature and velocity gradients occur, hence a wall clustered mesh system is generated close to the surface and also higher mesh concentration is introduced in the area of the computational domain with higher temperature and velocity gradients. Grid independence study is performed with three different mesh system viz. 0.8, 2.1, and 4.05 million cells with lateral averaged film cooling effectiveness used as assessment parameter for grid independence study. The Re No-based calculation on the mainstream inlet reveals that the flow is turbulent. The realizable k-ε model turbulence with EWT and thermal effects is used. The FCE predicted with turbulence model R-k-ε show good agreement on experimental results. Mainstream is specified with constant velocity 13 m/s and the temperature ratio of the hot air to coolant air is 0.883. The film coolant hole velocity is changed as per the change in BR and the temperature of the coolant stream was maintained constant. All the lateral side vertical boundaries are specified with periodic boundaries.

The sides of the domain are specified with non-heated and non-slip walls. Turbulence intensity for mainstream inlet and film hole inlet is 5% and 2%, respectively. The hydraulic diameter calculated based on mainstream and film hole inlet are specified at their respective boundaries. The continuity, momentum, energy equation and turbulence closure terms are solved in segregated method for three-dimensional steady incompressible flows. The SIMPLE scheme is adapted for coupling the pressure and velocity terms and SOUS is used for space discretization terms. The convergence criteria were set for scaled residuals to drop five orders of magnitude for continuity, momentum, turbulence equations and nine orders of magnitude for energy equation.

3 Experimental Investigation

The experimental study was performed on a custom fabricated suction type film cooling facility. The experimental set up comprises of different sub modules starting with air inlet whose sides are contoured to allow uniform air entry through inlet. Adjacent to the air inlet section is a heater assembly for rising the temperature of air entering the section and the heater element used is tubular finned type air heater with power of 12 kW. The temperature of heater module is controlled with a PLC temperature controller assembled adjacent to heater module. The heater module is covered with heat insulation blanket to reduce the heat loss to atmosphere. The test section is a C- shaped arrangement where the test plates with plenum can be inserted from behind the test section. Except the test section, all other modules are fabricated with MS plates of thickness 3 mm. The rubber gaskets are used to seal and connect the test section with adjacent modules, and asbestos fiber gasket sheet is used to seal the gap and prevent the leakage between all other assembled modules. The test section is followed by square to circular transition section that connects a diverging circular duct to inlet section of the blower unit. The film cooling air is supplied from air storage tank which receives pressurized air from a high power compressor. The air for film cooling is supplied through pipeline and controlled with check value. The orifice plate assembly is utilized for mass flow measurement of film cooling air, and a digital manometer is used to measure the pressure difference between upstream and downstream location of orifice assembly. Temperature measurement was performed with thermocouples embedded on the test surface with trench film cooling model.

4 Results and Discussions

The numerical results need to be validated with experimental results to gain confidence in the computational methodology. Figure 2 shows the validation study performed at blowing ratio (BR) of 1.2 and trench depth of 0.7D with film hole compound angle of 90°. Computational results are close to experimental results. The film cooling performance of trench model embedded with compound angled film

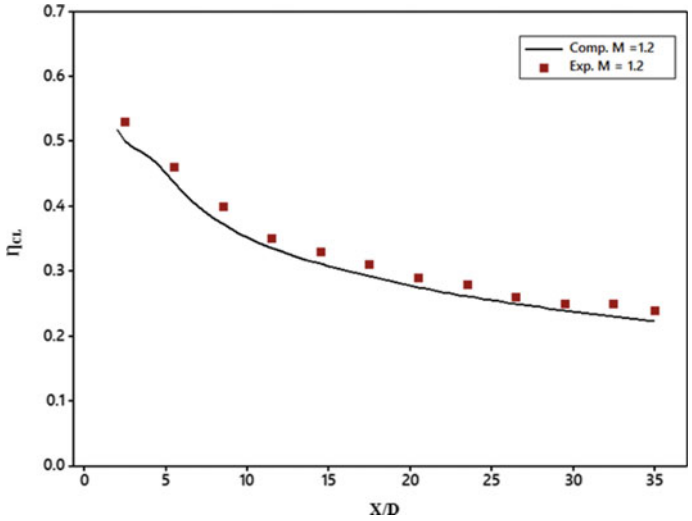

Fig. 2 Comparison of centerline FCE along test surface for numerical and experimental results

cooling hole is investigated with three major film cooling effectiveness parameters viz. local, lateral averaged and centerline FCE.

The lateral averaged FCE of 45°, 90° and 135° compound angles on test surface for BR of 1.2 as in Fig. 3, here the 90° compound angle film hole delivers higher FCE when compared to other compound angled hole models.

The 135° compound angle film hole delivers lower lateral averaged FCE. For higher BR 2, the lateral averaged FCE of different film hole compound angle is shown

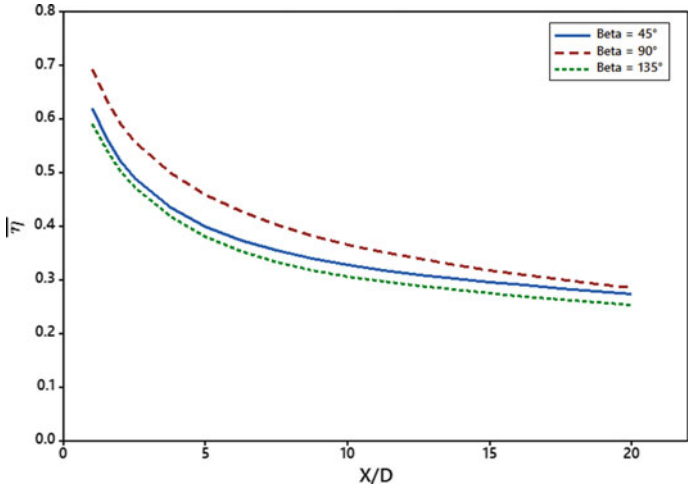

Fig. 3 $\overline{\eta}$ of different film hole compound angles at blowing ratio 1.2

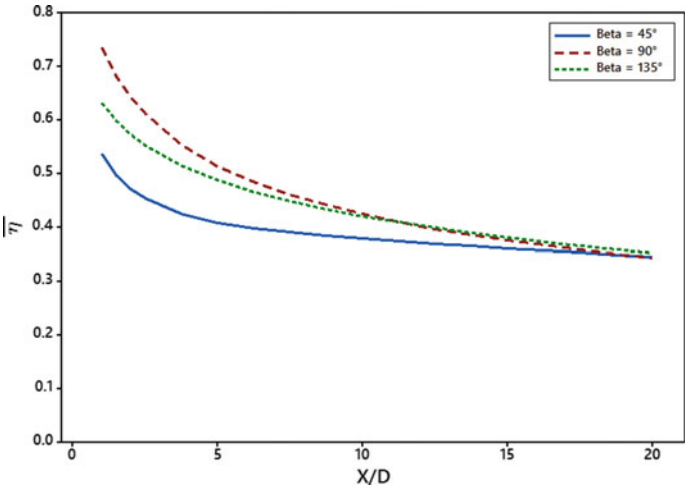

Fig. 4 $\overline{\eta}$ for various tested compound angle holes at BR 2

in Fig. 4, near the end of trench a significant level variation of lateral averaged FCE is observed.

Cooling effectiveness ($\overline{\eta}$) for three different film hole compound angle, however at downstream location the span averaged FCE of three tested hole compound angles (β of 45°, 90°, 135°) is uniform. The 90° compound angled film hole delivers higher span averaged FCE in comparison on other compound angles (45°, 135°) throughout the test surface and the 45° oriented film hole delivered lower $\overline{\eta}$ at higher blowing ratio 2. The 135° model produced lateral averaged FCE slightly lower than 90° oriented film hole. The variation of centerline FCE (η_{CL}) for three tested hole compound angles (45°, 90° and 135°) along longitudinal axis for BR 1.2 is shown in Fig. 5.

The compound angle film hole (90°) delivers higher centerline FCE near to trailing region of trench and film hole, however the centerline effectiveness of 90° oriented film hole is slightly reduced between X/D—1.25 to 3.25 and after that 90° model deliver higher FCE along the test surface. The 135° oriented compound angled film hole delivers lower centerline film cooling effectiveness. For higher BR of 2, the centerline FCE of test surface for three different film hole compound angle is shown in Fig. 6 and the 90° compound angle film hole delivers higher centerline FCE along central axis on test surface.

5 Conclusion

Film cooling performance of trenched model embedded with three different compound angle (45°, 90° and 135°) film cooling holes was investigated. The local, lateral averaged and centerline film cooling effectiveness were used as assessment

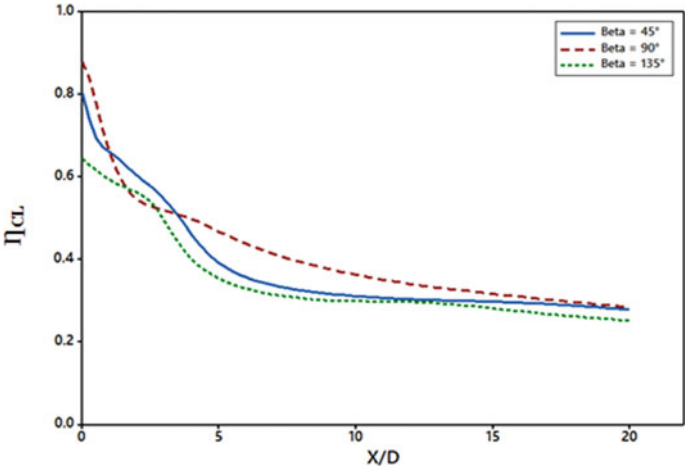

Fig. 5 η_{CL} for different film hole compound angles at blowing ratio 1.2

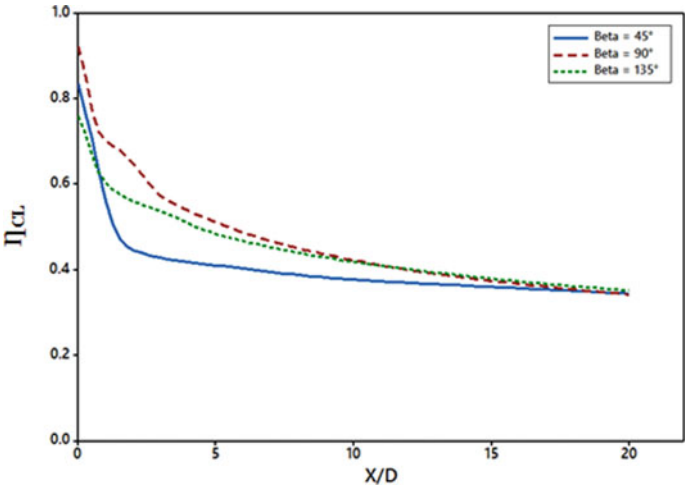

Fig. 6 η_{CL} for different film hole compound angles at blowing ratio 2

parameter to study the behavior on cooling effectiveness. Experiential studies performed on custom fabricated film cooling facility with 90° oriented film hole for blowing ratio of 1.2 shows close agreement with computational results. The film cooling hole oriented at compound angle 90° delivers higher local, lateral averaged and centerline FCE for two tested BR (1.2 and 2). 90° oriented compound angle film hole delivered uniform coolant coverage along lateral and longitudinal axis of test surface and this phenomenon results in higher film cooling effectiveness.

Acknowledgements The first person acknowledges DST, Government of India (GOI) for award of DST INPSIRE fellowship.

References

1. Dorington JR, Bogard DG, Bunker RS (2007) Film effectiveness performance for coolant holes embedded in various shallow trench and crater depressions. In: Proceedings of ASME turbo expo 2007: power for land, sea and air, GT-2007-27992, pp 749–758, ASME, Canada, 14–17 May 2007
2. Kross B, Pfitzner M (2012) Numerical and experimental investigation of the film cooling effectiveness and temperature fields behind a novel trench configuration at high blowing ratio. In: Proceedings of ASME turbo expo 2012: turbine technical conference and exposition, GT-2012-68125, pp 1197–1208, ASME, Denmark, 11–15 June 2012
3. Goldstein RJ, Jin P (2000) Film cooling downstream of a row of discrete holes with compound angle. ASME J Turbomach 123(2):222–230
4. Taslim ME, Khanicheh A (2005) Film effectiveness downstream of a row of compound angle film holes. ASME J Heat Transf 127(4):434–440
5. Chandran PM, Halder P, Panda RK, Prasad BVSSS (2012) A comparative study of film cooling effectiveness on a flat plate with adiabatic and conjugate conditions for different hole shapes. In: Proceedings of ASME turbo expo 2012: turbine technical conference and exposition, GT-2012-69142, pp 1571–1580, ASME, Denmark, 11–15 June 2012
6. Krishna Anand VG, Parammasivam KM Optimization of trenched film cooling using RSM coupled CFD. Inter J Turbo Jet Engines, Article in press. https://doi.org/10.1515/tjj-2018-0038
7. Lu Y, Dhungel A, Ekkad SV, Bunker RS (2008) Trench film cooling-effect of trench downstream edge and hole spacing. In: Proceedings of ASME turbo expo 2007: power for land, sea and air, GT-2008-50606, pp 563–569, ASME, Germany, 9–13 June 2008
8. Oguntade HI, Andrews GE, Ad B, Ingham DB, Pourkashanian M (2013) Improved trench film cooling with shaped trench outlets. ASME J Turbomach 135(2):1–15
9. Mcgoven KT, Leylek JH (2000) A detailed analysis of film cooling physics: part II—compound-angle injection with cylindrical holes. ASME J Turbomach 122(1):113–121

Identifying and Modelling of Constructs for Innovation Management of MSMEs: An ISM Approach

Bisma Mannan, Sonal Khurana and Abid Haleem

Abstract Both MSMEs and large organizations show the evidence that innovation is not only the result of technological knowledge and change, moreover, it also severely relies on the managerial aspect of innovation which is known as 'Innovation Management'. Although innovation management is recognized as the most important driving force for competitiveness, the available literature in the innovation management area is still highly fragmented. Thus, in this paper, we endeavour to do a systematic review and identify constructs for innovation management from perspectives of MSMEs and develop an ISM model. So, this paper helps in learning and understanding constructs that influence innovation management in MSMEs.

Keywords Innovation management · Systematic review · MSMEs · Construct · Interpretive structure modelling (ISM)

1 Introduction

Innovation is becoming vital for both developed as well as developing economy. Innovation is the main driving force for development and growth of an organization. Accordingly, much energy is put in developing innovative products, developing tacit and explicit innovative knowledge and progressive technologies. The existing enterprises or the start-ups are benefited from the innovations in the form of more income and more revenues. Innovation can be dealt as a discipline and has a capability of being learned and practiced [64].

Innovation is vital in the present business scenario. The condition of progress in competitive condition has turned out to be more challenging [69]. In this way, innovation is exceptionally domineering and becomes the principle need for the organization to achieve superior development and competitiveness. As organizations

B. Mannan (✉)
Sharda University, Greater Noida, Uttar Pradesh 201310, India
e-mail: bismamannan@gmail.com

S. Khurana · A. Haleem
Department of Mechanical Engineering, Jamia Millia Islamia, Delhi 110025, India

H. Kumar and P. K. Jain (eds.), *Recent Advances in Mechanical Engineering*,
Lecture Notes in Mechanical Engineering,
https://doi.org/10.1007/978-981-15-1071-7_13

are facing increased pace of technological change and competition, they must consider managerial aspect of innovation [66] which may add long-lasting competitive advantage.

In this study, we attempt to identifying constructs that represent innovation management in MSMEs with the help of available literature. The concept of literature review has lately gained attention in the literature of management [59] and after that we develop a conceptual model with the help of ISM.

2 Need for the Research

Researchers from a multidisciplinary background analyse, investigate and research on a phenomenon which is intricate and multidimensional. The innovation management literature is scattered and fragmented, and it is problematic to recognize a specific study in which an inclusive discussion of innovation management constructs for MSMEs are compiled. In this research, there is an identification and assessment of major constructs that are the basis of innovation management. The systematic review and the ISM model of constructs of innovation management further help management practitioners to understand innovation management environment in their organizations.

2.1 Objectives of the Research Constructs of Innovation Management

- Understanding the concept and paradigm shift of innovation.
- Identification of major construct that governs innovation management in organization.
- Develop a model that helps in achieving innovation management.

3 Constructs of Innovation Management

Innovation management is a key domain for practitioners as well as academicians. The ability of organizations to innovate is controlled by various constructs. These constructs are governed by their internal organizational condition as well as external conditions. There are ten major constructs which are the basis of innovation management in organization that are identified and compiled in a tabular form in the below section (Table 1).

Table 1 Constructs of Innovation management identified from the past literature

Construct	Authors
Knowledge management	Blackler [10], Hull et al. [32], Adams et al. [3], Khurana et al. [35], Tushman and Nadler [70], Van de Ven and Huber [72], Wong et al. [75], Zemaitis [77]
Organization culture	Ekvall [21], Dougherty [19], Mathisen and Einarsen [51], Tidd et al. [67], Mannan et al. [45]
Diffusion and adoption	Kotler and Trias de Bes [37], Baker [6], Kinnear et al. [1], Winer [74], Cooper et al. [14], Tidd [68], Hoffman [29], Roger [62]
Communication	Hameed et al. [27], Anuar et al. [4], Dahnil et al. [16], Abed et al. [2], Mannan et al. [46, 48, 49]
Collaboration	Preissl [60], Robson and Bennett [61], Pickernell et al. [58], Autio [5], Agarwal (2006), Packham et al. [57], Lee and Win [39], Khurana et al. [36]
Top management	Vaccaro et al. [71], Damanpour [17], Birkinshaw [9], Mihalache [54], Mannan et al. [44, 47, 49], Mannan and Khurana [43], Manoharan et al. [50], McAdam [53]
Portfolio management	Bard et al. [7], Cebon and Newton [11], Wadhwa et al. [73], Faems et al. [23], Davis [18], EU [20], Hisrich and Kearney [28], Hsiao and Liu [31], Jha and Devaya [33]
Benchmarking	Cooper and Kleinschmidt [13], Cooper et al. [12], Giovannoni and Pia Maraghini [25], Gomes and Yasin [26], Madsen et al. [40]
Government policies	Escribá-Esteve et al. [22], Czarnitzki and Hottenrott [15], Sharma et al. [65], Newman et al. [56], Mannan and Khurana [43], Mannan et al. [47], Manoharan et al. [50], Saxena et al. [63], Nelson and Winter [55]
Financial resources	Robson and Bennett [61], Escribá-Esteve et al. [22], Struhařová (2010), Czarnitzki and Hottenrott [15], Newman et al. [56], Bhunia [8], Xia [76], Mannan et al. [42], Saxena et al. [63], Hsiao et al. [30]

3.1 Interpretive Structural Modelling (ISM)

ISM is a methodology which permits users to deal with the intricacy of the system and without difficulty resolves the system into structured and comprehensible form by finding out the different level of the construct of a system. To develop the framework for innovation management in Indian MSMEs, one should enhance and simplify the knowledge of the constructs and the underlying interconnections. The exploration in the area is commenced on the recognizable proof of underlying contextual relationships amongst circumstances and end results that can prompt to knowledge generation of a system. ISM technique satisfies this necessity as it basically analyses the constructs, identifies the interrelationship between variables, and the hierarchy is developed according to the significance of these constructs and grouping of different constructs on different levels can also be performed. Consequently, in this chapter, the ISM is created for generic innovation management model in the context of Indian MSMEs.

Interpretive structural modelling (ISM) is the methodology which is algebraic in nature for framework development and investigation that was first presented by Warfield, which lessens the complexity of a system by creating a legitimately arranged hierarchical model Kang et al. [34]. ISM has been used in different research fields like vitality administration, data innovation, production and manufacturing technique, association conduct, execution and performance administration and project administration.

3.2 Development of ISM-Based Structural Model

ISM method is described. The six steps that are utilized in ISM methodology are discussed below:

Ten constructs that were discussed in Chap. 2 were organized and put in a form of a matrix so that the specialist/experts of innovation management area can easily share their opinion when the constructs are being compared in the matrix. The ten constructs are (1) knowledge management; (2) organization culture; (3) diffusion and adoption; (4) communication; (5) collaboration; (6) benchmarking; (7) top management; (8) portfolio management; (9) government policies; (10) financial resources. The number displayed in the parenthesis cites the construct's numbers.

The contextual relationship is established and analysed between constructs by comparing one construct with other constructs on the basis of their dependencies.

Structural self-interaction matrix (SSIM) is developed with the help of constructs to exhibit the contextual relationship between constructs on innovation management in MSMEs. The relationship data that is filled in the SSIM matrix was gathered with the help of the selected specialists from academics and industry. The four experts are from MSMEs of a managerial position, and three experts are from academic. All specialists were requested to recognize the relationships between the ten constructs of innovation management for Indian MSMEs and develop a model using their expert knowledge of constructs of innovation management. Worksheet is given to each expert each having a SSIM to fill. In these SSIM matrixes, the pair-wise comparison is utilized to develop a different contextual relationship. To develop a different contextual relationship among the constructs of innovation management in MSMEs, the specialists were requested to answer on a worksheet by representing '*V*', '*A*', '*X*' and '*O*' with respect to each cell of the matrix.

Every expert was appropriately briefed of the constructs of innovation management in Indian MSMEs, and the worksheet is given to accumulate the relationship feedback given by the experts. Subsequent to explaining the objective of research to the experts, every expert was asked to answer the worksheet. Worksheets were gathered from experts, and then the compiled result was assessed. If the connection amongst ith and the jth components is consistent at that point, respective alphabet was assigned to the corresponding cell. In this way, after a few associations, the final SSIM of the innovation management in Indian MSMEs was developed. Then, the SSIM has been transformed into a matrix which is binary, and it is known as

the reachability matrix by replacing *V*, *A*, *O* and *X* by 0 and 1. Next, transitivity is checked, after developing the reachability matrix, and then dependence and driving power are assessed (Table 2).

After several iterations, we get the final level partitioning table which is shown below (Table 3).

4 ISM Model

By using the level partitioning table, four levels of the interpretive structural model (ISM) are developed. Top management, financial support and government policies are on the fourth level having the highest driving power which means all the other factors of innovation management are directly or indirectly dependent on these three factors. On the third level, there are three factors, i.e. communication, organization culture and communication. These factors are also very critical for innovation management as it has high driving power. Next is the second level which also comprises with three factors, i.e. knowledge management, portfolio management and benchmarking. This level has a high dependence power. Lastly, diffusion and adoption are on level first with highest dependence power.

Figure 1 shows the ISM or the conceptual model of innovation management in MSMEs. This model is entirely based on the expert opinion and on the constructs, which are defined using the literature review. But, the available literature from which the constructs are identified is not in Indian context.

5 MICMAC Analysis

MICMAC analysis Mathiyazhagan et al. [52] will aid us in plotting the graph to categorize and recognize constructs for the innovation management in MSMEs. The purpose of MICMAC analysis is to recognize the core constructs that drive the system (Fig. 2).

With the help of dependence and driving power, all the ten constructs are divided into four categories which are discussed below [41]:

- Cluster I (Autonomous): These are the constructs having less dependence and driver powers. They are positioned near to the origin and do not much affect the system. Considering the current case, there are no such factors.
- Cluster II (Dependent). They are highly conditional constructs. They have very less driving power. In the present case, diffusion and adoption, knowledge management, benchmarking and portfolio management are dependent constructs.
- Cluster III (Linkage). The third group has correlating constructs which has both high dependence and high driving power. In this case, organization culture, communication and collaboration come in this category.

Table 2 Driving power verses dependence power

Codes	1	2	3	4	5	6	7	8	9	10	Driving power
1	1	0	1	0	0	1	0	1	0	0	4
2	1	1	1	1	1	1	0	1	0	0	7
3	0	0	1	0	0	0	0	0	0	0	1
4	1	1	1	1	1	1	0	1	0	0	7
5	1	1	1	1	1	1	0	1	0	0	7
6	1	0	1	0	0	1	0	1	0	0	4
7	1	1	1	1	1	1	1	1	1	1	10
8	1	0	1	0	0	1	0	1	0	0	4
9	1	1	1	1	1	1	1	1	1	1	10
10	1	1	1	1	1	1	1	1	1	1	10
Dependence power	9	6	10	6	6	9	3	9	3	3	64/64

Table 3 Final level partitioning of the constructs of innovation management in MSMEs

Elements	Reachability set	Antecedent set	Intersection	Level
1	1, 3, 6, 8	1, 2, 4, 5, 6, 7, 8, 9, 10	1, 6, 8	II
2	1, 2, 3, 4, 5, 6, 8	2, 4, 5, 7, 9, 10	2, 4, 5	III
3	3	1, 2, 3, 4, 5, 6, 7, 8, 9, 10	3	I
4	1, 2, 3, 4, 5, 6, 8	2, 4, 5, 7, 9, 10	2, 4, 5	III
5	1, 2, 3, 4, 5, 6, 8	2, 4, 5, 7, 9, 10	2, 4, 5	III
6	1, 3, 6, 8	1, 2, 4, 5, 6, 7, 8, 9, 10	1, 6, 8	II
7	1, 2, 3, 4, 5, 6, 7, 8, 9, 10	7, 9, 10	7, 9, 10	IV
8	1, 3, 6, 8	1, 2, 4, 5, 6, 7, 8, 9, 10	1, 6, 8	II
9	1, 2, 3, 4, 5, 6, 7, 8, 9, 10	7, 9, 10	7, 9, 10	IV
10	1, 2, 3, 4, 5, 6, 7, 8, 9, 10	7, 9, 10	7, 9, 10	IV

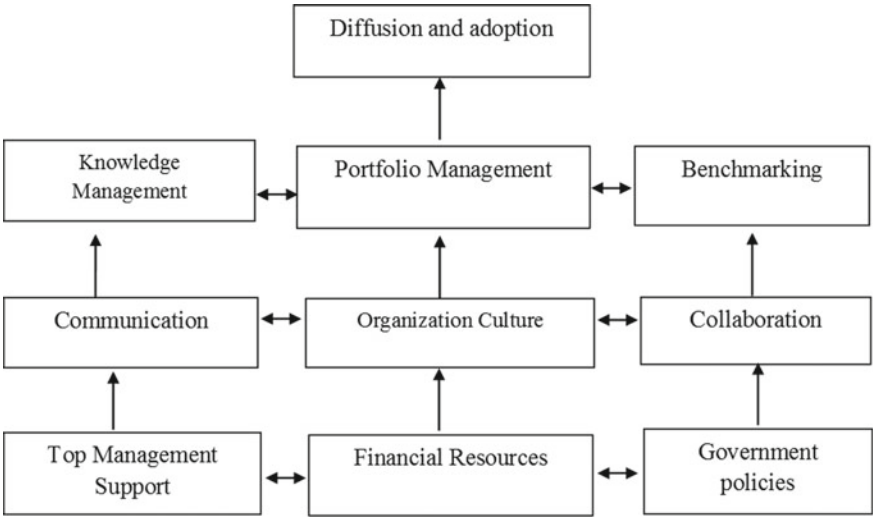

Fig. 1 ISM/conceptual model of innovation management in MSMEs

- Cluster IV (Independent). The fourth group consists of independent constructs with high driver power and is extremely discrete. Top management support, government policies and financial resources are independent constructs.

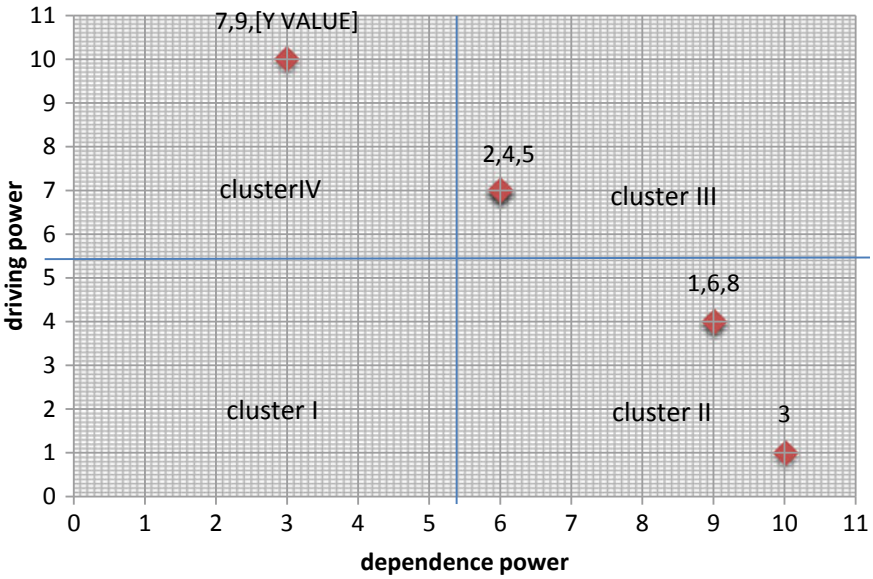

Fig. 2 Driving power and dependence graph for constructs

6 Result and Discussion

MSMEs require searching the sources of innovation, the modifications and their sign that show chances of success in innovation, and they require the knowledge and application of the principles of successful innovation. In this paper, we have identified ten constructs for developing a model for innovation management of Indian MSMEs. By using ISM approach, the hierarchical model is developed which helps in establishing the contextual relationship between the constructs of innovation management for Indian MSMEs. ISM has four hierarchical level, i.e. at the first level, it has diffusion and adoption which has high dependence power; second level has knowledge management, benchmarking and portfolio management; third level has communication, organization culture and collaboration; fourth and the last level have highest driving power which consists of top management, government policies and financial resources.

7 Research Implications

Identifying construct that represents innovation management in MSMEs within a structured outline is a challenging task. We have given a reasonable conceptualization of constructs of innovation and form ten hypotheses for each construct to advance our understanding in the area of innovation.

We believe that this paper gives insight and stimulates the perception of researchers and practitioners on innovation management and its constructs.

8 Limitation of ISM Modal and MICMAC Analysis

The results of ISM are subjective or may be biased because ISM inputs are entirely based on expert opinion. There may be a region-specific biasedness as the experts were from the specific region of India and the study is for Indian MSMEs. MICMAC analysis groups the constructs in the different cluster according to their driving or dependence power but it did not give the correlation value of these constructs. ISM gives the contextual relationship between the constructs but cannot quantify the relationship or statistically validate the relationship or the model. So, for this SEM can be used.

9 Conclusion

Innovation is astonishingly a standout topic amongst most of the topics discussed by academician and practitioners, and most of the studies tend to perceive innovation as the improvement of product, service or technology. Due to this, technological innovation has ruled innovation studies. So, most researches are mainly focused on product innovation and its diffusion and adoption in the market. Moreover, innovation is more dependent on the managerial aspects and on the constructs like financial resources, government policies and top management support. These constructs help in developing market strategies and keeping up with the competition. This involves not only looking for new technology and new advances in the product but also requires administration in the organization, that is, innovation management.

References

1. Kinnear TC, Bernhardt KL, Krentler KA (1995) Principles of marketing (4th ed). Harper Collins, New York
2. Abed S, Dwivedi Y, Williams M (2015) Social media as a bridge to e-commerce adoption in SMEs: a systematic literature review. Mark Rev 15(1):39–57. https://doi.org/10.1362/146934715x14267608178686
3. Adams R, Bessant J, Phelps R (2006) Innovation management measurement: a review. Inter J Manag Rev 8(1):21–47. https://doi.org/10.1111/j.1468-2370.2006.00119.x
4. Anuar J, Musa M, Khalid K (2014) Smartphone's application adoption benefits using Mobile Hotel Reservation System (MHRS) among 3 to 5-star city hotels in Malaysia. Procedia-Social Behav Sci 130:552–557. https://doi.org/10.1016/j.sbspro.2014.04.064
5. Autio E (1997) New, technology-based firms in innovation networks: symplectic and generative impacts. Res Policy 26(3):263–281

6. Baker M (1999) The IEBM encyclopedia of marketing. International Thomson Business, London
7. Bard JF, Balachandra R, Kaufmann PE (1988) An interactive approach to R&D project selection and termination. IEEE Trans Eng Manag 35:139–146
8. Bhunia A (2012) Association between default behaviors of SMEs and the credit facets of SMEs owners. Eur J Bus Manag 4(1)
9. Birkinshaw J (2010) Reinventing management. Wiley, Chichester
10. Blackler F (1995) Knowledge, knowledge work and organizations: an overview and interpretation. Organ Stud 16:1021–1046
11. Cebon P, Newton P (1999) Innovation in firms: towards a framework for indicator development. Melbourne Business School
12. Cooper RG, Edgett SJ, Kleinschmidt EJ (2004) Benchmarking best NPD practices. Res Technol Manag 47:50–59
13. Cooper RG, Kleinschmidt EJ (1995) Benchmarking the firm's critical success factors in new product development. J Prod Innov Manag 12:374–391
14. Cooper RG, Edgett SJ, Kleinschmidt EJ (2001). Portfolio Management for New
15. Czarnitzki D, Hottenrott H (2011) R&D investment and financing constraints of small and medium-sized firms. Small Bus Econ 36(1):65–83
16. Dahnil M, Marzuki K, Langgat J, Fabeil N (2014) Factors influencing SMEs adoption of social media marketing. Procedia-Social Behav Sci 148:119–126
17. Damanpour F (1991) Organizational innovation: a meta-analysis of effects of determinants and moderators. Acad Manag J 34:555–590
18. Davis MC (1998) Knowledge management. Inf Strat Executive's J 15:11–22
19. Dougherty D (1995) Managing your core competencies for corporate venturing. Entrepreneurship Theor Pract 19(3):113–135
20. EU European Commission (2004) Innovation Management and the Knowledge-Driven Economy. Directorate-General for Enterprise, ECSC-EC-EAEC, Brussels
21. Ekvall G (1996) Organizational climate for creativity and innovation. Eur J Work Organ Psychol 5:105–123
22. Escribá-Esteve A, Sánchez-Peinado L, Sánchez-Peinado E (2008) Moderating influences on the firm's strategic orientation-performance relationship. Int Small Bus J 26(4):463–489
23. Faems D, Janssens M, Neyens I (2012) Alliance portfolios and innovation performance. Group Organ Manag 37(2):241–268. https://doi.org/10.1177/1059601112441246
24. Fogel G, Zapalska A (2001) A comparison of small and medium-size enterprise development in central and eastern Europe. Comp Econ Stud 43(3):35–68. https://doi.org/10.1057/ces.2001.13
25. Giovannoni E, Pia Maraghini M (2013) The challenges of integrated performance measurement systems. Acc Auditing Accountability J 26(6):978–1008. https://doi.org/10.1108/aaaj-04-2013-1312
26. Gomes C, Yasin M (2011) A systematic benchmarking perspective on performance management of global small to medium-sized organizations. Benchmarking Inter J 18(4):543–562. https://doi.org/10.1108/14635771111147632
27. Hameed M, Counsell S, Swift S (2012) A conceptual model for the process of IT innovation adoption in organisations. J Eng Technol Manage 29(3):358–390. https://doi.org/10.1016/j.jengtecman.2012.03.007
28. Hisrich RD, Kearney C (2014) Managing innovation and entrepreneurship. SAGE Publications
29. Hoffman K (2005) Marketing principles and best practices. Thomson/South-Western, Mason
30. Hsiao SW, Ko YC, Lo CH, Chen SH (2013) An ISM, DEI, and ANP based approach for product family development. Adv Eng Inform 27(1):131–148
31. Hsiao SW, Liu E (2005) A structural component-based approach for designing product family. Comput Ind 56(1):13–28
32. Hull R, Coombs R, Peltu M (2000) Knowledge management practices for innovation: an audit tool for improvement. Int J Technol Manag 20:633–656
33. Jha KN, Devaya MN (2008) Modelling the risks faced by Indian construction companies assessing international projects. Constr Manag Econ 26(4):337–348

34. Kang HY, Lee AHI, Chang CC, Kang MS (2012) A model for selecting technologies in new product development, mathematical problems in engineering. https://doi.org/10.1155/2012/358129
35. Khurana S, Khan J, Mannan B (2013) A study on technology management: enablers and barriers in its implementation in the case of SMEs in India, sustainability and development. In: International conference on rural innovation, capacity building, knowledge management, entrepreneurship and technology (ICRICKET). New Delhi. http://dx.doi.org/10.13140/RG.2.1.4397.4640
36. Khurana S, Mannan B, Haleem A (2014) Integrating innovation with sustainability: a study of practices/status for Indian manufacturing industries (SMEs). In: AGBA 11th world congress conference. IIT, Delhi. http://dx.doi.org/10.13140/RG.2.1.2824.6005
37. Kotler P, Trias de Bes F (2003) Lateral marketing (1st ed). Wiley, Hoboken
38. Kovacˇicˇ A (2007) Benchmarking the Slovenian competitiveness by system of indicators. Benchmarking Inter J 14(5):553–574
39. Lee J, Win HN (2004) Technology transfer between university research centers and industry in Singapore. Technovation 24(5):433–442
40. Madsen D, Slåtten K, Johanson D (2017) The emergence and evolution of benchmarking: a management fashion perspective. Benchmarking Inter J 24(3):775–805. https://doi.org/10.1108/bij-05-2016-0077
41. Mangla S, Madaan J, Chan FT (2013) Analysisof flexible decision strategies for sustainability-focused green product recovery system. Int J Prod Res 51(11):3428–3442
42. Mannan B, Khurana S, Haleem A (2016) Modeling of critical factors for integrating sustainability with innovation for Indian small- and medium-scale manufacturing enterprises: an ISM and MICMAC approach. Cogent Bus Manag 3(1):1–15. https://doi.org/10.1080/23311975.2016.1140318
43. Mannan B, Khurana S (2012) Enablers and barriers for introduction of robotics as an AMT in the Indian industries (case of SME's). Inter J Comput Appl, 19–24. http://dx.doi.org/10.13140/2.1.2625.5368
44. Mannan B, Jameel S, Haleem A (2013) Knowledge management in project management. LAP LAMBERT Academic Publishing, Saarbrücken. http://dx.doi.org/10.13140/RG.2.1.4921.7527
45. Mannan B, Khan J, Khurana S (2012) Information technology: a green supply chain enable emerging paradigms in marketing. In: National conference on emerging paradigms in marketing. New Delhi, JMI. http://dx.doi.org/10.13140/RG.2.1.3556.1205
46. Mannan B, Khan J, Khurana S (2013) Enablers and barriers to KM in project based organization, sustainability and development. In: International conference on rural innovation, capacity building, knowledge management, entrepreneurship and technology (ICRICKET). New Delhi. http://dx.doi.org/10.13140/RG.2.1.3873.1762
47. Mannan B, Khurana S, Haleem A (2012) Identification and analysis of critical factors of KM in project management: an interpretive structural modeling approach. In: XVI annual international conference of society of operation management. IIM, IIT Lucknow, New Delhi. http://dx.doi.org/10.13140/RG.2.1.1776.0240
48. Mannan B, Khurana S, Haleem A (2015a) Study of factors that influences diffusion and adoption in innovation management. In: National seminar on solar robotics. JMI, Delhi
49. Mannan B, Khurana S, Haleem A (2015b) Technological innovation challenges and opportunities in India and the developing countries. In: 2015 annual IEEE india conference (INDICON), pp 1–6. http://dx.doi.org/10.1109/INDICON.2015.7443854
50. Manoharan TR, Muralidharan C, Deshmukh SG (2010) Analyzing the interaction of performance appraisal factors using interpretive structural modelling. Perform Improv 49(6):25–35
51. Mathisen GE, Einarsen S (2004) A review of instruments assessing creative and innovative environments within organizations. Creativity Res J 16:119–140
52. Mathiyazhagan K, Govindan K, Noorul Haq A, Geng Y (2013) An ISM approach for the barrier analysis in implementing green supply chain management.J Clean Prod 47:283–297
53. McAdam RMS (1999) The process of knowledge management within organizations: a critical assessment of both theory and practice. Knowl Process Manag 6:101–113

54. Mihalache OR (2012) Stimulating firm innovativeness: probing the interrelations between managerial and organizational determinants. Erasmus Research Institute of Management (ERIM), Rotterdam
55. Nelson RR, Winter SG (1982) An evolutionary theory of economic change. Harvard University Press, Cambridge, MA
56. Newman A, Gunessee S, Hilton B (2012) Applicability of financial theories of capital structure to the Chinese cultural context: a study of privately owned SMEs. Int Small Bus J 30(1):65–83
57. Packham G, Pickernell D, Brooksbank D (2010) Introduction: the changing role of universities in knowledge generation, dissemination and commercialization. Inter J Entrepreneurship Innov 11(4):261–263
58. Pickernell D, Packham G, Brooksbank D, Jones P (2010) A recipe for what? UK universities, enterprise and knowledge transfer: evidence from the federation of Small Businesses 2008 survey. Inter J Entrepreneurship Innov 11(4):265–272
59. Pittaway L, Robertson M, Munir K, Denyer D, Neely A (2004) Networking and innovation: a systematic review of the evidence. Inter J Manag Rev 5–6(3–4):137–168. https://doi.org/10.1111/j.1460-8545.2004.00101.x
60. Preissl B (2006) Research and technology organisations in the service economy. Developing Anal Tools Changing Innov Patterns Innov 19(1):131–145
61. Robson PJA, Bennett RJ (2000) SME growth: the relationship with business advice and external collaboration. Small Bus Econ 15(3):193–208
62. Rogers E (2003) Diffusion of innovations. Free Press, New York
63. Saxena JP, Sushil Vrat P (1992) Scenario building: a critical study of energy conservation in the Indian cement industry. Technol Forecast Soc Change 41(1):121–146
64. Schumpeter J (1934) The theory of economic development. Harvard University Press, New York: Harper & Row
65. Sharma OP, Bambawale OM, Gopali JB, Bhagat S, Yelshetty S, Singh SK, Anand R, Singh OM (2011) Field guide Mung bean and Urd bean. Government of India, Department of Agricultural and Co-operation, NCIPM, ICAR, New Delhi, India
66. Teece D (2007) Explicating dynamic capabilities: the nature and micro-foundations of (sustainable) enterprise performance. Strateg Manag J 28(13):1319–1350. https://doi.org/10.1002/smj.640
67. Tidd J, Bessant J, Pavitt K (1997) Managing innovation: integrating technological, market and organizational change. Wiley, Chichester, UK
68. Tidd J (2001) Innovation management in context: environment, organization and performance. Int J Manage Rev 3(3):169–183. https://doi.org/10.1111/1468-2370.00062
69. Tranfield D, Denyer D, Smart P (2003) Towards a methodology for developing evidence-informed management knowledge using systematic review. Br J Manag 14(3):207–222. https://doi.org/10.1111/1467-8551.00375
70. Tushman MT, Nadler D (1986) Organizing for innovation. Calif Manag Rev 28:74–92
71. Vaccaro IG, Volberda HW, Van Den Bosch FAJ (2012) Management innovation in action: the case of self-managing teams. In: Pitsis TS, Simpson A, Dehlin E (eds) Handbook of organizational and managerial innovation. Edwar Elgar, Cheltenham, pp 138–162
72. Van de Ven A, Huber G (1990) Longitudinal field research methods for studying processes of organizational change. Organ Sci 1(3):213–219. https://doi.org/10.1287/orsc.1.3.213
73. Wadhwa A, Phelps C, Kotha S (2016) Corporate venture capital portfolios and firm innovation. J Bus Ventur 31(1):95–112. https://doi.org/10.1016/j.jbusvent.2015.04.006
74. Winer (2007) Marketing management (3rd ed.) Prentice Hall
75. Wong P, Lee L, Foo M (2008) Occupational choice: the influence of product vs. process innovation. Small Bus Econ 30(3):267–281. https://doi.org/10.1007/s11187-006-9044-8
76. Xia L (2014) Analysis on the small and medium-sized enterprise financing bank loans availability. Appl Mech Mater 687–691:4799–4802. https://doi.org/10.4028/www.scientific.net/amm.687-691.4799
77. Zemaitis E (2014) Knowledge management in open innovation paradigm context: high tech sector perspective. Proc Soc Behav Sci 110:164–173

Investigation of Drivers Towards Adoption of Circular Economy: A DEMATEL Approach

Annayath Maqbool, Shahbaz Khan, Abid Haleem and Mohd Imran Khan

Abstract The increased population, scarcity of resources and environmental consciousness put the tremendous stress on the organisations to fulfil the demand in sustainable way. The current linear model is based on the take-make-use-destroy model, which has many limitations in terms of resource utilisation and environmental impact. To overcome such limitation, circular economy is proposed. The main aim of circular economy is to create a circular system that maximises the resource value and enhances the material and product. However, the adoption of the circular economy is challenging and required some essential/motivational factor. This study is identifying the ten major drivers towards the adoption of circular economy. Further, these drivers are categorised into two groups utilising the decision-making trial and evaluation laboratory (DEMATEL). The result of this study explored that most influential drivers are 'government policies for cleaner production' and 'urbanisation', while 'enhanced material and energy efficiency' and 'improving product quality' are the most influenced. This study can support the policy makers to develop the strategies in the adoption of circular economy.

Keywords Circular economy · Drivers · DEMATEL · Supply chain management

A. Maqbool · S. Khan · A. Haleem (✉) · M. I. Khan
Department of Mechanical Engineering, Jamia Millia Islamia, New Delhi 110025, India
e-mail: ahaleem@jmi.ac.in

A. Maqbool
e-mail: anayatmir56@gmail.com

S. Khan
e-mail: shahbaz.me12@gmail.com

M. I. Khan
e-mail: imrankhan@st.jmi.ac.in

H. Kumar and P. K. Jain (eds.), *Recent Advances in Mechanical Engineering*,
Lecture Notes in Mechanical Engineering,
https://doi.org/10.1007/978-981-15-1071-7_14

1 Introduction

The population of the world has been predicted to be about 9 billion by 2050 and 10.1 billion by 2100 [1]. This massive population growth puts tremendous stress on the environment and the resource [2]. So, there is the requirement of more extraction of raw materials and consequently more waste.

The current economic model is linear in nature [3] and aims at producing products from raw material, sold and dumped as waste after serving the purpose of use [4]. This economic model is called the take-make-use-destroy model [5]. This linear model is not sustainable in the long run as this model continuously destroys the limited natural resources [6]. The adoption of the circular economy (CE) can surmount the limitations of the linear model of the economy. A CE as described by the authors of [7] is 'an economic system that is based on business models which replace the 'end-of-life' concept with reducing, alternatively reusing, recycling and recovering materials in production/distribution and consumption processes, thus operating at the micro level (products, companies, consumers), meso level (eco-industrial parks) and macro level (city, region, nation and beyond), with the aim to accomplish sustainable development, which implies creating environmental quality, economic prosperity and social equity, to the benefit of current and future generations'.

The aim of the CE was to limit the extraction of raw materials and the production of waste by recovering and reusing as many of the materials possible. The CE has many significant advantages over the traditional economy as it is evident in literature through various studies and researches [8]. The linear economy flow model is causing several serious environmental impacts such as global warming and natural resource depletion. Unlike linear economy practices, CE-oriented approach focuses on reuse, remanufacturing, refurbishment, repair of products by cascading and upgrading. CE also emphasise on the exploitation of renewable energies such as solar, wind and biomass energy throughout the product value chain.

The switching of a linear economy to a CE is a very challenging task and demands motivational factors. These drivers facilitate in the adoption of the CE which makes it necessary for the identification and evaluation of the drivers before the adoption of the CE. With the use of DEMATEL, this study acknowledges the position of each driver in the CE system along with their degree of effectiveness on the system and on the other drivers. With the help of experts, the results obtained by the DEMATEL provide the major dominant drivers [9]. The focus is put on these influential drivers to make better the overall system. The other benefits of this technique are that the DEMATEL technique is suitable with limited data, [10]. Understanding the drivers and their driving potential will be beneficial in formulating the strategies in order to decrease the effect of barriers. In this paper, the objective of research is to find the drivers of the CE and explore the causal relationships among the drivers.

The remaining paper is structured as follows: Sect. 2 reviews the literature on the CE. Section 3 identifies the significant drivers of the CE. Section 4 presents the research methodology of the paper. The results are illustrated in Sect. 5. Sections 6, 7 and 8 present the discussions, implications and conclusions, respectively.

2 Literature Review

A CE approach is to facilitate growth and, at the same, time minimises resource usage by closing all resource loops and reconnecting them at various nodes, thereby reducing and ultimately eliminating waste [11].

To reveal the current status of adoption of the CE, various research scholars have generally reviewed the concepts of CE. Ghisellini et al. [5] first reviewed the CE and compared CE adoption and practices of China with Europe, Japan and the world. Govindan et al. [8] presented a comprehensive review of barriers, drivers and practices that affect the adoption of the CE through supply chain perspective.

Sun et al. [12] assessed the concepts, practices and assessment tools of CE in china. Geng et al. [13] evaluated the advancement and extent of adoption of the CE in China. Kirchherr et al. [7] examined the various conceptualisations of the CE to clarify the present interpretation of CE concepts by analysing 114 definitions. Lewandowski [14] assessed the current business models of circular to find out gaps that continued to be in the literature and presented a proposal for a new structure for better adoption of the CE. Ellen McArthur Foundation [15] presented a study that provides a toolkit for the policymakers who want to design a policy to step up the changes towards the CE. Liguori and Faraco [16] analysed the various conceptions of biotreatment such as biorefineries and waste management that encourage the adoption of the CE. Ghisellini et al. [5] analysed the changes involved with interlinking the systems of environment and economy.

3 Drivers Towards the Adoption of the Circular Economy

Drivers are the motivational requirement for the effective adoption of CE in a supply chain. For the successful implementation, these drivers are identified and investigated, and Table 1 describes the selected drivers.

4 Research Methodology

The paper aims to investigate the drivers of the CE through causal relationship. After finding the drivers through literature review and expert's input, the drivers are examined using DEMATEL technique [27].

DEMATEL is the MCDM technique which was proposed and developed by the Battle Memorial Institute of Geneva during the period of 1972 and 1976. DEMATEL technique is summarised in the following steps.

Table 1 Drivers towards the adoption of circular economy

Drivers	Description	References
Government policies for cleaner production (D_01)	Governments of almost every country made laws and policies for the promotion of cleaner production, consumption and waste management for the protection of resources health and safety. These laws act as drivers for the implementation of CE	[17–21]
Economic growth through adoption of CE (D_02)	With the adoption of circular economic activities, i.e. reduce, reuse and recycle, remanufacturing effectively helps in generating long-term profitability	[2, 19, 22]
Environmental protection laws (D_03)	The amount of waste produced could result in the generation of greenhouse gases and lead to global warming. Due to these climatic changes, air quality and water quality will be degraded, and landscapes may be lost forever. Therefore, it becomes necessary for the implementation of laws for environmental protection which is possible by the adoption of the CE	[19–21, 23, 24]
Demand for renewable energy (D_04)	The renewable resources need to be secured as the demand for these resources is increasing	[24, 25]
Urbanisation (D_05)	As people are moving towards the big cities, they require more development in the form of roads, bridges, dams, sewage and the need for transport thus put more pressure on the environment	[26]
Consumer awareness (D_06)	For the effective execution of the CE, consumer awareness is necessary	[19]
Enhanced material and energy efficiency (D_07)	Through the strategic adoption of CE, effectiveness of materials and energy use will be increased	[12]

(continued)

Table 1 (continued)

Drivers	Description	References
Improving product quality (D_08)	Product quality will be increased by adopting the CE in the supply chain	[19]
Cost reduction and financial profitability (D_09)	The product cost is reduced due to the use of recycled materials and alternative energy utilisation	Recommended by expert
The scarcity of resources (D_10)	Major resources such as raw materials and conventional energy sources are limited; these materials need to be preserved for future use	Recommended by expert

Step I: Construction of direct influence matrix

A questionnaire is used to collect the response experts about the effect of one factor over another factor. The pairwise comparison values between factor 'i' and 'j', by kth expert, were expressed using a five-point linear scale ranging between 0 and 4; the numerals are used to indicate the strength of a relationship (please see Table 2).

The notation of x_{ij} indicates the influence of variable i on variable j. The elements of diagonal (i.e. $i = j$) of the direct relation matrix are zero. For every expert, a non-negative $n \times n$ matrix is acquired as $X^k = x_{ij}^k$ where k represents the kth experts ($1 \leq k \leq H$). The direct relation matrix is acquired from each expert (number of expert is H) in the form of $X^1, X^2, X^3 \ldots X^H$.

Step II: Construct an overall direct relation matrix from H experts, the average matrix $A = [a_{ij}]$ can be acquired from the Expression [1]:

$$a_{ij} = \frac{\sum_{k=1}^{H} x_{ij}^k}{H} \tag{1}$$

Step III: Construct a normalised initial direct relation matrix, B from Expressions (2) and (3).

Table 2 Scale and their interpretation

Scale	Interpretation
0	No influence
1	Very low influence
2	Medium influence
3	High influence
4	Very high influence

$$B = A \cdot S \tag{2}$$

$$\text{where } S = \frac{1}{\max_{1 \le i \le n} \sum_{j=1}^{n} a_{ij}} \tag{3}$$

The elements of matrix B lie between zero and one.

Step IV: Construct the total relation matrix 'T' from Expression (4)

$$T = B \cdot (I - B)^{-1} \tag{4}$$

where 'I' is the identity matrix.

Step V: Evaluate the causal parameters through Expressions (5) and (6):

$$R_i = \sum_{j=1}^{n} t_{ij} \text{ for all } i \tag{5}$$

$$C_j = \sum_{i=1}^{n} t_{ij} \text{ for all } j \tag{6}$$

where R_i indicates the sum of rows and C_j indicates the sum of columns.

Step VI: Construct a cause and effect diagram using the data of $(R + C)$ and $(R–C)$ given in Table 6, computed from Eqs. (7) and (8):

$$P_i = R_i + C_j | i = j \tag{7}$$

$$E_i = R_i - C_j | i = j \tag{8}$$

The difference $(R_i - C_i)$ indicates the net influence that variable i adds to the system. Furthermore, if the value of $(Ri - Ci)$ is positive, variable i is a net cause, and if the value of $(Ri - Ci)$ is negative, variable i is a net receiver.

5 Results

The drivers towards the adoption of the CE are obtained through literature review. After discussing, the drivers with a five-member experts' group for the deeper insights and ten drivers were finalised on the recommendations of experts (Table 1). After

finalising the drivers, the decision makers were asked to assess the direct relation among the drivers of the CE on the scale of 0–4 (Table 2). The overall direct relation matrix is calculated using Expression 1 (Table 3).

Then, the normalised direct relation matrix (B) is computed from Expressions (2) and (3) as shown in Table 4.

After that, this matrix is changed into total relation matrix (T) using Expression (4) as shown in Table 5.

In matrix T, the summation of rows and columns is denoted by R and C, respectively, using Expression (5).

Where R_i denotes the total influence of driver 'i' to the other drivers, and Ci denotes net effect on driver 'j' from other drivers. Following the computations of values R and C for every row and column, the prominence (P_i) and net effect (E_i) is computed utilising the Expressions (7) and (8) as shown in Table 6. The net cause/effect of each driver is determined through 'E_i (i.e. $R - C$)'. If the value E_i is positive, then the driver produces the net cause, and if negative, then the driver is the net effect. Figure 1 shows the plots of $R + C$ and $R - C$, which thereby depicts the causal relationship among the drivers of the CE. We have discussed these results with experts for further insights.

6 Discussion on Results

In this research, the relationship among the various factors was investigated by using DEMATEL, which crammed the space left by conventional models that have only considered the direct effects of a factor [28].

The results that show the driver effects on the system alongside on each other are shown in Table 5. Based on the '$R + C$' values, the importance order of the drivers is D_05 > D_01 > D_10 > D_06 > D_09 > D_08 > D_02 > D_03 > D_07 > D_04. Thus, from the '$R - C$' values, the drivers are classified into cause and effect groups. The drivers 'government policies for cleaner production (D_01)', 'urbanisation (D_05)', 'consumer awareness (D_06)', 'cost reduction and financial profitability (D_09)' and 'scarcity of resources (D_10)' having the positive values of $R - C$ are categorised under cause group. The drivers 'economic growth through adoption of CE (D_02)', 'environmental protection laws (D_03)', 'demand for renewable energy (D_04)', 'enhanced material and energy efficiency (D_07) and 'improving the product quality (D_08)' having the negative values of $R - C$ are categorised under effect group.

The categorisation of drivers into cause and effect groups will facilitate the experts to recognise the cause group drivers, which are necessary to be controlled [29]. The matter of fact is that the variables in the influential group are hard to transform while the variables in the influenced group can be easily transformed [30]. The drivers who need improvement on priority basis will be recognised by the decision makers with the help of prioritisation of drivers while focusing on that driver will improve the other drivers as well as the whole system [31].

Table 3 Overall direct relation matrix as obtained through expert inputs

Drivers	D_01	D_02	D_03	D_04	D_05	D_06	D_07	D_08	D_09	D_10
D_01	0	3.6	3.8	3.4	3.6	3.6	3.8	4	3.4	3.4
D_02	1.6	0	1.6	1.4	2	2.4	2.4	2	3	2
D_03	3.2	2.4	0	1.6	2	2.8	1.4	1.6	1.4	2.4
D_04	1.4	1.6	1.6	0	2.8	1.4	1.6	2.4	2	1.4
D_05	3.4	3.2	3.8	3.8	0	3.4	3.8	3.8	3.2	4
D_06	3	2.4	2.8	2.8	3	0	3	3.4	3.2	3.6
D_07	2	1.6	1.6	1.6	1.6	2.4	0	1.6	1.4	1.6
D_08	1.6	2	1.6	2.4	2	2.4	1.6	0	2	2
D_09	3.4	3.6	3.2	3	3	2.8	3	3	0	3.2
D_10	3.4	3.2	3	3.2	4	3.4	3	3.4	3.2	0

Table 4 Normalised direct relation matrix (*B*)

Drivers	D_01	D_02	D_03	D_04	D_05	D_06	D_07	D_08	D_09	D_10
D_01	0.000	0.110	0.117	0.104	0.110	0.110	0.117	0.123	0.104	0.104
D_02	0.049	0.000	0.049	0.043	0.061	0.074	0.074	0.061	0.092	0.061
D_03	0.098	0.074	0.000	0.049	0.061	0.086	0.043	0.049	0.043	0.074
D_04	0.043	0.049	0.049	0.000	0.086	0.043	0.049	0.074	0.061	0.043
D_05	0.104	0.098	0.117	0.117	0.000	0.104	0.117	0.117	0.098	0.123
D_06	0.092	0.074	0.086	0.086	0.092	0.000	0.092	0.104	0.098	0.110
D_07	0.061	0.049	0.049	0.049	0.049	0.074	0.000	0.049	0.043	0.049
D_08	0.049	0.061	0.049	0.074	0.061	0.074	0.049	0.000	0.061	0.061
D_09	0.104	0.110	0.098	0.092	0.092	0.086	0.092	0.092	0.000	0.098
D_10	0.104	0.098	0.092	0.098	0.123	0.104	0.092	0.104	0.098	0.000

Table 5 Total relation matrix (T)

Drivers	D_01	D_02	D_03	D_04	D_05	D_06	D_07	D_08	D_09	D_10
D_01	0.255	0.361	0.360	0.352	0.365	0.372	0.366	0.388	0.348	0.356
D_02	0.201	0.157	0.200	0.196	0.217	0.232	0.226	0.225	0.237	0.215
D_03	0.250	0.233	0.161	0.209	0.225	0.250	0.207	0.223	0.202	0.234
D_04	0.176	0.185	0.182	0.137	0.219	0.185	0.185	0.216	0.192	0.180
D_05	0.349	0.349	0.359	0.362	0.265	0.365	0.365	0.382	0.341	0.370
D_06	0.305	0.294	0.299	0.302	0.314	0.235	0.310	0.335	0.308	0.326
D_07	0.187	0.179	0.176	0.178	0.182	0.206	0.133	0.188	0.170	0.180
D_08	0.192	0.206	0.192	0.216	0.210	0.223	0.196	0.159	0.203	0.207
D_09	0.320	0.331	0.315	0.312	0.319	0.319	0.315	0.330	0.224	0.321
D_10	0.334	0.335	0.324	0.332	0.359	0.350	0.330	0.357	0.328	0.247

Table 6 Prominence (P_i) and net effect (E_i)

Drivers	R	C	$R + C$	$R - C$
D_01	3.524	2.569	6.093	0.955
D_02	2.105	2.630	4.734	−0.525
D_03	2.194	2.568	4.763	−0.374
D_04	1.857	2.595	4.452	−0.737
D_05	3.506	2.673	6.179	0.833
D_06	3.026	2.737	5.763	0.289
D_07	1.779	2.633	4.412	−0.854
D_08	2.004	2.803	4.807	−0.799
D_09	3.106	2.554	5.659	0.552
D_10	3.296	2.636	5.932	0.660

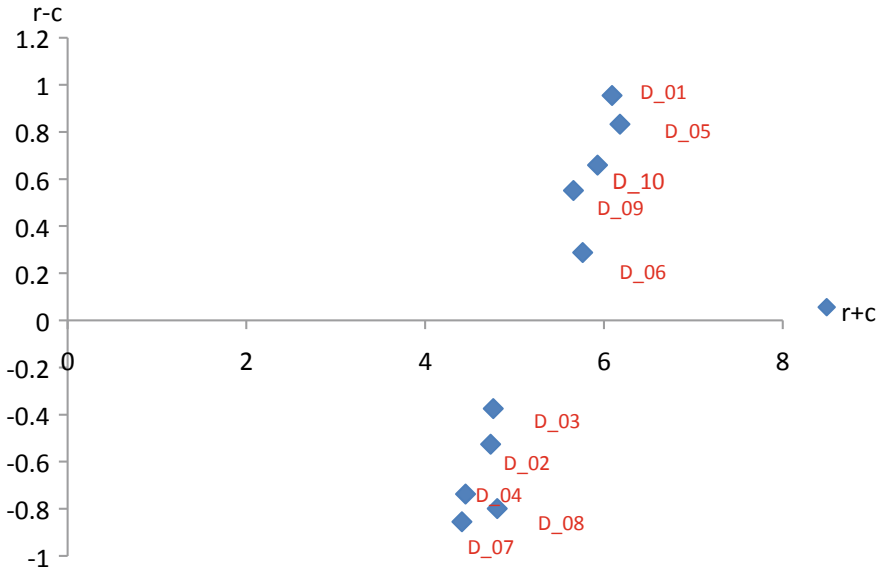

Fig. 1 Cause and effect diagram

6.1 Influential Drivers

Among the influential drivers, the 'government policies for cleaner production (D_01)' has been identified as the most influential driver. This is justified because the government laws are vital for adopting and implementing CE practices in the supply chain. The second most influential driver is 'urbanisation (D_05)'; the developmental changes necessitated by the shifting of people towards cities put pressure on the environment and hence demand a change. The adoption of the CE addresses this

demand. The next influential driver is 'scarcity of resources (D_10)', as the natural resources such as water, non-renewable energy and raw material are limited. Growing population stresses the limited availability of resources and leads to non-sustainable development. The CE reduces the need for new raw materials by reusing existing materials. 'Cost reduction and financial profitability (D_09)' is another influential driver for the implementation of the CE practices. The least influential driver identified is 'consumer awareness (D_06)' which is significant for the adoption of the CE.

6.2 Influenced Drivers

The most influenced driver identified is 'improving the product quality (D_08)'. It can be influenced by consumer awareness (D_06). The next most influenced driver identified is 'enhanced material and energy efficiency (D_07)'; it is influenced by 'scarcity of the resource (D_10)' and 'government policies for cleaner production (D_01)'. The next influenced driver is 'demand for renewable energy (D_04)'; it could be influenced by 'consumers awareness (D_06)' and 'environmental protection laws (D_03)'. The least influenced drivers are 'economic growth through adoption of the CE (D_02)' and 'environmental protection laws (D_03)'.

7 Implications

This research can be useful for the successful implementation of the CE. The decision makers can get help from identified interrelationships between drivers. The categorisation of the drivers into an influential and influenced group may help the policymakers to develop the policies for the adoption of the CE. The organisation needs to primarily focus on the influential group drivers for the successful adoption of the CE. This study can be beneficial for the academia to develop the understanding of the drivers of the CE and interrelationship among them.

8 Conclusion

The drivers of the successful implementation of the CE practices are recognised through the systematic literature review and affirmed through expert's opinion. After finalising the drivers, the relationship among the identified driver is determined using the DEMATEL approach. These drivers are classified into 'influenced' and 'influential' groups. The results of this study are discussed with the experts, and helpful cognisance is given in the discussion section. Finally, the research implication of this

paper is provided. The result of this study suggested that most influential are 'government policies for cleaner production' and 'urbanisation'. The most influenced drivers are 'enhanced material and energy efficiency' and 'improving product quality'. The influential drivers are the major focus while drafting the policies to implement the CE. This study also has some limitations such as the expert's opinion may be biased and subjective. To overcome such limitations, DEMATEL can be integrated with fuzzy and grey theory in future studies. Further, these drivers can be evaluated using the other MCDM technique such as fuzzy AHP, TOPSIS and BWM techniques.

References

1. Bastein T, Roelofs E, Rietveld E, Hoogendoorn A (2013) Opportunities for a circular economy in The Netherlands. TNO, Report commissioned by the Netherlands Ministry of Infrastructure and Environment
2. Franklin-Johnson E, Figge F, Canning L (2016) Resource duration as a managerial indicator for circular economy performance. J Clean Prod 133:589–598
3. MacArthur E (2015) Towards a circular economy: business rationale for an accelerated transition. Accessed November, 2018. https://www.ellenmacarthurfoundation.org/assets/downloads/TCE_Ellen-MacArthur-Foundation_9-Dec-2015.pdfFoundation_9-Dec-2015.pdf
4. Jawahir IS, Bradley R (2016) Technological elements of circular economy and the principles of 6R-based closed-loop material flow in sustainable manufacturing. Procedia CIRP 40:103–108
5. Ghisellini P, Cialani C, Ulgiati S (2016) A review on circular economy: the expected transition to a balanced interplay of environmental and economic systems. J Cleaner Prod 114: 11–32
6. Kok L, Wurpel G, Ten Wolde A (2013) Unleashing the power of the circular economy. Report by IMSA Amsterdam for Circle Economy
7. Kirchherr Julian, Reike Denise, Hekkert Marko (2017) Review conceptualizing the circular economy: an analysis of 114 definitions. Resour Conserv Recycl 127(2017):221–232
8. Govindan K, Hasanagic M (2018) A systematic review on drivers, barriers, and practices towards circular economy: a supply chain perspective. Int J Prod Res 56(1–2):278–311
9. Khan S, Imran Khan M, Haleem A (2018a) Towards effective management of cold chain: A DEMATEL approach. In: IOP conference series: materials science and engineering, vol 404, pp 012019
10. Chang B, Chang CW, Wu CH (2011) Fuzzy DEMATEL method for developing supplier selection criteria. Expert Syst Appl 38(3):1850–1858
11. McKinsey & Company (2016, October) The circular economy: moving from theory to practice. Special edition. Accessed November 2018. https://www.mckinsey.com/~/media/McKinsey/Business%20Functions/Sustainability%20and%20Resource%20Productivity/Our%20Insights/The%20circular%20economy%20Moving%20from%20theory%20to%20practice/The%20circular%20economy%20Moving%20from%20theory%20to%20practice.ashx
12. Sun B, Heshmati A, Geng Y, Yu X (2013) A review of the circular economy in China: moving from rhetoric to implementation. J Cleaner Prod 42:215–227
13. Geng Y, Zhu Q, Doberstein B, Fujita T (2009) Implementing China's circular economy concept at the regional level: a review of progress in Dalian, China. Waste Manag 29(2):996–1002
14. Lewandowski M (2016) Designing the business models for circular economy—towards the conceptual framework. Sustainability 8(1):43
15. Ellen MacArthur Foundation (2015) Delivering the circular economy, a toolkit for policymakers. Ellen MacArthurFoundation, Cowes
16. Liguori R, Faraco V (2016) Biological processes for advancing lignocellulosic waste biorefinery by advocating circular economy. Bioresorc Technol 215:13–20

17. Park J, Sarkis J, Wu Z (2010) Creating integrated business and environmental value within the context of China's circular economy and ecological modernization. J Clean Prod 18(15):1494–1501
18. Xinan L, Yanfu L (2011) Driving forces on China's circular economy: from Government's perspectives. Energy Procedia 5:297–301
19. Ilić M, Nikolić M (2016) Drivers for development of circular economy—a case study of Serbia. Habitat Int 56:191–200
20. Hazen BT, Mollenkopf DA, Wang Y (2017) Remanufacturing for the circular economy: an examination of consumer switching behavior. Bus Strategy Environ 26(4):451–464
21. Quina MJ, Soares MA, Quinta-Ferreira R (2017) Applications of industrial eggshell as a valuable anthropogenic resource. Resour Conserv Recycl 123:176–186
22. Geng Y, Zhu Q, Doberstein B, Fujita T (2008) Implementing China's circular economy concept at the regional level: a review of progress in Dalian, China. Waste Manag 29(2):996–1002
23. Pringle T, Barwood M, Rahimifard S (2016) The challenges in achieving a circular economy within leather recycling. Procedia CIRP 48:544–549
24. Clark JH, Farmer TJ, Herrero-Davila L, Sherwood J (2016) Circular economy design considerations for research and process development in the chemical sciences. Green Chem 18(14):3914–3934
25. Schiller G, Müller F, Ortlepp R (2017) Mapping the anthropogenic stock in Germany: metabolic evidence for a circular economy. Resour Conserv Recycl 123:93–107
26. Sun L, Li H, Dong L, Fang K, Ren J, Geng Y, Fujii M, Zhang W, Zhang N, Muduli K, Barve A (2013) Establishment of a sustainable development framework in small-scale mining supply chains in India. Int J Intell Enterp 2(1):84–100
27. Khan, S., Imran Khan M., Haleem, A., (2018b) Facilitating fair trade practices as a development strategy. In: IOP conference series: materials science and engineering, vol 404, pp 012009
28. Horng J-S, Liu C-H, Chou SF, Tsai C-Y (2013) Creativity as a critical criterion for future restaurant space design: developing a novel model with DEMATEL application. Int. J. Hosp. Manag. 33:96–105
29. Lin Y-T, Yang Y-H, Kang J-S, Yu H-C (2011) Using DEMATEL method to explore the core competences and causal effect of the IC design service company: an empirical case study. Expert Syst Appl 38:6262–6268
30. Wu WW, Lee YT (2007) Developing global managers' competencies using the fuzzy DEMATEL method. Expert Syst Appl 32(2):499–507
31. Govindan K, Muduli K, Devika K, Barve A (2016) Investigation of the influential strength of factors on adoption of green supply chain management practices: an Indian mining scenario. Resour. Conserv Recycl 107(2016):185–194

Simulation-Based Analysis of Performance Parameters of Thrust Pad Bearing Under Thin Film Lubrication with Chamfered Inlet

Poonam Kumari and Mohammad Sikandar Azam

Abstract An elastohydrodynamic numerical simulation of a thrust pad bearing with chamfering at inlet has been studied in this paper. To model the problem, a one-dimensional Reynolds equation along with elastic deformation equation in non-dimensional form has been discretized using finite difference method and solved iteratively by using an improved method. On chamfering at inlet of the bearing pad, a pressure peak gets generated near the inlet zone. This pressure peak, which is absent in non-chamfered pad, ultimately increases the load-carrying capacity of the thrust pad bearing at lower value of film thickness ratios and small film thickness. At large value of film thickness, the load capacity decreases at all film thickness ratios when chamfering is done on the bearing pad. On increasing minimum film thickness, the load capacity and coefficient of friction show more sensitivity at low value of film thickness ratios. At very high value of film thickness ratio, the change in load capacity and coefficient of friction with increasing film thickness ratios become almost negligible.

Keywords Thrust pad bearing · Thin film lubrication · Chamfered pad

Nomenclature

E_1 Elastic modulus of moving surface (Pa)
E_2 Elastic modulus of stationary surface (Pa)
E' Equivalent elastic modulus of moving surface (Pa)
f Frictional force (N)
F Dimensionless frictional force
h_0 Film thickness at exit of bearing pad (m)
h_1 Film thickness at inlet of chamfer (m)

P. Kumari · M. S. Azam (✉)
Department of Mechanical Engineering, Indian Institute of Technology (ISM) Dhanbad, Dhanbad, Jharkhand 826004, India
e-mail: mdsazam@gmail.com; mdsazam@iitism.ac.in

H. Kumar and P. K. Jain (eds.), *Recent Advances in Mechanical Engineering*, Lecture Notes in Mechanical Engineering,
https://doi.org/10.1007/978-981-15-1071-7_15

h_2 Film thickness at exit of chamfer (m)
h Film thickness (m)
K Film thickness ratio
l Total width of bearing pad (m)
l_1 Chamfer length (m)
p Fluid film pressure (Pa)
q Mass flow rate (kg/(ms))
q_1 Couette mass flow rate (kg/(ms))
q_2 Poiseuille mass flow rate (kg/(ms))
u Moving surface sliding velocity (m/s)
w Load capacity (N)
W Dimensionless load-carrying capacity
δ Elastic deformation of the moving surface (m)
η Lubricants viscosity (Pa s)
η_0 Viscosity at $p = 0$ (Pa s)
μ Friction of coefficient
μ' Dimensionless friction of coefficient
ν_1 Poisson's ratio of moving surface
ν_2 Poisson's ratio of stationary surface
ρ Lubricant's density (kg/m^3)
ρ_0 Density at $p = 0$ (kg/m^3)

1 Introduction

In recent years, the topic of thin film lubrication has been major domain of research. A lubricant with low viscosity is used for obtaining high operating efficiency at high sliding speed under high load conditions. Under this operating condition, the lubrication regime becomes more severe. Thrust pad bearings are used in turbines, compressors, pumps, and marine drive, automotive, and aerospace applications. Thrust pad bearing is fluid film bearing, which uses an oil wedge to support a load without shaft to bearing contacts. They are specially engineered for reduced power loss, oil flow, pad temperatures and offer high fluid film stiffness along with damping coefficients for the most reliable-efficient machine performance. For enhancing the bearing performance modifications in design such as different surface profiles, texturing and coatings over pads are used.

The pressure generated in a lubricant film is transmitted to the bounding surfaces, which elastically deforms. Due to elastic deformation, the geometrical shape of the bounding surfaces can have significant change [1, 2]. Reynolds equation was solved by Dowson and Higginson [3] and Dowson [4] numerically considering the bounding surfaces' elastic deformation and piezoviscous effect on lubricant. It was shown by Johnson [5] that in terms of both the elastic deformation and piezoviscous effect, the four regimes in which hydrodynamic lubrication can be categorized as: isoviscous

and rigid (IR), piezoviscous and rigid (PR), isoviscous and elastic (IE), and piezoviscous and elastic (PE). Kumar et al. [6] reviewed on experimental techniques of elastohydrodynamic lubrication over 70 years of span. Sharma et al. [7] studied the static and dynamic performances of a circular thrust pad hydrostatic bearing with different geometrical shape of recesses. Zouzoulas and Papadopoulos [8] investigated thermodynamic lubrication in pivoted pad thrust bearing exhibiting different types of surface treatment. Kumar et al. [9] conducted an investigation of thermo-piezoviscous effect and elastic deformation with deterministic surface roughness on thrust plane slider bearing. Kumar et al. [10] analyzed the deterministic roughness and elastic deformation effect on performance parameters of the Rayleigh step bearing under thin film lubrication. The performance of water lubrication tilting pad thrust bearing was studied by Wang et al. [11] during start-up and shut-down. Under the condition of thermo-elastohydrodynamic lubrication, Kumar et al. [12] investigated Rayleigh step bearing using optimized scheme of progressive mesh densification (PMD). Numerical simulation under condition of elastohydrodynamic lubrication using variable mesh density was carried by Kumar et al. [13] for rough thrust pad bearing. Performance of Rayleigh step bearing with influence of stochastic roughness considering shear flow factor under thermo-elastohydrodynamic lubrication has been done by Kumar et al. [14].

All above discussed literature suggest that very less work has been done in the area of bearings with different inlet conditions operating under elastohydrodynamic lubrication regime. Although these works in the area of elastohydrodynamic lubrication have been carried out for thrust pad bearing performance evaluation with different geometric recess, roughness and deformation, thermal effect, etc., no literature reports the effect of different inlet conditions. Present study showcases the effect of chamfering at inlet of thrust pad bearing operating under thin film lubrication. Different performance parameters of the bearing with chamfered pad at inlet have been compared to those with non-chamfered pad.

2 Methodology

To study inlet chamfering effect on performance parameters of the bearing, the finite difference method (FDM) has been used to discretize the non-dimensional related equations, and these are further solved iteratively using improved iteration method. The schematic representation of the one-dimensional thrust pad bearing with chamfering at inlet is shown in Fig. 1.

The one-dimensional expression of Reynolds equation for thrust pad bearing is expressed as:

$$\frac{\partial}{\partial x}\left(\frac{\rho h^3}{\eta}\frac{\partial p}{\partial x}\right) = 6u\frac{\partial(\rho h)}{\partial x} \tag{1}$$

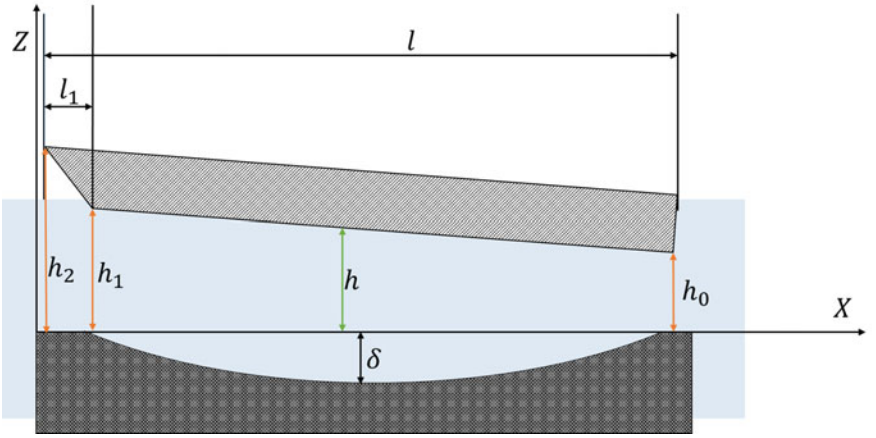

Fig. 1 Schematic diagram of chamfered thrust pad bearing

The film thickness h, with inlet chamfering and elastic deformation (δ) is expressed as:

$$h = \begin{cases} h_2 - \frac{(h_2 - h_1)}{l_1}(x) + \delta, & 0 \le x < l_1 \\ h_0 + \frac{(h_1 - h_0)}{(l - l_1)}(l - x) + \delta, & l_1 \le x \le l \end{cases} \tag{2}$$

where

$$\delta = -\frac{4}{\pi E'} \int_{x_{\text{in}}}^{x_{\text{out}}} \ln\left(x - x'\right) p\left(x'\right) \mathrm{d}x' \tag{3}$$

$$\frac{2}{E'} = \frac{1 - \nu_1^2}{E_1} + \frac{1 - \nu_2^2}{E_2} \tag{4}$$

The lubricant density and viscosity are expressed as:

$$\rho = \rho_0 \left[1 + \frac{0.6 \times 10^{-9} \times p}{1 + 1.7 \times 10^{-9} \times p}\right] \tag{5}$$

$$\eta = \eta_0 \exp\left\{[\ln \eta_0 + 9.67] \times \left[-1 + \left(1 + 5.1 \times 10^{-9} \times p\right)^z\right]\right\} \tag{6}$$

where

$$z = \frac{\alpha}{(\ln\, \eta_0 + 9.67) \times \left(5.1 \times 10^{-9}\right)}$$

The load capacity of unit length bearing is calculated by integration of the pressure over the contact area as:

$$w = \int_0^l p \, \mathrm{d}x \tag{7}$$

Frictional force expression for the moving surface is expressed as:

$$f = \int_0^l \eta \frac{\mathrm{d}u}{\mathrm{d}z} \mathrm{d}x = \int_0^l -\eta \frac{u}{h} - \frac{h}{2} \frac{\mathrm{d}p}{\mathrm{d}x} \mathrm{d}x \tag{8}$$

Coefficient of friction is given by:

$$\mu = -\frac{f}{w} \tag{9}$$

For lubricating oil total mass flow rate is expressed as:

$$q = q_1 + q_2 \tag{10}$$

where

$$q_1 = \rho u \frac{h}{2}, \quad q_2 = -\rho \frac{h^3}{12\eta} \frac{\partial p}{\partial x}$$

q is total mass flow rate, q_1 is Couette mass flow rate, and q_2 is Poiseuille mass flow rate.

The finite difference method (FDM) has been used to discretize the related equations and progressive mesh densification (PMD) method given by Zhu [15] is employed to iteratively solve these equations in order to obtain pressure distribution in the contact area. Pressures at inlet and exit were assigned zero value as the boundary condition for pressure distribution. During iterative process, all negative pressure values encountered are set at zero.

3 Results and Discussion

Table 1 catalogs the values of basic parameters being used in solving the related equations. In the present study, chamfered pad at the inlet of thrust pad bearing with chamfer height (h_2–h_1) and chamfer length (l_1) has been considered.

Figures 2, 3 and 4 showcases higher pressure generation in chamfered inlet thrust pad bearing as compared to non-chamfered. Pressure generated at $h_0 = 200$ nm is

Table 1 Parameters of thrust pad bearing and lubricant

Parameters	Value
Slider width	10 mm
Equivalent elastic modulus	230.76 GPa
Viscosity of the lubricant	0.01 Pa s
Pressure-viscosity coefficient	10 GPa^{-1}
Sliding speed	0.05 m/s
Chamfered thickness	0.5 mm
Chamfered height	100 nm

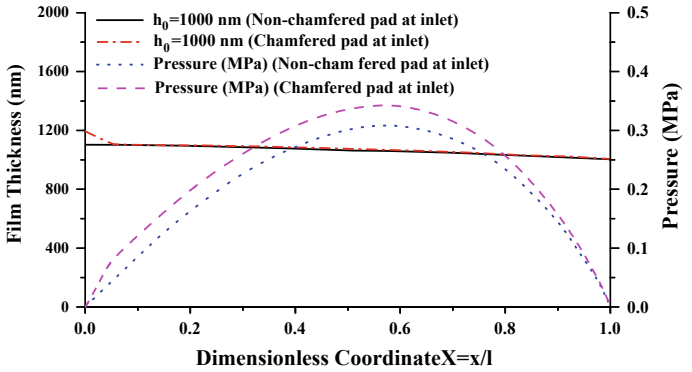

Fig. 2 Film thickness and distribution of pressure at $h_0 = 1000$ nm

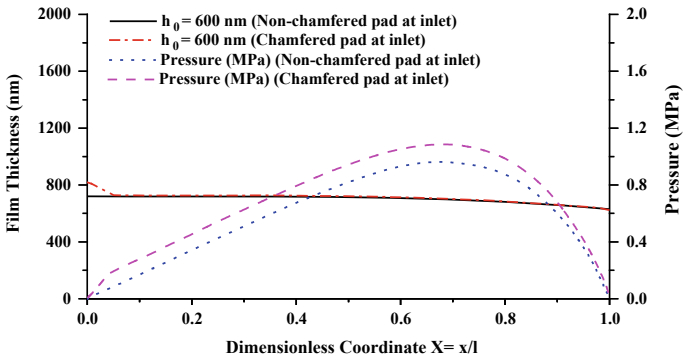

Fig. 3 Film thickness and distribution of pressure at $h_0 = 600$ nm

higher in comparison with pressure at $h_0 = 600$ nm and $h_0 = 1000$ nm. In Fig. 4, a secondary peak pressure under chamfered condition is observed at inlet and a no pressure zone is observed at inlet under non-chamfered condition. Film thickness in Figs. 2, 3 and 4 for corresponding pressure distribution is larger in case of chamfered

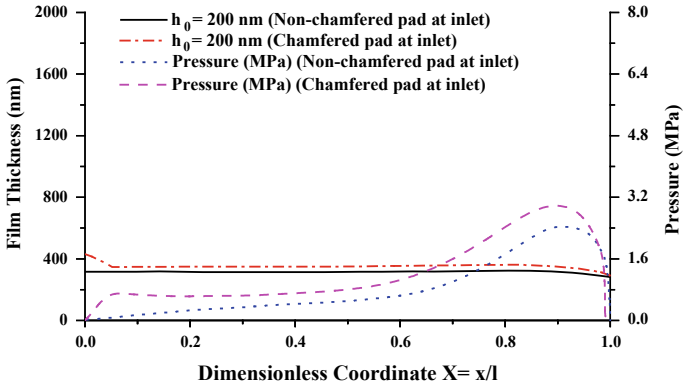

Fig. 4 Film thickness and distribution of pressure at $h_0 = 200$ nm

inlet compared to non-chamfered. At $h_0 = 200$ nm, there exists a large difference between film thickness of observed chamfered and non-chamfered inlet condition. For all minimum film thickness, the chamfering exists even after deflection of the bounding surfaces. Due to existence of secondary pressure peak at inlet, growth in pressure distribution is witnessed in the no pressure zone, which ultimately leads to larger load-carrying capacity. With reduction in film thickness, primary pressure peak shifts more toward outlet. At very small film thickness, there exists a constant pressure zone between two pressure peaks. Under both inlet conditions, the flow rates (Couette and Poiseuille) remain identical throughout the contact area with an exception at inlet. There exists a slight increase in both the flow rates (Couette and Poiseuille) under chamfered condition at inlet.

Table 2 shows the values of non-dimensional load-carrying capacity at different h_0 and K. Figures 5 and 6 showcases the effect of film thickness ratios (K) on non-dimensional load-carrying capacity. The load-carrying capacity under chamfered pad and non-chamfered pad at inlet are shown in Figs. 5 and 6, respectively, for all minimum film thickness. From both Figs. 5 and 6, it can be observed that the variation of non-dimensional load-carrying capacity with respect to K at different film thickness follows the trend:

- For the film thickness, i.e., $h_0 = 200$ nm
  - (b) When $1.2 \leq K \leq 2.3$
    $\boldsymbol{W}_{\textbf{chamfered}} > \boldsymbol{W}_{\textbf{non-chamfered}}$
  - (a) When $2.3 < K \leq 10$
    $\boldsymbol{W}_{\textbf{non-chamfered}} > \boldsymbol{W}_{\textbf{chamfered}}$
- For $h_0 = 400$–600 nm
  - (a) When $1.2 \leq K \leq 1.4$
    $\boldsymbol{W}_{\textbf{chamfered}} > \boldsymbol{W}_{\textbf{non-chamfered}}$
  - (b) When $1.4 < K \leq 10$

Table 2 Non-dimensional load-carrying capacity at different h_0 and K

K ↓	h_0 (nm) →									
	Non-chamfered pad at inlet					Chamfered pad at inlet				
	200	400	600	800	1000	200	400	600	800	1000
1.2	0.000453	0.003377	0.008263	0.010664	0.011611	0.00167	0.004943	0.008962	0.010738	0.011264
1.5	0.001112	0.00795	0.014661	0.018094	0.019739	0.001658	0.007743	0.013692	0.016705	0.018133
2	0.002193	0.011612	0.018392	0.022069	0.023929	0.002334	0.010919	0.017069	0.020362	0.02201
3	0.004252	0.012957	0.018571	0.021421	0.022809	0.004118	0.012118	0.017255	0.019826	0.021065
4	0.004832	0.012332	0.016628	0.018616	0.019533	0.004568	0.011542	0.015472	0.017262	0.018081
5	0.004902	0.011286	0.014523	0.015901	0.016508	0.004623	0.01057	0.013522	0.014757	0.015297
6	0.004796	0.010201	0.012649	0.013618	0.01403	0.004525	0.009554	0.011776	0.012641	0.013005
7	0.004616	0.009191	0.011059	0.011755	0.012042	0.004358	0.008605	0.010292	0.010911	0.011163
8	0.004405	0.008286	0.009729	0.01024	0.010445	0.004161	0.007754	0.00905	0.009501	0.009681
9	0.004185	0.00749	0.008617	0.008998	0.009149	0.003954	0.007003	0.00801	0.008346	0.008477
10	0.003967	0.006792	0.007682	0.007973	0.008085	0.003748	0.006345	0.007137	0.007391	0.007489

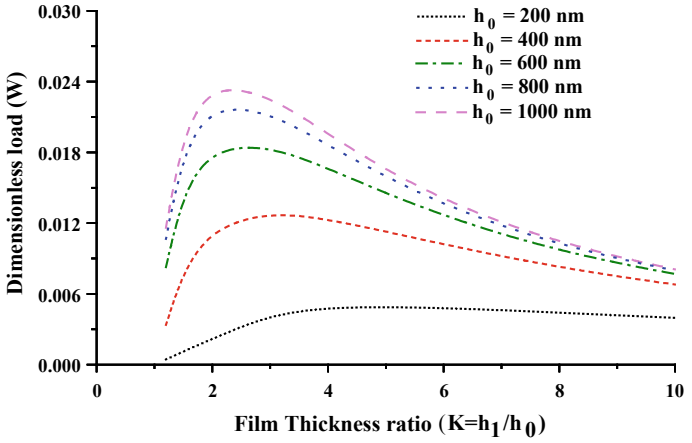

Fig. 5 Effect of film thickness ratios on non-dimensional load-carrying capacity under non-chamfered pad

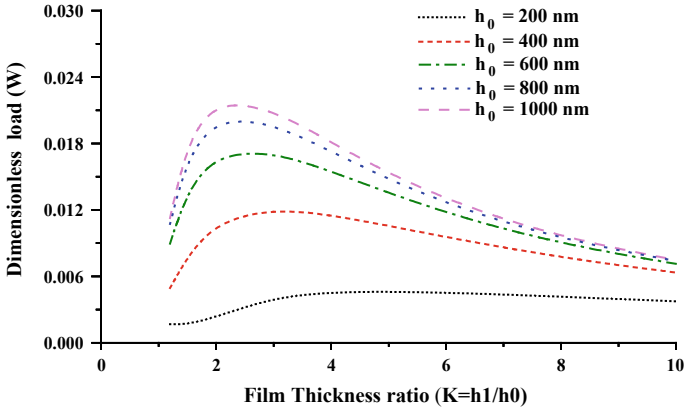

Fig. 6 Effect of film thickness ratios on non-dimensional load-carrying capacity under chamfered pad

$$W_{\text{non-chamfered}} > W_{\text{chamfered}}$$

- For $h_0 = 800$–1000 nm, at $1.2 \leq K \leq 10$
  $W_{\text{non-chamfered}} > W_{\text{chamfered}}$

Table 3 shows the values of non-dimensional friction coefficient at different values of h_0 and K. Figures 7 and 8 showcases the effect of film thickness ratios (K) on non-dimensional friction coefficient. The non-dimensional friction coefficient under chamfered pad and non-chamfered pad at inlet are shown by Figs. 7 and 8, respectively, for all minimum film thickness. From both Figs. 7 and 8, it can be observed

Table 3 Non-dimensional friction coefficient at different h_0 and K

K ↓	h_0 (nm) →									
	Non-chamfered pad at inlet					Chamfered pad at inlet				
	200	400	600	800	1000	200	400	600	800	1000
1.2	586.5957	241.8729	101.9913	82.18194	77.09882	379.7803	156.745	93.00814	81.31461	79.33032
1.5	583.4694	83.10092	50.08634	43.32187	41.03511	352.7178	85.42343	53.93113	47.11654	44.80919
2	222.7487	48.54154	35.82153	32.24121	30.86174	204.5653	52.34894	39.01594	35.23304	33.78745
3	83.64084	39.24516	32.43516	30.28992	29.43333	87.98763	42.80676	35.45195	33.16162	32.26515
4	67.88383	39.67905	34.52529	32.90495	32.26477	73.86994	43.37579	37.81322	36.10201	35.44782
5	65.06441	42.30267	38.00148	36.67725	36.16213	71.16021	46.33374	41.72591	40.35371	39.84646
6	65.71308	45.79105	42.03829	40.91022	40.47754	71.94582	50.26719	46.29033	45.15102	44.74608
7	67.83728	49.71451	46.35577	45.36876	44.99446	74.34768	54.70884	51.19746	50.23278	49.90527
8	70.74163	53.88915	50.83222	49.95178	49.62081	77.62477	59.45589	56.31149	55.48545	55.22018
9	74.11448	58.22237	55.40624	54.60905	54.31131	81.43976	64.40504	61.56314	60.85194	60.63903
10	77.79328	62.66219	60.04362	59.31306	59.04145	85.6145	69.49774	66.91342	66.30054	66.13335

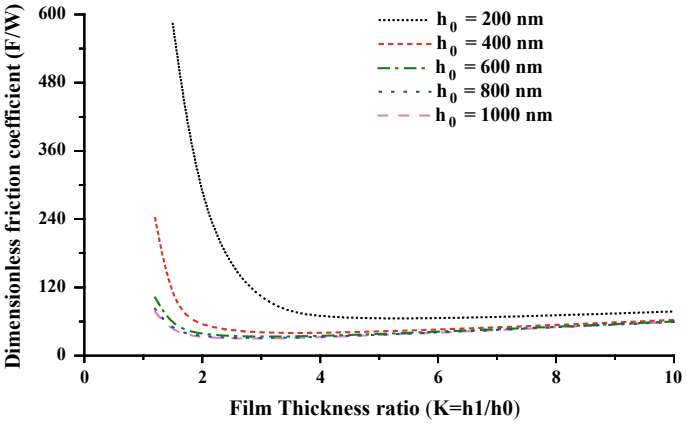

Fig. 7 Effect of film thickness ratios on non-dimensional friction coefficient under non-chamfered pad

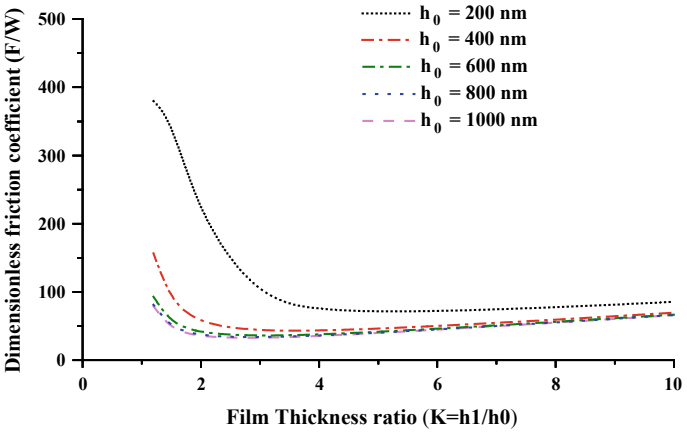

Fig. 8 Effect of film thickness ratios on non-dimensional friction coefficient under chamfered pad

that the variation of non-dimensional friction coefficient with respect to K for various film thickness follows the trend:

- For the film thickness, i.e., $h_0 = 200$ nm

  (b) When $1.2 \leq K \leq 2.3$

$$\mu'_{\text{non-chamfered}} > \mu'_{\text{chamfered}}$$

  (c) When $2.3 < K \leq 10$

$$\mu'_{\text{chamfered}} > \mu'_{\text{non-chamfered}}$$

- For $h_0 = 400$–600 nm

  (c) When $1.2 \leq K \leq 1.4$

$$\mu'_{\text{non-chamfered}} > \mu'_{\text{chamfered}}$$

  (d) When $1.4 < K \leq 10$

$$\mu'_{\text{chamfered}} > \mu'_{\text{non-chamfered}}$$

- For h_0= 800–1000 nm, at $1.2 \leq K \leq 10$

$$\mu'_{\text{chamfered}} > \mu'_{\text{non-chamfered}}$$

Table 4 shows an increase in non-dimensional load-carrying capacity due to chamfered pad at inlet. For all film thickness, values of load capacity increase under chamfered pad. The load capacity increase at $h_0 = 800$ nm and $h_0 = 1000$ nm is almost same, i.e., about 13%. At $h_0 = 200$ nm, the increase in load capacity is around 49%, which is maximum when compared all minimum film thickness values from $h_0 =$ 200–1000 nm.

Table 5 shows a decrease in non-dimensional frictional force due to chamfered pad at inlet. For all film thickness, frictional force of the bearing decreases when the pad is chamfered at inlet. At $h_0 = 200$ nm, the decrease in frictional force is around

Table 4 % change in non-dimensional load-carrying capacity at h_1–h_0 = 100 nm

h_0 (nm)	Load capacity with chamfered pad (W_c)	Load capacity non-chamfered pad (W_{nc})	Change (+)% = $\frac{(W_c - W_{nc})}{W_{nc}}$
200	0.00165822	0.00111193	49.13
400	0.00534516	0.00423304	26.27
600	0.00826044	0.00715979	15.37
800	0.00846578	0.00747471	13.26
1000	0.00764912	0.00676674	13.04

Table 5 % change in non-dimensional frictional force at h_1–h_0 = 100 nm

h_0 (nm)	Frictional force with chamfered pad (μ_c)	Frictional force non-chamfered pad (μ_{nc})	Change (−)% = $\frac{(\mu_c - \mu_{nc})}{\mu_{nc}}$
200	0.58488351	0.64877925	9.85
400	0.75289896	0.78198098	3.72
600	0.84904067	0.86192269	1.49
800	0.90611544	0.91340557	0.79
1000	0.93511747	0.94000716	0.52

10% and for more than $h_0 = 600$ nm, meager decrease (less than 1%) in friction force is noted.

4 Conclusion

The effect of chamfering on bearing pad has been studied in this paper. In the present study, numerical investigation of a bearing pad with and without chamfering at inlet has been done using PMD method. The conclusions drawn from the study are as follows:

1. Chamfering at inlet of bearing pad leads to generation of secondary pressure peak which ultimately increases the load-carrying capacity of the bearing. The no pressure zone vanishes with an existence of inlet chamfering. A constant pressure zone exists between the two pressure peaks at very small film thickness.
2. There exist sensitivity in load capacity and friction coefficient at all values of minimum film thickness.
3. When $K \geq 2.3$ for $h_0 = 200$ nm, $K \geq 1.4$ for $h_0 = 400$–600 nm and for all K more than $h_0 = 800$ nm minimum film thickness, chamfered pad shows decrease in load-carrying capacity in comparison with non-chamfered pad inlet.
4. When $K \geq 2.3$ for $h_0 = 200$ nm, $K \geq 1.4$ for $h_0 = 400$–600 nm and for all K more than $h_0 = 800$ nm minimum film thickness, chamfered pad shows an increase in friction coefficient values in comparison with non-chamfered pad inlet.

In future, performance analysis of thrust pad bearing with different types of inlet conditions like, roundness or filleting, can be done to improve the performance of the bearing.

References

1. Martin HM (1916) Lubrication of gear teeth. Engineering 102:119
2. Grubin AN (1949) Investigation of the contact of machine components. Central Sci Res Inst Tech Mech Eng 337:30
3. Dowson D, Higginson GR (1959) A numerical solution to the elasto-hydrodynamic problem. J Mech Eng Sci 1(1):6–15
4. Dowson D (1967) Elastohydrodynamics. In: Proceedings of the institution of mechanical engineers, conference proceedings. Sage, London, pp 151–167
5. Johnson KL (1970) Regimes of elastohydrodynamic lubrication. J Mech Eng Sci 12(1):9–16
6. Kumar R, Azam MS, Ghosh SK, Yadav S (2018) 70 years of Elastohydrodynamic Lubrication (EHL): a review on experimental techniques for film thickness and pressure measurement. MAPAN 33(4):481–491
7. Sharma SC, Jain SC, Bharuka DK (2002) Influence of recess shape on the performance of a capillary compensated circular thrust pad hydrostatic bearing. Tribol Int 35(6):347–356
8. Zouzoulas V, Papadopoulos CI (2017) 3-D thermohydrodynamic analysis of textured, grooved, pocketed and hydrophobic pivoted-pad thrust bearings. Tribol Int 110:426–440

9. Kumar R, Azam MS, Ghosh SK (2017) Effect of temperature on rough EHL in slider bearing. In: 2017 International Conference on Advances in Mechanical, Industrial, Automation and Management Systems (AMIAMS). IEEE, Allahabad, pp 156–163 (2017)
10. Kumar R, Azam MS, Ghosh SK, Khan H (2017) Effect of surface roughness and deformation on Rayleigh step bearing under thin film lubrication. Ind Lubr Tribol 69(6):1016–1032 (2017)
11. Wang Z, Liu Y, Wang Y, Liu X, Wang Y (2018) Influence of squeezing and interface slippage on the performance of water-lubricated tilting-pad thrust bearing during start-up and shutdown. Lubr Sci 30(4):137–148
12. Kumar R, Azam MS, Ghosh SK, Khan H (2018) Thermo-elastohydrodynamic lubrication simulation of the Rayleigh step bearing using the progressive mesh densification method. Simulation. https://doi.org/10.1177/0037549718788727
13. Kumar R, Ghosh SK, Azam MS, Khan H (2018) Numerical Simulation of rough thrust pad bearing under thin-film lubrication using variable mesh density. Iran J Sci Technol Trans Mech Eng 1–22 (2018)
14. Kumar R, Azam MS, Ghosh SK (2019) Influence of stochastic roughness on performance of a Rayleigh step bearing operating under Thermo-elastohydrodynamic lubrication considering shear flow factor. Tribol Int 134:264–280
15. Zhu D (2007) On some aspects of numerical solutions of thin-film and mixed elastohydrodynamic lubrication. Proc Inst Mech Eng Part J: J Eng Tribol 221(5):561–579

Workplace Safety Improvement Through Quality Control Circle Approach in Heavy Engineering Industry

D. Dinagaran, K. R. Balasubramanian, S. P. Sivapirakasam and Kuruva Gopanna

Abstract The heavy engineering industrial environment is one of the most critical working environments because of its job nature. This case study presents the quality control circle (QCC) approach for workplace safety improvement in the heavy engineering industry. This approach focuses on changing unsafe work environment into a safe work environment by using quality control concepts. The aim of this study was to examine and define safety culture through quality control circles by exploring worker's experiences and perceptions of safety and risks. A quality control circle team was formed in the heavy engineering industry, and the situation of workplace safety was deliberated with problem-solving techniques. The team identified the work-related problems and that problems are analysed through various QC tools and techniques with systematic steps. The efforts of the QCC approach reduced workplace hazard situation which paved the way to a reduction in injuries and reportable incidents.

Keywords Quality control circle · Workplace safety · Problem-solving steps

1 Introduction

A quality control circle (QCC) involves a small group of frontline workers who continually control the defects and improve the quality of the work, products and services. These QCC groups function independently, employ QCC concepts and techniques with the related tools by utilizing each member's ideas and promote mutual development for the self and the organization. Implementation of QCC activities in an organization is important to build positive work culture among workers, to reduce cycle time routine jobs, to improve productivity, quality, safety and other activities

D. Dinagaran (✉) · K. R. Balasubramanian · S. P. Sivapirakasam
National Institute of Technology, Tiruchirappalli 620015, India
e-mail: dinagar28960@gmail.com

K. Gopanna
Bharat Heavy Electricals Limited, Tiruchirappalli 620014, India

H. Kumar and P. K. Jain (eds.), *Recent Advances in Mechanical Engineering*,
Lecture Notes in Mechanical Engineering,
https://doi.org/10.1007/978-981-15-1071-7_16

such as TQM. The occupational safety problems reduce the efficiency of productivity and cause injuries to the workers in manufacturing companies. The principle of QCC is to fully utilize the worker skills to solve the work-related problems, to respect the peer workers to create a pleasant, dynamic and satisfying workplace and to contribute their skills and suggestions to the development of the organization.

1.1 Literature Review

A significant number of literature on quality control circles have developed since the inception of QCC in Japan in 1962. Lozano and Thompson [1] state that quality control circles are a formal, institutionalized mechanism for productive and participative problem-solving interaction among workers. According to Udupa, who introduced QCC concept in India [2] "Quality control circle is a small group of workers in the similar work centre or doing similar kind of task who meet voluntarily and regularly for about an hour every week to identify, systematic analyse and resolve work-related problems, leading to improvement in their total performance, and enrichment of their work life". Piczak [3] states the benefits of QCCs that it develops worker by directly involving them into the work-related problems like safety improvement, quality improvement, productivity enhancement, costs reduction, developing effective communication skills, avoiding absenteeism and workforce turnover.

Johns and Chesterton [4] specified that the implementation of QCC method in the manufacturing division of the ICL of UK was saved from bankruptcy in 1983. Lee and Lam [5] mentioned that in their research work about Kowloon–Canton Railway Corporation. The industry has realized the use of QCCs along with the ISO 9001 quality system resulted in a momentous rise in the reliability of the electric passenger train service and reduction in the maintenance costs. Mark Goh [6] issued a call for management to re-examine the use of QCs as a potential strategy and to integrate QCs with other team type initiatives for continuous improvement of the Singapore housing development board.

Slack et al. [7] stated that workplace safety is an important measure which is used to judge an effective layout in manufacturing companies. The workers need to be educated in the right procedures and attitudes, and they can contribute to a reduction in accidents by pointing out the hazards which have potential to cause harm in the workplace to the management. Stevenson [8] cited that ensuring safety of the worker in the organization is one of the main factors of risk. It is difficult for the effective motivation of the workers when they feel that they are working in a risky atmosphere. Abo-Alhol et al. [9] stated that quality circle activities improve positive behaviour and job satisfaction among workers which makes to feel their companies are a good place to work. Salaheldin and Zain [10] conducted an experimental study in the manufacturing industry of the Middle East country through the QCC approach to improve and ensure a safe work environment for the workers. In a case study of a hospital in Taiwan, Liu et al. [11] concluded that a QCC team was a major role

player to implement the TQM activities for the improvement of services. Kannan and Govinda Rajan [12] conducted a study in six organizations (three public sectors and three private sectors) and concluded that QCC members from both sectors experienced their high level of job satisfaction in their routine work after involving themselves in the QCC activities.

Tyagi and Srivastava [13] concluded that the well-equipped implementation of QCC concept in any industry will result in remarkable benefits and it will facilitate to create a better work atmosphere. Shantanu Welekar [14] presented a comparative discussion of various features of quality circle and evaluated the effectiveness of QC approach through a case study in the chemical industry. Jatt [15] discussed the key elements, benefits, rewards and drawbacks in the quality control circle in the organization. Krishnan et al. [16] found that the awareness of workplace safety and the technology supporting become a significant impact in the operation processes in the organization. Yuan et al. [17] summarized that the improvement of the accurate rate of hand hygiene (HH) of laboratory staff implementation is possible with QCC approach and it improved the confidence level of the team. Lin et al. [18] concluded that QCC technique is best suited for standardization and optimization of accurate intraocular lens (IOL) power calculation process for the cataract surgery patients.

Furthermore, the literature review exposes the significance of the QCC in many organizations for productivity improvement, improving job satisfaction among workers, but worker safety is one of the most important which is studied less. Therefore, in this research work, it is aimed to initiate and implement a QCC approach to improve workplace safety in the heavy engineering industry. This case study attempts to reveal that to reduce unsafe work atmosphere into an improved safe work atmosphere by systematic application of the QCC tools and techniques.

2 Experimental Procedure

The waterwall panel fabrication workplace of heavy engineering industry consists of 6-panel fabrication group with 30 workers like fitter, welder and gas cutters. A group of same wavelength workers includes a leader, deputy leader and two members with a line executive as a facilitator is accepted for involving and implementing the QCC approach in waterwall panel fabrication area of the heavy engineering industry. This QCC team meets regularly for about an hour every week after working hours and daily in some projects. The team educated to follow the Deming's circle concept plan-do-check-act (PDCA), 12 QC steps of problem-solving methodology with seven QC tools for solving the work-related problems. The following steps are used for workplace safety improvement in the heavy engineering industry with a systematic way to solve the problem in the proper perspective but also to make use of the problem-solving technique at the appropriate place.

Step 1: Identification of a Work-Related Problem

Brainstorming (round-robin method) sessions were conducted to identify various work-related problems, and 52 work-related problems were identified by the QCC team. These identified problems were categorized into "A", "B" and "C". A-category problem means that can be solved by QCC team itself, B-category problem means involvement of other departments is a necessary to solve the problem and C-category problem means management sanction may be needed in implementing the solution. So the QCC team focused to solve the A-category problems.

Step 2: Selection of Problem (First from "A" Category List)

A-category (which can be solved by QCC team itself) problems were sorted out to find out the vital problem in the work centre so that the problem can be solved by the team itself without depending on other departments. Rating method is used to select the problem, and the ratings were given by the team members by considering the criteria like quality, cost, delivery and safety (Fig. 1; Table 1).

Based on the rating method analysis, the high-scored problem was selected as a top priority to solve by the QCC team. The selected problem to solve is the work area which is not in a safe condition. Then, the team prepared an activity planning chart to ensure timely and successful completion of the selected project and planned to complete the project in 15 days (Table 2).

Step 3: Define the Problem

The selected problem was analysed elaborately with a detailed flow diagram. Using of air hoses for cleaning and grinding, handling of welding cables for welding in different locations at waterwall panels ranging up to 24 m in length, handling of oxy-acetylene gas hoses at different locations of the waterwall panels are the major work

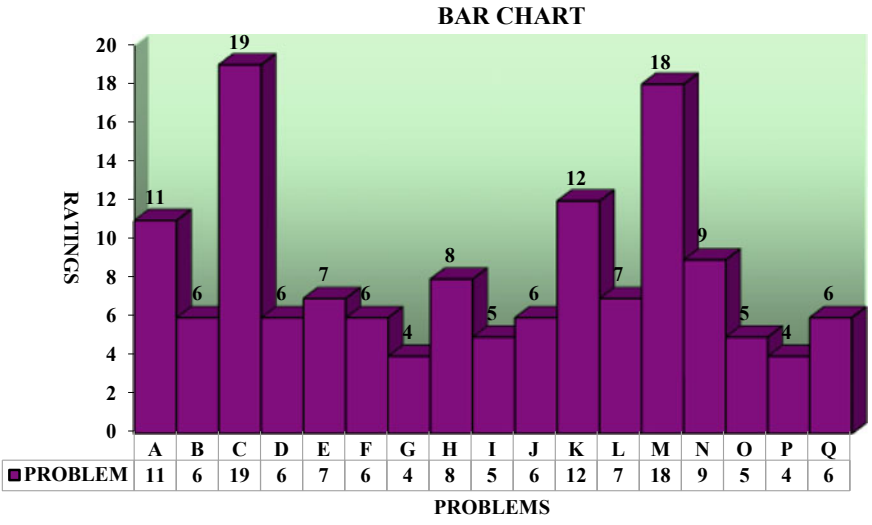

Fig. 1 List of A-category (which can be solved by QCC team itself) problems with rating

Table 1 List of A-category (which can be solved by QCC team itself) problems with rating

Sl. No.	Problem	Rating				Total ratings	Priority No.
		Team leader	Deputy leader	Member 1	Member 2		
A	Difficulties in panel matching	4	2	3	2	11	IV
B	Difficulties in the movement of the panel	2	1	1	2	6	VIII
C	**The work area is not in a safe condition**	**5**	**4**	**5**	**5**	**19**	**I**
D	Over bow in panel	2	2	1	1	6	VIII
E	Over noise while panel tilting	2	2	1	2	7	VII
F	Difficulties in nozzle cleaning	1	1	2	2	6	VIII
G	Skip welding in a panel	1	1	1	1	4	X
H	Frequent disturbance in weld torch	2	2	2	2	8	VI
I	Wastage of tubes	1	2	1	1	5	IX
J	Difficulties in side plate mounting	1	2	2	1	6	VIII
K	Difficulties in thin tube close pitch	2	3	3	4	12	III
L	Weld defect in panel	2	2	2	1	7	VII

(continued)

Table 1 (continued)

Sl. No.	Problem	Rating				Total ratings	Priority No.
		Team leader	Deputy leader	Member 1	Member 2		
M	The problem in torch angle setting	4	4	5	5	18	II
N	The problem in nozzle cleaning	2	3	3	1	9	V
O	Difficulties in flat fin pressure setting	1	1	2	1	5	IX
P	Tube damage	1	1	1	1	4	X
Q	Bow in flat	1	2	2	1	6	VIII

Table 2 Activity planning chart to complete the project

Sl. No.	Activity	No.of .days										Target
		1	1	2	2	1	2	1	1	2	2	
1	Define the problem											1
2	Analyzing the problem											1
3	Identifying the causes											2
4	Find out root cause											2
5	Data analysis											1
6	Developing solution											2
7	Foreseeing possible resistance											1
8	Trial implementation											1
9	Regular implementation											2
10	Follow up / review											2
												15

in the panel fabrication centre. Handling of air hose, welding cable and oxyacetylene gas hose leads to more unsafe workplace due to the welding cables and hoses are kept in the workplace itself after completion of the work. Hence, the workplace becomes more hazardous due to poor housekeeping and unsafe for the workers. EOT crane remote also kept anywhere in the workplace after completion of the work. There are three EOT cranes used in the panel fabrication work centre (Fig. 2).

Step 4: Analysis of the Problem

The selected problem was analysed with the **4W** and **1H** analysis for the clear understanding of the problem.

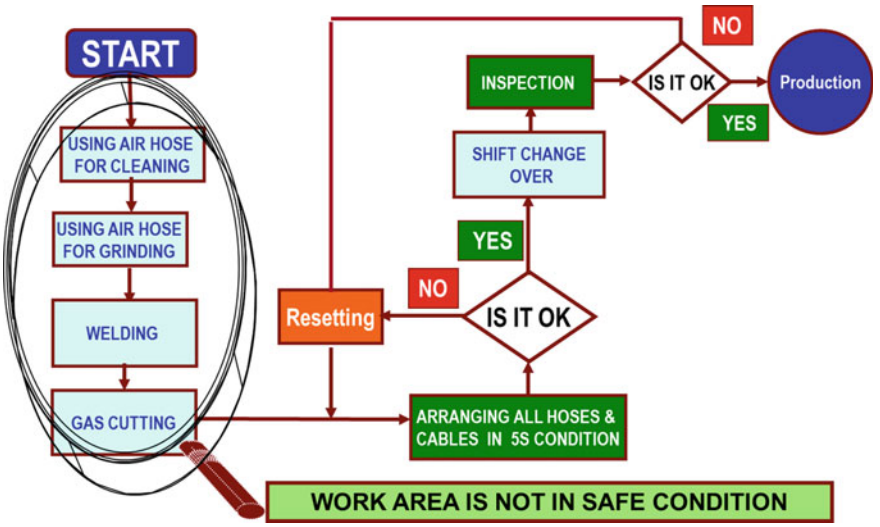

Fig. 2 Detailed flow diagram of waterwall panel work centre

- **W**hat is the problem? The workplace is not in a safe condition.
- **W**here does it occur? In waterwall panel fabrication area.
- **W**hen does it arise? While working in the waterwall panel area.
- **W**hich place? Welding cable, crane remote, air and gas hoses using areas.
- **H**ow to solve the problem? By using the problem-solving techniques (Fig. 3).

Then, the data collected to identify the usage of welding cable, crane remote, air and gas hoses provided areas for a week (Table 3).

These collected data were attributed to the Pareto chart to identify the vital few from the useful many. Based on the Pareto analysis, it is found in 80–20 line, welding cable, crane remote, air and gas hoses are the vital few causes for the unsafe work environment in waterwall panel fabrication workplace (Fig. 4).

Fig. 3 Welding cable, air hose, oxyacetylene gas hoses and EOT crane remotes are placed in an unsafe condition

Table 3 List of welding cable, crane remote, air and gas hoses usage

Sl. No.	Particulars	No. of times used/week	% of time	Cum %
1	Crane remote	120	41.1	41.1
2	Air hose	48	16.4	57.5
3	Gas hose	48	16.4	74.0
4	Welding cable	48	16.4	90.4
5	Edge bar	16	5.5	95.9
6	Straight edge	12	4.1	100.0
	Total	292	100	100

Step 5: Identification of Causes

The QCC team members conducted a brainstorming session to identify the probable causes for the unsafe condition of the workplace. The following possible causes were identified during the brainstorming session.

- Welding cable is too length
- No proper place for welding cables arrangement
- No proper place for pneumatic hose arrangement
- No proper place for oxyacetylene hose arrangement
- No proper place for placing crane remotes
- The work area is too large in size

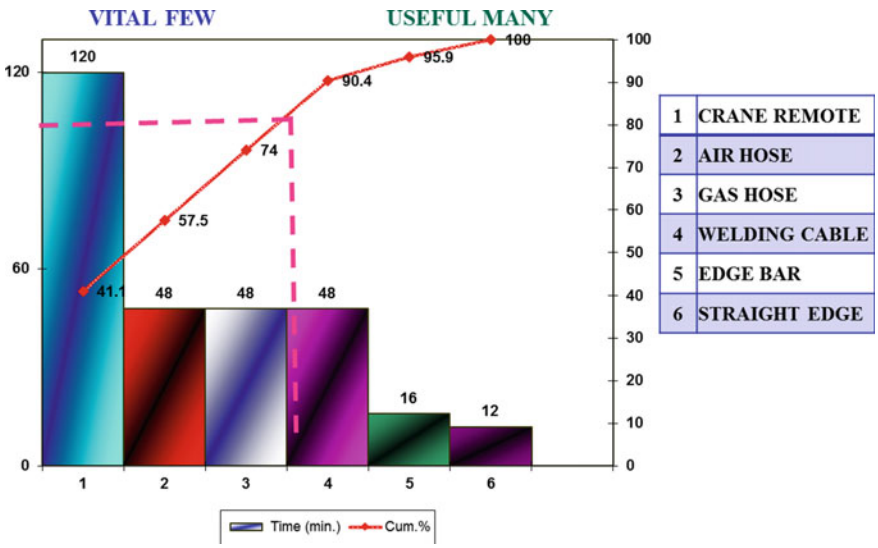

Fig. 4 Pareto chart to identify the vital few from the useful many

- Air hose is not provided properly
- Untrained operator
- Lack of knowledge
- Operator mistake.

The brainstormed various causes were stratified into the cause and effect diagram in the category of man, machine, method and materials for valid cause analysis. The detailed analysis was carried out in each category, while analysing the man, there is no valid cause because workers are trained and educated. Material and machines are a standard one. So there is no valid cause in this category. In method 4 valid causes are found as follows

- No proper place for arranging the welding cable,
- No proper place for arranging the oxyacetylene gas hose,
- No proper place for arranging the crane remotes and
- No proper place for arranging the pneumatic hoses (Fig. 5).

Step 6: Finding Out the Root Causes

Based on the valid cause analysis, the identified valid causes are taken as root causes for the unsafe condition of the workplace, then these root causes were analysed with why-why analysis to find out the solution for the problem.

Why? Why? Analysis

- **Root cause no: 1** no proper place for welding cables arrangement.
  Why no proper place for welding cables arrangement? There is no provision.

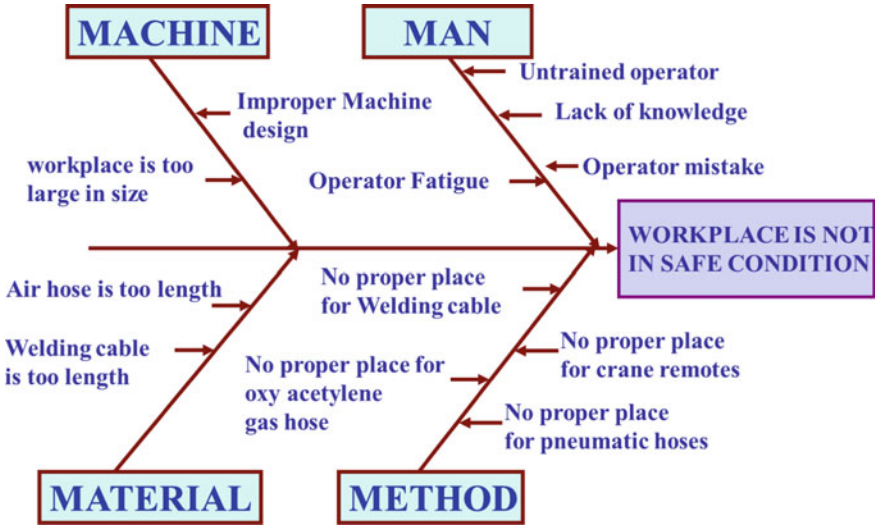

Fig. 5 Cause and effect diagram analysis to identify the valid causes

Why there is no provision? Because of the design.
How to solve it? By providing the proper stand for welding cables arrangement.

- **Root cause no: 2** no proper place for pneumatic hose arrangement.
  Why no proper place for pneumatic hose arrangement? There is no provision.
  Why there is no provision? Because of the design.
  How to solve it? By providing the proper stand for pneumatic hose arrangement.
- **Root cause no: 3** no proper place for oxyacetylene hose arrangement.
  Why no proper place for oxyacetylene hose arrangement? There is no provision.
  Why there is no provision? Because of the design.
  How to solve it? By providing the proper stand for oxyacetylene hose arrangement.
- **Root cause no: 4** no proper place for placing crane remotes.
  Why no proper place for placing crane remotes? There is no provision.
  Why there is no provision? Because of the design.
  How to solve it? By providing the proper stand for placing crane remotes.

Step 7: Data Analysis

The QCC team conducted several brainstorming sessions with various alternatives and outcomes for the development of the solution. Finally, the team came up with the solution that to provide stands for welding cable, air hose, oxyacetylene gas hose and crane remotes.

Step 8: Developing a Solution

The QCC team collected the panel stand from the scrap yard with scrap bend tubes and fabricated the stand for welding cable, air hose and oxyacetylene gas hose. The

team designed to fabricate to place all the welding cables, gas cutting hoses and air hoses in the single stand in each work centre. Likewise, six stands were fabricated for the entire work of the waterwall fabrication. A separate stand for placing EOT crane remotes also fabricated from the scape materials (Fig. 6).

Step 9: Foreseeing Probable Resistance

Identifying the probable constraints was carried out by the brainstorming session by the team members and finding ways to overcome probable constraints and also discussed in detail so that the stand may not be complicated for the workplace safety and other operations in the waterwall panel fabrication area. The following probable resistance was anticipated with the solution (Table 4).

Fig. 6 Fabricating the stand for welding cable, air hose and oxyacetylene gas hose

Table 4 Foreseeing probable resistance

Sl. No.	Probable resistance	Remedial action
1	The stand may disturb each other	No. all the stands are separately provided
2	The stand may fall down	No. jointed by welding joint
3	The stand may disturb the other function	It cannot disturb
4	Misalignment to other	There is no chance

Step 10: Trial Implementation and Check Performance

The fabricated stands for welding cable, air hose, oxyacetylene gas hose and crane remotes were located in each work centre for arranging them in a safe manner without any disturbance to the existing work. The workers were suggested to follow safe working practices like arranging the welding cable, air hose and oxyacetylene gas hose after completion of the work every day. The crane remote stand is provided with three EOT cranes, and the crane operators are also asked to place crane remotes at the stand after completion of the work (Fig. 7).

Step 11: Regular Implementation

The safe work practices were accepted by most of the workers, and they were following safe working practices like arranging the welding cable, air hose and oxyacetylene gas hose after completion of the work. The EOT crane remotes also placed regularly in the stand after completion of the work. Then, the regular implementation was effected.

Step 12: Follow-Up/Review

This new method of providing a stand for arranging of welding cable, air hose, oxyacetylene gas hose and EOT crane remote after completion of the work was disseminated to other departments for the improvement of workplace safety.

Fig. 7 Worker is placing the welding cable, air hose and oxyacetylene gas hose after completion of the work on the newly fabricated stand

3 Results and Discussions

Implementation of quality control circle enhanced the workplace safety in the water-wall panel fabrication area of the heavy engineering industry. Application of QCC concept improved the unsafe work atmosphere into safe work centre by utilizing the systematic approaches of the QC tools and techniques. The team followed the Deming's circle concept plan-do-check-act (PDCA), quality control steps of problem-solving methodology with quality control tools for solving the workplace safety-related problems. Stratification and brainstorming technique is used for identification of work-related problems, and rating method is used for the selection of problem. Process flow diagrams and 4W and 1H techniques are used for analysing the problem.

To identify the vital few from the useful, many Pareto charts were used. Again brainstorming technique is used for identification of causes for the problem, and the valid root causes for the problem was analysed with the Ishikawa diagram. The effective analysis of the man, material, method and machine was resulted to find the cause and effects of the problem. Based on that, the root causes were identified and analysed for the development of the solution to the problem. The root causes were analysed with the why-why analysis, and the data collection and brainstorming techniques are used for finding out the solution for the problem with various alternatives and outcomes. Development of the solution was found suitable after analysing with the foreseeing the probable resistance. Regular implementation is carried out with 5W and 1H analysis, and the same method is incorporated into other departments. This QCC team provided creative ideas to solve the work-related problems among the peer group workers.

The team members gained intangible benefits like team spirit, creative thinking skills, decision-making ability and communication skills, and the team members QCC knowledge also improved which resulted in the right solution for their workplace safety by fabricating the stands for welding cable, air hose, oxyacetylene gas hose and crane remotes. The QCC team members effectively utilized the waste material for the stand fabrication with the available resources. This research paper signifies at reporting a realization of the effective application of the QCC approach to improving the safety of workers within the heavy engineering industry. This case study delivers valuable insight into the practical application of a QCC method in the company in its efforts to provide a safe working environment for its workers. The efforts initiated by the QCC team were facilitated to identify the safety-related problems in their work centre. These problems were analysed with the problem-solving steps which led to improving the workplace safety and then improved the quality of the tasks.

4 Conclusion

The QCC concept empowered the members to resolve the unsafe work situation into the safe work situation in the waterwall fabrication area of the heavy manufacturing industry. The QCC team members benefited with improved self-confidence, teamwork culture and technical skills in attempting difficulties. In this case study, QCC concept has played a vital role as an innovative tool to manage workplace safety within a heavy engineering industry. The unsafe work situation which was having a potential hazard to cause injuries was minimized by providing the proper stand for arranging of gas hoses, air hoses, gas cutting hoses and EOT crane remotes after completion of work in waterwall fabrication area. The QCC approach showed that it is an effective method for solving the work-related problem with the QCC team members for the heavy engineering industry. Effective utilization of the quality control circle approach resulted to minimize the unsafe work culture, enhancement of safe work practices, improvement in morale and development of a sense of team spirit among the workers. The results of this case study is proved that QCC approach is beneficial to the workers and the company as a whole.

Suggestions for Future Research

This research work delivers a groundwork for further research regarding the implementation of QCCs in the industrial sector. Further studies may be necessary in order to prove that safety can be benchmarked in critical work industries. This study recommends further research into the methods to use QCCs for continuous improvement of worker's safety, productivity and quality of a company's operations.

Acknowledgements The authors are grateful to the management of Bharat Heavy Electricals Limited, Tiruchirappalli, India, for their support and consent to carry out the study.

References

1. Lozano R, Thompson PC (1980) Implementation in the space shuttle external tank program at Michoud assembly facility of the Martin Marietta Corporation. In: ASQC Technical Conference Transactions, Atlanta, vol 34, pp 42–86
2. Udpa SR (1986) Quality circles, progress through participation. McGraw-Hill Publishing Company Limited, New Delhi
3. Piczak W (1988) Quality circles come home. Qual Prog 37–39
4. Johns N, Chesterton J (1994) ICL Kidsgrove: engineering a quality culture. Int J Contemp Hospitality Manag 6(1/2):25–29
5. Lee S, Lam K (1997) Managing quality at an engineering maintenance center: from QCC to ISO 9001 and beyond. Int J Qual Reliab Manag 14(2):118–137
6. Goh M (2000) Quality circles: the journey of an Asian public enterprise. Int J Qual Reliab Manag 17(7):784–799
7. Slack N, Chambers S, Johnston R (2003) Operations management, 3rd edn. Prentice Hall, London

8. Stevenson W (2005) Operations management, 8th edn. Mc-Graw-Hill, London
9. Abo-Alhol TR, Ismail MY, Sapuan SM, Hamdan MM (2006) Effects of quality circle participation on employee perception and attitude in five Malaysian companies. J Sci Ind Res 65:970–976
10. Salaheldin SI, Zain M (2007) How quality control circles enhance work safety: a case study. The TQM Mag 19(3):229–244
11. Liu SC, Wu HH, Chen HK (2010) Improving organizational performance by a quality control circle: a case of medication improvement team at a hospital in Taiwan. Inf Technol J 9(4):692–697
12. Kannan S, Govinda Rajan SR (2011) Organisations' support to quality circles: a comparative study of public and private sector in India. Asian J Manage Res 2(1):217–227
13. Tyagi A, Srivastava V (2012) A study of the quality circles concept in indian industry (A Case Study on Bharat Electronics Limited, Ghaziabad). Int J Manage Res Rev 2(9):1445
14. Shantanu Welekar S (2013) Quality circle to improve productivity. Int J Eng Res Appl, Training 3(2):814–819
15. Jatt DV (2016) The importance of quality circle in an organisation. Paripex-Indian J Res 5(5):1402–1412
16. Krishnan S, Hizam SM, Saffian AKM, Baharun NAS, Azman N (2017) Safety at workplace enhance productivity. Hum Resour Manage Res J 7(1):33–37
17. Yuan PZ, Wang XL, Hu JH, Zhou ZZ, Li LL (2017) Application of quality control circle to improve the correct rate of hand hygiene of laboratory staff. Chin J Infect Control 16(12):1169–1172
18. Lin L, Chang P, Xie J, Li Z, Zhang H, Lu F, Zhao YE (2017) Sustained accuracy improvement in intraocular lens power calculation with the application of quality control circle. Sci Rep 7(1):14852

A Bio-inspired Climbing Robot: Dynamic Modelling and Prototype Development

Asesh Patra, Meet Patel, Priyabrata Chattopadhyay, Anubhab Majumder and Sanjoy Kumar Ghoshal

Abstract The utilization of bio-inspired robots on various growing issues has turned into an interesting subject. This paper presents a novel bio-inspired climbing robot which imitates the locomotion of an inchworm. The robot contains four indistinguishable modules associated with three revolute joints. At present, the climbing environment is confined to a ferromagnetic flat plane by providing switchable electromagnets to the front and rear modules. The dynamic analysis is performed using both Lagrange model and bond graph model, and a comparative study is carried out. The results obtained from the dynamic analysis are further used to estimate the essential joint torques required for actuator sizing. Finally, the prototype has been developed and the predefined inchworm gait is successfully implemented.

Keywords Bio-inspired robots · Bond graphs · Inchworm locomotion · Magnetic adhesion · Modular approach

1 Introduction

Nowadays, one of the important focuses in research is the climbing robots. There is an increase in demand for climbing robots due to first developing of high altitude and complex structures where human accessibility is difficult. In order to make climbing robot possible, two key aspects should be taken into account: (a) climbing locomotion and (b) adhesion. Sufficient research and various prototypes have been developed in which the means of locomotion are wheels, legs, limbs, etc., but due to some limitations and drawbacks in their flexibility or stability, there is a shift of interest from the previous one to the bio-inspired limbless one in which locomotion

A. Patra (✉) · M. Patel · A. Majumder · S. K. Ghoshal
Department of Mechanical Engineering, Indian Institute of Technology (ISM), Dhanbad 826004, India
e-mail: aseshpatra21@gmail.com

P. Chattopadhyay
CSIR-Central Mechanical Engineering Research Institute, M. G. Avenue, Durgapur 713209, India

H. Kumar and P. K. Jain (eds.), *Recent Advances in Mechanical Engineering*, Lecture Notes in Mechanical Engineering,
https://doi.org/10.1007/978-981-15-1071-7_17

is achieved by body undulation. Adhesion depends on the working environment like magnetic, pneumatic, and chemical. Design aspects and technologies have been designed by Schimdt and Berns which are discussed in reference [1]. Out of various bio-inspired robots, researchers are more fascinated by mainly three kinds of limbless creatures like caterpillar, inchworm, and snake. The shape of the snake type robot is investigated by Hirose and Morishima [2], and kinematic model with control mechanism is discussed by Chen et al. [3]. Moreover, the design and control system of caterpillar [4] and inchworm [5] are explained.

Within this framework, the objective of this work is to present a novel bio-inspired modular climbing robot with magnetic adhesion. This work limits the climbing condition in a level ferromagnetic plane and depicts an inchworm stride for the robot. An open-loop model is put forth to analyse the dynamics of the locomotion. This model is used to estimate the required joint torques for actuator sizing. Thereafter, a prototype has been developed on the basis of actuator sizing and model prediction, which performs satisfactorily. The equations of motion that describe the dynamics of a robot can be obtained by two classical methods, i.e. the Newton–Euler method [6, 7] and Lagrange method [8, 9]. These approaches become complex when a multibody system (like a robot) is associated with nonlinearity and coupled dynamic characteristics have been discussed in [10]. These techniques also circumvent the physical interaction between the elements in the system. The bond graph is an alternative approach which was developed in 1960 for modelling the dynamic system with different energy domains such as electrical, mechanical, and hydraulic system [11–17]. Bond graph model gives an overview of how energy is exchanged between the elements in the physical system. The exchange of energy is expressed in terms of effort and flow variable. In this approach, a graphical representation of the system is conveyed to the computer in order to generate the system equations.

The following part of this paper, Sect. 2, describes the design overview and represents a 3D CAD model of the robot. The locomotion strategy and associated motion kinematics are elaborated in Sect. 3. In Sect. 4, the dynamic analysis is exemplified and a comparative study has been carried out between the classical Lagrange's formulation and the bond graph approach. The experimental prototype development and the robot performance are discussed in Sects. 5 and 6, respectively. Finally, conclusions and future scopes are presented in Sect. 7.

2 Design Overview

Figure 1 shows the 3D CAD model of an inchworm robot. This robot made of four modules serially connected with one another by the help of set screws that plays the role of bearing during rotation. The modules are made of aluminium and 1-DOF revolute joints those are actuated by servo motors. An exploded view of the first two modules of the robot assembly is illustrated in Fig. 2. As adhesion required during climbing on the ferromagnetic surface, the electromagnets are connected to

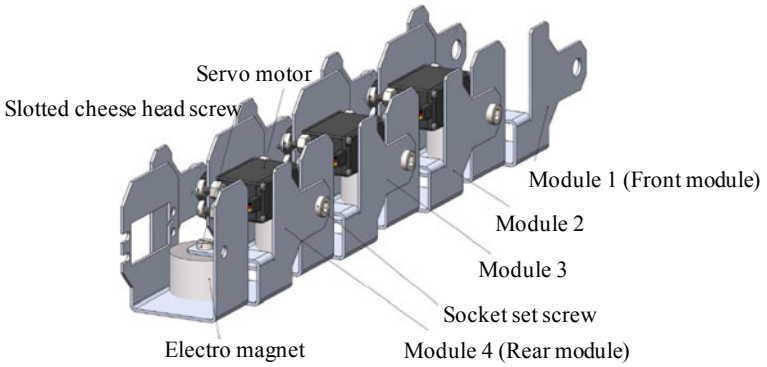

Fig. 1 3D CAD model of the inchworm robot

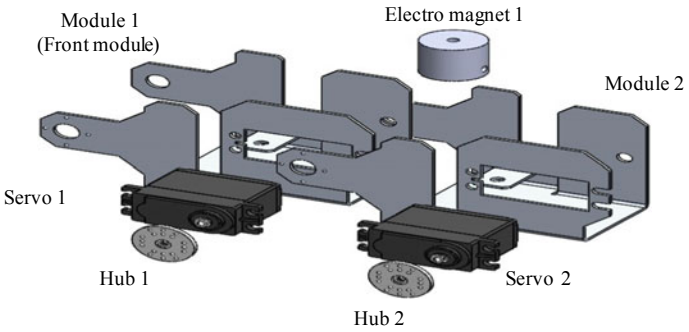

Fig. 2 Exploded view of the first two modules of the robot assembly

the front and rear module [18]. The modular concept optimizes the design of the robot configuration and minimises the overall weight of the robot.

3 Gait Description and Kinematics

The straightforward locomotion on a vertical planner wall has been explained in this section. In order to execute this gait, three revolute joints are simultaneously actuated for a time interval as shown in Fig. 3. The steps during one cycle of the locomotion are presented as follows:

Step 1: During the first interval of time (t_0 to t_1), the first link is in contact with the surface and joint angels remain unchanged.

Step 2: From t_1 to t_2, the first link remains in contact with the surface and the rest of the modules move towards the front module by giving simultaneous rotation to the joints.

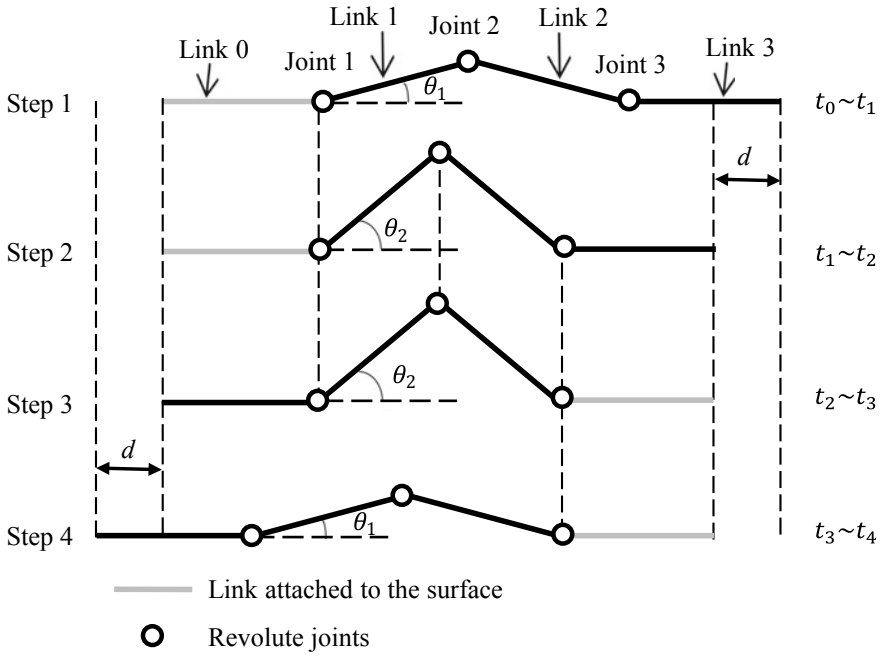

Fig. 3 Progression of the gait generation

Step 3: From t_2 to t_3, the first link is released and the last link is in contact with the surface and amid this process, the joint angles remain unchanged.

Step 4: During t_3 to t_4, similar to Step 2, in opposite direction a synchronous rotation is given to link joints except last link remaining modules moves in the forward direction.

Successful operation in this gait is obtained by formulating joint operations using piecewise sine functions which are a function of the time domain. These functions control the rotation of servos and are called joint orientation functions (JOFs) [19, 20]. The JOFs for one cycle of the gait are given in Eqs. (1)–(3) that are fed to the microcontroller during the real-time experiments [24, 25].

$$\varphi_1(t) = \begin{cases} \theta_1, & t \in [t_0, t_1] \\ \theta_1 + (\theta_2 - \theta_1)\left[\Delta_1 - \frac{\sin(2\pi\Delta_1)}{2\pi}\right], & t \in [t_1, t_2] \\ \theta_2, & t \in [t_2, t_3] \\ \theta_2 - (\theta_2 - \theta_1)\left[\Delta_2 - \frac{\sin(2\pi\Delta_2)}{2\pi}\right], & t \in [t_3, t_4] \end{cases} \tag{1}$$

$$\varphi_2(t) = -2.\varphi_1(t) \tag{2}$$

$$\varphi_3(t) = \varphi_1(t) \tag{3}$$

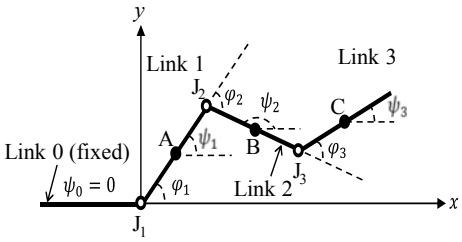

Fig. 4 Schematic diagram of the inchworm robot

where $\Delta_1 = \frac{t-t_1}{t_2-t_1}$, $\Delta_2 = \frac{t-t_3}{t_4-t_3}$.

The base and greatest angle of link 1 regarding the line of motion has been denoted as θ_1 and θ_2. In one cycle, the displacement achieved by the robot is designated as d that can be determined from condition (4) where l is distance between two neighbouring joints. The φ_1, φ_2, and φ_3 are time-dependent JOFs of Joint 1, Joint 2, and Joint 3, respectively. $\psi_i (i = 0{-}3)$ is the orientation of nth$(n = 0{-}3)$ link with respect to the positive x-axis as shown in Fig. 4, and the relationship between ψ_i and φ_i is given in Eq. (5). The angular velocity of a link can easily be calculated by differentiating Eq. (5).

$$d = 2l(\cos\theta_1 - \cos\theta_2) \tag{4}$$

$$\psi_0 = 0; \quad \psi_i = \psi_{i-1} + \varphi_i \tag{5}$$

4 Dynamic Analysis

In this section, the dynamic model of the inchworm robot is developed by considering the robot as a 3-DOF planar mechanism with revolute joints. It can be observed from Fig. 3; the robot remains idle during Step 1 as well as Step 3 when alternate switching between the electromagnets takes place. Figure 5 describes the symmetrical nature of the motion sequences during Step 2 and Step 4 where the origin of the coordinate system is shifted from Joint 1 to Joint 3 and the direction of x-axis is reversed. Hence, dynamic modelling of Step 2 is sufficient to investigate the dynamic behaviour. In the following subsections, the dynamic model is developed by involving two different approaches: the first attempt is based on the Lagrangian formulation, and subsequently, a bond graph model of the robot is presented. Afterwards, the joint torque values are estimated by using both models and the results are compared. In both the cases, the contact between the links and the surface is assumed to be frictionless.

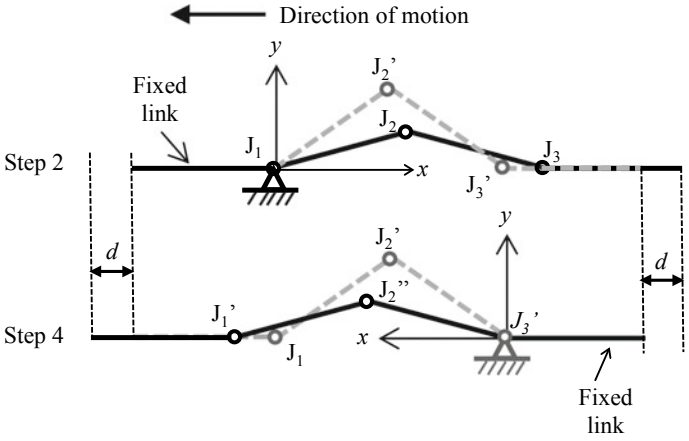

Fig. 5 Coordinate system during Step 2 and Step 3

4.1 Dynamic Model Based on the Lagrangian Formulation

The Lagrangian formulation is based on computing kinetic and potential energy of each link of a manipulator with respect to generalized coordinates. The difficulties in the calculation of equation of motion can be avoided by considering the position of centroid lies at the midpoint of each link. Let $A\ (x_1, y_1)$, $B\ (x_2, y_2)$, $C\ (x_3, y_3)$ are the centre of masses of link 1, link 2, and link 3, respectively (see Fig. 4). The position of x and y coordinates of point A, B, C can be given by:

$$\begin{cases} x_1 = \frac{l}{2}\cos\varphi_1 \\ y_1 = \frac{l}{2}\sin\varphi_1 \end{cases} \tag{6}$$

$$\begin{cases} x_2 = l\cos\varphi_1 + \frac{l}{2}\cos(\varphi_1 + \varphi_2) \\ y_2 = l\sin\varphi_1 + \frac{l}{2}\sin(\varphi_1 + \varphi_2) \end{cases} \tag{7}$$

$$\begin{cases} x_3 = l\cos\varphi_1 + l\cos(\varphi_1 + \varphi_2) + \frac{l}{2}\cos(\varphi_1 + \varphi_2 + \varphi_3) \\ y_3 = l\sin\varphi_1 + l\sin(\varphi_1 + \varphi_2) + \frac{l}{2}\sin(\varphi_1 + \varphi_2 + \varphi_3) \end{cases} \tag{8}$$

Let v_n be the velocity of the centroid of nth link and its square will be:

$$v_n^2 = \dot{x}_n^2 + \dot{y}_n^2 \quad (n = 1 \ldots 3) \tag{9}$$

Using Eqs. (5)–(9) becomes:

$$v_n^2 = l^2\left(\frac{1}{4}\dot{\psi}_n^2 + \sum_{i=1}^{n}\sum_{j=1}^{n-1}\dot{\psi}_i\dot{\psi}_j C_{ij}\right) \tag{10}$$

where $C_{ij} = \cos(\psi_i - \psi_j)$, and henceforward, we use the abbreviation $S_{ij} = \sin(\psi_i - \psi_j)$. Considering identical link length (l) and mass (m) for each link, the moment of inertia about the centroidal axis of each link is $J = \frac{1}{12}ml^2$. Thus, the total kinetic energy is calculated as:

$$K = \frac{1}{2}\sum_{n=1}^{3}\left(mv_n^2 + I\dot{\psi}_n^2\right) \tag{11}$$

The total potential energy is given by:

$$P = mgl\sum_{n=1}^{3}\left(\sum_{j=1}^{n}\sin\psi_j - \frac{1}{2}\sin\psi_n\right) \tag{12}$$

The Lagrangian function ($\mathcal{L}$) is defined as the difference between the total kinetic energy and the total potential energy of the system.

$$\mathcal{L} = K - P \tag{13}$$

Considering joint torques, τ_i as the externally applied generalized forces associated with generalized coordinates ψ_i, the Lagrangian equations of motion for the dynamic response of the mechanism can be written as:

$$\frac{\mathrm{d}}{\mathrm{d}t}\left(\frac{\partial\mathcal{L}}{\partial\dot{\psi}_i}\right) - \frac{\partial\mathcal{L}}{\partial\psi_i} = \tau_i \quad (i = 1\ldots3) \tag{14}$$

The equation of joint torques, i.e. Eq. 15, can be obtained by substituting Eqs. (11–13) into Eq. (14).

$$\begin{aligned}
&\frac{ml^2}{6}\begin{bmatrix} 14 & 9C_{12} & 3C_{13} \\ 6C_{12} & 8 & 3C_{23} \\ 3C_{13} & 3C_{23} & 2 \end{bmatrix}\begin{bmatrix} \ddot{\psi}_1 \\ \ddot{\psi}_2 \\ \ddot{\psi}_3 \end{bmatrix} \\
&+\frac{ml^2}{6}\begin{bmatrix} 0 & 9S_{12} & 3S_{13} \\ -9S_{12} & 0 & 3S_{23} \\ -3S_{13} & -3S_{23} & 0 \end{bmatrix}\begin{bmatrix} \dot{\psi}_1^2 \\ \dot{\psi}_2^2 \\ \dot{\psi}_3^2 \end{bmatrix} \\
&+\frac{mgl}{2}\begin{bmatrix} 5\cos\psi_1 \\ 3\cos\psi_2 \\ \cos\psi_3 \end{bmatrix} = \begin{bmatrix} 1 & -1 & 0 \\ 0 & 1 & -1 \\ 0 & 0 & 1 \end{bmatrix}\begin{bmatrix} \tau_1 \\ \tau_2 \\ \tau_3 \end{bmatrix}
\end{aligned} \tag{15}$$

4.2 Bond Graph Modelling of the Dynamic System

Bond graph model as shown in Fig. 6 uses the kinematic equation of joint velocities to compute the dynamic behaviour of the system. The input velocities are $\dot{\varphi}_1$, $\dot{\varphi}_2$, and $\dot{\varphi}_3$ indicated by SF-elements in the bond graph model. The joint velocities are presented in the bond graph model by $1_{\dot{\psi}_1}$, $1_{\dot{\psi}_2}$,and $1_{\dot{\psi}_3}$ junctions, respectively, which are determined by the moment of inertias (I elements) attached to the 1 junctions. The frictional loss occurred at each joint is modelled by inserting a pad [21] containing high value of compliance (K_h) and damping (R_h) in between the joint and the source. Joint velocity for link 2 is obtained by adding $\dot{\psi}_1$ and $\dot{\varphi}_2$ in a 0 junction. Similarly for link 3, $\dot{\varphi}_3$ is added with $\dot{\psi}_2$ in another 0 junction to obtain $\dot{\psi}_3$. The flow activated C-element on the 1 junction (effort summing junction) records the contemporary angular position of the links $\psi_i, i = 1 \ldots 3$, in terms of the measured states, Q_1, Q_2, Q_3, respectively, which is expressed as:

$$\psi_i = Q_i = \int f_i \mathrm{d}t \tag{16}$$

The linear velocities of the centre of mass of link in Cartesian coordinate are expressed in terms of joint velocity as follows:

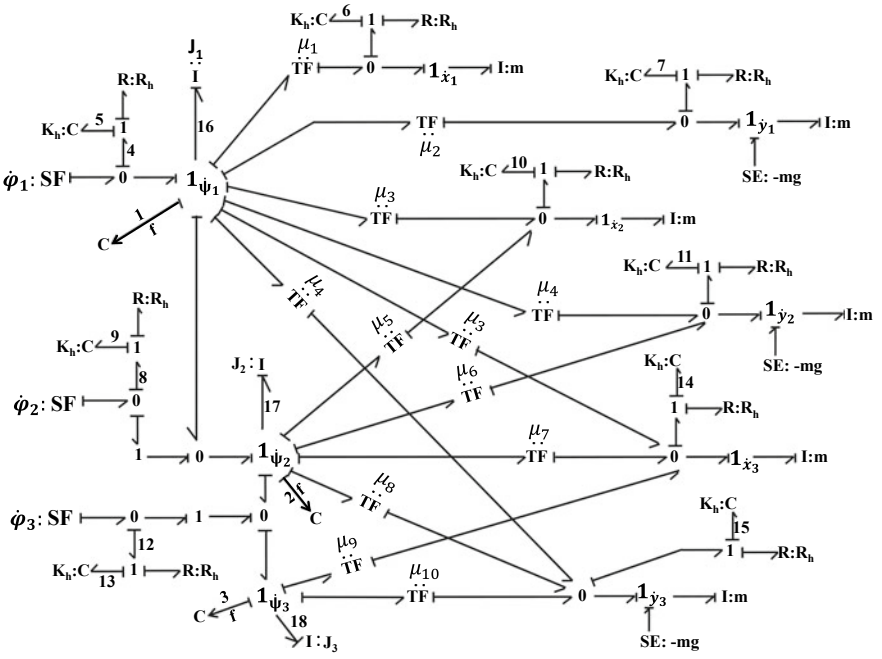

Fig. 6 Bond graph model of the inchworm robot

$$\begin{cases} \dot{x}_1 = -\frac{l}{2}\dot{\psi}_1 \sin\psi_1 \\ \dot{y}_1 = \frac{l}{2}\dot{\psi}_1 \cos\psi_1 \end{cases} \tag{17}$$

$$\begin{cases} \dot{x}_2 = -l\dot{\psi}_1 \sin\psi_1 - \frac{l}{2}\dot{\psi}_2 \sin\psi_2 \\ \dot{y}_2 = l\dot{\psi}_1 \cos\psi_1 + \frac{l}{2}\dot{\psi}_2 \cos\psi_2 \end{cases} \tag{18}$$

$$\begin{cases} \dot{x}_3 = -l\dot{\psi}_1 \sin\psi_1 - l\dot{\psi}_2 \sin\psi_2 - \frac{l}{2}\dot{\psi}_3 \sin\psi_3 \\ \dot{y}_3 = l\dot{\psi}_1 \cos\psi_1 + l\dot{\psi}_2 \cos\psi_2 + \frac{l}{2}\dot{\psi}_3 \cos\psi_3 \end{cases} \tag{19}$$

The transformer moduli of TF elements are $\mu_1 = -(l/2)\sin\psi_1$, $\mu_2 = (l/2)\cos\psi_1$, $\mu_3 = -l\sin\psi_1$, $\mu_4 = l\cos\psi_1$, $\mu_5 = -(l/2)\sin\psi_2$, $\mu_6 = (l/2)\cos\psi_2$, $\mu_7 = -l\sin\psi_2$, $\mu_8 = l\cos\psi_2$, $\mu_9 = -(l/2)\sin\psi_3$, and $\mu_{10} = (l/2)\cos\psi_3$. The velocity components $(\dot{x}_i, \dot{y}_i)$ are determined by the mass inertias m of the respective links appended to 1 junctions. The gravity force acts in the negative y-direction, which is modelled by adding an effort source SE (: $-m_i g$) element to the $1_{\dot{y}_i}$ junction.

The system equations are generated from the bond graph model by using a well-established algorithm [11, 22], which are given as:

$$m\ddot{x}_1 = R_h\left(\mu_1\dot{\psi}_1 - \dot{x}_1\right) + K_h Q_6 \tag{20}$$

$$m\ddot{y}_1 = R_h\left(\mu_2\dot{\psi}_1 - \dot{y}_1\right) + K_h Q_7 - mg \tag{21}$$

$$m\ddot{x}_2 = R_h\left(\mu_5\dot{\psi}_2 + \mu_3\dot{\psi}_1 - \dot{x}_2\right) + K_h Q_{10} \tag{22}$$

$$m\ddot{y}_2 = R_h\left(\mu_6\dot{\psi}_2 + \mu_4\dot{\psi}_1 - \dot{y}_2\right) + K_h Q_{11} - mg \tag{23}$$

$$m\ddot{x}_3 = R_h\left(\mu_9\dot{\psi}_3 + \mu_7\dot{\psi}_2 + \mu_3\dot{\psi}_1 - \dot{x}_3\right) + K_h Q_{14} \tag{24}$$

$$m\ddot{y}_3 = R_h\left(\mu_{10}\dot{\psi}_3 + \mu_8\dot{\psi}_2 + \mu_4\dot{\psi}_1 - \dot{y}_3\right) + K_h Q_{15} - mg \tag{25}$$

$$e_4 = \tau_1 = R_h\left(\dot{\varphi}_1 - \dot{\psi}_1\right) + K_h Q_5 \tag{26}$$

$$e_8 = \tau_2 = R_h\left(\dot{\varphi}_2 - \dot{\psi}_2 + \dot{\psi}_1\right) + K_h Q_9 \tag{27}$$

$$e_{12} = \tau_3 = R_h\left(\dot{\varphi}_3 - \dot{\psi}_3 + \dot{\psi}_2\right) + K_h Q_{13} \tag{28}$$

$$\begin{aligned} e_{16} = {} & K_h Q_5 + R_h\left(\dot{\varphi}_1 - \dot{\psi}_1\right) - \mu_1\left\{R_h\left(\mu_1\dot{\psi}_1 - \dot{x}_1\right) + K_h Q_6\right\} \\ & - \mu_2\left\{R_h\left(\mu_2\dot{\psi}_1 - \dot{y}_1\right) + K Q_7\right\} - K_h Q_9 - R_h\left(\dot{\varphi}_2 - \dot{\psi}_2 + \dot{\psi}_1\right) - \mu_3\{K_h Q_{10} \\ & + R_h\left(\mu_5\dot{\psi}_2 + \mu_3\dot{\psi}_1 - \dot{x}_2\right)\} - \mu_4\left\{K_h Q_{11} + R_h\left(\mu_6\dot{\psi}_2 + \mu_4\dot{\psi}_1 - \dot{y}_2\right)\right\} \\ & - \mu_3\left\{K_h Q_{10} + R_h\left(\mu_9\dot{\psi}_3 + \mu_7\dot{\psi}_2 + \mu_3\dot{\psi}_1 - \dot{x}_3\right)\right\} - \mu_4\left\{K_h Q_{11} + R_h\left(\mu_{10}\dot{\psi}_3\right.\right. \end{aligned}$$

$$+\mu_8\dot{\psi}_2 + \mu_4\dot{\psi}_1 - \dot{y}_3)\} \tag{29}$$

$$\begin{aligned} e_{17} = {} & K_h Q_9 + R_h(\dot{\varphi}_2 - \dot{\psi}_2 + \dot{\psi}_1) - \mu_5\{R_h(\mu_5\dot{\psi}_2 + \mu_3\dot{\psi}_1 - \dot{x}_2) \\ & + K_h Q_{10}\} - R_h(\dot{\varphi}_3 - \dot{\psi}_3 + \dot{\psi}_2) - K_h Q_{13} - \mu_6\{R_h(\mu_6\dot{\psi}_2 + \mu_4\dot{\psi}_1 - \dot{y}_2) \\ & + K_h Q_{11}\} - \mu_7\{R_h(\mu_9\dot{\psi}_3 + \mu_7\dot{\psi}_2 + \mu_3\dot{\psi}_1 - \dot{x}_3) + K_h Q_{14}\} - \mu_8\{R_h(\mu_{10}\dot{\psi}_3 \\ & + \mu_8\dot{\psi}_2 + \mu_4\dot{\psi}_1 - \dot{y}_3) + K_h Q_{15}\} \end{aligned} \tag{30}$$

$$\begin{aligned} e_{18} = {} & K_h Q_{13} + R_h(\dot{\varphi}_3 - \dot{\psi}_3 + \dot{\psi}_2) - \mu_9\{R_h(\mu_9\dot{\psi}_3 + \mu_7\dot{\psi}_2 + \mu_3\dot{\psi}_1 - \dot{x}_3) \\ & + K_h Q_{14}\} - \mu_{10}\{R_h(\mu_{10}\dot{\psi}_3 + \mu_8\dot{\psi}_2 + \mu_4\dot{\psi}_1 - \dot{y}_3) + K_h Q_{15}\} \end{aligned} \tag{31}$$

where Q stands for the generalized displacement associated with C elements, e represents generalized effort, and τ_i, $(i = 1 \ldots 3)$ refer to torque required for the ith joint. The system Eqs. (20–31) are solved using Symbols-Shakti® software which adopts fifth-order Runge–Kutta Gill method to integrate the equations numerically [23].

4.3 Comparing Results Between Lagrange's Model and Bond Graph Simulation

The joint torque values required to actuate the robot are obtained by using both Lagrange's model and the bond graph model. All the parameters used during calculation are given in Table 1. It can be observed from Eq. (1) to (3) that the direction of rotation given to Joint 2 is opposite of Joint 1 and Joint 3; therefore, negative torque values are obtained at Joint 2 for both Lagrange and bond graph models. Figure 7 shows the similarity of dynamic behaviour between two models, and Fig. 8 shows the deviation percentages of torque values which have been calculated using Eq. (32).

Table 1 Parameters used for joint torque estimation

Parameter	Value
Mass of each link, m	0.12 kg
Link length, l	0.091 m
Moment of inertia, J	8.28e−5
Initial value of φ_1	0.261 rad
Initial value of φ_2	−0.261 rad
Initial value of φ_3	0.261 rad
Gravitational acceleration, g	9.81 m/s^2
Minimum inclination of link 1, θ_1	0.261 rad
Maximum inclination of link 1, θ_2	0.61 rad
Duration of Step 2, $(t_2 - t_1)$	2 s

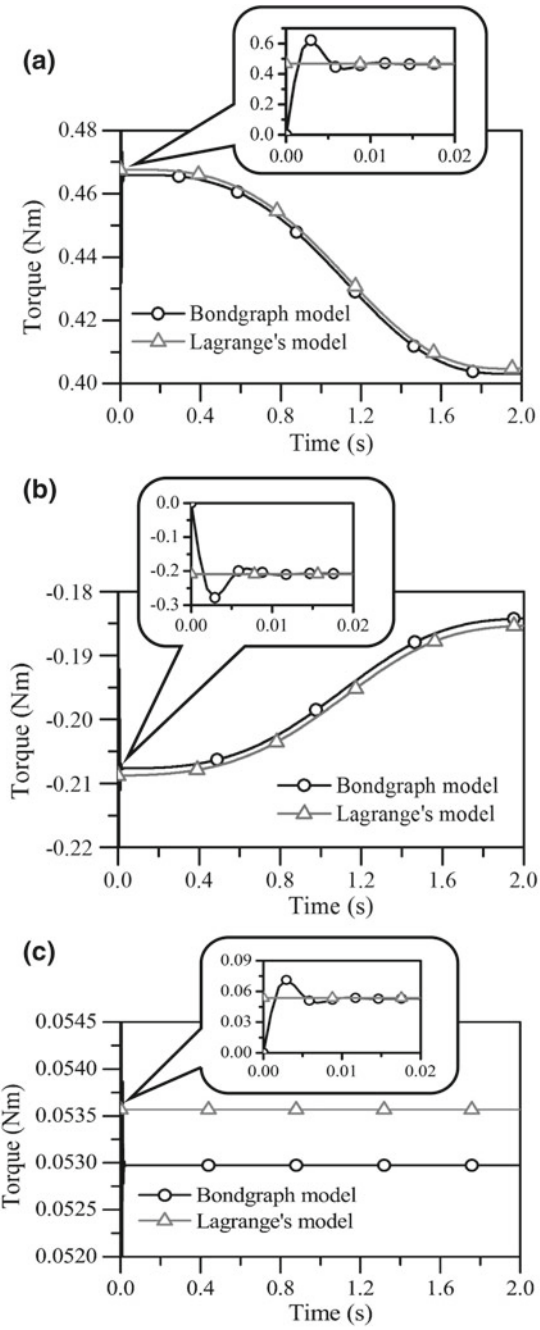

Fig. 7 Estimated joint torques from both Lagrangian formulation and bond graph model. **a** Comparison of torque required at Joint 1, **b** comparison of torque required at Joint 2, and **c** comparison of torque required at Joint 3

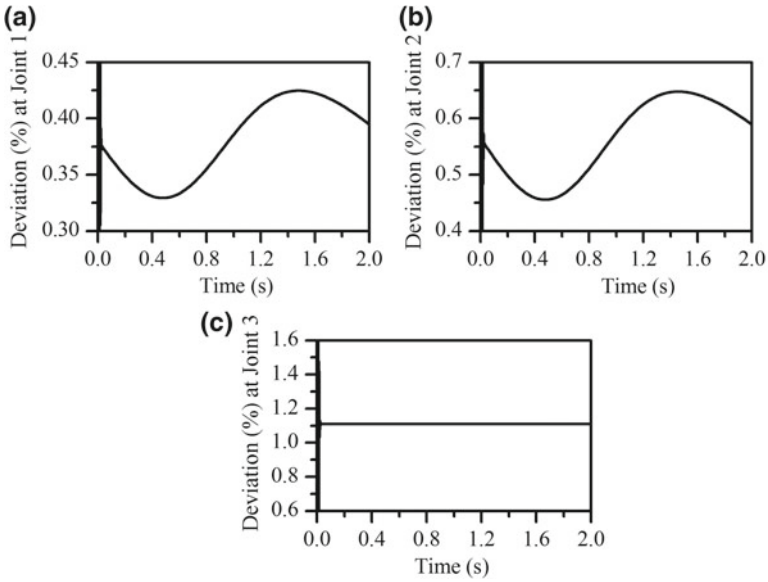

Fig. 8 Percentage deviation of torque values between Lagrange's formulation and bond graph model **a** deviation at Joint 1, **b** deviation at Joint 2, and **c** deviation at Joint 3

$$\text{Deviation}\,(\%) = \frac{\sqrt{\left(\tau_{\text{lagr}} - \tau_{\text{bond}}\right)^2}}{\tau_{\text{lagr}}} \times 100 \tag{32}$$

where τ_{lagr}, τ_{bond} are the joint torque values obtained from Lagrange's model and bond graph model, respectively. The deviation occurs due to the presence of additional joint flexibility or pads in the bond graph model which also causes high-frequency vibration in the system at the commencement of simulation as indicated in Fig. 7.

4.4 Torque Variation During Climbing up on a Vertical Surface

In this case, the gravity force acts in the positive x-direction. Hence, the effort source (SE: $m_i g$) element is added to the $1_{\dot{x}_i}$ junction instead of adding effort source (SE:$-m_i g$) element to the $1_{\dot{y}_i}$ junction as shown in Fig. 9. After the modification of the bond graph model, dynamic simulation process has been carried out and the estimated joint torque values are shown in Fig. 10.

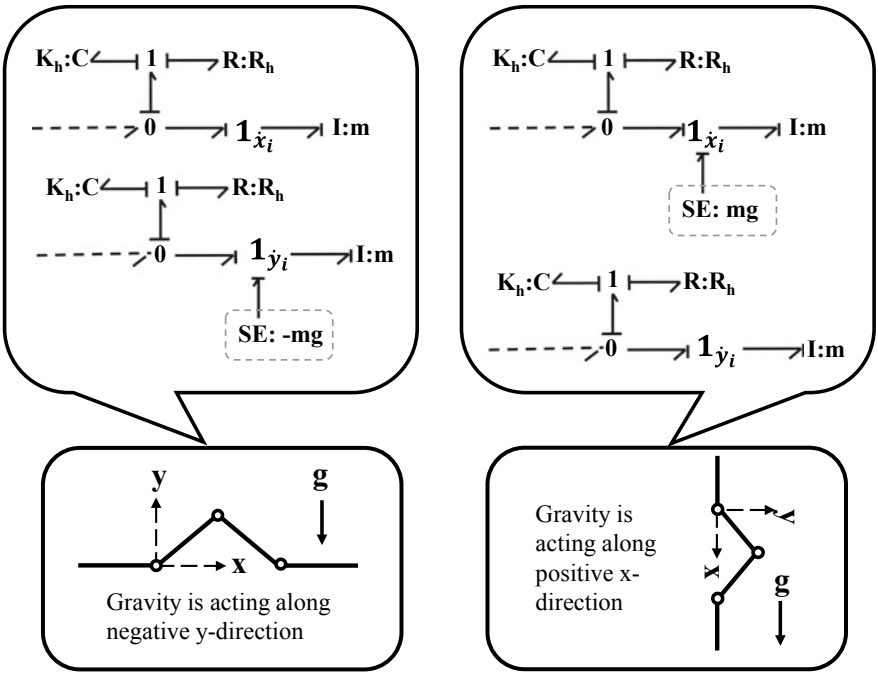

Fig. 9 Changes in the bond graph model required to represent the dynamic model of the robot while climbing up on a vertical surface

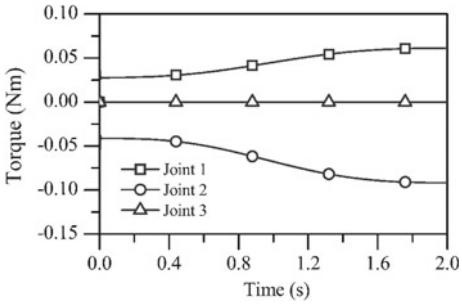

Fig. 10 Variation of joint torques during climbing up on a vertical surface estimated by using the bond graph model

4.5 Servo Motor Selection Based on the Dynamic Analysis

The results obtained from the dynamic analysis indicate that the maximum joint torque required to drive the robot on a horizontal plane is about 0.5 Nm and the value is well within 0.1 Nm while climbing up on the vertical plane. The torque requirement may be increased during practical experiments as the contact between the surface and the links is assumed to be frictionless in the dynamic analysis. Therefore, the rated torque of the servo motors should be more than 0.5 Nm.

5 Prototype Development

5.1 Mechanical Design

Figure 11 shows the assembled prototypes of inchworm robots where modules are identical and connected serially.

HS-5645MG DC servo motors are used for actuation which provides precise control of the angular position. Servos consist of an electric motor coupled to a position feedback sensor and have a range of motion between −90° and +90°. The pinion gear on the motors' output shaft transfers rotation through a metal gear train which delivers a high torque (10.3 kg cm with operating voltage 4.8 V). All the design specifications are given in Table 2.

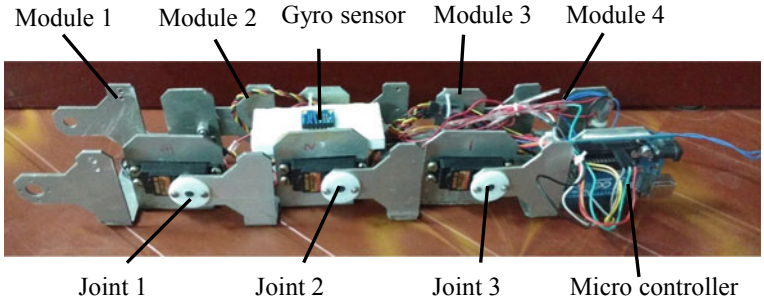

Fig. 11 Experimental prototype

Table 2 Design specification

Mass of each module	52.89 g
Module dimension	120 mm × 68 mm × 64 mm
Mass of servo motor	60 g
Mass of electromagnet	49 g
Joint to joint distance	91.01 mm
Rated torque of the servo motor	10.3 kg cm
Maximum holding force of the electromagnet	50 N

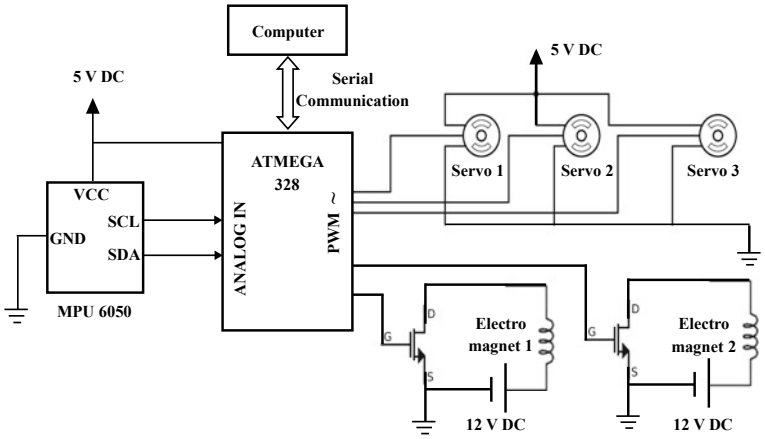

Fig. 12 Schematic diagram of the electronic architecture

5.2 Electronic Integration

In order to automate the robot, rear module houses a microcontroller board (ATmega328) which features a serial communication interface and provides an integrated development environment (IDE). The microcontroller board has 14 digital ports from which 6 can be used as PWM output and 6 analog inputs. In order to operate electromagnets, SRD-05V DC-SL-C relays are used as switches. The MPU-6050 gyro sensor is utilized to measure the angular displacement of the joints about the axis of rotation. It uses the I2C (Inter-Integrated Circuit) bus interface to communicate with the microcontroller board. A complete block diagram of the electronic architecture is shown in Fig. 12.

6 Experimental Results

The on-site climbing experiment is successfully executed on a ferromagnetic vertical wall by the inchworm robot, and the robot is able to accomplish the proposed locomotion strategy as shown in Fig. 3. Figure 13 illustrates a sequence of snapshots taken from a video recorded during the experiment. The $t_i (i = 0 \ldots 4)$ in Fig. 12 resembles the time $t_i (i = 0 \ldots 4)$ as shown in Fig. 3. The values of θ_1 and θ_2 are specified as 15° and 35°, respectively. The time duration for Step 1 and Step 3 is 1 s, and for Step 2 and Step 4, the time duration is 2 s; i.e., total time taken by the robot to complete one cycle of the gait is 6 s.

Figure 14 depicts the resemblance between the angular rotations of Joint 1 during

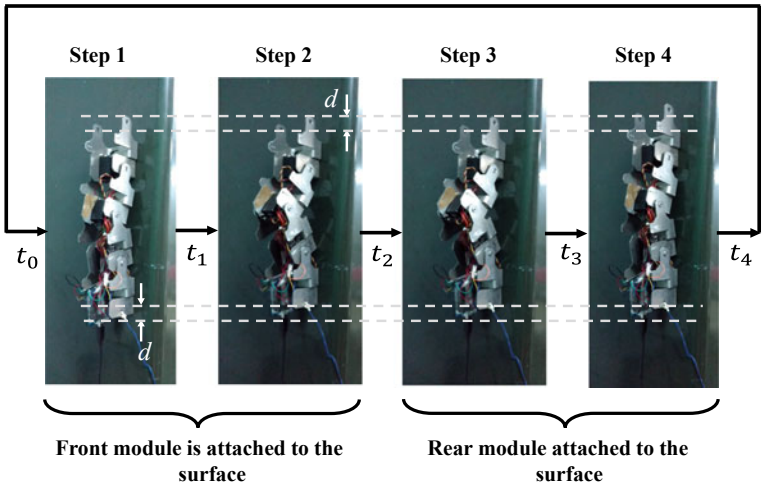

Fig. 13 Snapshots of the gait sequence

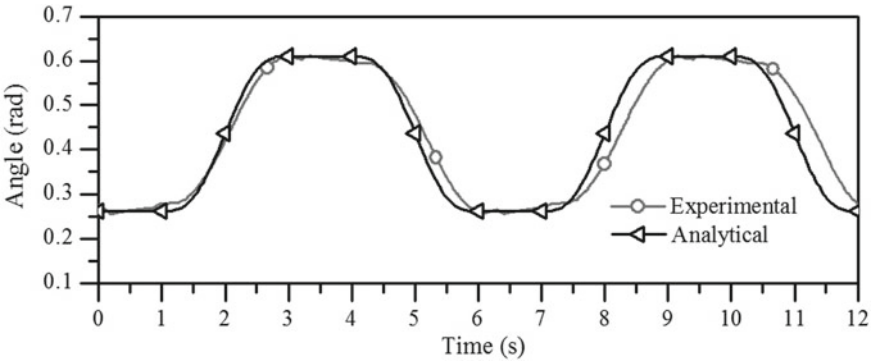

Fig. 14 Analytical and experimental angular rotation of Joint 1

the experiment with the predefined Joint Orientation Function (JOF). The experimental values of the angular rotation are further used to compute the real-time angular velocities of the joints. The analytical angular velocity of Joint 1 is calculated for two consecutive cycles of gait, and the values are compared with the real-time experimental values as shown in Fig. 15.

The net displacement of the front and rear module along the direction of motion is derived from the gait kinematics and the experimental data which are represented in Figs. 16 and 17, respectively. It has been observed that the distance travelled per complete gait cycle by the robot along the direction of motion, $\boldsymbol{d}$, is 25.48 mm which is about 95.4% of the calculated value from Eq. (4).

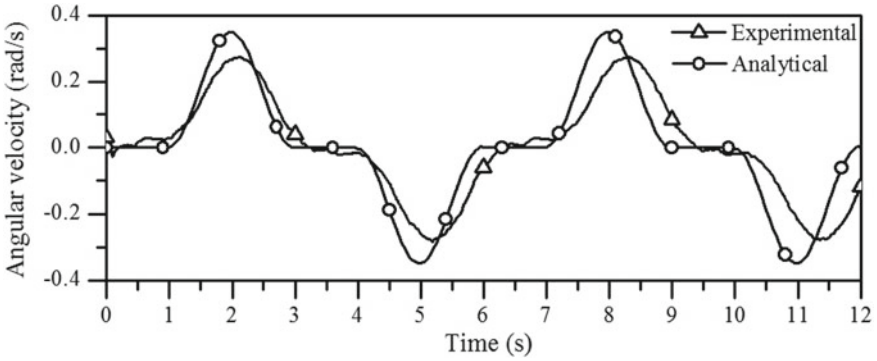

Fig. 15 Analytical and experimental angular velocity of Joint 1

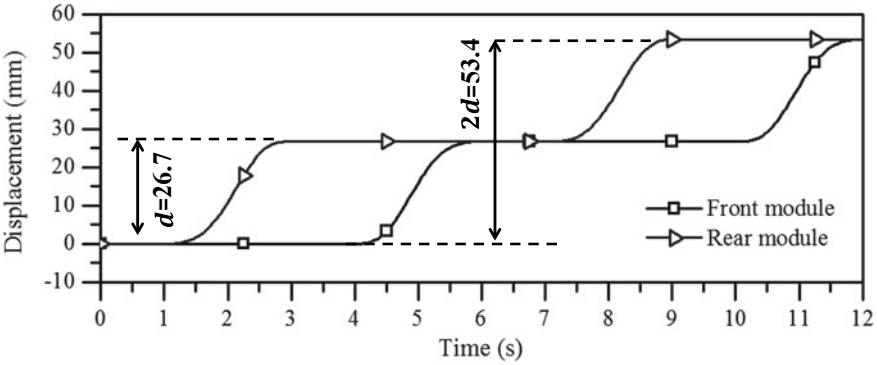

Fig. 16 Net displacement of the front and rear module along the direction of motion derived from the gait kinematics

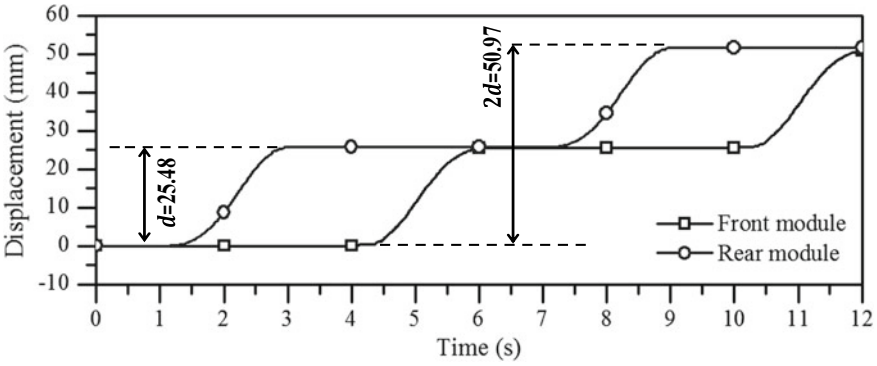

Fig. 17 Net displacement of the front and rear module along the direction of motion derived from the experimental data

7 Conclusion

So, basically a bio-inspired limbless robot that follows the example of an inchworm locomotion is displayed in this paper. A bond graph model of the robot has been created by considering the robot as a four-link planar mechanism with three revolute joints. The bond graph model is used to estimate the joint torques which are important for selection of actuators. The results obtained from the bond graph simulation are compared with results obtained from Lagrangian formulation by confining the motion of the robot on a horizontal flat surface. The satisfactory comparison between the bond graph and lagrangian models ensures the suitability of bond graph for predicting system's dynamic behaviour. The bond graph model eases the mathematical iterations in comparison to the Lagrangian formulation. Further, the proposed locomotion strategy has been successfully employed on an experimental prototype.

In future work, the flexibility of the robot can be enhanced by increasing the degree of freedom of each revolute joint so that it can steer during routing. Further modules can be added to enhance the flexibility of the robot. An extra control framework can likewise be presented for operating the servos that will upgrade the accuracy and smooth running amid the activity.

References

1. Schmidt D, Berns K (2013) Climbing robots for maintenance and inspections of vertical structures—a survey of design aspects and technologies. Robot Auton Syst 61(12):1288–1305
2. Hirose S, Morishima A (1990) Design and control of a mobile robot with an articulated body. Int J Rob Res 9(2):99–114
3. Chen L, Wang Y, Ma S, Li B (2003) Analysis of traveling wave locomotion of snake robot. In: Proceedings of 2003 IEEE international conference on robotics, intelligent systems and signal processing, vol 1. IEEE, pp 365–369
4. Wang K, Wang W, Zhang H (2013) The mechanical properties of a wall-climbing caterpillar robot: analysis and experiment. Int J Adv Rob Syst 10(1):34
5. Wang W, Zhang HX, Wang K, Zhang JW, Chen WH (2009) Gait control of modular climbing caterpillar robot. In: IEEE/ASME international conference on advanced intelligent mechatronics, 2009. AIM 2009. IEEE, pp 957–962
6. Djuric A, Jovanovic V, Filiovic M, Kevac L (2016) Comparison between Newton-Euler and automatic separation method for SCARA dynamic modeling. In: SoutheastCon, 2016. IEEE, pp 1–8
7. Becke M, Schlegl T (2012) Extended Newton-Euler based centrifugal/Coriolis matrix factorization for geared serial robot manipulators with ideal joints. In: Mechatronika, 2012 15th international symposium. IEEE, pp 1–7
8. Ghanbari A, Noorani SMRS (2011) Optimal trajectory planning for design of a crawling gait in a robot using genetic algorithm. Int J Adv Rob Syst 8(1):6
9. Caux S, Zapata R (1999) Modeling and control of biped robot dynamics. Robotica 17(4):413–426
10. Ghosh AK, Mukherjee A, Faruqi MA (1991) Computation of driving efforts for mechanisms and robots using bond graphs. J Dyn Syst Meas Contr 113(4):744–748
11. Merzouki R, Samantaray AK, Pathak PM, Bouamama BO (2012) Intelligent mechatronic systems: modeling, control and diagnosis. Springer Science & Business Media

12. Martens HR (1973) Simulation of nonlinear multiport systems using bond graphs. J Dyn Syst Meas Control 95(1):49–54
13. Merzouki R, Ould-Bouamama B, Djeziri MA, Bouteldja M (2007) Modelling and estimation of tire–road longitudinal impact efforts using bond graph approach. Mechatronics 17(2–3):93–108
14. Cohodar M, Borutzky W, Damic V (2009) Comparison of different formulations of 2D beam elements based on Bond Graph technique. Simul Model Pract Theory 17(1):107–124
15. Vaz A, Singh K, Dauphin-Tanguy G (2015) Bond graph model of extensor mechanism of finger based on hook–string mechanism. Mech Mach Theory 91:187–208
16. Pathak PM, Mukherjee A, Dasgupta A (2005) Impedance control of space robots using passive degrees of freedom in controller domain. J Dyn Syst Meas Control 127(4):564–578
17. Borutzky W (2009) Bond graph modelling and simulation of multidisciplinary systems—an introduction. Simul Model Pract Theory 17(1):3–21
18. Plaut RH (2015) Mathematical model of inchworm locomotion. Int J Non-Linear Mech 76:56–63
19. Maity A, Majumder S, Ghosh S (2010) An experimental hyper-redundant serpentine robot. In: 2010 IEEE international conference on Systems Man and Cybernetics (SMC). IEEE, pp 3180–3185
20. Maity A, Majumder S (2011) Serpentine robot moves and postures. In: 2011 IEEE conference on Robotics, Automation and Mechatronics (RAM). IEEE, pp 202–207
21. Tripathi JP, Ghoshal SK, Dasgupta K, Das J (2017) Bond graph modelling of a hydraulic cylinder-actuated planar manipulator. J Braz Soc Mech Sci Eng 39(11):4275–4287
22. Samantaray AK, Bouamama BO (2008) Model-based process supervision: a bond graph approach. Springer Science & Business Media
23. Samantaray AK, Mukherjee A (2006) Users manual of SYMBOLS Shakti, High-Tech Consultants, STEP, Indian Institute of Technology, Kharagpur
24. Chattopadhyay P, Majumder A, Dikshit H, Ghoshal SK, Maity A (2018) A bio-inspired climbing robot: design, simulation, and experiments. In: IOP conference series: materials science and engineering, vol 377, issue no. 1. IOP Publishing, p 012105
25. Chattopadhyay P, Dikshit H, Majumder A, Ghoshal S, Maity A (2018) Dynamic analysis of a bio-inspired climbing robot using ADAMS-Simulink co-simulation. In: AIP conference proceedings, vol 1952, issue no. 1. AIP Publishing, p 020015

Effect of Electrochemical Micromachining Process Parameters on Surface Roughness and Dimensional Deviation of Ti6Al4V by Tungsten Electrode

Venkatasreenivasula Reddy Perla, Subbarama Kousik Suraparaju, K. J. RathanRaj and A. Sreenivasulu Reddy

Abstract The electrochemical micromachining (ECMM) is a special form of conventional ECM process in which the tool electrode is at micro-level used to produce micro-features. This article aims to determine the parametric influence of process parameters in ECMM using Taguchi's experimental design and ANOVA. The objective variables are surface roughness (SR) and dimensional deviation (DD). Experiments were designed as per Taguchi's L16 orthogonal array (OA) by considering applied voltage (V), duty cycle (DC), feed rate (F) and frequency (f) as input parameters. Experiments carried on Ti6Al4V using sodium chloride (NaCl) salt solution with concentration 20 g/lt by producing blind holes of depth 250 μm. Surface roughness is measured with non-contact surface roughness tester Talysurf CCI (coherence correlation interferometry) having < 0.01 nm as least count and dimensional deviation is measured with vision measuring machine. ANOVA technique is performed to get percentage influence of each process parameter on performance characteristics, and it is observed that duty cycle has more influence on surface roughness and applied voltage has more influence on dimensional deviation.

Keywords Electrochemical micromachining · Electrolyte · Tungsten tool · Taguchi L16 OA · ANOVA

V. R. Perla (✉) · S. K. Suraparaju · A. Sreenivasulu Reddy
Mechanical Engineering Department, Sri Venkateswara University, Tirupati, Andhra Pradesh, India
e-mail: perlasreenu@gmail.com

V. R. Perla · K. J. RathanRaj
Industrial Engineering and Management Department, B.M.S. College of Engineering, Bengaluru, Karnataka, India

S. K. Suraparaju
Department of Mechanical Engineering, National Institute of Technology Puducherry, Karaikal, Ut of Puducherry, India

H. Kumar and P. K. Jain (eds.), *Recent Advances in Mechanical Engineering*,
Lecture Notes in Mechanical Engineering,
https://doi.org/10.1007/978-981-15-1071-7_18

1 Introduction

The significant electrochemical machining (ECM) was developed during 1959, and it is mainly operated for materials that are hard to machine with conventional machining operations. Electrochemical micromachining (ECMM) is an application of ECM for a precise shape in the micromachining range, in which micromachining is the component machining in dimension ranging between 1 and 999 μm [1, 2]. Micromachining is directly not possible to achieve by a conventional technique because micron-dimensional accuracies are involved in it.

The exigency towards the use of more micro-parts is demanded due to drastic changes in the utilization of various industrial components. For example, fuel injection nozzle design is changed according to environmental constraints and made it more compact with high accuracy. ECCM is best suited for this high-end usage of micro-parts, due to its various advantages such as higher machining rate, machining a wide range of materials, better precision and control, economical and also it is environmentally friendly. This method can effectively process the electrically conductive, hard and difficult to machine materials without any defects and deformation. During machining, there is no residual stresses development and no tool wear problem because there is no direct contact between tool electrode and workpiece. Since the electrolysis principle is the cause for mechanism of material removal, there is no heat generation during the process. These capabilities and qualities of ECMM make it useful in many industries where difficult-to-cut materials are to be processed [3–7] (Fig. 1).

The miniaturization components in various applications through the micromachining process are the current trend in machining. Micromachining is the key technology in microelectromechanical systems (MEMS). This technology lasts long and

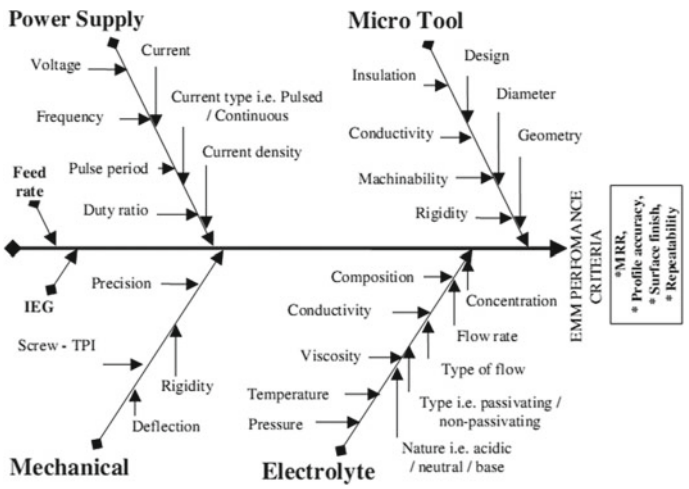

Fig. 1 Fishbone diagram of electrochemical micromachining (ECMM) [19]

will be more effective due to its effective space utilization, and also it has high accuracy and efficacy. ECMM can be operated in maximum applications associated with the micromachining due to its economic efficacy and the achievable high precision [8–11]. The process variables like applied machining voltage (V), duty cycle (%), feed rate (μm) and frequency (Hz) influence the surface roughness of the machined component. These parameters are to be optimized in such a way that the machined surface has an acceptable surface roughness. The surface roughness of this hole is measured by a highly precise instrument with minimum least count and also by a non-contact method such as light interferometry [12–15]. In recent years, a double-pulsed wire electrochemical micromachining is developed to cut profiles on the workpiece electrode like wire electrical discharge machining and also improve the stability in machining [16, 17]. Advanced engineering materials like bulk metallic glasses are also processed using ECMM [18].

2 Experimental Details

2.1 Experimental Set-up

The set-up employed for micro-hole drilling (500 μm diameter) is shown in the Fig. 2. This set-up comprises power supply system, electrolytic system, tool holding arrangement, controller unit, working platform and machining chamber. Experiments were conducted using NaCl (20 gm/l) as an electrolyte. Machining chamber is comprised of a work holding device, an LED light and a blow-off system. Even though there is a provison for the electrolyte flow in the set-up, in order to perform the vibration-less and smooth experimentation (to reduce tool vibration due to electrolyte pressure), die-sinking-type electrochemical machining is performed in this investigation. ECMM provides a smaller inter-electrode gap (IEG) without electrolyte boiling in the gap ranging from 10 to 80 μm which requires limiting the IEG valve across tool and workpiece. Model experiments performed to fix the inter-electrode gap, and it is fixed as 25 μm. The short-circuiting between workpiece and tool has occurred for the IEG which is smaller than the 25 μm. For smaller IEG, i.e. less than 25 μm, there is a chance of short-circuiting which causes defective machined surfaces.

ECMM experimental set-up works with the pulsed power supply of rectangular pulsed shape with a controller monitor connected to it. Since it is a pulsed power supply, pulse on time and pulse off time are the major electrical parameters along with applied current and voltage. The current and voltage indicators are shown in orange and yellow colours when the machining is performed and current is adjusted by the machine automatically based on the machining feed rate and other machining conditions, whereas voltage can be manually changeable. The other important parameter in ECMM is feed rate; it can be varied by using the controller through machine attached monitor and the input is given in the range of μm/s. The work platform is a plastic rectangular vessel having work holding platform with strong

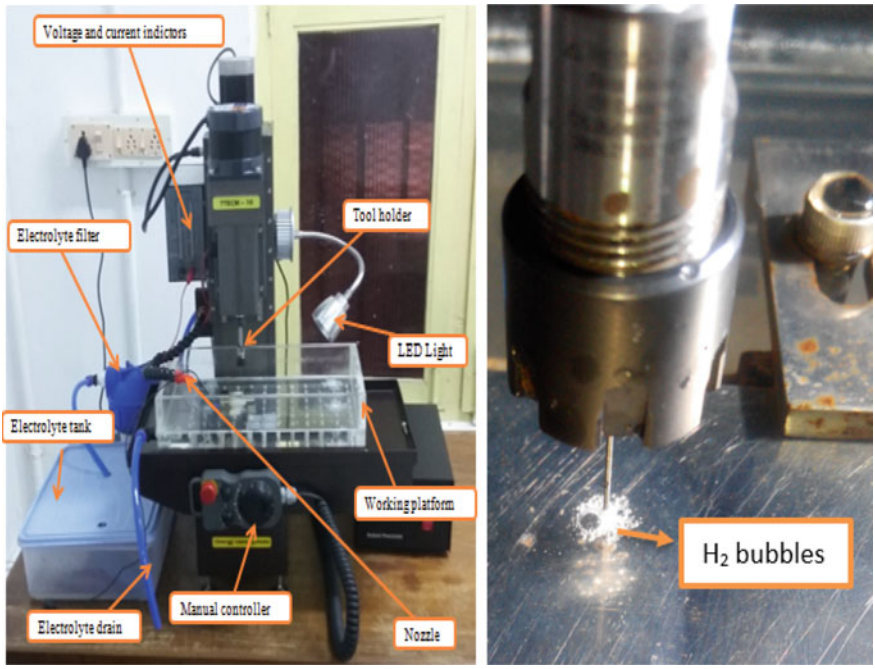

Fig. 2 ECMM experimental set-up and tool holder arrangement

magnets above and below the holder which holds the electrode during the machining without any movement. Along with this, electrolyte flowing system is attached to tank, filter, nozzle and recirculation system. A manual control is provided for giving instructions to the working platform and movement of tool holder in *X-Y-Z* directions.

2.2 Experimental Design

In the current study, an experimental study has been performed to find out the parametric influence on the output responses of the ECMM method. Due to its inherent properties and importance in manufacturing and aerospace industries, the titanium alloy (Ti6Al4V) of 100 mm X 60mm X 0.9mm is selected and employed as workpiece in the current study.

2.2.1 Selecting Factors and Factor Levels

The Taguchi method is an effective technique for designing and conducting experiments in various effective manufacturing systems because of its simplicity and applicability for producing robust designs. Taguchi technique gives the least number of experimental runs to be carried out for yielding optimum results. In order to fix a relation between the input parameters and output responses, an extensive information was collected on machine capability, available limits in the machine parameters along with the previous records and literature surveys. Thus, four variables chosen for experimental design are applied voltage (V), duty cycle (%), feed rate (μm) and frequency (Hz). From the collected data, four levels are selected for each parameter and thus the design is made by the combination of four parameters and four levels. The input parameters and their levels are shown in Table 1. Duty cycle and frequency are determined by using the following formulas:

$$T_{\text{total}} = T_{\text{on}} + T_{\text{off}}$$

$$\text{Duty cycle} = \frac{T_{\text{on}}}{T_{\text{total}}}$$

$$\text{frequency} = \frac{1}{T_{\text{total}}}.$$

2.3 *Machining of Titanium Alloys*

Titanium alloys are known for the better bio—compatibility and having a wide range of applications in the medical field like surgical instruments, bone implants, tooth implants and knee implants, etc. All these mentioned applications are shaped out with the operation of micro machining process for better viability. The micromachining of titanium and titanium alloys particularly in electrochemical micromachining (ECMM) is different when compared with any other commonly used metals. Titanium alloys have a tendency to develop thin tenacious film of oxide when it is exposed

Table 1 Levels and actual values of input parameters in ECMM

S. No.	Input parameter	Level 1	Level 2	Level 3	Level 4
1	Applied voltage (V)	12	14	16	18
2	Duty cycle (%)	20	40	60	80
3	Feed rate (μm/s)	0.3	0.6	0.9	1.2
4	Frequency (Hz)	30	40	50	60

to the surrounding containing oxygen. Because of this developed oxide layer, machining of titanium alloy is very difficult. During electrolysis to dissolute the titanium metal atoms into titanium ions, higher voltages are required when compared to other materials. The authors have performed some trial experiments within the range 5–25 V machining voltage with combination of various machining parameters viz. electrolyte concentration, duty cycle, frequency and tool feed rate. From the data of trial experiments, it has been revealed that the machining can only be possible normally at machining voltages 10–20 V. The selection of suitable electrolyte and its concentration is another deciding factor for machining of titanium alloys. In the present work, the saltwater containing sodium chloride with 20 grams per litre is used. The accuracy and precision of the final machined component in ECMM are highly influenced by the process parameters viz. applied voltage, pulse duty cycle, tool feedrate and frequency. Therefore, in achieving the desired results during machining of titanium alloys proper selection and controlling of these parameters play an important role.

2.3.1 Electrolysis

Electrolysis is the process in which electric current is used to make chemical changes in any electrically conducting substance. In ECMM, workpiece is connected to a positive terminal of power supply and tool is connected to a negative power supply. Electrolyte used in this experimentation (NaCl electrolyte) conducts electricity, and the current is carried by the atoms (group of atoms) of electrolyte not by the electrons. These atoms are going to lose or gain electrons by obtaining either negative or positive charges and also known as ions. The ions having negative charge are attracted by anode, and they moved through the electrolyte in the direction of negative current and named as anions. Similarly, the positively charged ions attracted towards negative electrode (cathode) and these are referred as cations. As the potential difference applied, due to electrolysis the water is dissociated into hydrogen and hydroxide ions and electrolyte dissolved into both sodium ions and chloride ions.

The free electrons are gained by the hydrogen ion to become hydrogen gas and liberated at cathode during machining as shown in Fig. 2. The metal ions at anode are also participated in the chemical reaction to form respective metal hydroxide precipitations. Along with this, sodium hydroxide and metal chlorides also formed since the amount of chlorine and aluminium and vanadium very small amount of these products are resulted. If the pulse off time is very small then the available electrolyte to remove the sludge is very small and it results in improper machining surface. All the chemicals used in the research are shown below (Figs. 3 and 4).

2.3.2 Chemical Reactions

As the applied potential difference reaches breakdown, electrolysis comes into action and the electrolyte dissociates water and NaCl as follows:

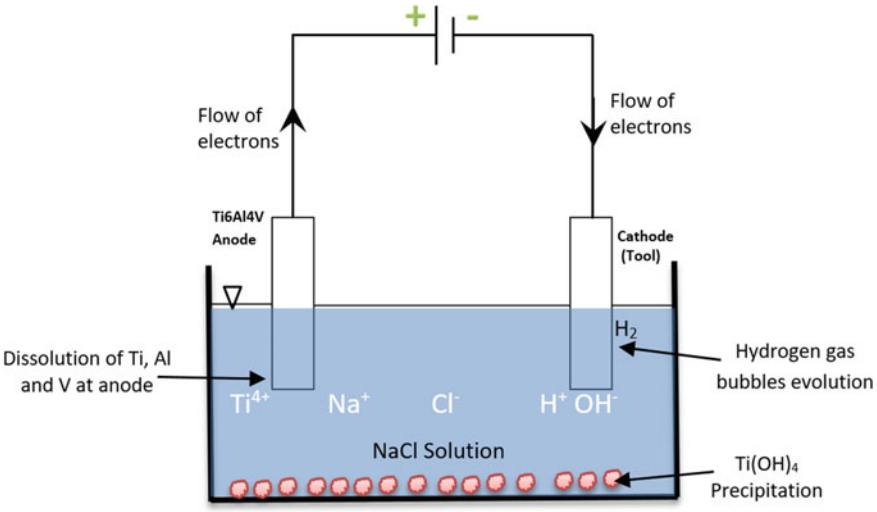

Fig. 3 Electrolysis of titanium alloy with NaCl electrolyte

Fig. 4 NaCl electrolyte before and after machining

$$NaCl \rightarrow Na^+ + Cl^-$$

$$H_2O \rightarrow H^+ + OH^-$$

At anode, the metal atoms become metal ions by losing electrons.
Reactions at anode:

$$Ti \rightarrow Ti^{4+} + 4e^-$$

$$2Al \rightarrow 2Al^{3+} + 6e^{-}$$

$$2V \rightarrow 2V^{5+} + 10e^{-}$$

By gaining the free electrons from anode, hydrogen ions are converted to hydrogen gas and appeared as bubbles.

Reactions at cathode:

$$20H^{+} + 20e^{-} \rightarrow 10H_2 \uparrow$$

The outcome of the electrochemical reaction is that the combination with other ions to precipitate as metal hydroxides and little bit chlorides

$$Ti^{4+} + 4OH^{-} \rightarrow Ti(OH)_4 \downarrow$$

$$Al^{3+} + 3OH^{-} \rightarrow Al(OH)_3 \downarrow$$

$$V^{5+} + 5OH^{-} \rightarrow V(OH)_5 \downarrow$$

$$Ti^{4+} + 4Cl^{-} \rightarrow TiCl_4$$

$$Na^{+} + OH^{-} \rightarrow NaOH$$

Since the percentage of aluminium (Al) and vanadium (V) is very less, the products formed from these elements like $Al(OH)_3$, $V(OH)_5$ are also very small in amount.

2.4 Output Parameters

The output parameters considered for this study are dimensional deviation and surface roughness. Dimensional deviation is measured with the help of vision measuring machine by measuring the diameter of the hole on the topmost surface of the workpiece material. This diameter is calculated by considering 6–8 points on the periphery of the hole, and according to the suggestions, machine covers all the points with a diameter value. Dimensional deviation is determined with the following formula.

$$\text{Dimensional Deviation} = \frac{D_h - D_t}{2}$$

where

D_h Diameter of the hole at top surface of the workpiece;
D_t Diameter of the tool 500 μm.

Surface roughness is measured with non-contact surface roughness tester (Talysurf-CCI). To determine surface roughness value, blind holes are performed with 250 μm as the depth of the hole. The surface roughness tester works with coherence correlation interferometry principle. The white light beam produced by the optical fibre is supplied to the equipment. The white light beam passes through a beam splitter, which splits the beam into two parallel splits. One split of the beam is reflected towards the target sample, while the second passes towards an internal reference mirror. Both beams again combine and give a local interference image; this is directed towards charge-coupled device detector (CCD). The microscope has optical measuring head which is coupled to piezoelectric actuators (PZT). Location of different points on the sample surface is found out using the analysis of mutual temporal coherence of interfering waves, which are applied individually to each surface point. The monitor connected to the equipment generates surface topography. Based on the magnification of the instrument, the number data points to be check is determined [16–19]. The equipment sample reading contains 2D and 3D and advanced 3D views and waviness graphs of surface profiles in pseudo-colours. With the help of surface profile and topography, all surface parameters (R_p, R_v, R_z, R_c, R_a and R_t, etc.) are determined (Figs. 5, 6 and 7).

3 Results

The ECMM experiments are conducted with Tungsten tool of 500 μm as diameter for titanium alloy (Ti6Al4V). In order to achieve proper circularity of machined holes, the anode tool is properly ground. The test job specimen of size 100 mm × 60 mm × 0.9 mm is prepared by using WEDM machine, and the electrolyte used for this experimental work is sodium chloride (NaCl) solution with twenty grams per litre as electrolyte concentration. Inter-electrode gap is also maintained constantly throughout the experiment (Table 2).

It can be seen from the experimental results of Ti6Al4V that the obtained dimensional deviation (DD) ranges from 156 to 477 μm and these values are measured with vision measuring machine (VMS-10). High-dimensional deviation is due to high applied voltage and with the use of non-coating tool (electrode). The results of surface roughness are 0.142–1.260 μm, and these readings are measured using non-contact surface roughness measuring machine (Talysurf-CCI) with the accuracy of < 0.01 nm (Tables 3 and 4).

The main effect plot for dimensional deviation shows that the major contributor for minimum dimensional deviation. From Table 5, it is applied voltage, followed by the feed rate. The increase in the applied voltage increases the current density at the machining zone. Hence, the high current density supported with voltage has

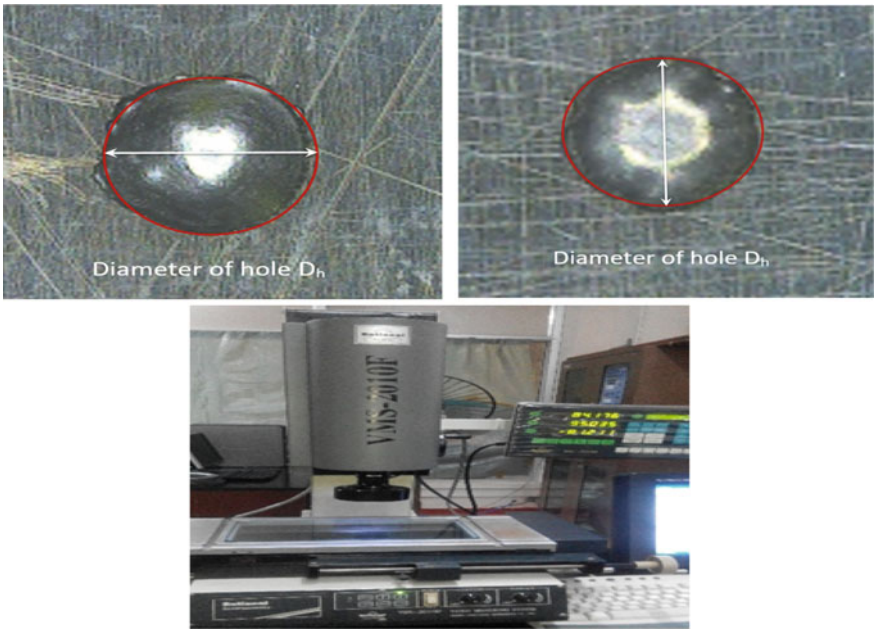

Fig. 5 Measurement of hole diameter (D_h) by vision measuring machine (VMS)

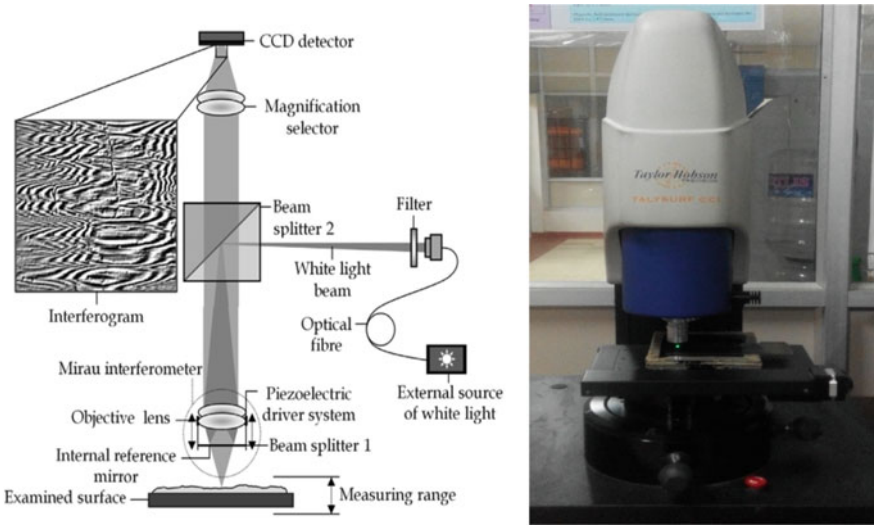

Fig. 6 Working principle of the non-contact surface roughness tester Talysurf-CCI [20]

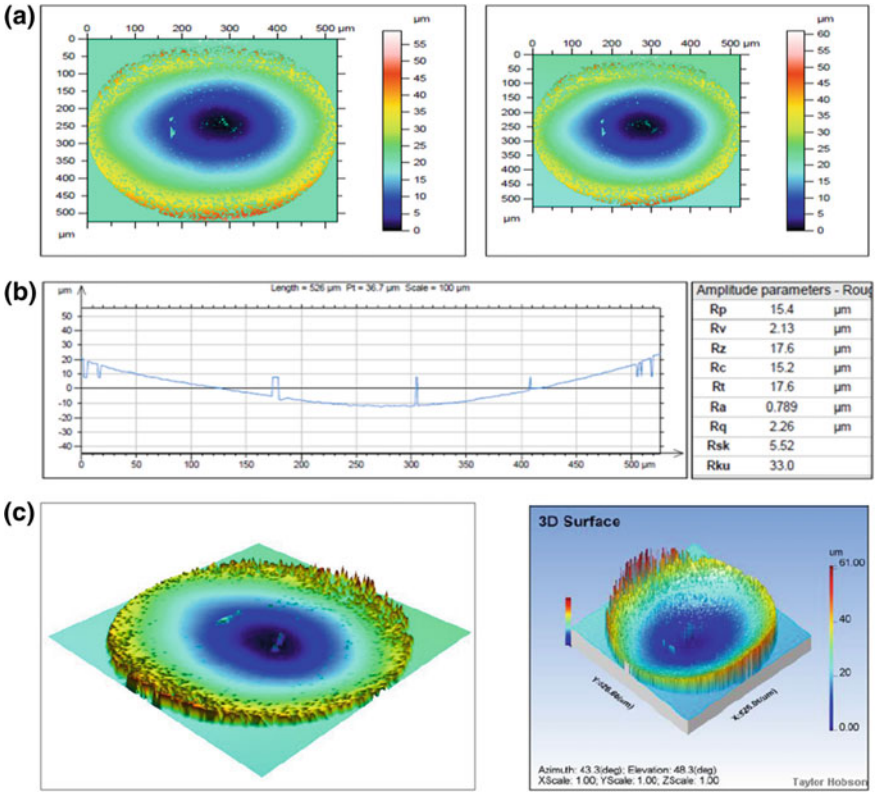

Fig. 7 Sample reading of non-contact surface roughness tester **a** 2D view pseudo-colour surface map, **b** surface profile with sample length and surface parameters and **c** 3D and advanced 3D views of surface topography

emerged as a major contribution to dimensional deviation for Ti6Al4V. Similarly, the main effect plot for surface roughness shows that the major contributor for minimum surface roughness is duty cycle followed by frequency of the pulse from Table 6. Due to increase in duty cycle, pulse on time increases and pulse off time reduces which results in very less time available to remove the machined debris which causes improper surface finish.

3.1 Results of ANOVA

See Tables 5 and 6.

Table 2 Experimental design and output response values

Expt. No.	Applied voltage (V)	Duty cycle (%)	Feed rate (μm/s)	Frequency (Hz)	Dimensional deviation (mm)	Surface roughness (μm)
1	12	20	0.3	30	0.286	0.820
2	12	40	0.6	40	0.201	0.142
3	12	60	0.9	50	0.214	0.615
4	12	80	1.2	60	0.256	0.789
5	14	20	0.6	50	0.190	0.230
6	14	40	0.3	60	0.346	0.208
7	14	60	1.2	30	0.156	0.882
8	4	80	0.9	40	0.230	0.775
9	16	20	0.9	60	0.225	0.176
10	16	40	1.2	50	0.253	0.834
11	16	60	0.3	40	0.366	0.143
12	16	80	0.6	30	0.298	0.461
13	18	20	1.2	40	0.432	0.215
14	18	40	0.9	30	0.295	0.155
15	18	60	0.6	60	0.390	0.198
16	18	80	0.3	50	0.477	1.260

Table 3 Response table for S/N ratios—dimensional deviation

Level	Applied voltage (V)	Duty cycle (%)	Feed rate (μm/s)	Frequency (Hz)
1	12.509	11.386	8.813	12.032
2	13.137	11.424	11.764	10.681
3	11.035	11.610	12.429	11.546
4	8.126	10.386	11.800	10.547
Delta	5.011	1.223	3.616	1.485
Rank	**1**	**4**	**2**	**3**

Table 4 Response table for S/N ratios—surface roughness

Level	Applied voltage (V)	Duty cycle (%)	Feed rate (μm/s)	Frequency (Hz)
1	6.240	10.733	7.562	6.433
2	7.427	12.091	12.628	12.353
3	10.071	9.068	9.430	4.139
4	10.401	2.248	4.519	11.213
Delta	4.161	9.843	8.109	8.214
Rank	**4**	**1**	**3**	**2**

Table 5 ANOVA for dimensional deviation

Source	DF	Adj. SS	Adj. MS	*F*-value	*P*-value	% influence
Applied voltage (V)	3	0.695	0.231	9.62	0.048	60.35
Duty cycle (%)	3	0.039	0.013	0.54	0.686	3.39
Feed rate (μm/s)	3	0.359	0.119	4.97	0.110	31.18
Frequency (Hz)	3	0.058	0.019	0.81	0.566	5.08
Error	3	0.072	0.024			
Total	15	1.223				

Table 6 ANOVA for surface roughness

Source	DF	Adj. SS	Adj. MS	*F*-value	*P*-value	% influence
Applied voltage (V)	3	0.064	0.021	0.24	0.863	4.98
Duty cycle (%)	3	0.485	0.162	1.84	0.315	38.18
Feed rate (μm/s)	3	0.344	0.114	1.30	0.417	26.97
Frequency (Hz)	3	0.380	0.127	1.44	0.386	29.87
Error	3	0.234	0.088			
Total	15	1.537				

3.2 Effect of Process Parameter on Dimensional Deviation

As shown in Fig. 8, the influence of the process parameters on dimensional deviation (DD) of ECMM process are plotted in main effect plots. From Fig. 8, it is clear that all the four parameters have considerable amount of effect on DD. It has been observed that applied voltage has huge impact on the dimensional deviation compared to other input parameters. Because, as the applied voltage increases, the

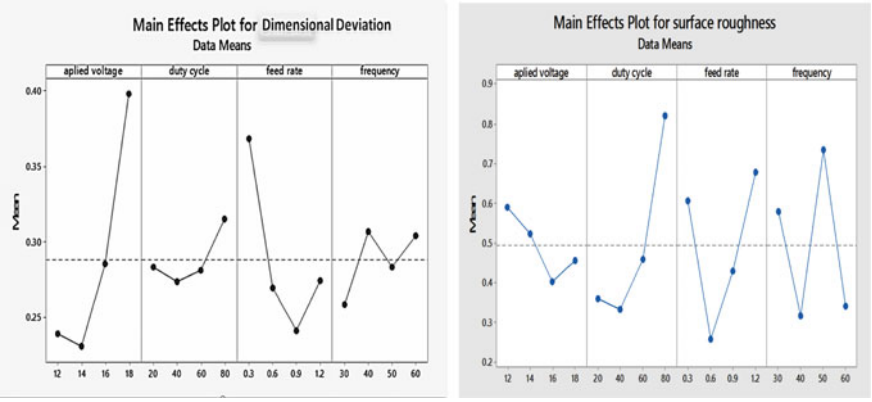

Fig. 8 Main effect plots for means of dimensional deviation and surface roughness

electrolysis process gains more momentum towards machining and the peripheral surface of the tool also comes into machining which results in increase of hole diameter that in turn increase the dimensional deviation. As the voltage becomes very low, the energy required to break the titanium bonds is very less, so machining cannot be initiated. Hence, the applied voltage should be moderate for good dimensional accuracy of micro-holes in ECMM. Second variable that affects the dimensional deviation is feed rate, which can be observed from the main effect plots. As the feed rate increases, the amount of material to be removed from the titanium alloy increases with time. This will lead to rapid removal of the material and leads to poor dimensional accuracy. Duty cycle and frequency are not affecting this output response significantly.

3.3 Effect of Process Parameters on Surface Roughness (SR)

The influence of process parameters on surface roughness of titanium alloy (Ti6Al4V) are plotted in main effect plot and is shown in Fig. 8. From the figure, it has been clearly understood that duty cycle has more impact on SR. It has been cleared that SR increases with increase in duty cycle; this causes increase in pulse on time and decrease in pulse off time. Reducing pulse of time causes less time to remove the debris; hence, the improper surface finish is obtained. The pulse on time also increases material removal rate which resulted in higher surface roughness. SR first decreases and then increases by increasing tool feed rate (μm/s). This is due to increasing feed rate up to optimum value, the results of SR are good, because fair amount of material is removed. Beyond this rapid removal causes irregular surfaces in the machining zone. Also, the feed rate influences the current density which causes the stray current effect significantly. Frequency is related to pulse on time and off time and depends on duty cycle and total time values. Hence, it has considerable effect on surface roughness based on experimental design values of pulse parameters.

4 Conclusions

The current investigation focuses on the influence of process parameters of ECCM on dimensional deviation and surface roughness. Producing micro-holes on titanium-based alloy using ECMM process requires more voltage compared to commonly used metals and its alloys. The colour of the electrolyte is changed to yellow after machining due to titanium hydroxide [Ti $(OH)_4$] and titanium chloride. Since the non-coated tool electrode is used, at higher voltage values the peripheral surface of the microtool comes in action during machining resulted in attaining the higher dimensional deviation values higher applied voltages. Non-contact surface roughness tester given the most accurate results, since the least count of the machine is in the range of less than 0.01 nm. From the results of ANOVA, it is concluded that applied voltage (60.35) has

more influence on dimensional deviation and duty cycle (38.18) has more influence on surface roughness.

Acknowledgements The authors would like to express gratitude towards **DST-FIST sponsored laboratories** of the Department of Manufacturing Engineering, Anna University, Chennai, for giving permission to use non-contact surface roughness testing machine facilities.

References

1. Geethapriyan T, Kalaichelvan K, Muthuramalingam T (2016) Multi performance optimization of electrochemical micro-machining process surface related parameters on machining Inconel 718 using Taguchi-grey relational analysis. Metallurgia Italiana 108(4):13–19
2. Bhattacharyya B, Malapati M, Munda J (2005) Experimental study on electrochemical micro-machining. J Mater Process Technol 169(3):485–492. https://doi.org/10.1016/j.jmatprotec.2005.04.074
3. Rama Rao S, Sravan CRM, Pandu Ranga V, Padmanabhan G (2009) Fuzzy logic-based forward modeling of electro chemical machining process. In: Proceedings on 2009 world congress on nature and biologically inspired computing, NABIC 2009, pp 1431–1435
4. Kalaimathi M, Venkatachalam G.S (2013) Experimental investigation on the electrochemical machining characteristics of monel 400 alloys and optimization of process parameters. Jordon J Mech Ind Eng 8(3):143–151. No. 3, ISSN 1995-6665
5. Dharmalingam S, Marimuthu P, Raja K (2017) Experimental investigation on electrochemical micro machining of Al-10%wt SiCp based on Taguchi design of experiments. IRME 7 (2014)
6. Sathiyamoorthy V, Sekar T, Suresh P, Vijayan R, Elango N (2015) Optimization of processing parameters in electrochemical machining of AISI 202 using response surface methodology. J Eng Sci Technol 10(6):780–789
7. Bhattacharyya B, Doloi B, Sridhar PS (2001) Electrochemical micro-machining: new possibilities for micro-manufacturing. J Mater Process Technol 113(1–3):301–305. https://doi.org/10.1016/S0924-0136(01)00629-X
8. Bhattacharyya B, Mitra S, Boro AK (2002) Electrochemical machining: new possibilities for micromachining. Robot Comput-Integr Manuf 18(3–4):283–289. https://doi.org/10.1016/S0736-5845(02)00019-4
9. Bhattacharyya B, Munda J (2003) Experimental investigation into electrochemical micromachining (EMM) process. J Mater Process Technol 140:287–291
10. Rajurkar KP, Zhu D, McGeough JA, Kozak J, De Silva A (1999) New developments in electro-chemical machining. CIRP Ann Manuf Technol 48(2):567–579. https://doi.org/10.1016/S0007-8506(07)63235-1
11. Senthil Kumar KL, Sivasubramanian R, Kalaiselvan K (2009) Selection of optimum parameters in non-conventional machining of metal matrix composite. Portugaliae Electrochimica Acta 27(4):477–486. https://doi.org/10.4152/pea.200904477
12. Sekar T, Marappan R (2008) Experimental investigations into the influencing parameters of electrochemical machining of AISI 202. J Adv Manuf Syst 07(02):337–343. https://doi.org/10.1177/0218492313489696
13. Kumar J, Khamba JS, Mohapatra SK (2008) An investigation into the machining characteristics of titanium using ultrasonic machining. Int J Mach Mach Mater 3(1/2):143. https://doi.org/10.1504/IJMMM.2008.017631
14. Dhobe SD, Doloi B, Bhattacharyya B (2011) Surface characteristics of ECMed titanium work samples for biomedical applications. Int J Adv Manuf Technol 55(1–4):177–188. https://doi.org/10.1007/s00170-010-3040-5

15. Blunt RT (2006). White Light Interferometry–a production worthy technique for measuring surface roughness on semiconductor wafers. Proc of CS MANTECH Conf 44(0):59–62. https://doi.org/10.1017/CBO9781107256514
16. Gao C, Qu N, He H, Meng L (2019) Double-pulsed wire electrochemical micro-machining of type-304 stainless steel. J Mater Process Technol 266: 381–387 (2019). https://doi.org/10.1016/j.jmatprotec.2018.11.018
17. Cole KM, Kirk DW, Singh CV, Thorpe SJ (2017) Optimizing electrochemical micromachining parameters for Zr-based bulk metallic glass. J Manuf Process 25:227–234. https://doi.org/10.1016/j.jmapro.2016.11.015
18. Meng L, Zeng Y, Zhu D (2017) Investigation on wire electrochemical micro machining of Ni-based metallic glass. Electrochim Acta 233:274–283. https://doi.org/10.1016/j.electacta.2017.03.045
19. A lecture notes on Micro Machining Processes by V.K. Jain, Mechanical Engineering Department, I.I.T Kanpur.
20. Kaplonek W, Lukianowicz C (2012) Coherence correlation interferometry in surface topography measurements. Recent interferometry applications in topography and astronomy, Ivan Padron, IntechOpen. https://doi.org/10.5772/35059

Transmissibility Along Human Segments When Exposed to Vibration

Arvinder Singh, Harkirat Singh, Ishbir Singh and Sachin Kalsi

Abstract Human body suffers from maximum effect of vibration while travelling and driving. So, it becomes important to study the response of human body when excitations are transferred while travelling. A realistic Indian male human body has converted into 3-D CAD model using anthropometric data available in existing literature. Transmissibility is from seat to lower torso, seat to upper torso and seat to head in frequency range of 0–20 Hz using finite element method. It has been found that maximum effect of vibration is noticeable at lower torso and head as compared to other human body segments. The results obtained using this study will be useful in designing seats and other components of tractor.

Keywords FEM · Indian human subject · Transmissibility

1 Introduction

With the change in lifestyle and technology, people have become more dominated towards their health and want to live a comfortable and luxurious life. Human body suffers from whole-body vibration (WBV) generated from many sources, i.e. while travelling, driving, working on machines, etc. WBV induces ill-effects like headache, lower back pain, spinal problem, motion sickness, etc. Because of the adverse effect on human body, it becomes important to study the effect of vibration and minimize its effects. Components for human use are designed to reduce the effects of vibration and should be beyond resonant frequency of human body.

To overcome the effects of vibration and to increase comfort level of human body; most of the researchers have worked in this area using different human models and methods. Kitazaki and Griffin [1] developed a 2-D human model using FEM technique by considering beam, spring, mass damper system, in which the six modes were founded with 5 Hz of primary and 8 Hz of secondary frequency. Mansfield and Griffin [2] conducted an experiment on twelve human subjects to check the

A. Singh · H. Singh · I. Singh (✉) · S. Kalsi
Chandigarh University, Mohali 140413, India
e-mail: ishbir@rediffmail.com

H. Kumar and P. K. Jain (eds.), *Recent Advances in Mechanical Engineering*,
Lecture Notes in Mechanical Engineering,
https://doi.org/10.1007/978-981-15-1071-7_19

nonlinearity of apparent mass and transmissibility when exposed to WBV. Singh et al. [3] conducted experiments to study the effect of vertical harmonic vibration on human body while sitting posture at different inclination angles of 0°, 15° and 30°. The amplitude accelerations were 0.5, 1 and 1.5 m/s^2 and the frequencies were 5, 8, 12, 16 and 20 Hz. Nigam and Malik [4] presented a human model with 15 degree of freedom spring-mass damper with 50th percentile anthropometric data of 76 kg mass. Adam and Jalil [5] calculated the vertical seat suspension transmissibility and seat effective amplitude transmissibility when a seated human subject is exposed to WBV and the results were found to be 2–3 Hz.

Liang and Chiang [6] developed the 14 degree of freedom human model recommended for studying the vertical body vibration biodynamic response in automotive seating posture. Nag et al. [7] performed a test on fifteen human subjects sitting on a simulated to analyze the distribution of body weight to the component of the seat. Singh et al. [8] developed a lumped parameter model from 54 kg Indian male subject in seated conditions without backrest support with 50th percentile anthropometric data. Singh et al. [9] conducted an experiment on WBV among Indian tractor driver and it was found that the z-axis was more dominant and vibration dose value was exceeding the limits given by ISO-2631-1. Rakhejaet al. [10] observed dynamics response of human body in seating posture with and without backrest inclinations and declination. Zhang et al. [11] conducted an experiment with 17 degree of freedom human subject model with included backrest and interaction between feet and ground.

Xueyanet al. [12] study found that the upper arm resonance frequency was 7–12 Hz, back and neck 6–7 Hz and shoulders were observed with the range of 7–9 Hz. Dewanganet al. [13] performed an experiment on male and female subject to find the transmissibility from seat to head in vertical and fore-and-aft to study the dynamic behaviour, magnitude of vertical vibrations were taken as 0.2, 0.5 and 0.75 m/s^2 and the frequency range was 0.5–20 Hz observed in all excitations. Shibata and Maeda [14] observed that in the frequency range of 1–20 Hz, backrest inclination between 10 and 30° was found to be the most effective in order to prevent the back pain disorders. Marchettiet al. [15] used a laser vibrometer to measure the vibration and the resonant frequency; it was observed around 8 Hz in the arms while using a single axis electrical shaker. Zimmermann and Cook [16] calculated the transmissibility in head and pelvic motion which were found to be greater in posterior orientation at below the frequency of 6 Hz, and above 6 Hz the acceleration transmissibility was greater in head and trunk in anterior position.

Basri and Griffin [17] performed an experiment with the acceleration value ranging from 0.2 to 2 m/s^2 with the frequency range of 1–20 Hz. It is found that the frequency of 8 Hz was more dominant in all posture positions. Kim et al. [18] developed a biomechanical model in sitting posture and resonance frequencies were found to be 5.35 and 8.34 Hz in whole body when exposed to random vibration. Cho and Yoon [19] conducted an experiment for evaluating the seating comfort quality using a biomechanical human seated subject model with backrest position having a nine degree of freedom. Shakhlavi et al. [20] developed a six degree of human seated position model without backrest and biomechanical response at all body segments

were calculated at different road conditions. Yoshimura et al. [21] developed a ten degree of freedom model using multi-body dynamics to calculate the transmissibility in human body.

From existing literature, it has been found that maximum work has been performed on European and US anthropometric data using experimental approach. Very less work on Indian anthropometric data has been reported in the literature. Taking this research gap into consideration, an attempt has been made in the current study to analyze the effects of WBV on Indian human subject.

2 Methodology

In the present study, the response of Indian human subject with 76 kg mass has been evaluated using FEM. Human body material properties have been modelled into 3-D CAD model using 95th percentile anthropometric data of Indian male human population available in existing literature [21]. Response of human subject has been evaluated using FEM in terms of transmissibility from seat to different parts of human body at different frequencies of vibration.

2.1 CAD Model of Human Subject

To model a 3-D CAD model of human subject using Solid Works 2014, physical dimensions have been taken from 95th percentile anthropometric data of Indian male with 76 kg mass. As shown in Fig. 1a, a human subject is sitting on a vehicle seat and Fig. 1b shows a CAD model of human subject in same posture with seat as it can be replaced with fixed support in FEM analysis.

2.2 Material Properties and Meshing

The material of human subject has been taken to be isotropic and homogenous in nature and the properties are considered to be as E (Modulus of elasticity) = 13 MN/m^2 [8], density of 1.062×10^3 kg/m^3 [8] and value of Poisson's ratio as 0.3 [8]. Automatic mesh technique has been used to create the mesh on the CAD human model in FEM-based software ANSYS 16.0 as shown in Fig. 2. The reason to use these elements is because of complexity of geometry and at this size of element, saturation of results was attained. The nodes generated during meshing are 20,588 and elements are 11,048. Due to complex shape of geometry and integration of body segments with seat model, i.e. buttock to seat face area, tetrahedral meshing has been used. The values of meshing quality parameters, i.e. Jacobian, skewness, volumetric skewness satisfies with limits as defined in existing literature [22].

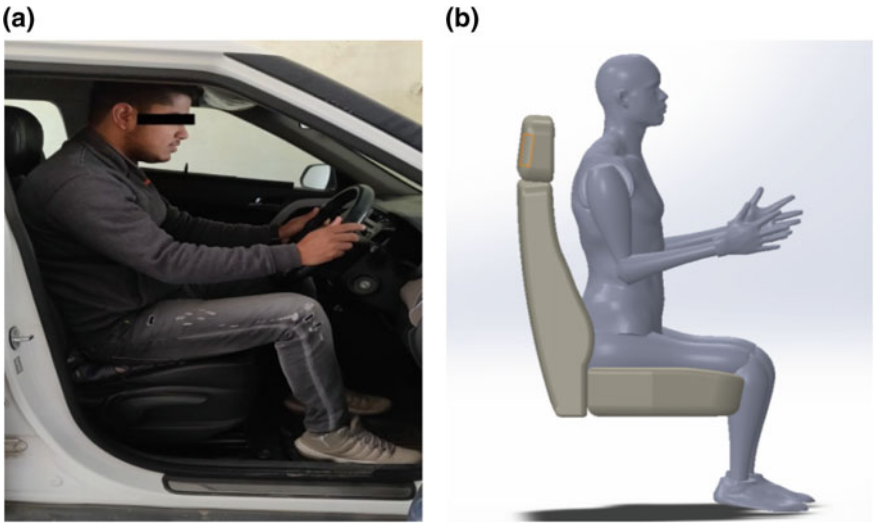

Fig. 1 **a** Realistic model of human body; **b** 3-D CAD model of human subject

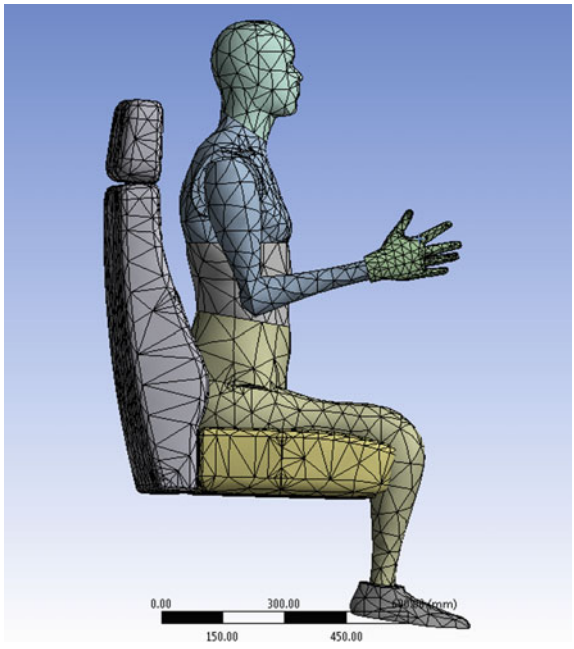

Fig. 2 Meshed model of human subject

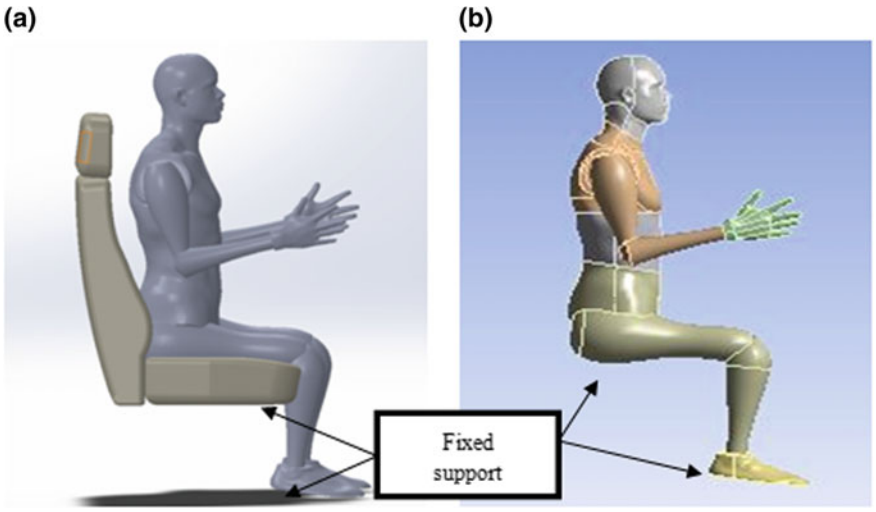

Fig. 3 Boundary conditions of driving posture; **a** With Seat; **b** Seat replaced with fixed support

2.3 Boundary Conditions

Boundary conditions are applied to calculate the results of human subject model, where the feet and buttock are assumed to be fixed in seated position as shown in Fig. 3.

The excitation has been given to seat from the base at different frequencies 0–20 Hz. The response or effect of vibration at different parts of human subject has been calculated in terms of transmissibility.

3 Results and Discussions

A case of Indian male human subject with an input as sinusoidal excitation has been considered. An acceleration of 1 m/s^2 [20] has been applied at driver seat and the base along with boundary conditions.

3.1 Seat to Head Transmissibility in Vertical Direction

An acceleration of 1 m/s^2 has been applied at the base of driver seat in range of 0–20 Hz [20]. It has been found from graph as shown in Fig. 4 that maximum acceleration travels at head when a value of frequency lies in a range of 2–4 Hz. Shakhlavi et al. [20] illustrated a study using analytical approach and found that

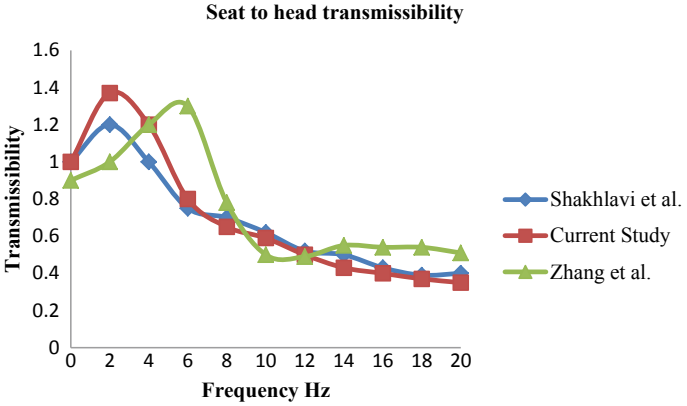

Fig. 4 Seat to head transmissibility

the maximum transmissibility was 1.2 from seat to head at frequency of 2 Hz. At frequency of 3 Hz, seat to head transmissibility was found as 1.4. Zhang et al. [11] calculated transmissibility in term of apparent mass along primary resonance frequency. Primary peak has been observed between frequency ranges of 5–7 Hz and secondary peak has been observed between frequency ranges of 10–12 Hz. The reason of secondary peak may be observed due to different inclination angles of seat and due to different damping ratio has been taken during the experiment.

3.2 Seat to Upper Torso Transmissibility in Vertical Direction

It becomes important to find the effect of vibration at other parts apart from head for designing a seat using ergonomics and its material properties. In this study, transmissibility was found to be 1.7 from seat to upper torso at frequency of 2 Hz as shown in Fig. 5. With the increase in frequency at acceleration amplitude of 1 m/s^2, transmissibility decreases. Two significant peaks were observed at 2 Hz and 10 Hz, respectively. The results obtained using FEM found to be in validation with existing literature [20].

3.3 Seat to Lower Torso Transmissibility in Vertical Direction

Taking human health into consideration, it is also important to find out the effect of vibration in lower torso which is shown in Fig. 6. It has been found that maximum transmissibility from seat to lower torso was 1.8 Hz at a frequency of 3 Hz. Shakhlavi et al. [20] found transmissibility with a value of 1.5 at frequency of 3 Hz.

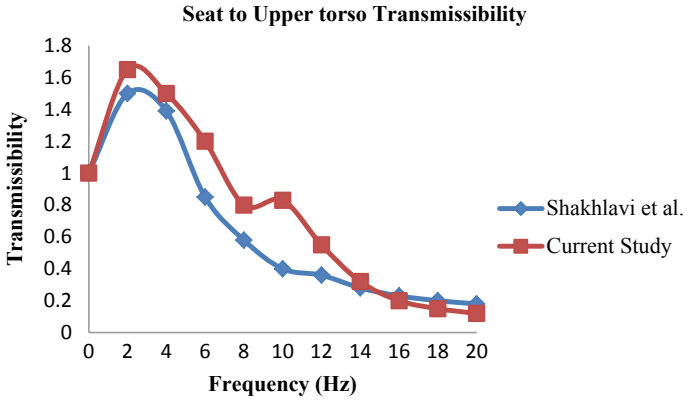

Fig. 5 Seat to upper torso transmissibility

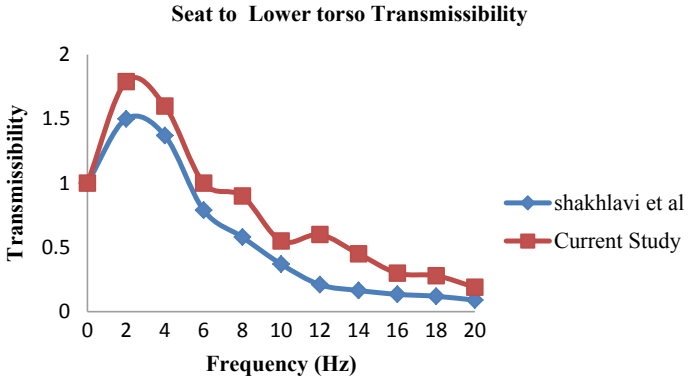

Fig. 6 Seat to lower torso transmissibility

4 Conclusion

A complex and dynamic human body has been modelled to 3-D CAD model using physical dimensions available in existing literature [21]. 95th percentile anthropometric data of Indian human population has been taken into consideration in CAD modelling. In this study, acceleration value of 1 m/s^2 has been applied to the 3-D CAD model in sitting posture with the frequency range of 0–20 Hz. Transmissibility from seat to different parts of human subject, i.e. head, upper and lower torso has been calculated using FEM approach. It has been found that the maximum effect of vibration was at head as compared to other parts of human body. The frequency range of 2–4 Hz has been found to be dominant in terms of transmissibility values. The results obtained in the current study are in validation with existing literature.

References

1. Kitazaki S, Griffin MJ (1998) Resonance behaviour of the seated human body and effects of posture. J Biomech 31:143–149
2. Mansfield NJ, Griffin MJ (2000) Non-linearities in apparent mass and transmissibility during exposure to whole-body vibration. J Biomech 27:933–944
3. Singh I, Nigam SP, Saran VH (2014) Modal analysis of human body vibration model for Indian subjects under sitting posture. Ergonomics 58:1117–1132
4. Nigam SP, Malik M (1987) A study on a vibratory model of a human body. J Biomech Eng 109:148–153
5. Aisyahadam S, Abduljalil NA (2017) Vertical suspension seat transmissibility and seat values for seated person exposed to whole-body vibration in agricultural tractor preliminary study. Procedia Eng 170: 435–442
6. Liang CC, Chiang CF (2006) A study on biodynamic model of seated human subject exposed to vertical vibration. Int J Industrial Ergonomics 36:869–890
7. Nag PK, Pal S, Kotadiya SM, Nag A, Gosai K (2008) Human-seat interface analysis of upper and lower body weight distribution. Int J Ind Ergonomics 38: 539–545
8. Singh I, Nigam SP, Saran VH (2016) Effect of backrest inclination on sitting subjects exposed to WBV. Procedia Technol 23:76–83
9. Singh A, Singh LP, Singh S, Singh H, Parkash C (2018) Investigation of occupational whole-body vibration exposure among indian tractor driver. Int J Human Factors Ergonomics 5:151–165
10. Rakheja S, Dong RG, Patra S, Boileau PE, Marcotte P, Warren C (2010) Biodynamics of the human body under whole body vibration: synthesis of the reported data. Int J Ind Ergonomics 40:710–732
11. Zhang X, Qiu Y, Griffin MJ (2015) Developing a simplified finite element model of a car seat with occupant for predicting vibration transmissibility in the vertical direction. Ergonomics 58:1220–31
12. Xu XS, Dong RG, Welcome DE, Warren CW, McDowell TZ, Wu J (2010) Vibration transmitted from human hands to upper arm, shoulder, back, neck and head. Int J Ind Ergonomic 1–12
13. Subashi GHMJ, Matsumoto Y, Griffin MJ (2008) Modelling resonances of the standing body exposed to vertical whole body vibration: effects of posture. J Sound Vibr 317:400–418
14. Shibata N, Maeda S (2010) Determination of backrest inclination based on biodynamic response study for prevention of low back pain. J. Med. Eng. Phys. 32:577–583
15. Marchetti E, Sisto R, Lunghi A, Sacco F, Sanjust F, Giovanni RD, Botti T, Morgia F, Tirabasso A (2017) An investigation on the vibration transmissibility of the human elbow subjected to hand-transmitted vibration. Int J Ind Ergonomics 62:82–89
16. Zimmermann CL, Cook TM (1997) Effect of vibration frequency and postal changes on human response to seated whole-body vibration exposure. Int Arch Occup Environ Health 69:165–179
17. Basri B, Griffin MJ (2013) Predicting discomfort from whole-body vertical vibration when sitting with an inclined backrest. Appl Ergonomics 44:423–434 (2013)
18. Kim TH, Kim YT, Yoon Y.S (2005) Development of a biomechanical model of the human body in a sitting posture with vibration transmissibility in the vertical direction. Int J Ind Ergonomics 35:817–829
19. Cho Y, Yoon Y.S (2001) Biomechanical model of human on seat with backrest for evaluating ride quality. Int J Ind Ergonomics 27:331–345
20. Shakhlavi SJ, Marzbanzard J, Tavoosl V (2018) Various vehicle speeds and road profile effects on transmitted accelerations analysis to human body segments using vehicle and biomechanical models. Cogent Eng 5:1–17
21. Yoshimura T, Nakai K, Tamaoki G (2005) Multi body dynamics modelling of seated human body under exposure of whole body vibration. J Ind Health 43:441–447
22. Chakrabarti D (1997) Indian anthropometric dimensions: for ergonomic design practice. National Institute of Design, Ahmedabad

A Comprehensive Review on Microfluidics Technology and its Applications

Su. Venkatesan, J. Jerald, P. Asokan and R. Prabakaran

Abstract In modern fields of science, the urge for analysing the characterization of fluid flow as well as fabricating micro level devices to facilitate fluid flow is increasing noticeably. The technology that provides detailed information about the aforesaid concepts is referred to as microfluidics. Microfluidics, in substance, considers the flow in the microchannels. It proved its mettle exclusively in the field of medical diagnostics. In this paper, the prerequisites such as molecular analysis, biodefence, molecular biology and microelectronics which emphasized the need for microfluidic technology are reported, and the microfluidics technology is reviewed in view of materials used fabrication methodologies and applications. This review article finally intends to look out for the alternative material such as biocompatible metal rather than plastics, to have a better production rate. In recent times, the research works on microfluidics are increasing significantly, and this article will be useful for future research work on microfluidics area.

Keywords Biocompatible · Characterization · Microchannels · Microfluidics · Plastics

Su. Venkatesan (✉) · J. Jerald · P. Asokan · R. Prabakaran
Department of Production Engineering, National Institute of Technology Tiruchirappalli, Tiruchirappalli 620015, India
e-mail: venkatesansu90@gmail.com

J. Jerald
e-mail: jerald@nitt.edu

P. Asokan
e-mail: asokan@nitt.edu

R. Prabakaran
e-mail: rpraba@nitt.edu

H. Kumar and P. K. Jain (eds.), *Recent Advances in Mechanical Engineering*,
Lecture Notes in Mechanical Engineering,
https://doi.org/10.1007/978-981-15-1071-7_20

1 Introduction

Microfluidics considers the migration of fluids in prototype kind alike featuring micro dimensional parts [1]. Initially, Microfluidics defined pertaining to the principles involving the movement of small quantities of fluids through chambers having sub-millimetre dimensions but later the term microfluidics defined often in association with the lab on a chip (LoC) device or micro total analysis systems (μ-TAS) [2]. Lab on chip refers to integrating various aspects of laboratory tests involving extracting a clear-cut quantity of chemical product, sample transportation, blending with reagents, etc. on a single system of the minimal area [3]. In 1990, the field-portable microfluidic systems intended to act as spotters for biological and chemical threats were developed as a preventive criterion with assistance from the defence advanced research projects agency (DARPA) of the US Department [4]. Microfluidics proved its competence astonishingly by alleviating the time required in the field of estrangement and espial of malfunctioning cells from onerous hours to tidy minutes and probably to seconds too [5]. The might of the microfluidics field exists at the interaction between the medicinal industry, biotechnology, micro-electro-mechanical systems, and chemistry [6]. A microfluidic device, with the updated design capable of detecting C-reactive protein (CRP) at very minute quantities, such that five times lower than the typical microfluidic chip without rugged channel wall [7]. Microfluidics enabled cell culture methods to exhibit numerous innate leverages than typical cell culture methods and also furnish adaptable ways to recreate on par in vivo-like extracellular ambiance, to have sensible cell-based drug research [8]. Utilization of microfluidic technology in cell separation results in considerable curtailment of reagents and samples required and also enables in avoiding surplus extraction of blood from the patients. Microfluidics also offers a high level of portability not only in terms of cell separation but also for diagnosing diseases at the doorstep of patients without compromising the desired accuracy and sensitivity [9]. The progression of the electronics field with microfluidic technologies leads to the generation of new domain microfluidic electronics, and in specific the integration of micro antenna as well as the necessary electronic circuits onto a PDMS microfluidic substrate elevated the microfluidic electronics domain to new heights in wirelessly sensing large strains over areas of 100 cm^2. Further, this technology is widened by utilization in the form of straps to assess the fitness [10]. The development of microfluidic devices to observe single cell electrical and mechanical characteristics resulted in a high level of fidelity, for differentiating normal cells from their faulty counterparts [11]. The microfluidic approach is utilized in chemistry laboratories for its nature of consuming very low volume material. This approach safeguards students from precarious bases and acids and also cuts down the duration of the experiment [12]. Microfluidic paper–based device, due to its' nominal cost and easier accessibility, plays an important role in numerous epidemiology studies and different analytical measurements [13]. The measured data can be relayed wirelessly to anywhere in the world, leading to a contemporary level of unified medical diagnostics [14]. Advancements in 3D printing technology facilitate concatenation of investigative tools onto the microfluidic

devices, leading to assist sample creation and even chromatographic estrangements. Also, the successful optimization of spray ionization on the 3D microfluidic chips can be routed to fabricate electrophoresis chips, a potential tool for bio-analytical applications [15]. Microfluidic chips concatenated with electrode setups placed over the silicon or glass substrate is utilized to monitor the epithelial cell growth and this technology proves fruitful for biomedical diagnostic applications [16]. The novel approach of electronics instilled in microfluidic paper-based analytical devices is employed to perceptibly measure the level of concentrations of the micronutrients, and these devices can act as efficient point-of-care devices [17]. The concept of blending microfluidics with microelectronics existed since many years, but the recent idea of concatenating magneto resistive sensor with microfluidic chips gained significance owing to its indispensable contribution in the bio-medicinal arena, particularly in the field of neural sciences for measurement of neural synaptic activity [18]. Efforts made to achieve the status of a point-of-need application for microfluidic technology by utilizing capillary action for fluid flow instead of intricate external pumps [19]. Analysis of cells at the single entity level needs special attention to avoid the heterogeneity characteristics of cells. Such analytical techniques are carried out by the development of microfluidic systems that can incarcerate single entities in limited reaction volumes; examples of such systems include droplet microfluidic systems and microchamber-based microfluidic systems [20]. 3D-printed microfluidic devices had a wide range of materials and intricate designs in their repertoire. Such capabilities push them to assist in the exploration of the material science domain for analysing wider range of materials [21]. The generation of paper-based microfluidics leads to the significant development of almost obviating the pumps required in a microfluidic system and this technology with fine tuning can be potentially the tipping point in the field of point-of-care (POC) diagnostics [22]. The purpose of this review paper is to highlight the bottleneck of not trying enough metallic materials as compared to polymers in the field of microfluidics and as well as not expanding the fabrication strategies to full commercialization rather got inclined with photolithographic fabrication techniques predominantly. Moreover, this review paper also intended to showcase the fact that the applications of microfluidics technology are developing monotonously towards biomedical applications, and this could be a matter of thought to utilize the microfluidic technology in different engineering streams. The field of microfluidics cannot be contained only in the diagnostic oriented applications rather it travels across multi-domain.

2 Materials Employed in Microfluidics

In the initial stages, silicon and glass were considered as the suitable materials for microfluidics technology but later when analysing biological samples in water, these materials were found to be inappropriate. When the field of microelectronics emerged, steel along with glass and silicon again captured the importance due to the requirement of the rigid walls of the microchannels [4]. Rolland et al. [23] reported

that utilization of photocurable perfluoropolyether (PFPE) based elastomer, to fabricate a microfluidic device, exhibited substantial defiance against organic solvents. Vulto et al. [24] identified the importance of dry film resist (Ordyl SY300/550) over both research and industrial applications, and the author attributed this importance to factors of low cost and small number of processing steps; the author also emphasized the dry film resist participation in the creation of hybrid chips with responsive elements in both top and bottom substrates. Heng et al. [25] pointed out that the porous nature of polymethyl methacrylate (PMMA) abbreviated the defilement created by biomolecule adsorption, and also stated that the low-cost criterion of PMMA when merged with excimer laser micromachining method, would sparkle the interest in the field of throwaway microfluidic biochips. Salk et al. [26] discussed the utilization of the powdered form of metal along with binders to create a microfluidic structure alike photoreactor with the help of photocatalytically active TiO_2 coating, applied through dip coating. The author used the aforementioned photoreactor for water purification. Grimes et al. [27] identified a technology to create intransigent moulds by initially laser imprinting the desired features onto the substrate material (shrinky dinks the children's toy) and subsequently exposing the substrate material to oven for heating. The author claimed that this technology favoured easy fabrication of deep channels and rounded patterns. Becker et al. [28] exhibited a comparative analysis among the group of different polymer materials such as thermoset polymers, technical thermoplastics (e.g. PMMA, PC, PEEK), and elastomers along with the glass and silicon, with respect to various criteria such as material price, possible geometries, organic solvent stability, alkaline stability, interconnections, microfabrication, structuring processes, mechanical stability, assembly, optical transparency, acid stability, and temperature stability and represented in a tabular format. The author conveyed that the technical thermoplastics proved to be competitive among others when considered the overall criterion. Abdelgawad et al. [29] insinuated about using copper and gold condensed disks, as substrate materials for fabrication of microfluidic chips with assistance from firm markers, to depict and replicate schematics of an electrode array. The above approach circumvents the complexity in photolithography. Different materials are compatible with different manufacturing processes for example, polydimethylsiloxane compatible with lithography, and polymethyl methacrylate compatible with sandblasting or wire EDM and microend milling, and aluminium alloy compatible with abrasive water jet [30]. Polycarbonate and polyethylene terephthalate, used in the creation of the test microfluidic device, and the influence of surface roughness on the desired flow, are analysed. For this purpose, the fluid samples of water, and whole horse blood utilized [31]. Polymethyl methacrylate (PMMA) and cyclic olefin copolymer (COC) are chosen for producing a very fine quality surface finish microfluidic devices ranging lower than 15 nm surface roughness. Such very fine quality attained through novel vapour solvent treatment. Polymer's regurgitation is responsible for that high-quality surface finish [32]. The vast number of materials, employed in microfluidics and their rapport with chemical conditions, ranging from full rapport to medium rapport, and no rapport were described in tabular format in the journal paper [33]. Suriano et al. [34] selected three different materials namely polymethyl methacrylate, cyclic olefin copolymer, and

polystyrene as substrates on which microchannels fabricated through femtosecond laser treatment to exhibit the fact that the surface roughness value achieved, comparatively lower than micro-milling process. The author also reported polymethyl methacrylate as the befitting material for laser processing compared to the cyclic olefin copolymer (COP) and polystyrene (PS). Wu and Gu [35] found out that for effective sensing through microfluidic components, an embodiment of a wide range of distinctive nanocomposites and bio- or chemical-configured nanoscale materials with a microfluidic environment must be carried out. The author claimed that this unification would help in irresolute restructuring and system adjustment suitable for different applications inclined towards sensing methodologies. Wu et al. [36] tried at using polyurethane (PU) material as a competent succedaneum to polydimethylsiloxane in microfluidic applications involving body-fluid interfacing. The author succeeded at the above effort by surface transformation with hydrophilic polyethylene oxide (PEO) which alleviated the adsorption of protein. The author also claimed that the PEO blended polyurethane befits the above microfluidic applications better than PDMS. Other than metals, glass, and silicon, polymers emerged as a vital replacement for microfluidic chips due to its versatility in properties [37]. Polymers had been classified under two major sectors such as chemical and physical classification. The chemical classification includes acrylates and vinyl polymers, epoxy resins, thiol–enes, polyurethanes, and siloxanes. The physical classification includes duroplastic polymers (thermosets, duroplasts), thermoplastic polymers (thermoplasts), and elastomers [33]. Ceramic materials obtained significance over silicon, glass, and polymer due to low-temperature cofired ceramic technology which simplifies the integration of heaters, sensors, and electronics into one module. This technology simplifies the measurement system [38]. Hoople et al. [39] suggested the utilization of acrylic material in the laser ablation technique for fabrication of microfluidic devices. The authors attributed this selection to the material's pervasiveness in fabrication methodologies and to the parity shown in relation to the 3D-printed material. The usage of obscure materials such as graphite, thorium oxide, niobium, and zirconium oxide is proposed for inquisitive environments such as microfluidic systems handling plasma and flames [1]. Polydimethylsiloxane (PDMS), utilized to design a microfluidic chip by recreating the framework from the lotus leaf substrate through soft lithography, and other polymer substrates such as polystyrene and polymethylmethacrylate (PMMA) are also compatible with the above techniques [7]. The polymer, acrylonitrile butadiene styrene (ABS), is employed in the 3D printing of microfluidic accessories [15]. Silicone polymer is exploited in the fabrication of microfluidic assays and optoelectronics equipment [17]. The microfluidic system was first employed to synthesize the nanoporous silver microstructures (np-AgMSs), and np-AgMSs successfully implemented as on-chip SERS substrates for the identification of thiocyanate level in the saliva of human species [40]. At earlier stages of microfluidics technology, the choice of materials reported to be silicon and glass, and at later stages, polymer materials captured the limelight and still existing over decades. The research has to be explored in material selection itself for choosing different biocompatible metals and various biocompatible shape memory alloys.

3 Fabrication Strategies Adopted

In the introductory stages of microfluidic technology, the soul fabrication method persisted was photolithography, and later on, the fabrication repertoire increased with the inclusion of etching techniques and so on. Imprinting methods, two such kinds employed to produce microchannels in plastic substrates. One involves the use of low radius wire to stamp channels to have a basic straight channel structure and the other one, involves the imprinting of previously crafted design on silicon master template on to the device substrate, allowing numerous perplexed microfluid channel structures [41]. Fu et al. [42] identified layer-stack soft lithography as a fabrication technique to fabricate a concatenated cell sorter device which instilled with different microfluidic components. McDonald et al. [43] discovered a nonphotolithographic technique called solid-object printing, to fabricate a microfluidic device from PDMS. The author reported that SOP had a competitive edge to photolithography in covering larger areas say approximately 150 cm^2, and also claimed that the SOP technique exhibited distinct competence in producing parallel, crossway channels. The microcutting processes involving groove milling, face milling, and drilling performed on the surface of PTFE to generate microelements for the creation of a microfluidic device. Optimized machining settings reported for the individual microcutting process, to have reduced burr generation and in turn reduced surface roughness. For groove milling, the optimized settings were ball mill cutter having 0.05 mm nose radius, the speed of rotation 25,000 rpm, cutting depth below 0.025 mm, and rate of feed 250 mm/min. For face milling, the optimized settings were square end mill cutter having 0.4 mm tool radius, the speed of rotation spanning between 10,000 and 25,000 rpm, the width of cut 0.2 mm, and rate of feed 100 mm/min. For drilling, the optimized condition was the drillbit dia of 0.5 mm instead of 0.1 and 0.2 mm because of the plausible higher cutting speed at higher drillbit dia, and no burr creation observed at this above setting [44]. Different structuring methods for paper-based microfluidic devices, and their corresponding plausible pros and cons reported in tabular format in the journal [45]. Wilson et al. [46] insinuated the blending of two fabrication technologies such as micro milling and soft lithography, for the creation of intricate channel profiles. At first, through micro milling, intersecting, and curved (serpentine-like) channel, produced on brass and aluminium, respectively. Later the patterns were transferred onto the PDMS substrate through soft lithography. The parameters for micro milling such as rotary speed, the rate of feed, and cutting depth were set to 150,000 rpm, 10 mm/s, and 20 μm, respectively. Similar to the previous work, Schubert et al. [47] tried at the merging of two techniques, laser structuring and micro milling, in sequence to produce intricate microfluidic structures. This strategy also helped in complementing each other's disadvantages such as low material removal rate of microlaser processing, compensated by micro milling, and limited miniaturization (size $\gg$ 0.01 mm) of micro milling, compensated by laser processing. Three materials aluminium, stainless steel, and titanium alloy subjected to micro milling for the generation of microchannels on the surfaces. Process parameters employed were profile depth, feed per tooth, cutting depth per pass, coolant

application, and rotation speed. Response parameters were surface roughness, channel geometry deviation, burr generation, and dimension. Surface finish was better for austenitic stainless steel, and it had the lowest burr generation compared to the other materials. Titanium alloy showed less percentage of error in profile width when compared to the other two. Good surface finish and less burr generation observed due to the major influence of low depth of cut and coolant utilization [48]. Au et al. [49] presented stereolithography (SL) as a rapid and cost-saving technology, able to produce the intricate 3D profiles which were not plausible with simple PDMS molding (soft lithography), and had a delivery rate, appealing to commercialization. Zhou et al. [50] developed an unprecedented idea of introducing conciliatory molding with soft lithography enabled to produce glass-PDMS-glass (G-P-G) microfluidic device at ease. This rapidity of the process facilitated the G-P-G microfluidic device to circumvent the limitations associated with usual PDMS devices. Heng et al. [25] adopted an excimer laser direct machining methodology employed to fabricate microfluidic components on PMMA surface. Higher fluence resulted in higher depth and increased surface roughness of the channel. For different voltages, different excimer fluences obtained and the surface obtained through this methodology subjected to further excimer polishing to improve surface finish. The surface exposed to lower fluence for a range of pulse times to examine surface roughness. For shorter pulse time, surface roughness (SR) was more and it got reduced with an increase in pulse time, but at later stages, SR again increased due to flimsy streaks generation on small edges of channel walls. Matellan et al. [51] utilized the three processes (laser micromachining, solvent-based vapour treatment, adhesive bonding) effectively to fabricate PMMA microfluidic device in an economical manner. Laser micromachining encouraged the design recurrences but produced comparatively rougher surface than soft lithography. Solvent-based vapour treatment subsequently carried out to improve the surface finish. Adhesive bonding performed between the microfluidic device and the substrates for easy transfer of structures. The combination of the above three processes effected in transforming the microfluidic device from mere showcase to clinic oriented applications. Two parameters such as laser power and distance to focus (DF) controlled laser micromachining. Low DF resulted in narrow and deep channels and vice versa for a given power. Higher the power deeper the channels and lower the power shallower the channels. Surface finish depends on exposure to the desired temperature for an apt period and smooth finish obtained by exposing at 25 °c to 10 min. Adhesive bonding produced high bonding strength when cured for longer times. The fabrication strategies depended on the choice of materials pertaining to microfluidic technology and at budding stages only glass and silicon employed. This imposed restriction on the fabrication methods used but later on with the advent of new materials such as polymers and some metals the fabrication methods evolved to the concept of one step manufacturing. The research has to be further explored in proper utilization of fabrication techniques such as laser processing, 3D printing, and micro milling.

4 Applications of Microfluidic Technology

In the past five to six years, the utilization of microfluidics technology emerged as an inevitable phenomenon in the field of cooling of 3D integrated circuits [52]. Microfluidics, in recent times, deepened its roots in the domain of quantitative biology which requires exact assessments and skill to control the ambiance exquisitely [53]. Complementary metal oxide semiconductor (CMOS) supported microfluidics technology provided a significant contribution to the real-time monitoring of health in aspects of detecting cancer cell, in situ pH sensing, DNA synthesis, real-time drug delivery, portable microscope, portable RBC and WBC counter, airborne virus disclosure. The above assistance made the expensive laboratory setup to go down to point-of-care (PoC) devices [54]. Absorption photometry assisted microfluidic chip comprising necessary arrangements developed to notify the presence of elements in the blood that are significant contributors to human health [55]. Microfluidics technology in association with electrodialysis principle performed effectively in retrieving the elements from ichorous wastes [56]. The circulating cell-free DNA in the given pattern of blood can be analysed with the help of microfluidic chips [57].

5 Conclusive Remarks

In summary, the microfluidics technology has diversified areas of interest. In this paper, the microfluidic domain has been characterized under limited areas of materials used and fabrication strategies adopted as well as applications. The thought process in this paper depicted that the choice of materials could be diverse rather being inclined to polymers alone. Similarly, the fabrication methodologies also adhere to predominantly photolithographic techniques, and the concept of one step manufacturing should be further exploited. Regarding the applications also, major researchers have focussed on biomedical applications, and it is believed in future, the applications relating to some other domains such as microfluidic cooling of integrated circuits, and microfluidic heat dissipation in heat exchangers will be identified and pursued to enhance the border of microfluidics technology.

References

1. Whitesides GM (2011) What comes next? Lab Chip 11:191–193. https://doi.org/10.1039/c0lc90101f
2. Haber C (2006) Microfluidics in commercial applications; an industry perspective. Lab Chip 6:1118–1121. https://doi.org/10.1039/b610250f
3. Abgrall P, Gué AM (2007) Lab-on-chip technologies: making a microfluidic network and coupling it into a complete microsystem—a review
4. Whitesides GM (2006) The origins and the future of microfluidics

5. Ohno K, Tachikawa K, Manz A (2008) Microfluidics: applications for analytical purposes in chemistry and biochemistry. Electrophoresis 29:4443–4453. https://doi.org/10.1002/elps.200800121
6. Franke TA, Wixforth A (2008) Microfluidics for miniaturized laboratories on a chip. ChemPhysChem 9:2140–2156. https://doi.org/10.1002/cphc.200800349
7. Liu C (2010) Rapid fabrication of microfluidic chip with three-dimensional structures using natural lotus leaf template. Microfluid Nanofluidics 9:923–931. https://doi.org/10.1007/s10404-010-0615-2
8. Wu M-H, Huang S-B, Lee G-B (2010) Microfluidic cell culture systems for drug research. Lab Chip 10:939. https://doi.org/10.1039/b921695b
9. Bhagat AAS, Bow H, Hou HW, Tan SJ, Han J, Lim CT (2010) Microfluidics for cell separation. Med Biol Eng Comput 48:999–1014. https://doi.org/10.1007/s11517-010-0611-4
10. Cheng S, Wu Z (2011) A microfluidic, reversibly stretchable, large-area wireless strain sensor. Adv Funct Mater 21:2282–2290. https://doi.org/10.1002/adfm.201002508
11. Chen J, Li J, Sun Y (2012) Microfluidic approaches for cancer cell detection, characterization, and separation. Lab Chip 12:1753–1767. https://doi.org/10.1039/c2lc21273k
12. Greener J, Tumarkin E, Debono M, Dicks AP, Kumacheva E (2012) Education: a microfluidic platform for university-level analytical chemistry laboratories. Lab Chip 12:696–701. https://doi.org/10.1039/c2lc20951a
13. Cate DM, Adkins JA, Mettakoonpitak J, Henry CS (2015) Recent developments in paper-based microfluidic devices. Anal Chem 87:19–41. https://doi.org/10.1021/ac503968p
14. Steinhubl SR, Muse ED, Topol EJ (2015) The emerging field of mobile health. Sci Transl Med 7:1–6. https://doi.org/10.1126/scitranslmed.aaa3487
15. Duarte LC, De Carvalho TC, Lobo-Júnior EO, Abdelnur PV, Vaz BG, Coltro WKT (2016) 3D printing of microfluidic devices for paper-assisted direct spray ionization mass spectrometry. Anal Methods 8:496–503. https://doi.org/10.1039/c5ay03074a
16. Hediger S, Fontannaz J, Sayah A, Hunziker W, Gijs MAM (2000) Biosystem for the culture and characterisation of epithelial cell tissues. Sensors Actuators B Chem 63:63–73. https://doi.org/10.1016/S0925-4005(00)00292-6
17. Lee S, Aranyosi AJ, Wong MD, Hong JH, Lowe J, Chan C, Garlock D, Shaw S, Beattie PD, Kratochvil Z, Kubasti N, Seagers K, Ghaffari R, Swanson CD (2016) Flexible opto-electronics enabled microfluidics systems with cloud connectivity for point-of-care micronutrient analysis. Biosens Bioelectron 78:290–299. https://doi.org/10.1016/j.bios.2015.11.060
18. Cardoso S, Leitao DC, Dias TM, Valadeiro J, Silva MD, Chicharo A, Silverio V, Gaspar J, Freitas PP ()2017 Challenges and trends in magnetic sensor integration with microfluidics for biomedical applications. J Phys D Appl Phys 50:aa66ec. https://doi.org/10.1088/1361-6463/aa66ec
19. Epifania R, Soares RRG, Pinto IF, Chu V, Conde JP (2018) Capillary-driven microfluidic device with integrated nanoporous microbeads for ultrarapid biosensing assays. Sensors Actuators B Chem 265:452–458. https://doi.org/10.1016/j.snb.2018.03.051
20. Ven K, Vanspauwen B, Pérez-Ruiz E, Leirs K, Decrop D, Gerstmans H, Spasic D, Lammertyn J (2018) Target confinement in small reaction volumes using microfluidic technologies: a smart approach for single-entity detection and analysis. ACS Sensors 3:264–284. https://doi.org/10.1021/acssensors.7b00873
21. Alizadehgiashi M, Gevorkian A, Tebbe M, Seo M, Prince E, Kumacheva E (2018) 3D-printed microfluidic devices for materials science. Adv Mater Technol 1800068:1–8. https://doi.org/10.1002/admt.201800068
22. Cost L, Free P (2018) Multidimensional paper networks : a new review. J Indian Inst. Si. xxx:1–34 https://doi.org/10.1007/s41745-018-0077-1
23. Rolland JP, Van Dam RM, Schorzman DA, Quake SR, DeSimone JM (2004) Solvent-resistant photocurable [ldquo]liquid Teflon[rdquo] for microfluidic device fabrication. J Am Chem Soc 126:2322–2323. https://doi.org/10.1021/ja040811t
24. Vulto P, Glade N, Altomare L, Bablet J, Del Tin L, Medoro G, Chartier I, Manaresi N, Tartagni M, Guerrieri R (2005) Microfluidic channel fabrication in dry film resist for production and prototyping of hybrid chips. Lab Chip 5:158–162. https://doi.org/10.1039/b411885e

25. Heng Q, Tao C, Tie-chuan Z (2006) Surface roughness analysis and improvement of microfluidic channel with excimer laser. Microfluid Nanofluidics 2:357–360. https://doi.org/10.1007/s10404-006-0078-7
26. Salk N, Seemann T, Rota A, Schlüter M, Hoffmann M, Harms C (2007) New functions for microfluidic components by using micro metal injection molding (μ-MIM). Chem Eng Commun 194:859–866. https://doi.org/10.1080/00986440701193886
27. Grimes A, Breslauer DN, Long M, Pegan J, Lee LP, Khine M (2007) Shrinky-dink microfluidics: rapid generation of deep and rounded patterns. Lab Chip 8:170–172. https://doi.org/10.1039/b711622e
28. Becker H, Gärtner C (2008) Polymer microfabrication technologies for microfluidic systems. Anal Bioanal Chem 390:89–111. https://doi.org/10.1007/s00216-007-1692-2
29. Abdelgawad M, Wheeler AR (2008) Low-cost, rapid-prototyping of digital microfluidics devices. Microfluid Nanofluidics 4:349–355. https://doi.org/10.1007/s10404-007-0190-3
30. Jáuregui AL, Siller HR, Rodríguez CA, Elías-Zúñiga A (2010) Evaluation of micromechanical manufacturing processes for microfluidic devices. Int J Adv Manuf Technol 48:963–972. https://doi.org/10.1007/s00170-009-2326-y
31. Prentner S, Allen DM, Larcombe L, Marson S, Jenkins K, Saumer M (2010) Effects of channel surface finish on blood flow in microfluidic devices. Microsyst Technol 16:1091–1096. https://doi.org/10.1007/s00542-009-1004-1
32. Ogilvie IRG, Sieben VJ, Floquet CFA, Zmijan R, Mowlem MC, Morgan H (2010) Reduction of surface roughness for optical quality microfluidic devices in PMMA and COC. J Micromech Microeng 20. https://doi.org/10.1088/0960-1317/20/6/065016
33. Waldbaur A, Rapp H, Länge K, Rapp BE (2011) Let there be chip—towards rapid prototyping of microfluidic devices: one-step manufacturing processes. Anal Methods 3:2681–2716. https://doi.org/10.1039/c1ay05253e
34. Suriano R, Kuznetsov A, Eaton SM, Kiyan R, Cerullo G, Osellame R, Chichkov BN, Levi M, Turri S (2011) Femtosecond laser ablation of polymeric substrates for the fabrication of microfluidic channels. Appl Surf Sci 257:6243–6250. https://doi.org/10.1016/j.apsusc.2011.02.053
35. Wu J, Gu M (2011) Microfluidic sensing: state of the art fabrication and detection techniques. J Biomed Opt 16:080901. https://doi.org/10.1117/1.3607430
36. Wu WI, Sask KN, Brash JL, Selvaganapathy PR (2012) Polyurethane-based microfluidic devices for blood contacting applications. Lab Chip 12:960–970. https://doi.org/10.1039/c2lc21075d
37. Ren K, Zhou J, Wu H (2013) Materials for microfluidic chip fabrication. Acc Chem Res 46:2396–2406. https://doi.org/10.1021/ar300314s
38. Nge PN, Rogers CI, Woolley AT (2013) Advances in micro fluidic materials. Integration, and Applications, Functions
39. Hoople GD, Rolfe DA, McKinstry KC, Noble JR, Dornfeld DA, Pisano AP (2014) Comparison of microscale rapid prototyping techniques for microfluidic applications. In: Volume 1: materials; micro and nano technologies; properties, applications and systems; sustainable manufacturing. ASME, p. V001T03A001
40. Lawanstiend D, Gatemala H, Nootchanat S, Eakasit S, Wongravee K, Srisa-Art M (2018) Microfluidic approach for in situ synthesis of nanoporous silver microstructures as on-chip SERS substrates. Sens. Actuators B Chem 270:466–474. https://doi.org/10.1016/j.snb.2018.05.051
41. Martynova L, Locascio LE, Gaitan M, Kramer GW, Christensen RG, Maccrehan WA (1997) Fabrication of plastic microfluid channels by imprinting methods. Anal Chem 69:4783–4789. https://doi.org/10.1021/ac970558y
42. Fu AY, Chou HP, Spence C, Arnold FH, Quake SR (2002) An integrated microfabricated cell sorter. Anal Chem 74:2451–2457. https://doi.org/10.1021/ac0255330
43. Mcdonald JC, Chabinyc ML, Metallo SJ, Anderson JR, Stroock AD, Whitesides GM (2002) Prototyping of microfluidic devices in poly (dimethylsiloxane) using solid-object printing. Anal Chem 74:1537–1545. https://doi.org/10.1021/ac010938q

44. Hira S (2007) Micro-cutting of polytetrafluoroetylene (ptfe) for application of microfluidic devices. Key Eng Mater 329:577–582. https://doi.org/10.4028/www.scientific.net/KEM.329.577
45. Martinez AW, Phillips ST, Whitesides GM, Carrilho E (2010) Diagnostics for the developing world: micro fluidic paper-based analytical devices. Anal Chem 82:3–10. https://doi.org/10.1007/s10337-013-2413-y
46. Wilson ME, Kota N, Kim Y, Wang Y, Stolz DB, Leduc PR, Ozdoganlar OB (2011) Fabrication of circular microfluidic channels by combining mechanical micromilling and soft lithography. Lab Chip 11:1550–1555. https://doi.org/10.1039/c0lc00561d
47. Schubert A, Groß S, Schulz B, Eckert U (2011) Sequential combination of micro-milling and laser structuring for manufacturing of complex micro-fluidic structures. Phys Procedia 12:221–229. https://doi.org/10.1016/j.phpro.2011.03.127
48. Monroy-Vázquez KP, Attanasio A, Ceretti E, Siller HR, Hendriqchs-Troeglen NJ, Giardini C (2013) Evaluation of superficial and dimensional quality features in metallic micro-channels manufactured by micro-end-milling. Materials (Basel) 6:1434–1451. https://doi.org/10.3390/ma6041434
49. Au AK, Lee W, Folch A (2014) Mail-order microfluidics: evaluation of stereolithography for the production of microfluidic devices. Lab Chip 14:1294–1301. https://doi.org/10.1039/c3lc51360b
50. Zhou L, Zhuang G, Li G (2018) A facile method for the fabrication of glass-PDMS-glass sandwich microfluidic devices by sacrificial molding. Sens Actuators B Chem 261:364–371. https://doi.org/10.1016/J.SNB.2018.01.158
51. Matellan C, Del Río Hernández AE (2018) Cost-effective rapid prototyping and assembly of poly(methyl methacrylate) microfluidic devices. Sci Rep 8:1–13. https://doi.org/10.1038/s41598-018-25202-4
52. Wang S, Yin Y, Hu C, Rezai P (2018) 3D integrated circuit cooling with microfluidics. Micromachines 9:1–14. https://doi.org/10.3390/mi9060287
53. Gao M, Wen L, He C, Chen Y, Liu C, Fu X, Huang S (2018) Technology, A.: applications of microfluidics in quantitative biology. Biotechnol J 13
54. Khan SM, Gumus A, Nassar JM, Hussain MM (2018) CMOS enabled microfluidic systems for healthcare based applications. Adv Mater 30:1–26. https://doi.org/10.1002/adma.201705759
55. Gao R, Wu Y, Huang J, Song L, Qian H, Song X, Cheng L, Wang R, Luo L, Zhao G, Yu L (2019) Development of a portable and sensitive blood serum test system using LED-based absorption photometry and pump-free microfluidic technology. Sens. Actuators B Chem 286:86–93. https://doi.org/10.1016/j.snb.2019.01.065
56. Allioux F-M, Kapruwan P, Milne N, Kong L, Fattaccioli J, Chen Y, Dumée LF (2018) Electrocapture of heavy metal ions with carbon cloth integrated microfluidic devices. Sep Purif Technol 194:26–32. https://doi.org/10.1016/J.SEPPUR.2017.10.064
57. Malbec R, Cacheux J, Cordelier P, Leichlé T, Joseph P, Bancaud A (2018) Microfluidics for minute DNA sample analysis: open challenges for genetic testing of cell-free circulating DNA in blood plasma. Micro Nano Eng 1:25–32. https://doi.org/10.1016/J.MNE.2018.10.003

Drilling Process Improvements in EN31 Steel Under Different Environments

Manoj Kumar Sinha, Jamil Ahmad, Harish Kumar and Ranganath M. Singari

Abstract Drilling is an important manufacturing process. This process is difficult and becomes complex in drilling of the high strength materials like EN31 steel, which finds wide industrial applications due to its favourable mechanical properties. The present work is the experimental investigations in drilling of EN31 steel under different drilling environments. The number of experimental runs has been decided using the Box-Behnken design methodology. The experiments have been performed under dry and wet conditions using soluble oil as drilling medium. Initially, the work is focused on the improvement in drilling characteristics under wet drilling as compared to the dry drilling. Later on, the effect of drilling input parameters while drilling of EN31 steel on output responses for has been studied using analysis of variance (ANOVA). The finding has been studied based on the main effect and interaction plots. Regression models in actual form for the output responses have been presented using ANOVA analysis for dry and wet drilling conditions separately. Mean surface roughness values under dry and wet drilling are also shown. From this work, it can be concluded that the wet drilling is better suited for drilling of high strength materials like EN31 steel owing to its better cooling the lubricating nature of the drilling medium used.

Keywords EN31 · Drilling · Thrust force · Surface roughness · Cutting torque

M. K. Sinha (✉)
National Institute of Technology, Hamirpur, India
e-mail: manoj.coet@gmail.com

J. Ahmad · H. Kumar
National Institute of Technology, Delhi, India

R. M. Singari
Delhi Technological University, Delhi, India

H. Kumar and P. K. Jain (eds.), *Recent Advances in Mechanical Engineering*,
Lecture Notes in Mechanical Engineering,
https://doi.org/10.1007/978-981-15-1071-7_21

1 Introduction

The present scenario of increased customer awareness as well as the demand for the quality products leads to the rapid growth in huge competition amongst the producers globally. It resulted in the optimum usage of the resources and optimisation of the machining parameters. Nowadays, many conventional and non-conventional machining processes are used in the manufacturing of quality products using different materials. Still, use of the conventional machining operations covers a substantial portion of the total manufacturing processes. Out of the widely used conventional operations, drilling is the most versatile conventional machining operation used in machining of important engineering materials. Drilling operation covers around 40% of all conventional machining processes [1]. In the present scenario, achieving high quality to improve the performance of the component is the prime necessity of almost all industries. However, many production industries encounter certain challenges such as dimensional as well as geometrical tolerances, better surface finish, and high production rate at reduced tool wear. Increase in the metal removal rates leads to high productivity in machining operations. It is quite difficult to balance between high material removal rate and close tolerance limits [2]. Therefore, study of the drilling parameters becomes essential to improve the product quality and to reduce the overall cost of the product.

Drilling is a conventional machining operation of producing a cylindrical hole in a solid workpiece using a revolving tool called drill bit. The drilling of cylindrical holes is one of the most generic processes amongst all the machining processes and is more complex than other metal removal processes due to its inherent problems and associated complexities. The decline in performance level under severe drilling conditions is another important difficulty associated with the drilling tools. The drills are interred in the work sample, which hinders the removal of metallic chips away from the working zone [3]. As shown in Fig. 1, from Ishikawa diagram of hole quality in EN31 steel, it can be seen that the quality of drilling operation is influenced by the many internal as well as external factors such as feed rate,

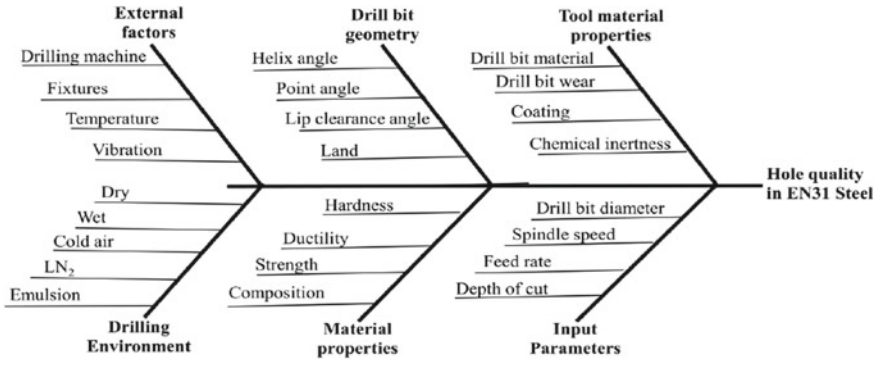

Fig. 1 Ishikawa diagram representing the hole quality in EN31 steel

Table 1 Drilling factors and their level

Input factor	Factor level		
	−1	0	+1
Spindle speed (rpm)	56	248	440
Feed rate (mm/rev)	0.10	0.20	0.30
Drill bit diameter (mm)	8	10	12

vibration, temperature, spindle speed, drill bit, drill type, and diameter of the drill bit. Since there are many parameters which affect the quality of drilling operation, it became necessary to investigate drilling input parameters for the improved quality of drilling products. Marimuthu et al. [4] investigated experimentally and numerically the laser-based micro-drilling operation in a high strength Nickel-based superalloy. They experimentally estimated the drilling time based on the hole size, laser energy, and pulse duration. Further, Wang et al. [5] studied the outcomes in experiments using water-based ultrasonic drilling in a Ni-based plate of thickness 12 mm. They focused on the drilled hole quality influence based on the ultrasonic-assisted drilling and found that this process generates drilled hole of better quality. Ramkumar et al. [6] investigated the drilling performance in a Ti/TiB-based composite material. They critically investigated the effect of important drilling parameters on the drilled-hole quality. Additionally, they proposed a wear mode of drill edges and analysed the work surface damage. They also minutely examined and studied chip morphology and its dependence on the drilling parameters.

From a comprehensive literature review, it has been found that most of the research in fields of conventional drilling operations, improvement is concentrated towards easy-to-drill materials such as aluminium alloys, and composites [7]. The present work focuses on drilling process improvement of difficult-to-drill material (EN31 steel) using Box-Behnken design and ANOVA analysis under the dry and wet drilling conditions (Table 1).

2 Materials and Methods

The commercially available, difficult-to-drill, EN31 steel bar of 40 mm diameter and 70 mm length has been chosen as work material. EN31 steel is basically a high carbon steel alloy, has a high degree of hardness (34–35 HRC), high compressive strength, lower thermal conductivity, and high abrasion resistance. Due to its low thermal conductivity, the temperature at the cutting zone interface raises abundantly during the drilling, results into rapid tool wear [8]. In addition, because of its high hardness and ability to retain strength at higher temperatures, it deforms the drill bit during the drilling which finally affects the dimensional accuracy of the drilled hole [8]. The chemical composition testing has been done by using ASTM E 415-17 method in a Spectro-lab for the exact characterisation of workpiece material, and obtained value of chemical composition has been given in Table 2. Some of the

Table 2 Chemical composition of EN31 Steel

Element	C	Si	Mn	Cr	Mo	Ni	Cu	Al	S	P	Fe
wt%	1.0121	0.2349	0.4760	1.2090	0.0310	0.0889	0.0288	0.0225	0.0240	0.0208	Rest

typical applications of EN31 steel include gauges, swaging dies, taps, ball and roller bearings, ejector pins, etc. Box-Behnken design chosen from the response surface methodology (RSM) is used to decide and customise the number of experimental runs.

For the present study, as shown in Table 1, three factors with three levels having five centre points have been selected, which gives 17 runs for every drilling conditions. The experiment was conducted for each run of input factor, and the value of two output responses (thrust force and cutting torque) was noted from the display unit of the drill dynamometer. The mean of the two replicates for thrust force and cutting torque has been used in the text. The readings obtained from the dynamometer were in Kg and Kg-m for the thrust force and cutting torque, respectively, and the multiplication with acceleration due to gravity has been done to convert it into N and Nm, respectively. The surface roughness was measured by using "Taylor Hobson Talysurf" surface roughness measuring instrument at 0.8 mm cut-off length. For each sample. at least three readings of surface roughness were taken, and the average of the same was taken as representative reading.

The setup for the drilling of workpiece in wet condition as shown in Fig. 2 has been developed by using low cost setup techniques. In this setup, a low-cost cooler's pump has been used for pumping the coolant at drill bit and workpiece interface. A plastic tub has been used for the collecting and storing of the coolant fluids. Since dynamometer has various electronic components, it must be sealed from the coolant to avoid the damage of electronic component, and hence, for this purpose, "Anabond 666" has been used for the complete sealing of the drill dynamometer. In Table 3, the complete details of experimental runs with corresponding input parameters and output responses obtained after experimentations have been presented.

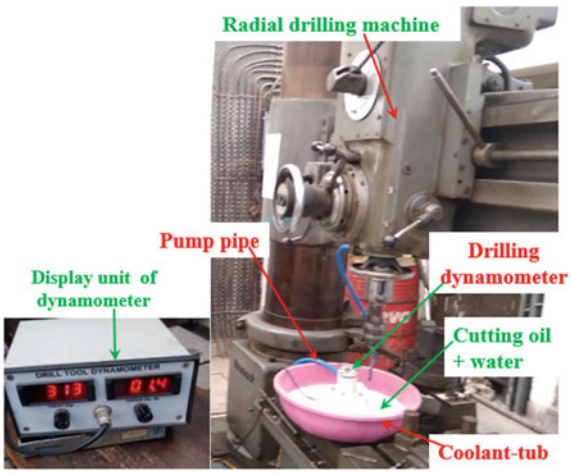

Fig. 2 Pictorial view of experimental setup for drilling in wet condition

Table 3 Input factor and output responses obtained after drilling experimentation

Run	Spindle speed	Feed rate	Drill bit diameter	Thrust force (N)		Cutting torque (Nm)		Surface roughness (μm)	
				Dry	Wet	Dry	Wet	Dry	Wet
1	056.00	0.20	12.00	4700	6000	19.0	24.0	5.30	3.51
2	248.00	0.30	12.00	9065	7000	32.0	36.0	6.48	2.85
3	248.00	0.30	08.00	3525	2200	10.0	06.0	5.25	2.25
4	248.00	0.20	10.00	5400	4900	14.0	14.0	4.66	2.10
5	248.00	0.20	10.00	5350	4600	13.5	14.0	4.69	2.36
6	056.00	0.10	10.00	3575	1250	10.5	04.5	2.86	0.57
7	248.00	0.20	10.00	5450	4650	14.5	14.5	2.69	1.88
8	440.00	0.20	08.00	3850	1900	10.0	05.5	2.12	1.56
9	248.00	0.10	12.00	3730	3600	13.5	14.0	4.52	3.87
10	056.00	0.30	10.00	7700	7050	23.0	18.0	6.87	3.95
11	056.00	0.20	08.00	3425	1850	09.0	06.0	4.33	1.91
12	248.00	0.20	10.00	5600	4700	13.5	13.5	3.36	2.35
13	440.00	0.30	10.00	7700	6900	21.0	22.5	2.90	2.24
14	248.00	0.20	10.00	5125	4750	13.5	13.0	3.32	1.89
15	440.00	0.20	12.00	8900	6100	26.5	29.0	3.79	1.93
16	440.00	0.10	10.00	4300	3100	10.0	08.0	3.58	1.94
17	248.00	0.10	08.00	2000	1800	5.50	05.0	2.32	0.81

3 Results and Discussions

The measurement of thrust force, cutting torque, and surface roughness is important aspects in the drilling hole quality of an engineering material. The thrust force and cutting torque generated during the drilling significantly contribute to the quality of the drilled product and power consumption. The mean surface roughness gives a valuable insight into the surface quality of the drilled product.

3.1 ANOVA Analysis of Output Responses

ANOVA of the output responses has been performed using Design Expert 7 software package. With the individual drilling input parameters' effect, the first-order expression between the input parameters has been obtained through F test at significance level of 5%. The estimated F values for the output responses have been compared to an F value taken from the F distribution table data for both dry and wet drilling conditions which is depicted in Table 4. The significant terms have been chosen and marked with a star (*) mark comparing the relative F values, Further, insignificant terms were removed, and the second-order multiple regression models in actual form have been fitted for output responses which have been given in Table 5. Additionally,

Table 4 Comparison of F values for output responses for dry and wet drilling conditions

Source of variation	Degree of freedom	F Value					
		Thrust force		Cutting torque		Surface roughness	
		Dry	Wet	Dry	Wet	Dry	Wet
Model	9	22.42*	9.03*	33.38*	149.40*	5.85*	6.32*
N-Spindle speed	1	11.45*	0.61	1.80	20.29*	11.87*	3.70
F-Feed rate	1	82.77*	31.80*	108.19*	337.79*	16.51*	18.70*
D-Drill bit dia	1	73.92*	39.58*	159.73*	841.59*	9.00*	15.41*
NF	1	0.42	1.42	0.23	0.26	10.75*	13.64*
ND	1	11.40*	0.0009	4.23	7.86*	0.24	2.18
FD	1	11.61*	3.19	19.61*	114.55*	0.46	3.07
N^2	1	3.87	0.042	4.31	0.12	0.41	0.060
F^2	1	0.14	0.31	0.89	2.22	2.34	0.0072
D^2	1	6.65*	4.22	0.89	20.46*	1.10	0.12
Residual	7						
Total	16						

$F_{0.05,\,1,\,16} = 4.49$ (from F distribution table) [9]

Table 5 Multiple regression mathematical model for output responses

Thrust force (N)	F_t (Dry) =	$-8719.17 - 21.09 \times N - 29643.7 \times F + 2679.69 \times D + 2.45768 \times N \times D + 4762.50 \times F \times D - 169.60 \times D^2$ ($R^2 = 0.9455$, Adj $R^2 = 0.9129$)
	F_t (Wet) =	$-8437.86 + 16750.00 \times F + 934.37 \times D$ ($R^2 = 0.8087$, Adj $R^2 = 0.7814$)
Cutting torque (Nm)	T_c (Dry) =	T_c (Dry) $= 3.29 - 116.87 \times F + 0.031 \times D + 17.50 \times F \times D$ ($R^2 = 0.9352$, Adj $R^2 = 0.9203$)
	T_c (Wet) =	$+ 63.15 - 0.027 \times N - 198.75 \times F - 11.76 \times D + 3.58\text{E}{-}003 \times N \times D + 26.25 \times F \times D + 0.53 \times D^2$ ($R^2 = 0.9929$, Adj $R^2 = 0.9887$)
Surface roughness (μm)	R_a (Dry) =	$-3.69 + 7.67 \times 10^{-3} \times N + 25.41 \times \text{F} + 0.38 \times D - 0.06 \times N \times F$ ($R^2 = 0.8062$, Adj $R^2 = 0.7416$)
	R_a (Wet) =	$-3.62 + 6.54 \times 10^{-3} \times N + 16.32 \times F + 0.29 \times D - 0.04 \times N \times F$ ($R^2 = 0.8053$, Adj $R^2 = 0.7404$)

to ensure the adequacy of the presented models, the predicted and actual values have been compared, and the relations between the predicted and the actual values for output responses have been mentioned in Fig. 3. Along with the R^2 value, the adjusted R^2 value of the drilling responses in all situations has been calculated using the software package and has been given along with regression equation. The adjusted R^2 values output responses have been found to be fairly close to R^2 values. This closeness specifies that the accepted quadratic regression models are good enough to capture the random variations in the collected experimental data. Also, it also delivers the information that by further increasing the degree of the proposed regression model, there will not be any significant improvement in the regressions obtained.

From the ANOVA table, feed rate and drill bit diameter have been found as the most affecting input parameter on the thrust force and cutting torque in dry as well as wet drilling conditions. Spindle speed has comparatively less effect on thrust force in case of dry drilling, while in case of wet drilling; the effect of spindle speed on thrust force is insignificant. Spindle speed has comparatively less effect on cutting torque in case of wet drilling, while in case of dry drilling, the effect of spindle speed on cutting torque is insignificant. Feed rate has been found as most influencing input parameter on the surface roughness in dry as well as wet drilling conditions.

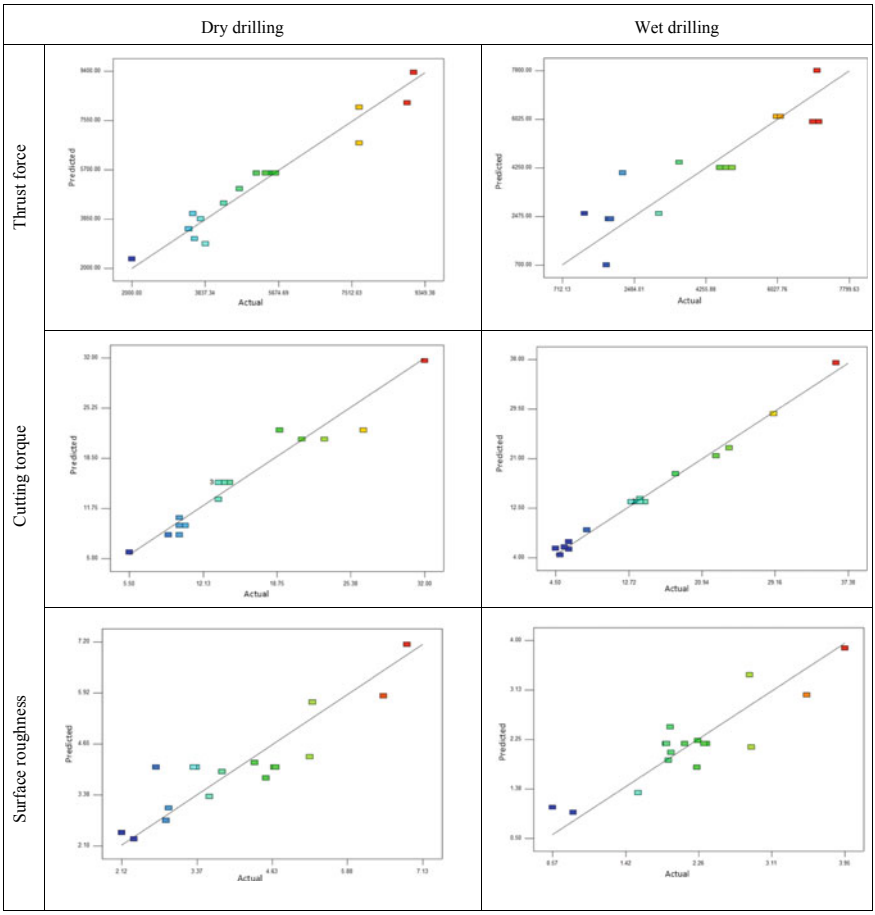

Fig. 3 Comparison between actual and predicted values of output responses

3.2 Graphical Analysis of Output Responses

For the graphical analysis of output responses, the software package "Minitab 18" has been used. In this, fitted means plot has been preferred over data means plot because fitted means plot generally gives more precise results, as it uses least-square method for predicting of mean response value. The main effect plot for mean thrust force gives a clear idea of how the output responses were affected by the different input parameters individually. The interaction plot gives a clear idea of the combined effect of two input parameter on the output responses, i.e. how the interaction of one input parameters in combination with other input parameter affecting the output responses.

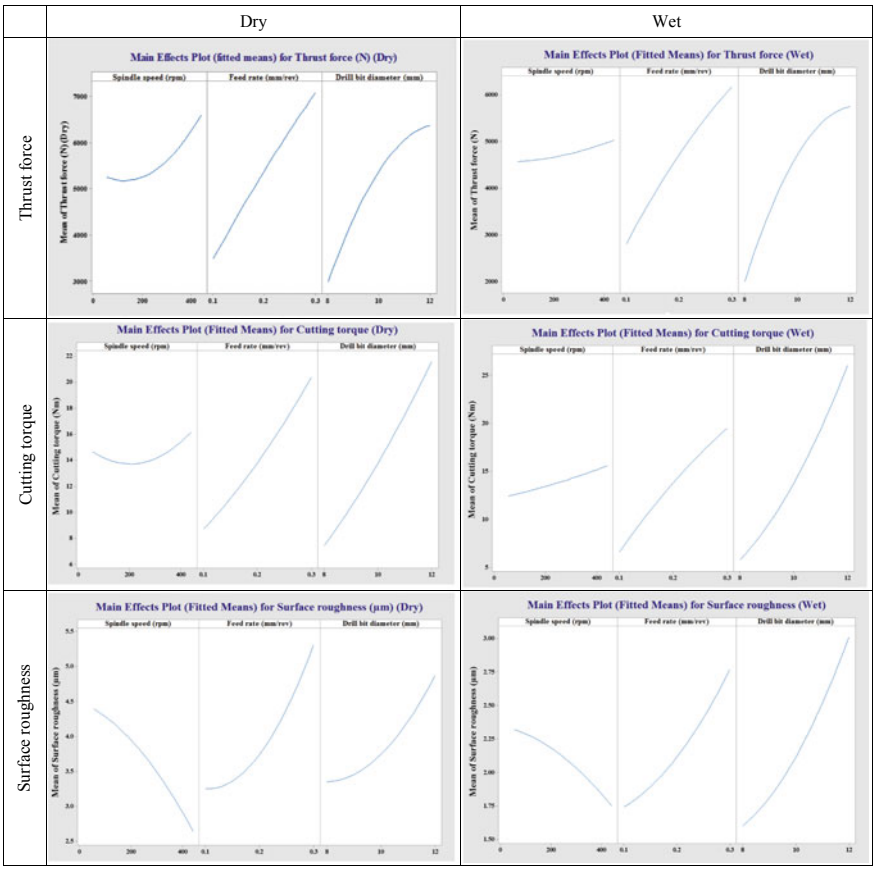

Fig. 4 Main effect plot for mean output responses

From the main effect plot of mean output responses as shown in Fig. 4, it has been found that feed rate and drill bit diameter have constantly increasing effect on the thrust force and cutting torque, whereas spindle speed has initially decreasing and then increasing effect on the thrust force and cutting torque. The initial decreasing trend of the thrust force and cutting torque with respect to spindle speed is in contradiction with the convention that with increase in the spindle speed, thrust force and cutting torque should increase. This trend generally found in lower diameter drill hole. The one reason for this could be at lower spindle speed and lower feed rate, the drill time is more, and hence, the higher heat generation inside the cutting zone interface leads to lower thrust force and cutting torque [8]. The unusual effect of spindle speed on the thrust force and cutting torque has been eliminated in case of wet drilling conditions. From the main effect plot of thrust force and cutting torque in wet drilling, it has been found that feed rate and drill bit diameter have highly dominant and constantly increasing effect on the thrust force whereas spindle speed

have, although increasing effect on the thrust force but the rate of the is very less compare to others.

The interaction plot for mean output responses as shown in Fig. 5 gives a further clarification and supports the reason given for the initial decreasing trend of thrust force and cutting torque with spindle speed. The interaction plot gives a clear idea of the combined effect of two input parameter on the output resonses, i.e. how the interaction of one input parameters with other input parameter affecting the output responses.

From the main effect plot of surface roughness (Fig. 4), it has been found that feed rate and drill bit diameter have consistently increasing effect on the surface roughness, whereas spindle speed has decreasing effect on the surface roughness. The effect of input parameter found on the surface roughness is in compliance with the established convention of drilling. The interaction plot for mean surface roughness as shown in Fig. 5 gives a clear idea of the combined effect of the most influential two input parameters on the surface roughness. For better clarity and understanding

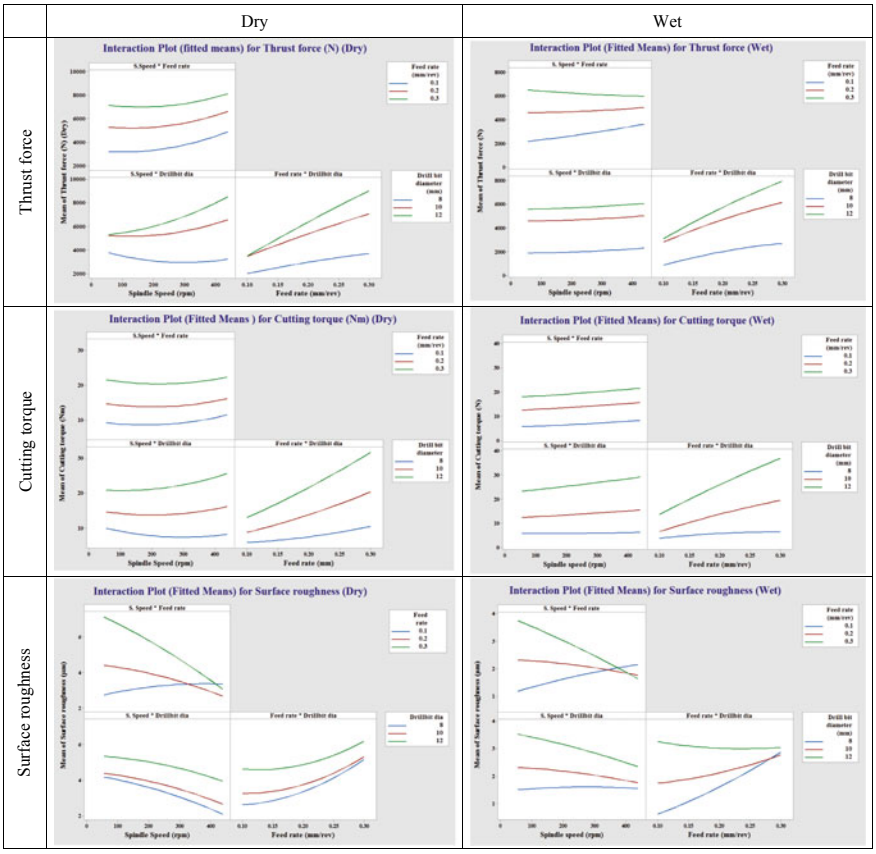

Fig. 5 Interaction plot for mean output responses

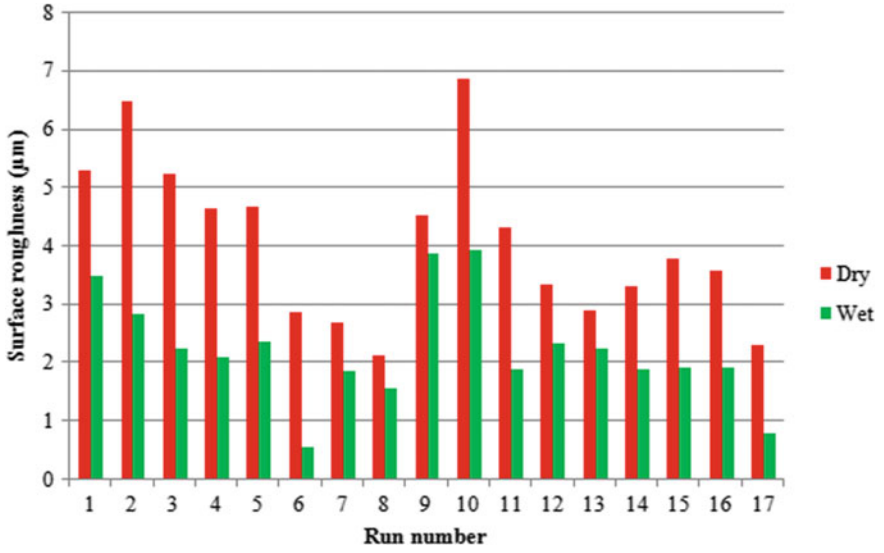

Fig. 6 Comparative representation of surface roughness in dry and wet drilling

of the mean surface roughness (R_a) obtained after dry and wet drilling, a comparison has been made between them as shown in Fig. 6, and it has been observed that the dry drilling conditions have always greater Ra value in comparison with Ra value in wet drilling conditions.

4 Conclusions

The present work presents a comprehensive experimental study for enhancing the quality of the drill hole of highly useful EN31 steel. Firstly, the present work explores the effect of effective media, i.e. drilling in wet condition for the drilling of hole in EN31 steel. Further the effect of the input drilling parameters on output the responses for drilling of EN31 steel in dry and wet drilling conditions have been studied in detail by using ANOVA analysis and RSM based graphical plot such as main effect plot and interaction plot. The multiple regression mathematical model in actual form has been fitted for the output responses by using ANOVA for dry and wet drilling conditions separately. In the last, a comparative study of output responses has been presented for the better clarity differences for drilling in dry and wet drilling conditions. The major findings derived from the present work are as follows:

I. From the comparison of output responses obtained from drilling of hole for EN31 steel in dry and wet drilling conditions, wet drilling condition has been found far better than dry drilling condition.

II. From the ANOVA for thrust force and cutting torque, the feed rate and drill bit diameter have been found as the most influencing input parameter for drilling of hole in dry as well as wet drilling conditions.
III. From the ANOVA for surface roughness, the feed rate has been found as the most influencing input parameter for drilling of hole in both dry as well as wet drilling conditions. The spindle speed has been found as more influencing parameter on surface roughness in dry drilling condition as compared to wet drilling condition.
IV. From RSM-based main effect plots, it has been found that with the increase in spindle speed, the value of thrust force and cutting torque is increasing, while the surface roughness value has decreased in both the drilling environments.

Refrences

1. Ku WL, Hung CL, Lee SM, Chow HM (2011) Optimization in thermal friction drilling for SUS 304 stainless steel. Int. J Adv Manuf Technol 53(9–12):935–944
2. Sheth S, George PM (2016) Experimental investigation, prediction and optimization of cylindricity and perpendicularity during drilling of WCB material using grey relational analysis. Precis Eng 45:33–43
3. Huang MF, Lin TR (2004) Application of grey-Taguchi method to optimise drilling of aluminium alloy 6061 with multiple performance characteristics. Mater Sci Technol 20(4):528–532
4. Marimuthu S, Antar M (2019) Dunleavey: characteristics of micro-hole formation during fibre laser drilling of aerospace superalloy. Precis Eng 55:339–348
5. Wang Houxiao Xu, Guoxiang Zhu Sukai, Wei Zhou, Naifei Ren, Kaibo Xia (2018) Comparison of percussion laser drilling quality with and without water based ultrasonic assistance. J Manuf Process 36:175–180
6. Ramkumar T, Selvakumar M, Mohanraj M, Chandrasekar P (2019) Experimental investigation and analysis of drilling parameters of metal matrix (Ti/TiB) composites. J Brazilian Soc Mech Sc. Eng 41:8
7. Ahmad J, Verma T, Sinha MK (2017) A comprehensive review of optimisation techniques employed in conventional drilling operation. In: Proceedings of 4th international conference on industrial engineering (ICIE)—2017, December 21–23, 2017. S. V. National Institute of Technology, Surat, Gujrat, India, pp. 509–514. (ISBN: 978-93-86238-39-9)
8. Prasanna J, Karunamoorthy L, Raman MV, Prashanth S, Chordia DR (2014) Optimization of process parameters of small hole dry drilling in Ti–6Al–4V using Taguchi and grey relational analysis. Measurement 48:346–354
9. Montgomery DC (2008) Design and analysis of experiments. Wiley, Hoboken, NJ

A New 3D Benchmarking Artifact to Evaluate Dimensional Accuracy and Geometric Tolerancing of Additive Manufacturing Technique

Md Qamar Tanveer, Mohd Suhaib and Abid Haleem

Abstract A variety of additive manufacturing (AM) techniques is available commercially based on a different principle. Benchmarking is a technique to investigate the overall performance of manufacturing technique with the aid of benchmark artifact. This paper aims to propose a new 3D artifact to check dimensional accuracy and geometric tolerancing in all three dimensions. The artifact can predict the effect of machine movement on variation in dimensional accuracy of artifact in a respective direction. Thus, the design of artifact covers maximum geometrical allowance. The artifact can be used to examine the dimensional accuracy and geometric tolerancing of single AM technique or for comparing two different AM techniques along the three dimensions.

Keywords Additive manufacturing · Benchmarking artifact · GD&T · Dimensional accuracy

1 Introduction

Additive manufacturing (AM) technique is the method of manufacturing objects by joining materials in layers from 3D model data [1]. The advantage of AM technologies is the capability to build complex, individually customised parts and rapid art-to-part [2]. Several AM techniques are commercially present. There is a need for a tool or procedure to evaluate the overall performances. Many researchers proposed benchmark artifact to assess the performance of different AM techniques [3]. A benchmark artifact is a 3D block which includes different features, design and developed to study the rapid prototyping (RP) machine. This paper proposes a new benchmarking artifact to evaluate dimension accuracy performance of the AM technique. The benchmarking can broadly be classified into three categories. First is the geometric benchmarking which is done to measure the geometric features dimensional

M. Q. Tanveer (✉) · M. Suhaib · A. Haleem
Department of Mechanical Engineering, Faculty of Engineering and Technology, Jamia Millia Islamia, New Delhi 110025, India
e-mail: mohdqamar26@gmail.com

H. Kumar and P. K. Jain (eds.), *Recent Advances in Mechanical Engineering*, Lecture Notes in Mechanical Engineering,
https://doi.org/10.1007/978-981-15-1071-7_22

accuracy. Second is the mechanical benchmark which investigates the mechanical properties. Last is the process benchmark which examines the process parameters like support structures, speed, layer thickness, and so forth. Due to the diversity of the working fundamental of AM technologies, it is difficult to develop a universal artifact for geometric benchmark and process benchmark, whereas standards are used for the mechanical benchmark [4].

The first benchmark was a real object introduced to assess the performance of RP techniques [5]. Since the efficacy of real-life object found limited, few researchers suggest to standardise the artifact for performance evaluation [6, 7]. Dimensional accuracy of the geometric feature has been the principal factor in designing an artifact. The design of existing artifacts considered not only dimensional accuracy but also focused on repeatability [8], minimum achievable feature size [9], and reducing the form errors [10]. Byun and Lee [11] suggested that the resolutions of RP technologies depend on the capability to manufacture a minimum dimensional size of fine features. The artifact consists of many small features on the large rectangular base. Pennington [12] proposed a bench part which includes six common features which are commonly found in products, including an overhang, horizontal boss, horizontal cylinder, vertical boss, vertical cylinder, and thin wall. As the artifact contains overhangs, it required support structure. Grimm [13] proposed a simple bench part to compare three commercial FDM printers. The reason for the simplicity was to reduce the build material and avoid the support structure. Brajlih et al. [14] proposed an artifact to evaluate the build speed versus build volume of AM machine. The artifact is designed considering ease of production and measurement. The cube artifact can be joined repetitively in all the axes to get a bigger artifact to check the work envelope of the RP machine. Due to the small size of the artifact, it was difficult to compare manufacture accuracy of machines. From the study, it has been found that the movement of the moving parts is not considered in the process of design and development of an artifact. The two significant motions of any AM machine are the horizontal movement in an x–y plane and the vertical movement in the z-axis. The accuracy and the small feature manufacturing capabilities of any AM machine heavily depend on the mention motions.

The paper proposes a new 3D artifact with an ability to check the dimensional accuracy in the x-axis, y-axis, and z-axis. The design and development of a new artifact are done by combining the salient features of the artifacts mentioned above. The significant features of the discussed artifacts considered while the development of the new artifact are summarised as follows. (i) Multidimensional: the features should be located in all three dimensions, (ii) simple design: the artifact must be quick and simple to manufacture to save time and build material, and (iii) measurement: simple enough to find the dimensional accuracy with ease on CMM and any other measuring machine. Along with the factors discussed, the proposed artifact includes all the geometric dimensioning and tolerances in all three dimensions.

2 Design of Test Part for Dimensional Accuracy

The prime purpose of the proposed artifact is to check the geometrical dimensional accuracy and tolerances in all three axes. There are already several existing artifacts for accuracy evaluation for AM machines. The artifact proposed by Ippolito et al. [15] allows an assessment of geometrical dimensions and tolerances according to ANSI-ISO standards, but unable to conclude the minimum achievable feature size and it was not suitable for the study of non-flat surfaces. Dimitrov et al. [16] proposed an artifact with a capability to examine the linear dimensional accuracy, repeatability, and the build area of the RP machine in all three dimensions. However, the artifact overlooked any circular and angular dimensional accuracy. Johnson et al. [17] designed and developed a small artifact on which geometric and dimensional tolerances, repeatability, dimensional accuracy, geometry feature (overhangs, square notch, and thin wall) can be studied.

Figure 1 shows the proposed artifact. The overall dimension of the test part is 50 × 50 × 50 mm. The square base consists of three corners and one fillet. This feature will help to check the linear and radial dimensional accuracy. The same feature is repeated with shrunk dimension with a height which results in a staircase. A small round feature is proposed to serve a dual propose; primarily, it will evaluate the minimum feature capability of AM machine and, secondly, as an aid to distinguish between the axes as the artifact is tri-symmetric.

Further, a boss feature is incorporated to check the circularity and cylindricity. An internal hole is created to check the concentricity with the internal hole of the boss.

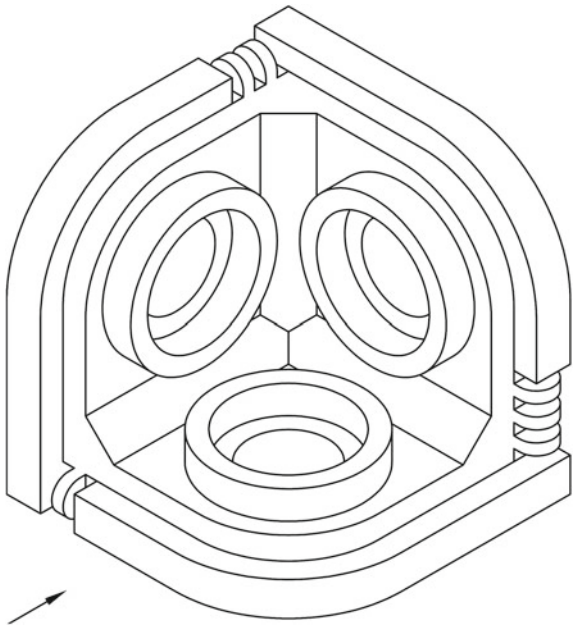

Fig. 1 Proposed 3D artifact

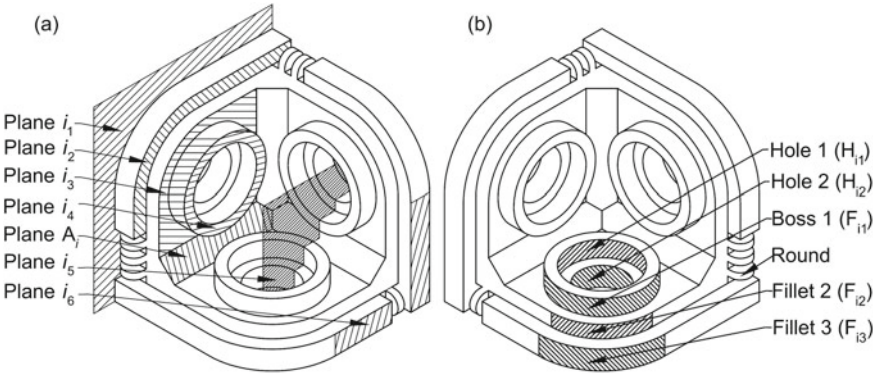

Fig. 2 **a** Planes consideration for linear dimensional accuracy, **b** Radial features consideration for radial dimensional accuracy

A surface (plane A_i) inclined to 45° added to check the angularity of the feature. The plane and radius are used for linear and radial dimensional accuracy (see Fig. 2). The linear dimensional accuracy can be checked between plane i_1, plane i_2, plane i_3, plane i_4, and plane i_6 (where i is the axis of consideration). A virtual plane i_5 considered to check the position of the centre of hole 1 and hole 2 in the perpendicular directions. A range of radius (see Fig. 2b) will help to examine the radial dimensional accuracy.

3 Design of Test Part for Geometric Tolerancing (GD&T)

The artifact designed to incorporate the maximum number of geometric tolerancing (GD&T). GD&T broadly classified into five categories: form, profile, location, orientation, and runout [18]. Orientation and location primarily considered, as there are the foremost desired characteristics of additive manufacturing. These characters help to predict the accuracy of the AM technique. Form and profile geometrical characteristics are later considered, as these characteristics will be more material driven in case of AM. Runout characteristic is not considered in the course of designing the test part. The following section explains the features which will help to evaluate GD&T in all three axes.

3.1 Orientation

3.1.1 Parallelism

A parallelism according to American Society of Mechanical Engineers (ASME) is defined as “two parallel planes parallel to a datum plane or axis, within which the

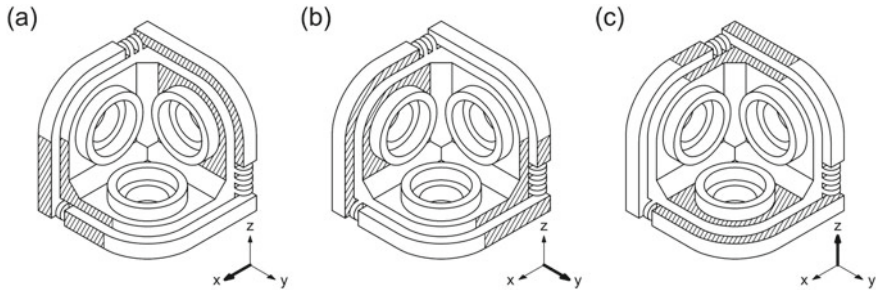

Fig. 3 Features used to measure parallelism through. **a** *x*-axis, **b** *y*-axis, **c** *z*-axis

surface or centre plane of the considered feature must lie" [18]. Parallelism can be evaluated between plane i_1, plane i_2, plane i_3, plane i_4, and plane i_6. The planes at a varying distance are considered to check the deviation of the parallelism. The observation will help conclude the effect of the distance of plane on parallelism. The considered plane is shown in Fig. 3.

3.1.2 Perpendicularity

ASME stated "Perpendicularity is the condition of a surface, centre plane, or axis at a right angle to a datum plane or axis. A tolerance zone is two parallel planes perpendicular to a datum plane or axis, within which the surface or centre plane of the considered feature must lie" [18]. Plane i_3 and plane i_4 will examine the perpendicularity. Plane i_4 is a top surface of the boss feature (see Fig. 4). The change in axis can convert the boss feature into an overhang. This plane will give an insight change in deviation due to an overhang feature.

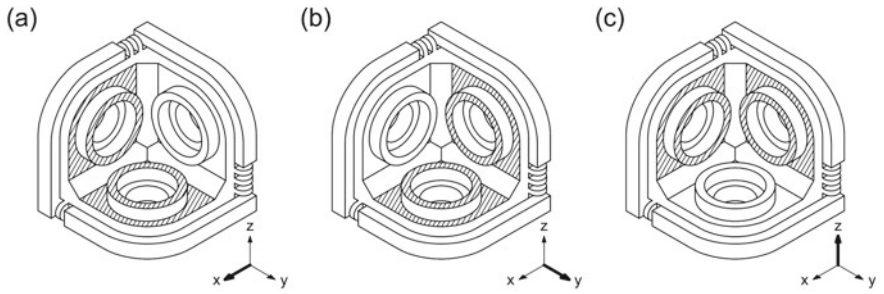

Fig. 4 Features to measure perpendicularity through. **a** *x*-axis, **b** *y*-axis, **c** *z*-axis

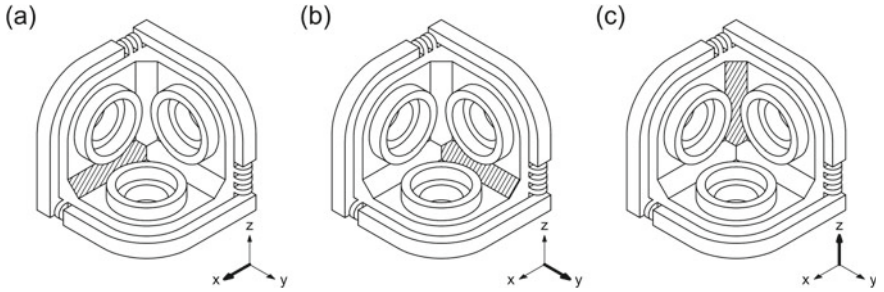

Fig. 5 Features to measure angularity through. **a** *x*-axis, **b** *y*-axis, **c** *z*-axis

3.1.3 Angularity

Angularity is the situation of a surface, plane, or axis at a specified angle (other than 90°) from a datum axis or plane [18]. Plane A_i is aligned at 45° from the plane i_3 of two perpendicular directions. This feature will help to check the angular dimensional accuracy. Increasing the number of aligned surfaces will make the feature difficult to measure. Figure 5 represents the considered plane A in all three dimensions.

3.2 Location

3.2.1 Position

The position tolerance examined with the aid of the centre of the hole 2. The shift of location of the hole centre from nominal value will be deviation of the position value. Examining the holes located in all three directions will predict position tolerance. Figure 6 shows the centre line to examine the position value.

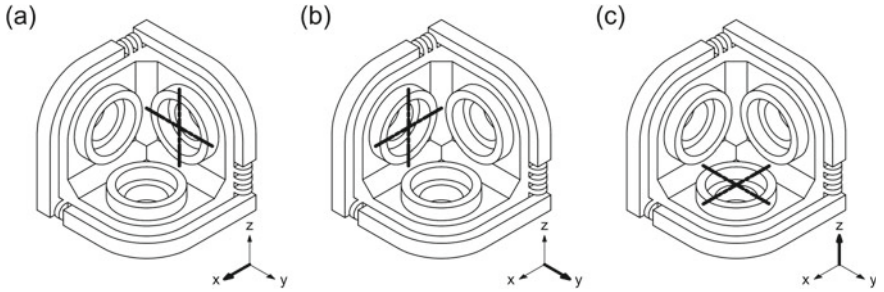

Fig. 6 Features to measure position through. **a** *x*-axis, **b** *y*-axis, **c** *z*-axis

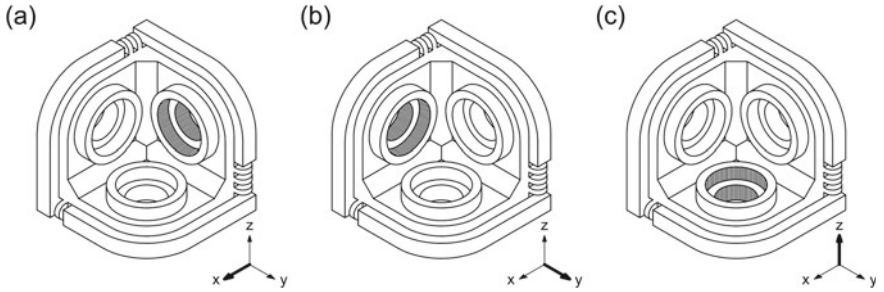

Fig. 7 Features to measure concentricity through. **a** *x*-axis, **b** *y*-axis, **c** *z*-axis

3.2.2 Concentricity

Concentricity is a condition where the locus of points traced from centre point to develop elements of a figure of revolution is corresponding with the centre point or centre axis of a datum feature [18]. The comparative shift between the axis location of hole 1 and hole 2 will give the value of concentricity tolerance (see Fig. 7). The artifact will able to give the concentricity in all dimensional. However, if no comparative study was will be done, then the result will be position tolerance value as it will depict the location shift of the centre of the hole.

3.2.3 Symmetry

Symmetry is that situation where the points of all correspondingly located features of two or more features plane are harmonious with the centre axis or centre plane of a datum feature [18]. The figure shows the small semi-round feature with a triple purposes. The first two is to differentiate the axis and to check the minimum feature size ability of the AM machine. The third is to check the symmetry tolerance along the respective axis. The symmetry tolerance will be across the virtual plane perpendicular to the round feature as shown in Fig. 8.

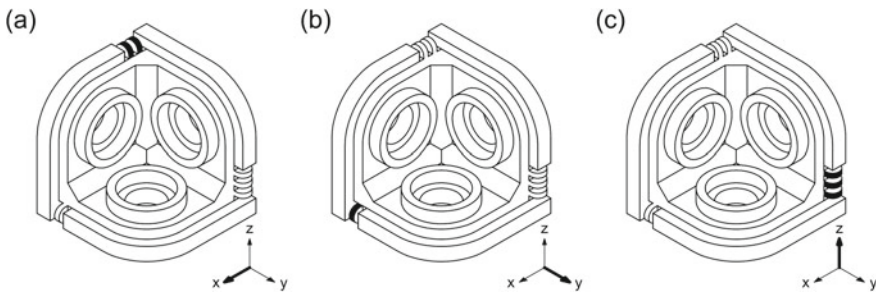

Fig. 8 Features to measure symmetry through. **a** *x*-axis, **b** *y*-axis, **c** *z*-axis

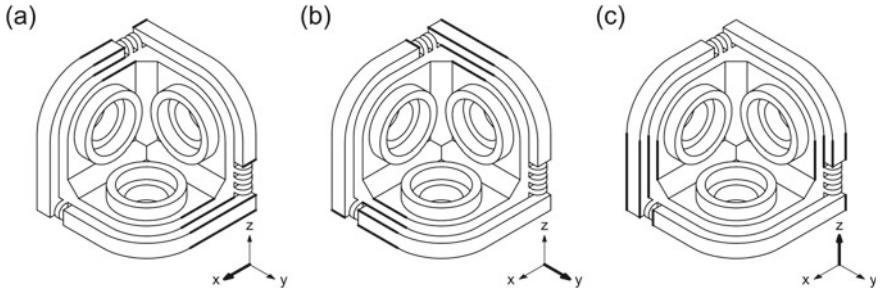

Fig. 9 Features to measure straightness through. **a** *x*-axis, **b** *y*-axis, **c** *z*-axis

3.3 Form

3.3.1 Straightness

Straightness is an elementary feature of an axis, or of a surface is a straight line. A straightness tolerance stipulates tolerance limits within which the measured element of the feature or line must lie [18]. The investigation of straightness is done through the edge of the plane i_1, plane i_2, and plane i_3 along with the three directions, respectively (see Fig. 9).

3.3.2 Flatness

Within flatness tolerance, all the elements in one directional plane are considered on the surface. Flatness is curtailed tolerance area defined by two parallel planes within which the surface whose flatness is required must lie [18]. The flatness can be studied on plane i_1, plane i_2, and plane i_3 along with the three directions, respectively. The surfaces for flatness tolerance on the three directions are shown in Fig. 10.

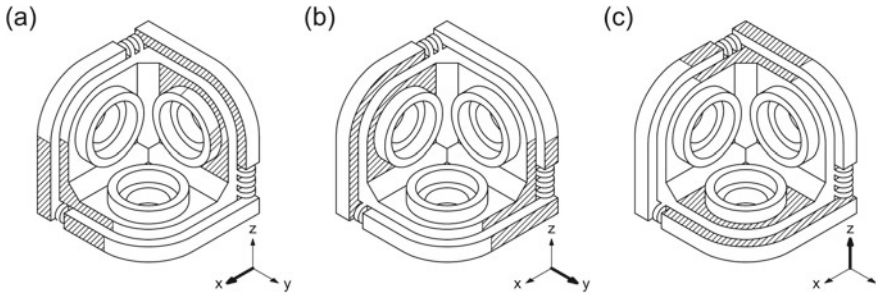

Fig. 10 Features to measure flatness through. **a** *x*-axis, **b** *y*-axis, **c** *z*-axis

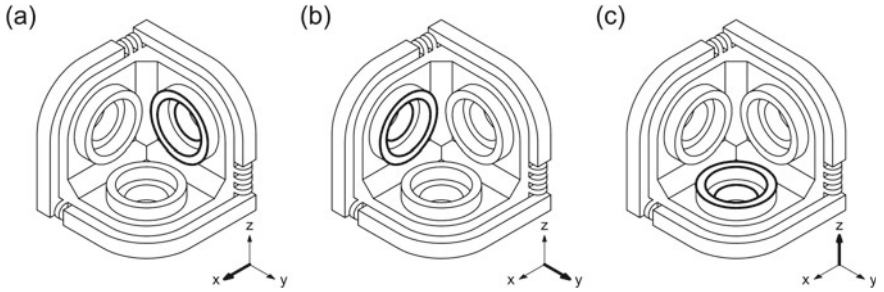

Fig. 11 Features to measure circularity through. **a** *x*-axis, **b** *y*-axis, **c** *z*-axis

3.3.3 Circularity

According to ASME, "Circularity is a condition of a surface where features other than a sphere, all points of the surface intersected by any plane perpendicular to an axis are equidistant from that axis. A circularity tolerance specifies a tolerance zone bounded by two concentric circles within which each circular element of the surface must lie, and applies independently at any plane" [18]. The circularity tolerance is observed on the edge of the boss feature and hole as shown in Fig. 11.

3.3.4 Cylindricity

Cylindricity is a condition when all the points lie on the circular surface are equidistant from a common central axis. The tolerance zone is bounded by two concentric circular surfaces within which the circular plane must lie. As cylindricity is a surface property, the tolerance applies simultaneously to both longitudinal and circular elements of the circular surface [18]. The circularity tolerance can be checked outside surface around the boss feature and the inside surface of hole 1 and hole 2 as shown in Fig. 12.

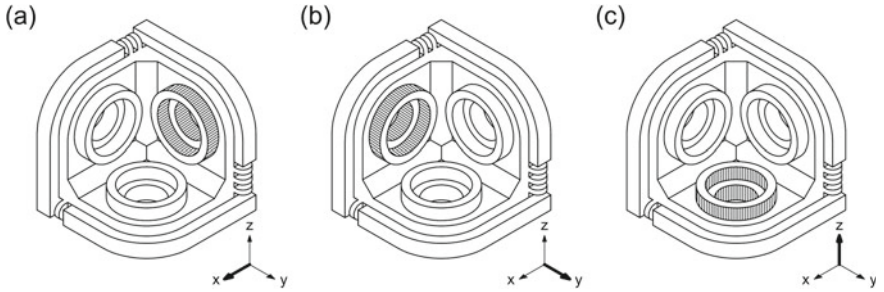

Fig. 12 Features to measure cylindricity through. **a** *x*-axis, **b** *y*-axis, **c** *z*-axis

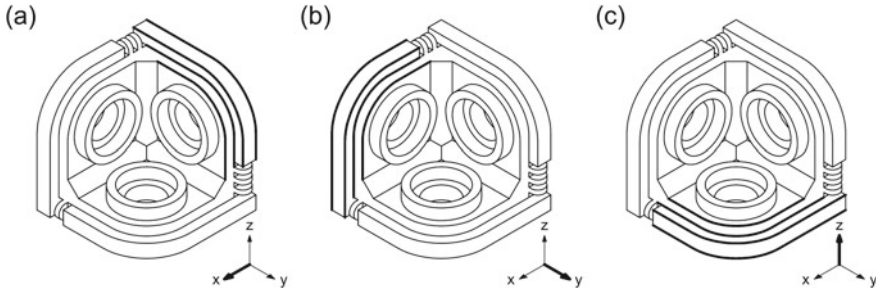

Fig. 13 Features to measure profile of line through. **a** *x*-axis, **b** *y*-axis, **c** *z*-axis

3.4 Profile

According to ASME, "A profile is the outline of an object in a given plane (two-dimensional figure). Profiles are formed by projecting a three-dimensional figure onto a plane or by taking cross-sections through the figure. The elements of a profile are straight lines, arcs, and other curved lines" [18].

3.4.1 Profile of a Line

The tolerance zone is established by extending the length along the considered feature. The profile of a line tolerance is a two-dimensional tolerance [18]. The tolerance is examined along with the complete round edge combining with the straight edge of plane i_1, plane i_2, and plane i_3 in all three dimensions, respectively (see Fig. 13).

3.4.2 Profile of a Surface

Unlike profile of line, the profile of a surface is a three-dimensional tolerance, extending along the width and length (or along circumference) of the considered feature [18]. The profile of surface is observed along the complete round surface of plane i_1, plane i_2, and plane i_3 in all three dimensions, respectively (see Fig. 14)

4 Discussion

The artifact can be manufactured by any of the available additive manufacturing processes. After development, the artifact can be measured by any coordinate measuring machine. The set of actual measurement data can be compared with the nominal measurement in any software platform. The design of proposed 3D artifact has various salient features as compared to the existing artifact. The robust design of artifact

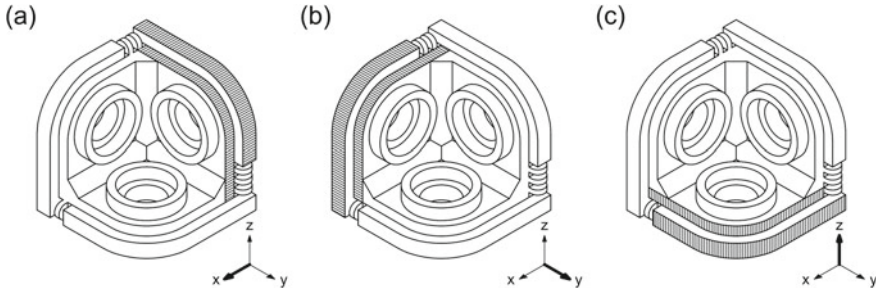

Fig. 14 Features to measure profile of surface through. **a** *x*-axis, **b** *y*-axis, **c** *z*-axis

gives the advantage to examine linear, radial, and angular dimension accuracy. The small size of the artifact will give the benefit to check the dimensional accuracy of the whole test part, not limited to particular features. The features of the artifact repeat with a change in dimension within one direction. The change in feature size will depict the percentage change in the dimensional accuracy. These observations help to make a correlation between the dimensional accuracy and the feature size. All features in a particular axis are again emulated in two other axes. The advantage of the tri-symmetric artifact envisages the dimensional accuracy in all three directions. In any AM machine, the motions of parts are predefined in the respective direction. By using the proposed 3D artifact, the effect of particular motion on dimensional accuracy can be observed. For example, the motion in fused deposition modeling machine can be divided into three directions, i.e. *x*-axis and *y*-axis movement of either nozzle along with *z*-axis movement of the platform. The deviation of the measurements can be found in particular direction eventually giving the advantage to the user to detect the particular motion for the manufacturing error.

The design aspect of artifact is further refined by adding the geometrical tolerancing. Again, the study of deviation of geometrical tolerance in all three directions can be done. These observations will help to improve the working of any AM machine in any particular direction to improve the overall geometrical performance.

5 Conclusion

The paper aims to propose a 3D artifact to study dimensional accuracy and geometrical tolerances in the three dimensions. The effect of machine part movement on dimensional accuracy and geometrical tolerances along three directions can be observed with the help of 3D artifact. The linear, angular, and radial dimensional accuracy of any AM machine can be investigated in three dimensions. The use of build material is optimized keeping view the economical aspect. The small size of the artifact saves significant time to manufacture. The proposed artifact gives an

Fig. 15 3D-printed artifact

insight into the dependency of dimensional accuracy on machine movement in particular direction. Figure 15 shows a printed artifact using the proposed 3D model in this paper. The 3D-printed artifact is manufactured by binder jetting technique for physical visualization.

The limitation of the developed artifact is the boss feature, which is an integral part of the artifact. If the axis is changed, the boss feature will convert into an overhung part which may require support structure while printing by any other additive technique. The future work is to improve the design of the artifact.

References

1. ASTM International (2013) F2792-12a—standard terminology for additive manufacturing technologies. American Society for Testing and Materials, pp 10–12
2. Moylan S, Slotwinski J, Cooke A, Jurrens K, Donmez MA (2012) Proposal for a standardized test artifact for additive manufacturing machines and processes. In: 23rd annual international solid freeform fabrication symposium, Austin, TX, pp 902–920
3. Rebaioli L, Fassi I (2017) A review on benchmark artifacts for evaluating the geometrical performance of additive manufacturing processes. Int J Adv Manuf Technol 93:2571–2598
4. Mahesh M (2004) Rapid prototyping and manufacturing benchmarking. https://scholarbank.nus.edu.sg/bitstream/10635/14697/1/ThesisManiMahesh.pdf
5. Kruth JP (1991) Material increase manufacturing by rapid prototyping techniques. CIRP Ann Manuf Technol 40:603–614
6. Jayaram D, Bagchi A, Jara-Almonte CC, O'Reilly S (1994) Benchmarking of rapid prototyping systems—beginning to set standards. In: Solid freeform fabrication symposium proceedings, pp 146–153
7. Moylan S, Slotwinski J, Cooke A, Jurrens K, Alkan Donmez M (2014) An additive manufacturing test artifact. J Res Nat Inst Stand Technol 119:429–459
8. Childs THC, Juster NP (1994) Linear and geometric accuracies from layer manufacturing. CIRP Ann—Manuf Technol 43:163–166

9. Xu F, Wong YS, Loh HT (2001) Toward generic models for comparative evaluation and process selection in rapid prototyping and manufacturing. J Manuf Syst 19:283–296
10. Zhou JG, Herscovici D, Chen CC (2000) Parametric process optimization to improve the accuracy of rapid prototyped stereolithography parts. Int J Mach Tools Manuf 40:363–379
11. Byun H-S, Lee KH (2003) Design of a New Test Part for Benchmarking the Accuracy and Surface Finish of Rapid Prototyping Processes, pp 731–740
12. Pennington RC, Hoekstra NL, Newcomer JL (2005) Significant factors in the dimensional accuracy of fused deposition modelling. Proc Inst Mech Eng, Part E: J Process Mech Eng 219:89–92
13. Grimm T (2002) Fused deposition modeling: a technology evaluation
14. Brajlih T, Valentan B, Balic J, Drstvensek I (2011) Speed and accuracy evaluation of additive manufacturing machines. Rapid Prototyp J 17:64–75
15. Ippolito R, Iuliano L, Gatto A (1995) Benchmarking of rapid prototyping techniques in terms of dimensional accuracy and surface finish. CIRP Ann—Manuf Technol 44:157–160
16. Dimitrov D, Van Wijck W, Schreve K, De Beer N (2006) Investigating the achievable accuracy of three dimensional printing. Rapid Prototyp J 12:42–52
17. Johnson WM, Rowell M, Deason B, Eubanks M (1997) Benchmarking evaluation of an open source fused deposition. In: Proceedings of the 22nd annual international solid freeform fabrication symposium, pp 197–211
18. American Society of Mechanical Engineers (2005) Dimensional and Tolerancing ASME Y1.5M-1994

Effect of 3D-Printed Ankle Foot Orthosis During Walking of Foot Deformities Patients

Harish Kumar Banga, Parveen Kalra, Rajendra M. Belokar and Rajesh Kumar

Abstract Lower leg foot orthoses are orthotic contraptions that help the decline leg joint and are suitable for a few pathologies, for the most part those that enhance the foot drop situation, that is by virtue of a lower leg joint inadequacy. In the common works of art, a specially crafted rendition of lower leg foot orthosis connected as a piece of the human casing has been made. Additive manufacturing frameworks have been used to make the decline leg foot orthosis (selective laser sintering technology). Kinematic estimations were gotten in a walk lab from foot drop sufferers, with and without 3D plastic-printed decline leg foot orthoses on unmarried feet. The results were given shown that with the orthoses, the lower leg joint conduct is kind of an immediately torsional spring, without a hysteresis. With an objective to test the adequacy of the AFO, clinical gait analysis of foot drop patients has been finished. Altered 3D distributed ankle foot orthosis has been mounted to give better gait cycle execution. The effects of this research exhibited that the patients in foot drop sufferers with 3D appropriated lower leg foot orthosis is assessed through Clinical Gait assessment.

Keywords Additive manufacturing · Ankle foot orthosis (AFO) · Gait analysis · Foot drop · Human biomechanics

1 Introduction

Foot drop is a misleadingly real name for a conceivably complicated issue. It tends to be depicted as a noteworthy insufficiency of lower leg and toe dorsiflexion. The foot and decrease leg dorsiflexors incorporate that the tibia is most irreplaceable, the extensor hallucis longus (EHL), and the extensor digitorum longus (EDL) as showed

H. K. Banga (✉) · P. Kalra · R. M. Belokar
PEC, Chandigarh, India
e-mail: drhkbanga@gmail.com

R. Kumar
UIET, Panjab University, Chandigarh, India

H. Kumar and P. K. Jain (eds.), *Recent Advances in Mechanical Engineering*,
Lecture Notes in Mechanical Engineering,
https://doi.org/10.1007/978-981-15-1071-7_23

Fig. 1 Foot drop disease

up in Fig. 1. These muscles empower the body to lift the foot amidst swing level and control plantar flexion of the foot on impact point strike [1].

The exam is organized to develop new orthoses to help the, as often as, feasible watched stroll variations from the norm pertaining to the human decrease leg foot complex using CAD showing. PC showing is a viewpoint approach for perfect plan of prosthesis and orthoses. Using CAD geometry various tests might be made without loosing of material and essential characterize elements can be changed [2–4].

Dynamic KAFOs are developed to control every stance and swing stages. But those currently available are inconvenient to use and feature complex manipulate systems. This research is directed at the usage of super elastic alloys to expand a biologically inspired dynamic knee actuator that may be hooked up on a traditional passive KAFO [5–8].

Anatomy

Strands from the dorsal parts of the ventral rami of L4-S1 are found in the peroneal nerve [9]. These are composed with the tibial nerve to symbolize the sciatic nerve as insisted in Fig. 1. The sciatic nerve leaves the pelvic hole at the extra essential sciatic foramen, just underneath average emerged from the performs. It bifurcates to plot the peroneal and tibial nerves each inside the distal 1/3 of the thigh or at the mid-thigh degree. The peroneal nerve investigates the lower back edge of the fibular neck to the basic compartment of the lower leg, constraining into shallow and far-reaching branches [10]. The shallow office is going among the two pioneers of the peronei and continues down the diminishing leg to lie among the peroneal tendon and the parallel edge of the gastrocnemius. By then it branches to the decrease leg anterolaterally to supply sensation to the dorsum of the foot (see Fig. 1).

2 Literature Review

The investigations include three-dimensional development examination of stride parameters and additionally, measure of assembling methods. The papers recognized were assessed in view of accompanying incorporation criteria (1) Design for foot drop/stroke patients and (2) Manufacturing procedures of lower leg foot orthoses, and (3) clinical trial populace utilizing AFO's.

2.1 Ankle Foot Orthoses Design

It have definite headways in non-meddling three-dimensional inspecting that have made it possible to get automated models of free-form surfaces ordinary of the human body. Joined with quick prototyping (RP) methodology, these progressions can change singular restorative devices by streamlining creation and giving quantitative plans to screen constant physiology. A novel system designing was delivered to utilize 3D photogrammetric checking as the patient-specific shape data information, and particular laser sintering (SLS) as the patient-specific RP outline yield ideally suited for restorative orthoses where shape fit and comfort are imperative [11–15].

They have uncovered a framed lower leg foot orthosis (MAFO's) a principal gadget to help walking limit and accordingly opportunity to a significant number of people with comprehensively fluctuating pathologies. The quantity of MAFO choices and the procedure, by which they are directed [16].

2.2 Ankle Foot Orthoses Manufacturing Techniques

Parametric examinations uncovered that the version turned into sensitive to the flexible moduli of the AFO and of the delicate tissue, but changed into fairly coldhearted to the tendon firmness. The effects affirmed the concept that top issues within the orthosis show up inside the mend and neck regions of the orthosis [17–20].

The enormous outcomes of the anterior AFO in lengthy-time period hemiplegic patients have been on lateral weight moving and weight bearing via affected leg after weight shifted to the affected side. Postural sway, postural symmetry, and anterior–posterior weight moving have been now not drastically affected [21]. Comprehensive clinical approach is a revolutionary and comprehensive new text that offers important records about modern-day orthoses to manual the pupil and clinician in prescribing and utilizing that home equipment in neuromuscular, musculoskeletal, and integumentary rehabilitation [22–25].

It describe the manufacturing of bodily fashions from CT records the usage of speedy prototyping and gift their clinical application. MDCT data acquisition

of isotropic voxels and modern post-processing techniques offer superb detail for clinicians and radiologists [26].

In the human body, discover what humans are manufactured from and the way the body works. In this captivating and complete guide to human anatomy, the whole thing you will ever want to know about the workings of your frame is presented in full-color element. The e-book is structured from the pinnacle to the toe, and is classified into nine sections: head, neck, thorax, top limbs, stomach, reproductive machine, pelvis, decrease limbs, and whole body systems [27].

It take a look at is to expand a motorized device to quantitatively look at the AFO alignment and mechanical houses. The motorized device includes a servo motor and an inline gear box with a 25:1 equipment ratio. A thermoplastic articulated AFO with Tamarack dorsiflexion help flexure joint changed into investigated within the look [28].

The previous research founds that there are nevertheless scientific, financial, and technological limitations for full-scale usage of AM in an administration framework for custom orthoses and prostheses [29].

The prototyped orthoses fabricated in this examination gave strong match of the subject's life frameworks appeared differently in relation to a pre-amassed AFO while store vering equivalent limit (for example mechanical sway on the biomechanics of walk) [30].

It has enhanced the fit resistance of customized lower leg and foot orthoses by 20%. This was accomplished by assessing and choosing a 3D checking procedure to give advanced models of surface life systems and moving all orthotic outlines from mortar throws, layouts, and diagrams to computerized plan arrangements and furthermore coordinating co-made computerized configuration, customized plan streamlining, and advanced manufacturing to give finish geometrical outline opportunity [31]. It have been represented on this paper, we favoring the mechanical blueprint, supervise set of rules, and deliberate assessment of a semi standoffish pleasing position control knee-bring down leg foot orthosis. The orthosis realizes a spring in parallel with the knee joint in the midst of the position segment of the progression and licenses extricated upset in the midst of the swing segment [32]. The plan is excited by strategies for the minute mindset examination of the knee joint revealing that the knee trademark approximates that of a straight torsional spring in the position territory of the gait [33]. The latest composition demonstrates that the supposition of using assorted procedures for gathering orthotic contraptions is commonsense. A couple of examinations tried to show how the condition of the orthotic devices can be adjusted to save weight, upgrade useful properties, be more fitting and patient changed.

2.3 Clinical Trials of Ankle Foot Orthoses

It have said lower leg foot orthoses utilized particularly if there should be an occurrence of handicap of neurological starting (cerebral paralysis, stroke, spinal rope harm) or musculoskeletal starting (injury, maturing). The look at is situated to grow

new orthoses to help the oftentimes found walk variations from the norm bearing on the human lower leg foot complex the use of CAD displaying [34]. It have said pre-assembled orthotic contraptions presently intended to fit as a fiddle, a significant number sufferers and thusly, they do not offer individualized solace and feature [35]. Custom-coordinate orthoses are better than pre-assembled orthotic gadgets from both of the above-expressed points of view. Be that as it may, growing a custom-coordinate orthosis is a cumbersome and time top-to-bottom manual framework completed through gifted orthotist [36].

The previous research suggests AFO solidness can supplant lost lower leg muscle work and give useful additions. In the investigation, two patients who had encountered stroke wore a latent unique AFO intended to be worn without a shoe, with twisting firmness customized for their level of plantar flexor shortage. At the gauge visit, 3D milestones on every patient's lower leg were digitized and used to redo their AFO's fit [37].

3 Methodology

This procedure of 3D checking CAD structuring with a sensible nature of picture as far as its goals and the generation of an AFO in 3D printing innovation. Based on the observed result, the project purpose is feasible but further refinement of the process is necessary at this stage. It has been concluded that using a 3D laser scanner can provide a high quality of image of scanning for the AFO. The CAD design tools have been suitably used to reduce the size of the original, large scan, the mesh in order to make 5 mm thickness final AFO design, and the extrusion from the scan by sketching on CATIA V and Delmia Solid Works design software the complete process [38]. The scanning of foot drop patient's leg has been carried out as shown in Fig. 2.

The value of material deformation with minimum load of 400 N at calf height 34 cm in carbon fiber is higher then other materials but the Nylon Polyamide is greater value than poly propylene in all thickness of ankle foot orthosis and much closer to the value of carbon fiber.

The AFO deformation calf height 34 cm at minimum constant load of 400 N having different curves for carbon fiber, Nylon Polyamide and polypropylene materials. The curve for Nylon Polyamide having thickness 5 mm is closer to the value carbon fiber of thickness 5 mm. The poly propylene material is least value in comparison of other materials. Gait analysis of foot drop patients has been carried out and gait analysis with old and new ankle foot orthosis in PGIMER Chandigarh has been studied.

The comparison of cadence and stride time with and without 3D printed ankle foot orthosis is shown in Fig. 3a, b. The cadence and stride time improvement in deformed foot and correct is improved by 3D-printed ankle foot orthosis.

The interaction of movement, standing security, and vitality protection brings about a complex and consistently changing relationship among the different appendage fragments as the body propels over the supporting foot and the toe is

Fig. 2 3D Scanning of foot drop patients

lifted to clear the ground. Each joint plays out a delegate example of movement. Amid position the postural changes are actuated inactively by the impact of body weight. Swing-stage movement relies upon muscle activity.

Lower leg edge shifted in two phases of plantar flexion and dorsiflexion are knowledgeable about every stance and swing time as appeared in Fig. 4a, b with old AFO and with new AFO. At the beginning of position, the lower leg has a 90-degree position. As the rear area is stacked, the foot drops into 10° of plantar flexion. At that point, the activity turns around and step by step achieves 10° of dorsiflexion. As of now plantar flexion is continued and achieves 20° before the finish of position, in spite of the fact that the last bend of movement happens in the twofold position time frame when the appendage is in effect quickly emptied. With toe-off, the foot is immediately raised to unbiased dorsiflexion and kept up in this position all through swing.

Lower leg plantarflexors control had been concentrated because of the reality those muscle ligament unit are key power makers for the span of taking strolls. Most of this power is delivered in a burst-like form all through the push-off period of strolling, which happens at some phase in sort of 45–65% of the walk cycle, straight away before the foot lifts off the floor. Push-off helps support up the leg into swing and divert/quicken the body's focal point of mass, which can presumably reduce collisional vitality misfortunes after contralateral foot contact and along these lines encourage low-estimated stride. Misestimating lower leg or foot energy ought to affect our comprehension, i.e. wherein quality is produced/consumed inside the casing human step, which has suggestions on musculoskeletal recreations that depend

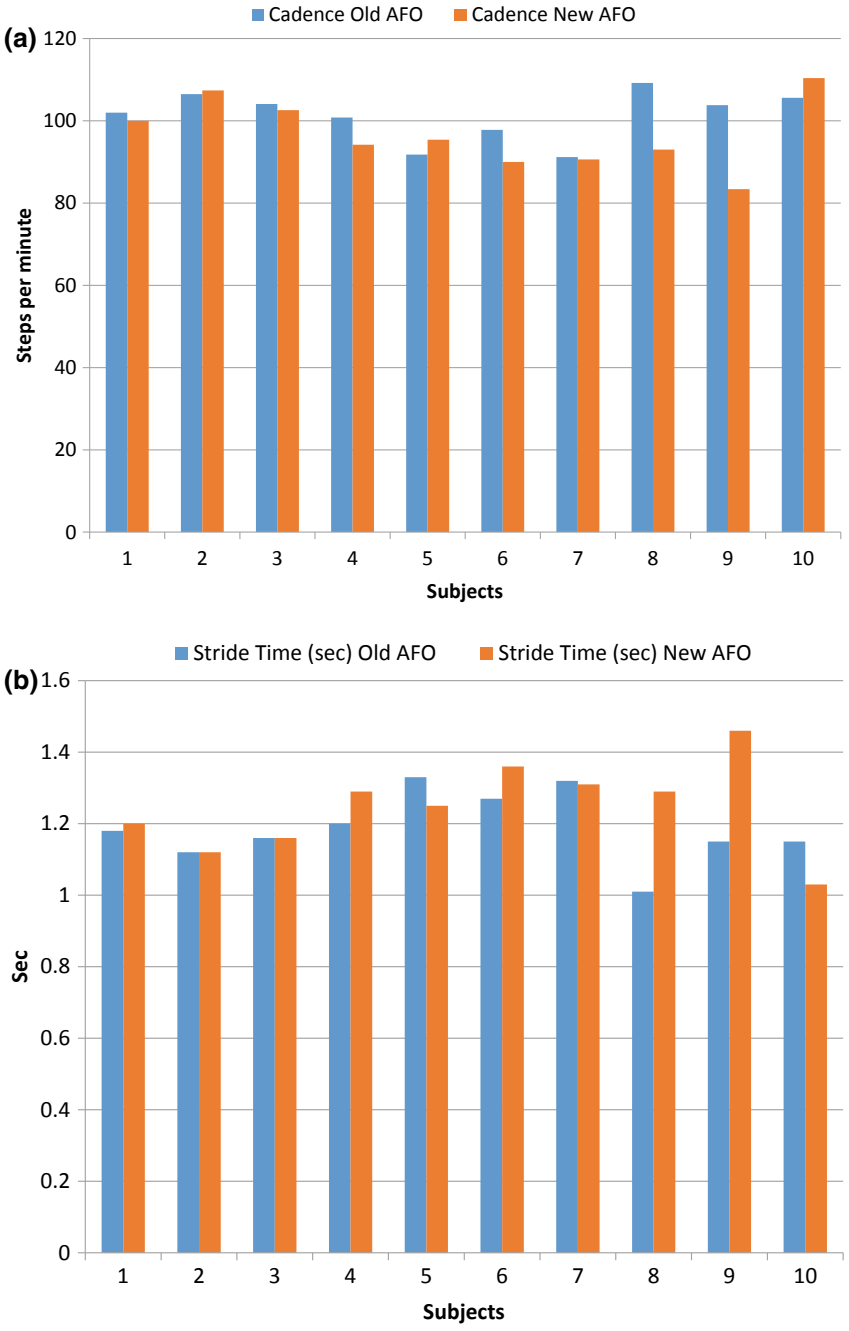

Fig. 3 **a** Cadence difference of left foot of foot drop patients with old and new AFO. **b** Stride time difference of left foot of foot drop patients old and new AFO

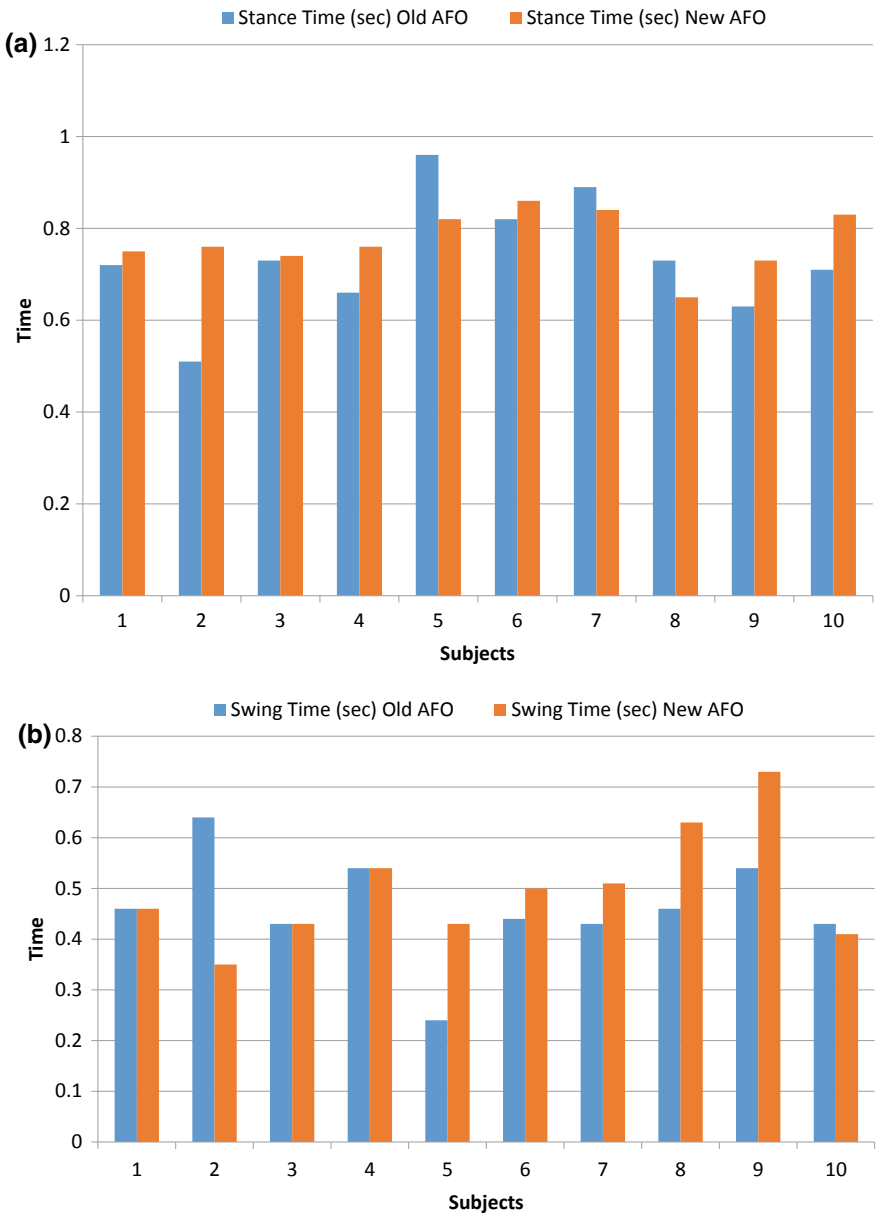

Fig. 4 **a** Stance time difference of left foot of foot drop patients old and new AFO. **b** Swing time difference of left foot of foot drop patients old and new AFO

(immediately or randomly) on observational energy gauges, and on assistive gadgets (e.g., foot prostheses) which are normally intended to mimic organic trademark. For instance, overestimating natural lower leg quality should result in controlled prostheses. The lower leg dorsiflexion and step length wrapped up by method for antique AFO and new AFO is appeared in Fig. 5a, b separately.

Figure 6 confirmed that the gate profile difference of left foot of foot drop patients old and new AFO and also shows that horizontal floor response pressure acted as generating dorsiflexion torque in the course of the first half of the stance phase and as producing plantar flexion torque at some stage in the second one half of. Therefore, the ankle joint torque from the simulated calculation underestimated the dorsiflexion torque clearly after heel touch and the plantar flexion torque at push-off.

A *T*-test was performed on left foot of foot drop patients during walking with old and new ankle foot orthosis with confidence interval of 90%.

Null hypothesis	H_0: μ_difference $= 0$
Alternative hypothesis	H_1: μ_difference $\neq 0$

The *P*-value is characterized as the likelihood under the suspicion of no impact or no distinction (invalid speculation), of getting an outcome equivalent to or more outrageous than what was really watched. The *P* represents likelihood and measures how likely it is that any watched contrast between gatherings is because of possibility. Being likelihood, *P* can take any an incentive somewhere in the range of 0 and 1. Qualities near 0 show that the watched distinction is probably not going to be because of shot, while a *P*-value near 1 recommends no contrast between the gatherings other than because of possibility. In this manner, usually in restorative diaries to see descriptive words, for example, "exceptionally critical" or "noteworthy" in the wake of citing the *P*-value contingent upon how near zero.

4 Results

The initial step time in foot drop patients was altogether longer than that in solid controls amid self-created walk inception ($P < 0.01$), however, it was not fundamentally extraordinary between the gatherings amid signal activated stride commencement. The second and third step times were not altogether unique between the gatherings amid either self-produced or prompt activated walk inception (Table 1). Step length and step speed in foot drop patients were fundamentally not exactly those in sound controls amid both self-produced and sign activated stride commencement ($P < 0.01$), aside from the initial step speed amid prompt activated walk inception. The progression width was not fundamentally unique between the gatherings amid either self-created or signal activated stride commencement. The DLS/Cycle proportions were not essentially unique between the gatherings amid either self-created or prompt activated walk inception, aside from the second DLS/Cycle proportion,

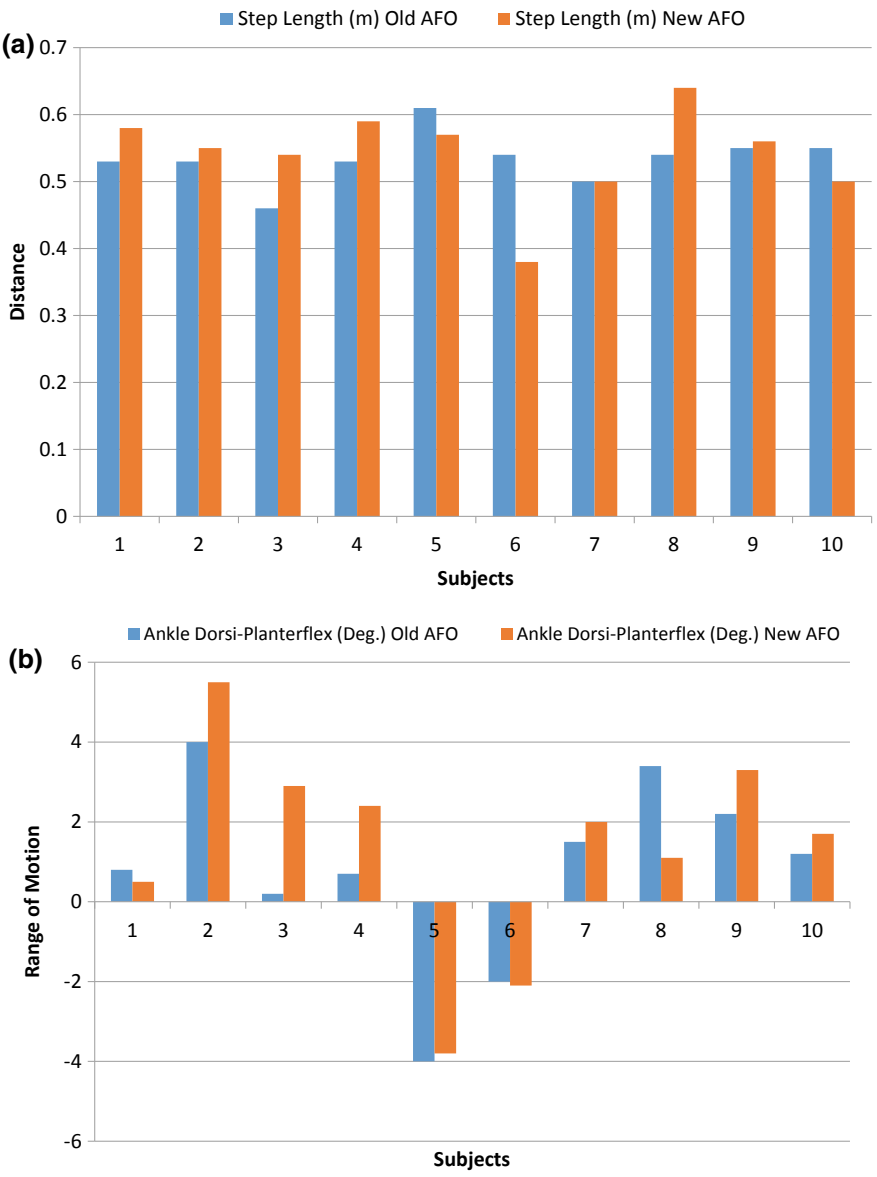

Fig. 5 **a** Step length difference of left foot of foot drop patients old and new AFO. **b** Ankle dorsi-planterflex of left foot of foot drop patients difference old and new AFO

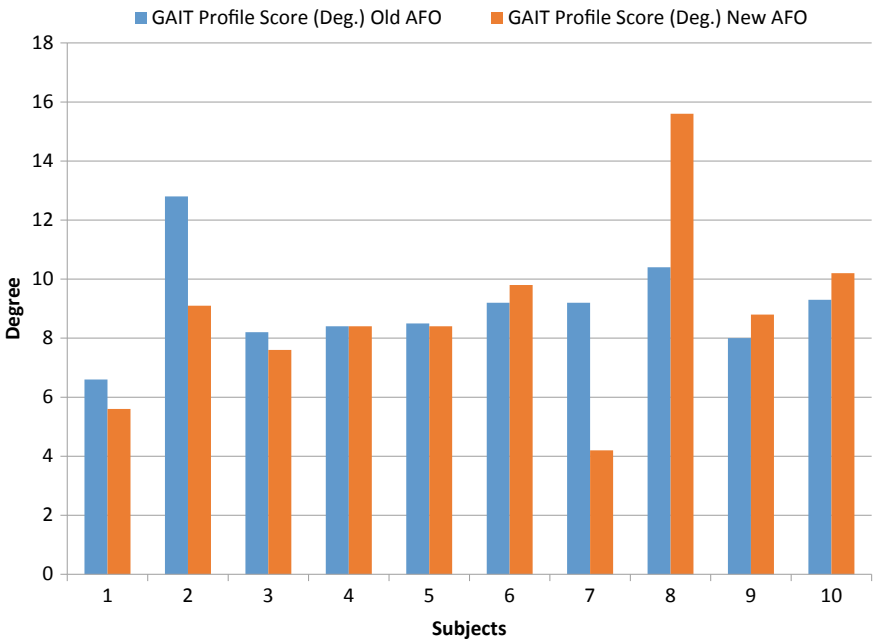

Fig. 6 Gait profile score difference of left foot of foot drop patients old and new AFO

Table 1 Paired *T*-test for left foot of foot drop patients during walking

Foot	S. No	Factor undertaken	*(LL < μ < UL)	*T*-value	*P*-value	Significance (yes/no)
Left foot	1	Cadence	$-0.22 < \mu < 9.38$	−1.75	0.099	Yes
	2	Stride time	$-0.1396 < \mu < 0.0236$	−1.30	0.092	Yes
	3	Stance time	$-0.1031 < \mu < 0.0271$	−1.07	0.093	Yes
	4	Swing time	$-0.1202 < \mu < 0.0442$	−0.85	0.099	Yes
	5	Step length	$-0.0512 < \mu < 0.0372$	−0.29	0.097	Yes
	6	Ankle dorsi-planterflex	$-2.259 < \mu < 0.439$	−1.24	0.097	Yes
	7	Gait	$-1.304 < \mu < 1.884$	−0.33	0.091	Yes

*Two-tailed

which was fundamentally bigger in foot drop patients as contrasted and solid controls amid self-produced step commencement ($P < 0.05$).

5 Conclusion

The process of 3D scanning and CAD designing the production of an AFO, with a reasonable quality of image in terms of its resolution, before sending it to a 3D printer. Based on the observed result, the research purpose is feasible but further refinement of the process is necessary at this stage.

It was concluded that using a 3D laser scanner can provide a high quality of image of scanning for the AFO making purposes compared to those that used in previous studies. The CAD design tools were suitable to reduce the size of the original, large scan, mesh making and offsetting the mesh in order to make 5 mm thickness for the final AFO design. Future works on the development of the AFO test-bed will focus on the design of the clamp elements so as to provide quantitative body weight during the gait. Actual human gait cycle data and ankle stiffness could be implemented into the control system so as to verify the functional analysis of the AFO. Further study of the energy return in gait will be analysis in this AFO test-bed.

Declaration of conflicting interests No potential conflicts of interest with respect to the research, authorship, and publication of this article as declared by Author(s).

Funding The author(s) received no financial support for the research, authorship, and publication of this article.

References

1. Abboud RJ (2002) Relevant foot biomechanics. Curr Orthop 6:165–179
2. Alexander MA, Xing SY, Bhagia S (2011) MLower limb orthotics [Online]. Webmd Llc. Available: http://Emedicine.Medscape.Com/Article/314838-Overview#Aw2aab6b5. Accessed 22-09-2011
3. American Orthotic and Prosthetic Association Inc. Evidence Note (2008) The use of ankle-foot orthoses in the management of stroke. 5(12):120–128
4. Banga HK, Kalra P, Belokar RM, Kumar R (2014) Rapid prototyping applications in medical sciences. Int J Emer Technol Comput Appl Sci (IJETCAS) 5(8):416–420
5. Banga HK, Belokar RM, Madan R, Dhole S (2017) Three dimensional gait assessments during walking of healthy people and drop foot patients. Def Life Sci J
6. Banga HK, Belokar RM, Kalra P, Madan R (2018) Fabrication and stress analysis of ankle foot orthosis with additive manufacturing. Rapid Prototyp J, Emerald Publ, Rapid Prototyp J 24(1):301–312
7. Banga HK, Belokar RM, Kumar R A novel approach for ankle foot orthosis developed by three dimensional technologies. In: 3rd international conference on mechanical engineering and automation science (ICMEAS 2017), vol 8. University of Birmingham, UK, No 10, pp 141–145 (2017)

8. Boehler W, Marbs A 3D scanning instruments. In: Proceedings of the CIPA WG 6 international workshop on scanning for cultural heritage recording, vol 3. Ziti, Thessaloniki. No 12, pp 9–18 (2002)
9. Brackx B, Van Damme M, Matthys A, Vanderborght B, Lefeber D (2012) Passive ankle-foot prosthesis prototype with extended push-off. Int J Adv Robotic Syst 1(10):19–28
10. Bennett BC, Russell SD, Abel MF (2012) The effects of ankle foot orthoses on energy recovery and work during gait in children with cerebral palsy. Clin Biomech (Bristol, Avon). 27(3):287–291
11. Bregman DJJ, Rozumalski A, Koops D, De Groot V, Schwartz M, Harlaar J (2009) A new method for evaluating ankle-foot orthosis characteristics. Gait Posture 30(6):144–149
12. Brehm M-A, Harlaar J, Schwartz M (2008) Effect of ankle-foot orthoses on walking efficiency and gait in children with cerebral palsy. J Rehabil Med 4(9):529–534
13. Bowker P (1993) Biomechanical basis of orthotic management Oxford England 2(10):19–28
14. Chen C-L, Yeung K-T, Wang C-H, Chu H-T, Yeh C-Y (1999) Anterior ankle-foot orthosis effects on postural stability in hemiplegic patients. Arch Phys Med Rehabil 8(5):1587–1592
15. Chu TM, Reddy NP, Padovan J (1995) Three-dimensional finite element stress analysis of the polypropylene, ankle-foot orthosis: static analysis. Med Eng Phys 17(5):372–379
16. Cook D, Gervasi V, Rizza R, Kamara S, Xue-Cheng L (2010) Additive fabrication of custom pedorthoses for clubfoot correction. Rapid Prototyp J 16:189–193
17. Mavroidis C, Ranky RG, Sivak ML, Patritti BL, Dipisa J (2011) Patient specific ankle-foot orthoses using rapid prototyping. J Neuroeng Rehabil 1(5):252–259
18. Crabtree CA, Higginson JS (2009) Modeling neuromuscular effects of ankle foot orthoses (AFO's) in computer simulations of gait. Gait Posture 29:65–70
19. De Burgh J (2003) The human body—an essential guide to how the body works. Grange Books, Rochester
20. Schrank ES, Stanhope SJ (2011) Dimensional accuracy of ankle-foot orthoses constructed by rapid customization and manufacturing framework. J Rehabil Res Dev 48:31–42
21. Edelstein JE, Bruckner J (2002) Orthotics: a comprehensive clinical approach. Wiley, Slack, New Jersey, USA
22. Gao F, Carlton W, Kapp S (2009) Development of a motorized device for quantitative investigation of AFO's. 15(3):112–119
23. Foot Drop Disease (Web Source: www.epainassist.com)
24. Anatomy of ankle nerve system (Web Source: www.epainassist.com)
25. Silva P, Silva MT, Martins J (2009) A review of thermoplastic ankle-foot orthoses adjustments/replacements in young cerebral palsy and spina bifida patients. JPO: J Prosthet Orthot 7:15–22
26. Milusheva SM, Tosheva EY, Toshev YE, Taiar R (2012) Ankle foot orthosis with exchangeable elastic elements series on biomechanics 23(1):322–330
27. Milusheva S, Tochev D, Stefanova L, Toshev Y Virtual models and prototype of individual ankle foot orthosis In: ISB XXth Congress—ASB 29th Annual Meeting July 31–August 5, Cleveland, Ohio (2011)
28. South BJ, Fey NP, Bosker G, Neptune RR (2009) Manufacture of energy storage and return prosthetic feet using selective laser sintering. J Biomech Eng 132:015001–015001
29. Staats TB, Kriechbaum MP (1989) Computer aided design and computer aided manufacturing of foot orthoses. JPO: J Prosthet Orthot 1:182–186
30. Sungjae H, Jungyoon K, Jinbock Y, Kisik T, Kihong R, Youngho K Development of an active ankle foot orthosis for the prevention of foot drop and toe drag. In: International conference on biomedical and pharmaceutical engineering, ICBPE, 11–14 Dec, vol. 1, pp 418–423 (2006)
31. Chu T-M, Reddy NP (1995) Stress distribution in the ankle-foot orthosis used to correct pathological gait. J Rehabil Res Dev 32(4):349–360
32. Tortora GJ, Derrickson BH (2008) Principles of anatomy and physiology. Wiley. New Jersey, USA
33. Kobayashi T, Leung AKL, Hutchins SW (2011) Techniques to measure rigidity of ankle-foot orthosis: a review. J Rehabil Res Dev 48(5):565–576

34. Van Swigchem R, Roerdink M, Weerdesteyn V, Geurts AC, Daffertshofer A (2014) The capacity to restore steady gait after a step modification is reduced in people with poststroke foot drop using an ankle-foot orthosis. Phys Ther 1(94):654–663
35. Waters RL, McNeal D, Perry J (1975) Experimental correction of footdrop by electrical stimulation of the peroneal nerve. J Bone Joint Surg 8(57):1047–1054
36. Whittle M (2007) Gait analysis: an introduction. Butterworth-Heinemann Elsevier, Philadelphia, USA
37. Winter DA (2009) Biomechanics and motor control of human movement. Wiley, New Jersey, USA
38. Ai YW, He Y, Wang ZJ, Wang Y (2014) A new method of digital manufacturing of orthoses. Comput Model New Technol 3(18):271–275

Robust Taguchi Based Optimization of Surface Finish During Hard Turning EN 31 with Carbon Nanotubes-Based Nano-Coated Tip

Navriti Gupta, R. S. Walia and A. K. Agrawal

Abstract In this paper, we report development of carbon nanotubes-based nanocoating on turning tooltip. Then the same tooltip was used in hard turning of EN-31 steel 48HRC. Taguchi optimization methodology was utilized in optimizing the most important machining indicator or output viz. surface finish. The input machining parameters taken in this study were a type of cutting tool, cutting conditions, cutting speed, feed rate, and depth of cut. Taguchi orthogonal array L27 (OA) was selected for design of experiments. ANOVA and S/N ratio 'smaller the better' was used for analysis of recorded observations. The primary findings of this research were the effectiveness of the carbon nanotubes-based nanocoating as predicted by results. Depth of cut, cutting speed, cutting conditions, type of coating, and feed rate in the given order had a role in determining the surface finish. The characterization of carbon nanotubes-based nanocoating was done using Scanning Electron Microscopy and Tunnel Electron Microscopy.

Keywords Hard turning · Coated tool · Carbon nanotubes · S/N ratio · Surface roughness · Cutting conditions

1 Introduction

Machining of hard materials/difficult-to-machine materials always posed a challenge for the machinists. The materials having hardness over 45 HRC are termed as hard materials [1]. These materials have higher melting points, higher hardness, and dense structures as alloys of Ni, Cr, and hardened industrial steels. Such materials are widely used in nuclear, aerospace, automobile, thermal power plants, etc. sectors due to their mentioned attributes. Their machining was a challenge as previously grinding was the only method available for their machining. However, after the

N. Gupta (✉) · A. K. Agrawal
DTU, Bawana, New Delhi 110042, India
e-mail: Navritiguptadtu@gmail.com; Navritigupta22@gmail.com

R. S. Walia
On Lien, PEC University of Technology, Chandigarh, India

H. Kumar and P. K. Jain (eds.), *Recent Advances in Mechanical Engineering*,
Lecture Notes in Mechanical Engineering,
https://doi.org/10.1007/978-981-15-1071-7_24

invention of hard turning, it overtook grinding because of its versatility. It is superior as compared to grinding as it allows complex shapes to be machined, closer tolerances can be achieved, and shapes that were more complex can be machined. Last but not the least is hard turning consumes 60% less time than grinding and the process is more efficient. The material removal rates (MRR) were also higher [2, 3]. To model any machining process statistically, input and output parameters must be defined. The input parameters are required to find out the design of experiments so as to achieve output parameters. The different inputs of hard turning process are cutting tool, cutting speed, feed rate, cutting conditions, tool geometry, etc. The output parameters/machining performance indicators are surface finish, cutting forces, tool wear rate, tool life, material removal rates, tool–chip interface temperature, etc. In this research work, five different input parameters viz. cutting speed, feed rate, depth of cut, type of coating, and cutting conditions were chosen and surface finish was chosen as the output parameter to be optimized. The novelty of the research was working with a newly and indigenously developed carbon nanotubes-based nano-coated tool using Taguchi design of experiments technique in form of L27 orthogonal array.

2 Tools in Hard Machining

Hard metals having hardness above 45 HRC are very difficult to machine by ordinary tools. Their machining calls for specially coated carbide tooltips, ceramics, or CBN tools. However, ceramics and CBN are very expensive options. Researchers are working on hard turning with carbide tools. These are formed by a powder metallurgy process. Coating on a carbide tool can be deposited by Chemical Vapor Deposition or Physical Vapor Deposition (PVD) process. The difference lies in the process of deposition of coating. In Physical Vapor Deposition process, a physical source is placed in a vacuum chamber and is vaporized. The vapors are deposited on the target or the substrate. On the other hand, in a Chemical Vapor Deposition (CVD) process, the ionization of carrier gas is done and it dissociates into atoms to be deposited on the substrate. This process is performed at relatively lower temperatures. Carbide tools with different Chemical Vapor Deposition and Physical Vapor Deposition coatings are widely used in precision hard turning. Some of Physical Vapor Deposition coatings are TiN, AlCrN, and TiAlN [4] while some of Chemical Vapor Deposition coatings are Al_2O_3, ZrN, Zr(C,N), Ti-Zr-C, TiB_2, etc. [5]. Xioying et al. developed CrAlTiN coating doped with carbon element for a reduction in the coefficient of friction using closed field unbalanced magnetron sputtering system (CFUMS) [6]. In the year 1969, TiC was the first CVD coating to be introduced for commercial usage [7–9]. It leads to huge success for CVD coatings in CNC machining center. About 20 years later, in the year 1980, TiN was the first commercially developed PVD coating available commercially [10]. Therefore, these coatings open up a new area of machining that is high-speed machining (HSM). Therefore, it can be concluded that both PVD and CVD have contributed significantly to increasing performance of advanced metal-cutting techniques [11]. However, there is a lack of literature for the

development of some alternate coating, which can be a possible substitute for PVD and CVD coatings.

3 Taguchi Design of Experiments

The experimental observations are translated into signal-to-noise (S/N) ratios. Signal-to-noise (S/N) ratio was used by Taguchi as the quality characteristics of choice and can be characterized into three categories [12]:

Smaller the better, $S/N = 10 \log 1/n\left(\sum y^2\right)$
Nominal is the best, $S/N = 10 \log \sum\left(y^2/S_y^2\right)$
Larger the better, $S/N = 10 \log 1/n\left(\sum 1/y^2\right)$
where 'y' is the average of experimentally observed data,
'S^2 y' the variance of 'y,'
'n' the number of observations taken in experiment,
and 'y' the observation of the conducted experiment.

For each type of observed data and response value required, we take a higher or lower value of S/N ratio [13]. In this research work, the response parameter surface finish was analyzed using 'smaller the better.'

4 Taguchi in Hard Turning Parameters Optimization: An Overview

Ucun et al. [14] researched machining performance of coated carbide tools while machining AISI 52100 grade bearing steels. They studied the effect of cutting parameters on tool wear and surface roughness. Kopac et al. [15] have performed machining of C15 E4. They took cutting speed, cutting tool materials, feed rate, and depth of cut as cutting parameters to be optimized using the Taguchi methodology. They chose orthogonal array (O.A.) of L16 (25), having two levels. The signal-to-noise ratio 'smaller the better' was used. Thamizhmanii et al. [16] used the Taguchi approach for optimization of cutting conditions to get smaller value of surface roughness. The authors found out from research that depth of cut significantly contributed toward surface roughness. Coated carbide tools have wear resistance, less heat generation, and lower forces. They usually are high-performance tools when compared with noncoated carbides. More than 40% of carbide tools are coated carbides [17, 18].

5 Experimental Study

5.1 Material and Experimental Setup

In this experimental process, experiments were performed on HMT Type22 center Turning Lathe. EN 31 rods of diameter 50 mm and length 900 mm were taken as raw material. The rod was hardened to HRC 48. Three different carbide cutting tools were used in this research viz. carbide insert, carbon nanotubes-based nano-coated insert, and Ti-based coated insert.

Surface finish was measured with Talysurf which was shown in Fig. 1. It had a ruby probe which was making linear movement over the machined surface. This instrument is very sensitive to the surface irregularities. If the surface was too rough, Talysurf reading was showing as ERROR.

5.2 Tool Inserts

In this research work, three tool bits have been used viz. bare carbide bit, carbide coated with carbon nanotubes-based nano-coated bit and carbide coated with Ti-based layer. Carbon nanotubes-based nanocoating is deposited indigenous at DTU, Delhi. Characterization of CNTs-based coating was done with Scanning Electron Microscopy and Tunnel Electron Microscopy. The tests revealed dominant presence of coiled mass of CNTs in the coating.

Figure 2 above showed the SEM and TEM images of CNTs-based nano-coated carbide bit. SEM images showed the presence of CNTs. The CNTs appeared to have fungus growth. TEM images further elaborated presence of multiwalled carbon nanotubes (MWCNTs) in the coating.

Talysurf

Fig. 1 TALYSURF-Surface Measuring Instrument, Metrology Lab, DTU, New Delhi

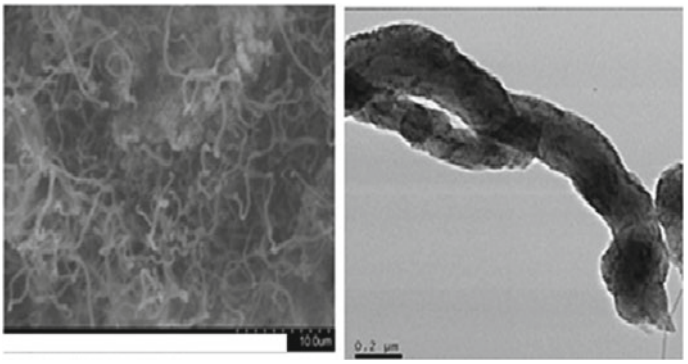

Fig. 2 SEM and TEM images of CNTs-based nanocoating

Table 1 Control parameters and their levels

Control parameter	Nomenclature	Level 1	Level 2	Level 3
Cutting tool	D	1 (wc)	2 (wc + CNT based)	3 (wc + Ti based)
Cutting conditions	C	Dry	Wet (cutting fluid)	Cool air
Spindle speed (rpm)	B	285	480	810
Feed rate (mm/min)	E	0.16	0.19	0.22
Depth of cut (mm)	A	0.53	0.81	1.06

5.3 Response Parameters and TAGUCHI DoE

In this research, the responses and their level were as per Table 1.

Three levels were taken for lower, intermediate, and higher values. Five input parameters viz. cutting tool, cutting conditions, spindle speed, feed rate, and depth of cut were chosen at three different levels.

Taguchi experiments were conducted as per Table 2. Sequence was as per Table 2. S/N ratios for different responses were calculated and were mentioned in Table 2. Complete ANOVA analysis was done using the one way ANOVA. In the following section graphs and tables were explained for each response.

6 Results and Discussion

6.1 Surface Finish

Surface finish indicates the quality of machined surface. If surface finish was too low or surface roughness was too high, it indicates poor quality of surface machined. The S/N ratio was analyzed and ANOVA table was used for interpretations of results.

Table 2 Taguchi L27 design of experiments

	A	B	C	D	E
S. No.	DoC	Speed	C cond.	C T	Feed
1	1	1	1	1	1
2	1	1	2	2	2
3	1	1	3	3	3
4	1	2	1	2	2
5	1	2	2	3	3
6	1	2	3	1	1
7	1	3	1	3	3
8	1	3	2	1	1
9	1	3	3	2	2
10	2	1	1	2	3
11	2	1	2	3	1
12	2	1	3	1	2
13	2	2	1	3	1
14	2	2	2	1	2
15	2	2	3	2	3
16	2	3	1	1	2
17	2	3	2	2	3
18	2	3	3	3	1
19	3	1	1	3	2
20	3	1	2	1	3
21	3	1	3	2	1
22	3	2	1	1	3
23	3	2	2	2	1
24	3	2	3	3	2
25	3	3	1	2	1
26	3	3	2	3	2
27	3	3	3	1	3

Table 3 is ANOVA of S/N ratio for surface finish. P-value was giving % contribution of each of control parameter in variation of the response of surface finish. Depth of cut being the most significant factor, the percentage contribution was highest at 14.76%. Cutting speed was the second-highest contributing factor at 14.49%. Here, cutting conditions have contribution of 13.34% in the overall surface finish determination. Type of coating was contributing 10.94% in temperature distribution and least contributing factor was feed rate of 9.81%.

The significance order for factors was ACBDE. Depth of cut was the most significant factor in determining surface finish while hard turning of EN 31 among the

Table 3 ANOVA surface finish (S/N ratio)

Source	SS	DOF	V	*P*-value	*F*-value	*F* critical
A	19.0299	2	9.51496912	14.75536016	43.19246751	19
B	17.1987	2	8.59936957	13.33549206	39.03617406	19
C	18.6881	2	9.34403619	14.49028553	42.41653069	19
D	14.1109	2	7.05545081	10.94125652	32.02767411	19
E	12.6497	2	6.32487285	9.80831106	28.71127185	19
A × B	21.5754	4	5.39384612	16.72903846	24.48494791	19.25
A × C	23.021	4	5.75525629	17.84995376	26.12554147	19.25
B × C	1.81469	4	0.45367168	1.407064795	2.059407557	19.25
Error	0.88117	4	0.22029233	0.683237657		

selected factors. Similarly, cutting speed was also a significant factor in determining the surface finish. Higher the cutting speed, higher is value of surface finish. Often, the finish turning operations are performed at very high cutting speeds. In the research work by Davim et al. [19] regarding the machinability of D2 steel, 60 HRC, it was concluded that with the right choice of cutting parameters, surface roughness with Ra < 0.8 lm can be obtained. Han et al. [20] investigated surface roughness in microgrooving and finally, proposed an empirical model of surface roughness which suggested Ra as a function of depth of cut. Bougharriou et al. [21] conducted research and developed a sophisticated surface roughness model for Rt, which can predict surface roughness at different cutting depths and feed rates with higher accuracy.

Surface finish was the most preferred outcome of any machining operation, as this will determine the quality of the machining operation as rough, semifinish, and finishing operation.

Figure 3 is showing S/N ratio plots were constructed and analyzed for this research, as shown in Fig. 3. Plots were drawn taking surface finish and S/N ratios along primary and secondary *Y*-axis and control parameters viz. depth of cut, cutting speed, cutting conditions, coating type, and feed rate along *X*-axis. On analyzing S/N ratio plots, it was observed that depth of cut and feed had direct effect on surface roughness. While Ti-based coating was giving highest value of surface finish, followed by carbon nanotubes-based nanocoating and bare coated tool was giving rough surface. At higher cutting speed, good surface finish was obtained. On increasing the cutting speed, a decrease in the cutting force and increase in cutting temperature is observed. As a result, the hardness and strength of the workpiece material will reduce. Also, shear yield strength will be decreased.

This will cause less tool wear. It will result in a good cutting effect. Also, depth of cut also played an important role in determining the surface finish. Increase in cutting speed and decrease in cutting depth provide good surface finish [22].

In the case of finishing operations, wet condition was highly preferred followed by cooled air. As per experiments conducted by Ahmed et al. [23], they found out

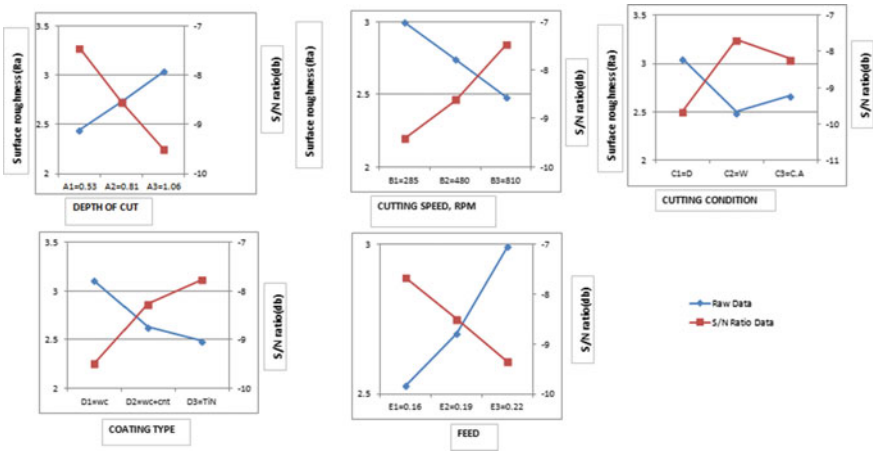

Fig. 3 S/N ratio plots for response surface finish versus control factors

that contribution of the depth of cut and cutting speed in outcome of surface quality was significantly larger as compared to the contribution of feed rate.

7 Conclusions

The primary finding of this research was related to effectiveness of carbon nanotube-based coating with Ti-based coated tool as compared with bare tool. In this research, a comparison was drawn among bare bit, carbon nanotubes-based nano-coated bit, and superior Ti-based coated bit. The Taguchi DoE L27 OA was used to conduct turning experiments. The responses were analyzed in terms of % contribution or the P-value of input factors using the S/N ratio table. For response of surface roughness, the % contribution of input control factors was in descending order as depth of cut, cutting conditions, cutting speed, coating type, and feed rate. Manufacturing of precision parts demands final finish machining operations, which may constitute up to 15% of the total manufacturing costs [24]. Surface finish is considered as the main quality assessment feature in metal removal operations. Coating type also played an important role in determining surface finish. As per the observations of this research, there was substantial improvement in surface finish value achieved with the carbon nanotubes-based nano-coated tool as compared to that with bare tool. It was observed that carbon nanotubes-based nano-coated bit was better than bare bit. The surface finish is dependent on several factors as determined by the S/N ratio plots.

Feed rate and depth of cut exhibited linear relationship with the surface finish. Cutting speed also showed linear relationship. Choice of coolant while hard turning EN 31 also influenced surface quality. Good surface finish was obtained with usage of lubricant.

Acknowledgements This researched was enriched by the contributions of Dr. P. K. Tyagi, Applied Physics Department, DTU, New Delhi, India, Mr. Manjit Singh, Mr. Rajesh Bora, Mr. Rajesh Kumar, Mr. Sunil Kumar, Mechanical Engineering Dept. DTU, Delhi.

References

1. Tonshoff H, Arendt C, Ben Amor R (2000) Cutting of hardened steel. Ann CIRP, 49:547–566
2. Tonshoff H, Wobker H, Brandt D (1995) Hard turning–Influence on the work piece properties. Trans NAMRI/SME 23:215–220
3. Tonshoff H, Wobker H, Brandt D (1996) Tool wear and surface integrity in hard turning. Prod Eng 3:19–24
4. Gupta KM, Kamakoti R, Dharmateja S, Sivarajan S(2018) Cutting characteristics of PVD coated cutting tools. Mater Today: Proc 5(5):11260–11267
5. Haubner R (2017) Evolution of conventional hard coatings for its use on cutting tools. Int J Refract Metals Hard Mater 62:210–218
6. Li X, Wu W, Dong H (2011) Microstructural characterisation of carbon doped CrAlTiN nanoscale multilayer coatings. Surf Coat Technol 205(10):3251–3259
7. Rebenne H, Bhat D (1994) Review of CVD TiN coatings for wear-resistant applications: deposition processes, properties and performance. Surf Coat Technol 63:1–13
8. Ettmayer P, Kolaska H, Ortner H (2014) History of hardmetals. In: Sarin VK (ed) Comprehensive hard materials. Elsevier Ltd. ISBN 978-0-08-096528-4
9. Broszeit E, Gabriel H (1980) Beschichten nach den CVD-Verfahren. Materialwissenschaft und Werkstofftechnik 11:31–40
10. Matthews A (1985) Titanium nitride PVD coating technology. Surf Eng 1:93–104
11. Knotek O, Loffler F, Kramer G (2001) Applications to cutting tools. In: Bunshah RF (ed) Handbook of hard coatings. Noyes Publications/William Andrew Publishing, New York, pp 370–410. ISBN 0-8155-1438-7
12. Mahapatra S, Patnaik A (2009) Study on mechanical and erosion wear behavior of hybrid composites using Taguchi experimental design. Mater Des 30:2791–2801
13. Ghani J, Choudhury I, Hassan H (2004) Application of Taguchi method in the optimization of end milling parameters. J Mater Process Technol 145:84–92
14. Ucun I, Aslantas K (2009) Investigation of performance of carbide cutting tool in turning Hardened 52100 tool steel. In: IATS. Karabuk, Turkey
15. Kopac J, Bahor M, Sokovic M (2002) Optimal machining parameters for achieving the desired surface roughness in fine turning of cold preformed steel work pieces. Int J Mach Tools Manuf 42:707–716
16. Thamizhmanii S, Saparudin S, Hasan S (2007) Analysis of surface roughness by using Taguchi method. Ach Mater Manuf Eng 20:503–505
17. Singh H, Kumar P (2004) Tool wear optimization in turning operation by Taguchi method. Indian J Eng Mater Sci 11:19–24
18. Davim JP (2003) Design of optimization of cutting parameters for turning metal matrix composites based on the orthogonal arrays. J Mater Process Technol 132:340–344
19. Davim JP, Figueira L (2007) Machinability evaluation in hard turning of cold work tool steel (D2) with ceramic tools using statistical techniques. Mater Design 28:1186–91
20. Han J, Li L, Chan C, Lee W (2017) Investigation on the formation of surface defects of OFHC copper in diamond micro-grooving process. Int J Adv Manuf Technol 93(9–12):4133-4141
21. Bougharriou A, Bouzid W, Sai K (2014) Analytical modeling of surface profile in turning and burnishing. Int J Adv Manuf Technol 75(1–4):547–558
22. Li Bin (2014) An experimental investigation of dry cutting performance for machining gray cast iron with carbide coating tool. Int J Adv Manuf Technol 71:1093–1098

23. Sayeed GM et al (2015) Optimization of feed and radial force in turning process by using Taguchi design approach. Mater Today: Proc 2:3277–3285
24. Walia RS, Shan HS, Kumar P (2006) Parametric optimization of centrifugal force-assisted abrasive flow machining (CFAAFM) by Taguchi method. Mater Manuf Process 21:375–382

Convection of Viscoplastic Fluid in U-Tube Bends

N. H. Khan, M. K. Paswan and M. A. Hassan

Abstract Viscoplastic fluids are found among both man-made and natural materials frequently. They are characterized by the presence of yield stress, which results in complex fluid rheology. During heat treatment, such materials undergo convection. The convection patterns are expected to be complex due to the presence of yield stress and delayed fluid movement. In this work, heat transfer and flow characteristics of viscoplastic fluid in a square duct with 180° sharp bend have been studied numerically. The duct is filled with viscoplastic fluid obeying Herschel–Bulkley model. The flow is assumed to be two dimensional, laminar and steady. Finite volume-based scheme is used to obtain the flow domain behavior. The effects of Reynolds number, input height to output height ratio (IOR), Yield number and power law index on the flow and heat transfer characteristics of the viscoplastic fluid have been investigated. Results are presented in terms of streamlines, isotherms and velocities under different heating conditions. Yielded and unyielded regions in the flow domain have been identified. It has been found that vortices are emanating near the sharp corner. A strong correlation of the size of vortices, reattachment length and heat flow with variable parameters has been obtained.

Keywords Yield stress · Convection · Herschel–Bulkley model · Reynolds number

1 Introduction

Heat exchanger with 180° sharp bend is being widely used in lowering the thermal load on the material by providing internal cooling passage in it. Additionally, these convective passages could be found in the cooling arrangement in food processing industries. An experimental study of heat and fluid flow characteristics inside the straight, rectangular channels connected with 180° sharp bend was reported, and investigations of convective heat transfer rate for both smooth and rib-roughened

N. H. Khan · M. K. Paswan · M. A. Hassan (✉)
Nanofluid Laboratory, Department of Mechanical Engineering, National Institute of Technology, Jamshedpur 831014, India
e-mail: hassan.me@nitjsr.ac.in

H. Kumar and P. K. Jain (eds.), *Recent Advances in Mechanical Engineering*,
Lecture Notes in Mechanical Engineering,
https://doi.org/10.1007/978-981-15-1071-7_25

ducts had been presented in [1]. Hirota et al. [2] used naphthalene sublimation method to explore heat and mass transfer characteristics in the smooth rectangular two-pass channel with sharp bend for different Reynolds number and turn clearances (30, 50 and 70 mm). They found that heat/mass transfer exhibits steep variation at sharp corner and suggested a strong dependency on Reynolds number and turn clearances. Chung et al. [3] studied flow structures, reattachment lengths and heat transfer characteristics of unsteady laminar flow numerically in 180° sharp bend in the range of $50 \leq \mathrm{Re} \leq 1000$. A strong dependency of heat transfer on flow oscillations is found, whereas flow remains steady till $\mathrm{Re} \leq 600$ (unsteady for $\mathrm{Re} > 600$). The effects of input height to output height ratio (IOR) of the 180° sharp bend channel on the flow and thermal characteristics for varying Reynolds number ranging from 100 to 900 have been investigated numerically [4]. Considering the fact that mist injection into steam enhances the heat transfer of turbine blade which in turn increases the efficiency of gas turbine, Dhanasekaran and Wang [5] proposed a laboratory validated CFD model and studied the cooling performance of mist/steam at gas turbine working conditions.

Majority of the studies on sharp U-tube bend involve Newtonian fluid, though we are surrounded by large of non-Newtonian fluids where shear stress is not directly proportional to the rate of shear strain. Among non-Newtonian fluids, those which require a minimum critical shear stress, termed as yield stress, to flow otherwise they behave as a solid are categorized as viscoplastic fluid, also called yield stress fluid. In addition to processed food and dairy products, materials of geophysical interest such as mud, lava, debris and glaciers exhibit viscoplasticity [6–8]. Materials like toothpaste, mayonnaise, hair gel and mortar are viscoplastic fluid. Bio-fluids such as mucus and saliva have been studied as yield stress fluids. Detailed information about viscoplastic fluid is well documented in many review articles [9–13].

The duct flow of viscoplastic materials is a matter of importance due to its application in food and dairy processing and polymer industry. Numerical investigation of viscoplastic fluid obeying Bingham model inside a rectangular duct has been reported by Taylor and Wilson [14]. Flow of viscoplastic fluid was assumed to be steady, laminar and two dimensional. The impact of non-dimensional yield stress and aspect ratio on flow pattern, i.e., yielded and unyielded region was explored. The central plug zone and corner dead regions expanded with rise in yield stress. Pham and Mitsoulis [15] extended the work of Taylor and Wilson [14] and proposed a master curve between reduced flow rate (ratio of viscoplastic to Newtonian flow rates) and Bingham number for generalized duct. Many efforts to understand viscoplastic flow inside duct can be found in the literature [16–18]. In several situations, such as food processing, drawing of fiber optics, the operating temperature of yield stress fluid plays a vital role. Several studies have been carried out to explain the convection heat transfer in viscoplastic fluid in different geometries [19–22]. However, the flow of the yield stress fluid through 180° sharp bend has not been addressed.

In this current work, numerical analysis of thermal and flow characteristics of viscoplastic fluid inside a rectangular duct having 180° sharp bend has been performed. The rheological behavior of yield stress fluid is assumed to be described by Herschel–Bulkley model.

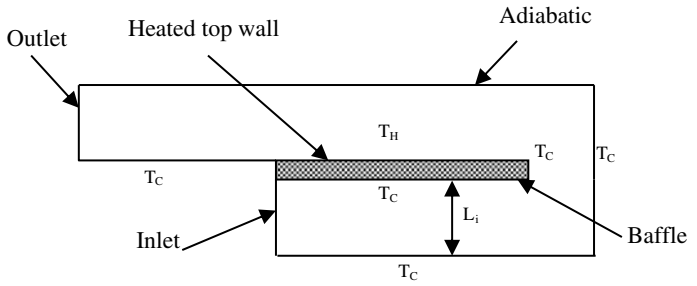

Fig. 1 Schematic diagram of square duct with sharp bend

2 Problem Formulation

The heat transfer and fluid flow inside a square duct having 180° sharp bend with top sided heated baffle have been studied numerically. Yield stress fluid enters in the square duct from its lower end then passes downstream through the sharp bend further allowed to flow over heated baffle and finally after heat interaction it exits from the upper end of the duct. The flow is assumed to be steady, laminar, incompressible and two dimensional. The flow is allowed to fully develop by providing long enough lower branch of the duct. The constitutive viscosity relation is assumed to comply with Herschel–Bulkley law. The schematic diagram of the computational domain is shown in Fig. 1. The topmost wall of the upper branch of the channel is presumed to be adiabatic, top surface of the baffle is kept at elevated temperature T_H, and rest of the walls have been kept isothermal at lowered temperature T_C. All thermo-physical properties except density are constant with temperature.

This numerical study of heat and fluid flow behavior has been carried out under different Reynolds number Re (10^2–10^4), Yield number Y_o (0.01–5) and IOR (1:2, 1:1.5, 1:1, 1.5:1, 2:1). Isotherms and streamlines have been plotted to explain the physics of fluid flow and heat transfer characteristics.

3 Governing Equations, Boundary Conditions and Solution Methodology

The governing equations for two dimensional, steady and laminar flow of yield stress fluid flow through inside a square duct with 180° sharp bend in non-dimensional form are as follows:

Continuity equation:

$$\frac{\partial U}{\partial X} + \frac{\partial U}{\partial Y} = 0 \tag{1}$$

Momentum equations:

$$U\frac{\partial U}{\partial X}+V\frac{\partial U}{\partial Y}=-\frac{\partial P}{\partial X}+\frac{1}{\mathrm{Re}}\frac{\partial}{\partial X}\left\{\tau_{xx}^{*}+\tau_{xy}^{*}\right\} \tag{2}$$

$$U\frac{\partial V}{\partial X}+V\frac{\partial V}{\partial Y}=-\frac{\partial P}{\partial Y}+\frac{1}{\mathrm{Re}}\frac{\partial}{\partial Y}\left\{\tau_{yx}^{*}+\tau_{yy}^{*}\right\}+g^{*} \tag{3}$$

Energy equation:

$$U\frac{\partial \theta}{\partial X}+V\frac{\partial \theta}{\partial Y}=\frac{1}{\mathrm{Re\,Pr}}\left\{\frac{\partial^{2}\theta}{\partial X^{2}}+\frac{\partial^{2}\theta}{\partial Y^{2}}\right\} \tag{4}$$

X and Y are the non-dimensional coordinates. U, V, θ and P are the non-dimensional x-velocity, y-velocity, temperature and pressure, respectively. Non-dimensionalization has been done by using inlet height L_i as characteristic length, free stream velocity u_∞ as characteristic velocity in the following manner:

$$X=\frac{x}{L_i},\ Y=\frac{y}{L_i},\ U=\frac{u}{u_\infty},\ V=\frac{v}{u_\infty},\ \theta=\frac{T-T_{\mathrm{C}}}{T_{\mathrm{H}}-T_{\mathrm{C}}},\ P=\frac{p}{\rho u_\infty^{2}},\ g^{*}=\frac{g}{u_\infty^{2}/L_i}$$

The non-dimensional numbers Reynolds number (Re) and Prandtl number (Pr) that appear in the governing equations can be defined as follows:

$$\mathrm{Re}=\frac{\rho u_\infty L_i}{\eta_{\mathrm{B}}}\quad\text{and}\quad\mathrm{Pr}=\frac{\eta_{\mathrm{B}}c_p}{k}$$

where $\eta_{\mathrm{B}}=K\dot{\gamma}^{n-1}$ is the plastic viscosity. Viscoplastic fluid having constant value of thermal conductivity $k=0.6$ W/m K has been selected. The rheological properties of the yield stress fluid are modeled by Herschel–Bulkley constitutive relation, and it can be written in dimensionless form as follows:

$$\left.\begin{array}{ll}\tau^{*}=\left[|\dot{\gamma}|^{n-1}+\frac{Y_o}{|\dot{\gamma}|}\right]\dot{\gamma} & \tau^{*}>Y_o\\ \dot{\gamma}=0 & \tau^{*}<Y_o\end{array}\right\} \tag{5}$$

where $\tau^{*}=\frac{\tau}{K(u_\infty/L_i)^{n}}$ and Y_o are the Yield number and are given by $Y_o=\frac{\tau_y L_i}{\eta_{\mathrm{B}}u_\infty}$

Negligible effect of temperature on yield stress fluid has been observed in an experimental study by Peixinho et al. [23], for a temperature range of 0–90 °C. Forrest and Wilkinson [24] observed an insignificant response of yield stress with temperature, as yield stress is mainly dependent on the mechanical locking of the fluid which is temperature independent. Therefore, the effects of temperature on viscosity and yield stress of Herschel–Bulkley fluid have been neglected in the present study.

The topmost wall of the upper channel is assumed to be adiabatic, top surface of the baffle is maintained at relatively higher temperature T_{H}, and the rest five walls of

the computational domain are isothermally cooled at constant temperature T_C. No slip condition has been applied on all walls of the square duct having sharp bend.

Boundary Conditions:

$$\text{Inlet} : U = 1, V = 0, \theta = 0, \frac{\partial P}{\partial n} = 0$$

$$\text{Outlet} : \frac{\partial U}{\partial X} = \frac{\partial V}{\partial X} = \frac{\partial \theta}{\partial X} = 0, P = 0$$

$$\text{Top surface of the baffle} : U = V = 0, \theta = 1, \frac{\partial P}{\partial n} = 0$$

$$\text{Top most wall of the duct} : U = V = 0, \frac{\partial \theta}{\partial n} = 0, \frac{\partial P}{\partial n} = 0$$

Solution Methodology:

The coupled equations of mass, momentum and energy together with boundary conditions have been solved numerically by commercially available finite volume code ANSYS FLUENT 17.0. The discretization of viscous and thermal diffusion terms has been achieved through central differencing scheme. Second-order upwind scheme is used to discretize the advection terms. Semi-Implicit Method for Pressure-Linked Equations (SIMPLE) algorithm has been adapted to achieve the coupling of pressure and velocity fields, which implicitly takes care of the divergence-free nature of incompressible fluid flow. The convergence criteria have been set to 10^{-6} for all the relative (scaled) residuals.

4 Results and Discussion

Herschel–Bulkley fluid is permitted to enter from lower part of the channel then it encounters a sharp bend, furthermore it flows over a heated top surface of the baffle and is finally allowed to exit from the upper channel of the computational domain. Fluid structures and heat flow characteristics of viscoplastic fluid flow in a square duct with 180° sharp bend have been studied numerically under different parameters. The important parameters are Reynolds number Re, Yield number Y_o, Prandtl number Pr, power law index n and inlet height to outlet height ratio IOR. This current investigation has been carried out for different values of Y_o, Re, IOR and heat input at a fixed value of Pr = 7.0.

4.1 Effect of Reynolds Number

Flow Characteristics: Reynolds number is a dimensionless number which represents the ratio of inertia forces to viscous forces. The flow pattern, whether it is laminar or turbulent, can be predicted by observing Reynolds number.

The contour plots of stream function for different Re ranging 10^2–10^4 for fixed values of $Y_o = 0.1$ and IOR $= 1$ have been depicted in Fig. 2. The expected flow separation at the corner of the baffle appears due to adverse pressure gradient. It is clearly shown that the strength of the vortices near the corner of the baffle in the upper part of the channel is augmented with Re, which indicates the rise in velocity.

The streamlines of vertical component of velocity are plotted for different Re which is in turn flow velocity at a fixed value of $Y_o = 0.1$ and IOR $= 1$ in Fig. 3. At the inlet, yield stress fluid is allowed to enter horizontally along the length of the lower channel of the duct. The vertical component of the velocity is observed only at the 180° sharp bend after which the direction of flow reverses. It is seen that this y-velocity component intensifies and sustains itself up to a relatively broader region with rise in Reynolds number as anticipated. Moreover, the position of maximum y-velocity shifts upward negligibly with rise in Re.

Flow separation appears near the sharp corner of the baffle, where fluid itself reattaches to the heated wall of the baffle. The degree of flow separation can be

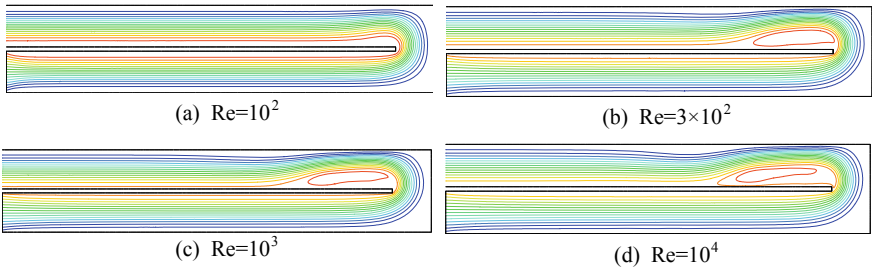

Fig. 2 Streamline for $Y_o = 0.1$, IOR $= 1$

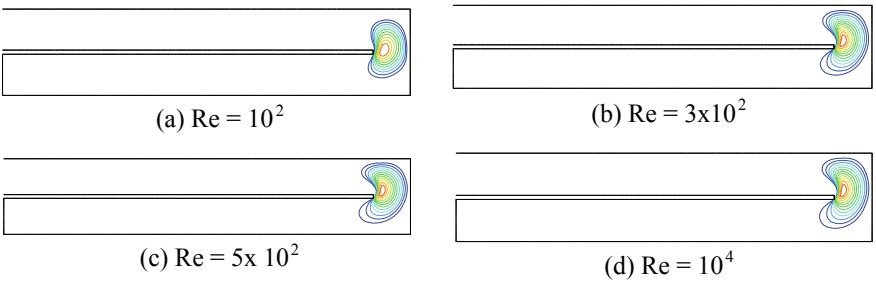

Fig. 3 Contour plot of y-velocity for $Y_o = 0.1$ and IOR $= 1$

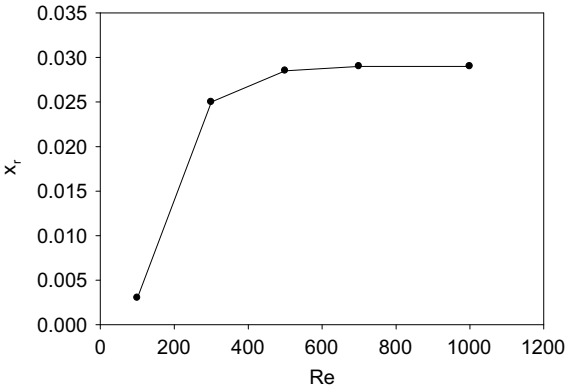

Fig. 4 Reattachment length for $Y_o = 0.1$ and IOR $= 1$

visualized through the investigation of reattachment length. The reattachment length as a function of Re is depicted in Fig. 4. As Re is increased, Herschel–Bulkley fluid reattaches itself at relatively larger length to the baffle. Furthermore, the curve is much steeper for lower value of Re, and it becomes almost horizontal at relatively higher Re as shown in Fig. 4. In other words, the reattachment length increases at a faster rate for lower Re in comparison with the higher values of Re.

Heat Transfer Characteristics: The rate of heat dissipation from the heater which is situated at the top surface of the baffle is achieved through the flow of the yield stress fluid in the present work. This heat dissipation can be analyzed by considering Nusselt number which can be viewed as the ratio of convective heat transfer to the conductive heat transfer. So, higher the Nusselt number, higher is the convective heat transfer which results in augmented rate of cooling.

To understand the effects of Re on the heat flow rate, distribution of Nu along the heater length has been depicted in Fig. 5. The flow enters at $x = 0.10$ of the upper part of the baffle. In Fig. 5, fluctuation of local Nusselt number can be seen for all values of Re > 100. For Re = 100, the distribution of Nu along the heater is almost

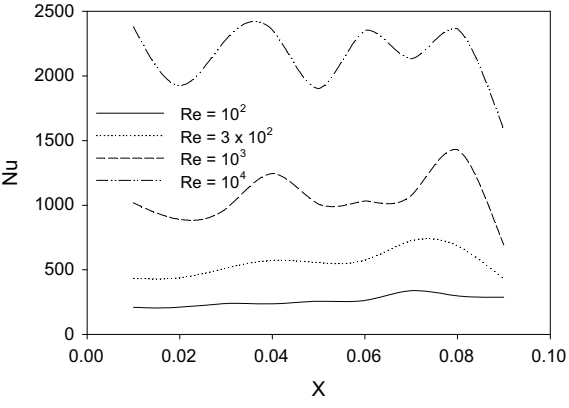

Fig. 5 Variation of Nu along the heated wall at IOR $= 1$, $Y_o = 0.1$

linear. Furthermore, these fluctuations become more pronounced for higher values of Re as can be seen in Fig. 5 (for $\mathrm{Re} = 10^4$). The increasing value of averaged Nu is observed with rise in Re. It is a known fact that the advection of heat rises with increase in velocity of fluid, and hence, Nu increases with rise in Re as suggested by numerical results.

4.2 *Effect of Yield Stress*

Flow characteristics: As it is earlier mentioned that viscoplastic fluids are that class of fluids which need a shear stress more than the critical value called yield stress to flow, and otherwise it behaves as a solid. In other words, yield stress is a characteristic of the viscoplastic fluid that governs the flowability of yield stress fluid. Lower yield stress corresponds to enhanced flowabilty in the fluid. The non-dimensional parameter Yield number is appropriately selected in such a manner that yield stress is directly proportional to it.

In attempt to find out the impact of yield stress on flow structures, several numerical simulations have been performed for different Yield number while keeping other parameters constant. The results of contour plot of stream function for carefully chosen different yield numbers ranging from 0.01 to 5 at a particular value of other parameters $\mathrm{Re} = 10^3$ and $\mathrm{IOR} = 1$ are sketched in Fig. 6. It can be seen that the vortices appear with greater intensity for the lowest selected value of Yield number ($Y_o = 0.01$). Moreover, it still appears up to $Y_o = 0.15$ but with lesser intensity, and ultimately it completely disappears for relatively higher values of Yield number. It

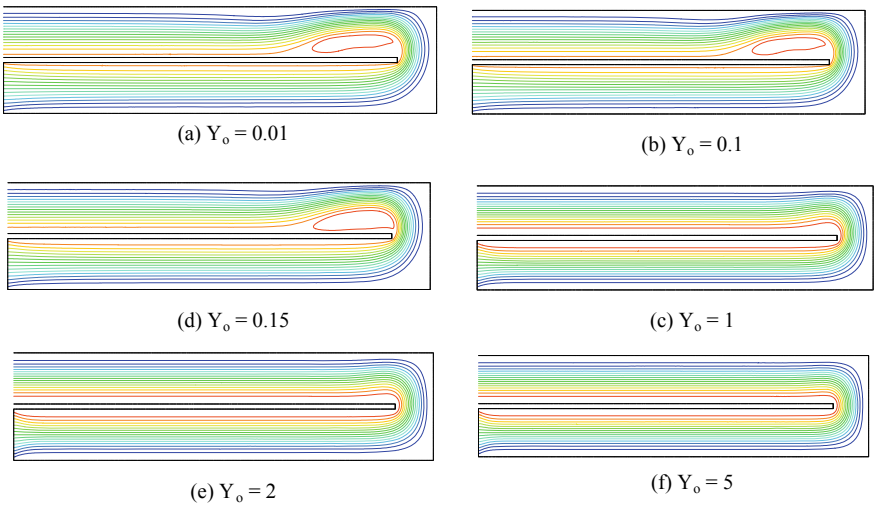

Fig. 6 Streamline for $\mathrm{Re} = 10^3$, $\mathrm{IOR} = 1$

is earlier stated that the yield stress, which is directly proportional to Yield number, mainly depends on the mechanical locking of fluid particles, and hence, it suppresses both the bulk fluid flow and the disturbances or fluctuations arising during the flow of viscoplastic fluids. So, it can be interpreted that with rise in Yield number, i.e., yield stress the suppressing ability of generated eddies within the fluid particles enhances, and therefore, the strength of vortices, that are emanated at the sharp corner of the baffle, continuously dies with increase in Yield number.

To further comprehend the dependency of flow structures on yield stress, another contour plot of vertical component of velocity for different Yield numbers ($Y_o = 0.01, 0.1, 0.15, 1, 2, 5$) has been depicted at a fixed value of $\mathrm{Re} = 10^3$ and $\mathrm{IOR} = 1$ in Fig. 7. It is seen that the y-velocity can be sensed to a farther region for the lower value of Y_o rather than the higher values. Furthermore, greater value of vertical component of velocity is observed for lower magnitude of Yield number and vice versa. The anticipated results of numerical simulations can be explained as it is earlier discussed that the flowability of fluid increases with fall in yield stress in turn Yield number. Therefore, fall in Yield number results in both larger strength and region of existence for y-velocity component near the corner of the baffle.

A plot between reattachment length and Y_o is shown in Fig. 8 in which Re and IOR are maintained at a fixed value. It is clearly seen that the reattachment length decreases with rise in Yield number. It may be explained as rise in Yield number means fall in flowability of the viscoplastic fluids, and hence, lower value of reattachment length.

Heat transfer characteristics: It is earlier stated that lower value of Yield number corresponds to higher ability to flow for viscoplastic fluids. Therefore, convective heat transfer enhances which in turn increases the Nusselt number as depicted in Fig. 9. The highest value of both local and average Nu is observed for the lowest $Y_o = 0.05$.

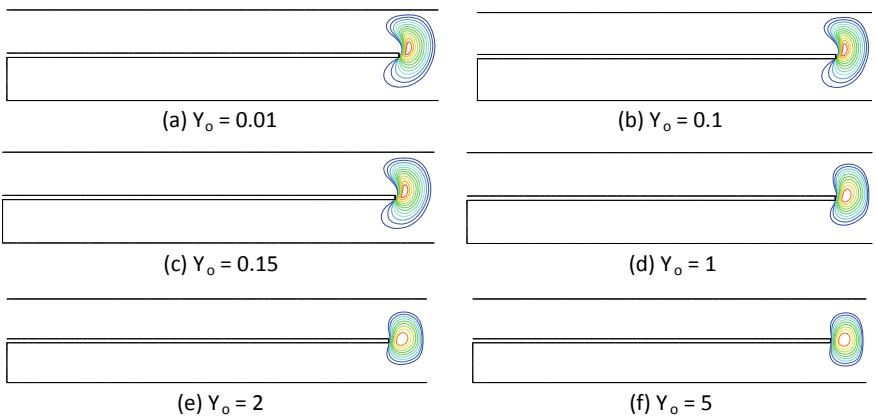

Fig. 7 Contour plot of y-velocity for $\mathrm{IOR} = 1$, and $\mathrm{Re} = 10^3$

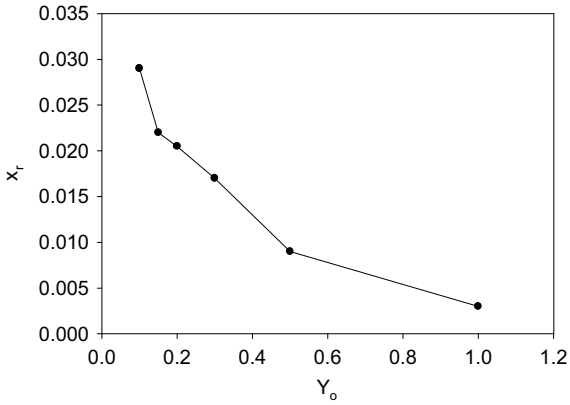

Fig. 8 Reattachment length for $\mathrm{Re} = 10^3$ and $\mathrm{IOR} = 1$

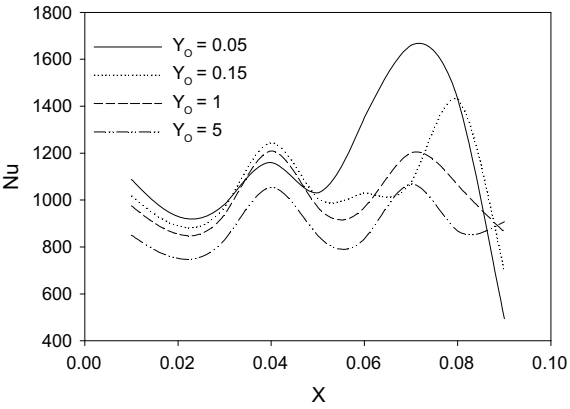

Fig. 9 Distribution of Nu along the heated wall

4.3 Effect of IOR

Flow characteristics: Several numerical simulations of the viscoplastic fluid flow inside the square duct have been performed to realize the effects of IOR on the flow structures and heat transfer. So, at a fixed value of $\mathrm{Re} = 10^3$ and $Y_o = 0.1$, numerical investigation is carried out and contour plot of stream function is depicted in Fig. 10 for different values of IOR. When $\mathrm{IOR} \leq 1$, vortices appear at the corner of the baffle while for $\mathrm{IOR} > 1$, they disappear altogether for the carefully selected values of other parameters as shown in Fig. 10. Furthermore, it is observed that the vortices, emanating from the corner of the baffle, are intensified as IOR decreases. The disturbances in the flow are generated through sharp bending, and it gets dissipated by the damping viscous forces. As IOR decreases, there is increase in height of the outlet branch which results in higher intensity of the inertia forces. Hence, vortices are observed and also they become more vibrant for the lower value of IOR. On the

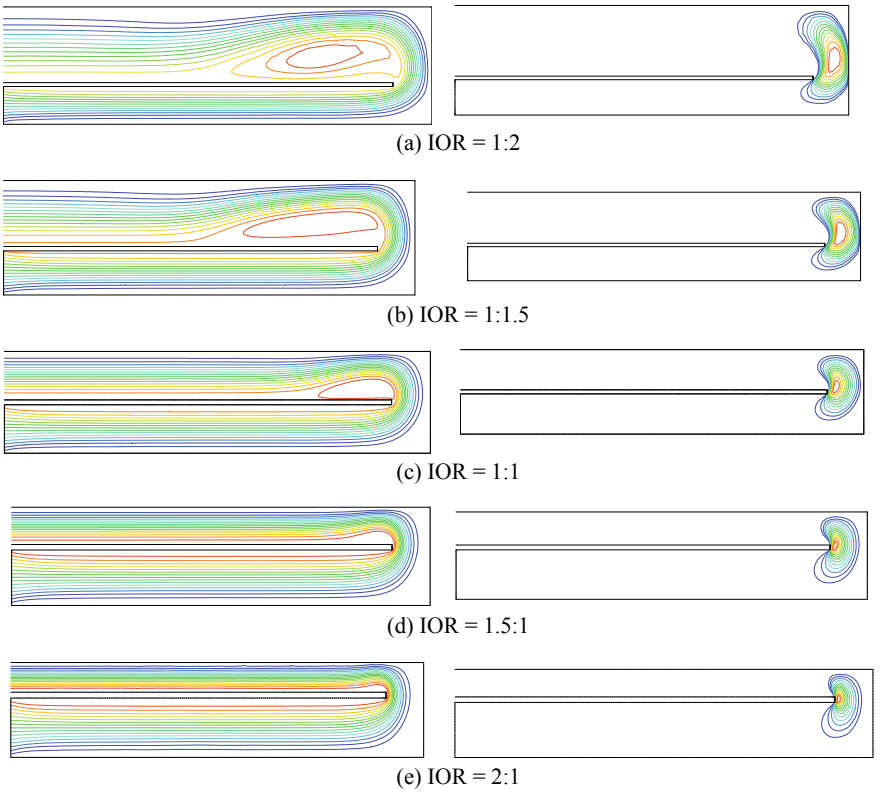

Fig. 10 Streamline for Re $= 10^3$, $Y_o = 0.1$ (Left). Contour plot of y-velocity for Re $= 10^3$, and $Y_o = 0.1$ (Right)

other hand, the vortex structure does not appear for the higher values of IOR which may be due to the weakening of inertia forces in comparison with viscous forces.

Figure 10 shows the contour plot of vertical component of velocity for different IOR for fixed value of Re and Y_o. It appears only at the bend section near the baffle corner where the flow reverses its direction. The region of y-velocity increases with increase in height of upper duct, i.e., with decrease in IOR. The region of maximum y-velocity also shifts toward the baffle corner as IOR increases.

The reattachment length for a fluid moving in a square upper duct increases with increase in its width, in other words reattachment length rises with fall in IOR as shown in Fig. 11. It may be due to the increased height of the duct which allows the incoming fluid from the lower portion of square duct to move more freely in vertical direction.

Heat Transfer Characteristics: Fig. 12 shows the distribution of Nu along the length of the heater for different IOR at fixed Re and Y_o. The lowest local and average Nu appear for IOR = 1:2 and the maximum for IOR = 1:1. With decrease in

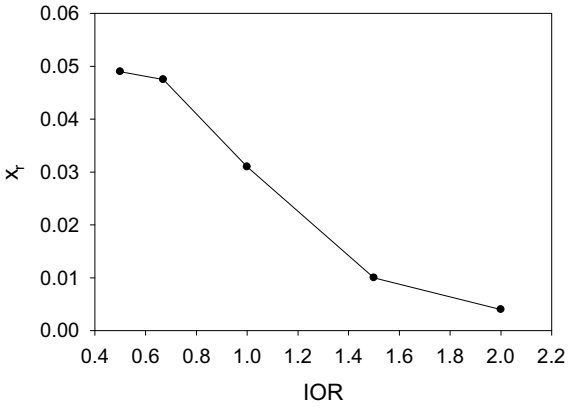

Fig. 11 Reattachment length for Re $= 10^3$ and $Y_o = 0.1$

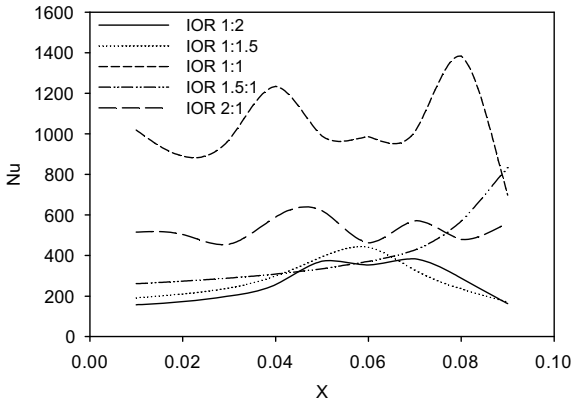

Fig. 12 Variation of Nu with IOR for Re $= 10^3$, $Y_o = 0.1$

the height of the upper duct, the degree of mixing of the fluid particles discourages, and hence, heat transfer.

5 Conclusions

The numerical study of fluid and heat flow for viscoplastic fluids inside a square duct having 180° sharp bend has been conducted. The effects of Re, Y_o and IOR have been investigated. The strong dependency of heat transfer on flow characteristics is illustrated. The maximum heat dissipation rate in present work is found to be at maximum Re, lowest Y_o and IOR $= 1$.

Acknowledgements The corresponding author *(M. A. Hassan)* is thankful to SERB, Department of Science and Technology, Government of India for support grant vide File number *ECR/2017/001003*.

References

1. Mochizukia S, Murataa A, Shibata R, Wang J (1999) Detailed measurements of local heat transfer coefficients in turbulent flow through smooth and rib-roughened serpentine passages with a 180° sharp bend. Int J Heat Mass Transf 42:1925–1934
2. Hirota M, Fujita H, Syuhada A, Araki S, Yoshida T, Tanaka T (1999) Heat/mass transfer characteristics in two-pass smooth channels with sharp 180-deg turn. Int J Heat Mass Transfer 42:3757–3770
3. Chung YM, Tucker PG, Roychowdhury DG (2003) Unsteady laminar flow and convective heat transfer in a sharp 180 bend. Int J Heat Fluid Flow 24:67–76
4. Wang TS, Chyu MK (1994) Heat convection in a 180-deg turning duct with different turn configurations. J Thermophy Heat Transf 8:595–601
5. Dhanasekaran TS, Wang T (2012) Numerical model validation and prediction of mist/steam cooling in a 180° bend tube. Int J Heat Mass Transf 55:3818–3828
6. Robson GR (1967) Thickness of Etnean lava. Nature 216:251–252
7. Johnson AM (1970) Physical processes in geology. Freeman Cooper, San Francisco
8. Hulme G (1974) The interpretation of lava flow morphology. Geophys J R Astr Soc 39:361–383
9. Bird RB, Dai GC, Yarusso BJ (1983) The rheology and flow of viscoplastic materials. Rev Chem Eng 1:1–70
10. Ancey C (2007) Plasticity and geophysical flows. J Non-Newtonian Fluid Mech 142:4–35
11. Coussot P (2014) Yield stress fluid flows: a review of experimental data. J Non-Newtonian Fluid Mech 211:31–49
12. Balmforth NJ, Frigaard IA, Ovarlez G (2014) Yielding to stress: recent developments in viscoplastic fluid mechanics. Annu Rev Fluid Mech 46:21–46
13. Mitsoulis E (2007) Flow of viscoplastic materials: model and computations. Rheol Rev 135:135–178
14. Taylor AJ, Wilson SDR (1997) Conduit flow of an incompressible. Yield-Stress Fluid J Rheol 41:93–101
15. Thong VP, Mitsoulis E (1998) Viscoplastic flows in ducts. The Can J Chem Eng 76:120–125
16. Moyers-Gonzalez MA, Frigaard IA (2004) Numerical solution of duct flows of multiple viscoplastic fluids. J Non-Newtonian Fluid Mech 122:227–241
17. Damianou Y, Kaoullas G, Georgiou GC (2016) Cessation of viscoplastic Poiseuille flow in a square duct with wall slip. J Non-Newtonian Fluid Mech 233:13–26
18. Muravleva EA, Muravleva LV (2009) Unsteady flows of a viscoplastic medium in channels. Mech Solids 44:792–812
19. Vola D, Boscardin L, Latche JC (2003) Laminar unsteady flows of Bingham fluids: a numerical strategy and some benchmark results. J Comput Phys 187:441–456
20. Hassan MA, Pathak M, Khan MK (2013) Natural convection of viscoplastic fluids in a square enclosure. ASME J Heat Transf 135:122501
21. Darbouli M (2013) Rayleigh-Bénard convection for viscoplastic fluids. Phys Fluids 25(2):023101
22. Karimfazli I, Frigaard IA, Wachs A (2016) Thermal plumes in viscoplastic fluids: flow onset and development. J Fluid Mech 787:474–507
23. Peixinho J, Desaubry C, Lebouche M (2008) Heat transfer of a non-Newtonian fluid in transitional pipe flow. Int J Heat Mass Transf 51:198–209
24. Forrest G, Wilkinson WL (1973) Laminar heat transfer to temperature-dependent Bingham fluids in tubes. Int J Heat Mass Transf 16:2377–2391

Performance Analysis of Temperature and MRR Using High-Speed Micro-Drilling on Incoloy 800 Superalloy

T. Venkatesan, J. Jerald and P. Asokan

Abstract Micro-drilling is one of the advanced levels of metal cutting processes in the manufacturing and assembly industry, thereby producing micro-holes with higher depth, greater surface finish and better-quality of roundness. In this research work, micro-drilling has been done on Incoloy 800 which is an iron-based superalloy which has good resistance to corrosion, oxidation at higher temperature and is used in various equipments like superheaters, pressure vessels, heat exchangers, etc. The temperature and material removal rate (MRR) are analysed by varying the processes parameters like diameter of the tool, spindle speed and feed as per Taguchi L_{27} orthogonal array design. From this experiment, it is found that MRR and temperature increase with the increase in feed and speed of spindle. The results obtained by the experiments are optimized by using grey relational analysis (GRA).

Keywords Micro-drilling · Material removal rate · Temperature · Grey relational analysis

1 Introduction

Micro-drilling is one of the developing fields in manufacturing and assembly of many miniature parts and products. Gupta et al. [1] have done a research work on various work material such as printed circuit board, mild steel and alloys of aluminium to find the best combination of the processes parameters. Redzuan and Kurniawan [2] have done an experiment by using spindle speed, feed and depth of drilling as input parameters. The roundness of the hole is measured. From the results, it is found that the roundness is affected by spindle speed and feed. Rahman et al. [3] used HSS drilling tool to find the role of speed of the spindle and feed on surface roughness by

T. Venkatesan (✉) · J. Jerald · P. Asokan
Department of Production Engineering, National Institute of Technology, Tiruchirappalli, Tiruchirappalli 620015, India
e-mail: venkatesan_st74@yahoo.com

H. Kumar and P. K. Jain (eds.), *Recent Advances in Mechanical Engineering*,
Lecture Notes in Mechanical Engineering,
https://doi.org/10.1007/978-981-15-1071-7_26

changing the processes parameters like tool diameter, spindle speed and feed. It was found that when the spindle speed and feed rate are increased, the surface roughness is decreased. Sivasankar et al. [4] studied a simple and efficient methodology and algorithms to evaluate the surface roughness, waviness and roundness. Roughness is measured using arithmetic deviation of the roughness and peak to peak height. Waviness is measured using waviness step height. These parameters were measured and studied using video measuring machine and image processing technology. Jindal [5] have conducted a micro-drilling experiment by using high-speed air spindle, and the holes are drilled by peck drilling method. It is recorded from the results that the feed rate is the main factor considered for micro-drilling. The removal of the burr from the drilled hole is a difficult one. Bhandari et al. [6] used a control chart for burr formation in drilling of PCB by using L9 orthogonal array. In the experiment, twist drills of tungsten carbide with HSS shank are used with three different tool diameters. The removal of the burrs obtained at the exit of the micro-holes plays an important role in the quality of the parts during assembly. Kim et al. [7] conducted and experimented for preventing the exit burr by applying metal foil to the exit of the micro-hole. In this experiment, by using cyanoacrylate adhesive with copy paper and metal foil, a low hardness material was used. Xavier and Elangovan [8] a have conducted an experiment to control the ship size and easy removal of chips without damaging the walls of the hole. Iwata et al. [9] had conducted micro-drilling experiments using two different types of machine and measured the quality of the hole. It is recorded that at higher speed of the spindle, the hole surface finish is high. Lin et al. [10] has monitored the failure of the micro-tool by considering the thrust force and current by using drill diameter varying from 0.1 to 0.3 mm on stainless steel plate. The thrust force is measured with the help of dynamometer. In this study, it is found that thrust is most important in detecting the tool breakage. It is understood from the review of literature that a limited number of research works have been done in the area of micro-drilling of superalloys.

2 Experimental Setup and Procedure

Micro-holes are drilled on Incoloy 800 work material by using DT 110-Multi-Process Micro-Machining Centre (Make: M/s. Mikro-Tools Pvt. Ltd., Singapore) which is a 3-axis machine. The micro-holes were drilled by tungsten carbide drill bit at higher speeds ranging from 16,000 to 26,000 rpm. The work material Incoloy 800 is fixed on the table with the help of a fixture. The size of the workpiece is 22 × 22 mm with a thickness of 2 mm. The temperature produced during the micro-drilling is measured by using infrared thermometer. The experiment setup is shown in Fig. 1

The main objective of this work is to maximize MRR, So that the production cost of small components is reduced and minimizes temperature produced during drilling of micro-holes on the work material which will reduce the wear of the tool

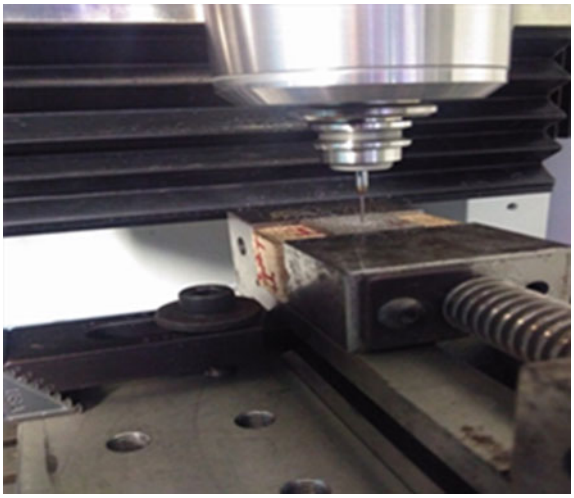

Fig. 1 Micro-drilling setup

Table 1 Parameter table

Processes parameters	Levels
Tool diameter	400, 600 and 800 μm
Speed of the spindle	16,000, 21,000 and 26,000 rpm
Feed	1, 2 and 3 mm/min

bit and improve the surface finish of the holes. Micro-drilling is done by changing the processes parameters such as tool diameter, feed and spindle speed. The levels of the processes variables are given in Table 1. During the experiment, one of the process variables is kept constant and the other parameters are changed as per the Taguchi L9 orthogonal array design. Taguchi L27 orthogonal array design is shown in Table 2.

Chemical composition of work material (Incoloy 800)

Elements	C	Al	Si	P	S	Ti	Cr	Mn	Fe	Ni	Cu
Composition (wt%)	0.02	0.11	0.48	0.009	0.004	0.29	21.5	0.47	46.3	30.9	0.01

3 Results and Discussion

In this section, the effect of the processes parameters on temperature and material removal rate are discussed based on the ANOVA analysis.

Table 2 L_{27} orthogonal array design table

S. No.	Tool dia (μm)	Feed (mm/min)	Speed (rpm)	Temperature (°C)	MRR (mm^3/min)
1	400	1	16,000	27.6	0.002
2	400	1	21,000	27.7	0.005
3	400	1	26,000	27.8	0.006
4	400	2	16,000	27.1	0.008
5	400	2	21,000	27.6	0.01
6	400	2	26,000	28.1	0.011
7	400	3	16,000	27.9	0.02
8	400	3	21,000	28.4	0.02
9	400	3	26,000	29.1	0.022
10	600	1	16,000	27.2	0.027
11	600	1	21,000	28.2	0.028
12	600	1	26,000	29.3	0.03
13	600	2	16,000	27.1	0.029
14	600	2	21,000	29.3	0.031
15	600	2	26,000	29.9	0.041
16	600	3	16,000	29.7	0.042
17	600	3	21,000	29.7	0.044
18	600	3	26,000	30.3	0.05
19	800	1	16,000	28.2	0.049
20	800	1	21,000	28.7	0.047
21	800	1	26,000	30.7	0.055
22	800	2	16,000	30.5	0.058
23	800	2	21,000	30.5	0.062
24	800	2	26,000	30.9	0.068
25	800	3	16,000	31.2	0.07
26	800	3	21,000	31.5	0.073
27	800	3	26,000	33.1	0.078

3.1 Temperature

Temperature obtained during micro-drilling is a vital factor which affects the drill bit tip and also the surface of the hole wall. It is found that the value of temperature is increasing for increasing value of tool diameter, feed and spindle speed. The results as per ANOVA are given in Table 3. It is noted that from the ANOVA table, the calculated value of "*F*" for tool diameter is 46.05 which is higher than the table value of "*F*", so tool diameter is more significant. The performance of temperature on different process parameters is given in Fig. 2.

Table 3 ANOVA for temperature

Source	DF	SS	MS	*F* cal	*F* tab
Tool dia	2	32.5007	16.2504	46.05	4.46
Feed	2	13.6896	6.8448	19.40	4.46
Speed	2	9.0763	4.5381	12.86	4.46
Tool dia * feed	4	3.2215	0.8054	2.28	3.84
Tool dia * speed	4	1.3815	0.3454	0.98	3.84
Feed * speed	4	0.4526	0.1131	0.32	3.84
Error	8	2.8230	0.3529		
Total	26	63.1452			

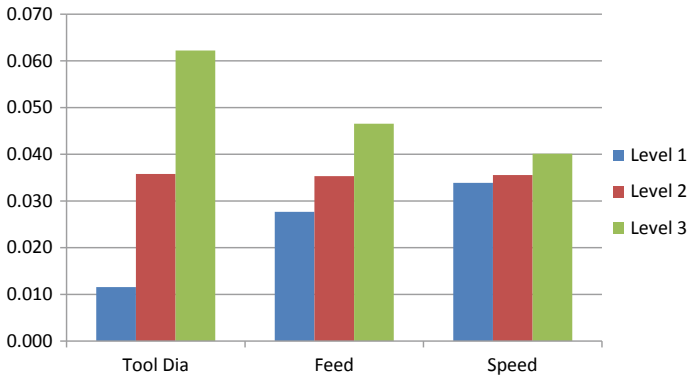

Fig. 2 Performance of temperature on process parameters

3.2 Material Removal Rate (MRR)

The spindle speed and feed play a major role in machining time. If there is increase in the feed rate and spindle speed, the time required to finish the micro-hole is less. The results as per ANOVA are given in Table 4. It is noted that from the ANOVA table, the calculated value of "*F*" for tool diameter is 1788.56 which is higher than the table value of "*F*", so tool diameter is more significant. The effect of MRR on various processes parameters is given in Fig. 3.

3.3 Grey Relational Analysis

In this work, grey relational analysis (GRA) is used to find the best combination of the processes parameters. According to this work, the machining time should be less

Table 4 ANOVA for material removal rate

Source	DF	SS	MS	F cal	F tab
Tool dia	2	0.01155941	0.00577970	1788.56	4.46
Feed	2	0.00162452	0.00081226	251.36	4.46
Speed	2	0.00018674	0.0009337	28.89	4.46
Tool dia * feed	4	0.00006281	0.00001570	4.86	3.84
Tool dia * speed	4	0.00003126	0.00000781	2.42	3.84
Feed * speed	4	0.00001215	0.00000304	0.94	3.84
Error	8	0.00002585	0.00000323		
Total	26	0.01350274			

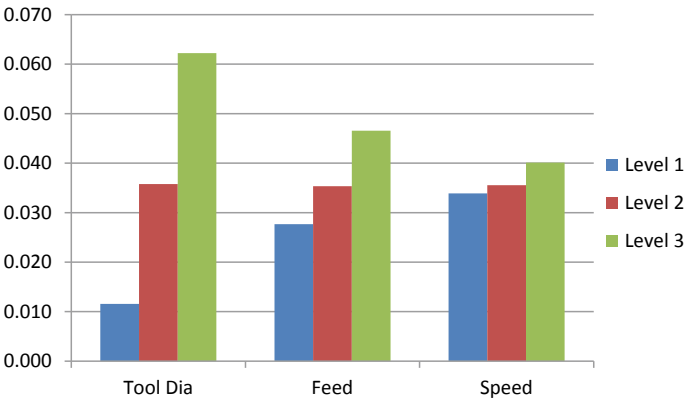

Fig. 3 Performance of MRR on process parameters

and the material removal rate must be high. To find the "larger-the-better" response parameter MRR, the following equation is used for calculating normalized value [10].

$$x_i^*(\mathrm{k}) = \frac{x_i^*(k) - \min x_i^0(k)}{\max x_i^0(k) - \min x_i^0(k)}$$

where $X_i(k)$ is sequence of data premerger. $K = 1$ for MRR; $i = 1, 2, \ldots, 9$ number of experiments. For "smaller-the-better" response parameter machining time, the following equation is used for calculating normalized value.

$$x_i^*(k) = \frac{\max x_i^*(k) - x_i^0(k)}{\max x_i^0(k) - \min x_i^0(k)}$$

The grey relational coefficient $\xi(k)$ is calculated by using the following equation

$$\xi(k) = \frac{\Delta_{\min} + \xi \cdot \Delta_{\max}}{\Delta_{0i}(k) + \xi \cdot \Delta_{\max}}$$

Table 5 shows the normalization values, grey relational coefficient and grey relational grade values for the response parameters temperature and material removal rate.

The best combination of processes parameters is obtained from the grey relational grade values for the response values temperature and material removal rate as per the table. The best combination obtained from grey relational analysis is given in Table 6.

Table 5 GRA readings

S. No.	Normalization		Sequ normal		GRC		GRG	Rank
	Temp	MRR	Temp	MRR	Temp	MRR		
1	0.9167	0.0000	0.0833	1.0000	0.8571	0.3333	0.5952	11
2	0.9000	0.0395	0.1000	0.9605	0.8333	0.3423	0.5878	13
3	0.8833	0.0526	0.1167	0.9474	0.8108	0.3455	0.5781	16
4	1.0000	0.0789	0.0000	0.9211	1.0000	0.3519	0.6759	3
5	0.9167	0.1053	0.0833	0.8947	0.8571	0.3585	0.6078	9
6	0.8333	0.1184	0.1667	0.8816	0.7500	0.3619	0.5560	18
7	0.8667	0.2368	0.1333	0.7632	0.7895	0.3958	0.5927	12
8	0.7833	0.2368	0.2167	0.7632	0.6977	0.3958	0.5468	19
9	0.6667	0.2632	0.3333	0.7368	0.6000	0.4043	0.5021	27
10	0.9833	0.3289	0.0167	0.6711	0.9677	0.4270	0.6974	2
11	0.8167	0.3421	0.1833	0.6579	0.7317	0.4318	0.5818	15
12	0.6333	0.3684	0.3667	0.6316	0.5769	0.4419	0.5094	26
13	1.0000	0.3553	0.0000	0.6447	1.0000	0.4368	0.7184	1
14	0.6333	0.3816	0.3667	0.6184	0.5769	0.4471	0.5120	24
15	0.5333	0.5132	0.4667	0.4868	0.5172	0.5067	0.5120	25
16	0.5667	0.5263	0.4333	0.4737	0.5357	0.5135	0.5246	23
17	0.5667	0.5526	0.4333	0.4474	0.5357	0.5278	0.5317	21
18	0.4667	0.6316	0.5333	0.3684	0.4839	0.5758	0.5298	22
19	0.8167	0.6184	0.1833	0.3816	0.7317	0.5672	0.6494	5
20	0.7333	0.5921	0.2667	0.4079	0.6522	0.5507	0.6014	10
21	0.4000	0.6974	0.6000	0.3026	0.4545	0.6230	0.5387	20
22	0.4333	0.7368	0.5667	0.2632	0.4688	0.6552	0.5620	17
23	0.4333	0.7895	0.5667	0.2105	0.4688	0.7037	0.5862	14
24	0.3667	0.8684	0.6333	0.1316	0.4412	0.7917	0.6164	8
25	0.3167	0.8947	0.6833	0.1053	0.4225	0.8261	0.6243	7
26	0.2667	0.9342	0.7333	0.0658	0.4054	0.8837	0.6446	6
27	0.0000	1.0000	1.0000	0.0000	0.3333	1.0000	0.6667	4

Table 6 Best combination

Tool diameter	600 (μm)
Feed	2 (mm/min)
Spindle speed	16,000 (rpm)

4 Conclusions

From this work, micro-holes were drilled on Incoloy 800 and the process parameters like tool diameter, spindle speed and feed rate were varied as per Taguchi's L_{27} orthogonal design and the following conclusions have arrived.

- It is recorded from the experiments temperature increases when the values of tool diameter, feed rate and spindle speed are increased.
- From ANOVA results, it is noted that tool diameter is influencing more on the temperature, which has a higher value of "*F*" than the table value.
- From the results, it is found that for increasing values of speed and feed, the material removal rate is increased. This is because the tool moves faster in the cutting direction.
- Tool diameter plays major role in material removal rate, and it has a higher calculated "*F*" value than the table value.

References

1. Gupta KK, Jain T, Deshmukh M (2013) Optimization of process parameters in high rpm micro drilling machine. Int J Innov Eng Technol 2:128–130
2. Redzuan N, Kurniawan D et al (2015) Evaluation of hole quality on microdrilling AISI304 austenitic stainless steel. Procedia Manuf 2:465–469
3. Rahman AA, Mamat A, Wagiman A (2009) Effect of machining parameters on hole quality of micro drilling for brass. Mod Appl Sci 3:221
4. Sivasankar S, Jeyapaul R, Kolappan S (2012) Procedural study for roughness, roundness and waviness measurement of EDM drilled holes using image processing technology. Comput Model Inf Process 16:49–63
5. Jindal A (2010) Experimental Investigation of process and response parameters in micro drilling using scanning electron microscope (SEM)
6. Bhandari B, Hong Y-S, Yoon H-S et al (2014) Development of a micro-drilling burr-control chart for PCB drilling. Precis Eng 38:221–229
7. Kim DW, Lee YS, Chu CN, Oh YT (2006) Prevention of exit burr in micro drilling of metal foils by using a cyanoacrylate adhesive. Int J of Adv Manuf Tech 27:1071–1076
8. Xavier LF, Elangovan D (2013) Effective parameters for improving deep hole drilling process by conventional method—a review. Intl J of Eng Res Tech 2:1
9. Iwata K, Moriwaki T, Hoshi T (1981) Basic study of high speed micro deep drilling. CIRP Ann Manuf Technol 30:27–30
10. Lin CL, Lin JL, Ko TC (2002) Optimisation of the EDM process based on the orthogonal array with fuzzy logic and grey relational analysis method. Int J Adv Manuf Technol 19:271–277

Design and Development of Zirconia-Dolerite Ball Plate for Error Mapping of Probe-Type Coordinate Measuring Machine

Vinay A. Kulkarni and B. B. Ahuja

Abstract Improved zirconia-dolerite ball plate is produced and calibrated depicting higher compactness, higher flexural strength, less weight with possibility of manual movement, enabling maximum parameter evaluation with respect to measuring volume periodic and interim checks at considerable lesser time. The manufactured ball plate shows considerable stability even at higher operating temperature of 24 °C with a maximum deviation of 4.1 μm with an average stability of 1.503 μm within the distinct-placed zirconia balls.

Keywords Metrology · CMM · Zirconia balls · Dolerite plate · Thermal stability

1 Introduction

As defined by IS 15635 Part–I: 2006, ISO 10360-1:2000 defines coordinate measuring machine (CMM) as a measuring system that provides movement to probing system and capability to measure spatial coordinates on job surface. CMM allows productive measurement of 3D components by collecting measurement data of geometrical points. The number of factors, like sampling strategy, rigid body errors, environmental conditions, dynamic errors, strategy of sampling, errors of probing, algorithms of fitments, affects accuracy by CMM measurement. Due to varying application requirements of CMM usage, manufacturers find it difficult to specify uncertainty precisely, before the measurement task on priority. Two levels of complexity and two levels of time intervals define verification of CMM performance. The

V. A. Kulkarni (✉)
Mechanical Engineering Department, DY Patil College of Engineering, Akurdi, Pune 411033, India
e-mail: kulkarnivinay@rediffmail.com

Savitribai Phule Pune University, Pune, India

B. B. Ahuja
Director and Professor, Production Engineering & Industrial Management, College of Engineering, Pune 411005, India
e-mail: bba.prod@coep.ac.in

H. Kumar and P. K. Jain (eds.), *Recent Advances in Mechanical Engineering*,
Lecture Notes in Mechanical Engineering,
https://doi.org/10.1007/978-981-15-1071-7_27

yearly cycle is the primary calibration of CMM which is annually adjusted enabling calibration results within the classification of equipment [1]. After the probe has been triggered, errors mapped in CMMs correct the noted point coordinates. Due to the absence of probe triggering event, retroreflector in RAM does not report the corrected coordinates. For such type of CMMs, instead of desired measuring accuracy, interferometer evaluation reports CMM's position accuracy. Non-vector-driven CMMs, which cannot move simultaneous three-axes, laser interferometer measurements, are difficult and slow. This capability requires during volumetric measurement. Apart from this technical requirement, ISO 10360-2 recommends the use of physical artefact as standard performance of evaluation [2]. To overcome the difficulty of measurement accuracy and not just positional accuracy of CMM, national and international standards are regularly developed and improved. Various designed artefacts are designed and manufactured along with special tests. More accurate CMM thus depends on higher degree of accurate artefacts featuring lower cost of interim checking or calibration [3]. Single, simplified artefact can be used with various orientations and locations to enhance calibration result. This approach yields similar result as that of simulation and experiments resulted by 3D artefact.

2 Geometrical Errors Affecting CMM Performance

A point is an adequate artefact, indicating similarities out of 3D space in measurement out of discrete point. Therefore, sphere is an effective artefact of the purpose of evaluation of CMM performance and reference points can be the centre of spheres [4].

ISO 230-2 defines 21 geometrical errors affecting performance of CMM as per Table 1.

ISO 10360 series contain tests with varying concepts of error measurements for CMM. Ball plate artefact enables determination of all X, Y and Z position error components, measuring entire workspace for the reference location as needed.

Artefact that replicates the workpiece orientation and geometry, repetitive measurement by it, enables to measure sampling error by CMM, capable of equivalent with traceable standards [5, 6].

As the probing spheres are provided by ball plate, it is a well-known artefact for calibration of CMMs or interim checks [7].

T. Liebrich, B. Bringmann et al. presented 2D ball plate that needs to be located by a kinematic correct coupling on a spacer or base plate [8]. P. Ramum, J. A. Ygu, R. J. Hocken, J. Miller explained the implementation of measurement procedure of the calibrated artefact for parametric errors [9]. B. Bringmann, A. Kung developed a 2D ball plate which can be shifted square to the plate (Fig. 1).

An attempt is made in this paper to design and develop a improved and stable zirconia-dolerite ball plate, having low coefficient of thermal expansion, scratch

Table 1 21 Geometrical errors affecting CMM performance

S. No.	Description	*X*-axis	*Y*-axis	*Z*-axis
1	Linear displacement errors	$\delta x(x)$	$\delta y(y)$	$\delta z(z)$
2	Vertical straightness errors	$\delta y(x)$	$\delta x(y)$	$\delta x(z)$
3	Horizontal straightness errors	$\delta z(x)$	$\delta z(y)$	$\delta y(z)$
4	Roll angular errors	εx(x)	$\varepsilon y(y)$	$\varepsilon z(z)$
5	Pitch angular errors	$\varepsilon y(x)$	$\varepsilon z(y)$	$\varepsilon x(z)$
6	Yaw angular errors	$\varepsilon z(x)$	$\varepsilon x(y)$	$\varepsilon y(z)$
7	Squareness errors	Sxy	Syz	Szx
δ—Linear error, subscript is error direction, ( ) is position coordinate				
ε—Angular error, subscript is angular error, ( ) is position coordinate				
Pitch—vertical up and down ↕	Yaw—horizontal left and right ↔	Roll—self-rotation around the axis ↻		

The measurement of these geometric errors will enable mathematical modelling required to be individually characterized by different CMMs due to different motions available for different CMMs

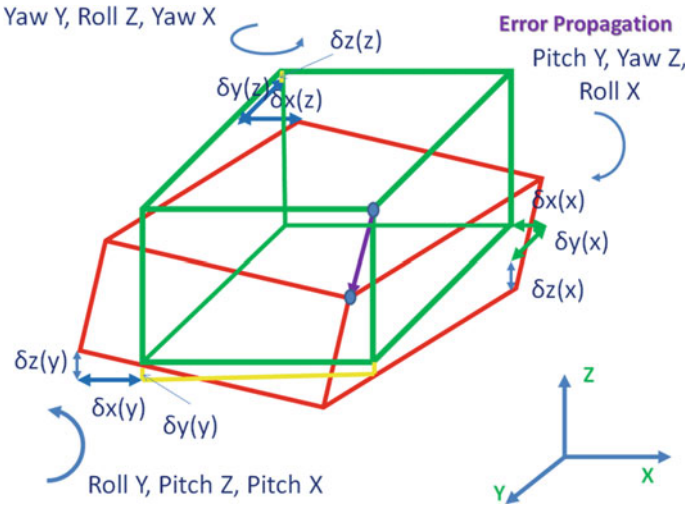

Fig. 1 Geometrical errors representation in measuring volume

resistance, high compactness degree with improved flexural strength of 1000 MPa, as shown in Fig. 2. Dolerite plate yields strength in design, very less thermal conductivity, lower weight movable manually, wide coverage of entire measurement volume, enabling maximum determination of parametric errors, volumetric errors enabling the operator for regular interim check along with tests for verification.

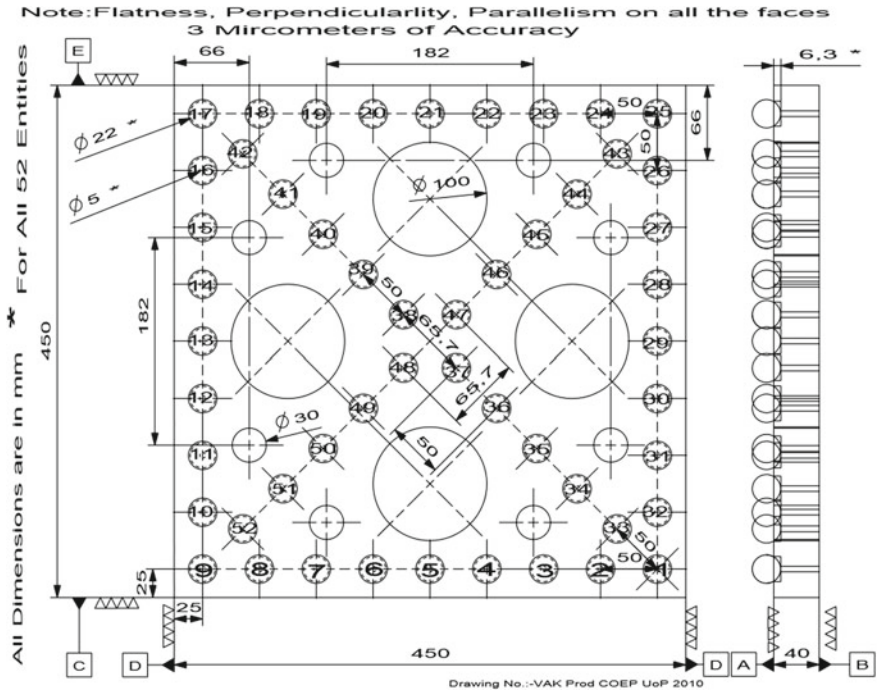

Fig. 2 Production drawing of zirconia-dolerite ball plate

3 Ball Plate: Suitable Artefact

As hole plate method uses only 2D measurements, a ball plate that can be customized to address 8 issues is manufactured as per the following steps.

3.1 Selection of Material

Material selection is vital as all above eight issues highlighted in design and development of artefact which is directly related to it.

3.2 Ball Material

Zirconia balls' features

- Resistance to abrasion and corrosion,
- Chemically inert to metals at high temperature,

- High strength at very high temperatures,
- Delivers transformation toughening depicting flexural strength.

3.3 Plate Material

Dolerite features

- Composed of plagioclase and pyroxene,
- Three times equivalent to stiffness of granite,
- Deflects one-third of granite under same load,
- Uniform in hardness with scleroscope reading of >Hs 95,
- As compared to any granite, dolerite gives higher wear resistance with coefficient of linear expansion as 2.4×10^{-6}/°C as compared to granite as 4.16×10^{-6}/°C,
- Porosity percentage of dolerite is NIL, showing no moisture absorption, whereas 1.5% porosity in nature is hold by granite. This results into considerably less deflecting the plate, causing almost nil deviation on flatness.

4 Development of Ball Plate

A dolerite plate for a specific geometry as shown in Fig. 1 is developed, on which zirconia balls are glued using structural bond adhesive Loctite H3101. The final assembly of zirconia-dolerite ball plate is shown in Fig. 3.

The technical characteristics of ball plates are as per Tables 2 and 3. The total weight of ball plate is 18 kg and can be manually handled (Table 4).

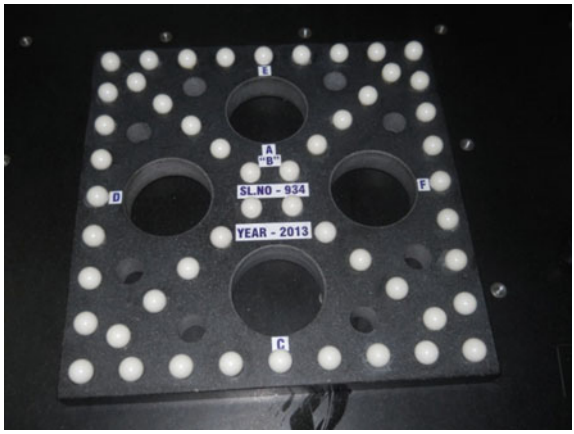

Fig. 3 Zirconia-dolerite ball plate

Table 2 Technical characteristics of dolerite plate manufactured in Guindy Machine Tools Limited, Metrology Division, Hosur, India

• Dimensions: 450 × 450 × 40 mm
• Flatness, parallelism, straightness, squareness, parallelism of all faces are within 2 μm

Table 3 Technical characteristics of zirconia balls manufactured in Precision and Ball Gauging Co. West Sussex, England

• Diameter—25 mm	• Specific density—6.05 g/cm^3
• Hardness—12.3 GPa	• Young's modulus—205 GPa
• Tensile strength—1560 MPa	• Thermal conductivity—3.8 W/m K

Table 4 Total directional deformation analysis

S. No.	Temperature (°C)	Total maximum deformation (μm) (resultant of *X*-, *Y*- and *Z*-directions)
1	20.5	0.39886
2	21	0.79772
3	21.5	1.1966
4	22	1.5954
5	22.5	1.9943
6	23	2.3921
7	23.5	2.792
8	24	3.1909

Maximum deformation value is 3.1909 μm for a ball plate dimension of 450 × 450 × 40 mm which will have very less impact on overall dimensional stability of artefact. However, this is once again tested with practical testing of dimensions over a temperature difference of +2 °C as per Table 5 [10]

5 Thermal Deformation Analysis of Ball Plate

Even after thermal compensation of CMM is used, the influence of job with it can cause considerable errors in measurements. Although 20 °C is theoretically a perfect measurement ambiance, practically it may not be as per the international standards [10]. This is due to the fact that CMMs are placed near to the production process with possibility of deviating from the idealized world.

Further, Jean-Pierre Kruth, Paul Vanherck, et al. [10] showed the influence of the thermal interaction of the job affects repeatability of CMMs in overcoming extended temperature range.

Workpiece is always subjected to soaking period during which it is kept at 20 °C as standard metrological temperature [11–14].

In this analysis, we consider various temperature conditions to determine the thermal deformation of ball plate. To analyse thermal distortion at 20.5, 21, 21.5, 22,

Table 5 Dimensions measured by CMM in calibration laboratory at Accurate Gauging and Instruments Pvt. Ltd., Pune, India

S. No.	Element distance	Actual dimension measurement at °C in μm			Max. deviation in μm
		20	22	24	
1	1–2	49.9654	49.9695	49.9693	4.1
2	1–3	99.9061	99.9101	99.9096	4
3	1–4	149.9338	149.9374	149.9369	3.6
4	1–5	200.1647	200.1681	200.1676	3.4
5	1–6	250.0814	250.0847	250.0843	3.3
6	1–7	299.8975	299.9007	299.9001	3.2
7	1–8	349.8052	349.8083	349.8077	3.1
8	1–9	399.9123	399.9155	399.9148	3.2
9	1–25	400.1492	400.1468	400.1466	2.6
10	1–26	350.1116	350.1094	350.1093	2.3
11	1–27	300.1497	300.1476	300.1475	2.2
12	1–28	250.1574	250.1554	250.1554	2
13	1–29	200.0519	200.0499	200.0496	2.3
14	1–30	150.1383	150.1363	150.136	2.3
15	1–31	100.0441	100.0421	100.0419	2.2
16	1–32	50.0464	50.0443	50.044	2.4
17	9–10	49.858	49.858	49.8581	0.1
18	9–11	99.8829	99.8829	99.883	0.1
19	9–12	149.8905	149.8907	149.8907	0.2
20	9–13	199.8033	199.8035	199.8036	0.3
21	9–14	249.9483	249.9485	249.9487	0.4
22	9–15	299.8911	299.8914	299.8916	0.5
23.	9–16	349.9368	349.9372	349.9372	0.4
24.	9–17	399.8921	399.8923	399.8924	0.3
25.	17–18	50.0005	50.0005	50.0006	0.1
26	17–19	100.0238	100.024	100.024	0.2
27	17–20	149.9551	149.9556	149.9557	0.6
28	17–21	199.9534	199.9535	199.9534	0.1
29	17–22	249.9106	249.911	249.9109	0.4
30	17–23	299.804	299.8042	299.8039	0.3
31	17–24	349.7521	349.7524	349.7522	0.3
32	17–25	399.7637	399.7641	399.7639	0.4
33	1–33	49.9835	49.9834	49.9829	0.6
34	1–34	99.9726	99.9726	99.972	0.6

(continued)

Table 5 (continued)

S. No.	Element distance	Actual dimension measurement at °C in μm			Max. deviation in μm
		20	22	24	
35	1–35	149.9113	149.9112	149.9108	0.5
36	1–36	199.8623	199.8625	199.862	0.5
37	1–37	249.9107	249.9106	249.9101	0.6
38	1–38	315.5788	315.5786	315.5783	0.5
39	1–39	365.3787	365.3783	365.3781	0.6
40	1–40	415.5511	415.551	415.5508	0.3
41	1–41	465.6812	465.6809	465.6807	0.5
42	1–42	515.7218	515.7212	515.7211	0.7
43	1–17	565.7309	565.7309	565.7303	0.6
44	9–52	49.3748	49.377	49.3761	2.2
45	9–51	100.0488	100.0513	100.0505	2.5
46	9–50	149.6783	149.6808	149.68	2.5
47	9–49	199.9566	199.9592	199.9583	2.6
48	9–48	249.5523	249.5547	249.5537	2.4
49	9–47	315.4193	315.4216	315.4207	2.3
50	9–46	365.6003	365.6027	365.6019	2.4
51	9–45	414.8572	414.8598	414.8591	2.6
52.	9–44	465.7893	465.7918	465.7909	2.5
53	9–43	515.5453	515.5474	515.5467	2.1
54	9–25	565.4408	565.4406	565.4408	0.2
Average					1.503704

Average max. Deviation of 1.503704 μm shows the stability of ball plate

22.5, 23, 23.5 and 24.5 °C, we assumed a basic reference temperature as 20 °C, which is then increased to respective temperature at which thermal distortion analysis is made by using FEA.

For this purpose, we assumed that reference temperature 20 °C to respective temperature at which temperature distortion to be analysed (e.g., 20.5 °C) in 43200 s and then kept constant till 86400 s as depicted in Figs. 4 and 5.

The resultant analysis is shown in the following tables (Fig. 6).

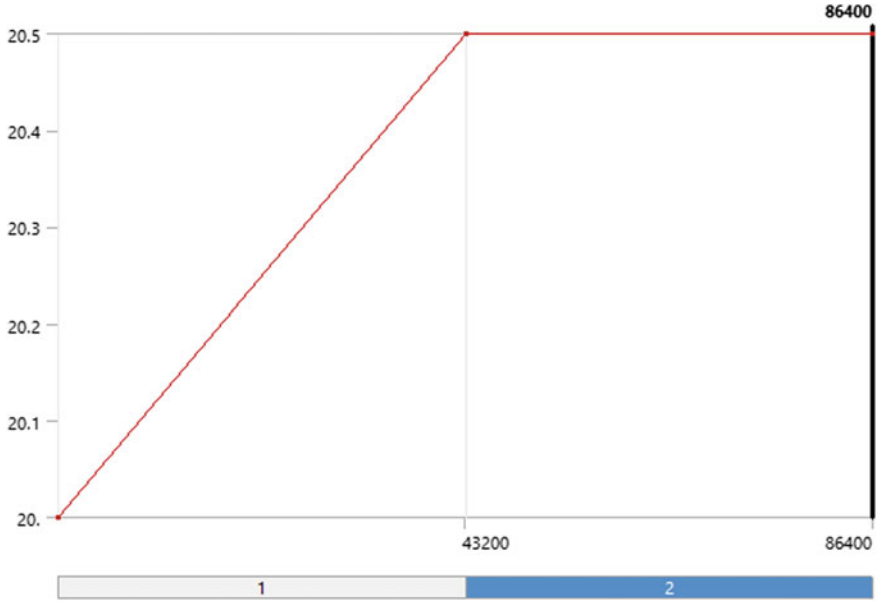

Fig. 4 Time versus temperature analysis (thermal conditions)

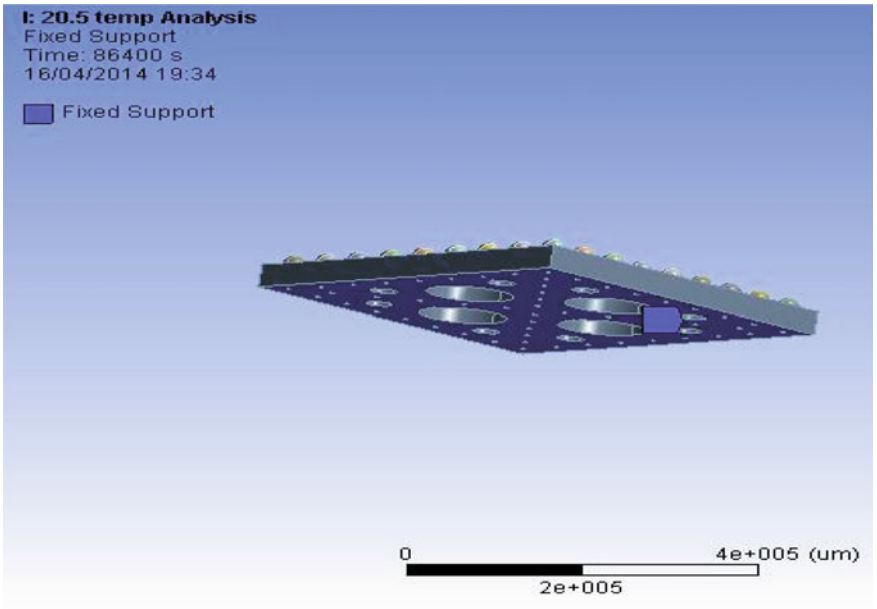

Fig. 5 Fixed support

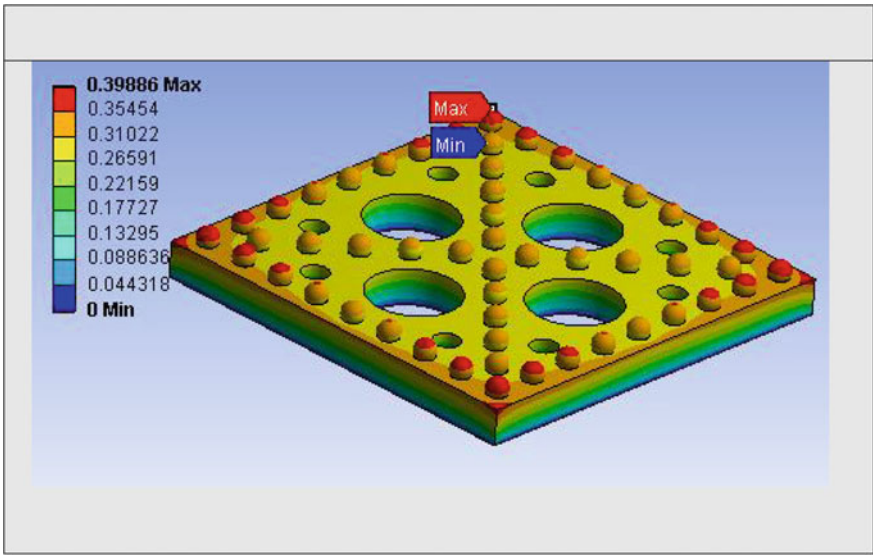

Fig. 6 Thermal distortion analysis

6 Conclusion

A zirconia-dolerite plate for a specific geometry is developed, on which zirconia balls are glued using structural bond adhesive Loctite H3101. The production and operational cost of this ball plate is low ₹ 1,19,041/– (one lakh nineteen thousand forty one rupees only) and interim check can be completed in single setup. The manufactured ball plate shows considerable stability even at higher operating temperature of 24 °C with a maximum deviation of 4.1 μm with an average stability of 1.503 μm within the distinct placed zirconia balls.

Acknowledgements Authors would like to thank, Savitribai Phule Pune University for providing research grant to carry out this research work as per Fin/Bill/2013–2014/1751. Also, to help improving quality of framework presented in paper, authors would like to thank anonymous reviewers.

References

1. Hocken RJ, Pereira PH (2011) Coordinate measuring machine and systems, 2nd edn. CRC Press, Boca Raton
2. Shen Y, Moon S (1997) Mapping of probe pretravel in dimensional measurements using neural networks computational technique. Comput Ind 34:295–306

3. Parkinson S, Longstaff AP, Crampton A, Fletcher S, Allen G, Myers A (2011) Representing the process of machine tool calibration in first-order-logic. In: Proceedings of the 17th international conference on automation and computing, Chinese Automation and Computing Society, Huddersfield, UK
4. Furutani Ryoshu, Shimojima Ken, Takamasu Kiyoshi (2003) Kinematical calibration of articulated CMM using multiple simple artefacts, XVII IMEKO world congress metrology in the 3rd Millenium, June 22–27. Dubrovnik, Croatia
5. Ibaraki Soichi, Hata Takafumi (2010) A new formulation of laser step diagonal measurement-three-dimension case. Precis Eng 34:516–525
6. Beaman Jonathan, Morse Edward (2010) Experimental evaluation of software estimates of task specific measurement uncertainty for CMMs. Precis Eng 34:28–33
7. Bringmann B, Kung A (2005) A measuring artefact for true 3D machine testing and calibration. CIRP Ann Manuf Technol 54:471–474
8. Liebrich T, Bringmann B, Knapp W (2009) Calibration of 3D-ball plate. Precis Eng 339:1–6
9. Ramu P, Yague JA, Hocken RJ, Miller J (2011) Development of parametric model and virtual machine to estimate task specific measurement uncertainty for a five-axis multi-sensor coordinate measuring machine. Precis Eng 35:431–439
10. Kruth Jean-Pierre, Vanherck Paul, Van den Bergh Christope, Schaht Benny (2002) Interaction between workpiece and CMM during geometrical quality control in non-standard thermal conditions. Precision Engineering 26:93–98
11. Kulkarni VA, Ahuja BB, Mulay AV (2015) Pooled error mapping of probe type coordinate measuring machine. Int J Sci Eng Res 76:242–245
12. Kulkarni VA, Ahuja BB (2015) Statistical performance analysis of zirconia-dolerite ball plate for dimensional stability. Int J Innov Technol Explor Eng 4:34–37
13. Kulkarni VA, Ahuja BB (2015) Autocorrelation of zirconia-dolerite ball plate artifact. Int J Mech Eng Res 3:1–4
14. Kulkarni, VA, Ahuja, BB (2015) Test specific uncertainty analysis of zirconia-dolerite ball plate by Monte Carlo simulation. MAPAN—J Metrol Soc, pp 1–8. Springer, India

Application of Industrial Internet of Things for Online Monitoring of Bearings

Saroj Kumar, Parminder Singh, Shankar Sehgal, Harmesh Kumar, Naveen Aggarwal, Sarbjeet Singh and Deepam Goyal

Abstract This paper discusses the application of an industrial internet of things (IIoT) based system which can be used to online monitor the acceleration based responses of a shaft and bearings assembly. The experimental set-up includes one shaft, two ball bearings (for supporting the shaft), one coupling (for connecting shaft to the motor), one electric motor (for providing input torque), one table (on which the complete set-up is mounted), one accelerometer (for measuring acceleration) and one mobile (as receiver for receiving the warning or preventive maintenance schedule based message). The system is developed in such a way that the accelerometer acquires the time domain vibration signal produced by the bearing. This signal is then sent further to SIM900A-based IIoT system for online data monitoring and transmission. In the event of any vibration response going away from the permissible range, it is considered as a fault in the system. In such cases of possible failure,

S. Kumar · S. Sehgal (✉) · H. Kumar
Mechanical Engineering, UIET, Panjab University, Chandigarh 160014, India
e-mail: sehgals@pu.ac.in

S. Kumar
e-mail: ksaroj700@gmail.com

H. Kumar
e-mail: harmesh@pu.ac.in

P. Singh · N. Aggarwal
Computer Science Engineering, UIET, Panjab University, Chandigarh 160014, India
e-mail: singh99parminder@gmail.com

N. Aggarwal
e-mail: navagg@gmail.com

S. Singh
Department of Mechanical Engineering, Government College of Engineering and Technology, Jammu 181122, India
e-mail: sarbjeet.gcet@gmail.com

D. Goyal
Department of Mechanical Engineering, National Institute of Technical Teachers Training and Research, Chandigarh 160019, India
e-mail: deepam.mech@nitttrchd.ac.in

H. Kumar and P. K. Jain (eds.), *Recent Advances in Mechanical Engineering*,
Lecture Notes in Mechanical Engineering,
https://doi.org/10.1007/978-981-15-1071-7_28

the system offers an early warning to the operator on personal mobile of the end-user regarding high vibration levels. Use of this type of IIoT-based system helps in avoiding unwanted and unplanned system shutdowns due to failure of the bearings.

Keywords Industrial internet of things · Vibration · Condition monitoring · Bearing assembly · Preventive maintenance

1 Introduction

In the era of globalization, manufacturing industries are facing intense pressure to prevent unexpected breakdowns, reduce maintenance cost and increase plant availability. Due to ever changing nature of working environment, it is desired to put into practice an effective e-maintenance strategy for evolving proper usage of existing assets and reliability and safety [1, 2]. The importance of real-time online monitoring is heightening persistently as the industries try to enhance the machine availability and have premature alarm of incipient breakdown and precautionary shutdown of machine to prevent further losses [3]. Therefore, it is required to design systems which can recognize and deal with different types of failures of machine elements for monitoring the health condition of the machine aiding timely maintenance decisions.

Recent developments in the networking systems, particularly through the use of internet has overcome the distance barriers, and allows for online data transfer to take place smoothly from various locations [4]. Zhao et al. [5] developed a remote condition monitoring and fault diagnosis system based on service-oriented architecture for detecting the faults and remote monitoring. During applications, the primary utility of service-oriented architecture comprised of runtime using already existing services that were utilized by Lazar et al. [6] to exhibit a visual surveying system in automation of manufacturing operations for pick-and-place process of dynamic equipments. Also, an integrated intelligent equipment maintenance decision structure based on service-oriented architecture was presented by Cao and Jiang [7] to sustain collective support decisions related to remote diagnosis and maintenance of machine elements. Later service-oriented architecture models and 2-D or 3-D digital software tools were consolidated to build up an engineering structure for acceptance, configuration, simulation, simple outline, control and tracking of manufacturing systems by Leitão et al. [8]. A time-constrained services model includes different functional layers viz. real-time infrastructural layer, support layer, hardware layer, and tool and real-time service layer which have been utilized for real-time web services in industrial automation [9]. Integration of dynamic e-maintenance system with a service-oriented architecture based enterprises can substantially strengthen decision-making processes aiding the growth concerning sustainable manufacturing [10]. Goyal and Pabla [11] developed laser-based non-contact vibration measurement system for monitoring the condition of the machine in real time. It verified the effectiveness and practicality of the system. Later a need was felt to develop a system

which can not only monitor the vibration level of a system but also send a warning message to end-user in case of increased vibration levels beyond threshold values.

This papers presents the applications of new technology i.e. industrial internet of things (IIoT) in the online vibration data analysis of ball bearings to check the condition of the bearings, so that a corrective and an appropriate decision could be taken at the right time to avoid the losses due to any unexpected shutdown or unwanted preventive maintenance of bearing system.

2 Materials and Methods

A mild steel shaft was supported at two locations with the help of two ball bearings as shown in Fig. 1. The shaft was connected to an electric motor through a rigid coupling. Vibration responses generated by the set-up were measured in mV by using three-axis accelerometer having sensitivity of 300 mV/g mounted on top of the housing of left hand side bearing B_L. Accelerometer was used to collect the vibration responses in *X*, *Y* and *Z* directions simultaneously. *X* direction was assumed to be passing through the centre of bearing B_L and towards the observer; *Y* direction was

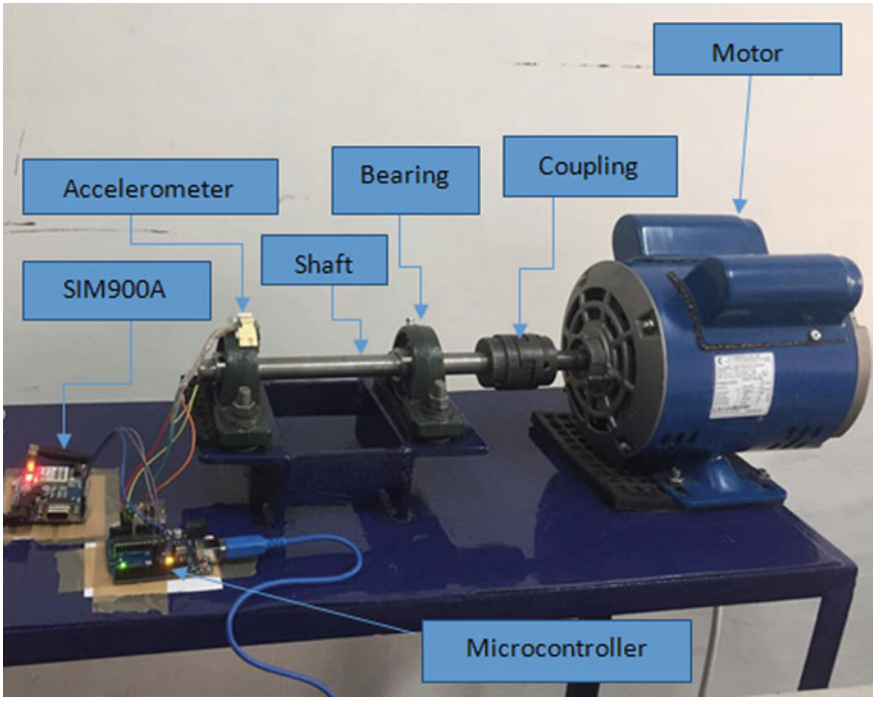

Fig. 1 IIoT-based system for online monitoring of vibration responses

Fig. 2 Accelerated testing of bearing

taken along vertical passing through the centre of the bearing B_L; and Z direction was taken along the axis of the shaft.

Initially both the bearings B_L and B_R (Right hand side bearing) were in good condition. Corresponding vibration responses were recorded and taken as standard reference condition monitoring signal of the set-up. With the passage of time, some fault is supposed to have occurred in one of the bearings. However, it could have taken very long time for such a fault to appear on its own. In order to save time, accelerated testing of the bearing was done in laboratory.

During accelerated testing, the bearing was held tightly using a bench vice as shown in Fig. 2. Compressive forces resulted in slight deformation of various bearing components. The bearing was kept under the effect of compressive forces for few hours after which the inner race of the bearing was rotated by using an adjustable spanner. Compressive forces combined with forced rotation of the bearing resulted in accelerated wear of the rolling elements as well as lubrication seals. It further led to an increased noise level and leaking of some lubricant from side of the bearing. Thus, a faulty bearing B_{LF} was created. Bearing B_L was then replaced by the faulty bearing B_{LF}. Use of faulty bearing B_{LF} in the experimental set-up resulted in slight leakage of lubricating oil, overheating and higher vibration responses. IIoT system was designed to send a short warning message to the mobile of end-user as soon as the vibration signal exceeded the specified limit. Such warning message was found to be very helpful in online condition monitoring of the bearing assemblies.

Figure 3 shows the working of proposed IIoT-based online monitoring system. Acceleration data was measured by the accelerometer and then transferred to micro-controller which checks whether the vibration level is below the prescribed threshold limit. Prescribed threshold limit was decided based upon the results of pilot experiments conducted during initial stages of this work. 0.12 g was prescribed as the threshold limit because it best suited the current set-up. If the vibration level

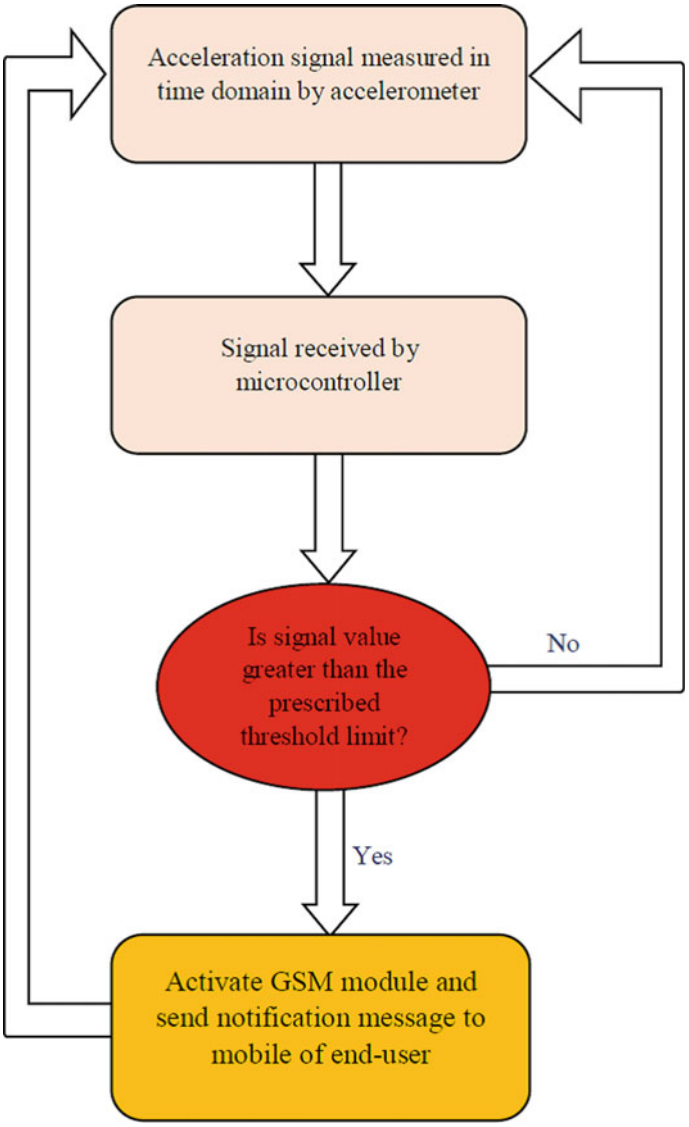

Fig. 3 Flow chart showing the working algorithm of IIoT-based system

exceeds the threshold limit then the microcontroller activates the SIM900A module for sending warning notification message to end-user on his or her mobile. SIM900A module was chosen because most of the mobile operators operate in 900 MHz band and SIM900A supports communication in this band in India. Further, it is well tested and easily available in the market. However, for other countries, where a different frequency band is prevalent, we may have to select a different module.

3 Results and Discussion

Figure 4 shows time domain acceleration signals while using healthy bearings B_L and B_R. Average vibration responses along *X*, *Y* and *Z* directions were found to be 0.0088, 0.0089 and 0.0356 mV, respectively. These average vibration responses were calculated from the time domain acceleration responses measured by the accelerometer in a defined time window. Acceleration signals of a faulty bearing-based system are shown in Fig. 5. Here the average signals were observed to be 0.0525, 0.0852 and 0.0479 mV along *X*, *Y* and *Z* directions, respectively. It is seen that average vibration response signals of faulty bearing-based system is 495, 851 and 34% higher than their counterparts in a healthy bearing system along *X*, *Y* and *Z* directions, respectively. The IIoT system rechecks the signal after a specified time interval and again finds the average, compares against the preset threshold limit and sends warning message to the end-user if required. A screenshot of the warning message received on one such test-mobile is shown in Fig. 6. Present system sends a warning message which includes name of machine and prescribed threshold limit value.

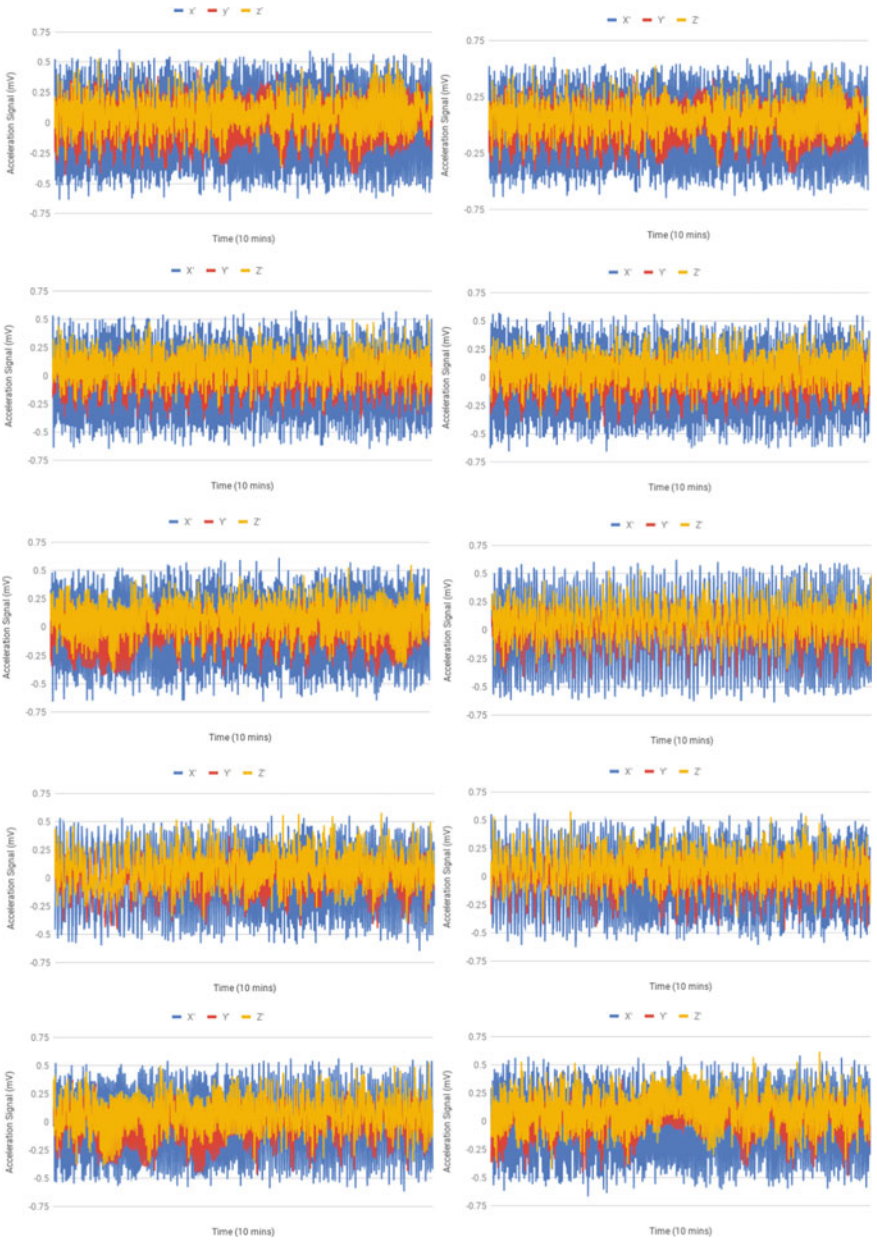

Fig. 4 Sample acceleration signals measured from healthy set-up

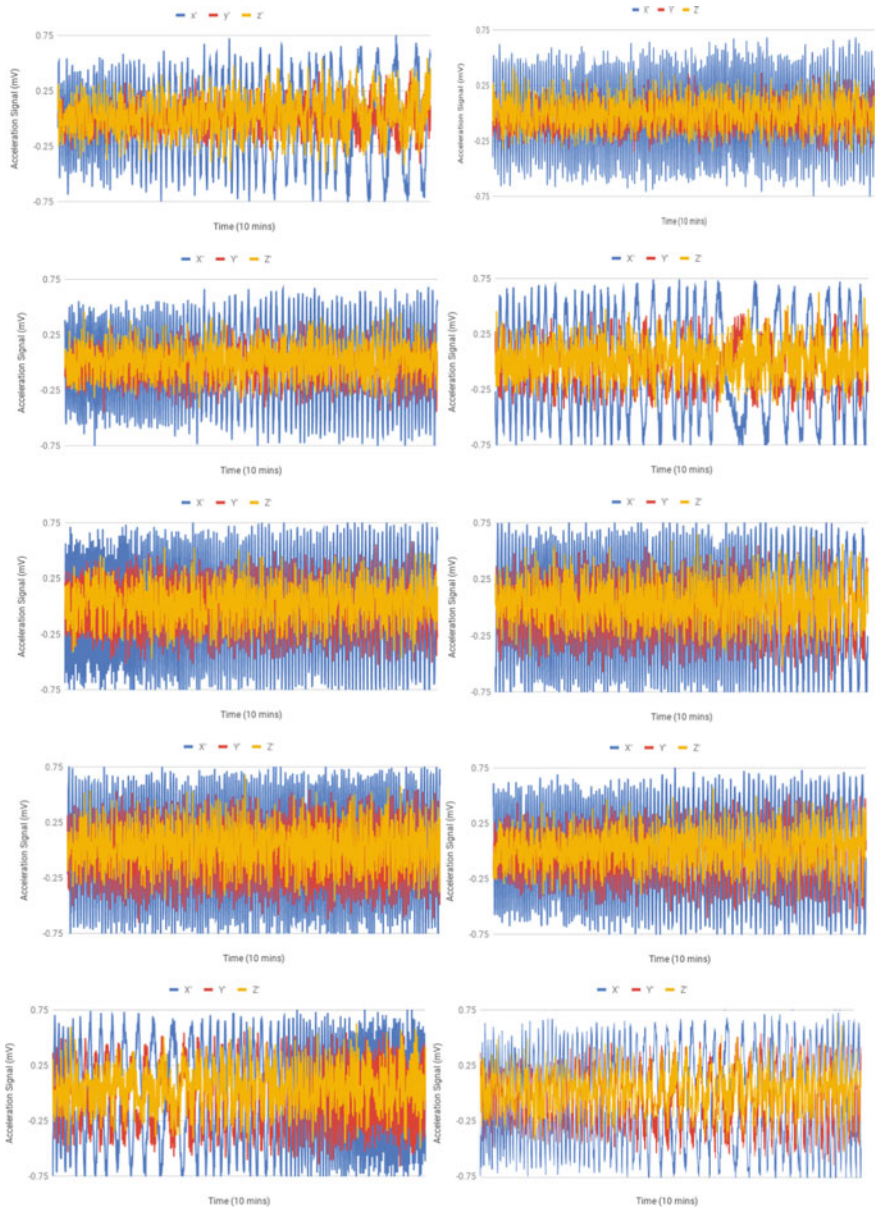

Fig. 5 Sample acceleration signals measured from faulty set-up

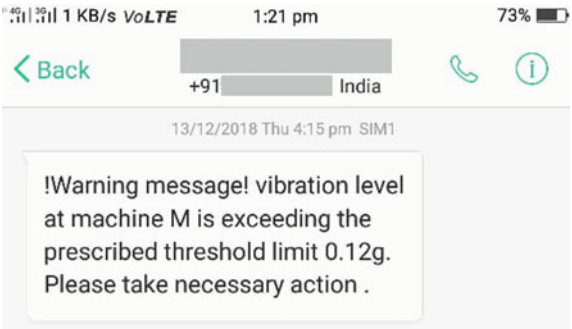

Fig. 6 Screenshot of the message received through IIoT system

4 Conclusion

IIoT-based low-cost system has been developed which is capable of performing three major IIoT tasks, viz. measuring the vibration responses of bearing set-up, comparing it with a reference signal and sending a warning message to mobile of end-user. Warning message will be sent only if average vibration response exceeds a predefined threshold limit. Such high vibration responses may be caused due to any fault in the bearing system. The IIoT system developed during this work performed successfully when tested in laboratory working conditions. Such a low cost IIoT-based condition monitoring system is very helpful for small and medium scale enterprises to avoid unplanned shutdowns due to unexpected failure of bearings.

Acknowledgements Authors acknowledge the support received from TEQIP-III and Design Innovation Centre, established by Ministry of Human Resource Development at UIET, Panjab University, Chandigarh, India.

References

1. Goyal D, Pabla BS (2016) The vibration monitoring methods and signal processing techniques for structural health monitoring: a review. Arch Comput Methods Eng 23(4):585–594
2. Goyal D, Pabla BS (2015) Condition based maintenance of machine tools—a review. CIRP J Manufact Sci Technol 10:24–35
3. Goyal D, Pabla BS, Dhami SS, Lachhwani K (2017) Optimization of condition-based maintenance using soft computing. Neural Comput Appl 28(1):829–844
4. Parida A, Kumar U (2010) Integrated strategic asset performance assessment. In: Kiritsis D, Emmanouilidis C, Koronios A, Mathew J (eds) Engineering asset lifecycle management. Springer, London, pp 25–30
5. Zhao F, Chen J, Dong G, Guo L (2010) SOA-based remote condition monitoring and fault diagnosis system. Int J Adv Manuf Technol 46(9–12):1191–1200
6. Lazar C, Burlacu A, Archip A (2014) Vision-guided robot manipulation predictive control for automating manufacturing. In: Borangiu T, Trentesaux D, Thomas A (eds) Service orientation in Holonic and multi-agent manufacturing and robotics, vol 544. Studies in computational intelligence. Springer, Cham, pp 313–328

7. Cao X, Jiang P (2008) Development of SOA based equipments maintenance decision support system. In: Xiong C, Liu H, Huang Y, Xiong Y (eds) Intelligent robotics and applications. ICIRA 2008. Lecture Notes in Computer Science, vol 5315, pp. 576–582. Springer, Berlin, Heidelberg
8. Leitão P, Mendes JM, Bepperling A, Cachapa D, Colombo AW, Restivo F (2012) Integration of virtual and real environments for engineering service-oriented manufacturing systems. J Intell Manuf 23(6):2551–2563
9. Mathes M, Stoidner C, Schwarzkopf R, Heinzl S, Dörnemann T, Dohmann H, Freisleben B (2009) Time-constrained services: a framework for using real-time web services in industrial automation. SOCA 3(4):239
10. Cannata A, Karnouskos S, Taisch M (2010) Dynamic e-maintenance in the era of SOA-ready device dominated industrial environments. In: Kiritsis D, Emmanouilidis C, Koronios A, Mathew J (eds) Engineering asset lifecycle management. Springer, London, pp 411–419
11. Goyal D, Pabla BS (2016) Development of non-contact structural health monitoring system for machine tools. J Appl Res Technol 14(4):245–258

Acquisition of Jugular Venous Pulse Waveform by a Non-invasive Technique

S. Bagyaraj, M. Ragumathulla and D. Vaithiyanathan

Abstract In this paper, a non-invasive technique has been proposed for the acquisition of jugular venous pulse (JVP) waveform using an accelerometer sensor. Waveform is obtained from the vibrations measured using the accelerometer sensor. The vibration signals present in the jugular vein regions are due to pressure created during the hemodynamic event of cardiac cycle. This pressure created during the cardiac cycle is measured using the sensor and is further processed. Finally, the JVP pattern is obtained by applying a suitable computation method. The JVP wave is obtained along with electrocardiogram (ECG) signal which is measured with the help of ECG electrodes. These collected signals from accelerometer sensor and electrodes are made to run in real time with the help of a DAQ system and a computer. The obtained pattern is compared with the electrocardiogram, and changes in JVP waveform's amplitude are correlated with heart activity during cardiac cycle.

Keywords Jugular vein anatomy · Jugular venous pulse · Heart diseases · Accelerometer

1 Introduction

The traditional method involves the measurement of jugular venous pressure by a physical examination. First, the patient was made to lie on a slanting bed with head inclined at an angle of 45° as shown in Fig. 1, and the veins elevation above the sternal angle (Louis angle) are measured When doing this examination, a light is made to fall on the neck region to get a clear view of the vein and a centimeter ruler is used to for measuring the venous pressure. Measure the distance from the sternal angle to the

S. Bagyaraj
Sri Sivasubramaniya Nadar College of Engineering, Kalavakkam 603110, India

M. Ragumathulla
College of Engineering Guindy, Anna University, Chennai 600025, India

D. Vaithiyanathan (✉)
National Institute of Technology Delhi, New Delhi 110040, India
e-mail: dvaithiyanathan@nitdelhi.ac.in

H. Kumar and P. K. Jain (eds.), *Recent Advances in Mechanical Engineering*,
Lecture Notes in Mechanical Engineering,
https://doi.org/10.1007/978-981-15-1071-7_29

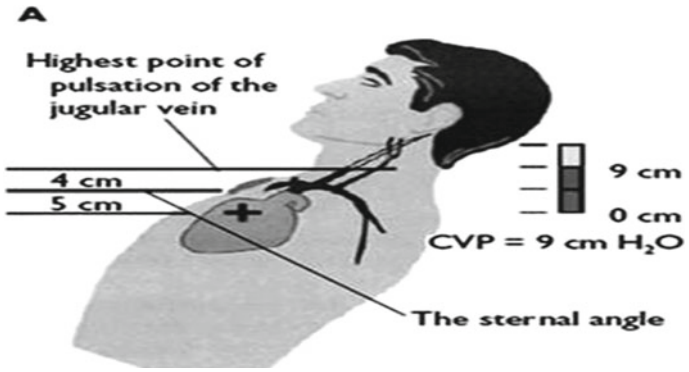

Fig. 1 Traditional JVP assessment

jugular vein's highest pulsation point level. A measurement of 5 cm is added to the measured value since it is the point where the right atrium lies below the sternal angle. This value gives the jugular venous pressure in cm of water [1].

This method of measuring the venous pressure requires more time, and it is also a difficult procedure which requires highly skilled physicians. Because of the vein's direct connectivity with heart, the vibration present on it reflects the activity of heart during cardiac cycle. The measurements taken from jugular vein can help in various diagnoses of heart diseases such as pericardial effusion, pulmonary hypertension, tricuspid stenosis, and constrictive pericarditis [2].

The aim of this proposed system involves in measuring the vibrations of the jugular vein in simple and non-invasive technique with the help of accelerometer sensor which is further analyzed by a suitable post-processing. This method comprises an easy and a comfortable way of measuring the jugular vein vibrations due to the hemodynamic events in the cardiac cycle. Acquisition is done in a non-invasive method by placing the sensor in a direction perpendicular to the axis of the jugular vein. This system driven by software will be easier to handle rather than the traditional method that involves in measure jugular venous pulse.

The non-invasive sensors are used to measure the vibrations of vein and artery. It is further processed to obtain the JVP waveform pattern that can help in various clinical diagnoses [3]. The accelerometer sensor has been used to measure the heart rate in various ambulatory situations along with ECG. The sensor gives information about the position of the subject. The measured vibration value is converted to corresponding heart rate for heart rate variability diagnosis [4].

The accelerometer sensor measures the tidal volume (TV) variability and the respiration rate by placing it on the chest region. The vibrations caused by inspiration and expiration are measured, and they correspond to tidal volume and respiration rate [5]. The normal jugular venous pressure with ultrasonography is estimated by determining the point at which the diameter of the internal jugular vein (IJV) began to decrease on ultrasonography (the taper). Experiment is carried out by recording the quadrant in the IJV's path from the clavicle to the angle of the jaw in which

the taper was located. Separate examiners measured the U-JVP of 15 participants to determine the reliability among inter-rater. The mean jugular venous pressure is found to be 6.35 cm [6].

2 JVP Physiology

The right jugular vein communicates directly with the right atrium through the superior vena cava and so it reflects the pressure build up in the right atrium in the form of vibrations at that region. On comparing the direct line between the right and left jugular vein, the right side jugular vein is preferred for assessing the venous pressure and pulse [7]. A typical jugular pulse wave has been explained with the help of a waveform shown in Fig. 2 [8]. In this waveform, '*a*' indicates the atrial contraction for the blood to flow into the ventricle and '*x*' follows '*a*' wave which represents the atrial relaxation due to the rapid filling [8]. The '*c*' wave corresponds to the right ventricular contraction causing the tricuspid valve to bulge toward atrium and x' represents right ventricle pulling tricuspid valve down during ventricular systole. The '*v*' wave indicates venous filling while tricuspid valve closes causing an increase in pressure. y' is caused by the rapid emptying of atrium into the ventricle followed by the opening of tricuspid valve [8].

JVP waveform is obtained based on the pressure build during the events that occur in the cardiac cycle. Amplitude of the waveform tends to increase when there is a rise in pressure and decrease in amplitude as a result of the decrease in the pressure level, respectively. The jugular venous pulse waveform is not given much importance in clinical diagnosis due to the challenges present in the traditional method of measurement. A typical electrocardiogram is compared with a JVP waveform in Fig. 3 [3] for clear and detailed information on the physiological activity of the heart, and its changes are reflected in the jugular vein vibrations.

The change in pressure builds up during the cardiac cycle is reflected in the vibrations of the vein which causes an increase and decrease in the amplitude of waveform obtained. There is also a difference in the timing of the JVP waveform amplitude and electrocardiogram which is due to the time taken by the pulse to reach the vein from the heart during each cycle.

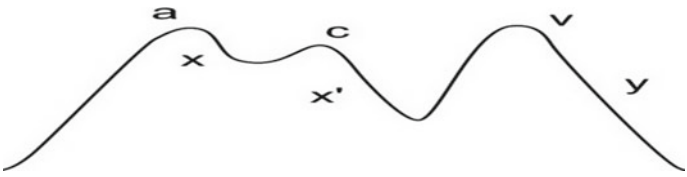

Fig. 2 JVP waveform

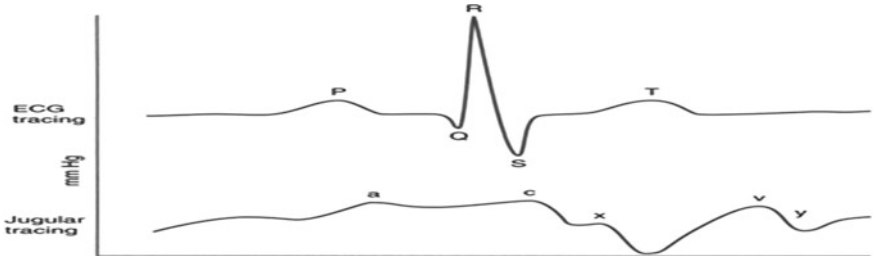

Fig. 3 ECG and JVP waveform

3 Experimental Results and Discussion

The acquisition and analysis of jugular venous pulse waveform along with electrocardiogram are carried out as shown in Fig. 4. The ADXL335 accelerometer and Ag–AgCl electrodes are the measurement elements that are used in the measurement of jugular vein's vibration and ECG signal, respectively. Signals recorded are made to run in real time using the DAQ and the PC system. Finally, the analog signals are analyzed and computed in offline with the help of MATLAB software.

The three-axis ADXL335 accelerometer is chosen by considering its wide frequency range (0.5–1600 Hz) and acceleration measurement range (±3 g) specification required for the acquisition of jugular vein vibration. It requires only a low power supply in the range of 1.83–3.6 V, and it can also withstand high temperature. The accelerometer is placed on the jugular vein region on the right side of the neck because to its clear visibility than a left-sided vein and the electrocardiogram is acquired with a bipolar lead I limb electrode configuration system. During this process, the subject is made to lie on a flat table for a clear view of identifying the jugular vein in the right side of the neck region. Signals are acquired with the NI USB 6009 model DAQ device with a supply voltage of 2.5 V. These collected raw data from the DAQ device are exported to an excel sheet for further offline processing. Finally, the collected analog data are analyzed offline using the MATLAB software. In offline computation, filters are used to remove the motion artifacts due to neck movement and the environmental noise at the time of signal acquisition.

The experiment is conducted with four male and three female healthy subjects within the age group of 22–24 years. Accelerometer sensor is placed on the right jugular vein with the help of surgical tape as shown in Fig. 5. The ECG is also acquired simultaneously along with the accelerometer data for one-minute duration

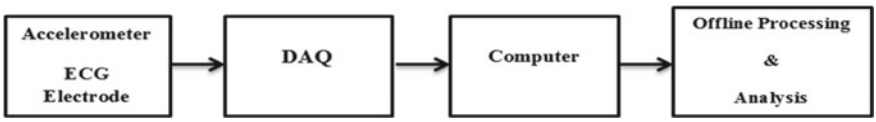

Fig. 4 Block diagram of system

Fig. 5 Accelerometer sensor placement

with 1000 Hz sampling rate. The acquisition setup and DAQ display panel are shown in Figs. 6 and 7. The sensitivity of ADXL335 accelerometer is 300 mv/g where g is gravitational force. The accelerometer is calibrated for its correct output value using the formula shown in Eqs. 1 and 2.

$$\text{Output} = \frac{\text{(Output-Zero gravity value)}}{\text{(Sensitivity)}} \tag{1}$$

Fig. 6 Acquisition setup

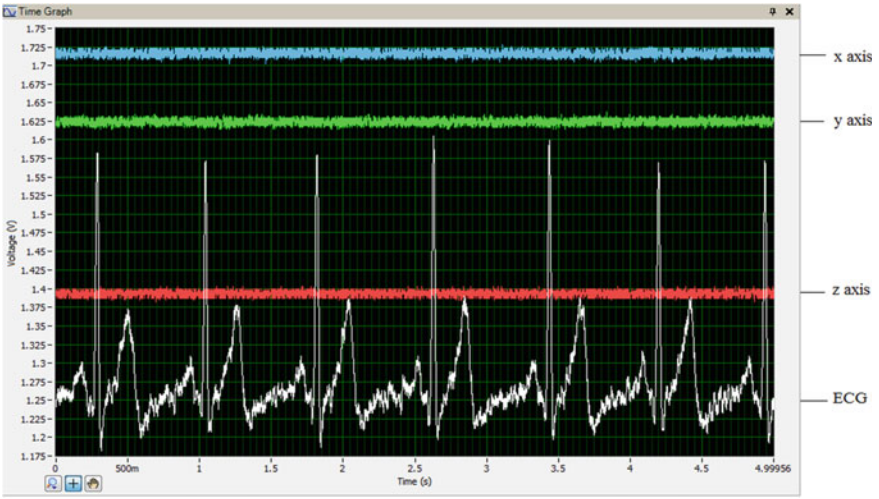

Fig. 7 Signal in DAQ display panel

$$\text{Zero gravity value} = \frac{\text{Supply Voltage}}{2} \tag{2}$$

The raw signal acquired from the accelerometer is shown in Fig. 8. Now the JVP raw signal and ECG is filtered simultaneously with a 50 Hz notch filter to remove the power interference noise and noises due to neck movements during the experiment procedure. The band-pass filter in the range 10–120 Hz is used to get the JVP signals from the collected raw data. Finally, a smoothening filter is applied to obtain clear and noise-free JVP waveform. This filtered signal is shown in Fig. 9. A trace is drawn connecting the JVP peaks throughout the signal for five and two ECG cycles. This trace taken for the peaks gives the jugular venous pulse waveform which is shown in Figs. 10 and 11. Both accelerometer and ECG signals which are measured and processed offline are shown together for a comparison.

In this work, it has been observed from Fig. 11 that the change in amplitude value of jugular venous pulse waveform occurs with respect to every ECG cycle. The rise in amplitude of JVP waveform '*a*' at the end of ECG's '*P*' wave corresponds to the atrial contraction. During atrial contraction, depolarization occurs and so the pressure in the chamber increases which makes the amplitude of the waveform to increase. The decrease in amplitude '*x*' at '*R*' wave corresponds to the atrial relaxation. Amplitude rise in JVP waveform '*c*' is seen at the '*S*' wave of every ECG wave which is due to the increase in pressure during right ventricular contraction. The amplitude of the JVP waveform tends to decrease further '*x*' with respect to the ECG and it is caused by the ventricular repolarization which makes the pressure to drop. There is also a rise in amplitude of the acquired JVP waveform '*v*' during the '*T*' wave of

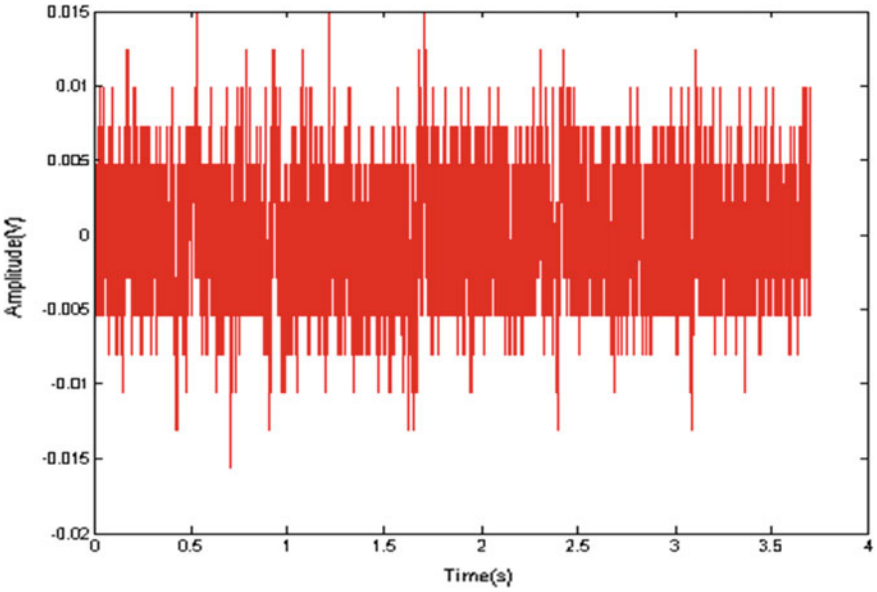

Fig. 8 Raw signal from accelerometer

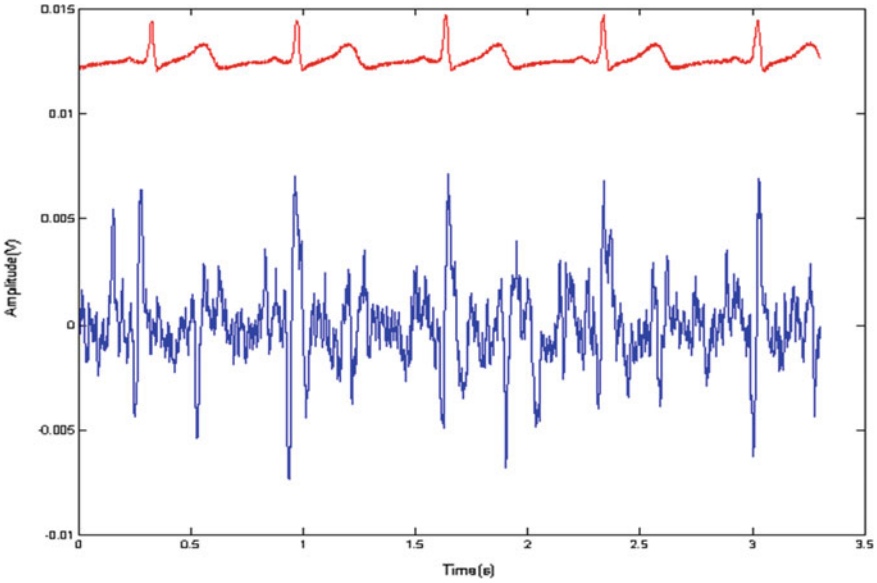

Fig. 9 Filtered JVP waveform

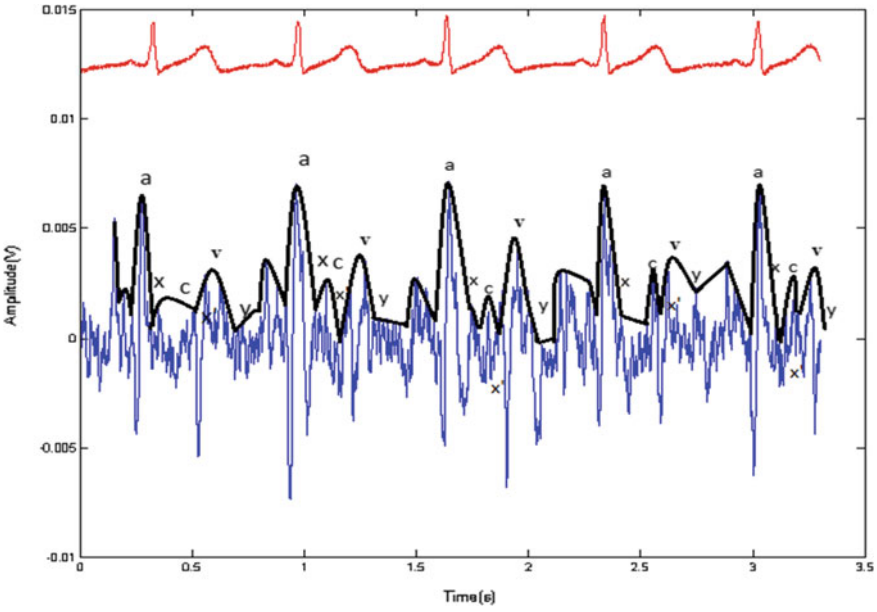

Fig. 10 Final ECG and JVP

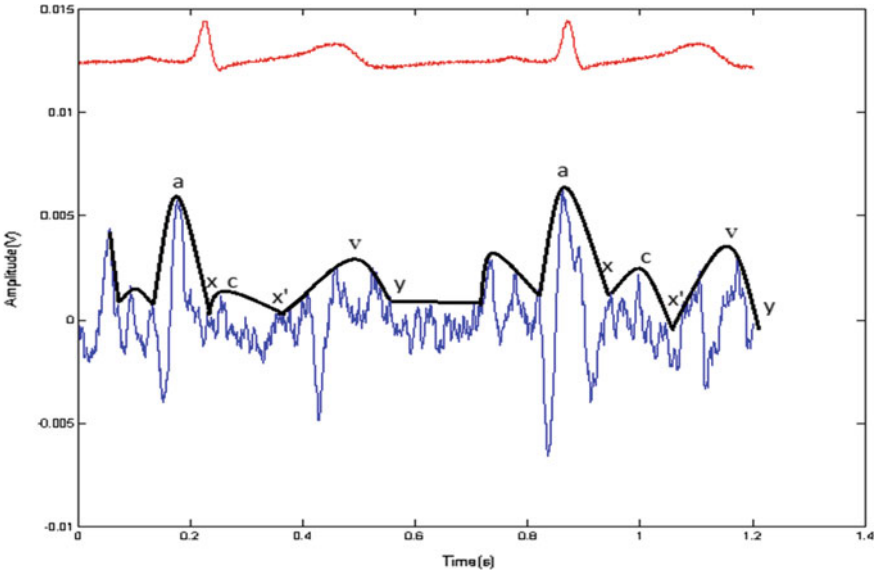

Fig. 11 Final ECG and JVP waveform

ECG which is because of venous filling when the tricuspid valve closes causing an increase in pressure. Finally, the '*y*' descent occurs due to the opening of tricuspid valve.

Delay in the amplitude of the JVP waveform with respect to ECG is caused by the time taken for the pulse from the heart to reach the jugular vein region which is measured by the accelerometer sensor. The JVP waveform has been obtained by measuring the vibration signals using two accelerometers from the jugular vein and carotid artery along with the ECG and PCG in the paper [3]. The signals taken from both accelerometers have been computed by taking the difference between the signals collected from both accelerometers and a corresponding preprocessing is done to get the final output waveform.

The peaks of the obtained JVP waveform have been compared with the ECG as well as the PCG signal, and it seems to match with both the signals in every cycle. In this work, the experiment is done by measuring the vibrations from jugular vein only with a single accelerometer sensor and appropriate processing is done to remove the movement artifacts and power line interference. The filtered signal is further smoothened to get a clear signal, and an envelope is taken which forms the final JVP waveform similar to the previous literature.

4 Conclusions

The proposed system involves the acquisition of jugular venous pulse waveform by measuring the vibrations over the jugular vein in a non-invasive manner. An accelerometer sensor is been used for the measurement of vibration which converts the analog vibration value into its corresponding voltage value. The data from the sensor are further processed to obtain the JVP waveform. This technique does not require any special training for the clinical technicians to handle the instrument on comparing with the existing traditional method. For future work, the amplitude and time interval of the obtained waveform can be studied and made useful in diagnosis of various heart diseases.

References

1. Mark M, Applefeld (2005) The jugular venous pressure and pulse contour. In: Clinical methods: the history, physical, and laboratory examinations, 3rd edn, vol 34. Elsevier, Cardiac Physiology, pp 1416–1427
2. Longmore M, Wilkinson I, Turmezei T, Cheung CK (2009) Clinical skills: the jugular venous pressure. In: Oxford handbook of clinical medicine, 7th edn. United States, Oxford University Press Inc., pp 30–31
3. Nguyen T, Dinh A, Bui FM, Toi, T (2015) A novel non-invasive system for acquiring jugular venous pulse waveforms. In: Research Article, the Korean Society of Medical and Biological Engineering

4. Van Steenis HG, Tulen JHM (1997) The effects of physical activities on cardiovascular variability in ambulatory. In: Proceedings of the 19th annual international conference of the IEEE, vol 1, pp 105–108
5. Fekr AR, Radecka K, Zilic Z (2014) Tidal volume variability and respiration rate estimation using a wearable accelerometer sensor. In: International conference on wireless mobile communication and healthcare—transforming healthcare through innovations in mobile and wireless technologies vol 6, pp 1–6
6. Socransky SJ (2010) Defining normal jugular venous pressure with ultrasonography. Can J Emerg Med 12:320–324
7. Mozaffarian D, Roger VL, Benjamin EJ, Berry JD, Borden WB, Bravata DM, Dai S (2013) Jugular venous pulse measurement. In: 35th annual international conference of the IEEE EMBS
8. Garg N, Garg N (2000) Jugular venous pulse: an appraisal. J Indian Acad Clin Med 1(3):261

Condition Monitoring of Induction Motor Using Internet of Things (IoT)

Anurag Choudhary, Shefali Jamwal, Deepam Goyal, Rajeev Kumar Dang and Shankar Sehgal

Abstract In the era of globalization, manufacturing industries are facing intense pressure to prevent unexpected breakdowns, reduce maintenance cost and increase plant availability. Due to increasing trend of Internet of things (IoT), numerous sensors deployed around the world are developing at a rapid pace. In this paper, an IoT-based wireless control and monitoring system has been presented for determining the health of induction motor (IM). A module of sensors has been employed to monitor the different parameters, viz. current, voltage, temperature, and speed which were processed using microcontroller for analysis and display purposes. Further, the Ethernet module has been used for sending the information from the microcontroller to cloud (Cayenne) database for wireless remote monitoring and controlling of induction motor. The system has been implemented to monitor and control various parameters in real time, and also improving the detectability of different faults due to over limiting of the current, voltage, temperature, and speed values. The proposed system has significant potential in industrial environment with complex systems to economically monitor the condition of machine safely in real time.

Keywords Condition monitoring (CM) · Internet of things (IoT) · Induction motor (IM)

A. Choudhary · S. Jamwal
Department of Electrical Engineering, National Institute of Technical Teachers Training and Research, Chandigarh 160019, India

D. Goyal
Department of Mechanical Engineering, National Institute of Technical Teachers Training and Research, Chandigarh 160019, India

R. K. Dang (✉)
Department of Mechanical Engineering, UIET, PUSSGRC, Hoshiarpur 146021, India
e-mail: dang.rajeev@pu.ac.in

S. Sehgal
Mechanical Engineering, UIET, Panjab University, Chandigarh 160014, India

H. Kumar and P. K. Jain (eds.), *Recent Advances in Mechanical Engineering*,
Lecture Notes in Mechanical Engineering,
https://doi.org/10.1007/978-981-15-1071-7_30

1 Introduction

Due to the ever-changing nature of working environment, it is the dire need of today's world to put into practice an effective e-maintenance strategy for evolving proper usage of existing assets and reliability and safety [1–3]. During applications, the primary utility of service-oriented architecture comprised of runtime using already existing services that were utilized by Lazar et al. [4] to exhibit a visual surveying system in automation of manufacturing operations for pick-and-place process of dynamic equipment's. Recent advances in the enhancement of wireless network technology, the uses of Internet-connected devices, viz. smartphones and laptops have made realization of smart sensor in combination with signal processing circuitry possibility. Therefore, it is required to implement Internet of things (IoT) which can recognize and deal with different types of failures within a machine for condition monitoring aiding timely maintenance decisions [5, 6].

Condition monitoring (CM) of rotary machines is the procedure of consistently observing or monitoring the status of machine health for increasing efficiency and productivity, reducing maintenance costs, and enhance machine availability [7]. Manufacturing imperfections and tolerance, installation, operating condition, and calendar of maintenance are the main considerations responsible for failures in electrical rotating machines [8]. An online CM system has been presented to record the temperature, frame, speed, line voltages, and vibrations from a three-phase induction motor (IM) for various working conditions. A real-time laser-based non-contact vibration measurement system has been developed for determining the health of the machine [9, 10]. The effectiveness and practicality of the proposed system have been validated with the accelerometer.

At the point, when extensive numbers of sensors are deployed and initiate producing data, the conventional application-based methodology (i.e., connect sensors directly to applications individually and manually) becomes infeasible. With a view to address this inefficiency, the present work proposes a wireless-based condition monitoring system for determining the health of IM. Different parameters, viz. current, voltage, temperature, and speed were monitored using sensors module and then processed using Arduino Uno microcontroller to analyze and display the parameters. Further, the Ethernet module has been used for sending the information from microcontroller to cloud (Cayenne) database for wireless remote monitoring and controlling of induction motor.

2 IoT-Based Condition Monitoring

In general, IoT is basically a network of physical devices, i.e., sensors, microprocessors, etc., where all the items around us are interlinked by the means of Internet and interact with each other with minimum human mediation [11]. One of its greatest advantages is an ease of integration with the existing technology and machinery to

create a better world for human beings [5, 12]. The primary motive of IoT is to know what we want, what we like, and what we need, and act in like manner without explicit guidelines. The use of sensors with the reduction in cost and size has augmented the way machines communicate with each other and has led to a manufacturing revolution [13, 14]. Manufacturing industries are tapping into this unprecedented technology to enhance the accuracy and quality of the existing monitoring and controlling system of the plant. By minimizing the need for human involvement, expanding connectivity, and simplifying the use of automation and analytics, the IoT redefines the cost of condition monitoring of rotating electrical machine and makes development of new solution both financially, practically and more valuable to the industries. The overall structure of IoT-based monitoring and controlling structure has been shown in Fig. 1.

A low-cost wireless monitoring system using Arduino Uno microcontroller helps to overcome the traditional application-based approaches and also to add controlling features from remote location. The hardware used in the present work provides wireless monitoring of three-phase induction motor from remote location using IoT as shown in Fig. 2. Induction motor, a critical component in industrial processes, are most significant prime movers in industrial applications due to their simplicity and reliability of construction. A 3 phase, 2-pole, 50 Hz, and 0.25 hp squirrel cage induction motor has been used to control and monitor as prototype in this study. The methodology adopted for online condition monitoring in the present work is illustrated in Fig. 3.

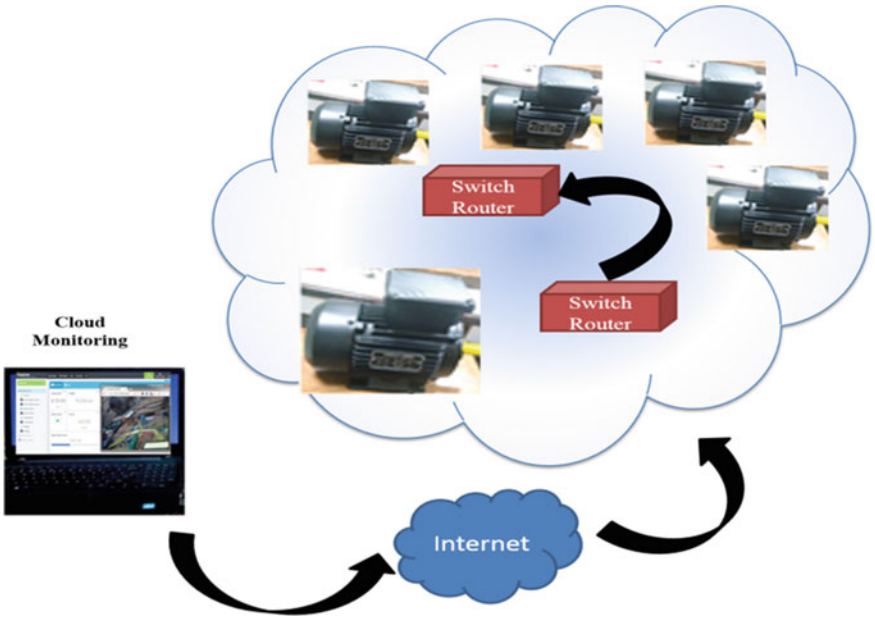

Fig. 1 IoT-based monitoring and controlling structure

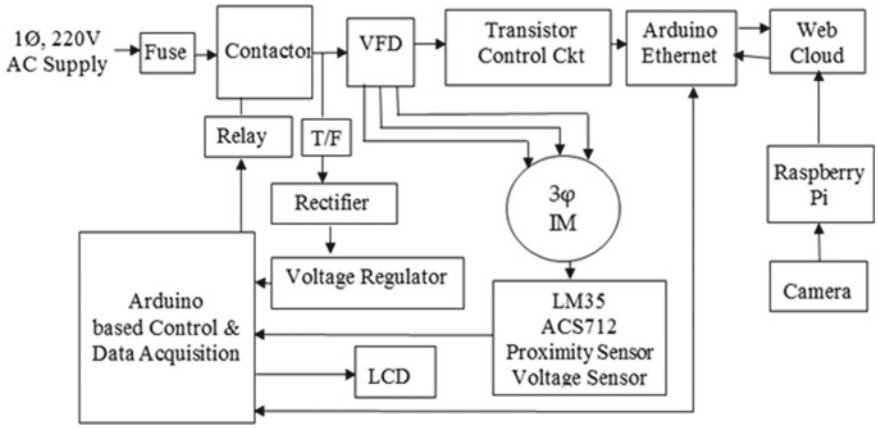

Fig. 2 Block diagram of IoT-based monitoring and control system of induction motor

The whole arrangement comprises transmitter and receiver. Transmitter system consists of sensors, transducers, and microcontroller which have been used to acquire the IM parameters such as current, voltage, temperature, and speed located at distant location. The acquired parameters then sent to a PC for display through microcontroller and transmitting end IoT user. Measured values are then compared with set values through Arduino program and if in any case the measured value exceeds the set value of any parameter, control signal will be generated by microcontroller to take corrective action such as to stop the motor, switch on fan on motor side, and adjust the speed depending on the measured value of the parameter.

3 Experimental Setup and Data Acquisition

In order to validate the proposed IoT-based monitoring system, the test-bed for parameter acquisition was set up as shown in Fig. 4. In this study, the various induction motor parameters have been acquired under different operating conditions and sent it to the IoT cloud (Cayenne).

All the acquired parameters have been compared with the existing standard meter in laboratory condition. The standardized sensor modules have been used for acquiring the motor parameters as discussed in Table 1.

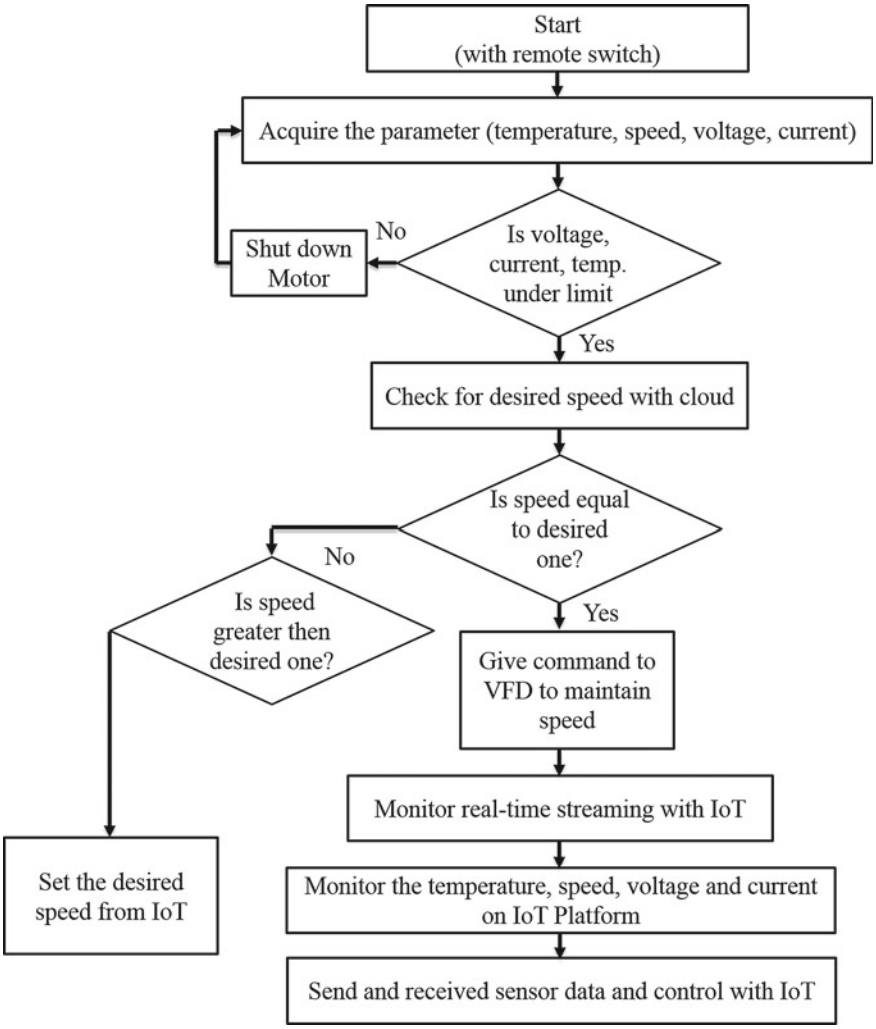

Fig. 3 Flow chart of the proposed methodology

3.1 Hardware Implementation

The hardware framework is divided into four categories including power supply, parameter sensors, and signal conditioning circuits, control and data acquisition system, and finally, transmitter system to send the information to the cloud.

Power supply: A 230 V AC was given to variable-frequency drive and converted to proper controlling and supply voltage for driving the microcontroller and other

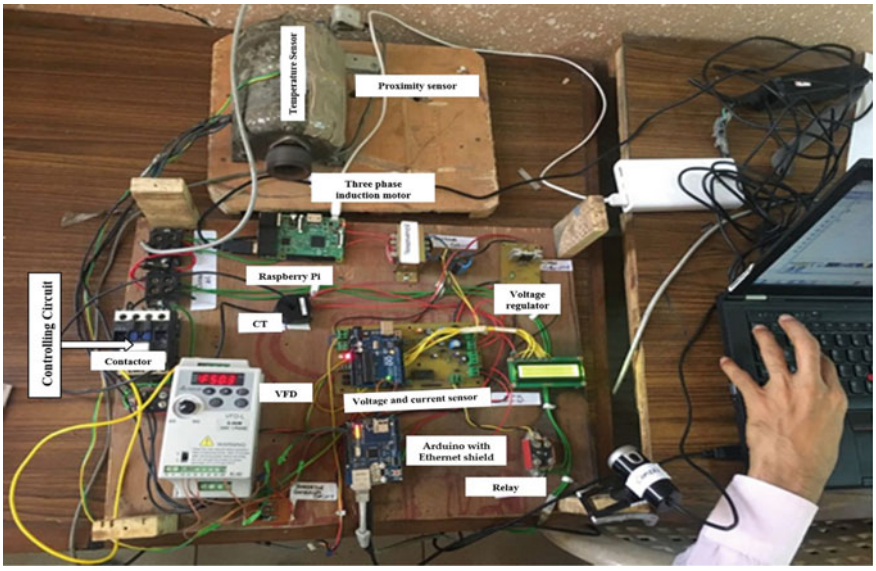

Fig. 4 Experimental setup

Table 1 Sensors description

Sensor	Description	Range
Current sensor	ACS712 follows	1–30 A
Voltage sensor	Voltage divider circuit	100–220 V
Temperature sensor	LM35	−55° to 150°
Proximity sensor	LJ12A3-4-Z/BX-5 V M12 NPN-NO Switch	DC 6–36 V

components. Input supply is fed to bridge rectifier through AC contractor and solid-state relay has been used for connecting and disconnecting the supply to the variable-frequency drive (VFD). The hardware implementation of power source is shown in Fig. 5. Bridge rectifier rectifies AC to DC, and output of rectifier is then fed to capacitor bank for smoothening the obtained 5 V DC output.

Variable-frequency drive: Variable-frequency drive (VFD) is the method of controlling the speed of induction motor by varying the supply frequency. It is possible to operate with different speeds by changing the supply frequency which has large industrial applications, viz. ventilation systems, pumps, elevators, etc. It consists of bridge rectifiers which convert 230/110 V AC to 300/150 V DC. The DC output from the bridge rectifier was smoothed by a high-value smoothing capacitor to eliminate the ripples from supply. Afterthought, constant DC supply is fed to the frequency generating circuit, which has been formed using MOSFET transistors and converts it into AC supply with variable frequency to control the speed of the IM. Hardware and its connection have been shown in Fig. 6.

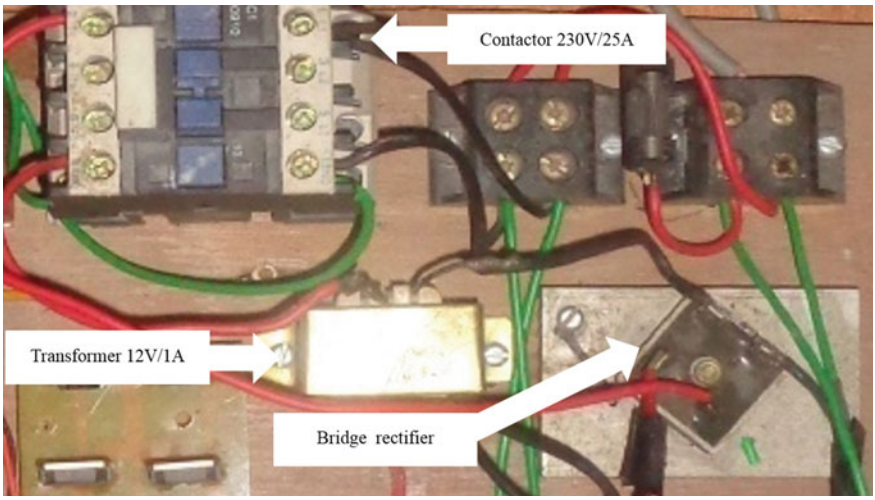

Fig. 5 Bridge rectifier for supply

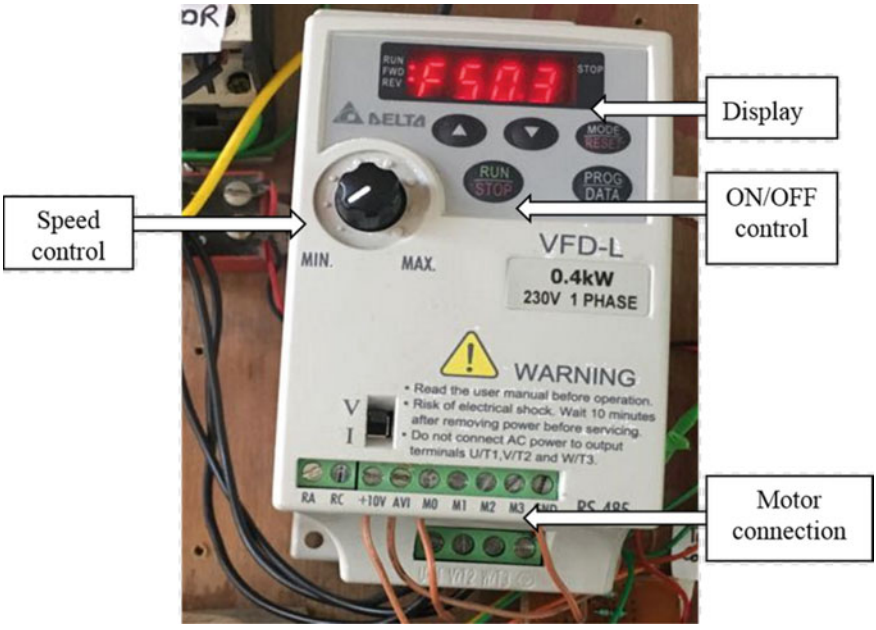

Fig. 6 Variable-frequency drive for speed control of induction motor

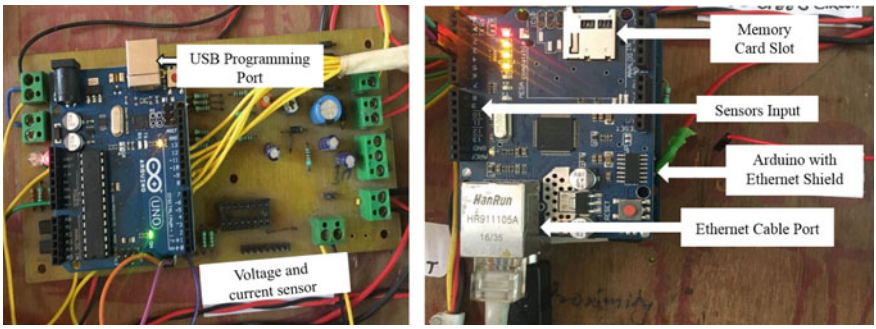

Fig. 7 Control and data acquisition system for the proposed work

Control and data acquisition system: The most important element of the system is a low-cost microcontroller (Arduino Uno), which is used to acquire the sensor values and control the external hardware connected to it as shown in Fig. 7. The voltage divider circuit has been used to measure supply voltage to the motor. Output from VT is rectified, filtered, stepped down, and fed to microcontroller. Current sensor (ACS712) is used to estimate input current to motor, filtered; stepped current is fed to Arduino Uno. LM35 sensor is used to measure surface temperature of motor. The proximity sensor is used to measure the speed of the induction motor. Arduino Uno starts 1 s delay and then counts all the pulses through proximity sensor by using the timer multiplied by 30 and then send. An Optocoupler provides isolation between proximity sensor, speaker and the controlling circuit. Arduino Ethernet shield has used as a transmitter of the monitoring system to connect to the Internet. This shield is able to send and receive data from worldwide with an Internet source. IoT platform (Cayenne) has been used as cloud or remote location. When any parameter received by Cayenne goes beyond set value, the microcontroller sends command to relay at transmitting end to disconnect the motor from power supply.

3.2 Software

In the system developed, Cayenne cloud has been used to connect monitoring system with Arduino Ethernet shield. After connecting system with Cayenne, data can be sent from the monitoring system to the Cayenne dashboard and display it using widgets. Commands may also be received from Cayenne, allowing remote control and live streaming of the motor. Graphical user interface (GUI) of IoT platform (Cayenne) is shown in Fig. 8.

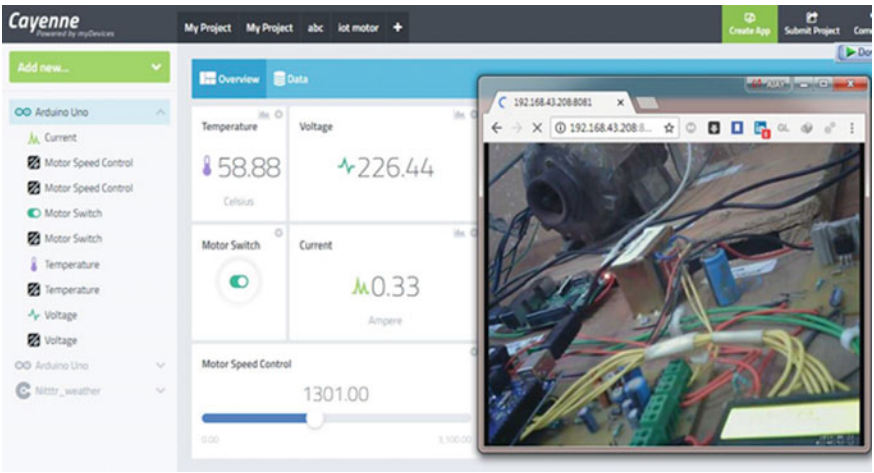

Fig. 8 GUI of IoT platform (Cayenne)

4 Results and Discussion

Several laboratory tests have been carried out to validate the performance of the wireless network, followed by direct measurements from an induction motor, whose results are discussed below. In the first stage, the hardware has been implemented as discussed in Sect. 3.1. The second stage is the application of the remote control of the induction motor using IoT. The error between the readings is then calculated. Graphical user interface (GUI) of IoT platform (Cayenne) is used to monitor and control the motor parameters on the laptop/smartphone or computer placed at remote locations as shown in Fig. 8. All the obtained values were compared and in case if value of any parameter beyond set value, then the command is sent to the microcontroller through GUI to take appropriate action to prevent failure of the motor parts. As seen in Fig. 9, the temperature will increases with increasing the operating time of the motor. A remote camera has been interfaced with Raspberry pi for real-time streaming with IoT on remote location.

As shown in Fig. 10, speed of the motor in operating condition follows the reference speed from IoT cloud (Cayenne). Figure 11 shows the rise time, settling time, settling maximum, and settling minimum with reference set speed from IoT cloud (Cayenne). In the staring of the induction motor, it takes a large current approximately to 7 times of normal current, the current drawn by induction motor during settling time with reference set speed from IoT cloud (Cayenne) as shown in Fig. 12. The operating current of the motor during continuous running mode is shown in Fig. 13. Finally, the terminal voltage drawn during settling time by induction motor with reference speed is shown in Fig. 14. It can be noticed that the speed will be reduced as the terminal voltage of the induction motor decreases.

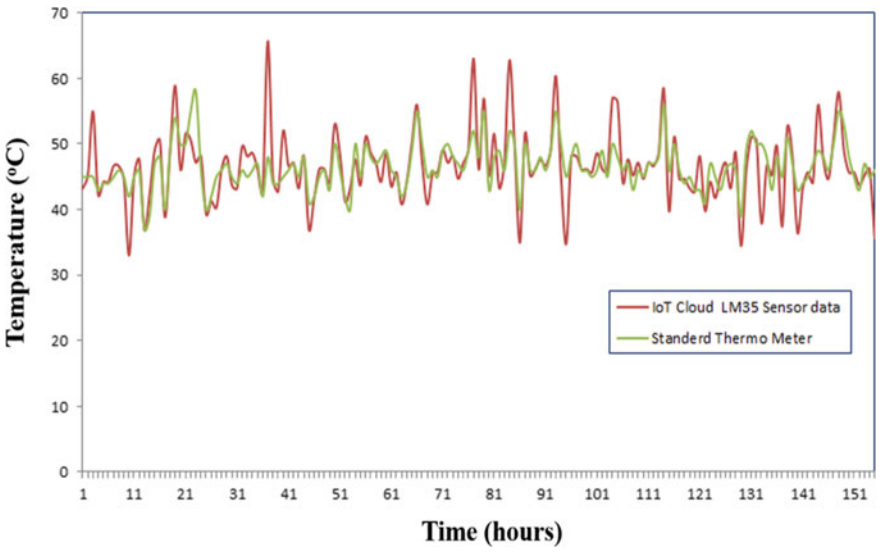

Fig. 9 Temperature of the motor surface in operating condition

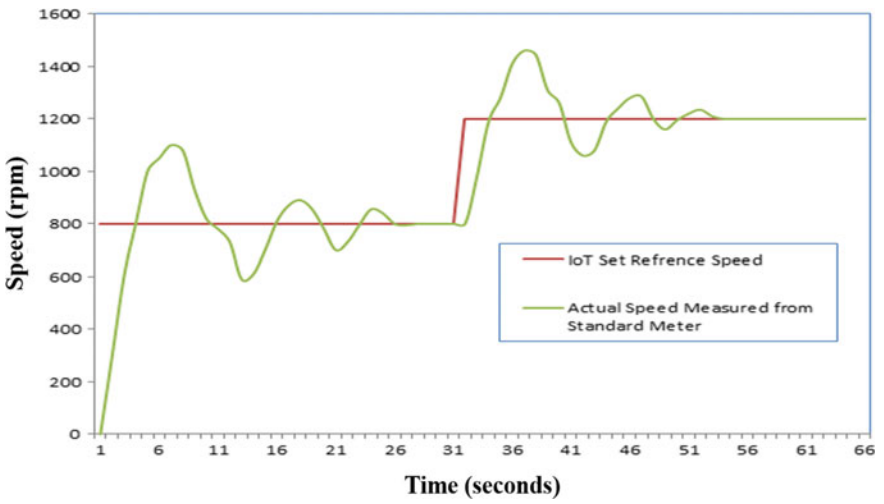

Fig. 10 Speed of the motor in operating condition with reference speed from IoT cloud

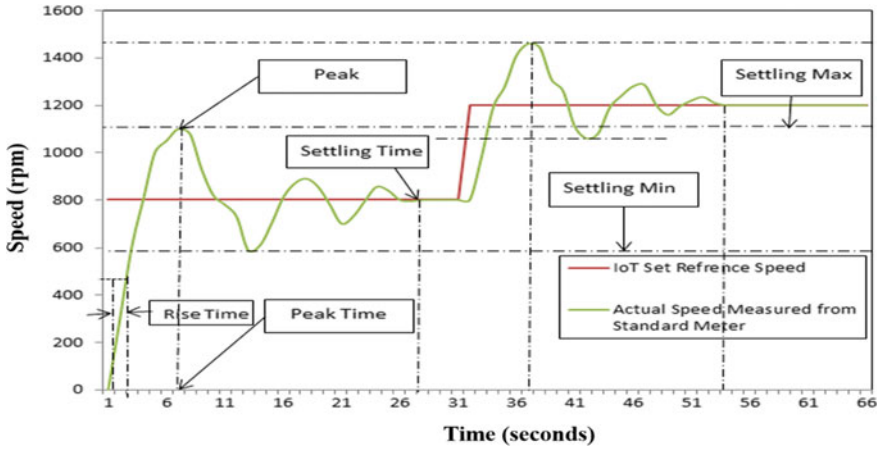

Fig. 11 Rise time, settling time, settling maximum, and settling minimum with reference set speed from IoT cloud

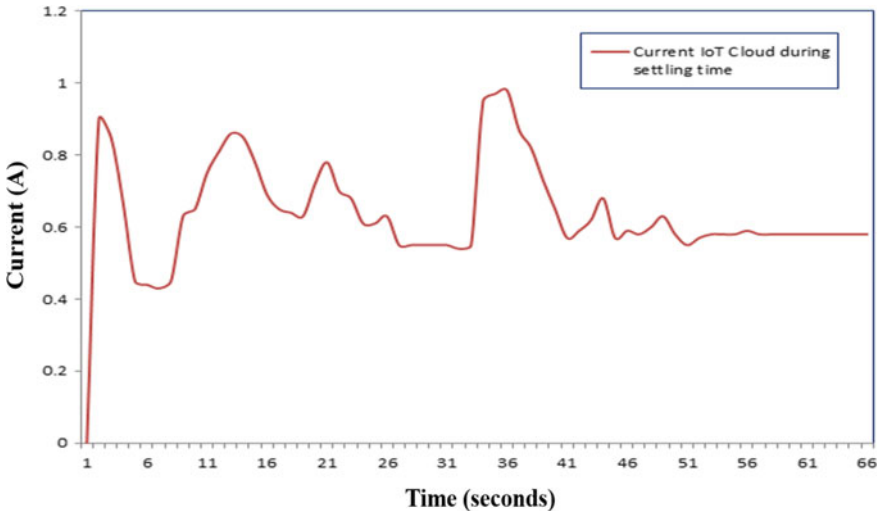

Fig. 12 Current drawn by induction motor during settling time with reference set speed from IoT cloud

5 Conclusion

The Internet of things has significantly attracted the attention of researchers throughout the most recent couple of years. With the progresses in sensor hardware technology and cost-effective materials, sensors are expected to be attached to all the items around us, so that these can interact with each other with minimal human mediation.

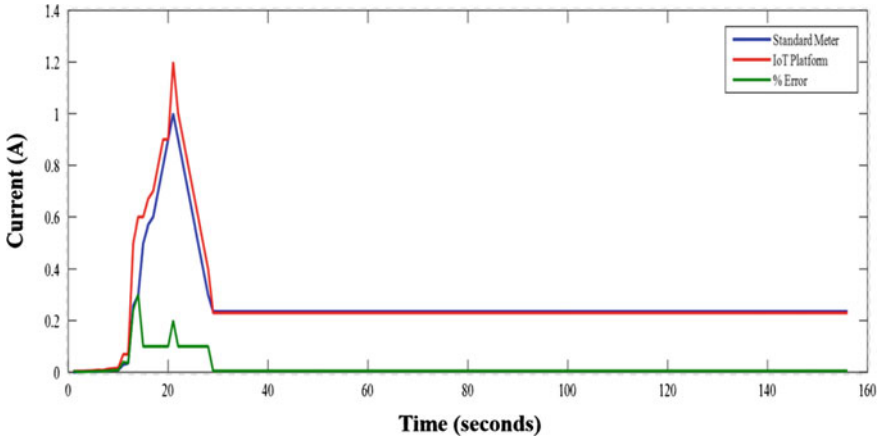

Fig. 13 Operating current of the motor during continuous running mode

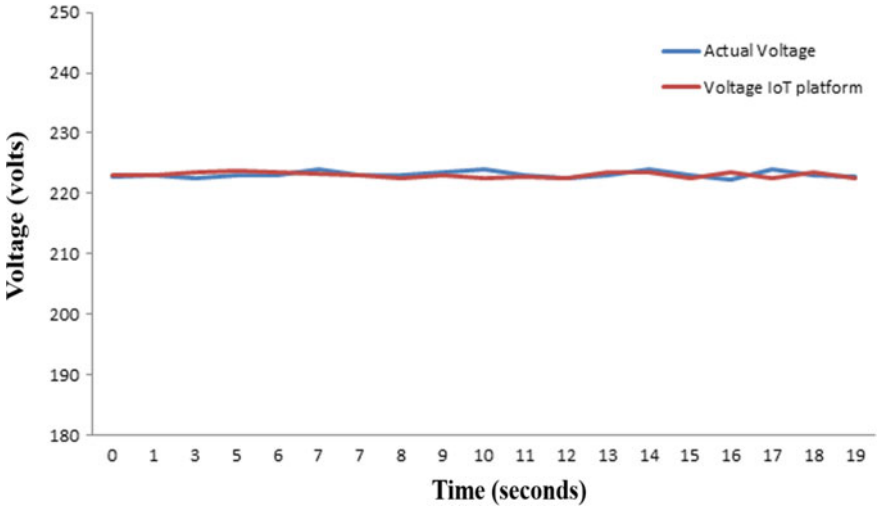

Fig. 14 Voltage drawn during settling time by induction motor with reference speed

In this paper, a wireless monitoring system has been developed to monitor the essential parameters of induction motor, and control it if any of the parameter goes beyond set value. These parameters were analyzed and visualized with an aid of Arduino Uno microcontroller which sends command to relay at transmitting end and cutout motor from supply. The system has been implemented to monitor and control various parameters in real time, and also improving the detectability of different faults due to over limiting of the current, voltage, temperature, and speed values. The results obtained using the proposed system have been compared and found to be in sync with the existing standard meter, relies solely on temperature. An Ethernet module

has been used for sending the information from microcontroller to cloud (Cayenne) database for wireless remote monitoring and controlling of induction motor. There is enormous potential for ideal utilization of IoT-based condition monitoring for determining the failure and maintenance aspects of machines.

References

1. Goyal D, Pabla BS (2016) The vibration monitoring methods and signal processing techniques for structural health monitoring: a review. Arch Comput Methods Eng 23(4):585–594
2. Choudhary A, Goyal D, Shimi SL, Akula A (2018) Condition monitoring and fault diagnosis of induction motors: a review. Arch Comput Methods Eng 26(4):1221–1238
3. Goyal D, Pabla BS (2015) Condition based maintenance of machine tools—a review. CIRP J Manufact Sci Technol 10:24–35
4. Lazar C, Burlacu A, Archip A (2014) Vision-guided robot manipulation predictive control for automating manufacturing. In: Service orientation in Holonic and multi-agent manufacturing and robotics. Springer, Cham, pp. 313–328
5. Xia M, Li T, Zhang Y, de Silva CW (2016) Closed-loop design evolution of engineering system using condition monitoring through internet of things and cloud computing. Comput Netw 101:5–18
6. Saez M, Maturana FP, Barton K, Tilbury DM (2018) Real-time manufacturing machine and system performance monitoring using internet of things. IEEE Trans Autom Sci Eng 99:1–14
7. Goyal D, Pabla BS, Dhami SS, Lachhwani K (2017) Optimization of condition-based maintenance using soft computing. Neural Comput Appl 28(1):829–844
8. Halem N, Zouzou SE, Srairi K, Guedidi S, Abbood FA (2013) Static eccentricity fault diagnosis using the signatures analysis of stator current and air gap magnetic flux by finite element method in saturated induction motors. Int J Syst Assur Eng Manag 4(2):118–128
9. Goyal D, Pabla BS (2016) Development of non-contact structural health monitoring system for machine tools. J Appl Res Technol 14(4):245–258
10. Goyal D, Vanraj, Pabla BS, Dhami SS (2019) Non-contact sensor placement strategy for condition monitoring of rotating machine-elements. Eng Sci Technol Int J 22(2):489–501
11. Perera C, Zaslavsky A, Christen P, Georgakopoulos D (2014) Context aware computing for the internet of things: a survey. IEEE Commun Surv Tutor 16(1):414–454
12. Jung JH, Lee JJ, Kwon BH (2006) Online diagnosis of induction motors using MCSA. IEEE Trans Industr Electron 53(6):1842–1852
13. Dohr A, Modre-Opsrian R, Drobics M, Hayn D, Schreier G (2010) The internet of things for ambient assisted living. In: 2010 seventh international conference on information technology: new generations, IEEE, pp 804–809
14. Kumar S, Singh P, Sehgal S, Kumar H, Aggarwal N, Singh S, Goyal D (2019) Application of industrial internet of things for online monitoring of bearings. Lect Notes Mech Eng: In Press.

Development of Aluminium-Yttrium Oxide Metal Matrix Composite Foam Through FSP

Sachin Rathore, Ratnesh Kumar Raj Singh and K. L. A. Khan

Abstract Nowadays safety is the most important concern in the automobile industries. The safety can enhance by applying high-strength materials, but in general high-strength material is heavy and reduces the fuel economy of the automobiles. Thus, there is a requirement of such a material which have high strength to weight ratio. One such type of material is aluminium foam having high strength to weight ratio and also has very good impact-absorbing capability. The friction stir processing (FSP) opens a new route for developing aluminium foam. Also, if it is possible to develop the foams by light metal matrix composite (MMC) materials, then it added more features into it. Thus in present work, aluminium-yttrium oxide ($Al–Y_2O_3$) MMC foam is developed by using FSP technique by adding TiH_2 and pure aluminium powder. The result shows proper foam is developed by using FSP route. The pores are uniform and equally distributed into the aluminium matrix. The compressive strength of the foam decreases with increasing the amount of TiH_2 (Titanium hydride) into the metal matrix. This is because of the increase in size of the pores which increases the distance between load-bearing matrix.

Keywords Friction stir processing · Aluminium composite · Foam · Compressive strength

1 Introduction

The human lives are dependent on the safety guard attached in the automobiles. The main factor for the loss of human lives is road accidents. These accidents cause high impact force occurring on the vehicle. To minimize the adverse effect of these impact forces, many safety factors are employed into the vehicle. One such safety factor is to applying the foaming material at different places in the vehicle which absorb the

S. Rathore · K. L. A. Khan
KIET Group of Institutions, Ghaziabad, UP, India

R. K. R. Singh (✉)
Thapar Institute of Engineering and Technology, Patiala, Punjab, India
e-mail: rkrs73@gmail.com

H. Kumar and P. K. Jain (eds.), *Recent Advances in Mechanical Engineering*,
Lecture Notes in Mechanical Engineering,
https://doi.org/10.1007/978-981-15-1071-7_31

impact forces during road accident. The aluminium is widely used to develop the foam material because of its lightweight and good strength. There are lots of methods available for development of aluminium foam [1]. Powder metallurgy is common method used for developing aluminium foam [2]. In this process, a "precursor" is fabricated [3], which contains a foaming agent and a stabilizer with the aluminium powder. Then, this precursor is heated to a desired temperature so that foaming agent decomposes and release gases. These gases entrapped in the metal matrix and produce pores into it and the structure is known as foam. There are various methods used for making of precursors [4]. But these conventional routes for developing aluminium foam are costly and time-consuming. The other routes for development of precursor are electro-deposition technique [5], accumulative roll bonding (ARB) route [6] and the compressive torsion processing (CTP) route [7]. However, various factors associated with these processes affect their application and enhance the cost of fabrication of foam [8]. So, it is required to develop a method which will support the sustainable development.

Recently, friction stir processing (FSP) is widely used for development of aluminium surface composite and also used for development of precursor [9]. In the friction stir processing technique, the mixing blowing agent powder used for fabrication of precursor [10] and powder (stabilization agent) into aluminium plates utilizing the huge mixing activity of FSP [11]. It reduces the processing cost [12] and enhances productivity of the process [13]. In this research, initially the FSP route is used to develop aluminium–Y_2O_3 MMC and then this fabricated composite is used to fabricate foam. In the FSP route, for development of foam, first the precursor is fabricated by mixing a foaming agent along with aluminium powder which acts as a stabilizer in the aluminium plates during the stirring action in FSP. In this study, AA7075–Y_2O_3 metal matrix campsite porous foam has been fabricated. Then the fabricated porous structure has been nondestructively observed by scanning electron microscopy. The mechanical properties of fabricated foam have been evaluated by compression testing.

2 Experimental Procedure

2.1 Composite Making

The Al–Y_2O_3 MMC was fabricated by friction stir processing. For development of composite, aluminium plates were chosen of 100 mm × 200 mm × 6 mm dimensions. A special tool is fabricated for grooves making on shaper machine. Then using this tool, grooves were developed on the aluminium plates along its length with 1.5 mm thickness and up to 3 mm depth. The spacing between two consecutive grooves was keeping 2.5 mm. These grooves then filled with Y_2O_3 powders with average powder size is 67 μm measured by SEM. The FSP is employed to mix the Y_2O_3 powder into the aluminium matrix. This mixing produces aluminium–Y_2O_3 metal matrix

composite. Then, this composite plate is machined on milling machine up to 0.5 mm depth to remove the irregularities present on the top of the plate. Further, these plates were used for development of aluminium foam.

2.2 Precursor Making

The Al–Y_2O_3 MMC plates were drilled with 3 mm diameter drill bit up to 3 mm depth (Fig. 1). Then these holes are filled by foaming material containing foaming agent as a TiH_2 and stabilizer as a pure aluminium powder. The size of TiH_2 particles is approximately 36 μm with ~10 μm aluminium powder have been used in this experiment. The percentage amount (weight %) of the TiH_2 was kept 10, 30 and 50% during the experimentation. After filling the holes, the plates are stacked and FSP was carried out on a vertical milling machine. Figure 2 shows a schematic diagram of the stacked plates and the position of tool used to do processing in this study. The FSP tool used in this study has a cylindrical pin with flat shoulder. The diameter of the tool shoulder is 20 mm, the diameter of the tool probe is 9 mm and its length is 8 mm. The H-13 hot-die steel is used as the tool material. The FSP parameters were selected based on the trial run experiments and best-suited parameters are chosen for processing. The tool rotation and traverse speed were kept 900 rpm and 100 mm/min, respectively. In this experiments, tool was kept 2° tilt from vertical axis of the machine. Figure 3 shows the plate on which FSP was carried out. The PSW was done in such a way that the tool is sifted little away (approximately about the diameter) when finished processing on a line and then moves back and so on.

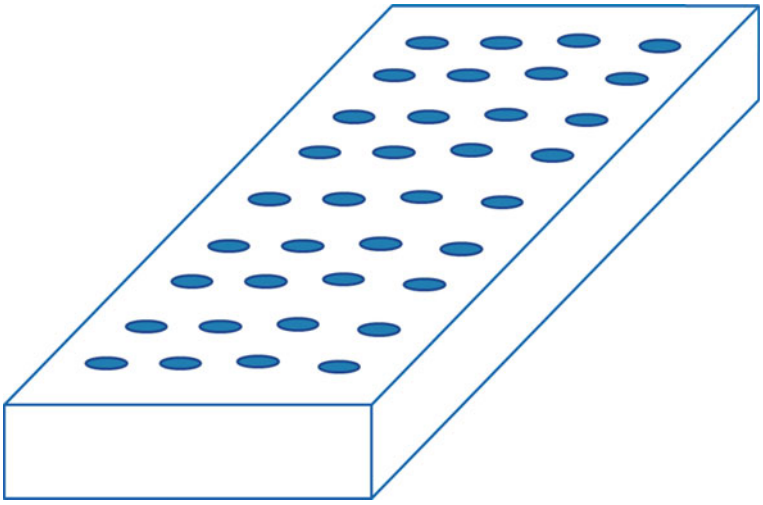

Fig. 1 Schematic diagram of drilled plate for developing precursor

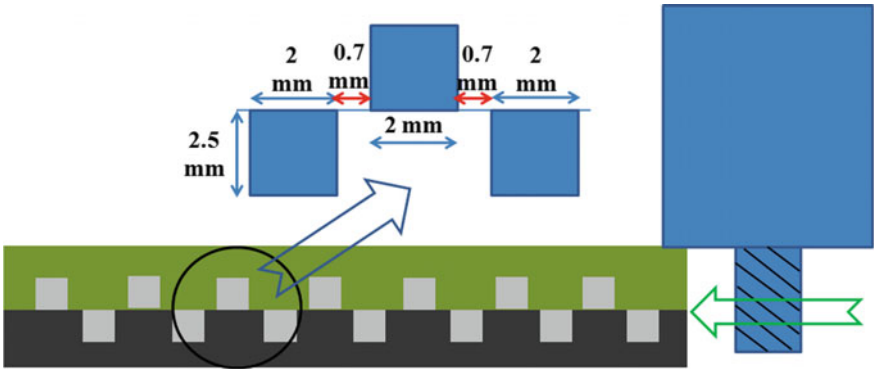

Fig. 2 Schematic diagram of precursor development by FSP

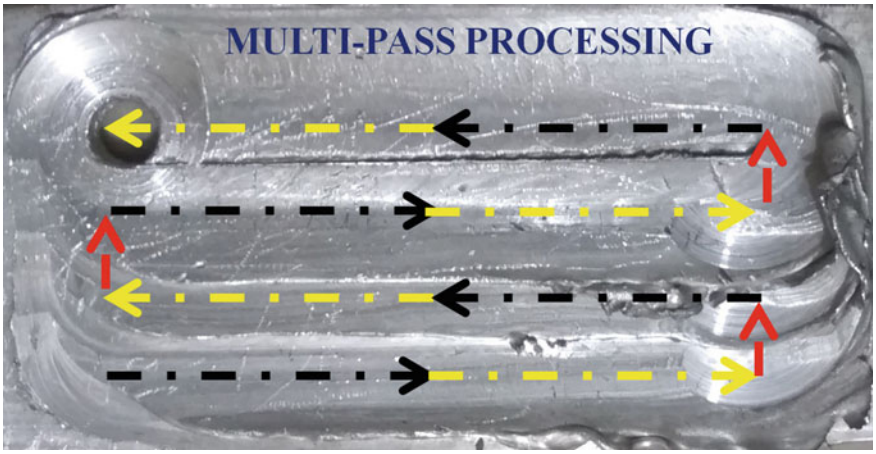

Fig. 3 Multi-pass FSP for development of precursor

2.3 Foam Making

The processed precursor is heat-treated in a preheated electric furnace to induce foaming. The holding temperature and the holding time have been kept 550 °C and 20 min, respectively. The sample was then cooled to room temperature under water. Then, the compression test specimen of 10 × 10 × 6 mm has been cut out from the foamed sample by wire electro-discharge machining.

3 Results and Discussion

3.1 SEM Inspection

The pores in the foam have been observed nondestructively by SEM using a tabletop SEM TM-3000 (made of Hitachi) at room temperature. The SEM analysis has been done to study the size of pores developed in different composition of TiH_2 powder. The samples were prepared with 10 mm × 10 mm × 6 mm in dimensions. Figure 4a shows images of a precursor obtained just after FSP. Grey regions represent the aluminium matrix while black one indicates pores. The pores occur in the matrix due to the heat generated during FSP. But the generated pores in the precursor are not uniformly distributed and a tunnel defect is also observed in precursor as shown in Fig. 4a. But roughly good circularity of pores was obtained but the size of these pores is very small. However, it is essential to reheat the precursor further to fabricate porous aluminium matrix with proper pores size and higher circularity. Figure 4b shows, foam produced after heating in furnace, indicating proper pores developed with greater in size. Then this fabricated foam is mechanically tested for their strength. The compression test is the most essential test to check the deformation behaviour of the foam. Figure 5 shows the stress–strain curve obtained from compression test for the precursor. From Fig. 5, it is clear that compression strength decreases with increasing the foaming agent. This is because, as the amount of foaming agent increases, the size of pores increases. Thus, the distance between the load-resisting metal matrix increases. It causes more deformation takes place on a given load and reduces the compressive strength of the foam. Generally, the characteristic of foam material is defined by the plateau stresses and its region [14]. The plateau region is a horizontal line occurred in the compressive stress–strain curve [15]. This plateau region shows

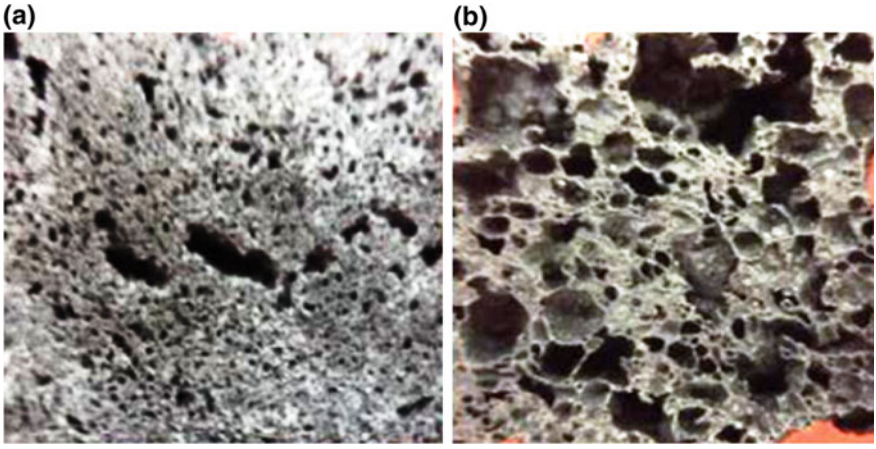

Fig. 4 **a** Precursor developed after FSP and **b** Foam developed after heat treatment

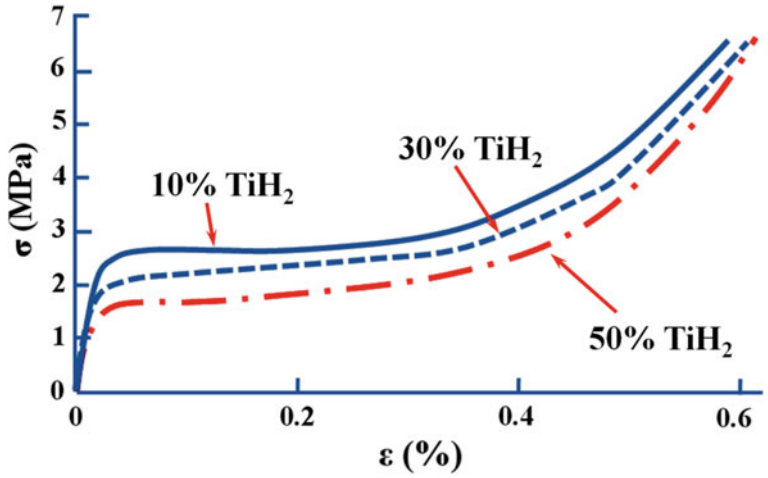

Fig. 5 Compression stress–strain curve obtained from porous foam fabricated by friction stir processing

the force absorbing capacity of the foam. Increasing the amount of plateau region increases the force absorbing capacity of the foam [16]. In this experiment, it is found that increasing the amount of TiH_2, increases the plateau region in the foam.

4 Conclusion

The successful Al-MMC foam has been developed by using FSP route. The preliminary study shows that as the weight % of foaming agent increases the tendency to resist the compressive load decreases. The composite has tendency to absorb impact energy by propagating crack at faster rate in all direction. This is also represented in the compression test as the compression strength decreases the collapse rate of pores in foam increases. This tendency increases the absorption of energy without transferring it. From the result, it is also clear that as the plateau region increases, it increasing the load-bearing capacity of the foam.

References

1. Alniak MO (2003) Changes of grain sizes and flow stresses of AA2014 and AA6063 aluminum alloys at high temperatures in various strain rates, 27:59–64
2. Andrews E, Sanders W, Gibson LJ (1999) Compressive and tensile behaviour of aluminum foams, 270:113–124
3. Hutchinson JW, Wadley HNG, Ashby MF, Evans AG, Fleck NA, Gibson LJ (2000) Metal foams: a design guide Butterworth-Heinemann

4. Banhart J (2000) Manufacturing routes for metallic foams. J Mater 52(December):22–27
5. Banhart J (2001) Manufacture, characterisation and application of cellular metals and metal foams. Prog Mater Sci 46:559–632
6. Banhart J (2005) Aluminium foams for lighter vehicles. Int J Veh Des 37(2005):114–125
7. Banhart BJ (2006) Metal foams: production and stability. Adv Eng Mater 8(9):781–794
8. Banhart J, Baurneister J, Weber M (1996) Damping properties of aluminium foams. Mater Sci Eng A 205(95):221–228
9. Hangai Y, Kamada H, Utsunomiya T, Kitahara S, Kuwazuru O, Yoshikawa N (2014) Aluminum alloy foam core sandwich panels fabricated from die casting aluminum alloy by friction stir welding route. J Mater Process Technol 214(9):1928–1934
10. Hangai Y, Ozeki Y, Utsunomiya T (2009) Foaming conditions of porous aluminum in fabrication of ADC12 aluminum alloy die castings by friction stir processing. Mater Trans 50(9):2154–2159
11. Hangai Y, Takahashi K, Utsunomiya T, Kitahara S, Kuwazuru O (2012) Fabrication of functionally graded aluminum foam using aluminum alloy die castings by friction stir processing. Mater Sci Eng A 534:716–719
12. Baumeister J, Banhart J (1998) Production methods for metallic foams. In: MRS symposium proceeding, vol 521. San Francisco, pp. 121–132
13. Cambronero LEG, Ruiz-roman JM, Corpas FA, Prieto JMR (2009) Manufacturing of Al–Mg–Si alloy foam using calcium carbonate as foaming agent. J Mater Process Technol 9(209):1803–1809
14. Davies SZGJ (1983) Review metallic foams: their production, properties and applications. J Mater Sci 18:1899–1911
15. Gergely V, Curran DC, Clyne TW (2003) The FOAMCARP process: foaming of aluminium MMCs by the chalk-aluminium reaction in precursors. Compos Sci Technol 63:2301–2310
16. Korner C, Singer RF (2000) Processing of metal foams—challenges and opportunities. Adv Eng Mater 4:159–165

Model-Based Adaptive Prognosis of a Hydraulic System

Sawan Kumar, Sumanta Kumar Dutta, Sanjoy Kumar Ghoshal and J. Das

Abstract Fault diagnostic and prognostic methods are the extensive topics of condition-based maintenance system. These publications include a wide range of statistical approaches for model-based approaches. Uncertainty in prediction cannot be avoided; therefore, algorithms are working to help manage these uncertainties. Remaining useful lives (RUL) are regularly updated through adaptive degradation models identified by using the concept of sampling importance resampling (SIR) filter. The SIR filter algorithm has become a popular choice for model-based progressive system. As a matter of study, we consider a hydraulic system and develop a detailed physics-based model and use extensive simulations to describe our prehistoric science approach and to evaluate its effectiveness and strength.

Keywords Hydraulic system · RUL · SIR filter

1 Introduction

Energy crisis and destabilization of fuel prices have accelerated the research on the fuel-efficient system. Model-based diagnostics approach is required for precise and infallible models of actual physical systems which incorporate several domains (such as mechanical, electrical and hydraulic). Behavior can be non-ambiguous, and it may be challenging to capture the connection between individual components and between the system and their environment.

Apart from this, different systems used in the real world are multi-models, i.e., operations are carried out in various configurations. An important challenge is modeling the system's mobility in a serious and effective way. In practice, the major challenge is balancing the details amalgamated into the model to ensure diagnosability, while keeping the complication in the model within controllable

S. Kumar (✉) · S. K. Dutta · S. K. Ghoshal
Department of Mechanical Engineering, IIT(ISM) Dhanbad, Dhanbad, India
e-mail: nawaskumar@gmail.com

J. Das
Department of Mining Machinery Engineering, IIT(ISM) Dhanbad, Dhanbad, India

H. Kumar and P. K. Jain (eds.), *Recent Advances in Mechanical Engineering*,
Lecture Notes in Mechanical Engineering,
https://doi.org/10.1007/978-981-15-1071-7_32

limits. Wu et al. [1] have discussed various types of energy saving techniques. The overall system efficiency depends upon the robustness of the system, which is only achievable with proper fault detection of the system. This is also related to the energy regeneration purpose [2]. Detecting faults (when something goes wrong), fault isolation (determining the fault location), identification of fault (determining fault mode) and prognostics (depending on the expected nature of continuous use, the occurrence of failure is predicted) are the sequential steps of complete fault diagnosis. Determination of fault detection and isolation (FDI) with a quantitative approach necessitates the generation of a mathematical model of the system. Use of the different constraints and different compatibility conditions has been presented in terms of known variables using the residual relations which are termed as analytical redundancy relations (ARRs) [3]. According to the normal operation of the model, the constraints are valid. The adaptive thresholds have been generated from the residual relations with small deviations of the constraints that are taken into account for the observation of the normal mode of operation. The number of sensors is proportional to the structured residuals. This is used for the fault detection and isolation purpose. Unstructured residual allows estimating the time-dependent behavior of the process parameters, which can be used for fault detection by comparison with the nominal values. Using the ARRs, the fault signature matrix (FSM) can be formed which is responsible for the identification of the faulty components. The unexpected deviations in the parameters of the system are termed as faults. Then, as faults transpire and stimulate the deviation of measurements, the observed deviations in measurements are compared to predicted values for the given particular faults, and any fault causing inconsistency when compared to the observed measurement deviations is removed from consideration [4]. The prediction for the end of the system's life is made by using a predictor on the basis of a mistake progress model integrated with nominal models for each hypothesized fault candidate. Many diagnostics and prognosis are used on the simulation model of the hydraulic system and the results are presented.

	Fault detection	Prognostics	Diagnostics
Machine learning	Clustering	Neural network	Decision trees
Physics-based	System theory	Damage propagation models	
Conventional numerical	Linear regression	Kalman filters	Logistic regression
AI-model-based	Expert systems		Finite-state machines

The paper structure is as follows. Section 2 accommodates the details of the behavioral and diagnostic model of the system. Section 3 explains in detail the method of diagnosis and prognosis used in this work. Section 4 includes experimental results and Sect. 5 provides a reasonable conclusion for the paper.

2 Modeling of the Hydraulic System

2.1 Model-Based Approaches

For the implementation of a model-based progressive approach, the components require a detailed physics-based model. Nominal behavior, as well as defective behavior of the component, should be described by the model. Apart from this, the progress of fault should be defined over time. It is with these models that can be predicted. Developing a nominal model based on the physical understanding of the system is the initial step in the way of developing models that meet the previously described requirements.

2.2 Physical Description of the System

The schematic representation of the setup being studied is shown in Fig. 1. Table 1 gives the names of the different components of the setup corresponding to the tags given in Fig. 1. The setup has a double-acting variable displacement pump (tag 2), driven by a 7.5 kW electric motor (tag 1), furnishing pressurized fluid to a bent axis hydromotor (tag 6). Before reaching the hydromotor, the fluid passes through a proportional flow control valve (tag 4), which is operated using a solenoid, which modulates the flow supplied to the hydromotor corresponding to the voltage imparted to the flow control valve. The hydromotor is used to drive a single-acting fixed displacement loading pump (tag 7) which in turn supplies fluid to the reservoir (tag 12.1–12.4) through a pressure relief valve (PRV) (tag 9). The load torque of the motor is regulated by varying the pressure setting of the PRV. The experiments are

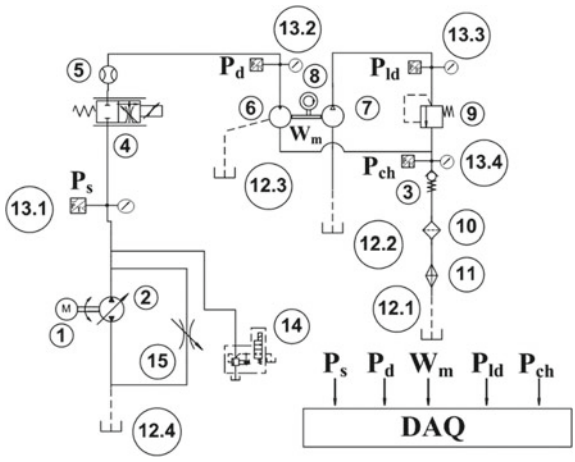

Fig. 1 Schematic representation of the setup

Table 1 The different components in the schematic diagram

Tag No.	Name of equipment
1	Electrical drive motor
2	Variable displacement pump
3	Spring-loaded check valve
4	Proportional flow control valve
5	Flow sensor
6	Motor
7	Loading pump (fixed displacement)
8	Speed sensor
9	Pressure relief valve
10	Filter
11	Oil cooler
12.1–12.4	Hydraulic reservoir
13.1–13.4	Pressure sensor
14	Flow control valve
15	Flow restrictor valve

conducted on the setup under well-aerated conditions. To obtain fluid with constant viscosity at different parts of the setup, suitable oil cooler and filter are used. The oil cooler maintains the temperature of the fluid in the range of 55–62 °C. The experimental setup has four pressure sensors (tag 13.1–13.4) and a speed sensor (tag 8) to measure the pressure at different sections of the system and the speed of the driven hydromotor which is recorded in the data acquisition system (DAQ). To ensure the accuracy of the setup, multiple test runs are conducted before collecting the data.

2.3 Mathematical Modeling of the System

The assumptions made for the mathematical modeling of the system are as follows:

- The fluid used in the system is a Newtonian fluid.
- The rate of flow through the flow control valve has a nonlinear relationship with the pressure difference across it.
- Details of valve dynamics assimilating spool inertia and friction effects are not taken into consideration.
- Compression of the fluid during flow through pipes is not considered.

2.3.1 Variable Displacement Pump

The volume flow rate lost due to compression in the pump can be mathematically given as

$$Q_p = D_p\omega_p - \frac{P_s}{L_p} - \left(C_D A\sqrt{\frac{2(|P_s - P_d|)}{\rho}}\mathrm{Sgn}(P_s - P_d)\right) \tag{1}$$

where

Q_p = Volume flow rate provided by the pump
D_p = Variable pump displacement
L_p = Resistance to leakage in variable displacement pump
D_s = Main pump pressure or system pressure
C_D = Coefficient of discharge
A = Orifice area of the proportional valve
P_d = Proportional relief valve pressure or delivery pressure = $k_{\text{bulk}} \int Q_m \mathrm{d}t$
$P_s = k_{\text{bulk}} \int Q_p \mathrm{d}t$, k_{bulk} = bulk modulus.

2.3.2 Hydraulic Motor

The volume flow rate lost due to compression in the hydraulic motor can be mathematically given as

$$Q_m = \left(C_D A\sqrt{\frac{2(|P_s - P_d|)}{\rho}}\mathrm{Sgn}(P_s - P_d)\right) - D_m\omega_m - \frac{P_d}{L_m} \tag{2}$$

where

Q_m = Volume flow rate lost due to compression in the hydraulic motor
D_m = Volumetric displacement of hydraulic motor
L_m = Resistance to leakage in hydraulic motor
ω_m = Angular velocity of hydraulic motor.

Now, torque lost in the motor to overcome rotational inertia is

$$T_m = D_m(P_d - P_{ch}) - f\omega_m - D_{lp}P_{ld} \tag{3}$$

where

P_{ch} = Check valve pressure at loading circuit
f = Viscous friction coefficient
D_{lp} = Loading pump displacement

P_{ld} = Discharge pressure of the loading pump.
$\omega_m = \frac{\int T_m \mathrm{d}t}{\text{Motor Inertia}} = \frac{\int T_m \mathrm{d}t}{J}$

Now, flow to the tank from the motor can be described as

$$Q_{m1} = D_m \omega_m - \left(C_d A_{\text{ch}} \sqrt{\frac{2(|P_{\text{ch}} - P_{\text{atm}}|)}{\rho}} \text{sgn}(P_{\text{ch}} - P_{\text{atm}}) \right) + \left(C_d A_l \sqrt{\frac{2(|P_{\text{ld}} - P_{\text{ch}}|)}{\rho}} \text{sgn}(P_{\text{ld}} - P_{\text{ch}}) \right) \tag{4}$$

And corresponding effort = $P_{\text{ch}} = k_{\text{bulk}} \int Q_{m1} \mathrm{d}t$
where

A_{ch} = Orifice area of the check valve at load circuit
P_{atm} = Atmospheric pressure.

2.3.3 Loading Pump

Loading pump which is coupled with the hydraulic motor also experiences some hydraulic losses during fluid flowing through the pump. Now, the flow from the pump is given as,

$$Q_{\text{lp}} = D_{\text{lp}} \omega_m - \left(C_d A_l \sqrt{\frac{2(|P_{\text{ld}} - P_{\text{ch}}|)}{\rho}} \text{sgn}(P_{\text{ld}} - P_{\text{ch}}) \right) \tag{5}$$

where the pressure at the inlet to the loading pump = $P_{\text{ld}} = k_{\text{bulk}} \int Q_{\text{lp}} \mathrm{d}t$

A_l = Orifice area of the load valve.

2.3.4 Residuals

In this application, five sensors are used, and therefore, the number of residuals will be five.

From Eq. (1), the first residual can be described as below:

$$\text{Rd}_1 = D_p \omega_p - \frac{\dot{P}_s}{k_{\text{bulk}}} - \left(\frac{P_s}{L_p} \right) - \left(C_D A \sqrt{\frac{2(|P_s - P_d|)}{\rho}} \text{Sgn}(P_s - P_d) \right) \tag{6}$$

and

$$\varepsilon_1 = \frac{|\dot{P}_s|}{\delta k_{\text{blk}}} + \left(\delta D_p |\omega_p|\right) + [\delta(C_D A)]\sqrt{\frac{2|P_s - P_d|}{\rho}} + \frac{|P_s|}{\delta L_p}$$

where δ is the uncertainty for the associated parameter and its value is considered as 0.1 (i.e., 10%).

Upper threshold value $= \text{Rd}_1 + \varepsilon_1$
Lower threshold value $= Rd_1 - \varepsilon_1$

The second residual corresponding to the second equation is

$$\text{Rd}_2 = \left(C_D A\sqrt{\frac{2(|P_s - P_d|)}{\rho}}\text{Sgn}(P_s - P_d)\right) - D_m\omega_m - \frac{\dot{P}_d}{k_{\text{bulk}}} - \frac{P_d}{L_m} \tag{7}$$

and

$$\varepsilon_2 = \frac{|\dot{P}_d|}{\delta k_{\text{blk}}} + (\delta D_m|\omega_m|) + [\delta(C_D A)]\sqrt{\frac{2|P_s - P_d|}{\rho}} + \frac{|P_d|}{L_m}$$

Upper threshold value $= \text{Rd}_2 + \varepsilon_2$
Lower threshold value $= \text{Rd}_2 - \varepsilon_2$

According to Eq. (3), the third residual is as follows:

$$\text{Rd}_3 = D_m(P_d - P_{\text{ch}}) - f\omega_m - D_{\text{lp}}P_{\text{ld}} - J\dot{\omega}_m \tag{8}$$

and

$$\varepsilon_3 = \delta D_m|P_d - P_{\text{ch}}| + (\delta f|\omega_m|) + \left(\delta D_{\text{lp}}|P_{\text{ld}}|\right) + (\delta J|\dot{\omega}_m|)$$

Upper threshold value $= \text{Rd}_3 + \varepsilon_3$
Lower threshold value $= \text{Rd}_3 - \varepsilon_3$

From Eq. (5), the fourth residual can be described as below:

$$\text{Rd}_4 = \frac{\dot{P}_{\text{ld}}}{k_{\text{blk}}} - D_{\text{lp}}\omega_m + C_D A_l\sqrt{\frac{2|P_{\text{ld}} - P_{\text{ch}}|}{\rho}}\text{sgn}(P_{\text{ld}} - P_{\text{ch}}) \tag{9}$$

and

$$\varepsilon_4 = \frac{|\dot{P}_{\text{ld}}|}{\delta k_{\text{blk}}} + \left(\delta D_{lp}|\omega_m|\right) + [\delta(C_D A_l)]\sqrt{\frac{2|P_{\text{ld}} - P_{\text{ch}}|}{\rho}}$$

Upper threshold value $= \mathrm{Rd}_4 + \varepsilon_4$
Lower threshold value $= \mathrm{Rd}_4 - \varepsilon_4$

From Eq. (4), the fifth residual can be described as

$$\mathrm{Rd}_5 = D_m\omega_m - \left(C_d A_{\mathrm{ch}}\sqrt{\frac{2(|P_{\mathrm{ch}} - P_{\mathrm{atm}}|)}{\rho}}\mathrm{sgn}(P_{\mathrm{ch}} - P_{\mathrm{atm}})\right) + \left(C_d A_l\sqrt{\frac{2(|P_{\mathrm{ld}} - P_{\mathrm{ch}}|)}{\rho}}\mathrm{sgn}(P_{\mathrm{ld}} - P_{\mathrm{ch}})\right) - \frac{\dot{P}_{\mathrm{ch}}}{k_{\mathrm{bulk}}} \tag{10}$$

and

$$\varepsilon_5 = (\delta D_m|\omega_m|) + \left(\delta(C_d A_{\mathrm{ch}})\sqrt{\frac{2(|P_{\mathrm{ch}} - P_{\mathrm{atm}}|)}{\rho}}\right) + \left(\delta(C_d A_l)\sqrt{\frac{2(|P_{\mathrm{ld}} - P_{\mathrm{ch}}|)}{\rho}}\right) + \frac{|\dot{P}_{\mathrm{ch}}|}{\delta k_{\mathrm{bulk}}}$$

Upper threshold value $= \mathrm{Rd}_5 + \varepsilon_5$
Lower threshold value $= \mathrm{Rd}_5 - \varepsilon_5$

From the five residual equations from Eqs. (6) to (10), the fault signature matrix is derived in Table 2, which correlates the components with their fault likelihood.

2.4 Simulink Model of the System

According to the mathematical equations of the above section, a block model is made in MATLAB/Simulink. The model has been divided into two parts—behavioral model and diagnostic model (Fig. 2). In the behavioral model, the constitutive relations given in Eqs. (1) through (5) are evaluated, whereas the diagnostic model is a simple computation of the residuals given in Eqs. (6) through (10).

3 Adaptive Prognosis Approach

3.1 Degradation Model and RUL Prediction

System input, $u(k)$, measurement, $t(0: k)$, and the initial state of the system are taken as input of small model supervisor, and state transition function, $f(k)$ and observation function, $h(k)$, state distribution, $y(k)$, and parameter, $\theta(k)$ is used to estimate $p(y(k),$

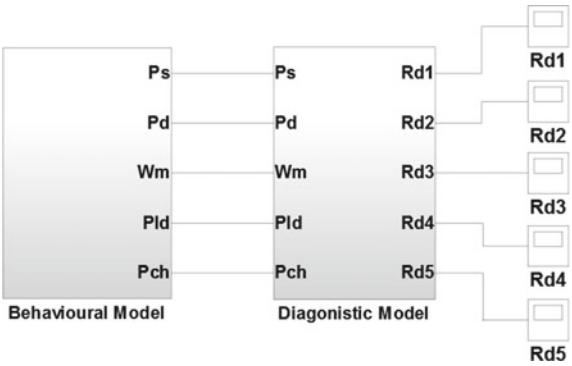

Fig. 2 Simulink model of the system

$z(k) \mid t(0{:}\,k)$. Any suitable filtering scheme, e.g., Kalman filter, extended Kalman filter, unscented Kalman filter, particle filter, SIR filter [5] and others, can be appointed as the nominal observer. According to the fault signature matrix (FSM), the probable components can be identified during the breakdown of the machine for a particular type problem. But there are some faults which cannot be isolated because of its nature. In the given FSM, if only the first residual (Rd_1) deviates, then it is not isolable between V_p and L_p. The reason is that fault signature is same, i.e., coherence vector $C^{'}$= [1 0 0 0 0] for V_p and L_p.

3.2 Proposed Prognosis Procedure

3.2.1 Damage Estimation

In the model-based paradigm, estimation of the loss reduces joint states-parameter estimation, i.e., calculation of $f(\boldsymbol{y}_k, z_k, |z_{0:k})$. For linear systems with additive Gaussian noise terms, the particle filter serves as the most appropriate option [6]. For nonlinear systems with additive Gaussian noise terms, the unscented Kalman filter or extended Kalman filter also works as suitable alternatives [7]. However, for nonlinear systems with non-Gaussian noise conditions, particle filters are most suitable and provide accurate (i.e., sub-adoption) solutions to the state calculation problem for those systems where the optimum solution is unrecoverable or unmanageable. In particle filters, a set of discrete weighted specimens called particle helps to estimate, almost accurate, state distribution. As the number of particles grows, increasing accuracy ensures that optimal solution stops. In addition, implementation of particle filters is relatively straightforward, and increasing or decreasing the number of particles controls the computational complexity, with respect to the preferred estimation performance. Furthermore, other filtering algorithms are unable to directly handle the discrete position sensors. For these reasons, our model-based prognostics framework utilizes sampling importance resampling (SIR) particle filters. With particle

filters, the particle approximation to the state distribution is given by

$$\left\{\left(\boldsymbol{y}_k^i, \boldsymbol{z}_k^i\right), \omega_k^i\right\}_{i=1}^N$$

where N denotes the number of particles, and for particle, i.e., $\boldsymbol{y}_k^i$ parameter shows the estimates, $\boldsymbol{z}_k^i$ denotes the parameter estimates and ω_k^i denotes the weight.

The posterior density is estimated by

$$f(\boldsymbol{y}_k, \boldsymbol{z}_k, |\boldsymbol{z}_{0:k}) \approx \sum_{i=1}^{N} \omega_k^i \delta_{\left(\boldsymbol{y}_k^i, \boldsymbol{z}_k^i\right)}(\mathrm{d}t_k \mathrm{d}z_k)$$

where $\delta_{\left(\boldsymbol{y}_k^i, \boldsymbol{z}_k^i\right)}(\mathrm{d}t_k \mathrm{d}z_k)$ denotes the Dirac delta function located at $(\boldsymbol{y}_k^i, \boldsymbol{z}_k^i)$.

The sample importance reproduction (SIR) employs particle filters, and by using systematic reproduction, the resampling phase is applied. The pseudo-code for single phase of SIR filter is shown as Algorithm 1 [8]. Each particle i is propagated periodically by sample of new parameter values. Here, the parameter $\boldsymbol{z}_k$ is developed by some unknown random process which is independent of the state $\boldsymbol{y}_k$. To assess the parameters within a SIR filter structure, however, we need to assign parameters to some type of development. Specific solutions are to use a random walk, i.e., for parameter $\boldsymbol{z}$, $\boldsymbol{z}_k = \boldsymbol{z}_{k-1} + \xi_{k-1}$ where ξ_{k-1} is typically Gaussian noise. After sampling parameter values from selected distribution, new states are taken sampling by implementing state equation f to $(\boldsymbol{y}_k^i, \boldsymbol{z}_k^i)$ with process noise $v(t)$ sampled from its assumed distribution. The particle weight is assigned using z_k. Specifically, the output equation h is applied to $(\boldsymbol{y}_{k+1}^i : \boldsymbol{z}_{k+1}^i)$ and the probability of this output is calculated using the probability of sensor noise using the probability density function. Weight is then normalized, followed by resampling step [9]. Therefore, within the algorithm, we believe that some sensor noise exists for these sensors.

3.2.2 Prediction

Prediction is started at a certain time t_p. Using the current state estimate, $f(\boldsymbol{y}_k, \boldsymbol{z}_k, |\boldsymbol{z}_{0:k})$ the goal is to compute $f(\mathrm{EOL}_{t_p}, |\boldsymbol{z}_{0:t_p})$ and $f(\mathrm{RUL}_{t_p}, |\boldsymbol{z}_{0:t_p})$. The particle filter computes

$$f\left(\mathrm{EOL}_{t_p} | \boldsymbol{z}_{0:t_p}\right) \approx \sum_{i=1}^{N} \omega_{t_p}^i \delta_{\left(\mathrm{EOL}_{t_p}^i\right)}\left(\mathrm{dEOL}_{t_p}\right).$$

To calculate EOL, we proliferate each particle ahead of its specific EOL and weigh the particle on t_p compute EOL, for its EOL prediction.

4 Results and Discussions

In our experiments, to find fault, we use the nominal system simulation model to produce the behavior of the nominal system. In our experiments and the parameters of the hydraulic system, fault signatures for defects are given in Table 2, and errors are used for isolation. For identifying the fault, we use sampling importance resampling (SIR) as its supervisor. Parameter is updated through the given weight to the EOL and RUL and gives the appropriate result.

4.1 System Identification and Experimentally Validation

Figure 3a through Fig. 3d compare the measured and simulated pressure at different points in the circuit for the purpose of fault diagnosis. The parameter values (given in Table 3) obtained from the product catalogue of the set-up are used for model simulation. In Fig. 3, experimental pressure is slightly more than the simulation pressure. The nature of curve is almost similar after adjusting some parameter. The

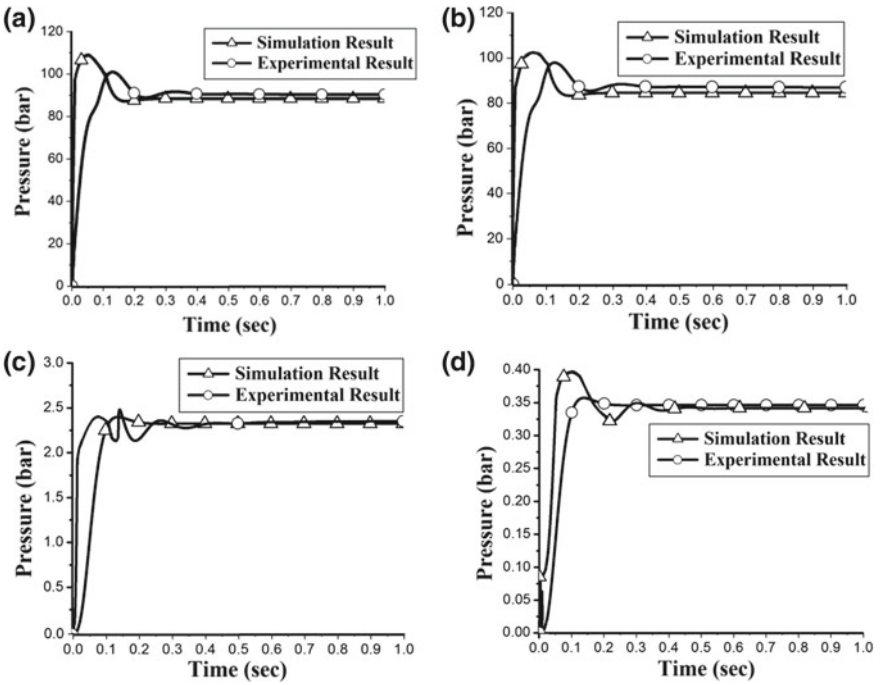

Fig. 3 **a** System pressure (E_s) versus time. **b** Delivery pressure (E_d) versus time. **c** Loading pressure (E_{ld}) versus time. **d** Check valve (E_{ch}) pressure versus time

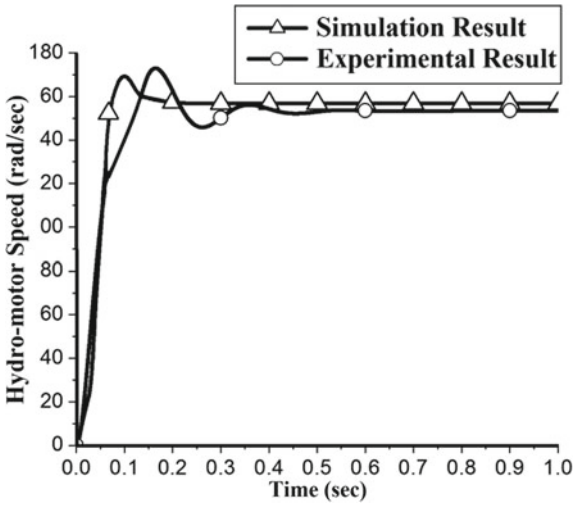

Fig. 4 Motor speed (ω_m) versus time

peak time is shifted in experimental behavior. The reason is that in the model simulations different nonlinearities caused by flow-force, pump ripples, etc. are not considered, while experimental analysis involves all such factors. Apart from that errors due to measurement and process noise are also reflected in the test data.

In Fig. 4, the experimental rotational speed of hydromotor is slightly less than simulation result. It is due to the viscous friction of the revolving component, which is not identified in the model.

4.2 Residual Evaluation Using Test Data

Two types of faults are imposed one after another. First one is the reduction of pump displacement (i.e., Vp reduced) and the next is the reduction of the leakage resistance across the variable displacement pump (i.e., Lp reduced) at 5 s. Only Rd_1 is crossing the threshold as shown in Figs. 5 and 6, respectively. Only Rd_1 is deflected beyond the range of the threshold. Now, the task is to isolate the faulty component through parameter estimation.

4.3 Demonstration of the Approach

The behavior received by the model supports the model-based approach in contrast to simple trending strategies. To demonstrate a general solution, the particle filter is permitted to estimate all the damage modes of the hydraulic system jointly. Taking into consideration the large state space, $T = 40000$ s is implemented. For each fault

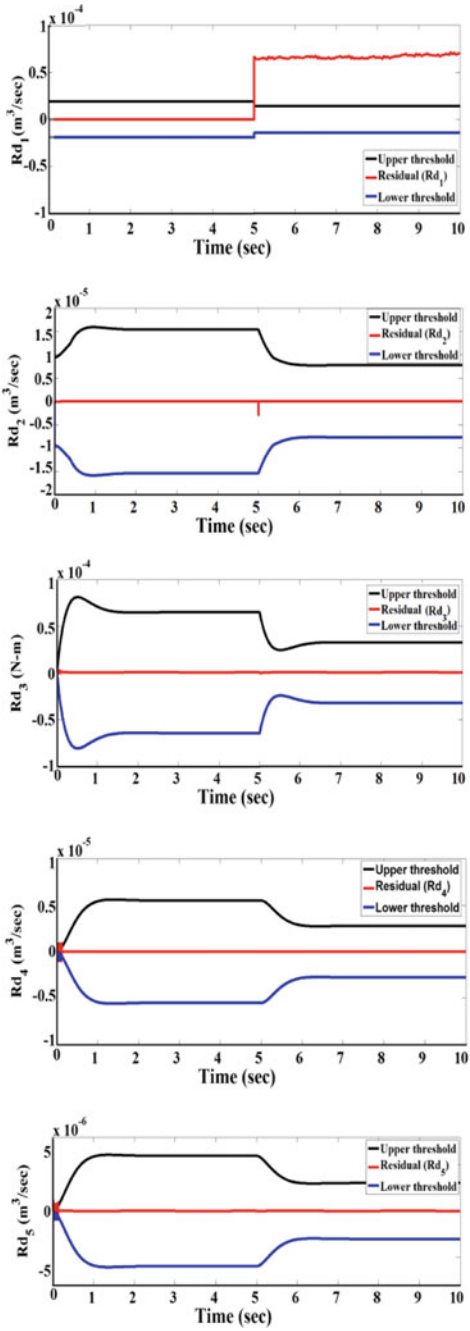

Fig. 5 Upper threshold, residual and lower threshold versus time after imposing the fault in the displacement of pump

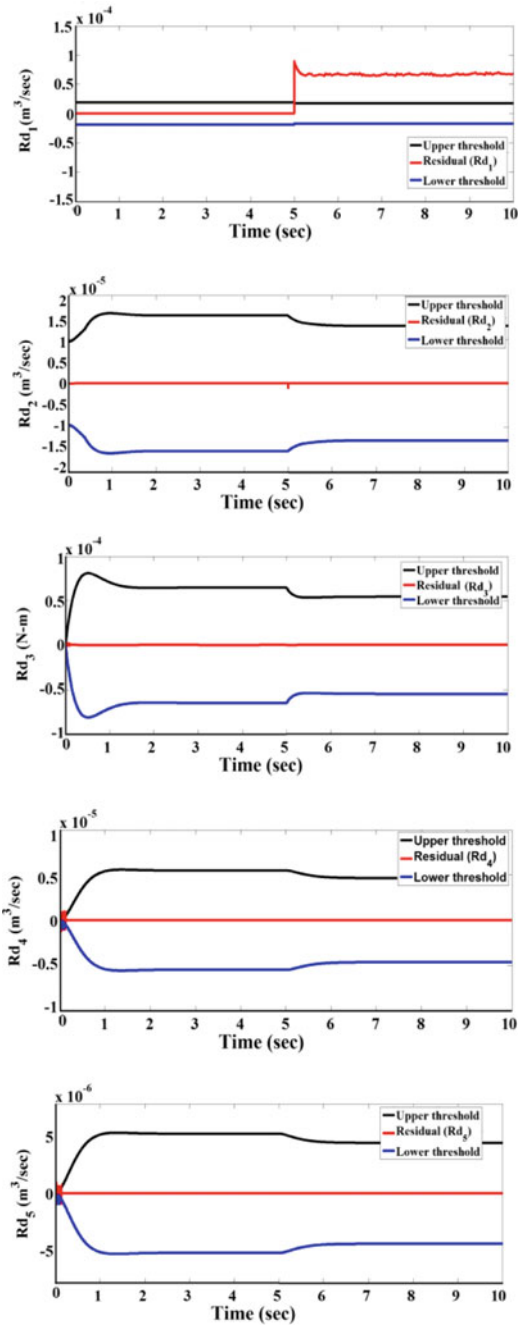

Fig. 6 Upper threshold, residual and lower threshold versus time after imposing the fault in the leakage of pump

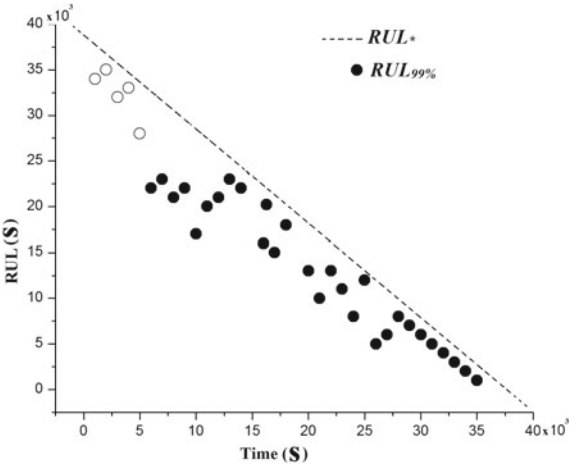

Fig. 7 RUL*(true) versus $RUL_{99\%}$

mode, the proposed algorithm provides the correct wear rate. The identified fault in this particular study is the external leakage from pump-plenum. Figure 7 captures the 99% confidence-level predictions, i.e., the value at which 99% of the prediction distribution is greater than or equal to that value. At this level of confidence, the predictions always remain below the true RUL and work as conservative estimates, and decisions can be taken on the basis of these risks. For more complete verification, a more flexible test is required, such that it may be run to fail the defect and/or the injection of hydraulic system.

For this, the estimated value of displacement of the pump (Dp) is obtained as 2.839×10^{-6} m^3/rad and leakage resistance (L_p) is 1.5×10^{11} N s/m^2, whereas the nominal values for D_p and L_p are 3.14×10^{-6} m^3/rad and 1×10^{11} N s/m^2, respectively (refer Tables 2 and 3). But the increase of leakage above the nominal is not admissible. Hence, the admissible solution is the reduction of pump displacement to 2.839×10^{-6} m^3/rad.

Table 2 Fault signature matrix

Components	Rd_1	Rd_2	Rd_3	Rd_4	Rd_5	I
D_p	1	0	0	0	0	0
D_m	0	1	1	0	1	1
A	1	1	0	0	0	1
A_l	0	0	0	1	1	1
D_{lp}	0	0	1	1	0	1
L_p	1	0	0	0	0	0
L_m	0	1	0	0	0	1
f	0	0	1	0	0	1

Table 3 Parameters of components used in Simulation

Parameters	Value
Electric motor speed (ω_p)	150 rad/s
Fixed pump displacement (D_p)	3.15×10^{-6} m^3/rad
Bulk stiffness (k_{bulk})	5×10^{12} N/m^2
Resistance to pump leakage flow path (L_p)	1×10^{11} N s/m^2
Coefficient of discharge (C_D)	0.64
Density of the fluid (ρ)	865.7 m^3/kg
Proportional leakage area (A)	2×10^{-5} m^2
Motor displacement (D_m)	1.91×10^{-6} m^3/rad
Inertia of motor (J)	0.01 kg m^2
Motor leakage (L_m)	1×10^{12} N s/m^2
Loading pump displacement (D_{lp})	1.75×10^{-6} m^3/rad
Proportional leakage area constant for loading circuit (A_l)	2×10^{-5} m^2
Proportional leakage area constant for motor (A_{ch})	1×10^{-4} m^2
Atmospheric pressure (P_{atm})	1×10^5 Pa
Viscous friction (f)	0.1 N s/m^2

5 Conclusions

In the course of this work, a model-based prognostics system approach making the use of SIR filters for updated parameter estimation has been developed. The estimated damage of the hydraulic system predicted EOL and forms EOL and RUL distributions. Applying this method to a hydraulic system, we develop an exhaustive physics-based model that includes models of damage progression. From the simulated experiments, it can be established that using only the discrete position sensors of the hydraulic system, successful prognostics can be achieved, and this approach is applied to experimental data under the same constraint. The effectiveness of a model-based approach is demonstrated by the results, and insight into the parameters considered for the selection of sensors for valve prognostics is given. A model-based approach is advocated, where the performance depends greatly upon the accuracy of the model provided. Undoubtedly, a key obstacle is presented in the development of such a model.

Acknowledgements I am grateful to DST project number YSS/2015/000397 "Design and development of series-parallel hydraulic hybrid energy efficient excavator having displacement con-trolled actuators" for providing the setup for doing future research in this field.

References

1. Wu W, Hu J, Jing C, Jiang Z, Yuan S (2014) Investigation of energy efficient hydraulic hybrid propulsion system for automobiles. Energy 73:497–505
2. Lin T, Huang W, Ren H, Fu S, Liu Q (2016) New compound energy regeneration system and control strategy for hybrid hydraulic excavators. Autom Constr 68:11–20
3. Shi H, Yang H, Gong G, Liu H, Hou D (2014) Energy saving of cutterhead hydraulic drive system of shield tunneling machine. Autom Constr 37:11–21
4. Kumar S, Das S, Ghoshal SK, Das J (2018) Review of different energy saving strategies applicable to hydraulic hybrid systems used in heavy vehicles. IOP Conf Ser Mater Sci Eng 377(1):012072. (IOP Publishing)
5. Roychoudhury I, Hafiychuk V, Goebel K (2013) Model-based diagnosis and prognosis of a water recycling system. In: Aerospace conference, IEEE, pp 1–9
6. Mahulkar V, McGinnis H, Derriso M, Adams DE (2010) Fault identification in an electro-hydraulic actuator and experimental validation of prognosis based life extending control. Air force research lab wright-patterson AFB OH air vehicles directorate
7. Prakash O, Samantaray AK, Bhattacharyya R, Ghoshal SK (2018) Adaptive prognosis for a multi-component dynamical system of unknown degradation modes. IFAC-PapersOnLine 51(24):184–191
8. Pandian A, Ali A (2009) A review of recent trends in machine diagnosis and prognosis algorithms. In: 2009 world congress on nature and biologically inspired computing. NaBIC 2009, IEEE, pp 1731–1736
9. Daigle MJ, Goebel K (2011) A model-based prognostics approach applied to pneumatic valves. Int J Progn Health Manag 2(2):84–99

Effect of Intercritical Heat Treatment and Volume Fraction on the Morphological Properties, Mechanical Properties, and Work Hardening Behaviour of Dual-Phase Steel

Shubham Sharma, Jujhar Singh, N. Jayarambabu, Chander Prakash, Sunpreet Singh, Abhinav Sharma and Harish Kumar

Abstract An investigation aimed at determining the importance of carbon percentage in the microstructure development of dual-phase steel is carried out by intercritically annealing the different samples of low-carbon steels which consists of different percentage of carbon (0.16, 0.18, and 0.20%). The samples are heated in muffle furnace to above Ac3 temperature (920 °C), soaked the sample for 30 min and quenched in ice brine solution to get complete martensitic structure. Later the samples are intercritically annealed at 740, 760, 780, 800, and 820 °C (between Ac1 and

S. Sharma (✉)
CSIR-Central Leather Research Institute, Regional Centre for Extension and Development, Leather Complex, Kapurthala Road, Jalandhar, Punjab 144021, India
e-mail: shubham543sharma@gmail.com

J. Singh · A. Sharma
Department of Mechanical Engineering, Inder Kumar Gujral Punjab Technical University, Kapurthala, Punjab 144603, India
e-mail: jujharsingh2085@gmail.com

A. Sharma
e-mail: abhinav.a939@gmail.com

N. Jayarambabu
Center for Nanoscience and Technology, Institute of Science and Technology, Jawaharlal Nehru Technological University Hyderabad, Hyderabad, Telangana 500085, India
e-mail: njayarambabu@gmail.com

C. Prakash · S. Singh
School of Mechanical Engineering, Lovely Professional University, Phagwara, Punjab 144411, India
e-mail: chander.mechengg@gmail.com

S. Singh
e-mail: sunpreet.21624@lpu.co.in

H. Kumar
Department of Mechanical Engineering, National Institute of Technology Delhi, New Delhi, Delhi 110040, India
e-mail: harishkumar@nitdelhi.ac.in

H. Kumar and P. K. Jain (eds.), *Recent Advances in Mechanical Engineering*,
Lecture Notes in Mechanical Engineering,
https://doi.org/10.1007/978-981-15-1071-7_33

Ac3) for 60 min and quenched in oil at room temperature. Microstructure examination revealed that steel containing 0.18%C yields a better microstructure which consists of around 46% martensite and remaining ferrite and minute amount of retained austenite, which is a good combination of strength and toughness. The uniaxial tensile test results show that at specimen containing 0.18%C with 46% martensite content yielded maximum tensile strength with comparatively higher toughness. Microhardness test shows that hardness increases with increasing carbon percentage and has higher values at 0.18%C.

Keywords Intercritical annealing · Martensite · Ferrite · Dual-phase (DP) steel · Intercritical heat treatment (ICHT)

1 Introduction

DP steels are a portion of the superior progressed high-potency steels (HPS) ancestor and were created to enhance steel quality as well as force and formability with improved limit of vitality retention. The simplest of the DP steel in this sort comprise 0.08–0.2% weight carbon (C), 0.5–1.5% weight manganese (Mn), except steels small scale alloyed with vanadium are likewise reasonable, whilst little augmentations of chromium (Cr) (0.5% weight) and molybdenum (Mo) (0.2–0.4% weight) are habitually utilized. These steels have relatively low yield stress of the order of 300–350 MN/m^2. The trail of advancement and progression of DP steel as illustrated by various specialists or examiners coordinate towards understanding the job of substantial number of microstructural erratic factors, which impact their mechanical possessions/assets [1]. Volume fraction, amount of retained austenite is some of the microstructural variables. The study on the structural-tensile property co-relations in DP steels has led to explain the relationship between strength and volume fraction of martensite. Attention has been paid to characterize toughness behaviour of DP steels in order to produce them for structural applications. There exist several methods to produce DP steels, which yield various types of distribution of ferrite and martensite in the microstructures. There appears an agreement that the strength of DP steel is linearly proportional to the percentage of martensite in the structure, in turn, the carbon content of present in the material [2, 3].

2 Literature Survey

An enhancement of the intercritical temperature enhances the segment of austenite shaped, which changes into martensite amid quick cooling, recuperating hardness, and force. Be that as it may, there is equalization between two inverse impacts: for low martensite divisions, carbon composition of this stage is high, whilst with expanding the division, carbon composition diminishes. This carbon composition of martensite

manages the hardness of the segment and thus influences the ultimate properties of material. It has been accounted for that there is a span of martensite segments (35–50%) in which mechanical assets of dual-phase steels are upgraded, allied to a equilibrium amid martensite segment and hardness of the mutual stages [4, 5]. The constituent too characterizes the probability to acquire the twin configuration in diverse bore dia. or thickness and hi-tech scientific perspectives like weldability [4]. In spite of the fact that it has been created a lot of data, there are still talks about the advancement of mechanical possessions of these dual-phase steels with carbon constituent. The goal of this research study is to consider the impact of the carbon ingredient on the acquired morphological and mechanical assets of dual phase from traditional tectonic steels.

3 Materials and Methods

3.1 Materials

Commercial low-carbon steels were chosen as the initial preliminary substance for creating dual-phase morphologies by suitable heat treatment. The as-received steels were as 8 mm deep hot rolled plates in extinguished and tempered situation. The elemental investigation of the DP steel was determined with the aid of an optical emission spectroscopy analysis. This determined chemical composition of the steel is as appeared in Table 1.

3.2 Heat Treatment Procedure

The as-received structural steels were then cut into specimens and subjected to double quenching, where they are first heated in muffle furnace shown in Fig. 1 and soaked at 920 °C for thirty min. and then extinguished in nine per cent ice brackish water arrangement (7 °C) as appeared in Fig. 2. Later the specimens were held at different intercritical temperatures individually (740, 760, 780, 800, and 820 °C) for 60 min and quenched in oil at room temperature. The schematic representation of the above heat treatment process is shown in Fig. 3. The specimens ‘A’ are named A74, A76, A78, A80, and A82; the specimens ‘B’ are named B74, B76, B78, B80, and B82; the specimens ‘C’ are named C74, C76, C78, C80, and C82 for identification.

Table 1 Chemical compositions of the DP steel

Samples	Carbon (%)	Manganese (%)	Sulphur (%)	Phosphorus (%)	Silicon (%)	Chromium (%)	Molybdenum (%)	Vanadium (%)	Boron (%)	Nickel (%)
A	0.16	1.32	0.002	0.013	0.44	0.03	0.09	0.056	0.0019	0.4
B	0.18	1.4	0.001	0.018	0.3	0.01	0.11	0.035	0.001	0.6
C	0.2	1.5	0.002	0.015	0.5	0.02	0.02	0.065	0.0018	0.8

Fig. 1 Muffle furnace

Fig. 2 Quenching performed on the specimen

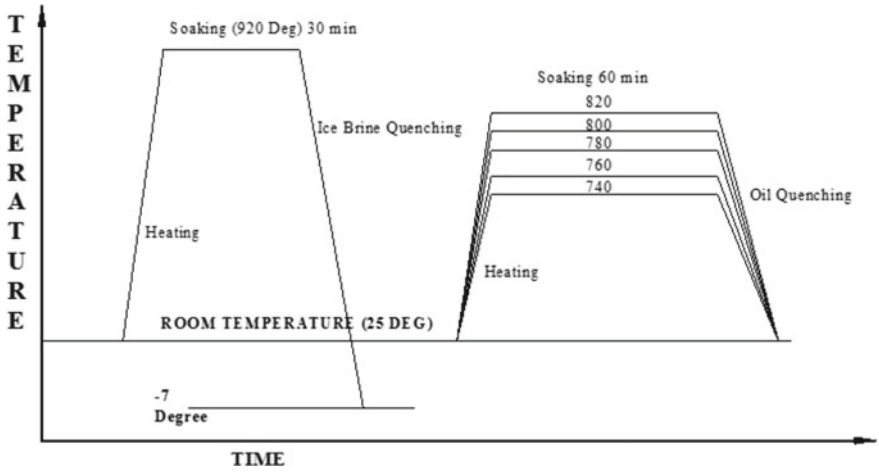

Fig. 3 Schematic representation of the heat treatment process carried out

4 Experimentation Work and Analysis

4.1 Microstructure Examination

Metallographic examinations are carried out on the heat-treated specimens to know the microstructure. Test samples for metallographic examinations were cut from the heat-treated blanks in the transverse direction of the rolled plates using a Buehler isomet 2000 diamond saw in order to avoid any deformation or burning on the surfaces [6–9]. These were first ground on successively finer silicon carbide abrasive papers, followed by polishing on Buehler metlap pattern no 8, platen no 4 and on a nylon cloth using 9-micrometer, and 1-micrometer diamond slurry, respectively. The final polishing was carried out on texmet paper cloth using a colloidal suspension (Buehler Masterpolish) at a wheel speed of 140 RPM. The polished test specimens were etched with proper etchants (Nital sodium meta bi sulphide) and subjected to microstructure examination using EPHIPHOTNIKON microscope with 400× magnification. The test results revealed the presence of ferrite and martensite phases in the microstructure with varying proportions and thus the specimen can now be called as dual-phase steel and are shown in the following Figs. 4, 5, 6, 7, 8, 9, 10, 11, 12, 13, 14, 15, 16, 17 and 18 as mentioned.

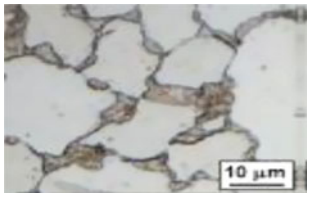

Fig. 4 Dual-phase microstructures of A74

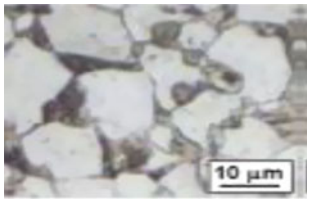

Fig. 5 Dual-phase microstructures of A76

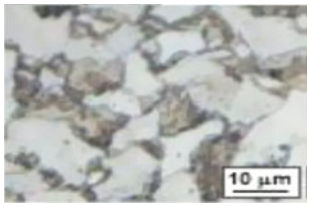

Fig. 6 Dual-phase microstructures of A78

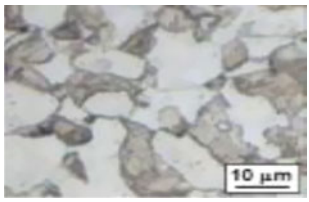

Fig. 7 Dual-phase microstructures of A80

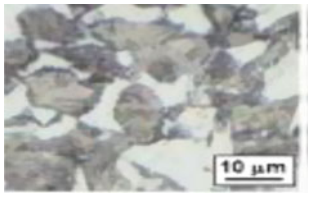

Fig. 8 Dual-phase microstructures of A82

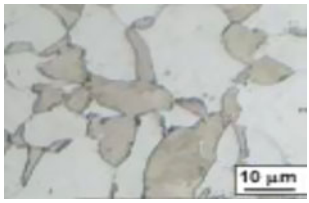

Fig. 9 Dual-phase microstructures of B74

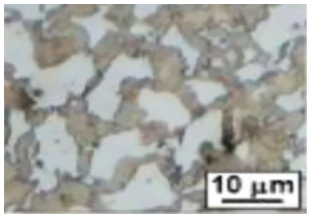

Fig. 10 Dual-phase microstructures of B76

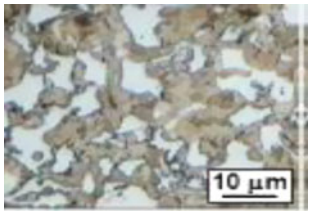

Fig. 11 Dual-phase microstructures of B78

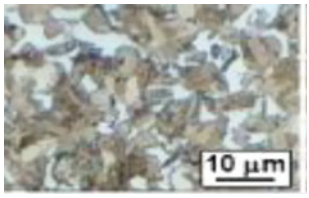

Fig. 12 Dual-phase microstructures of B80

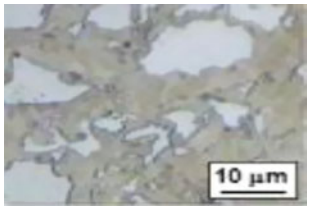

Fig. 13 Dual-phase microstructures of B82

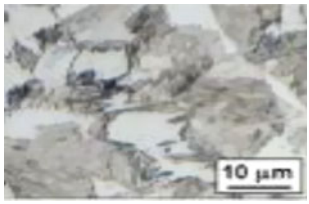

Fig. 14 Dual-phase microstructures of C74

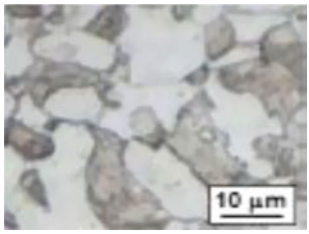

Fig. 15 Dual-phase microstructures of C76

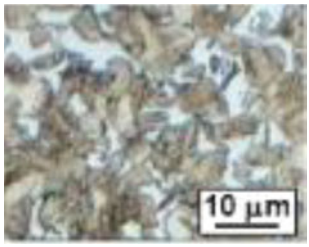

Fig. 16 Dual-phase microstructures of C78

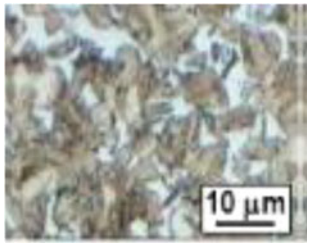

Fig. 17 Dual-phase microstructures of C80

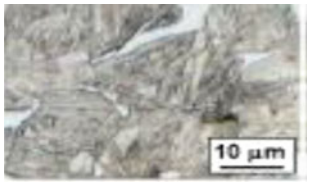

Fig. 18 Dual-phase microstructures of C82

In the above microstructures, the white field represents ferrite phase and the dark field represents the martensite phase. In every instance, it was examined a double structure comprising of equi-aligned granules of ferrite and martensite islets. Martensite enhanced with enhancing temp. ICHT, allied to a higher austenite segment shaped. Moreover, it is importance to remind that B78, B80, C78, and C80 steel presented smaller grain sizes than the rest of the specimens.

4.2 Volume Fraction Determination

To conclude the volume proportion of phases involved, via a systematic manual technique, in which point-counting technique was employed by following the ASTM standard E562 and thereby evaluating the volume proportion of a recognizable ingredient of stage from segments through the morphological analysis [8–11]. Table 2

Table 2 Microstructural phase constituents in volume percentage of DP steel

Specimen code	Volume percentage		Retained austenite (%)
	Ferrite (%)	Martensite (%)	
A74	70	30	2
A76	60	38	2
A78	57	42	1
A80	54	45	1
A82	49	50	1
B74	74	25	1
B76	64	35	1
B78	56	46	–
B80	48	52	–
B82	42	58	–
C74	71	28	1
C76	60	40	–
C78	48	52	–
C80	42	58	–
C82	38	62	–

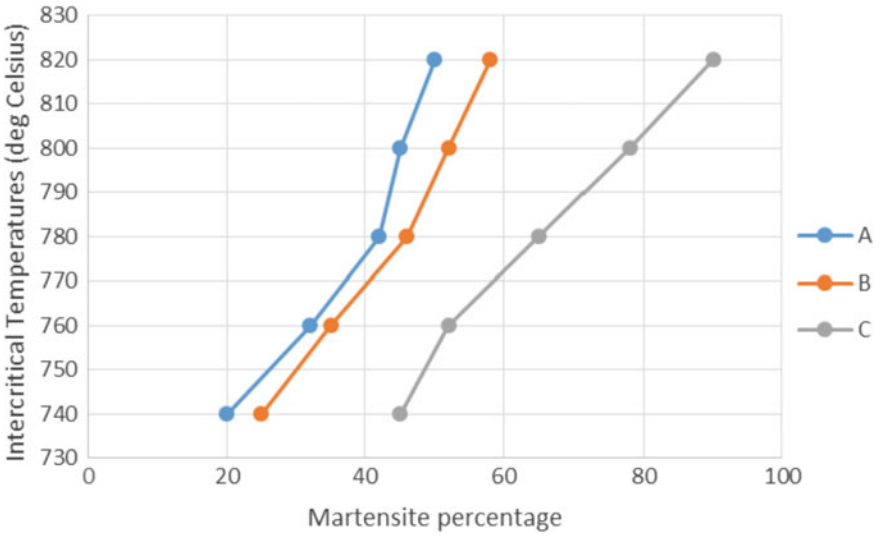

Fig. 19 Graph of ICT versus martensite %

and Fig. 19 show the variation of martensite volume percentage with respect to the increase in the intercritical temperature. From Fig. 19, it can be observed that the martensite volume percentage increases with increase in the ICHT where martensite is a function of percentage of carbon present in it.

4.3 Tensile Test

To determine the yield strength, tensile strength, and percentage elongation uniaxial tensile tests were carried out according to ASTM standards on all the DP steel specimens prepared by ICHT. The test results are tabulated in Tables 3, 4 and 5.

The tensile tests yielded the following results:

Table 3 Yield strength of heat-treated specimens

ICT↓	Specimens→		
	A	B	C
740	658	715	680
760	678	742	712
780	685	790	670
800	690	778	642
820	698	755	590

Table 4 Tensile strength of heat-treated specimens

ICT↓	Specimens→		
	A	B	C
740	725	870	970
760	748	930	935
780	770	980	895
800	790	955	850
820	765	940	810

Table 5 Percentage elongation of heat-treated specimens

ICT↓	Specimens→		
	A	B	C
740	15.2	17.3	18.2
760	14.8	20.5	14.7
780	13.8	25.4	12.5
800	12.4	24.1	10.1
820	10.2	22.5	8.7

- DP steels consist of 0.18% carbon has higher yield strength and higher tensile strength which is very much higher than regular low-carbon steels.
- Specimen B subjected to ICHT at 780o, i.e. B78 has higher yield and tensile strength compared to others, and this is because of the small grains present in the microstructure and the optimum martensite volume fraction present in the DP steel.
- B78 has better combination of ferrite and martensite. It has slightly higher percentage of ferrite which leads to higher ductility and elongation due to this elasticity. The presence of martensite increases the strength; hence, the ultimate tensile strength also got increased with increase in carbon content and increase in ICHT. But, increase in martensite volume increases the brittleness of the material which is not desirable.

The behaviours of different DP specimens discussed are reliable and steady with reports writing through deep survey and can be clarified from parcel division of internal resisting forces and strains amid the two stages, in view of the customized regulation of blends [3, 12]. As a whole, it was scrutinized a persistently yield conduct which is trait for this sort of double structures owing to the existence of elevated compactness of unconfined or untied disruptions/discontinuities in ferrite/martensite interfaces, due to austenite/martensite alteration [13, 14]. Additionally, it was commonly examined an elevated strain solidifying, usual of these stuffs. This facet is typically assessed by the internal resisting force liaison indicator [11, 15, 16, 17].

Table 6 Microhardness of heat-treated specimens

ICT↓	Specimens→		
	A	B	C
740	240	280	270
760	255	293	285
780	270	310	295
800	283	320	310
820	290	332	325

4.4 Hardness Test

Brinell hardness test was carried on each of the specimen and above are the results of the test. The test results of microhardness according to ASTM standards on all the DP steel specimens prepared by ICHT are tabulated in Table 6 as mentioned below:

From it can be observed that hardness value increases with increasing martensite volume fraction. But at higher hardness material becomes brittle and machining becomes cumbersome. If the material is brittle, catastrophic failure may occur and crack propagation will take place at faster rate. Obviously, this outcome demonstrates that dual-phase steel with magnificent or splendid dissemination of ferrite and martensite will have high hardness values. Hence, we can conclude that B78 has better combination of hardness and ductility with respect to crack propagation.

5 Conclusions

DP steels can be obtained from low-carbon steels with carbon percentage 0.16–0.20% through ICHT technique. The use of ice brine solution and oil for quenching gives finer microstructure comparatively. The intercritical temperatures also affect the martensite volume fraction. The increase in the intercritical temperature increases the martensite volume fraction, which is in turn dependent on the percentage of carbon present in the material. Carbon content highly influences the development of martensite phase, and all the mechanical properties mainly tensile strength, yield strength, and hardness increases with increase in carbon content, percentage elongation decreased with increase in martensite volume, but once the carbon content reaches 0.2% martensite volume fraction is too high that the material becomes too brittle and leads to catastrophic failure. The preeminent amalgamation of mechanical assets in the investigated dual-phase steels can be acquired with carbon composition of 0.18% with ICHT at 780 °C which consists of 46% martensite.

References

1. Gerbase J, Embury JD, Hobbs RM (1979) The mechanical behaviour of some dual-phase steels—with emphasis in the initial work hardening rate. In: Structure and properties of dual-phase steels, pp 118–144
2. Dzupon M, Parilak L, Kollarova M, Sinaiova I (2007) Dual phase ferrite-martensitic steels micro-alloyed with V-Nb. Metalurgija 46(1):15–20. Davenport AT (1979) Formable HSLA and dual-phase steel, conference proceedings. The Metallurgical Society of AIME, New York
3. Hayami S, Furukawa T (1977) A family of high-strength, cold rolled steels. In: Proceedings of micro alloying 75. Union Carbide Corp, New York, pp 311–321
4. Kott RA, Morris JW, Mohaved P, Kolahgar S, Marashia SPH (2009) The effect of intercritical heat treatment temperature on the tensile properties and work hardening behaviour of ferrite-martensite dual phase steels sheets. In: Structure and properties of dual-phase steels. Mater Sci Eng 518:1–6
5. Speich GR (1981) Physical metallurgy of dual-phase steels, fundamentals of dual-phase steels. In: Proceedings of a symposium at the 110th AIME annual meeting 1981, pp 3–45. The Metallurgical Society of AIME, Chicago
6. Crawley A, Shahata MT, Pussegoda N (1981) Processing properties and modelling of experimental batch-annealed dual-phase steels. In: Fundamentals of dual-phase steels, pp 181–197
7. Honeycombe RWK (1982) Application guidelines, steels: microstructure and properties international iron and steel institute: committee of automotive applications advanced high strength steel (AHSS) (2005)
8. Kang J, Ososkov Y, Embury JD, Wilkinson D (2007) Digital image correlation studies for microscopic strain distribution and damage in dual phase steels. Scripta Mater 56(11):999–1002
9. Kuang S, Kang Y, Yu H, Liu R (2009) Stress-strain partitioning analysis of constituent phases in dual phase steels based on the modified law of mixture. Metall Mater Int J Miner 16(4):393–398
10. Lorusso H (2009) Soldadura de aceros dual phase en chapafina: obtención, procesos, microestructuras y propiedadesmecánicas. Universidad deBuenos Aires, Buenos Aires
11. Maffei B, Salvatore W, Valentini R (2007) Dual-phase steels rebars for high-ductile R.C. structures, part 1: microstructural and mechanical characterization of steel rebars. Eng Struct 29(12):3325–3332
12. Hance B, Michael (2005) The influence of deformation-induced residual stresses on the post-forming tensile stress/strain behaviour of dual-phase steels. Doctoral Dissertation, University of Pittsburg
13. Kumara A, Singh SB, Rayb KK (2008) Influence of bainite/martensite content on the tensile properties of low carbón dual-phase steels. Mater Sci Eng A474(1–2):270–282
14. Matlock DK, Krauss G, Ramos LF, Huppi GS (1979) AIME symposium on structure and properties of highly formable dual-phase HSLA steels. A correlation of processing variables with deformation behaviour of dual-phase steels. Metall Trans A 10(2):259–261
15. Erman AM, Davies RG, Donlon WT (1981) Electron microscopic study of deformed dual-phase steels. The Metallurgical Society of AIME, pp 85–94
16. Speich GR, Miller RL (1979) Mechanical properties of ferrite-marten site steel. In: Structure and properties of dual-phase steels, pp 145–182
17. Tamura I, Tomota Y, Akao A, Yamaoha Y, Ozawa M, Kanatani S (1973) On the strength and ductility of two phase iron alloys. Trans ISIJ 13(4):283–292

Rheological Characterization and Finishing Performance Evaluation of Vegetable Oil-Based Bi-dispersed Magnetorheological Finishing Fluid

Vikas Kumar, Rajesh Kumar and Harmesh Kumar

Abstract Magnetorheological (MR) finishing fluids are the backbone of MR finishing technology. The abrading forces acting on a workpiece surface can be controlled flexibly and the fine finishing with close tolerances can be obtained by using proper machining conditions and MR finishing fluid compositions. The structure of MR finishing fluid under applied magnetic field provides useful rheological properties which are helpful during finishing operation. The rheological properties of fluid sample can be improved by the addition of magnetic nanoparticles which fills the structural micro-cavities of fluid sample. In the present work, iron oxide nanoparticles are used for preparation of bi-dispersed MR finishing fluid samples. Rheological properties and finishing performance of both mono-dispersed and bi-dispersed fluid samples are compared.

Keywords Magnetorheological finishing fluid · Magnetic field strength · Rheological properties · Surface roughness

1 Introduction

Surface finishing is one of the most desired operations used in manufacturing industries in the production of a final product. Surface quality of components plays an essential part for the better lifespan of components, because the service life of different engineering component depends on it. Components with undesired surface roughness exhibit various problems such as increased wear rate, undesired friction, fluid flow problems, low corrosion and oxidation resistance. Finishing operations are very time consuming and labor intensive which costs around 15% of the overall production cost for producing a final product [1]. The traditional finishing processes such as grinding, lapping and honing are most widely used in manufacturing industries. But such processes alone are incapable to produce required surface characteristics on complex shape parts due to the inability of rigid tool movement with respect to

V. Kumar (✉) · R. Kumar · H. Kumar
Department of Mechanical Engineering, U.I.E.T., Panjab University, Chandigarh 160014, India
e-mail: vdhanda07@gmail.com

H. Kumar and P. K. Jain (eds.), *Recent Advances in Mechanical Engineering*,
Lecture Notes in Mechanical Engineering,
https://doi.org/10.1007/978-981-15-1071-7_34

workpiece surface. Moreover, the heat generated during traditional finishing operation may cause certain defects on the surface of part being finished. To overcome the issues related to traditional finishing processes and to provide in-process determinism, a number of advanced finishing processes based on Magnetorheological (MR) fluid technology have been developed by researchers [2]. MR fluid possesses unique featured rheological property that can be tuned effectively with the help of magnetic field strength (on-state condition) as per requirements [3]. Similar to conventional finishing operations, MR fluid-based finishing operations are based on mechanism of mechanical abrasion but in a more controlled manner. The involvement of MR fluid technology in finishing operations provides selective control of abrading forces that are otherwise difficult to control in conventional finishing operations. The performance of MR finishing processes highly depends on various machining parameters as well as on the composition of MR finishing fluid [4]. Researchers are much interested in unique rheological properties (yield stress and viscosity) of MR finishing fluids which provides desired abrading force on a workpiece surface. MR finishing fluid comprises mixture of micron size magnetizable particles and non-magnetic abrasive particles which are dispersed in a carrier liquid along with additives.

The rheological behavior of MR finishing fluid can be controlled under applied magnetic field strength. The change in rheological behavior under applied magnetic field is reversible in nature after removal of magnetic field strength. Under the effect of magnetic field, the magnetizable particles present in MR fluid aligned along magnetic field lines and the non-magnetic abrasives embedded in between columnar chain like semi-solid structure of magnetizable particles [5]. The semi-solid structure thus formed exhibits a resisting force against the deformation applied and stiffen more with the increase in magnetic field strength. The stiffened structure acts as conformable finishing tool that adapts surface shape easily and eliminates the problem of "tool misfit," faced during the finishing of complex geometries. The stiffened structure gives a desired finishing action when moves selectively on a workpiece surface. The material is removed from the workpiece surface by selective action of active abrasives particles only or by combined action of abrasive and magnetic particles that actually acts on workpiece surface during finishing operation. A variety of components having different geometrical shape and material which have been nano-finished with the use of MR fluid-based advanced finishing processes includes BK7 glass [6], K9 glass [7], KDP crystal [8], nickel-coated aluminum mirrors [9], silicon micro-channel [10], aluminum [11], S.S work material [12], titanium alloy [13], austenitic S.S (AISI 304), EN31 (ferromagnetic) and copper [14], etc. The mentioned studies show that MR finishing processes have the ability to finish wide spectrum of materials.

To improve their application area in finishing of more hard materials, the rheological properties of MR finishing fluids need to be improved. Addition of nano-sized iron particles in fluid composition helps to improve the strength of fluid structure. Nanoparticles fill the micro-cavities of the fluid structure which is formed due to alignment of micron-sized particles [15]. Due to this reason, the fluid structure becomes more dense and rigid under applied same magnetic field. Therefore, in the present work, nano-iron particles-based bi-dispersed MR finishing fluid samples

have been prepared and their rheological properties have been compared with mono-dispersed MR finishing fluid. Moreover, vegetable-based oil which is biodegradable has been used as a carrier liquid in the present work. Most of carrier liquids used in preparation of MR finishing fluids are based on mineral oil, silicon oil and deionized water. Among all these carrier liquids, only deionized water is a biodegradable medium. But it does not provide better suspension to micron-sized iron particles as well as abrasive particles resulting in their fast sedimentation. Also, in water-based MR finishing fluids, corrosion of iron particles takes place which degrades the MR effect and hence the yield stress of the fluid sample. The finishing experiments have been also carried out to compare the finishing performance of mono-dispersed and bi-dispersed fluid samples.

2 Materials and Sample Preparation

In the present work, micron-sized flake shaped, spherical shaped-iron particles (Sigma-Aldrich, product 209309 and 12310) and silicon carbide (SiC) abrasives SFG LAP-25 (Speedfam Co. Ltd.) were dispersed in a vegetable oil (coconut oil)-based carrier liquid. Green additive guar gum was used as thixotropic agent. The nano-iron oxide particles (Sigma-Aldrich) with 50–100 nm mean particles size were used to prepare bi-dispersed MR finishing fluid samples. The morphology of iron particles and SiC abrasives was studied by scanning electron microscopy. The scanning electron microscopic (SEM) images of micron-sized flake shaped, spherical shaped-iron particles and SiC abrasives are shown in Fig. 1a, b and c, respectively.

The mono-dispersed MR finishing fluid sample has been prepared by mixing micron-sized iron particles, SiC abrasives and guar gum in carrier liquid. In the same way, three bi-dispersed fluid samples have been prepared by using different (5, 10, 15) vol.% fractions of iron oxide nanoparticles within total magnetic content of iron particles. The compositional detail of fluid samples is given in Table 1.

3 Rheological Characterization

Rheological characterization has been carried out using modular compact rheometer (MCR-102, Anton Paar, Germany) available at IIT, Ropar. The modular compact rheometer equipped with magnetorheological device (MRD 180) provides homogeneous magnetic field which acts perpendicular to the shear flow direction of fluid sample. All the fluid samples were tested at 25 °C using a parallel plate geometry (PP/20) with 1 mm gap. Rheological behavior of all the fluid samples was tested at 0.6 T magnetic field strength and the shear rate was varied from 0.1 to 1000 s^{-1} during testing.

The obtained flow curves (shear stress and viscosity as a function of shear rate) of each sample at applied magnetic field strength of 0.6 T is shown in Fig. 2. Figure 2a

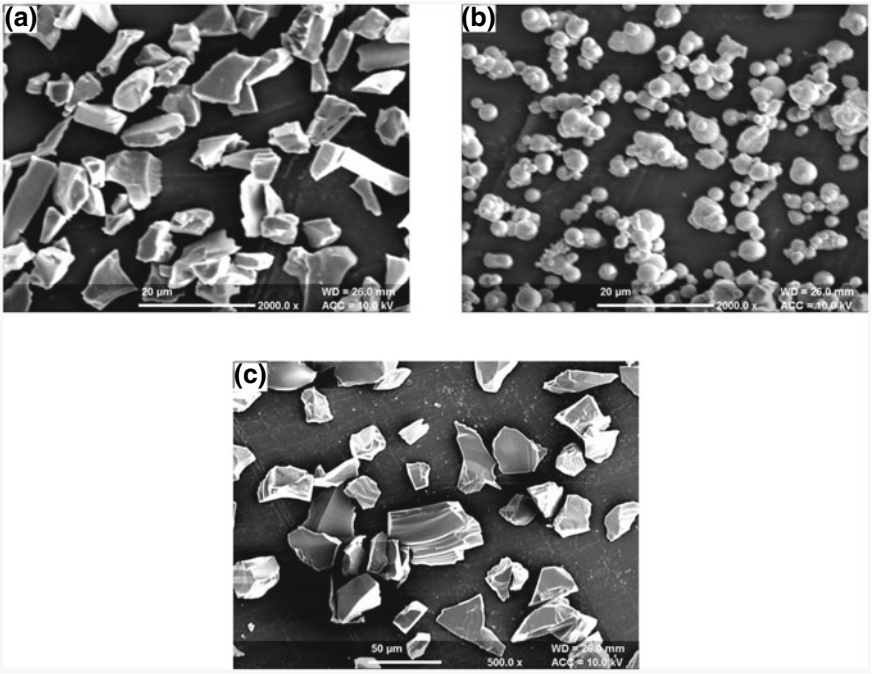

Fig. 1 SEM micrographs of **a** flake shaped iron particles, **b** spherical shaped iron particles and **c** SiC abrasives

Table 1 Fluid sample compositions

Sample no.	Sample type	Composition includes
1	Mono-dispersed	35 vol.% micron-sized iron particles, 10 vol.% micron-sized SiC abrasives and 5 vol.% guar gum in carrier liquid (remaining constituent)
2	Bi-dispersed	5 vol.% iron oxide nanoparticles, 30 vol.% micron-sized iron particles, 10 vol.% micron-sized SiC abrasives and 5 vol.% guar gum in carrier liquid (remaining constituent)
3	Bi-dispersed	10 vol.% iron oxide nanoparticles, 25 vol.% micron-sized iron particles, 10 vol.% micron-sized SiC abrasives and 5 vol.% guar gum in carrier liquid (remaining constituent)
4	Bi-dispersed	15 vol.% iron oxide nanoparticles, 20 vol.% micron-sized iron particles, 10 vol.% micron-sized SiC abrasives and 5 vol.% guar gum in carrier liquid (remaining constituent)

represents the change of shear stress vs shear rate for all fluid samples. From Fig. 2a, it can be seen that the flow curves of all the bi-dispersed fluid samples levelled up for the entire shear rate region as compared to the mono-dispersed fluid sample. The flow curve of bi-dispersed fluid sample with 10 vol.% of iron oxide nanoparticles shows

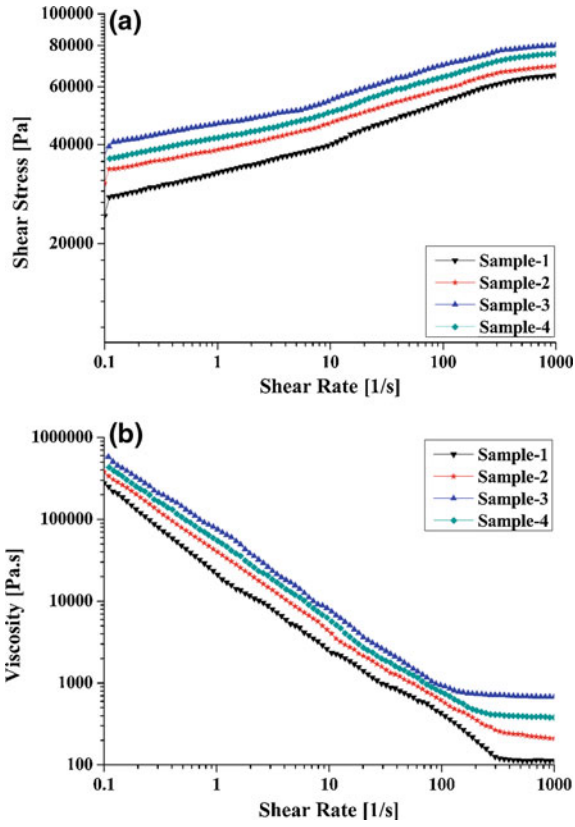

Fig. 2 **a** Shear stress versus shear rate and **b** viscosity versus shear rate, at a magnetic field strength of 0.6 T

the highest increase in shear stress for the entire range of shear rate. This may be due to the reason that the structural micro-cavities formed in between micron-sized particles are filled completely by iron oxide nanoparticles.

The appropriate filling of micro-cavities gives more robust structure of fluid sample under applied magnetic field strength. On the other hand, the flow curve of bi-dispersed fluid sample with 15 vol.% of iron oxide nanoparticles leveled down as compared to bi-dispersed fluid sample having 10 vol.% nanoparticles. This may be due to the reason that at higher concentration of iron oxide nanoparticles from optimum value, the overall magnetic properties of fluid sample decrease down. Figure 2b shows the change in viscosity of fluid samples as a function of shear rate at applied magnetic field strength. From Fig. 2b, it may be observed that the viscosity of all the fluid sample decreases with the increase in shear rate which shows shear thinning characteristics of fluid samples.

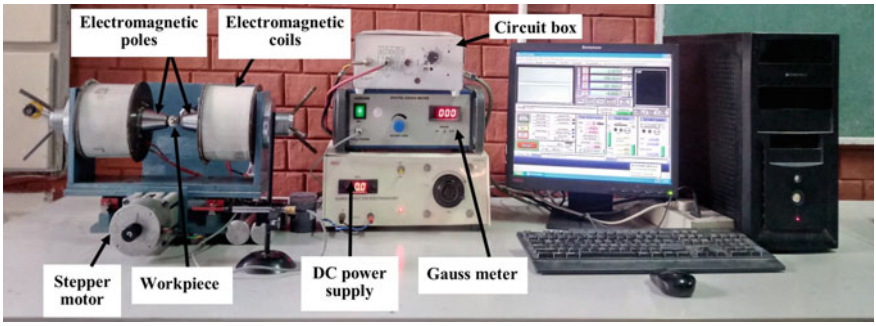

Fig. 3 In-house developed MR fluid finishing setup

4 Magnetorheological (MR) Finishing Process

4.1 Experimental Setup and Working Principle

MR finishing setup used in nano-finishing of external cylindrical surface of S.S-316L workpiece is shown in Fig. 3. A mandrel is used to hold the cylindrical workpiece of 20 mm outer diameter and 10 mm inner diameter. The workpiece mandrel holds in a collet chuck which is attached to the spindle of DC motor. A double coil electromagnet is placed on a Y-axis linear slide in such a way that both of the pole moves linearly along the longitudinal axis of workpiece and the workpiece rotates between them simultaneously. The linear movement of electromagnetic poles can be programmed according to the requirement by controlling the Y-axis linear slide with the help of stepper motor and control unit. The working gap between workpiece surface and electromagnetic poles can be adjusted manually as per the requirement. When the MR finishing fluid is supplied in the finishing region, it gets stiffened because of the applied magnetic field. The iron particles having embedded abrasives are absorbed immediately by the magnetic force and fill the gap between the electromagnet poles and workpiece. The material is removed from the workpiece surface by the active abrasive particles which are in contact with the surface asperities.

4.2 Experimental Work

After the rheological characterization of fluid samples, finishing experiments were carried out to compare the finishing performance of mono-dispersed sample (minimum yield stress) and bi-dispersed sample (maximum yield stress). Bi-dispersed fluid sample with 10 vol.% iron oxide nanoparticles was selected for finishing because it possesses maximum yield stress as compared to other bi-dispersed samples. The experimental machining conditions used in finishing operation are given in Table 2.

Table 2 Experimental conditions used during finishing

S. no.	Parameters	Values
1	Working gap	1 mm
2	Rotating speed	600 rpm
3	DC power supply	3 A
4	Linear feed	40 mm/min
5	Finishing time	30 min

Table 3 Roughness data before and after finishing operation

Finishing fluid type	Initial Ra (nm)	Final Ra (nm)	Change in Ra	Percentage change in Ra
Mono-dispersed fluid sample	517	273	244	47.19
Bi-dispersed sample having 10 vol.% iron oxide nanoparticles	498	156	342	68.67

5 Results and Discussion

The different surface roughness parameters, i.e., arithmetic mean of roughness (*Ra*), mean square of roughness (*Rq*) and maximum height (*Rz*) of workpiece samples were measured before and after finishing operation with Mitutoyo surftest SJ-410 roughness tester. The observed surface roughness (Ra) values are given in Table 3.

Figure 4a, b shows surface roughness profile before and after finishing with bi-dispersed MR finishing fluid sample having 10 vol.% of iron oxide nanoparticles. The obtained finishing results were found to be better with bi-dispersed sample as compared to mono-dispersed fluid sample. This may be due to the stronger fluid structure of bi-dispersed sample which exhibits higher yield stress and imparts higher magnitude of abrading forces on the workpiece surface.

6 Conclusion

In this research work, rheological characteristics and finishing performance of bi-dispersed MR finishing fluid samples have been carried out. The addition of iron oxide nanoparticles within fluid sample improves the rheological properties of fluid sample. Better rheological properties obtained only after addition of an optimum concentration of iron oxide nanoparticles. Bi-dispersed fluid sample having 10 vol.% iron oxide nanoparticles exhibits better rheological properties as compared to other samples. Better rheological properties of fluid sample found to be useful in finishing

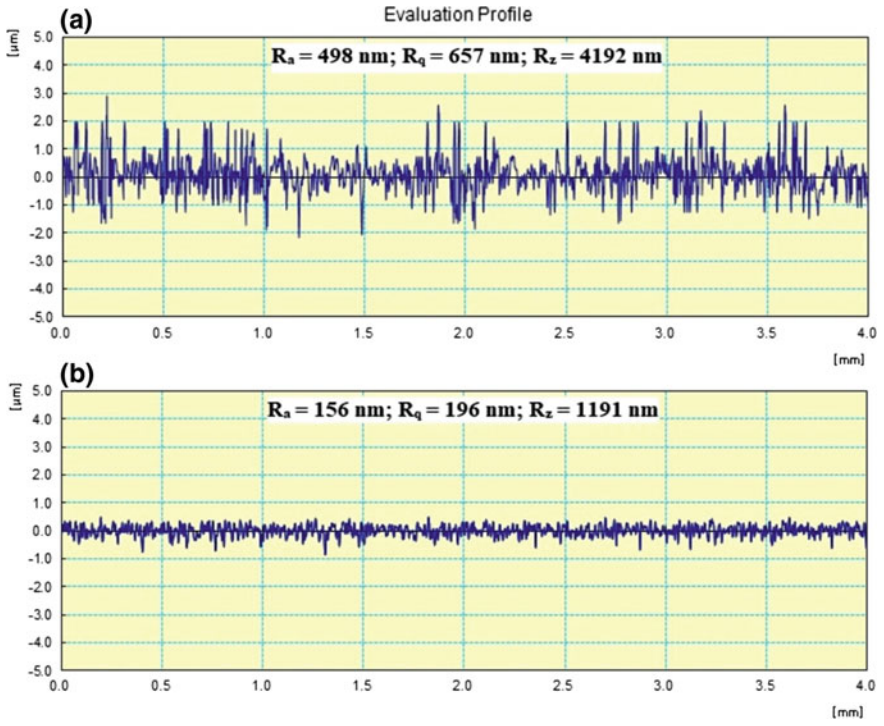

Fig. 4 Surface roughness profile **a** before and **b** after finishing operation

operation. Better finishing result has been obtained using bi-dispersed MR finishing fluid as compared to mono-dispersed fluid.

Acknowledgements Authors express gratitude to UGC, Government of India for providing BSR fellowship, Technical Education Quality Improvement Programme (TEQIP)-II, MHRD, Government of India and University Institute of Engineering and Technology (Panjab University) Chandigarh for providing funds to develop the experimental setup, Sophisticated Analytical Instrumentation Facility (SAIF), Panjab University, Chandigarh and Mechanical Engineering Department, Indian Institute of Technology, Ropar for providing their lab facilities for this research work.

References

1. Singh M, Singh A, Singh AK (2018) A rotating core-based magnetorheological nanofinishing process for external cylindrical surfaces. Mater Manuf Process 33(11):1160–1168. https://doi.org/10.1080/10426914.2017.1328116
2. Maan S, Singh G, Singh AK (2017) Nano-surface-finishing of permanent mold punch using magnetorheological fluid-based finishing processes. Mater Manuf Process 32(9):1004–1010. https://doi.org/10.1080/10426914.2016.1232823

3. Sidpara A, Das M, Jain VK (2009) Rheological characterization of magnetorheological finishing fluid. Mater Manuf Process 24(12):1467–1478. https://doi.org/10.1080/10426910903367410
4. Parameswari G, Jain VK, Ramkumar J, Nagdeve L (2017) Experimental investigations into nanofinishing of Ti6Al4V flat disc using magnetorheological finishing process. Int J Adv Manuf Technol 1–11. https://doi.org/10.1007/s00170-017-1191-3
5. Chaudhuri A, Wereley NM, Kotha S et al (2005) Viscometric characterization of cobalt nanoparticle-based magnetorheological fluids using genetic algorithms. J Magn Magn Mater 293:206–214. https://doi.org/10.1016/j.jmmm.2005.01.061
6. Kim DW, Cho MW, Seo TI, Shin YJ (2008) Experimental study on the effects of alumina abrasive particle behavior in MR polishing for MEMS applications. Sensors (Basel) 8:222–235. https://doi.org/10.3390/s8010222
7. Cheng H, Yeung Y, Tong H (2008) Viscosity behavior of magnetic suspensions in fluid-assisted finishing. Prog Nat Sci 18:91–96. https://doi.org/10.1016/j.pnsc.2007.07.007
8. Chen S, Li S, Peng X et al (2015) Research of polishing process to control the iron contamination on the magnetorheological finished KDP crystal surface. Appl Opt 54(6):1478–1484. https://doi.org/10.1364/AO.54.001478
9. Seok J, Kim Y, Jang K et al (2007) A study on the fabrication of curved surfaces using magnetorheological fluid finishing. Int J Mach Tools Manuf 47:2077–2090. https://doi.org/10.1016/j.ijmachtools.2007.05.007
10. Kim WB, Lee SH, Min BK (2004) Surface finishing and evaluation of three-dimensional silicon microchannel using magnetorheological fluid. Trans ASME J Manuf Sci Eng 126:772–778. https://doi.org/10.1115/1.1811113
11. Gheisari R, Ghasemi AA, Jafarkarimi M, Mohtaram S (2014) Experimental studies on the ultra-precision finishing of cylindrical surfaces using magnetorheological finishing process. Prod Manuf Res 2(1):550–557. https://doi.org/10.1080/21693277.2014.945265
12. Jha S, Jain VK (2006) Modeling and simulation of surface roughness in magnetorheological abrasive flow finishing (MRAFF) process. Wear 261:856–866. https://doi.org/10.1016/j.wear.2006.01.043
13. Sidpara AM, Jain V (2012) Nanofinishing of freeform surfaces of prosthetic knee joint implant. Proc IMechE Part B J Eng Manuf 226(11):1833–1846. https://doi.org/10.1177/0954405412460452
14. Singh AK, Jha S, Pandey PM (2012) Magnetorheological ball end finishing process. Mater Manuf Process 27:389–394. https://doi.org/10.1080/10426914.2011.551911
15. Leong SAN, Samin PM, Idris A et al (2016) Synthesis, characterization and magnetorheological properties of carbonyl iron suspension with superparamagnetic nanoparticles as an additive. Smart Mater Struct 25(2):1–12. https://doi.org/10.1088/0964-1726/25/2/025025

Experimental Investigation of Microstructure and Mechanical Properties of Brass–Iron Joined by TIG Welding Process

J. Nithin Kumar, M. Devaiah, P. Sandeep kumar and P. Sudheer Rao

Abstract Brass is widely used as engineering material in marine and process industry in light of its high quality, corrosion resistance, electrical, and high warm conductivity. It is easily shaped and possesses a gratifying appearance. Notwithstanding, it is hard to weld brass. The principal issue with brass alloy while welding is dissipation of zinc. Subsequent to welding, the weld area and warmth influenced zone end up permeable, since the measure of zinc in the metal combination is diminished because of vanishing, and it loses the physical and compound properties which it typically has. In this paper, a brass–iron, which is widely used in marine and process industries, is taken and welding is done with Tungsten Inert Gas (TIG) welding process with different parameters such as root gap, flow rate, diameter of electrode, and flow of current. The principal target of this paper was to determine mechanical properties, such as tensile strength, hardness, and microstructure of TIG welded brass joints. Weld zone and heat-affected zones of brass welded test are seen by scanning electron microscopy (SEM) to decide zinc dissipation in 2D pictures. Tensile strength and hardness tests are performed by utilizing universal testing machine (UTM) and Vickers hardness testing machine separately according to ASTM principles. Tensile strength of brass weld tests was found in the range of 27.102–263.62 N/mm^2, level of elongation was found in the range 0.72–3.80% and hardness of brass weld test was found in the range 85.9–160.33 HV. How evaporation of zinc is decreased in metal weld test is seen at weld zone (WZ), heat-affected zone 1 (HAZ1), and heat-affected zone 2 (HAZ2).

J. Nithin Kumar · M. Devaiah (✉) · P. Sandeep kumar · P. Sudheer Rao
Department of Mechanical Engineering, Geethanjali College of Engineering and Technology, Cheeryal (V), Keesara (M), Medchal District, Telangana 501301, India
e-mail: devaiah.malkapuram@gmail.com

J. Nithin Kumar
e-mail: nithinkumar.8787@gmail.com

P. Sandeep kumar
e-mail: skumarcharyp@gmail.com

P. Sudheer Rao
e-mail: sudheerraopolasani22@gmail.com

H. Kumar and P. K. Jain (eds.), *Recent Advances in Mechanical Engineering*, Lecture Notes in Mechanical Engineering,
https://doi.org/10.1007/978-981-15-1071-7_35

Keywords TIG welding · Brass · Root gap · Flow rate · SEM · Weld zone · Zinc and HAZ

1 Introduction

The utilization of brass materials requires advancement and methods in the welding. The nature of welding is influenced by numerous components that ought to be cautiously analyzed. Worried with this innovation, the capacity to providing great welded segments with the expanded infiltration, the nature of the surface structure, and the nonattendance of the pore in the joining parts are critical, since numerous essential parameters control the welding. The nature of the welded joints is influenced by numerous components, for example, welding current, welding speed bend length, and so on. In mid-nineteenth century, a few elements impacting on the warmth contribution to the weld pool had been inspected by Kovacevic and colleagues. In these works, the prime concerns were identified with the subject of welding technique, welding current, welding speed, the compound structure of workpiece, warm conductivity coefficient, welding position, circular segment length, the sort and width of the terminal, the stream rate and creation of protecting gas, the kind of the current and polarity [1].

As it was referenced in the content, the vanishing importantly affects the welding. The vanishing can be constrained by choosing appropriate welding current and welding speed as indicated by the circular segment length. In this paper, the relationships that supply the better welding surface have been gotten. Grating, grinding mix, and beat welding assume a vital position in welding because of the trouble in combination welding. Be that as it may, the forecast of the appropriate welding parameters may result in an augmentation of the utilization of the conventional combination welding [2].

To decrease the zinc vanishing, bending and porosity, the warmth contribution to the welding pool must be as low as could be expected under the circumstances and the welding time as short as would be prudent. The grayish zinc shaped at the outside of the welding dab in ordinary TIG welding does not show up with TIG heartbeat welding. This demonstrates TIG beat welding decreases Zn dissipation. At the point, when the beat recurrence expands, the entrance increments and the other way around. Restricted warmth contribution to the welding pool given in short welding occasions positively affects the weldability of metal materials. The use of the TIG beat welding technique in the welding of metal materials is effective. Heartbeat recurrence affects the state of the welding globule. Moreover, bend length modifies the state of the welding globule altogether [3].

Welding input parameters assume an extremely huge job in deciding the nature of a weld joint. The joint quality can be characterized as far as properties, for example, weld-dab geometry, mechanical properties, and mutilation. For the most part, all welding procedures are utilized with the point of getting a welded joint with the ideal weld-dot parameters, brilliant mechanical properties with least twisting. [4]

Quality and profitability assume essential job in the present assembling market. The fundamental goal of ventures uncovers with creating better quality item at least expense and increment productivity. TIG welding is most essential and basic task use for joining of two comparative or divergent part with warming the material or applying the weight or utilizing the filler material for expanding profitability with less time and cost compel [5].

Also, since the measure of the zinc in the compound is decreased because of vanishing, the metal material loses its physical and concoction properties which it ordinarily has. Not being tackled these issues adequate mixture welding of metal materials; it had been guided specialists to apply new techniques. It appears that grinding mix welding which is one of the new techniques grew these days will take care of these issues. Along these lines, it needs trial examinations in this subject. Despite the fact that there are such a large number of inquiries about grinding mix welding in aluminum and its amalgams, explores about copper and its compounds particularly metal are constrained. This examination, it was called attention to contact blend welding capacity particularly metal plates which are 3 mm in thickness. Hence, try conditions were resolved and grinding mix welding strategies was connected to metal plates in various turn and welding speeds. Gotten welded joints oppressed about physical virtual, mechanical tests, and microstructure examinations, and the outcomes had been assessed [6].

The main objective this paper is to find out tensile strength and hardness of the brass after welding and it compared with base metal, such that it can be used as engineering material in different areas like marine and process industries. And also we studied the zinc evaporation at different zones of the weld joints of the metal and compared with hardness test results and tensile strength results.

2 Experimental Procedure

In this study, effects on material properties and microstructure are founded for brass–iron plate which is cut into small pieces of 18 number of size 100 mm × 50 mm × 5 mm. All these pieces are then filed at single side to 30° using smooth filing half of the thickness. Now these pieces are ready for the Butt joint welding.

Each job is assigned with different parameters like root gap, current, electrode diameter and gas flow rate. As these all parameters are varied, the welding strength and the defects at the heat-affected zone (HAZ) and weld zone are to be carried out by different tests. Composition of brass–iron: copper (Cu)%—60.66, tin%—1.02, iron (Fe)%—1.74, and zinc (Zn)%—36.58 as shown in Table 1.

Table 1 Different TIG welding parameters assigned for welding of brass

Test piece	Root gap (mm)	Current (A)	Electrode diameter (mm)	Gas flow rate (L/min)
1	0.5	100	3	2
2	1	120	4	4
3	1.5	150	2.4	5
4	0.5	120	4	4
5	1	150	2.4	5
6	1.5	100	3	2
7	0.5	150	2.4	5
8	1	100	3	2
9	1.5	120	4	4

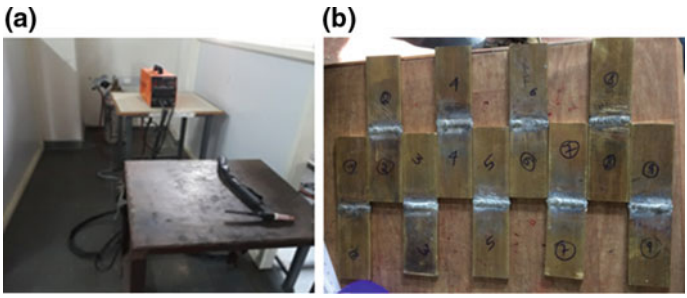

Fig. 1 **a** TIG welding apparatus setup, **b** TIG welded samples with different parameters

2.1 TIG Welding Apparatus

Trials have been led with the TIG welding set-up appeared in Fig. 1a. The test device is basically comprised of four segments. These are the anode holder, slide, and power supply and gas tube. Welding has been done under direct current. The workpiece is balanced as the positive shaft and the cathode as negative post. Protecting gas was argon (99.995%). The protecting gas should show laminar stream into the welding area. Choppiness protecting gas stream may happen in the welding pool and can make the oxidative gases noticeable all around enter the welding pool. The thickness of the brass material utilized in the investigations was 5 mm.

2.2 Tensile Strength Test and Hardness Test

Tensile testing, otherwise called strain testing, is a key materials science test in which an example is exposed to uni-pivotal pressure until disappointment. The outcomes

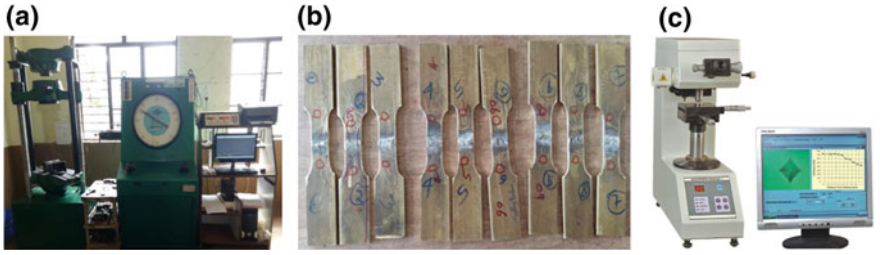

Fig. 2 **a** Tensile test apparatus (UTM). **b** Tensile test samples. **c** Vickers hardness testing machine

from the test are normally used to choose a material for an application, for quality control, and to foresee how a material will respond under different kinds of powers. Properties that are specifically estimated by means of a pliable test are extreme rigidity, most extreme prolongation and decrease in the region. An elastic example is an institutionalized example cross-segment. It has two shoulders and a check (area) in the middle. The shoulders are huge so they can be promptly held, though the check segment has a littler cross-area with the goal that the disfigurement and disappointment can happen in this are the shoulders of the test example can be produced in different approaches to mate to different holds in the testing machine. Their subtleties are given in Fig. 2a, b.

Hardness is a proportion of how safe strong material is to different sorts of lasting shape change when a compressive power is connected. It is subject to pliability, versatile solidness, pliancy, strain, quality, sturdiness, visco-flexibility, and thickness. The Vickers hardness test utilizes a square-base jewel pyramid as the indenter with the included edge between inverse appearances of the pyramid of 136°. The Vickers hardness number (VHN) is characterized as the heap isolated by the surface zone of the space.

2.3 Scanning Electron Microscopy (SEM)

To dissect the microstructure of acquired welding joints at various positions like warmth influenced zones and at welding locale with SEM investigation, the SEM (filtering electron magnifying instrument) utilizes an engaged light emission vitality electrons to produce an assortment of signs at the outside of strong examples. The signs that get from electron-test collaborations uncover data about the example including outside morphology (surface), substance piece, and crystalline structure and introduction of materials making up the example. In many applications, information is gathered over a chose zone of the outside of the example, and a two-dimensional picture is produced that shows spatial varieties in these properties. Territories running from around 1 cm–5 μm in width can be imaged in an examining mode utilizing traditional SEM methods (amplification going from 20X to roughly 30,000X, spatial goals of 50–100 nm). The SEM is additionally equipped

Fig. 3 Scanning electron microscope

for performing investigations of chose point areas on the example; this methodology is particularly helpful in subjectively or semi-quantitatively deciding synthetic pieces (utilizing Energy-Dispersive X-Ray Spectroscopy-EDS), crystalline structure, and precious stone introductions (utilizing Electron Backscatter Diffraction-EBSD). The plan and capacity of the SEM are fundamentally the same as the EPMA (Electron Prove Micro-Analyzer) and extensive cover in abilities exists between the two instruments. Figure 3 shows the SEM machine.

3 Results and Discussion

In this experimental investigation, we had taken four fundamental parameters like root gap, current, electrode diameter, and gas flow rate for every example distinctively and found the mechanical properties like tensile strength and hardness of welded joints.

3.1 Tensile Test

To determine mechanical properties of got weld joints, it has been performed tensile test on UTM as per ASTM guidelines B927/B927M. To measure the tensile strength, the tensile test specimen required to be prepared as Fish-bone shape as shown in Fig. 4. The results as plotted in Figs. 5 and 6 which also shown in Table 2.

The maximum tensile strength is determined at the test piece number **7** where the root gap and electrode diameter are low, current and gas flow rate are high. The maximum Ultimate load obtained from tensile test is 26.320 KN, maximum tensile

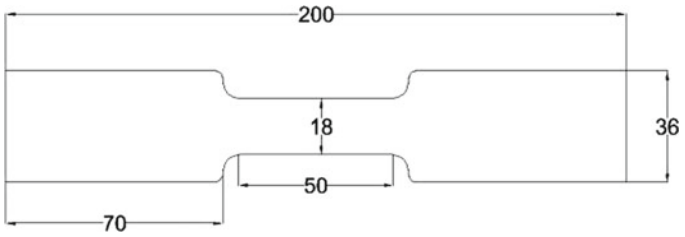

Fig. 4 Tensile test specimen (Fishbone diagram with dimensions according to ASTM standards)

Fig. 5 Ultimate load of welded samples

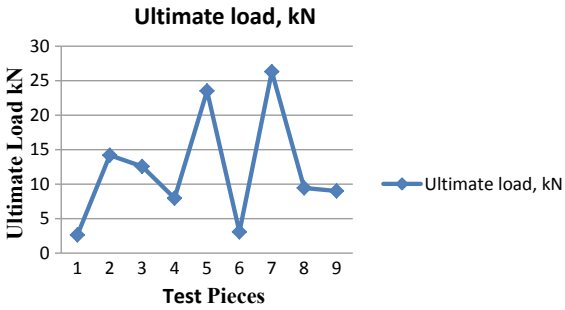

Fig. 6 Tensile strength of welded samples

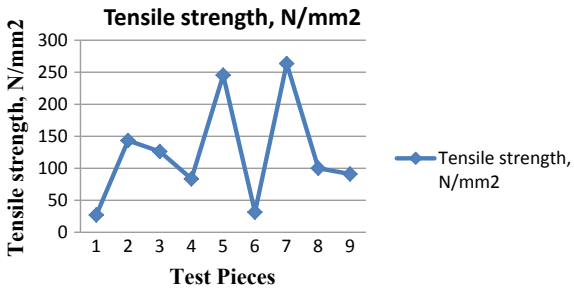

Table 2 Tensile test results for brass specimens

Test piece	Ultimate load (kN)	Tensile strength (N/mm^2)	Elongation (%)
1	2.64	27.102	1.600
2	14.2	143.347	2.600
3	12.560	126.295	1.920
4	7.960	83.464	0.720
5	23.520	245.563	4.700
6	3.080	31.454	1.240
7	26.320	263.622	3.800
8	9.440	100.053	1.800
9	9.000	90.964	1.160

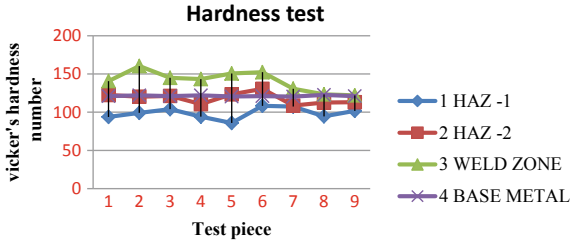

Fig. 7 Hardness values of welded samples at different zones

strength is 263.622 N/mm2 and the elongation at that point is 3.80 % as shown in Figs. 5 and 6.

3.2 Hardness Test

To determine mechanical properties of got weld joints, it has been performed hardness test on Vickers hardness testing machine as indicated by ASTM norms by planning nine test examples. The outcomes are plotted in Fig. 7 and also shown in Table 3.

The maximum hardness determined at the weld zone is 160.33 HV (hardness number) by Vickers hardness testing machine and averagely at test piece number 7 hardness at different zones is equal to base metal. Where root gap and electrode diameter are low, current and gas flow rate are maximum.

3.3 SEM Analysis

To watch microstructure of acquired weld joints, it has been performed SEM investigation by examining electron magnifying instrument for nine test examples. The outcome with electron voltage of 10 kV and amplification 500x with the width of 10.5 mm improved the situation weld tests at weld zone (WZ), heat-affected zone 1 (HAZ 1), heat-affected zone 2 (HAZ 2). At that point, how the evaporation of zinc is reduced or increased observed in 2D pictures.

In a large portion of the weld, examples observed that the zinc dissipation is high and because of that the rigidity and hardness esteems are low. Yet, in weld example number 7 it is seen that vanishing of zinc is medium contrasted with other weld tests in this way, it is having high elasticity high and hardness esteem is equivalent to base metal as shown in Fig. 8.

Table 3 Hardness test results for brass specimens

S. No.	Location	1	2	3	4	5	6	7	8	9
1	HAZ 1	93.80	99.17	104.0	94.15	85.9	108.3	107.3	94.53	101.7
2	HAZ 2	122.5	120.3	121.3	110.6	123.3	130.6	108.6	112.6	113.0
3	Weld zone	140.6	160.3	145.0	143.3	150.6	152.3	130.6	123.3	122.0
4	Base metal	121.0	122.0	121.0	122.0	120.6	121.0	120.3	122.6	121.0

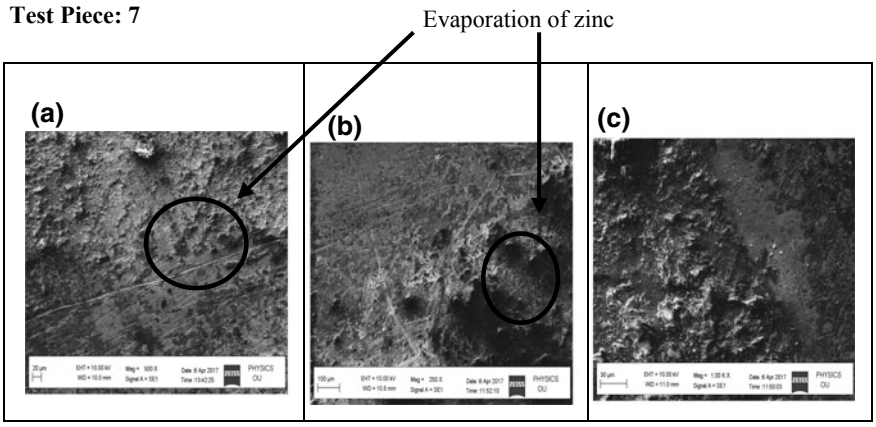

Fig. 8 Test piece number 7 is observed during SEM analysis is the porosity (evaporation of zinc) is medium at HAZ 1, HAZ 2, and welding zone

4 Conclusion

As subsequent to welding, the weld metal ends up permeable and the measure of zinc in the alloy is decreased because of vanishing, the metal material loses the physical and substance properties which it ordinarily has.

We found from the investigation that of TIG welding parameters for brass–iron that the porosity due to welding is medium in the job number 7 which may possess the properties as normal brass after welding.

1. When the root gap and electrode diameter were low values, current and gas flow rate are maximum, the tensile strength and ultimate load are maximum.
2. When the root gap and electrode diameter were minimum values, current and gas flow rate are maximum, the hardness at heat-affected zone and weld zone is nearer to base metal region.
3. Microstructure analysis by SEM we observed that job number 7 had medium evaporation of zinc present in metal. So, it is having high tensile strength and hardness.

Acknowledgements We are thankful to Principal, Management and Head of Mechanical Engineering Department—Geethanjali College of Engineering and Technology, Hyderabad, for their support during this work. Our special thanks to the experts who have contributed toward the development of the project. And our sincere thanks to Dr. T. Shiva Prasad for giving us the guidance whenever required and for his motivational support throughout the completion of the work.

References

1. Kovacevic R, Cao ZN, Zhang YM (1996) Eng Mater Technol 118:589–596
2. Meran C (2006) Prediction of the optimized welding parameters for the joined brass plates using genetic algorithm. Mater Design 27(5):356–363
3. Meran C, Yuksel M, Gulsoz A, Sekercioglu T (2004) Welding problems with thin brass plates and tungsten inert gas pulse welding. Sci Technol Weld Join 9(2):131–137. https://doi.org/10.1179/136217104225017053
4. Benyounis KY, Olabi AG (2008) Optimization of different welding processes using statistical and numerical approaches—a reference guide. Adv Eng Softw 39(6):483–496
5. Naitik SP, Rahul BP A review on parametric optimization of TIG welding. Int J Comput Eng Res 04(1)
6. Meran C (2006) The joint properties of brass plates by friction stir welding. Mat Design 27(9):719–726

Finite Element Modeling and Simulation of Projectile Impact on Ductile Target

Sanan H. Khan, Servesh K. Agnihotri, Ateeb A. Khan and Afsar Husain

Abstract The present study discusses the finite element modeling and simulation strategy of projectile impact on thin ductile target like aluminum. Ogive nose projectile was chosen to impact on aluminum target normally by velocities at and above the ballistic limit of the plate. Abaqus/Explicit finite element code was used to model the problem. To define the thermo-viscoplastic behavior of the metal target, Johnson-Cook flow stress was used in conjunction with damage initiation criterion to predict the complete perforation process. Further, Hillerborg's damage evolution proposal, based on stress-displacement response, was followed to observe the damage response after the failure has initiated in the material. Various parameters, like choice of element size, hourglassing, aspect ratio of elements, etc. which plays an important role in the simulation, have been studied. The result obtained with the presented model is compared with the results from the literature, and good agreement between them was found.

Keywords Ogive nose · Abaqus · Low velocity · Johnson-cook model

1 Introduction and Literature Review

Perforation of metals during projectile impact is a complex process involving elastic and plastic deformation, strain and strain rate hardening effects, thermal softening, crack formation, adiabatic shearing, plugging, petaling and even shattering. These effects depend on the properties and geometries of projectile, target and on the incident velocity. Various studies have been published by Backman and Goldsmith [1], Corbett et al. [2] and Goldsmith [3] which discusses the phenomenon of perforation

S. H. Khan (✉) · A. A. Khan · A. Husain
Department of Mechanical Engineering, Aligarh Muslim University (AMU), Aligarh 202002, India
e-mail: sananiitk@gmail.com

S. K. Agnihotri
Department of Mechanical Engineering, NIT Delhi, New Delhi 110040, India

H. Kumar and P. K. Jain (eds.), *Recent Advances in Mechanical Engineering*,
Lecture Notes in Mechanical Engineering,
https://doi.org/10.1007/978-981-15-1071-7_36

and various parameters involved in the problem. Gupta et al. [4] have studied normal impact on thin aluminum plates by ogive-nosed projectiles at impact velocities greater than the ballistic limit. They have studied the effects of plate thickness and projectile-related parameters on residual velocity and ballistic limit. Some results were also obtained by Gupta and Madhu [5] for hard-core steel projectiles.

Most of these analyses and others [6–8] were experimental in nature. Due to the dynamic nature of the transient phenomenon, the mechanics of perforation is so fast that it is quite difficult to analyze and observe the variation of all its parameters experimentally. Some of the studies have been published [9–14] which attempts to model the impact phenomenon by 2D numerical analysis. Recently, Iqbal et al. [11, 15] have reported 3D numerical model of the problem with shear failure criteria. The study was comprehensive in nature with inclusion of parametric failure study from different nose profiles of the projectile. However, they did not report the comprehensive modeling strategy undertaken by them. The present study is an effort in this direction.

In this study, an ogive nose projectile of CRH 2 was impacted on thin aluminum plate of 0.5 mm thickness and the failure behavior and damage modes were studied. The details of the modeling strategy and effect of various parameters in the simulation were highlighted. Further, improved damage evolution method was implemented in the constitutive law that incorporates stress-displacement response after the failure has initiated in the elements. The projectile and target dimensions were taken from the work of Gupta and Ansari [4, 16].

2 Modeling Methodology

2.1 Geometric Modeling, Boundary Condition and Contact

3D analytical rigid projectile was made in the preprocessing module of Abaqus/Explicit. The projectile was kept rigid as the aim is to see the perforation and deformation behavior of the target and not the projectile. The projectile was given a reference point at the center of gravity of its body with mass, inertia and initial velocity assigned to it. The metal target was modeled as a 3D deformable body with three partitions constructed on its face. The impact zone was further partitioned in four parts to simplify the geometry and improve the results as seen from Fig. 1. The progressive movement of the projectile is defined by the dynamic explicit procedure of the Abaqus finite element code. Surface-to-surface contact between the projectile and the plate was given by the kinematic contact algorithm with finite sliding. With the kinematic algorithm, the contact penetration of a slave node into a master surface is eliminated at the end of each time increment. During defining the contact, the bullet was considered as the master surface as it has more stiffness than the impact zone of the target which is a node-based slave surface [15]. Due to the small thickness of the target, the friction between the plate and the projectile was assumed negligible.

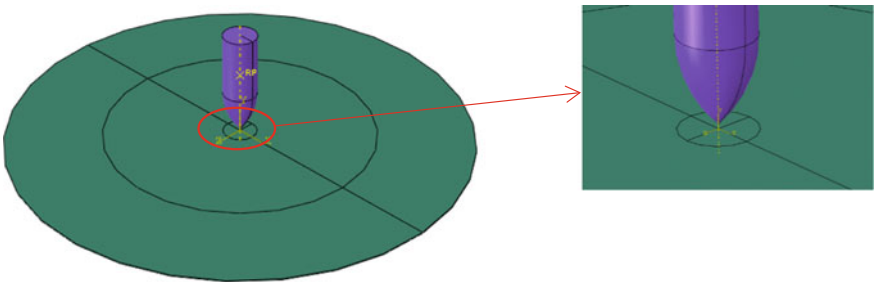

Fig. 1 Target plate partitioning strategy

The assumption was verified by taking two values of the coefficient of friction (0 and 0.05) but no significant difference in the results was observed. The circular plate is curtailed at its circumference with respect to all six degrees of freedom by using encastre boundary condition in the code.

2.2 Constitutive Relation and Failure Criteria

Deformable aluminum target was assigned material properties to predict the deformation behavior that occurred in experiments [4, 16]. Density and isotropic elasticity can be easily assigned to the model but predicting the plastic and damage behavior aluminum target requires correct failure model that incorporates these effects. The Johnson-Cook failure model is capable to predict the flow surface as it incorporates the elasto-viscoplastic behavior observed in aluminum at low-impact velocities. The model also takes into account the effect of high strain rate and thermal softening of the material. Moreover, this model is pre-implemented in Abaqus/Explicit. The flow stress is given by

$$\sigma_{\text{eq}} = \left[A + B\left(\bar{\varepsilon}^{\text{pl}}\right)^{n}\right]\left[1 + C\ln\left(\dot{\varepsilon}^{*}\right)\right]\left[1 + \left(T^{*}\right)^{m}\right] \tag{1}$$

where $\bar{\varepsilon}^{\text{pl}}$ is the equivalent plastic strain and $\dot{\varepsilon}^{*}$ is dimensionless strain rate with $\dot{\varepsilon}$ and $\dot{\varepsilon}_0$ being plastic strain rate and user-defined reference strain rate (typically 1.0 s^{-1}), respectively. The yield stress A and the hardening parameters (B and n) are determined by fitting first part of Eq. (1) to the experimental plastic flow surface of true stress stress–strain data. Moreover, T^{*} represents the non-dimensional temperature.

Failure accumulation in the Johnson-Cook model does not directly degrade the yield surface instead the model, [17, 18] defines the strain at fracture as

$$\bar{\varepsilon}_{f}^{\text{pl}} = \left[D_1 + D_2 e^{-D_3\sigma^{*}}\right]\left[1 + D_4\ln\left(\dot{\varepsilon}^{*}\right)\right]\left[1 + D_5 T^{*}\right] \tag{2}$$

where σ^* is stress triaxiality parameter and D_1, D_2, D_3D_4 and D_5 are model parameters. These parameters are determined from experiments on notched and axisymmetric specimens at different strain rates. The first set of brackets in Eq. (2) is intended to represent the observation that strain to fracture decreases as the hydrostatic tension increases. The second set of bracket is the strain to failure expression representing the effect of an increased strain rate on the material ductility, lastly the third set represent the effect of thermal softening.

The failure occurs in the model when the damage variable D exceeds unity. The evolution of D is given by the accumulated incremental effective plastic strain divided by the current strain at fracture as

$$D = \sum \frac{\Delta \bar{\varepsilon}^{\mathrm{pl}}}{\bar{\varepsilon}_f^{\mathrm{pl}}} \tag{3}$$

where $\Delta \bar{\varepsilon}^{\mathrm{pl}}$ is the equivalent plastic strain increment and $\bar{\varepsilon}_f^{\mathrm{pl}}$ is equivalent fracture strain.

In the past, studies [10, 15, 19] propose damage formulation of ductile materials by shear failure criteria which gives satisfactory results based on Johnson-Cook damage parameters ($D_1 - D_5$). But the criteria majorly depend upon the value of inertia of the target and aspect ratio of the elements in and around the impact zone. To make the aspect ratio close to unity (an essential condition for accurate results) in a circular geometry of target (as shown in Fig. 1) for 3D geometry is not possible and significant difference in the results were found when aspect ratio goes away from unity [18]. The improvement in the present study is proposed by using damage evolution criterion in conjunction with Johnson cook failure model. Further, it is to be noted that when failure occurs stress–strain relationship no longer accurately represents the material's behavior. Continuing to use the stress–strain relation after failure introduces a strong mesh dependency based on strain localization. Hence to overcome this Hillerborg's fracture, energy proposal [23] is used that incorporates a stress-displacement response after the damage has initiated. It defines the energy required to open unit area of crack as

$$G_f = \frac{\sigma_u \, \bar{u}_f^{\mathrm{pl}}}{2} \tag{4}$$

where σ_u is ultimate stress at damage initiation and $\bar{u}_f^{\mathrm{pl}}$ is the equivalent plastic displacement at failure. It is to be noted that before the damage starts $\bar{u}_0^{\mathrm{pl}}$ is zero but as the damage is initiated it becomes $\bar{u}_f^{\mathrm{pl}} = L\varepsilon_f^{\mathrm{pl}}$, where L is the characteristic length of the element and $\varepsilon_f^{\mathrm{pl}}$ is plastic strain at failure. The inclusion of characteristic length in the material response removes mesh sensitivity by preserving the fracture energy. The values of the Johnson-Cook model parameters used in the present work were obtained from Gupta et al. [10].

2.3 Mesh Definition

Meshing is done on the deformable target such that the results can be achieved accurately within the available computational facility. Aspect ratio is defined as the number of elements taken along the length to the number of elements along the thickness direction of the target. When the ratio approaches unity, Zukas and Scheffler [20] suggested that simulation approaches its optimal values. For meshing, numbers of elements were taken along the thickness direction from 1 to 5, and the attempt was made to keep the aspect ratio of the elements close to unity. The condition for a unity aspect ratio is recommended [20] as some dependency upon the mesh does remain but is not essential due to the incorporation of evolution criteria. The plate is meshed with different element sizes, which is defined as

$$\text{size} = \frac{h}{n} \tag{5}$$

where h, is the plate thickness and n is the number of elements in the thickness.

The solution convergence is obtained by meshing the plate with different element sizes and comparing the residual velocity of the projectile obtained with the experimental data [4, 16]. Figure 2a shows the meshed plate with finer mesh created at impact zone while Fig. 2b shows elements arranged in the thickness direction. Figure 2c observes the solution convergence with 1–5 elements arranged in the thickness of the impact zone of the plate. Finally, three elements were chosen in the thickness direction making the size of the element as 0.167 mm which gives 23,640 elements in the impact zone and 217,045 elements for the whole target plate.

2.4 Element Type and Hourglassing

The target plate was meshed using C3D8R elements (eight-node linear brick, reduced integration with hourglass control). These types of continuum elements are best suited for stress/displacement analysis [21]. The advantage of the reduced integration elements is that the strains and stresses are calculated at the locations (material integration point) that provide optimal accuracy. A second advantage is that the reduced number of integration points decreases CPU time and storage requirements.

However, reduced integration procedure can admit deformation modes that cause no straining at the integration points (for coarser meshing). This zero-energy mode makes the element rank deficient and causes a phenomenon called hourglassing. Hence to stabilize the element against the effect of hourglassing, some artificial stiffness is introduced to prevent some of these unusual deformation. There are several methods available in Abaqus/Explicit to introduce the artificial stiffness like enhanced, viscous, combined, relax stiffness, etc. to control the effect of hourglassing. The model is tested on different methods and enhanced hourglassing is chosen, based on solution convergence. However, the external energy occurring from the artificial

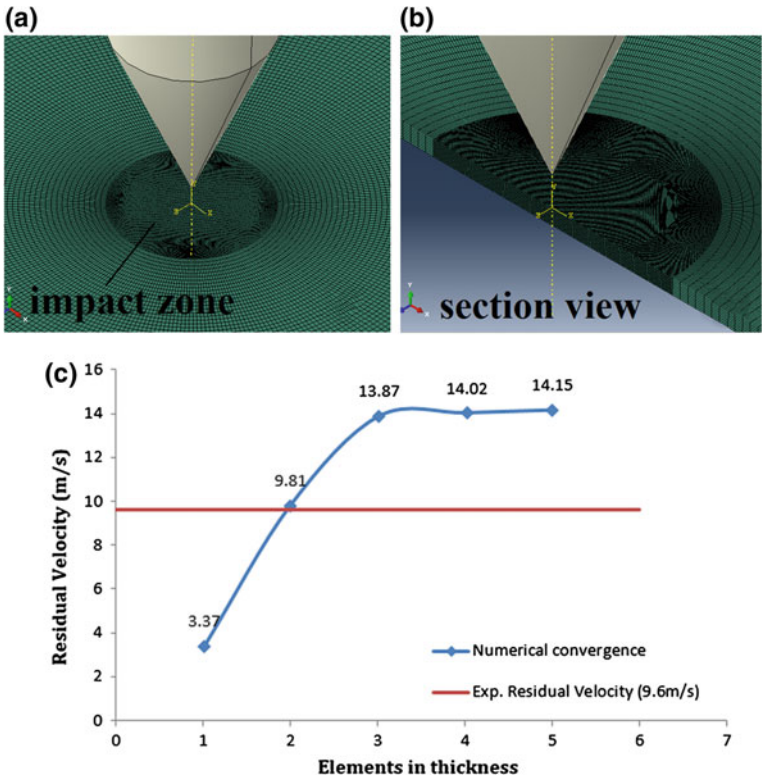

Fig. 2 **a** Meshing difference in impact zone and outside, **b** sectioned view and **c** mesh convergence study

stiffness needs to be monitored and ensured that its effect is minimal to the internal energy of the system. For the present study, it was found that this energy was below 1% of the internal energy of the system.

3 Results and Discussion

Many simulation runs were performed at different impact velocities to observe the perforation process of the target by ogive profile projectile. Table 1 compares the present work with Gupta and Ansari [4, 16]. The ballistic limit of the plate obtained from present model (13.87 m/s) quite closely matches (15.7 m/s) with the experiments [16]. Table 1 also shows the error or deviation of the values from the experimental results. It is found that after the ballistic limit the deviation was 28.54% which is large compared to other values. Further, the error reduces as the velocity is increased. This is because at lower impact velocities microstructural changes occur in the material

Table 1 Comparison of the results from the present study and Gupta and Ansari [4, 16]

Ogive projectile					Aluminum plate (1100-H12)						
Mass		55 g			Effective plate span 206 mm Thickness 0.5 mm						% Error $\left\lvert\frac{(V_r)e-(V_r)n}{(V_r)e}\right\rvert * 100$
Diameter		15 mm									
S. no	Specimen no.	V_i (m/s)	Gupta and Ansari [4, 16]				Present study				
			V_r (m/s)	V_d (m/s)	E_{ab} (J)	Status	V_r (m/s)	V_d (m/s)	E_{ab} (J)	Status	
1	**J113**	**15.7/13.87**	**0**	**15.7**	6.78	**NP**	**0**	**13.87**	5.29	**NP**	
2	J112	21.1	9.6	11.5	3.64	P/5	12.34	8.76	2.11	P/4	28.54
3	J13	25.7	18.7	7	1.35	P/4	20.13	5.57	0.85	P/4	7.64
4	J12	31.1	25.6	5.5	0.83	P/4	26.89	4.21	0.49	P/4	5.03
5	J11	32.1	26.88	5.22	0.75	P/4	28.04	4.06	0.45	P/4	4.31
6	J14	38.3	33.91	4.39	0.53	P/4	35.07	3.23	0.29	P/4	3.42
7	J15	53.9	50.36	3.54	0.34	P/4	51.49	2.41	0.16	P/4	2.24
8	J16	60	56.7	3.3	0.30	P/4	57.81	2.19	0.13	P/4	1.95
9	J17	64.8	61.77	3.03	0.25	P4	62.78	2.02	0.11	P/4	1.63
10	J110	68.3	65.45	2.85	0.22	P/4	66.34	1.96	0.11	P/4	1.35
11	J111	76.3	73.58	2.72	0.20	P/3	74.27	2.03	0.11	P/4	0.93

Note P—Perforated, NP—Not Perforated

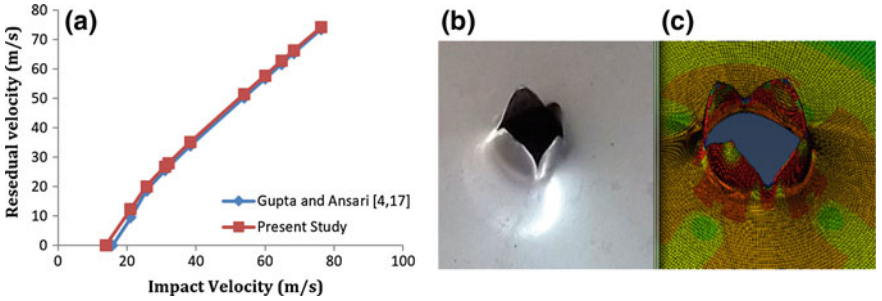

Fig. 3 Variation of the impact velocity with residual velocity and postmortem views of the perforated target

during the perforation process and hence the ballistic velocity V_{50} varies from sample to sample. This may be the reason for some difference between the experiment and simulation ballistic velocity.

Further, the absorbed energy (E_{ab}) is tabulated in Table 1. The absorbed energy is decreasing with the increasing impact velocity. This is because at higher impact velocity the target is not able to resist the projectile motion and hence the energy transfer from the projectile to the target decreases [22, 24]. This shows that at higher strain rate the deformation rate is affected in the target aluminum plate.

Figure 3a shows the variation of residual velocity with increasing impact velocity. The residual velocity increases with increasing impact velocity linearly as discussed by Gupta and Ansari. Figure 3b, c compare the damage occurred in the postmortem samples from experiment and present study. The petaling failure mode along with shear failure is clearly observed. The projectile created four petals of approximately same size and length oriented at 90° to the target plate. The present FEM model was able to reproduce the experimental failure modes accurately.

4 Conclusion

The present study investigates the failure modes of ogive nose projectile through FEM modeling. Johnson-Cook (J-C) failure model was used to predict the flow behavior of aluminum. The study discusses the various boundary condition and contact constrained used during the projectile/target modeling. Further, it was shown that hourglassing, mesh size and element type were important parameters that govern the behavior of the material in predicting correct failure modes during the perforation.

References

1. Backman ME, Goldsmith W (1978) The mechanics of penetration of projectiles into targets. Int J Eng Sci 16:1–99
2. Corbett GG, Reid SR, Johnson W (1996) Impact loading of plates and shells by free-flying projectiles: a review. Int J Impact Eng 18:141–230
3. Goldsmith W (1999) Non-ideal projectile impact on targets. Int J Impact Eng 22:95–395
4. Gupta NK, Ansari R, Gupta SK (2001) Normal impact of ogival nosed projectiles on thin plates. Int J Imp Eng 25:641–660
5. Gupta NK, Madhu V (1997) An experimental study of normal and oblique impact of hard-core projectile on single and layered plates. Int J Imp Eng 19:395–414
6. Prakash T, Sekhon GS, Gupta NK (2003) Adaptive finite element analysis of plastic deformation of plates under projectile impact. J Defence Sci 53(1):57–65
7. Borvik T, Langseth M, Hopperstad OS, Malo KA (2002) Perforation of 12 mm thick steel plates by 20 mm diameter projectiles with flat, hemispherical and conical noses: part I: experimental study. Int J Imp Eng 27:19–35
8. Ansari R, Khan SH, Khan AH (2010) Oblique impact of cylindro-conical projectile on thin aluminium plates CD. In: Proceedings ICTACEM 2010, Dec 27–29. IIT Kharagpur, India, pp 361–363
9. Borvik T, Langseth M, Hopperstad OS, Malo KA (2002) Perforation of 12 mm thick steel plates by 20 mm diameter projectiles with flat, hemispherical and conical noses: part II: numerical study. Int J Imp Eng 27:37–64
10. Gupta NK, Iqbal MA, Sekhon GS (2007) Effect of projectile nose shape, impact velocity and target thickness on deformation behavior of aluminium plates. Int J Solids Struct 44:3411–3439
11. Deb A, Raguraman M, Gupta NK, Madhu V (2008) Numerical simulation of projectile impact on mild steel armour plates using LS-DYNA, part I: validation. Defence Sci J 58:422–438
12. Husain Afsar, Ansari Raisuddin, Khan Arshad Hussain (2017) Experimental and numerical investigation of perforation of thin polycarbonate plate by projectiles of different nose shape. Latin Am J Solids Struct 14(2):357–372
13. Husain A, Hussain Khan A, Ansari R (2018) Ballistic performance evaluation of polycarbonate plate based on quasi-static perforation. IOP Conf Ser Mater Sci Eng 377:012087
14. Khan AA, Naushad Alam M, Rahman N, Wajid M (2016) Finite element modelling for static and free vibration response of functionally graded beam. Latin Am J Solids Struct 13(4):690–714
15. Iqbal MA, Chakrabarti A, Beniwalm S, Gupta NK (2010) 3D numerical simulations of sharp-nosed projectile impact on ductile targets. Int J Impact Eng 37:185–195
16. Ansari R (1998) Normal and oblique impact of projectiles on single and layered plates. PhD thesis, IIT Delhi
17. Johnson GR, Cook WH (1983) A constitutive model and data for metals subjected to large strains, high strain rates and high temperatures. In: Proceedings of the seventh international symposium on Ballistics. The Hague
18. Johnson GR, Cook WH (1985) Fracture characteristics of three metals subjected to various strain, strain rates. Temp Press Eng Fract Mech 21:31–48
19. Iqbal MA, Gupta G, Gupta NK (2010) 3D numerical simulations of ductile targets subjected to oblique impact by sharp nosed projectiles. Int J Solids Struct 47:224–237
20. Zukas JA, Scheffler DR (2000) Practical aspects of numerical simulations of dynamic events: effects of meshing. Int J Impact Eng 9:925–945
21. Version 6.11 ABAQUS analysis user's manual (2011) vol 2
22. Gupta NK, Madhu V (1992) Normal and oblique impact of a kinetic energy projectile on mild steel plates. Int J Impact Eng 12:333–343
23. Hillerborg A, Modeer M, Petersson PE (1976) Analysis of crack formation and crack growth in concrete by means of fracture mechanics and finite elements. Cem Conc Res 6:773–782
24. Khan WU, Ansari R, Gupta NK (2003) Oblique impact of projectile on thin aluminium plates. Defence Sci J 53:139–146

Characterization and Mechanical Properties of 2024/Y_2O_3 Composite Developed by Stir Rheocasting

Semegn Cheneke Lemessa and D. Benny Karunakar

Abstract Semi-solid cast 2024 matrix composites reinforced with 1.5, 2.5, and 3.5 wt% Y_2O_3 particles were developed using vertical muffle furnace equipped with a mechanical stirrer. The composites were successfully developed, and their morphological investigation showed reinforcement particles distribution was fair. The properties of the developed composites improved significantly with an increase in the Y_2O_3 particles in the alloy. The highest ultimate tensile and yield strengths achieved were 294 MPa and 178 MPa respectively corresponding to the 2024/1.5 wt% Y_2O_3 composite. 34 and 45% increments in ultimate tensile and yield strengths were achieved for the 2024/1.5 wt% Y_2O_3 composite compared to the stirred rheocast sample without reinforcement. A decrease in the percentage elongation was observed with an increase in the amount of the yttria particles due to the particle agglomeration and porosity.

Keywords Stir rheocasting · Characterization · Microstructure · Metal matrix composite · Mechanical properties

1 Introduction

The demand for aluminum alloys (lightweight materials) with enhanced strength and room and elevated temperature properties is increasing in the material world. Dispersion of rare earth elements while processing lightweight materials is one of the methods to improve the casting characteristics such as decrease of gasses, refinement of the microstructure, and grain size refinement [1–8]. Additional benefits are an improvement of mechanical properties [3], improvement of ambient and high-temperature properties [2, 9], and improvement of corrosion and wear properties

S. C. Lemessa (✉) · D. B. Karunakar
Mechanical and Industrial Engineering Department, Indian Institute of Technology Roorkee, Roorkee 247667, India
e-mail: semegncheneke@gmail.com

D. B. Karunakar
e-mail: bennyfme@iitr.ac.in

H. Kumar and P. K. Jain (eds.), *Recent Advances in Mechanical Engineering*,
Lecture Notes in Mechanical Engineering,
https://doi.org/10.1007/978-981-15-1071-7_37

[10]. Furthermore, the heat resistant and high melting point intermetallic formed can restrict the dislocation motion and grain boundary slide [11, 12]. The rare earth elements provide lightweight materials enhanced improvements in properties, but they are expensive and difficult for processing. Therefore, it needs to consider a suitable substitute material which gives comparable property compared to the pure rare earth elements. In this regard, the oxide form of the rare earth element becomes the best alternative due to their lower cost of processing, availability, and stability [10]. Y_2O_3 particle, without losing its corrosion property, strengthened aluminum alloy [13]. It was also reported that the dispersion of Y_2O_3 as a reinforcing material in the magnesium matrix improved the strength and ductility simultaneously [14]. Furthermore, Y_2O_3 particulate is thermally stable at high temperatures [14], and it was stated that there appears good integrity between the Y_2O_3 and the Mg matrix which is the result of good thermal stability [14].

For synthesizing metal matrix composites, various methods have been used by different researchers such as in situ methods, liquid, and solid-state methods. The liquid method which involves stirring has been the attractive and most applied method due to the economic benefit it offers compared to other methods. It provides one-third to half of the other methods in terms of the economic benefit, and it is suitable for high production volume [15, 16]. Composite development using conventional casting has some problems. Among them, mixing of the ceramic particles and the matrix is difficult due to the lack of wettability between them [17]. Therefore compocasting/stir rheocasting as an alternative method for the development of composites was developed.

Semi-solid metal casting is a recent processing technology developed due to its advantage over the conventional casting technique [17]. Some of the advantages are a smaller degree of macro-segregation and lower amount of shrinkage cavity. Particle distribution in the base matrix is relatively easier. Therefore, semi-solid casting (compocasting) is accepted as a powerful method for synthesizing composites [17].

There is very few literature reported on metal matrix composite development using semi-solid metal casting process. Some of the research works have been presented hereafter. Yoshida et al. [17] investigated AZ91D composites reinforced with whisker synthesized using semi-solid processing. In their study, they reported that by processing the composite using the semi-solid processing, a fair distribution of reinforcements in the base matrix is relatively easy [17].

Elsharkawi et al. [18] studied rheocasting of semi-solid Al359 matrix composite reinforced with 20% SiC particle employing SEED process. It was reported that nearly spherical α-Al grains were observed in the microstructure. It was reported that particle distribution in the base matrix was fairly uniform. They concluded that SSM is a preferable processing method to develop high-quality composites.

Kumar et al. [19] investigated the effect of pouring temperature on the microstructure evolution of a semi-solid cast in situ Mg_2Si-reinforced Al matrix composite. They reported that a uniform distribution of the reinforcements and the spheroidal

grain formations were achieved. They concluded that the microhardness of the composite increased due to the grain refinement level achieved and the improvement in morphology.

Curle and Ivanchev [20] studied wear of behavior of semi-solid cast Al matrix composites reinforced with SiCp. They reported that nearly spherical α Al globules were attained by processing the composite in the semi-solid region of the alloy. The addition of the particles in the base matrix increased the hardness of the composite.

Nagaral et al. [21] investigated the characterization of Al2618 matrix reinforced with nano B_4C composite synthesized by semi-solid processing. It was reported that a porosity free composite was obtained and particle distribution in the base matrix was fairly uniform. They concluded that the properties of the reinforced composites were superior to the unreinforced counterparts.

Inspired by the above research works, the oxide form of the rare earth element yttrium (yttrium oxide (Y_2O_3)) is used as a reinforcement material for the development of 2024 aluminum metal matrix composite. Stir rheocasting was used for synthesizing the composite, and metallographic samples were taken for microstructural investigations. X-ray diffraction analysis, differential thermal analysis, and scanning electron microscope were used for characterizing the developed samples. Tensile properties of the developed composites were also studied.

2 Materials and Methods

2.1 Materials

The base alloy used as a matrix for the experiments in this study is aluminum 2024 alloy. It was received in the form of a block from the supplier, and its composition is shown in Table 1. Yttrium oxide (Y_2O_3) particles with <10 μm received from Nano Partech, Chandigarh, India, is used as the reinforcement. The morphology of the Y_2O_3 particle used as reinforcement in this research is shown in Fig. 1.

2.2 Methods

Initially, the 2024 aluminum alloy was melted at 720 °C using a vertical muffle furnace. The melt was isothermally held at this temperature for 20 min for complete homogenization. After completely melting and mixing the alloy, 1 wt% of

Table 1 The chemical composition of 2024 aluminum alloy

Cu	Mg	Mn	Si	Fe	Others	Al
3.97	1.34	0.50	0.08	0.07	0.05	Bal

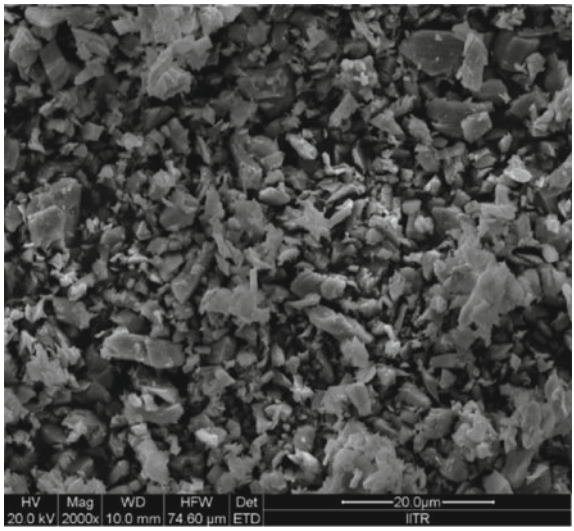

Fig. 1 SEM image showing as received Y_2O_3 particles

hexachloroethane (C_2Cl_6) was added for removing the slag and degassing. 1 wt% of mg was also added to the melt for improving its wettability.

Next, the temperature was set to a semi-solid temperature of 640 °C to keep the melt in a mesh region. According to the Scheil equation, this corresponds to 40% of solid fraction, Eqs. (1) and (2) [22],

$$f_{\mathrm{L}} = (T_{\mathrm{M}} - T)|(T_{\mathrm{M}} - T_{\mathrm{L}})^{-1/1-k} \tag{1}$$

$$f_{\mathrm{S}} = (1 - f_{\mathrm{L}}) \tag{2}$$

where f_{L} is the weight fraction of liquid in the liquid-solid zone, f_{S} is the weight fraction of solid in the liquid-solid zone, T_{M} is the melting point of pure aluminum, T is the working semi-solid temperature of the alloy, T_{L} is the liquidus temperature of the alloy, and k is constant.

The preheated reinforcements (1.5 wt% Y_2O_3, 2.5 wt% Y_2O_3, and 3.5 wt% Y_2O_3) were added to the slurry in series of the experiments. The preheating of reinforcements was performed at 300 °C for 2 h to remove moisture from them. The slurry was stirred thoroughly for 10 min at 500 RPM for each reinforcement level to distribute them uniformly in the melt. For each sample, approximately 300 g of the base alloy was melted. Sample without any reinforcement at the same semi-solid temperature, with the same procedure above, was also prepared for comparison purpose.

Finally, after holding the slurry for 10 min, it was directly transferred manually to the prepared split type die, which was preheated at 300 °C for 1 h. All the cast samples were solidified, and representative samples were taken for the investigation of microstructure and mechanical properties. Figure 2 shows the experimental setup

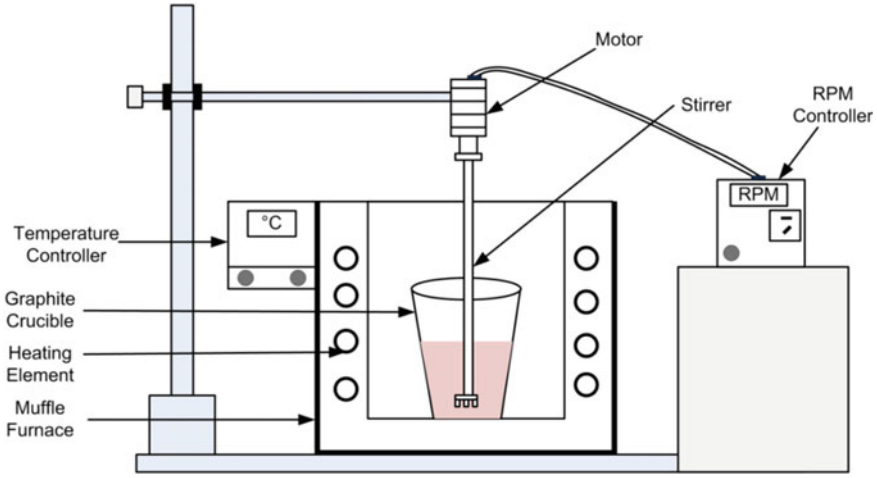

Fig. 2 Experimental setup used in the present study

Table 2 Compositions and designations of the developed alloy and composites

Processing method	Compositions (wt%)	Sample designation
Stir rheocasting	2024 alloy	RC-1
Stir rheocasting	AA2024 + 1.5 wt% Y_2O_3	RC-2
Stir rheocasting	AA2024 + 2.5 wt% Y_2O_3	RC-3
Stir rheocasting	AA2024 + 3.5 wt% Y_2O_3	RC-4

used in the present experiment. The compositions of the developed composites and their designations are given in Table 2.

2.3 Microstructure Characterization

Metallographic samples were cut and prepared for the purpose of microstructural analysis. The surfaces of the specimens were polished gradually using 320–1200 grit SiC emery papers, followed by velvet cloth dispersed with the Al_2O_3 suspension on a disk polisher. Finally, etching was done using Keller's solution (1.5% HCl, 1% HF, 2.5% HNO_3, and 95% H_2O). Microstructural characterization was done using field emission scanning electron microscope (FE-SEM), equipped with energy dispersive spectroscopy (EDS) (Make-FEI Model-FE-SEM QUANTA 200 FEG, Netherlands) and optical microscope (OM) (Model: TL LED, Germany). X-ray diffraction (XRD) (Make-Bruker, Model-D8-Advance, Germany) analysis with

CuKα ($k = 1.5418$ Å) was also carried out. Xpert Highscore plus-Philips XRD software was used for confirming the formation of phases and intermetallic compounds in the developed composites.

Differential thermal analysis (DTA) was carried out to determine the solidus and liquidus temperatures of the base alloy. The alloy was prepared in the form of powder for the purpose of DTA analysis. Heating and cooling of the samples were done at a rate of 10 °C/min in an argon atmosphere. The instrument used for thermal analysis was Make-EXSTAR (Model-SII 6300 EXSTAR).

2.4 Testing of Mechanical Properties

Tensile test: Standard tensile specimens were cut with the dimensions (diameter = 6 mm, gauge length = 30 mm). The tensile test was conducted on an Instron tensile testing machine (Model-5982, Make: Instron, USA) to assess the yield strength (YS), the ultimate tensile strength (UTS), and percent elongation (% EL). The loading rate used to perform the test was 0.5 mm/min. The 0.2% proof stress, UTS, and % EL were obtained from the stress–strain curves.

3 Results and Discussion

3.1 DTA Analysis

The DTA curves of the unreinforced alloy and the developed composites are shown in Fig. 3. Heating and cooling of the samples were performed at 10 °C/min in an argon atmosphere. The figure indicates that with an increase in the amount of Y_2O_3 particles in the matrix, the peaks were shifted to higher temperature values. The endothermic peaks show the melting point of the developed samples. As the reinforcement amount increases, the endothermic peak shifted to the right, and it means that the melting point of the developed composite rises to a higher temperature value. We can conclude that the high-temperature property of the developed composite could be improved with the addition of the high melting point Y_2O_3 particles in the matrix.

3.2 XRD Phase Analysis

XRD of the 2024 and 2024/Y_2O_3 composites are shown in Fig. 4. The phase composition analysis by XRD showed the distribution of the Y_2O_3 reinforcement in the

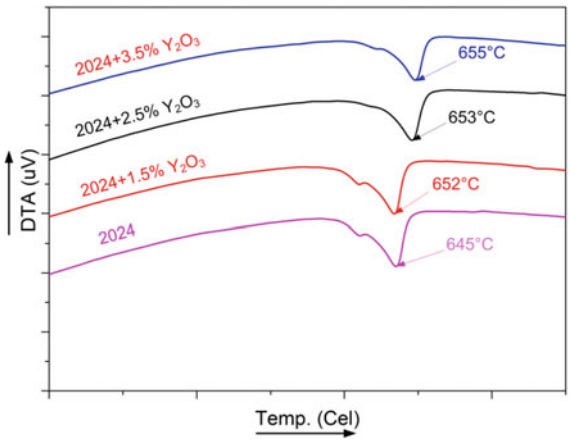

Fig. 3 DTA curve of the unreinforced alloy and developed composites

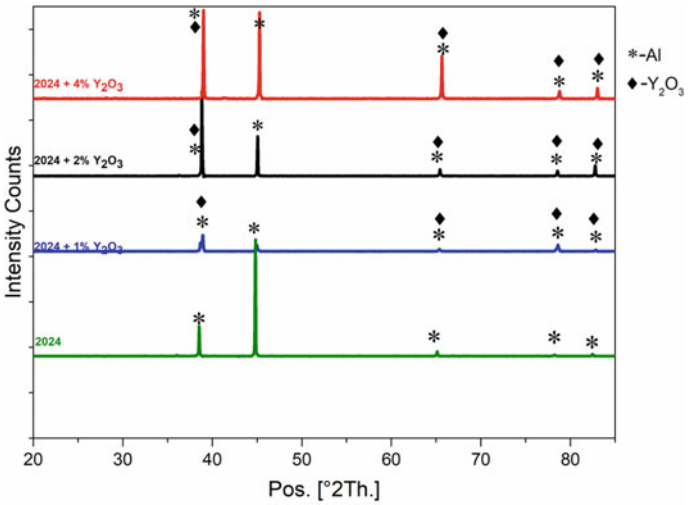

Fig. 4 XRD spectra of the developed composites

developed composite. As clearly seen on the XRD spectra, as the Y_2O_3 reinforcement increases in the composite, the corresponding peaks related to the reinforcement increased. This confirms the increase in the amount of reinforcement in the base matrix. The Al_3Y intermetallic phase was not observed in all the developed composites. The absence of the intermetallic phases further indicates that the Y_2O_3 particle is in equilibrium with the matrix and thermodynamically stable [23]. A small shift in Al peaks to higher 2θ angle was also observed. This is due to an increase in the content of reinforcement particles in the matrix.

3.3 The Effect of Semi-solid Metal Casting

During SSM casting, stirring the melt homogenizes the temperature distribution in the slurry. The homogenized temperature distribution and high cooling rate affect the final quality of the cast component. It provides minimized micropores, dispersion of eutectic nuclei, spheroidization of primary phase, and grain refinement [24]. In conventional (liquid) casting, the grains are dendritic in structure, whereas the developed rheocast samples have a spherical grain structure, as shown in Fig. 5. As shown clearly, the optical micrograph of the RC-1 reinforced rheocast sample (Fig. 5a) has a spherical grain structure. Figure 5b shows the optical image of the RC-2 composite. Compared to the micrograph of the developed rheocast sample without reinforcement, the microstructure of the composites was refined. With an increase in the amount of the yttria particles in the composite, the grain structures of the developed composites were refined (Fig. 5c and d). It was reported that the addition of rare earth oxides in the matrix could refine the grains of the matrix [1–4, 6]. In addition to the refining ability of the reinforcement particles, stirring has also further refined the grain structure of the rheocast composite samples, which would contribute to the improvement in mechanical properties. The globular microstructure obtained, as clearly seen in the figures, shows that the rheocasting technique

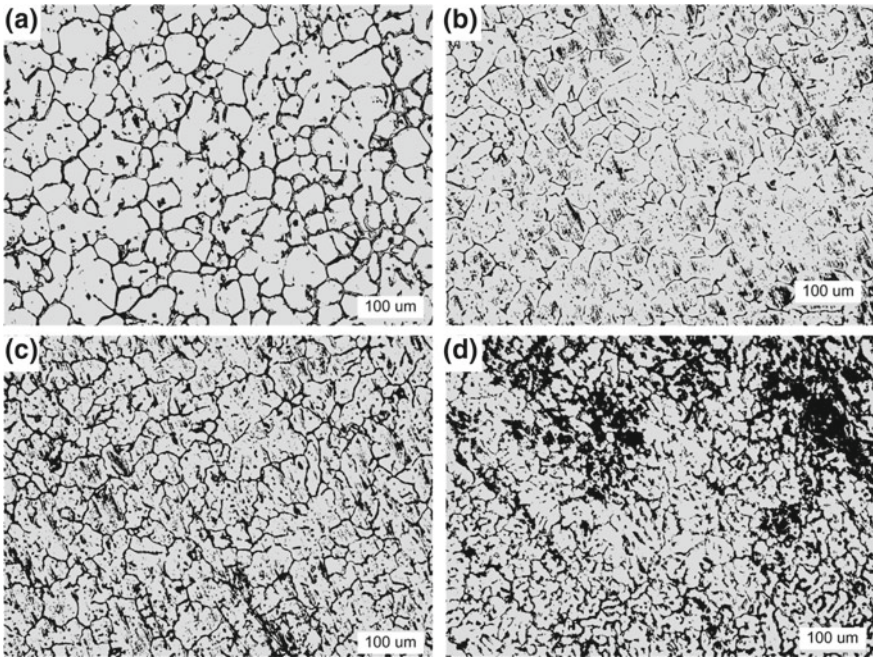

Fig. 5 Optical images of **a** RC-1, **b** RC-2, **c** RC-3, **d** RC-4

followed was effective in developing the composite. As a result, ductility, strength, and hardness were improved significantly, which are shown later.

3.4 Microstructure Evolution and Particle Distribution

Microstructural characterizations of all the developed samples were investigated using FE-SEM and are shown in Fig. 6. The microstructures mainly consist of the matrix (α Al) and grain boundaries (GB) eutectic phases and reinforcement particles, as confirmed by the XRD analysis.

The microstructural feature of the stirred rheocast sample without reinforcement is shown in Fig. 6a. The microstructural feature contains small micropores on the surface. The micropores formed might be due to contamination of the slurry with the atmospheric air while stirring. The microstructure of the stirred rheocast sample with 1.5 wt% Y_2O_3 reinforcement is shown in Fig. 6b in which fair uniform distribution of the reinforcements can be observed. Micropores were also observed on the microstructure. Figure 6c and d show the microstructural features of the composites 2024 + 2.5 wt% Y_2O_3 and 2024 + 3.5 wt% Y_2O_3, respectively. Particles got agglomerated due to the increase in the content of the reinforcement particles in the base matrix. Micropores were also observed in the samples.

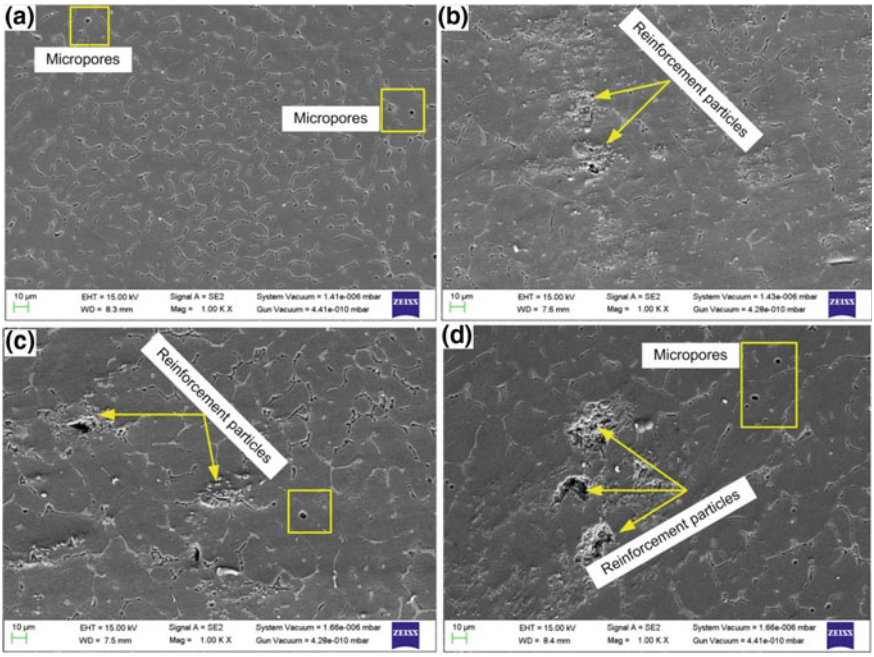

Fig. 6 SEM microstructure of **a** RC-1, **b** RC-2, **c** RC-3, **d** RC-4

EDS analysis. The magnified areas of the grains and the GB areas along with the EDS analysis of the samples are shown in Fig. 7. Figure 7a shows the agglomerates formed in the composite. Figure 7b shows the EDS point analysis which shows the compositions of the agglomerates. It confirmed the presence of Y element in the composite. As indicated clearly, the large peak of Y has been observed, but the peaks corresponding to other elements are very small. The line scan along the agglomerate is shown in Fig. 7c. The corresponding elemental map carried out along the agglomerates of the particles is shown in Fig. 7d. A line scan made along the agglomerated particles with its spectrum shows high peaks of Al, Y, and O elements in the structure. This confirms the agglomeration of Y_2O_3 particles in the composite.

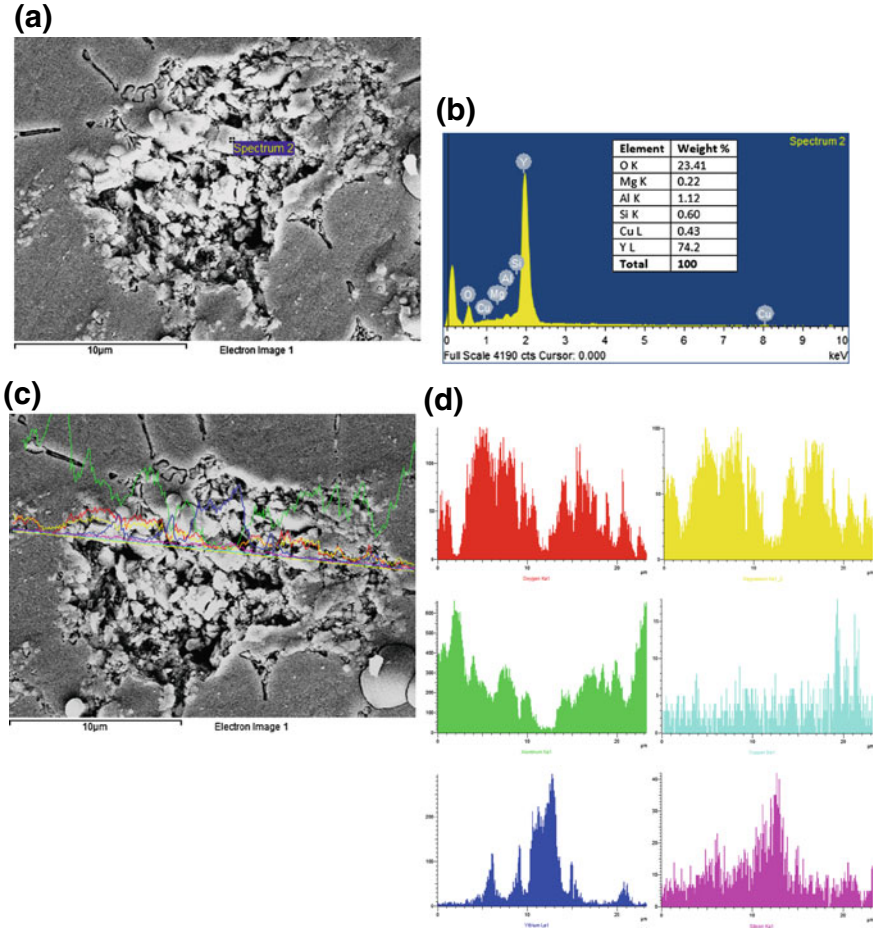

Fig. 7 SEM image showing **a** agglomerated yttria particles, **b** EDS point analysis, **c** the line scan along the agglomerate, **d** the corresponding elemental mapping of the agglomerate

3.5 Mechanical Characterization

Tensile properties: Figure 8 shows the stress–strain curves of the 2024 composites reinforced with varying amounts of Y_2O_3 particles. The semi-solid cast sample without reinforcement was considered for the purpose of comparison. The result shows that the semi-solid cast sample without reinforcement has exhibited UTS of 195 MPa. The UTS improved substantially with an increase in the content of the yttria particles. The UTS of RC-2 composite was found to be 294 MPa. 34% increment in UTS was achieved for the RC-2 composite, compared to the RC-1. The UTS of RC-3 and RC-4 was found to be 240 MPa and 193 MPa, respectively. 19% increment in UTS was achieved for the RC-3 composite, but the UTS of RC-4 decreased. Small additions of the hard ceramic particles into the matrix contribute to a substantial improvement in properties like strength and hardness compared to the unreinforced one [25]. The significant increase in UTS of the developed composites was due to particles distribution (Fig. 6) in the matrix. As the amount of the yttria reinforcement increases, the particles somewhat got agglomerated. The properties of the composite could be deteriorated due to the agglomeration of particles. This hinders particle distribution in the matrix that could increase the porosity level and voids in the developed composite [25]. In addition, the increase in the UTS achieved was due to the strong bond between the reinforcement and the matrix. Due to this, the load transfer is more efficient for the stir rheocast composites. Moreover, the grain refinement level increased with an increase in the addition of yttria particles, and thus, an improvement in tensile strength was achieved.

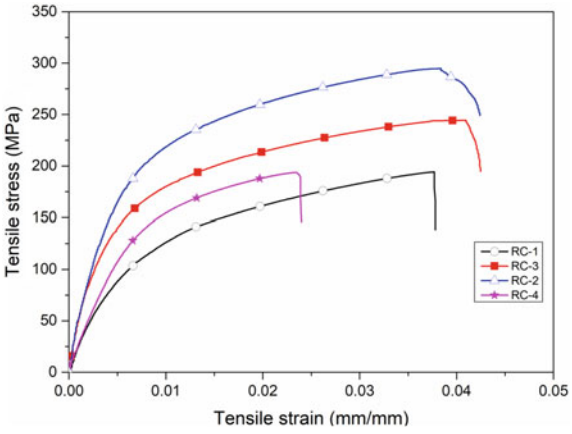

Fig. 8 Stress–strain curve of the developed composites

The 0.2% offset yield strengths of RC-1, RC-2, RC-3, and RC-4 composites were found to be 98 MPa, 178 MPa, 140 MPa, and 128 MPa, respectively. 45, 30, and 23% increments in 0.2% offset yield strengths were achieved for RC-2, RC-3, and RC-4 composites, respectively, compared to the RC-1 (the rheocast sample without reinforcement). The percentage elongation was also found to be 5, 4, 4, and 3% for RC-1, RC-2, RC-3, and RC-4 samples, respectively. The percentage elongation of the composites decreased with an increase in the content of the Y_2O_3 particles. The reduction in elongation of the developed hybrid composites is due to agglomeration of the particles around which voids have been formed. The other reason might be due to the irregularity in the shape of the yttria particles. There will be higher stress concentration around the corners of the particles due to the irregularity that contributes to the sudden initiation of cracks that lead to reduced elongation.

The UTS and the yield strengths of the composites increased with the addition of the yttria particles but at the expense of ductility.

Earlier, it was reported that there was a substantial decrease in the grains sizes of the matrix while increasing the content of reinforcement particles in the base matrix [26]. In their study, they reported that the grain size decreased from 1077.1 to 78.4 μm as the reinforcement of the particles in the matrix was increased from 0 to 7.0 wt%. Similarly, in the present study, substantial grain refinement level has been achieved with an increase in the amount of the reinforcement levels in the matrix. There appear to be two main reasons for the refinement of the grains. The first one was during the beginning of the solidification, during which some of the particles acted as nucleation sites for the aluminum matrix. Secondly, during the solidification process, the particulates around the aluminum matrix caused a pinning effect on the matrix, restricting the grain growth [27, 28].

To further describe the effect of the Y_2O_3 particles on the tensile strength and hardness of the developed composites, two main approaches have been presented [23]. The first approach was the load transfer on the particles. In this case, the load transferred to the particles from the matrix was due to the good bond existing between them. The second one was based on the load transfer of the particles. In this case, the load transferring effect of the particles to the matrix could contribute to an improvement in the yield strength of the composites. Figure 9 shows the overall material properties of the developed samples in the present study.

4 Conclusions

In the present work, 2024 composite reinforced with Y_2O_3 particles was developed successfully using the semi-solid casting method and the following conclusions were drawn.

1. The FE-SEM microstructure showed fairly a uniform distribution of the reinforcements in the composites due to good wettability between them. However, the particles got agglomerated as the reinforcement content increases in the matrix.

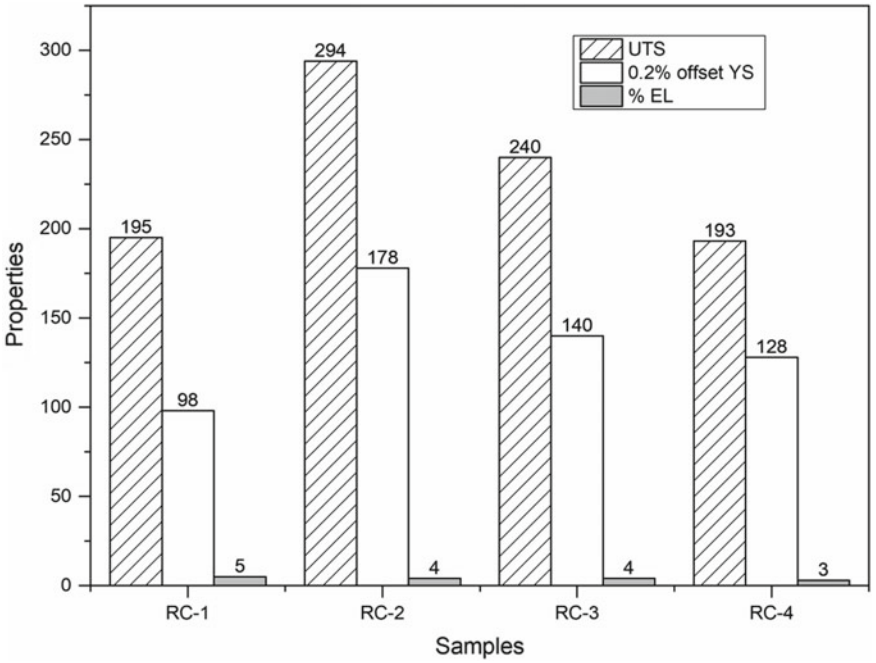

Fig. 9 Overall mechanical properties of the developed samples

2. The properties like ultimate tensile and yield strengths increased with an increase in the addition of Y_2O_3 particles, whereas the percent elongation decreased.
3. The highest values of yield and ultimate tensile strengths were achieved for the developed composite with the yttria content of 1.5 wt%. With an increase in the yttria particles in the matrix, the ultimate tensile and yield strengths were decreased due to the agglomeration of the particles.
4. There is no evidence of intermetallic compounds formed by processing the composite in the semi-solid region of the alloy.
5. The addition of the yttria in the base matrix increased the liquidus temperature of the developed composite as confirmed by the analysis using the differential thermal analyzer.

Acknowledgements The authors highly acknowledged Welding Lab Research laboratory, Department of Mechanical and Industrial Engineering and Institute Instrumentation Centre, IIT Roorkee, for providing the facilities and support to carry out the research work.

References

1. Zhang X, Sun J, Wang M, Zhang Y, Ma N, Wang H (2015) Improvement of yttrium on the hot tearing susceptibility of 6TiB_2/Al-5Cu composite. J Rare Earths 33:1335–1340. https://doi.org/10.1016/S1002-0721(14)60566-4
2. Pan FS, Chen MB, Wang JF, Peng J, Tang AT (2008) Effects of yttrium addition on microstructure and mechanical properties of as-extruded AZ31 magnesium alloys. Trans Nonferrous Met Soc China 18:s1–s6
3. Wang Y, Guan S, Zeng X, Ding W (2006) Effects of RE on the microstructure and mechanical properties of Mg-8Zn-4Al magnesium alloy. Mater Sci Eng A 416:109–118. https://doi.org/10.1016/j.msea.2005.09.104
4. Rosalbino F, Angelini E, De Negri S, Saccone A, Delfino S (2003) Influence of the rare earth content on the electrochemical behavior of Al-Mg-Er alloys. Intermetallics 11:435–441. https://doi.org/10.1016/S0966-9795(03)00016-5
5. Dong Y, Lin XP, Xu R, Zheng RG, Fan ZB, Liu SJ, Wang Z (2014) Microstructure and compression deformation behavior in the quasicrystal-reinforced Mg-8Zn-1Y alloy solidified under super-high pressure. J Rare Earths 32:1048–1055. https://doi.org/10.1016/S1002-0721(14)60182-4
6. Huang WX, Yan H (2014) Preparation and theoretic study of semi-solid Al_2Y/AZ91 magnesium matrix composites slurry by ultrasonic vibration. J Rare Earths 32:573–579. https://doi.org/10.1016/S1002-0721(14)60110-1
7. Li M, Li XG, Zhang K, Li YJ, Ma ML, Shi GL, Yuan JW, Liu JB (2015) Effects of isothermal homogenization on microstructure evolution of Mg-7Gd-5Y-1MM-0.5Zr alloy. J Rare Earths 33:439–444. https://doi.org/10.1016/S1002-0721(14)60438-5
8. Li KJ, Li QN, Jing XT, Chen J, Zhang XY (2009) Effects of Sb, Sm, and Sn additions on the microstructure and mechanical properties of Mg-6Al-1.2Y-0.9Nd alloy. Rare Met 28:516–522. https://doi.org/10.1007/s12598-009-0100-9
9. Xiao W, Jia S, Wang J, Wu Y, Wang L (2008) Effects of cerium on the microstructure and mechanical properties of Mg-20Zn-8Al alloy. Mater Sci Eng A 474:317–322. https://doi.org/10.1016/j.msea.2007.04.008
10. Zhang T, Li DYY (2001) Improvement in the resistance of aluminum with yttria particles to sliding wear in air and in a corrosive medium. Wear 251:1250–1256. https://doi.org/10.1016/S0043-1648(01)00774-8
11. Yang WG, Koo CH (2003) Tensile properties of Mg-8Al-xRE alloys from 300 K to 673 K. Mater Trans 44:1029–1035. https://doi.org/10.2320/matertrans.44.1029
12. Wu G, Fan Y, Gao H, Zhai C, Zhu YP (2005) The effect of Ca and rare earth elements on the microstructure, mechanical properties and corrosion behavior of AZ91D. Mater Sci Eng A 408:255–263. https://doi.org/10.1016/j.msea.2005.08.011
13. Bouaeshi WB, Li DY (2007) Effects of Y_2O_3 addition on microstructure, mechanical properties, electrochemical behavior, and resistance to corrosive wear of aluminum. Tribol Int 40:188–199. https://doi.org/10.1016/j.triboint.2005.09.030
14. Hassan SF (2011) Effect of primary processing techniques on the microstructure and mechanical properties of nano-Y_2O_3 reinforced magnesium nanocomposites. Mater Sci Eng A 528:5484–5490. https://doi.org/10.1016/j.msea.2011.03.063
15. Vembu V, Ganesan G (2015) Heat treatment optimization for tensile properties of 8011 Al/15% SiCp metal matrix composite using response surface methodology. Defence Technol 11:390–395. https://doi.org/10.1016/j.dt.2015.03.004
16. Nagaraj N, Mahendra KV, Nagaral M (2018) Investigations on mechanical behaviour of micro graphite particulates reinforced Al-7Si alloy composites. In: IOP conference series: materials science and engineering, vol 310, p 012131. https://doi.org/10.1088/1757-899x/310/1/012131
17. Yoshida M, Takeuchi S, Pan J, Sasaki G, Fuyama N, Fuj T, Fukunaga H (1999) Preparation and characterization of aluminum borate whisker reinforced magnesium alloy composites by semi-solid process. Adv Compos Mater 8:259–268. https://doi.org/10.1163/156855199X00254

18. Elsharkawi EA, Pucella G, Côte P, Chen XG (2014) Rheocasting of semi-solid Al359/20% SiC metal matrix composite using SEED process. Can Metall Q 53:160–168. https://doi.org/10.1179/1879139513Y.0000000120
19. Kumar S, Das P, Tiwari SK, Mondal MK, Bera S, Roy H, Samanta SK (2015) Study of microstructure evolution during semi-solid processing of an in-situ Al alloy composite. Mater Manuf Process 30:356–366. https://doi.org/10.1080/10426914.2014.952040
20. Curle UA, Ivanchev L (2010) Wear of semi-solid rheocast SiCp/Al metal matrix composites. Trans Nonferrous Met Soc China 20:852–856
21. Nagaral M, Kalgudi S, Auradi V, Kori SA (2018) Mechanical characterization of ceramic nano B_4C Al2618 alloy composites synthesized by semi-solid state processing. Trans Indian Ceram Soc 77:146–149. https://doi.org/10.1080/0371750X.2018.1506363
22. Flemings MC (1991) Behavior of metal alloys in the semisolid state. Metall Trans A 22:957–981. https://doi.org/10.1007/BF02661090
23. Rajan HM, Ramabalan S, Dinaharan I, Vijay SJ (2013) Synthesis and characterization of in situ formed titanium diboride particulate reinforced AA7075 aluminum alloy cast composites. Mater Des 44:438–445. https://doi.org/10.1016/j.matdes.2012.08.008
24. Natori K, Utsunomiya H, Tanaka T (2017) Improvement in formability of semi-solid cast hypoeutectic Al-Si alloys by equal-channel angular pressing. J Mater Process Technol 240:240–248. https://doi.org/10.1016/j.jmatprotec.2016.09.022
25. Yigezu BS, Mahapatra MM, Jha PK (2013) Influence of reinforcement type on microstructure, hardness, and tensile properties of an aluminum alloy metal matrix composite. J Miner Mater Charact Eng 1:124. https://doi.org/10.4236/jmmce.2013.14022
26. Chen F, Chen Z, Mao F, Wang T, Cao Z (2015) TiB_2 reinforced aluminum based in situ composites fabricated by stir casting. Mater Sci Eng A 625:357–368. https://doi.org/10.1016/j.msea.2014.12.033
27. Lu L, Lai MO, Chen FL (1997) Al-4 wt% Cu composite reinforced with in-situ TiB_2 particles. Acta Mater 45:4297–4309. https://doi.org/10.1016/S1359-6454(97)00075-X
28. Selvam JDR, Smart DR, Dinaharan I (2013) Microstructure and some mechanical properties of fly ash particulate reinforced AA6061 aluminum alloy composites prepared by compocasting. Mater Des 49:28–34. https://doi.org/10.1016/j.matdes.2013.01.053

Conversion and Utilization of Gravitational Potential Energy for Hydraulic Excavator

Tushar Kanti Saha, Abhinav Kr. Singh, Mohit Bhola, Sumanta Kumar Dutta and Sanjoy Kumar Ghoshal

Abstract Considering the loss of high throttling loss for open-circuit hydrostatic transmission at present, hydraulic excavation energy saving is important for removing the source of deficiency and protecting the environment. This paper deals with closed circuit gravitational potential energy recovery system (GPERS) based on energy storage element such as an accumulator, along with the generator. An estimated 16% total energy consumption is reduced when a system using accumulator-motor-generator system is used as compared to the simple motor system. The simulation result is carried out with Automation Studio and MATLAB/Simulink. At last, the paper put forward the future development of GPERS.

Keywords Boom potential energy · Hydraulic excavator · Energy recovery · Hydraulic accumulator

1 Introduction

In the past few decades, energy inadequacy and environmental pollution have become a serious problem throughout the world. So energy saving and emission reduction are very much required in all the fields. Waste energy recycling is a very good method for improving energy efficiency and it can be used to reduce energy requirement from different conventional energy sources. To increase energy efficiency in power industries, internal combustion engines, and in the iron and steel industry, misused heat and gas are recuperated [1–4]. The piezo-electric material is a device which converts mechanical vibration energy into electric energy. In this manner, mechanical vibration energy can be recuperated [5–7]. Braking energy in different vehicles can also be recuperated for reducing energy intake and performance can be improved [8, 9] and for saving energy in different systems hybrid concepts are used. In this

T. K. Saha (✉) · A. Kr. Singh · S. K. Dutta · S. K. Ghoshal
Department of Mechanical Engineering, IIT (ISM), Dhanbad 826004, India
e-mail: tusharkantisaha5@gmail.com

M. Bhola
Department of Mining Machinery Engineering, IIT (ISM), Dhanbad 826004, India

H. Kumar and P. K. Jain (eds.), *Recent Advances in Mechanical Engineering*,
Lecture Notes in Mechanical Engineering,
https://doi.org/10.1007/978-981-15-1071-7_38

way, exhaust emission and energy consumption can be reduced in excavators, wheel loaders, trucks, cars, earthmovers, and harvesters [10–14]. Sawan et al. [15] showed different renewable energies and different storing devices to store that energy to use in further stages.

Energy saving in construction machinery has become a very important issue due to the increase in fuel price and the environmental pollution, especially for a hydraulic excavator (HE), as it is very much popular device in construction machinery and it has low energy efficiency and bad exhaust. Dropping process wastes a lot of gravitational potential energy. Thus by recovering potential energy, energy consumption for mobile machinery can be reduced significantly.

Potential energy can be recovered by two strategies, hydraulic recovery, and electrical recovery. For electrical recuperation technique at first, hydraulic motor is driven by downstream fluid and then the electric generator is driven by a hydraulic motor; hydraulic energy is converted into electrical energy; and in the end; it is stored in super-capacitors or batteries. In hydraulic recovery, technique accumulator is used to storing potential energy by changing it into hydraulic energy. HO et al. [16] have proposed a hydraulic accumulator-based energy-saving hydraulic system, and this combination was investigated through modeling and analysis. The author revealed that, depending on motor and pump displacement energy recovery capacity of the system varies from 32 to 66%. They also showed that more motor displacement ratio shows higher energy recovery capacity. Chen Mingdong et al. [17] have come up with the principle of energy saving of hydraulic counterweight by the use of the accumulator. On the basis of the basic principle, the mathematical modeling of the system is done. Hydraulic excavator power can be reduced by connecting accumulator with the boom. By this process, system noise and damage of hydraulic component can be reduced. Andersen et al. [18] proposed an energy recovery system, in which battery is connected with an electric motor in forklift trucks. In comparison with conventional machines, efficiency at high velocity increased from 56 to 74% and at low velocity 39 to 69%.

Zhang et al. [19] proposed that during boom dropping operation accumulator is charged and this stored energy is used to generate electricity with the help of a hydraulic motor, and this operation improved the efficiency of the hydraulic excavator. Luo et al. [20] proposed a hydraulic circuit to convert potential energy of boom, arm, and bucket into electrical energy and then this energy is stored in a storage device. They found that 16T hybrid excavator is more efficient as compared to conventional one. Siebert et al. [21] have improved the efficiency of load sensing systems. In the proposed system, efficiency increment was done by diminishing the pressure loss occurred within the system. For achieving this objective, the traditional LS system was implemented with the developed hydraulic circuit. An approximately 44% decrement was observed in system inherent pressure loss through simulation. In a simulation study, Zimmerman et al. [22] found that by removing the directional control valves the possibility in energy saving can be achieved on the load sensing hydraulic excavator system. The results showed that the total energy loss was distributed toward three prime areas like actuator work, control, and pump losses. Ge et al. [23] found that the huge energy consumption in overrunning condition of the

hydraulic excavator can be improved by the proposed novel system. In their proposed design, the hydraulic elements like swing motor, boom cylinder, and stick cylinder were controlled with the separate meter in and meter out technique, a bucket cylinder and the motor travels by the traditional valves. Experimental results showed that the valve pressure loss is decreased significantly by the proposed system and simultaneously energy efficiency is also increased. As compared to load sensing system boom consumes 15% less energy and arm consumes 5.6% less energy and at the same time pressure shocks are removed significantly.

The energy efficiency and stability of the boom system were enhanced by Liu et al. [24]. This enhancement was manifested based on the independent metering circuit with flow strategy, valve coordinate in static, dynamic and in accordance with pressure pump. Experimental outcomes based on load sensing and implemented independent metering circuit shows that energy consumption of the boom system in independent metering was around 15% in comparison with load sensing system. Xu et al. [25] have reported on upcoming trends and developments in motion control technologies for designing a hydraulics system with multi-actuator for utilization of mobile machinery. Zhao et al. [26] designed a new hydraulic hybrid excavator with three-chamber cylinders (TCCs) and accumulators. Its work is to recover the potential energy of mechanical arms and excavator load. TCCs constitute three chambers with the piston rod, chamber without piston rod and chamber with counterweight. Simulation study shows that potential energy recovery system reduces 30 to 60% dissipated energy as compared to without potential energy recovery system and 50% of dissipated energy of engine is also reduced.

The aim of this paper is that proposing energy-saving solutions for hydraulic systems to improve the efficiency and permits a reduction in fuel consumption. Starting from the energy analysis of the circuit, through its validated mathematical model, the distribution of the energy losses within the system has been investigated. At last, a new hydraulic circuit has been proposed combining all energy-saving solutions. Simulation result showed 16% of less energy consumption and significant reduction in fuel saving.

2 Experimental Procedure

In the conventional hydraulic excavator system as shown in Fig. 1a, both the cylinders are directly connected to pump. In the conventional circuit during extension process all the load is lifted by pump only and in retraction process where boom is dropped all the gravitational potential energy of bulky boom is wasted through throttling losses. In modified circuit as shown in Fig. 1b, lifting and dropping of the boom are divided into four stages. In the first stage, boom is extended with the help of accumulator; in the second stage, boom is extended with the help of a pump and in return line fluid is passed through hydraulic motor which is coupled with an electric generator. In the third stage, when the boom drops down, the return line fluid is supplied to the accumulator. This fluid charges accumulator which is used further to lift boom in the

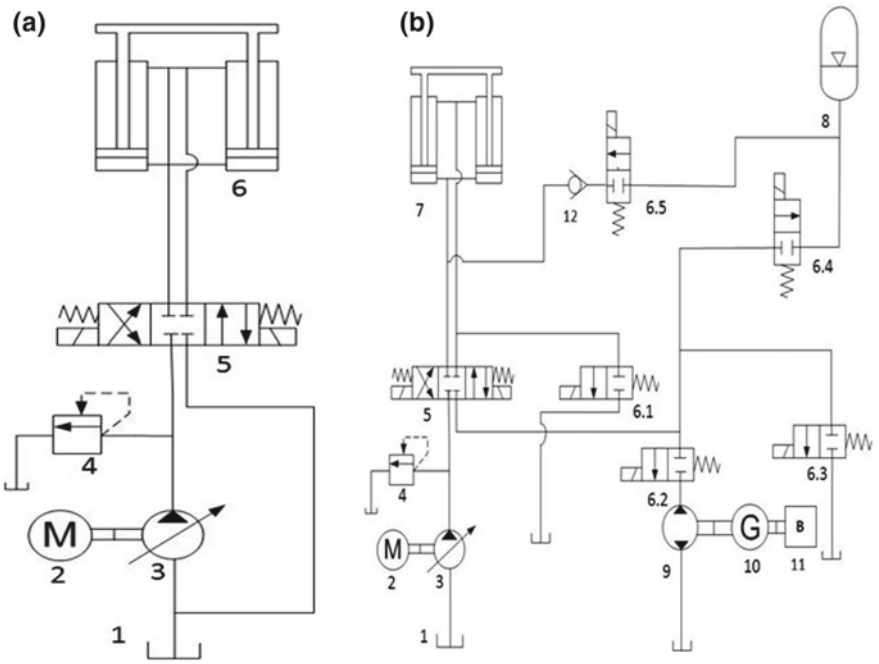

Fig. 1 **a** Conventional and **b** modified circuit

next operation. In the last stage during retraction of hydraulic cylinder, the return line flow is supplied to the tank after passing through the hydro-motor. This hydro-motor runs an electric generator, and the generated electricity is stored in super-capacitor for further use. This is best explained in terms of flow chart as shown in Fig. 2.

Tables 1 and 2 comprise the list of components for conventional circuit (Fig. 1a) and modified circuit (Fig. 1b), respectively. Table 3 gives specification about different components used to run the circuit in Automation Studio and MATLAB.

2.1 Mathematical Modeling

The mathematical equations of motor, pump, two-chamber cylinder, and accumulator are described below to explain the work principle and energy saving of the modified circuit as compared to conventional system.

Mathematical Model of Motor

The consumption of fuel is calculated by the equation is given below

$$m_f = \int T_e M_e(T_e, \alpha_e)\omega_e(T_e, \alpha_e)\mathrm{d}t \tag{1}$$

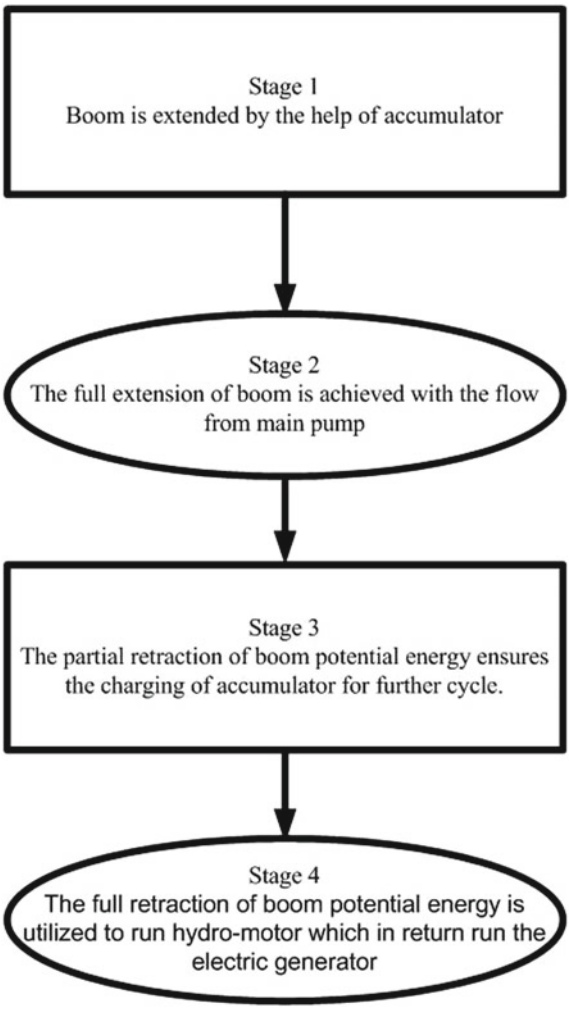

Fig. 2 Operational stages of modified circuit

Table 1 Component of conventional circuit

1	Hydraulic tank
2	Motor
3	Variable hydraulic pump
4	Pressure relief valve
5	Directional control valve (4/3)
6	Two-chamber hydraulic cylinder

Table 2 Components of modified circuit

1	Hydraulic tank
2	Motor
3	Variable hydraulic pump
4	Pressure relief valve
5	Directional control valve (4/3)
6	Directional control valve (2/2)
7	Two-chamber hydraulic cylinder
8	Hydraulic accumulator
9	Bi-directional hydraulic pump
10	Generator
11	Battery
12	Check valve

Table 3 Specification of different components

Component	Parameter	Specification
Electric motor	Mechanical power	200 kW
	Setting speed	2000 RPM
	Maximum angular speed	2010 RPM
	Maximum temperature	100 °C
	Maximum torque	1000 N m
Unidirectional variable displacement pump	Displacement	80 cm^3/rev
	Maximum pressure	400 bar
	Maximum temperature	100 °C
Pressure relief valve	Cracking pressure	150 bar
	Maximum flow	420 L/min
	Maximum pressure	450 bar
	Maximum temperature	100 °C
Twin hydraulic cylinder	Piston diameter	100 mm
	Rod diameter	50 mm
	Stroke	1000 mm
	Resistive force on extension	30 kN
	Driving force on retraction	15 kN
Gas loaded hydraulic accumulator	Total volume	20 L
	Pre-charge pressure	36 bar
	Initial liquid volume	10 L
	Internal diameter	200 mm

(continued)

Table 3 (continued)

Component	Parameter	Specification
Bi-directional hydraulic motor generator	Displacement	100 cm^3/rev
	Maximum angular speed	5000 RPM
	Maximum displacement	350 cm^3/rev
	Maximum pressure	450 bar
	Maximum temperature	100 °C
	Maximum torque Maximum output	400 N m 15 kW

m_f = fuel consumption of engine
M_e = fuel efficiency
T_e = output torque of engine
α_e = degree of engine throttle opening
ω_e = rotational speed of engine.

The torque delivered by the engine is obtained by the following equation.

$$T_e = J_e \frac{\mathrm{d}\omega_e}{\mathrm{d}t} + D_e\omega_e + T_1 \tag{2}$$

J_e = equivalent moment of inertia of engine
D_e = equivalent viscous damping coefficient of engine
T_l = rotational frictional torque.

Mathematical Model of Pump

The input power required by the pump is

$$W_p = T_p\omega_p \tag{3}$$

W_p= power of pump
T_p = torque of pump
ω_p = rotational speed of pump.

The total torque generated by the pump can be calculated by using the following equation.

$$\mathrm{T_p} = \mathrm{J_p}\frac{d\,\omega_p}{dt} + \mathrm{D_{viscous}}\omega_p + \Delta\mathrm{P_p}\mathrm{D_p} \tag{4}$$

J_p = equivalent rotational inertia of pump
D_p = pump displacement
D_{viscous} = viscous damping coefficient of pump
ΔP_p = difference in pressure between high and low pressure chamber of pump.

The rate of flow of pump is obtained by using the equation is given below.

$$Q_{\text{flow}} = \eta_{vp} D_p \omega_p \tag{5}$$

Q_{flow} = flow rate of pump
η_{vp} = volume efficiency of pump

The continuity of variable displacement piston pump can be shown by using the following equation.

$$\frac{V_{outlet}}{\beta_e}\frac{dP_p}{dt} = \mathrm{Q_{flow}} - \mathrm{C_p}\Delta\mathrm{P_p} \tag{6}$$

V_{outlet} = volume of pump outlet
β_e = equivalent bulk modulus of elasticity of hydraulic oil
P_p = pressure of pump outlet
C_p = Total leakage coefficient of pump (i.e., summation of internal coefficient and external coefficient leakage of pump).

Mathematical Model of Two-Chamber Cylinder

The kinematics of the boom cylinder is given by the following equation.

$$m_1 \frac{\mathrm{d}v_1}{\mathrm{d}t} = F_1 + P_A A_A - P_a A_a - B_1 v_1 - f_1 \tag{7}$$

m_1 = mass of the boom cylinder
v_1 = velocity of the boom cylinder
F_1 = Load
P_A = cylinder chamber pressure without piston rod
A_A = area of the cylinder chamber without piston rod
P_a = cylinder chamber pressure with piston rod
A_a= area of the cylinder chamber with piston rod
B_1 = viscous damping coefficient of boom cylinder
f_1 = friction force of boom cylinder.

The continuity equation of the boom cylinder chamber without piston rod can be given by the following equation.

$$\frac{V_A}{\beta_e}\frac{\mathrm{d}P_1}{\mathrm{d}t} = Q_1 - A_A v_1 - C_1 P_1 - C_3(P_1 - P_2) \tag{8}$$

V_A = cylinder chamber volume without piston rod
Q_1 = flow of closed pump controlled system
C_1 = coefficient of the external leakage chamber without piston rod
C_3 = coefficient of the internal leakage between the chambers.

The continuity equation of boom cylinder chamber considering piston rod is given by the equation.

$$\frac{V_a}{\beta_e}\frac{\mathrm{d}P_2}{\mathrm{d}t} = A_a v_2 - Q_1 - C_2 P_2 - C_3(P_2 - P_1) \tag{9}$$

V_a = volume of the cylinder chamber with piston rod
C_2= coefficient of the external leakage chamber considering piston rod.

Mathematical Model of Accumulator

The bladder type accumulator was selected as main energy storage element in modified circuit.

From Boyle's law, the accumulator equation can be written as

$$P_0 V_0^n = P_1 V_1^n = P_2 V_2^n = \text{constant} \tag{10}$$

P_0 = accumulator charging pressure
V_0 = accumulator size, charging volume of gas at P_0
P_1 = minimum system pressure
V_1 = gas volume corresponding to pressure P_1
P_2 = maximum system pressure
V_2 = gas volume corresponding to pressure P_2
n = polytropic exponent

where n can be determined by the working condition of accumulator.

$$q_{\text{acc}} = \frac{\mathrm{d}V_F}{\mathrm{d}t} \tag{11}$$

q_{acc} = flow supplied by accumulator
V_F = volume of fluid inside the accumulator.

3 Results and Discussions

To analyze the energy recovery of hydraulic excavator, one complete cycle of extension and retraction of the hydraulic cylinder is chosen. The boom is raised with a force of 30 kN opposing its upward movement and its retraction is assisted by a force of 15 kN. The engine is operated at a speed of 2000 rpm during the process. The displacement of piston rod of hydraulic cylinder with time is shown in Fig. 3. From this figure, it is observed that in the conventional circuit, the cylinder is extended from 0.5 to 8 s and retraction occurs from 10.5 to 17 s. In modified circuit, cylinder

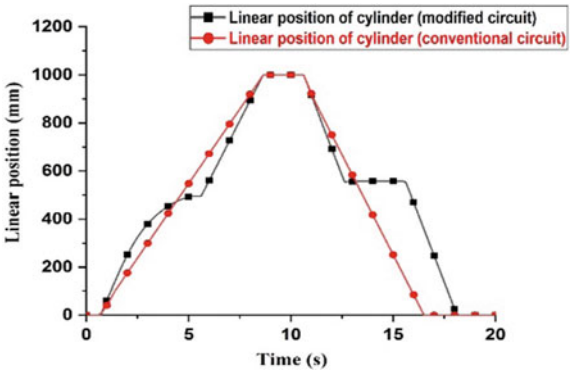

Fig. 3 Linear position of hydraulic cylinder

is extended in two stages: In the first stage, the cylinder is lifted with assistance from the accumulator and in the second stage cylinder is lifted with the help of a pump. In the first stage of the graph, non-linear displacement of the actuator is due to polytropic process decay of accumulator.

Figure 4 shows piston side chamber pressure of the hydraulic cylinder. It can be seen that in both the cases, the piston side pressure is almost the same in case of extension but during retraction, the accumulator is getting charged and the hydro-motor is also running. That is why the pressure increases in the piston side chamber of the hydraulic cylinder. From Fig. 5, it is observed that during the extension of the cylinder, the rod side chamber is connected to the tank, as a result, there will be very nominal pressure rise. But during the retraction operation, the pressure rises due to the charging of accumulator and operation of the hydro-motor. Figures 6 and 7 demonstrate the pressure and the fluid content inside the accumulator, respectively. In the first stage, the accumulator lifts the boom for five seconds while the liquid volume inside the accumulator decreases and hence pressure also decreases. In the

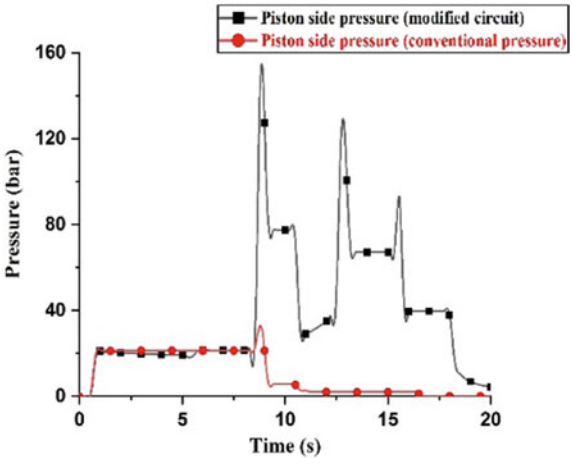

Fig. 4 Piston side pressure of hydraulic cylinder

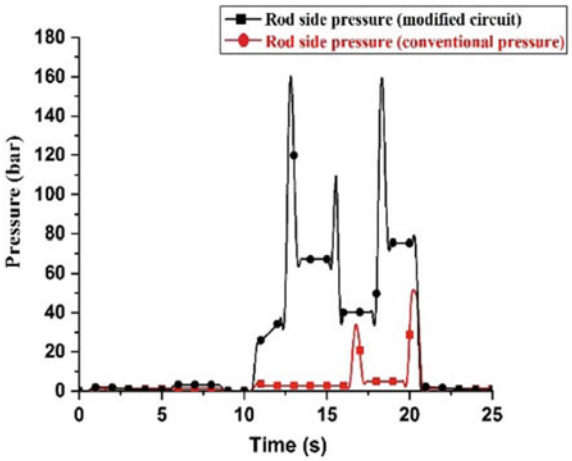

Fig. 5 Rod side pressure of hydraulic cylinder

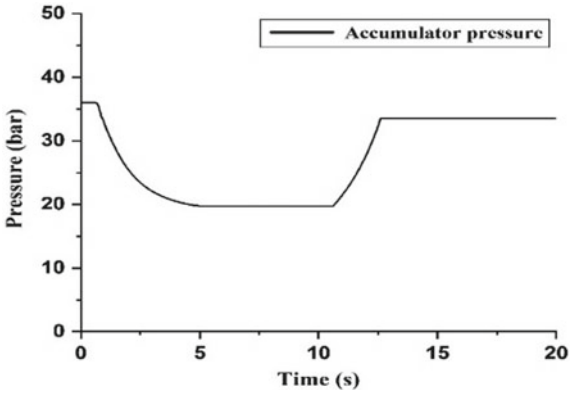

Fig. 6 Accumulator pressure

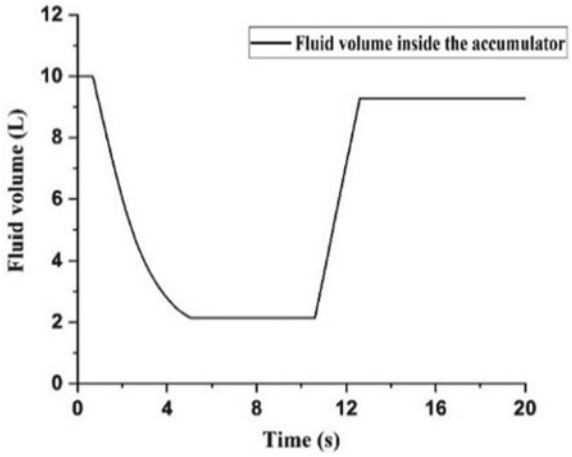

Fig. 7 Fluid volume inside the accumulator

third stage, the accumulator is getting charged. During the charging process, the fluid enters the accumulator and hence pressure is also increasing. The nature of the graph also justifies the discharging and charging of accumulator. Figure 8 shows the rotational speed of hydro-motor with time. From the graph, it can be seen that only during the fourth stage hydro-motor runs at 2000 rpm. In the first, second, and third stage, there is no fluid supplied to the hydro-motor so it does not run at that time. Inlet pressure and outlet pressure of hydro-motor are shown in Fig. 9. The outlet of the hydro-motor is always connected to the tank so there is very less pressure in the outlet line. Inlet pressure of the hydro-motor is due to the load on hydro-motor. This pressure difference across the hydro-motor generates power, which is further stored

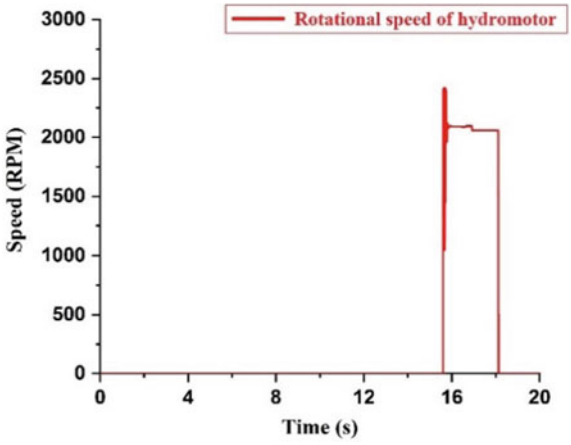

Fig. 8 Rotational speed of hydro-motor

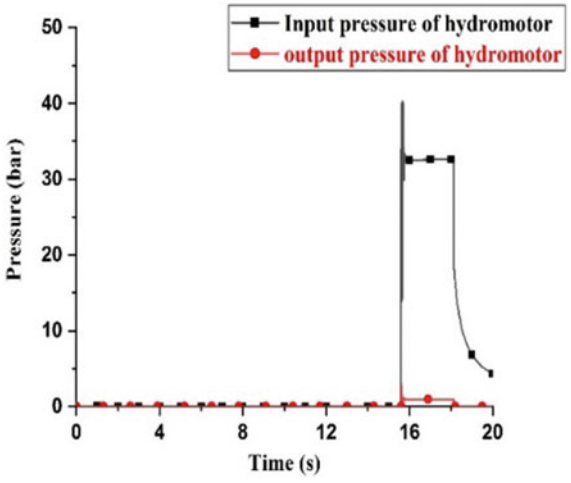

Fig. 9 Input and output pressure of hydro-motor

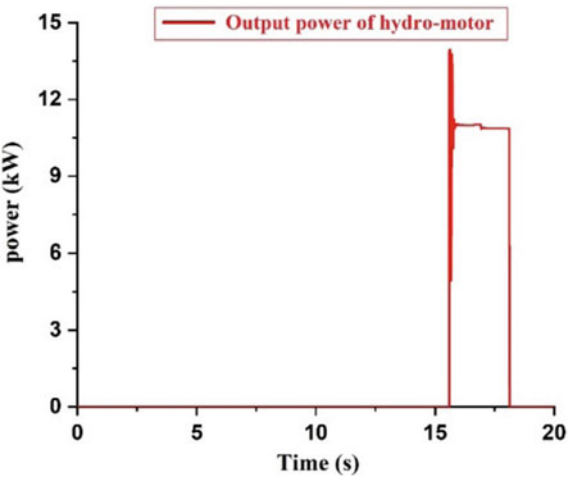

Fig. 10 Output power of hydro-motor

in the battery. From hydro-motor generator connection total 82.9 kJ of energy is saved in a duration of 60 s. Figure 10 represents output torque of the electric motor with respect to time. In case of conventional circuit, there is almost constant output torque due to absence of the fluctuation in the loading components. For modified circuit, the first stage comprises of almost zero output torque as accumulator supplies flow to the cylinder.

4 Conclusions

In this paper, the author has proposed an amalgamated hydraulic drive to be incorporated in the hydraulic excavator for the recovery of gravitational potential energy. This modified system comprises of an accumulator, hydro-motor, and generator. The model of conventional circuit and modified circuit is created by Automation Studio software and MATLAB software. From the calculation of the mathematical model and details simulation analysis following conclusions can be obtained.

- Total energy saved by the modified circuit is 16% as compared to conventional system circuit, when operated for a span of 60 s of operation.
- Experimental validation is required for modified circuit using advanced actuation system such as multi-chamber cylinders.

References

1. Fu J, Liu J, Deng B, Feng R, Yang J, Zhou F, Zhao X (2014) An approach for exhaust gas energy recovery of internal combustion engine: steam-assisted turbocharging. Energy Convers Manag 85:234–244
2. Sciubba E, Tocci L, Toro C (2016) Thermodynamic analysis of a Rankine dual loop waste thermal energy recovery system. Energy Convers Manag 122:109–118
3. Tabatabaeikia S, Ghazali NNBN, Chong WT, Shahizare B, Izadyar N, Esmaeilzadeh A, Fazlizan A (2016) Computational and experimental optimization of the exhaust air energy recovery wind turbine generator. Energy Convers Manag 126:862–874
4. Vale S, Heber L, Coelho PJ, Silva CM (2017) Parametric study of a thermoelectric generator system for exhaust gas energy recovery in diesel road freight transportation. Energy Convers Manag 133:167–177
5. Tan T, Yan Z (2016) Analytical solution and optimal design for galloping-based piezoelectric energy harvesters. Appl Phys Lett 109(25):253902
6. Tan T, Yan Z, Hajj M (2016) Electromechanical decoupled model for cantilever-beam piezoelectric energy harvesters. Appl Phys Lett 109(10):101908
7. Yan Z, Abdelkefi A, Hajj MR (2014) Piezoelectric energy harvesting from hybrid vibrations. Smart Mater Struct 23(2):025026
8. Qiu C, Wang G (2016) New evaluation methodology of regenerative braking contribution to energy efficiency improvement of electric vehicles. Energy Convers Manag 119:389–398
9. Hui S, Lifu Y, Junqing J, Yanling L (2011) Control strategy of hydraulic/electric synergy system in heavy hybrid vehicles. Energy Convers Manag 52(1):668–674
10. Shimoyama H, Ikeo S, Koyabu E, Ichiryu K, Lee S-K (2004) Study on hybrid vehicle using constant pressure hydraulic system with flywheel for energy storage. No. 2004-01-3064. SAE Technical Paper
11. Matheson P, Stecki J (2003) Modeling and simulation of a fuzzy logic controller for a hydraulic-hybrid powertrain for use in heavy commercial vehicles. No. 2003-01-3275. SAE Technical Paper
12. Kim YJ, Filipi Z (2007) Simulation study of a series hydraulic hybrid propulsion system for a light truck. SAE Trans 147–161
13. Enes AR, Book WJ (2008) A hardware-in-the-loop simulation testbed for emulating hydraulic loads representing the complete dig cycle of a construction machine. In: ASME 2008 International Mechanical Engineering Congress and Exposition. American Society of Mechanical Engineers, pp 185–192
14. Yang H, Sun Wei, Bing Xu (2007) New investigation in energy regeneration of hydraulic elevators. IEEE/ASME Trans Mechatron 12(5):519–526
15. Kumar S, Das S, Ghoshal SK, Das J (2018) Review of different energy saving strategies applicable to hydraulic hybrid systems used in heavy vehicles. In: IOP conference series: materials science and engineering, vol 377, issue no 1. IOP Publishing, pp 012072
16. Ho TH, Ahn KK (2010) Modeling and simulation of hydrostatic transmission system with energy regeneration using hydraulic accumulator. J Mech Sci Technol 24(5):1163–1175
17. Chen M, Dingxuan Z (2011) Research on boom energy recovery system with closed circuit in hydraulic excavators. In: 2011 international conference on Transportation, Mechanical, and Electrical Engineering (TMEE). IEEE, pp 954–957
18. Andersen TO, Hansen MR, Pedersen HC (2005) Regeneration of potential energy in hydraulic forklift trucks. In: Fluid Power Transmission and Control ICFP'2005, pp 302–306
19. Zhang X, Liu S, Huang Z, Chen L (2010) Research on the system of boom potential recovery in hydraulic excavator. In: 2010 international conference on Digital Manufacturing and Automation (ICDMA), vol 2. IEEE, pp 303–306
20. Luo W, Shi K, Li W, Xiao J (2011) Research on potential energy recovery of 16T wheeled hybrid excavator. In: 2011 Second International Conference on Digital Manufacturing and Automation (ICDMA). IEEE, pp 996–998

21. Siebert J, Wydra M, Geimer M (2017) Efficiency improved load sensing sytem—reduction of system inherent pressure losses. Energies 10(7):941
22. Zimmerman JD, Matteo P, Williamson CA, Ivantysynova M (2007) Energy consumption of an LS excavator hydraulic system. In: ASME 2007 international mechanical engineering congress and exposition. American Society of Mechanical Engineers, pp 117–126
23. Ge L, Dong Z, Huang W, Quan L, Yang J, Li W (2015) Research on the performance of hydraulic excavator with pump and valve combined separate meter in and meter out circuits. In: 2015 International Conference on Fluid Power and Mechatronics (FPM). IEEE, pp 37–41
24. Liu B, Quan L, Ge L (2017) Research on the performance of hydraulic excavator boom based pressure and flow accordance control with independent metering circuit. Proc Inst Mech Eng Part E: J Process Mech Eng 231(5):901–913
25. Xu B, Cheng M (2018) Motion control of multi-actuator hydraulic systems for mobile machineries: recent advancements and future trends. Front Mech Eng 13(2):151–166
26. Zhao P, Chen Y, Zhou H (2016) Potential energy recovery system of hydraulic hybrid excavator. In: BATH/ASME 2016 symposium on fluid power and motion control. American Society of Mechanical Engineers, pp V001T01A007–V001T01A007

Microstructure and Wear Study of Al 7075-T6/Eggshell/SiC/Al_2O_3 Hybrid Composites

Girija Moona, Vikas Rastogi, R. S. Walia and Rina Sharma

Abstract In present experimental investigation, hybrid aluminium metal matrix composites were fabricated using stir casting technique by infusing eggshell particles (0.5, 1 wt%), SiC particles (1, 1.5 wt%) and Al_2O_3 particles (1.5, 2.5 wt%) into Al 7075-T6 metal matrix. The developed composites were further characterized for microstructures using FESEM, X-ray diffractometry and EDS techniques. Tribological behaviour investigations were carried out using a pin-on-disk tribometer for comparative study between as-cast Al 7075-T6 alloy and Al-7075-T6/Eggshell/SiC/Al_2O_3 composites. During dry sliding wear test at room temperature, there was a decrease of 33% in wear rate, 20% in coefficient of friction and 20% in frictional force of composites, whereas in presence of lubricant, the developed composites exhibited maximum reduction of 85% in wear rate, 46% in coefficient of friction and 46% in frictional force as compared to their unreinforced counterparts. Due to augmented tribological properties, fabricated hybrid composites can reasonably be used for lightweight wear-resistant applications.

Keywords Stir casting · Reinforcement · Hybrid composites · Microstructure · Tribology

1 Introduction

Main objective of developing composite materials is to make the matrix and perform combinations to produce the best possible material characteristics that cannot be achieved by conventional materials. Aluminium metal matrix composites (AMCs) offer a wide spectrum of advantages with enhanced mechanical and physical properties to prefer their selection for most of the advanced engineering applications. They have always been one of the most prominent research interests of many material

G. Moona (✉) · V. Rastogi · R. S. Walia
Delhi Technological University, New Delhi 110042, India
e-mail: moonag@nplindia.org

G. Moona · R. Sharma
CSIR-National Physical Laboratory, Dr. K. S. Krishnan Marg, New Delhi 110012, India

H. Kumar and P. K. Jain (eds.), *Recent Advances in Mechanical Engineering*,
Lecture Notes in Mechanical Engineering,
https://doi.org/10.1007/978-981-15-1071-7_39

science researchers due to their applications in avionics, automobiles and defence sectors. AMCs are developed to attain desired material properties with an intention to cater the needs of component manufacturers for different utilizations in scientific fields. Advantageous attributes of aluminium composites provide cost-effective alternatives, replacing many conventional materials for intrinsic engineering applications. In aluminium composites, various reinforcements are mixed with pure aluminium/aluminium alloys to produce a combination of enhanced properties as compared to the base metal. Properties of aluminium composites can be tailored by varying metal matrix, reinforcements and process parameters. Mixing of Al_2O_3 with aluminium alloy Al 356 through stir casting route resulted into increased hardness [1]. Al 7075 infused with B_4C particles produced a composite with better hardness and enhanced wear resistance [2]. Al 2014/TiC composites exhibited increased hardness and strength [3]. Al 6061/SiC composites processed through liquid metallurgy route have high tensile strength and improved wear resistance as compared to the unreinforced alloy [4]. Aluminium alloy AK 12 reinforced with fly ash and fabricated through squeeze casting acquires reduced porosity and improved corrosion resistance [5]. Mixing of 6 wt% of fly ash particles with LM 6 alloy to fabricated aluminium composites resulted into increased hardness and tensile strength [6]. It has been observed that aluminium matrices reinforced with single reinforcements exhibited certain improved characteristics, while other significant attributes were compromised, such as, in case of Al 6061/fly ash composites, tensile strength and hardness were increased, while there was a reduction in ductility. In process of surmounting this issue, fabrication of hybrid composites with reduced interfacial area and reduced meniscus penetration defect is being encouraged in order to adopt them as more dependable and extensible materials [7]. Al 6061-SiC/Graphite hybrid composites with different reinforcement weight fractions demonstrated increased tensile strength [8]. AA6082 + (Si_3N_4 + Gr) hybrid composite investigated for hardness and tensile strength showed reduced percentage elongation and increased hardness [9]. There are many methods for fabrication of aluminium composites such as stir casting, powder metallurgy, squeeze casting, liquid infiltration and plasma deposition, etc. [10, 11]. In present experiment, aluminium hybrid composites were synthesized by using Al 7075-T6 as metal matrix and eggshell, silicon carbide and aluminium oxide particles as reinforcements through liquid metallurgy route, particularly adopting stir casting technique. It was noticed that generally composites processed via powder metallurgy route exhibited better mechanical characteristics yet stir casting was preferred mostly due to its simplicity, cost effectiveness, ability to cause better wettability between reinforcements and aluminium melt and uniform infusion of filler particles into aluminium metal matrix [12]. Synthesized hybrid aluminium composites were characterized for microstructure and wear investigations.

2 Experimental Procedure

Base metal matrix used for this experiment was Al 7075-T6 alloy with chemical composition 89% Al, 6% Zn, 2% Mg, 1.2% Cu, 0.5% Fe, 0.3% Mn, 0.4% Si, 0.2% Cr and 0.2% Ti. Three reinforcements, eggshell particles (0.5 wt% and 1 wt%, average particle size ~60 μm), SiC particles (1 wt% and 1.5 wt%, average particle size ~65 μm) and Al_2O_3 particles (1.5 wt% and 2.5 wt%, average particle size ~90 μm) were infused in metal melt to prepare hybrid aluminium composites using stir casting techniques. Calculated amount of base metal was weighed and put into graphite crucible in an electric furnace for melting at 900 °C. Simultaneously, the weighed amounts of reinforcements were preheated in a muffle furnace to remove absorbed gases and moisture content, hence improving wettability. The molten metal was stirred at a speed of 150 rpm using mechanical stirrer of stir casting setup (Fig. 1), and preheated reinforcements were added to metal vortex. After infusion of reinforcements into metal matrix, the crucible was kept in an electromagnetic stirrer (Fig. 1) for uniform dispersion.

After appropriate stirring and ensuring decent mixing of filler particles into molten metal, the fabricated castings were allowed to solidify (Fig. 2).

The fabricated composites were investigated for microscopic studies and wear behaviour. For microstructure study, polished pallets of dimension $10 \times 10 \times 5\ mm^3$ (Fig. 3) were prepared, whereas for wear study, the specimens were prepared as per ASTM G 99-17 (Fig. 4) and tested on a pin-on-disk tribometer against a rotating disk of EN 31 steel.

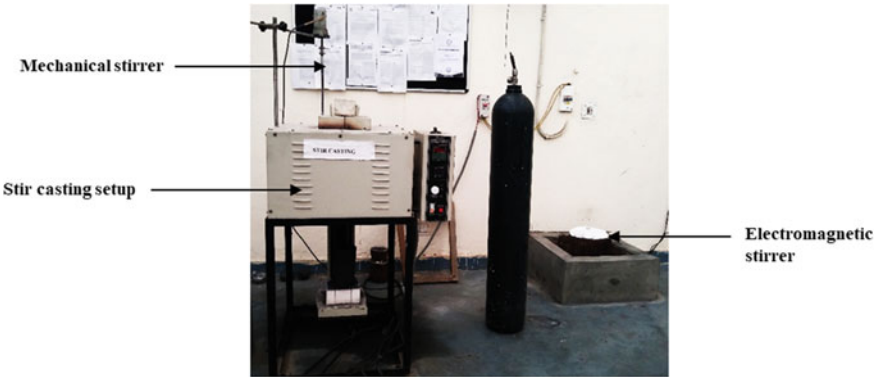

Fig. 1 Stir casting setup for composite fabrication

Fig. 2 Composite castings

Fig. 3 Specimens for microstructure study

Fig. 4 Specimens for wear study

3 Results and Discussions

3.1 Microstructure Study

As-cast Al 7075-T6 sample (marked as 0) and two aluminium hybrid composites samples (marked as 1 and 2) with different reinforcement contents were conventionally polished and cleaned for optical imaging using Field Emission Scanning Electron Microscope, Make: Zeiss; Model: Supra 40VP. On microstructural analysis, no reinforcement was noticed in as-cast Al 7075-T6 specimen optical micrograph (Fig. 5), while the hybrid composite images (Figs. 6 and 7) indicated presence of

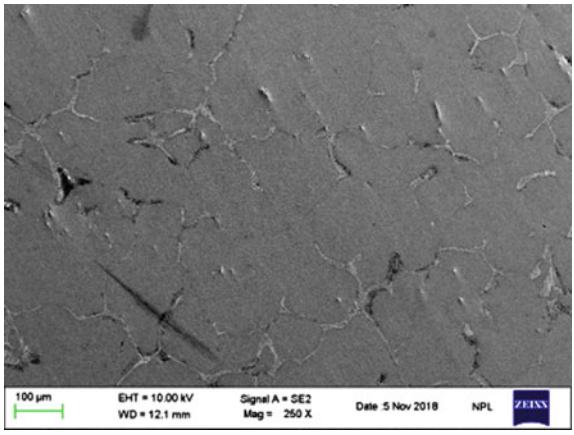

Fig. 5 Microstructure of as-cast Al 7075-T6

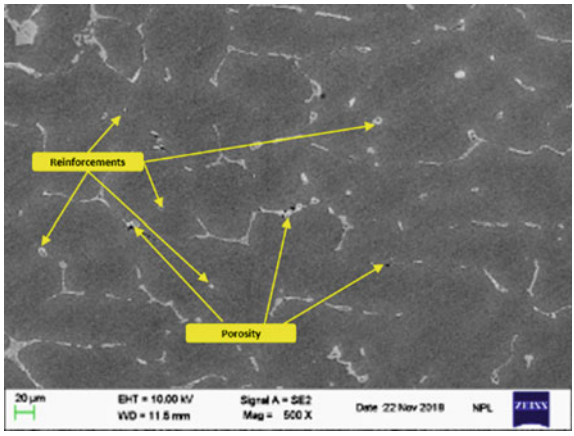

Fig. 6 Microstructure of Al 7075-T6/0.5 wt% eggshell/1.0 wt% SiC/1.5 wt% Al_2O_3 hybrid composite

reinforcement particles into Al 7075-T6 matrix. Some clusters of reinforcements due to agglomeration and porosity due to moisture on reinforcement particles surfaces and shrinkage during solidification were also observed.

The X-ray diffraction (XRD) analysis using X-Ray Diffractometer (Make: Rigaku Japan, Model—Miniflex-II) and Energy dispersive spectroscopy (EDS) using EFSEM (Make: Zeiss; Model: Supra 40VP) of as-cast Al 7075-T6 sample showed only aluminium alloy constituents peaks, ruling out the presence of any filler in base metal matrix (Fig. 8).

On conducting elemental analysis of hybrid aluminium composites using XRD and EDS, peaks of Si, Al and eggshell were visible in addition to Al 7075-T6 constituents peaks (Figs. 9 and 10). The oxygen and carbon contents in fabricated composites were found to be insignificant due to limited amount of reinforcements.

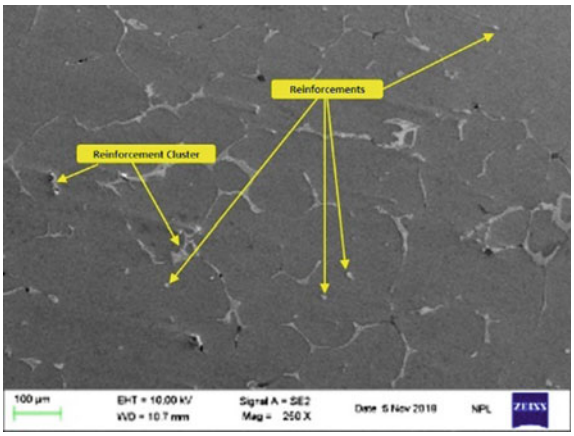

Fig. 7 Microstructure of Al 7075-T6/1 wt% eggshell/1.5 wt% SiC/2.5 wt% Al_2O_3 hybrid composite

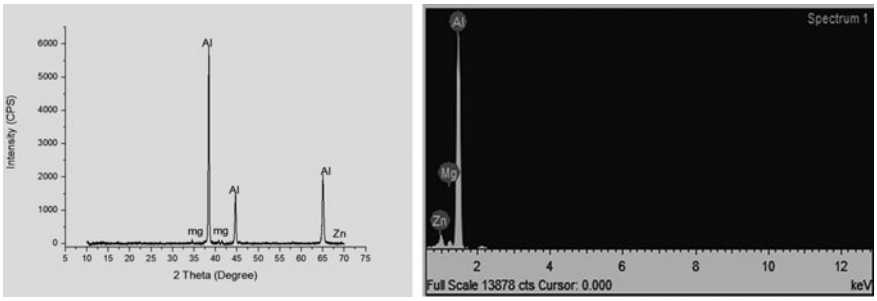

Fig. 8 XRD pattern and EDS profile of as-cast Al 7075-T6

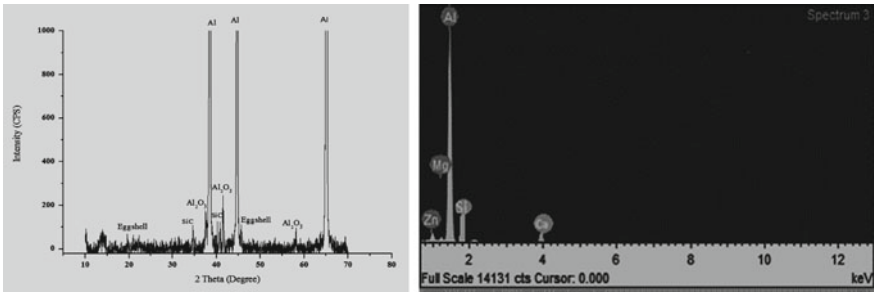

Fig. 9 XRD pattern and EDS profile of Al 7075-T6/0.5 wt% eggshell/1.0 wt% SiC/1.5 wt% Al_2O_3 hybrid composite

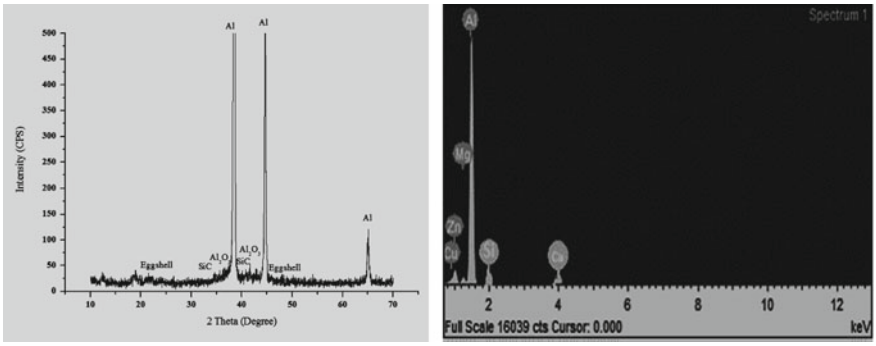

Fig. 10 XRD pattern and EDS profile of Al 7075-T6/1 wt% eggshell/1.5 wt% SiC/2.5 wt% Al_2O_3 hybrid composite

3.2 Wear Behaviour

Tribological behaviour of hybrid aluminium composites was investigated using a pin-on-disk rotary tribometer, Make: Atlas; TR-20L-PHM 800-DHM 850 (Fig. 11) by applying constant load of 20 N, for sliding distance of 2 km at a speed of 2 m/s at room temperature (32 °C) in accordance with dry sliding wear test conditions and in presence of lubricant for distinct wear-resistant applications.

Dry sliding wear tests were conducted at room temperature for as-cast Al 7075-T6 sample and hybrid aluminium composite samples. Graphs were plotted for wear rate, coefficient of friction and frictional force using experimental outcomes as shown in Fig. 12a–c.

During dry sliding wear tests at room temperature, as-cast Al 7075-T6 showed wear rate: 1.08 μm/s, average coefficient of friction: 0.121 and average frictional force: 2.247 N. Al 7075-T6/0.5 wt% eggshell/1.0 wt% SiC/1.5 wt% Al_2O_3 hybrid composite displayed wear rate: 0.797 μm/s, average coefficient of friction: 0.098 and average frictional force: 1.972 N, whereas Al 7075-T6/1 wt% eggshell/1.5 wt% SiC/2.5 wt% Al_2O_3 hybrid composite exhibited wear rate: 0.727 μm/s, average coefficient of friction: 0.096 and average frictional force: 1.938 N. Synthesized composites showed improved wear characteristics in terms of 33% reduced wear rate,

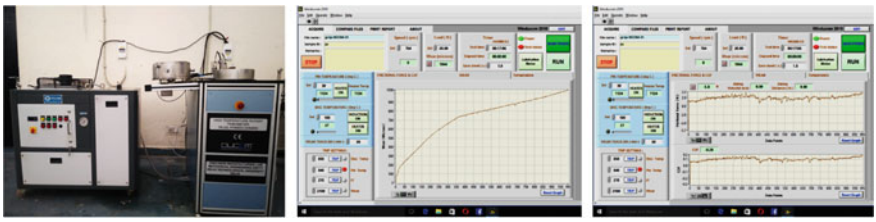

Fig. 11 High temperature pin-on-disk rotary tribometer for wear study

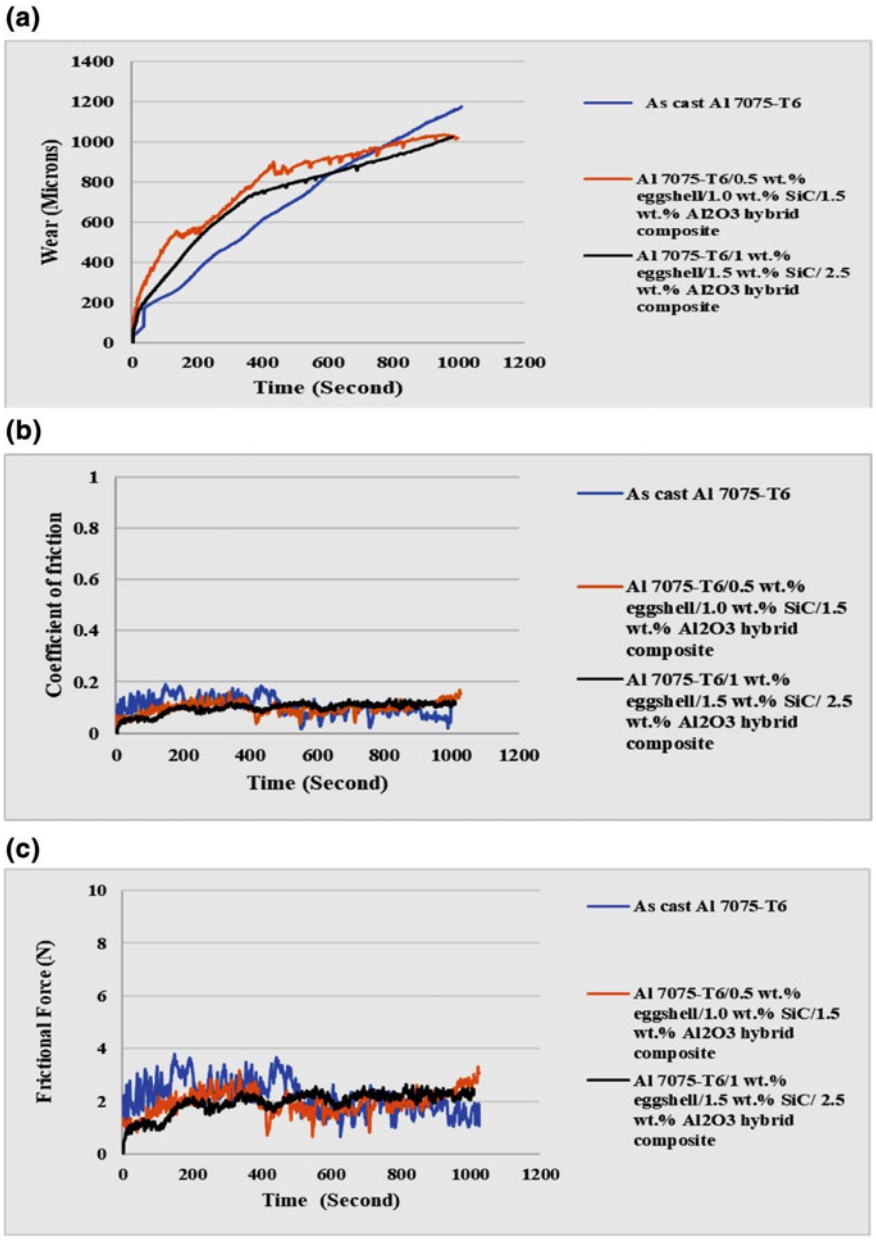

Fig. 12 **a** Wear versus time during dry sliding wear test. **b** Coefficient of friction versus time during dry sliding wear test. **c** Frictional force versus time during dry sliding wear test

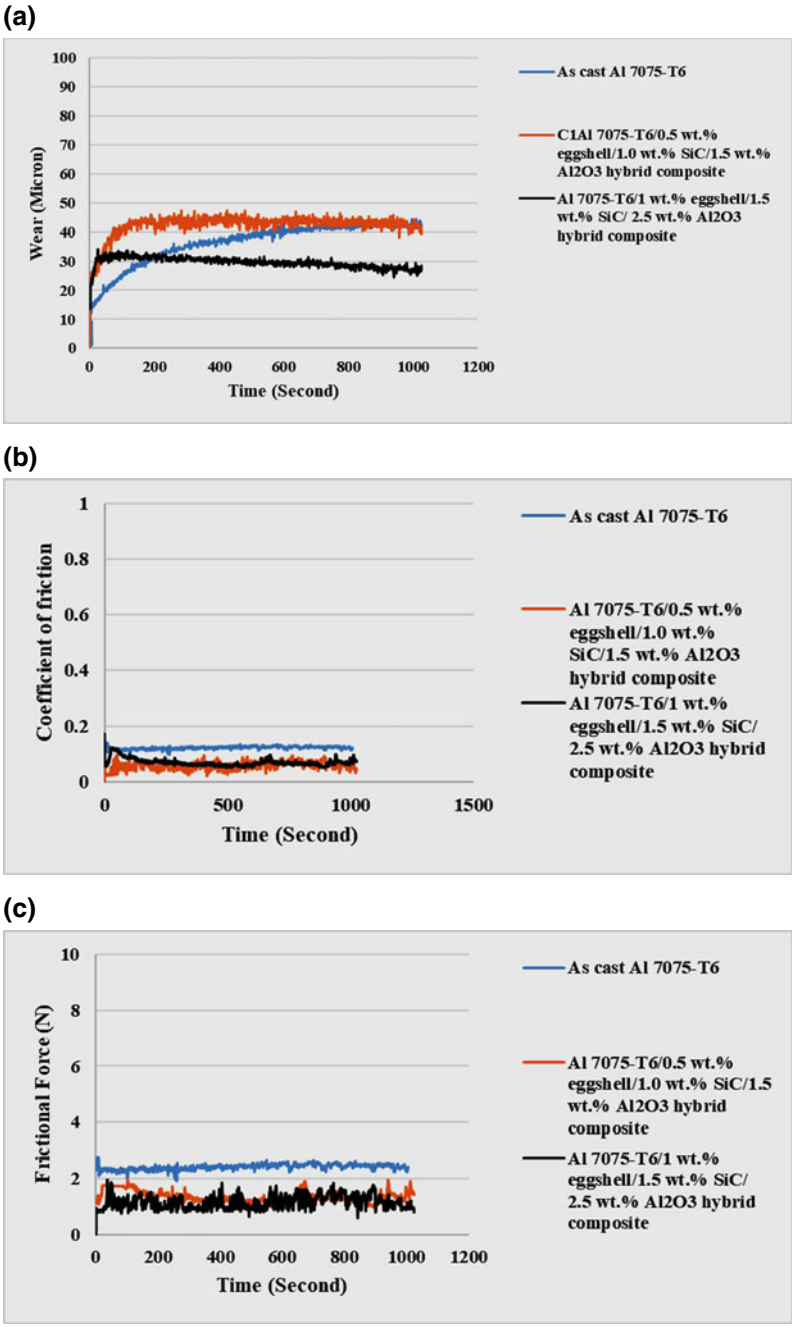

Fig. 13 **a** Wear versus time with lubrication. **b** Coefficient of friction versus time with lubrication. **c** Frictional force versus time with lubrication

20% reduced coefficient of friction and 20% reduced frictional force in comparison with as-cast Al 7075-T6 due to enhanced seizure resistance offered by reinforced particles. Additionally, wear properties were enhanced with filler content in hybrid composites.

Wear tests were also carried out in presence of a synthetic oil lubricant at room temperature. The developed composites exhibited phenomenal enhancement in tribological properties. Plots in Fig. 13 a, b and c exhibit wear properties of as-cast Al 7075-T6 sample and hybrid composites in aforesaid experimental conditions.

With lubrication, as-cast Al 7075-T6 offered wear rate: 0.022 μm/s, average coefficient of friction: 0.105 and average frictional force: 2.173 N. Al 7075-T6/0.5 wt% eggshell/1.0 wt% SiC/1.5 wt% Al_2O_3 hybrid composite demonstrated wear rate: 0.005 μm/s, average coefficient of friction: 0.070 and average frictional force: 1.340 N, whereas Al 7075-T6/1 wt% eggshell/1.5 wt% SiC/2.5 wt% Al_2O_3 composite showed wear rate: 0.003 μm/s, average coefficient of friction: 0.057 and average frictional force: 1.177 N.

The synthetic oil layer between specimen pin and rotating disk prevented direct contact of the two surfaces resulting into a maximum reduction of 85% in wear rate, 46% in coefficient of friction and 46% in frictional force as compared to the pure alloy metal casting.

4 Conclusion

In present investigation, hybrid aluminium metal matrix composites were prepared under specified experimental conditions using stir casting technique and characterized for elemental analysis and wear behaviour.

- Al 7075-T6/0.5 wt% eggshell/1.0 wt% SiC/1.5 wt% Al_2O_3 and Al 7075-T6/1 wt% eggshell/1.5 wt% SiC/2.5 wt% Al_2O_3 hybrid composites were fabricated successfully.
- Optical micrographs of synthesized composites exhibited uniform distribution of reinforcements into metal matrix, indicating their stable microstructure.
- EDS and XRD analysis of as-cast Al 7075-T6 and developed hybrid composites showed peaks of alloy constituents and reinforcements infused into metal matrix for fabrication of composites.
- During dry sliding wear test, there was a maximum decrease of 33% in wear rate, 20% in coefficient of friction and 20% in frictional force of composites in comparison with as-cast Al 7075-T6 alloy.
- Wear tests were also conducted in the presence of a synthetic oil lubricant. Synthesized composites exhibited a maximum reduction of 85% in wear rate, 46% in coefficient of friction and 46% in frictional force as compared to their unreinforced counterparts.

References

1. Mazahery A, Abdizadeh H, Baharvandi HR (2009) Development of high-performance A356/nano-Al_2O_3 composites. Mater Sci Eng A 518:61–64
2. Devaraju A, Kumar A, Kotiveerachari B (2013) Influence of addition of Grp/Al_2O_3p with SiCp on wear properties of aluminum alloy 6061-T6 hybrid composites via friction stir processing. Trans Nonferrous Met Soc China 23(5):1275–1280
3. Woo KD, Zhang DL (2004) Fabrication of Al-7 wt.% Si-04wt.% Mg/SiC nano-composite powder and bulk nano composite by high energy ball milling and powder metallurgy. Curr Appl Phys 4:175–178
4. Wang H, Li G, Zhao Y et al (2010) In-situ fabrication and microstructure of Al_2O_3 particle reinforced aluminium matrix composite. Mater Sci Eng A 527:2881–2885
5. Prasad DS, Shoba C, Ramanaiahet N (2014) Investigations on mechanical properties of aluminum hybrid composites. J Mater Res Technol 3(1):79–85
6. Sharma P, Sharma S, Khanduja D (2016) Production and characterization of AA6082-(Si_3N_4 + Gr) stir cast hybrid composites. Part Sci Technol 35(2):158–165
7. Veeresh Kumar GB, Rao CSP, Selvaraj N et al (2010) Studies on Al6061-SiC and Al7075-Al_2O_3 metal matrix composites. J Miner Mater Charact Eng 9:43–55
8. Krishna MV, Xavior AM (2014) An investigation on the mechanical properties of hybrid metal matrix composites. Procedia Eng 97:918–924
9. Ervina Efzan MN, Siti Syazwani1 N, Abdullah MM (2016) Microstructure and mechanical properties of fly ash particulate reinforced in LM6 for energy enhancement in automotive applications. Mater Sci Eng 133:1–11
10. Feng YC, Geng L, Zeng PQ, Zeng ZZ et al (2008) Fabrication and characterization of Al based hybrid composite reinforced with tungsten oxide particles and aluminium borate whisker by squeeze casting. Mater Des 29:2023–2026
11. Moona G, Walia RS, Rastogi V, Sharma R (2018) Aluminium metal matrix composites: a retrospective investigation. Indian J Pure Appl Phys 56:164–175
12. Bodunrin MO, Alaneme KK, Chown LH (2015) Aluminium matrix hybrid composites: a review of reinforcement philosophies; mechanical, corrosion and tribological characteristics. J Mater Res Technol 4:434–445

Determination of the Degradation Pattern of Pump Using Two-Phase Diagnostic Bond Graph

Sumanta Kumar Dutta, Sawan Kumar, Tushar Kanti Saha and Sanjoy Kumar Ghoshal

Abstract A bond graph-based approach has been applied for failure prognosis in the hydraulic circuit. The degradation function of a fault in the system is determined using a two-phase diagnostic bond graph model (DBG). By intentionally imparting a time-varying fault in the pump displacement, the capability of the DBG model is exhibited. The analytical redundancy relations (ARRs) evaluated from the first DBG helps to discern the manifestation of fault. Making use of ARRs of the first phase, the second DBG delivers the degradation pattern of the fault enabling the determination of remaining useful life (RUL) of the system.

Keywords DBG · RUL · ARRs

1 Introduction

Fault detection and isolation (FDI) is an important tool for ensuring the safety, efficiency, and reliability of the system. Wu et al. [1] have discussed various techniques of energy savings. Lin et al. [2] have discussed different techniques of FDI. The overall system efficiency depends upon the robustness of the system, which is only achievable with proper fault detection of the system. Determination of FDI with a quantitative approach necessitates the generation of a mathematical model of the system. Use of the different constraints, different compatibility conditions have been presented in terms of known variables using the residual relations which are dubbed as analytical redundancy relations (ARRs) [3–5]. Making use of bond graph model of the system, FDI is able to identify the cause and type of fault and also the necessary measures which need to be taken to control the impact of these faults based on analytical redundancy approach.

But FDI comes into the fray after the occurrence of the fault, and in some cases, it is unable to control the degradation of the fault. In such instances, determining the time to failure (TTF) and remaining useful life (RUL), with help of prognostics, play

S. K. Dutta (✉) · S. Kumar · T. K. Saha · S. K. Ghoshal
Department of Mechanical Engineering, IIT(ISM) Dhanbad, Dhanbad, India
e-mail: dutta.sumantakr@gmail.com

H. Kumar and P. K. Jain (eds.), *Recent Advances in Mechanical Engineering*,
Lecture Notes in Mechanical Engineering,
https://doi.org/10.1007/978-981-15-1071-7_40

a significant hand in estimating the duration for which the system can be run safely until complete failure. But in order to evaluate the RUL, knowledge of the degradation pattern with time is paramount. Ascertaining the RUL of a system can be carried using either one of data-based or model-based approach. Model-based diagnostics approach is required for precise and infallible models of actual physical systems which incorporate several domains (such as mechanical, electrical, and hydraulic). Model-based methods require an accurate mathematical model that describes the expected behavior of the system. Whereas the data-based approach is governed by on the availability of a database of the performance of the system. But either approach has its fair share of shortcomings. To overcome these limitations, Borutzky [6] has proposed a method involving the use of two-phase diagnostic bond graphs (DBG) to assess the time-varying degradation behavior of the fault. The first-phase DBG is used to identify the appearance of a fault. Using the DBG, the ARRs are determined and from these adaptive thresholds are generated by taking into consideration the uncertainty associated with the value of parameters. The number of sensors determines the number of residuals generated. The fault signature matrix (FSM), which assists in the identification of the faulty components, is generated using the ARRs. Whenever any of the residuals crosses the adaptive thresholds, it signals the manifestation of fault [7]. After the identification of the source of the fault and its isolation, it is replaced by a time-varying parameter in the second phase of the DBG which gives the degradation behavior of fault. As time progresses, the residuals will head toward the failure limits. By inverting the ARRs, the time for this intersection can be computed which gives the RUL.

In this paper, the authors have considered a hydraulic circuit which has been described below. The two-phase DBG approach has been applied to the circuit for fault diagnosis and prognostics. To test the ability and applicability of the two-phase DBG method in accurately determining the deterioration pattern of the fault with time and hence establish the RUL of the system, a fault has been deliberately introduced in the displacement volume of the variable displacement pump.

The above-mentioned approach finds its utility in the various automated processes some of which are automated manufacturing processes, in which the absence of human supervision demands the early detection of fault occurrence and estimation of the remaining life. This helps in the prompt determination of the faulty component and its subsequent repairing and replacement preventing the breakdown of the machines and ensuring a reduced shutdown period, hence safeguarding the interests of the manufacturer by reducing the incurred costs.

The paper structure is as follows. The second section of this paper provides detailed information about the physical hydraulic system and its mathematical model. The second section houses the details of the behavioral and diagnostic model of the hydraulic system and its bond graph model. Section 3 explains in detail the two-phase DBG approach used in this work. Section 4 supplies the experimental results, and Sect. 5 provides a reasonable conclusion for the paper.

2 Diagnostic Bond Graph Approach

2.1 Parameter Degradation

It is assumed that the fault has occurred and has been isolated after being detected. The DBG approach is applied to the system to detect the degradation of the parameter. It is assumed that the parameter consists of two parts: the first is the nominal value which remains constant throughout, and second is the time-varying factor which degrades over time. Combined together, these two components give the overall value of the parameter which takes the system toward failure.

2.2 Determining the Degradation Function

Using the residuals along with the adaptive thresholds of the system, the occurrence of faults is detected, by the inspection of the FSM, by the first phase DBG. Taking the initially assumed value of the different parameters $g(t)$ from Table 2 and the outputs of the different sensors $h(t)$, the ARRs are generated. These ARRs provide the residuals $R^1(t)$ which act as fault identifiers. In the case of a fit system, i.e. if the actual value of the system parameter is distracted by their nominal values within the small acceptable range only, then ARR residuals are neighboring zero. If they exceed the appropriate definitive user-defined or adaptive thresholds, which account for parameters uncertainty, they indicate the beginning of a fault with a magnitude, which could potentially progress over time. ARR residuals may lie outside fault thresholds but inside failure alarm limits provided the parameter variates within certain limits. Hence, irrespective of the fact that a fault has occurred, a system continues operating with reduced efficiency and at a lower performance level for a time duration which depends upon how the faulty parameters degrade, the prediction of which is our objective. The second-phase DBG accounts for the unknown time-varying parameter degradation. Let Ø be the parameter and be the time-varying degradation parameter. Then, $Ø(t) = Ø_n + (t)$. If the latter is known and if measured outputs given by the faulty system are taken as inputs into the DBG of the second phase, then the evaluation of the ARRs will give residuals close to zero. To determine the RUL estimates, the available values of the fall function can be extended further. Extrapolation can be repeated with ongoing time and RUL estimates can be improved in this way (Fig. 1).

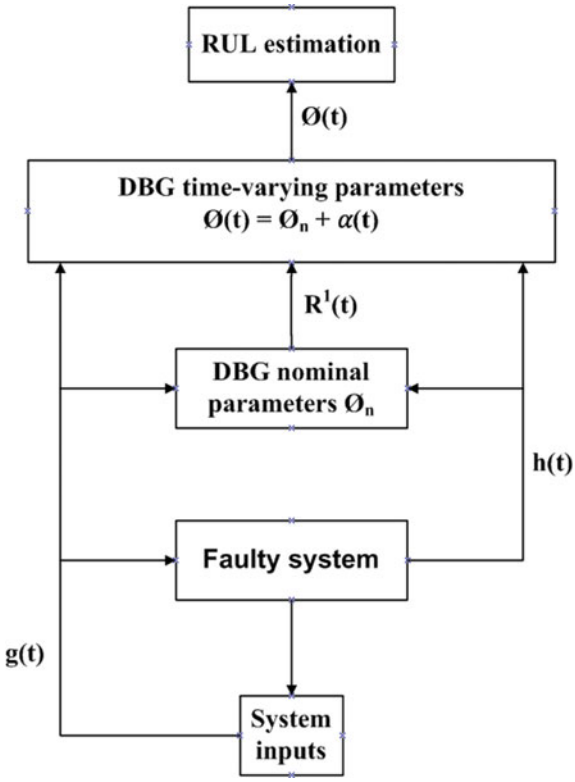

Fig. 1 Sequence of operation for determination of parameter degradation

3 The Hydraulic System

3.1 Physical Description of the System

The schematic representation of the setup being studied is shown in Fig. 2. Table 1 gives the names of the different components of setup corresponding to the tags given in Fig. 2. The setup has a double acting variable displacement pump (tag 2), driven by a 7.5 kW electric motor (tag 1), furnishing pressurized fluid to a bent axis hydro motor (tag 5). Before reaching the hydro motor, the fluid passes through a proportional flow control valve (tag 3), which is operated using a solenoid, which modulates the flow supplied to the hydro motor corresponding to the voltage imparted to the flow control valve. The hydro motor is used to drive a single-acting fixed displacement loading pump (tag 7) which in turn supplies fluid to the reservoir (tag 14.1–14.4) through a pressure relief valve (PRV) (tag 8). The load torque of the motor is regulated by varying the pressure setting of the PRV. The experiments are conducted on the setup under well-aerated conditions. To obtain fluid with constant viscosity at different parts of the setup, suitable oil cooler and filter are used. The oil cooler maintains the

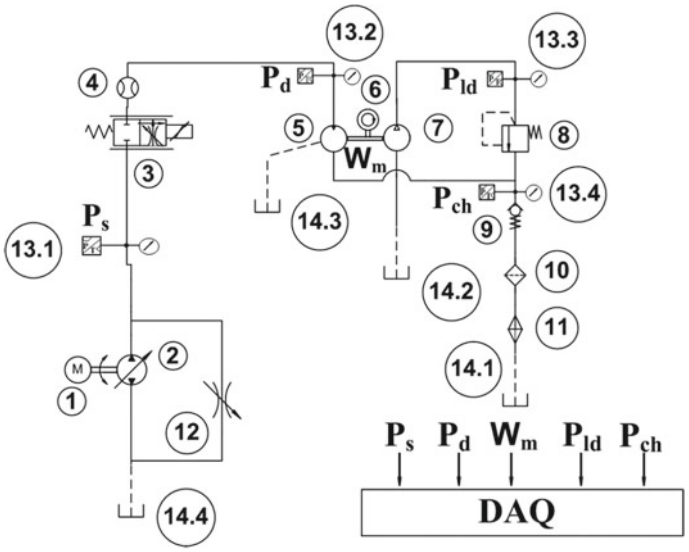

Fig. 2 Schematic representation of the setup

Table 1 Different components in the schematic diagram

Tag No.	Name of equipment
1	Electrical drive motor
2	Variable displacement pump
3	Proportional flow control valve
4	Flow sensor
5	Hydro motor
6	Speed sensor
7	Loading pump (fixed displacement)
8	Pressure relief valve
9	Spring-loaded check valve
10	Filter
11	Oil cooler
12	Flow restrictor valve
13.1–13.4	Pressure sensor
14.1–14.4	Hydraulic reservoir

temperature of the fluid in the range of 55–62 °C. The experimental setup has four pressure sensors (tag 13.1–13.4) and a speed sensor (tag 6) to measure the pressure at different sections of the system and the speed of the driven hydro motor which are recorded in the data acquisition system (DAQ). To ensure the accuracy of the setup, multiple test runs are conducted before collecting data.

3.2 The Bond Graph and Simulink Model of the System

The BG model of the hydraulic system is made with the storage elements having integrative causality. The system's Simulink model is prepared using this BG model.

According to the mathematical equations of the above section, a block model is made in MATLAB/Simulink. The model has been divided into two parts—Behavioral model and diagnostic model (Fig. 3). In the behavioral model, the constitutive relations given in Eqs. (1) through (5) are evaluated. Whereas, the diagnostic model is a simple computation of the residuals given in Eqs. (6) through (10) (Fig. 4).

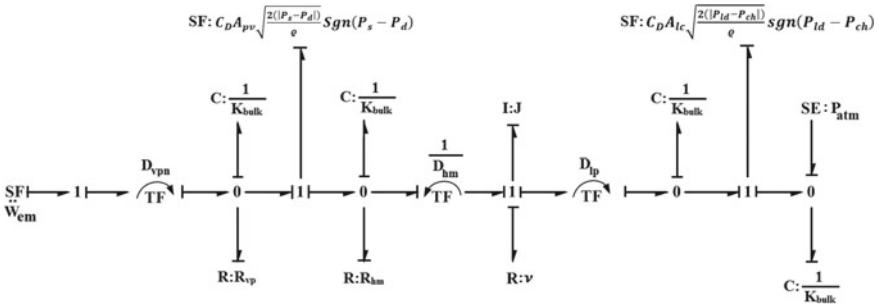

Fig. 3 Bond graph model of the hydraulic system

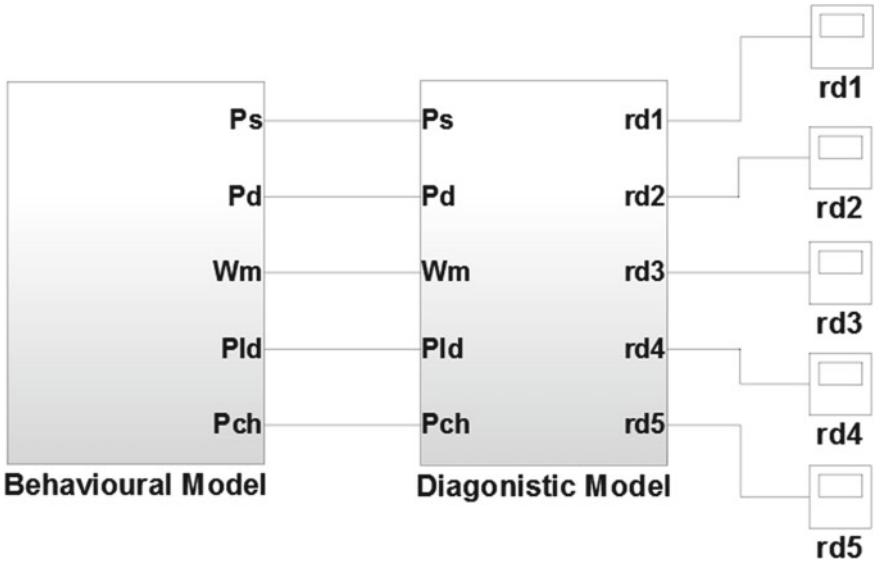

Fig. 4 Simulink model of the system

3.3 Mathematical Modeling of the System

The assumptions made for the mathematical modeling of the system are:

- Valve spool inertia and friction effects are not taken into consideration.
- Fluid does not get compressed while flowing through the pipes.
- The rate of flow through the flow control valve has a nonlinear relationship with the pressure differential across it.
- The fluid used in the system follows Newton's law of viscosity.

The mathematical equations for the different components in the system are derived with the combined use of bond graph and Simulink model.

Variable Displacement Pump

The volume flow rate lost due to compression in the variable pump can be mathematically given as

$$Q_{\mathrm{vp}} = D_{\mathrm{vp}}\omega_{\mathrm{em}} - \frac{P_{\mathrm{s}}}{R_{\mathrm{vp}}} - \left(C_{\mathrm{D}}A_{\mathrm{pv}}\sqrt{\frac{2(|P_{\mathrm{s}} - P_{\mathrm{d}}|)}{\varrho}}\mathrm{sgn}(P_{\mathrm{s}} - P_{\mathrm{d}})\right) \tag{1}$$

where,

Q_{vp}	Volume flow rate provided by the pump
D_{vp}	Variable pump displacement
R_{vp}	Resistance to leakage in variable displacement pump
P_{s}	Main pump pressure or system pressure
C_{D}	Coefficient of discharge
A_{pv}	Orifice area of the proportional valve
ω_{em}	Rotational speed of the driving electric motor
P_{d}	Proportional relief valve pressure or delivery pressure $= k_{\mathrm{bulk}} \int Q_{\mathrm{hm}}\mathrm{d}t$
$P_{\mathrm{s}} = k_{\mathrm{bulk}} \int Q_{\mathrm{vp}}\mathrm{d}t$, k_{bulk}	Bulk Modulus.

Fixed Displacement Loading Pump

Loading pump which is coupled with the hydraulic motor also experiences some hydraulic losses during fluid flowing through the pump. Now, the flow from the pump is given as,

$$Q_{\mathrm{lp}} = D_{\mathrm{lp}}w_{\mathrm{m}} - \left(C_{\mathrm{D}}A_{\mathrm{lc}}\sqrt{\frac{2(|P_{\mathrm{ld}} - P_{\mathrm{ch}}|)}{\varrho}}\mathrm{sgn}(P_{\mathrm{ld}} - P_{\mathrm{ch}})\right) \tag{2}$$

A_{lc}	Orifice area of the load valve
P_{ld}	Discharge pressure of the loading pump
P_{ch}	Check valve pressure at loading circuit

ϱ Density of fluid
w_{m} Angular velocity of the hydraulic motor.

Driven Hydraulic Motor

The torque provided by the hydro motor is,

$$T_{\mathrm{hm}} = D_{\mathrm{hm}}(P_{\mathrm{d}} - P_{\mathrm{ch}}) - \nu w_{\mathrm{m}} - D_{\mathrm{lp}} P_{\mathrm{ld}} \tag{3}$$

where

ν Viscous friction coefficient
D_{lp} Loading pump displacement

$w_{\mathrm{m}} = \frac{\int T_{\mathrm{hm}} \mathrm{d}t}{\text{Motor Inertia}} = \frac{\int T_{\mathrm{hm}} \mathrm{d}t}{J}$

where the pressure at the inlet to the loading pump $= P_{\mathrm{ld}} = k_{\mathrm{bulk}} \int Q_{\mathrm{lp}} \mathrm{d}t$.

The volume flow rate lost due to compression in the hydraulic motor can be mathematically given as

$$Q_{\mathrm{hm}} = \left(C_{\mathrm{D}} A_{\mathrm{pv}} \sqrt{\frac{2(|P_{\mathrm{s}} - P_{\mathrm{d}}|)}{\varrho}} \mathrm{sgn}(P_{\mathrm{s}} - P_{\mathrm{d}}) \right) - D_{\mathrm{hm}} w_{\mathrm{m}} - \frac{P_{\mathrm{d}}}{R_{\mathrm{hm}}} \tag{4}$$

where,

Q_{hm} Volume flow rate lost due to compression in the hydraulic motor
D_{hm} Volumetric displacement of the hydraulic motor
R_{hm} Resistance to leakage in the hydraulic motor.

Now, flow to the tank from the motor can be described as,

$$Q_{\mathrm{hm1}} = D_{\mathrm{hm}} w_{\mathrm{m}} - \left(C_{\mathrm{D}} A_{\mathrm{chv}} \sqrt{\frac{2(|P_{\mathrm{ch}} - P_{\mathrm{atm}}|)}{\varrho}} \mathrm{sgn}(P_{\mathrm{ch}} - P_{\mathrm{atm}}) \right) + \left(C_{\mathrm{D}} A_{\mathrm{lc}} \sqrt{\frac{2(|P_{\mathrm{ld}} - P_{\mathrm{ch}}|)}{\varrho}} \mathrm{sgn}(P_{\mathrm{ld}} - P_{\mathrm{ch}}) \right) \tag{5}$$

where,

A_{chv} Orifice area of the check valve at load circuit
P_{atm} Atmospheric pressure.

And corresponding effort $= P_{\mathrm{ch}} = k_{\mathrm{bulk}} \int Q_{\mathrm{hm1}} \mathrm{d}t$.

Residuals

In this application, five sensors are used; therefore, the number of residuals will be five. In this section, the first-phase residuals have been determined along with the adaptive thresholds.

From Eq. (1), the first residual can be described as below,

$$rd_1 = D_{\mathrm{vp}}\omega_{\mathrm{em}} - \frac{\dot{P}_{\mathrm{s}}}{k_{\mathrm{bulk}}} - \left(\frac{P_{\mathrm{s}}}{R_{\mathrm{vp}}}\right) - \left(C_{\mathrm{D}}A_{\mathrm{pv}}\sqrt{\frac{2(|P_{\mathrm{s}} - P_{\mathrm{d}}|)}{\varrho}}\mathrm{sgn}(P_{\mathrm{s}} - P_{\mathrm{d}})\right) \tag{6}$$

and

$$\varepsilon_1 = \frac{|\dot{P}_{\mathrm{s}}|}{\delta k_{\mathrm{bulk}}} + \left(\delta D_{\mathrm{vp}}|\omega_{\mathrm{em}}|\right) + \left[\delta(C_{\mathrm{D}}A_{\mathrm{pv}})\right]\sqrt{\frac{2|P_{\mathrm{s}} - P_{\mathrm{d}}|}{\varrho}} + \frac{|P_{\mathrm{s}}|}{\delta R_{\mathrm{vp}}}$$

Here, δ is the uncertainty for the associated parameter and its value is considered as 0.1 (i.e. 10%).

Upper threshold value $= rd_1 + \varepsilon_1$
Lower threshold value $= rd_1 - \varepsilon_1$

From Eq. (2), the second residual can be described as below,

$$rd_2 = \frac{\dot{P}_{\mathrm{ld}}}{k_{\mathrm{bulk}}} - D_{\mathrm{lp}}w_{\mathrm{m}} + C_{\mathrm{D}}A_{\mathrm{lc}}\sqrt{\frac{2|P_{\mathrm{ld}} - P_{\mathrm{ch}}|}{\varrho}}\mathrm{sgn}(P_{\mathrm{ld}} - P_{\mathrm{ch}}) \tag{7}$$

and

$$\varepsilon_2 = \frac{|\dot{P}_{\mathrm{ld}}|}{\delta k_{\mathrm{bulk}}} + \left(\delta D_{\mathrm{lp}}|w_{\mathrm{m}}|\right) + \left[\delta(C_{\mathrm{D}}A_{\mathrm{lc}})\right]\sqrt{\frac{2|P_{\mathrm{ld}} - P_{\mathrm{ch}}|}{\varrho}}$$

Upper threshold value $= rd_2 + \varepsilon_2$
Lower threshold value $= rd_2 - \varepsilon_2$

According to Eq. (3), the third residual is as follows,

$$rd_3 = D_{\mathrm{hm}}(P_{\mathrm{d}} - P_{\mathrm{ch}}) - \nu w_{\mathrm{m}} - D_{\mathrm{lp}}P_{\mathrm{ld}} - J\dot{w}_{\mathrm{m}} \tag{8}$$

and

$$\varepsilon_3 = \delta D_{\mathrm{hm}}|P_{\mathrm{d}} - P_{\mathrm{ch}}| + (\delta\nu|w_{\mathrm{m}}|) + \left(\delta D_{\mathrm{lp}}|P_{\mathrm{ld}}|\right) + (\delta J|\dot{w}_{\mathrm{m}}|)$$

Upper threshold value $= rd_3 + \varepsilon_3$
Lower threshold value $= rd_3 - \varepsilon_3$

The fourth residual corresponding to the Eq. (4) is,

$$rd_4 = \left(C_D A_{pv}\sqrt{\frac{2(|P_s - P_d|)}{\varrho}}\,\mathrm{sgn}(P_s - P_d)\right) - D_{hm} w_m - \frac{\dot{P}_d}{k_{bulk}} - \frac{P_d}{R_{hm}} \tag{9}$$

and

$$\varepsilon_4 = \frac{|\dot{P}_d|}{\delta k_{bulk}} + (\delta D_{hm}|w_m|) + \left[\delta\left(C_D A_{pv}\right)\right]\sqrt{\frac{2|P_s - P_d|}{\varrho}} + \frac{|P_d|}{R_{hm}}$$

Upper threshold value $= rd_4 + \varepsilon_4$
Lower threshold value $= rd_4 - \varepsilon_4$

From Eq. (5), the fifth residual can be derived as,

$$\begin{aligned} rd_5 = D_{hm} w_m &- \left(C_D A_{chv}\sqrt{\frac{2(|P_{ch} - P_{atm}|)}{\varrho}}\,\mathrm{sgn}(P_{ch} - P_{atm})\right) \\ &+ \left(C_D A_{lc}\sqrt{\frac{2(|P_{ld} - P_{ch}|)}{\varrho}}\,\mathrm{sgn}(P_{ld} - P_{ch})\right) - \frac{\dot{P}_{ch}}{k_{bulk}} \end{aligned} \tag{10}$$

and

$$\begin{aligned} \varepsilon_5 = (\delta D_{hm}|w_m|) &+ \left(\delta(C_D A_{chv})\sqrt{\frac{2(|P_{ch} - P_{atm}|)}{\varrho}}\right) \\ &+ \left(\delta(C_D A_{lc})\sqrt{\frac{2(|P_{ld} - P_{ch}|)}{\rho}}\right) + \frac{|\dot{P}_{ch}|}{\delta k_{bulk}} \end{aligned}$$

Upper threshold value $= rd_5 + \varepsilon_5$
Lower threshold value $= rd_5 - \varepsilon_5$ (Table 2).

Table 2 Fault signature matrix

Components	rd_1	rd_2	rd_3	rd_4	rd_5	I
D_{vp}	1	0	0	0	0	0
D_{hm}	0	0	1	1	1	1
D_{lp}	0	1	1	0	0	1
R_{vp}	1	0	0	0	0	0
R_{hm}	0	0	0	1	0	1
ν	0	0	1	0	0	1

4 Results and Discussions

For the purpose of testing the ability of this approach in successfully identifying the time-varying degradation pattern of different parameters, we intentionally introduce a fault in the volumetric displacement of the variable displacement pump, five seconds after the start of the system.

The variation of volumetric displacement of the pump with time occurs according to the following pattern (Fig. 5):

$$\begin{aligned} D_{vp} &= D_{vpn} && t < 5 \\ &= D_{vpn} * e^{-\lambda(t-5)} && 5 \leq t < 5.16095 \\ &= D_{vpn}/5 && t \geq 5.16095 \end{aligned} \tag{11}$$

Before the inception of the fault, the state equations of the variable pump (Eq. 1) take the form

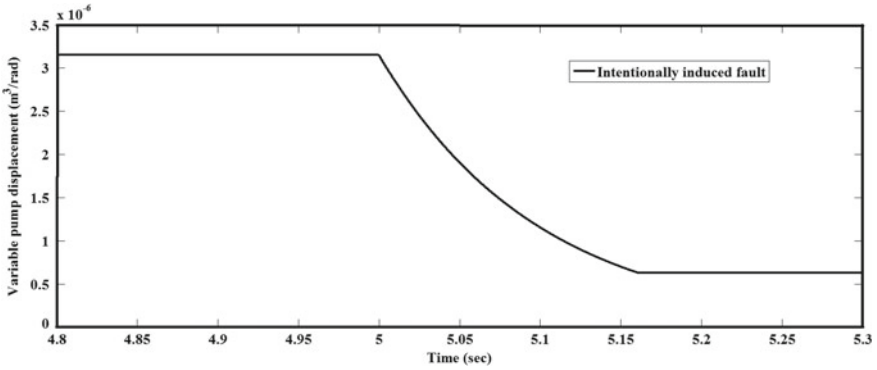

Fig. 5 Intentionally induced fault in the displacement volume of the variable displacement pump

$$Q_{\mathrm{p}} = D_{\mathrm{vp}}\omega_{\mathrm{em}} - \frac{P_{\mathrm{s}}}{R_{\mathrm{vp}}} - \left(C_{\mathrm{D}}A_{\mathrm{pv}}\sqrt{\frac{2(|P_{\mathrm{s}} - P_{\mathrm{d}}|)}{\varrho}}\mathrm{sgn}(P_{\mathrm{s}} - P_{\mathrm{d}})\right) \tag{12}$$

And residual obtained from the first phase of DBG,

$$rd_{1|1} = D_{\mathrm{vp}}\omega_{\mathrm{em}} - \frac{\dot{P}_{\mathrm{s}}}{k_{\mathrm{bulk}}} - \left(\frac{P_{\mathrm{s}}}{R_{\mathrm{vp}}}\right) - \left(C_{\mathrm{D}}A_{\mathrm{pv}}\sqrt{\frac{2(|P_{\mathrm{s}} - P_{\mathrm{d}}|)}{\varrho}}\mathrm{sgn}(P_{\mathrm{s}} - P_{\mathrm{d}})\right) \tag{13}$$

But when the inception of fault takes place, the D_{vp} becomes time variant. As a result of this, the state Eq. (12) changes to (14),

$$Q_{\mathrm{p}} = \widetilde{D_{\mathrm{vp}}}\omega_{\mathrm{em}} - \left(\frac{P_{\mathrm{s}}}{R_{\mathrm{vp}}}\right) - \left(C_{\mathrm{D}}A_{\mathrm{pv}}\sqrt{\frac{2(|P_{\mathrm{s}} - P_{\mathrm{d}}|)}{\varrho}}\mathrm{sgn}(P_{\mathrm{s}} - P_{\mathrm{d}})\right) \tag{14}$$

And residual becomes,

$$rd_{1} = \widetilde{D_{\mathrm{vp}}}\omega_{\mathrm{em}} - \frac{\dot{P}_{\mathrm{s}}}{k_{\mathrm{bulk}}} - \left(\frac{P_{\mathrm{s}}}{R_{\mathrm{vp}}}\right) - \left(C_{\mathrm{D}}A_{\mathrm{pv}}\sqrt{\frac{2(|P_{\mathrm{s}} - P_{\mathrm{d}}|)}{\varrho}}\mathrm{sgn}(P_{\mathrm{s}} - P_{\mathrm{d}})\right) \tag{15}$$

The BG model of the circuit accounting for the degradation in the volumetric displacement of the pump is given in Fig. 6.

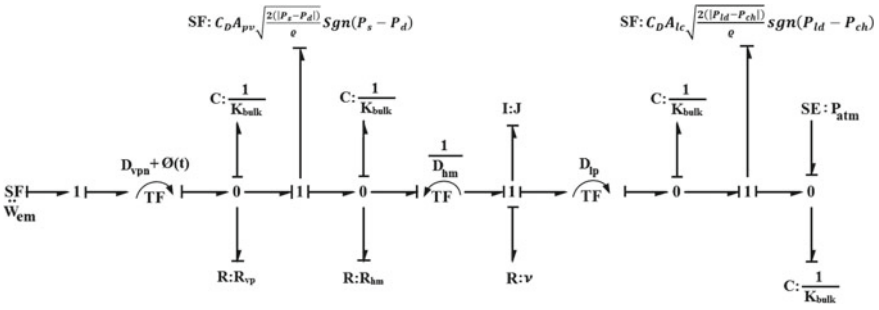

Fig. 6 Bond graph model of the hydraulic system considering the degradation pattern

As the cause for the deviation from the normal behavior of the system is the time-varying fault in the volumetric displacement of the pump so, the residual $rd_{1|1}$ deviates away from zero. As the time-varying degradation of the parameter is taken into account during the second phase of the DBG so the newly modified residual $rd_{1|2}$ approaches naught.

$$\begin{aligned} rd_{1|2} = {} & D_{\text{vpn}}\omega_{\text{em}} - \frac{\dot{P}_{\text{s}}}{k_{\text{bulk}}} - \left(\frac{P_{\text{s}}}{R_{\text{vp}}}\right) \\ & - \left(C_{\text{D}}A_{\text{pv}}\sqrt{\frac{2(|P_{\text{s}} - P_{\text{d}}|)}{\varrho}}\text{sgn}(P_{\text{s}} - P_{\text{d}})\right) + \varnothing(t)\omega_{\text{em}} \\ = {} & 0 \end{aligned} \tag{16}$$

or

$$rd_{1|1} = -\varnothing(t)\omega_{\text{em}}$$

or

$$\begin{aligned} & -\left(D_{\text{vpn}}\omega_{\text{em}} - \frac{\dot{P}_{\text{s}}}{k_{\text{bulk}}} - \left(\frac{P_{\text{s}}}{R_{\text{vp}}}\right) - \left(C_{\text{D}}A_{\text{pv}}\sqrt{\frac{2(|P_{\text{s}} - P_{\text{d}}|)}{\varrho}}\text{sgn}(P_{\text{s}} - P_{\text{d}})\right)\right) \Big/ \omega_{\text{em}} \\ & = \emptyset(t) \end{aligned} \tag{17}$$

Herein, $\emptyset(t)$ is the unknown degradation trend and $D_{\text{vp}}(t)$ is varying displacement volume of the variable pump. $\emptyset(t)$ is the solution of (17). The overall volumetric displacement of the pump can be given by,

$$D_{\text{vp}}(t) = D_{\text{vpn}} + \emptyset(t) \tag{18}$$

The evolution of residual $rd_{1|1}$ with time is shown in Fig. 7. Table 3 contains the details of initial values given to different parameters of the system for the purpose of simulation.

The comparison between the deliberately introduced time-varying fault and the obtained degradation pattern, as shown in Fig. 8, provides the necessary evidence which supports the applicability of the approach described in this work. To help in discerning the difference between the induced degradation pattern and the recovered degradation from the Simulink model, Fig. 9 presents the enlarged view of Fig. 8 at the instant the degradation starts and Fig. 10 represents the same at the instant the degradation pattern becomes nearly constant at 5.1609 s.

Figure 11 presents that the residual $rd_{1|2}$ approaches zero if the output of the faulty system is taken as input for the ARRs.

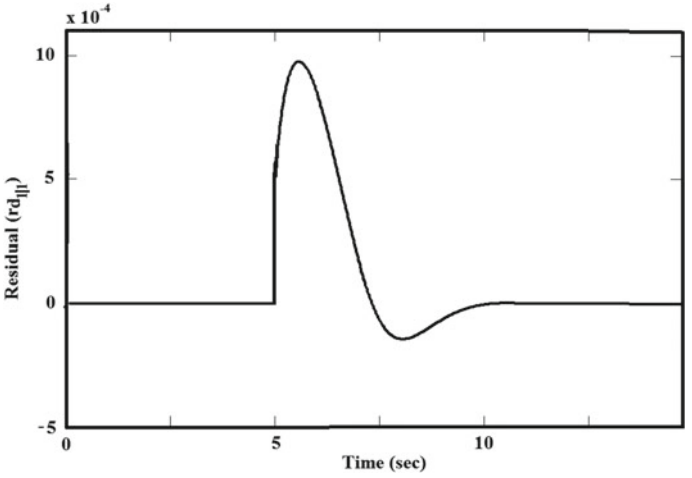

Fig. 7 Evolution of $rd_{1|1}$ with time

Table 3 Parameters of components used in simulation

Parameters	Value
Electric motor speed (ω_{em})	160 rad/s
Variable pump displacement (D_{vp})	3.15×10^{-6} m^3/rad
Bulk Stiffness (k_{bulk})	5×10^{12} N/m^2
Resistance to leakage in variable pump (R_{vp})	1.25×10^{11} N-s/m^2
Coefficient of discharge (C_D)	0.64
Density of the fluid (ϱ)	867.7 m^3/kg
Proportional valve orifice area (A_{pv})	2.25×10^{-5} m^2
Motor displacement (D_{hm})	1.91×10^{-6} m^3/rad
Inertia of motor (J)	0.012 kg m^2
Resistance to leakage in hydro motor (R_{hm})	1×10^{12} N-s/m^2
Loading pump displacement (D_{lp})	1.75×10^{-6} m^3/rad
Proportional leakage area constant for loading circuit (A_{lc})	2×10^{-5} m^2
Orifice area of check valve (A_{chv})	1.15×10^{-4} m^2
Atmospheric pressure (P_{atm})	1.01×10^5 Pa
Viscous friction (ν)	0.1 N-s/m^2
Degradation coefficient (λ)	10

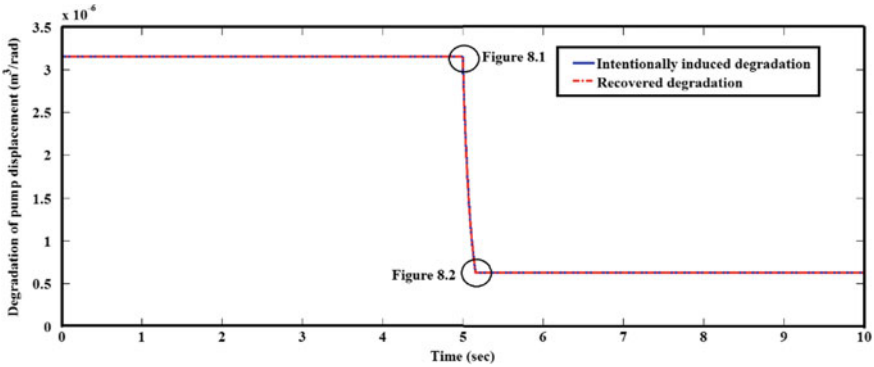

Fig. 8 Comparison between the intentionally introduced fault and the obtained degradation

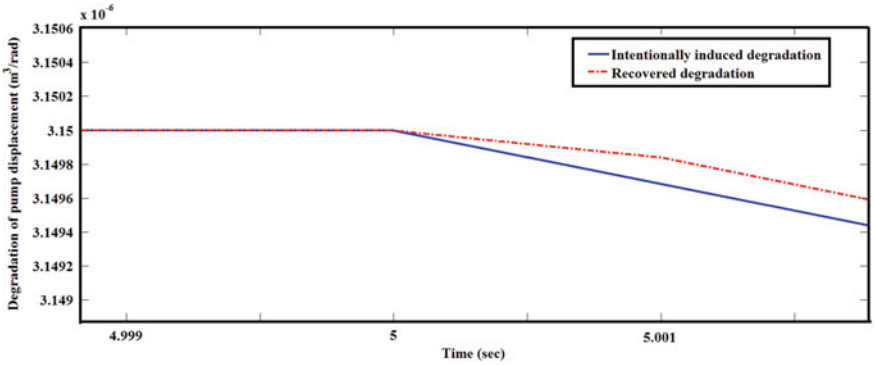

Fig. 9 Enlarged view at the instant degradation starts (i.e. at 5 s)

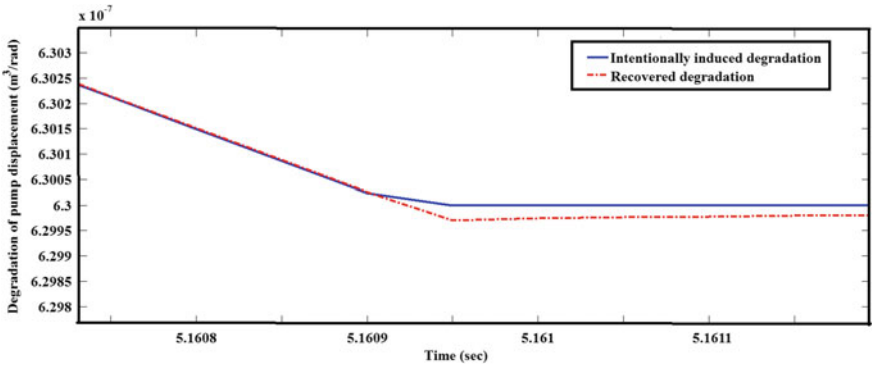

Fig. 10 Enlarged view at the instant degradation becomes constant (i.e. at 5.161 s)

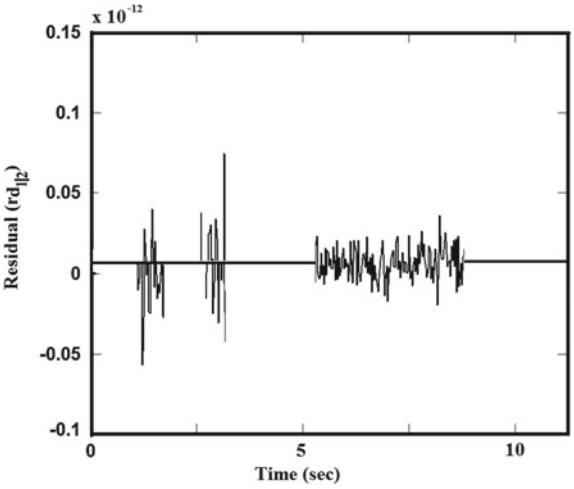

Fig. 11 Evolution of $rd_{|12}$ with time

5 Conclusions

The bond graph-based approach used in the course of this work helps to overcome the shortcomings of both model-based and data-based approach for prognosis. Using a two-phase DBG, the ARRs are established. The first-phase bond graph contributes to discerning the occurrence of fault and the second phase is utilized to determine the unknown time-varying parameter degradation with the help of the evaluated residuals. While the real system is monitored and its output signals are measured, simultaneous computation of the degradation functions is carried out. Once the time evolution of a degradation process has been computed up to some instant, an ARR residual using the values of the degradation function can be projected into the future in order to estimate the RUL. With the progression of time, repeated computation of the degradation process can be carried out resulting in improved RUL estimation.

References

1. Wu W, Hu J, Jing C, Jiang Z, Yuan S (2014) Investigation of energy efficient hydraulic hybrid propulsion system for automobiles. Energy 73:497–505
2. Lin X, Pan S, Wang D (2008) Dynamic simulation and optimal control strategy for a parallel hybrid hydraulic excavator. J Zhejiang Univ Sci A 9(5):624–632
3. Bouamama BO, Samantaray AK (2003) MSGD-T. Derivation of constraint relations from bond graph models for fault detection and isolation. In: Proceedings ICBGM'03, simulation series, vol 35, no 2. 104-109-56555-257-1
4. Samantaray AK (2017) Model-based diagnosis and prognosis of hybrid dynamical systems with dynamically updated parameters. In: Bond graphs for modelling, control and fault diagnosis of engineering systems, 2nd edn. Springer, Cham

5. Shi H, Yang H, Gong G, Liu H, Hou D (2014) Energy saving of cutterhead hydraulic drive system of shield tunneling machine. Autom Constr 37:11–21
6. Borutzky W (2018) Determination of a function for a degradation process by means of two diagnostic band graphs. IFAC-PapersOnLine 51(24):636–642
7. Kumar S, Das S, Ghoshal SK, Das J (2018) Review of different energy saving strategies applicable to hydraulic hybrid systems used in heavy vehicles. In: IOP conference series: materials science and engineering, vol 377, no 1. IOP Publishing, UK, p 012072

Ballistic Performance of Thin Aluminium Cylindrical and Hemispherical Shells

Nikhil Khaire and G. Tiwari

Abstract The objective of study was to carry out the numerical simulation to compare the ballistic resistance failure mode and energy-dispersed characteristic of Al-H1100 thin hemispherical shell and cylindrical shell. Span diameter (200 mm), thickness (0.7 and 1 mm) and mass of hemispherical and cylindrical shells kept constant for direct comparison. Ogive-nosed projectiles of 19 mm diameter, 50.8 mm length and 52 mass were impacted at tip of the both shells target. Finite element modelling was carried out by using Abaqus explicit solver. Numerical result of cylindrical shell was elucidated against experimental result of hemispherical shell. The response of both the targets was compared in terms of global deformation, residual velocity, ballistic limit, failure mode and energy dispersed in plastic deformation. Result shows that the cylindrical shell outperformed than the hemispherical shell due to the large global deformation. Also both the cylindrical and hemispherical target failed by hole enlargement with petal formation.

Keywords Cylindrical shell · Hemispherical shell · Ballistic limit · Energy absorption

1 Introduction

In recent year, lots of research has been carried out on the thin shell structure which is used in the form of cylindrical, spherical shell due to important applications in various engineering fields such as defence, aerospace, armoured vehicle and automotive industry. There is lots of research found in the literature for response of thin shell structure under the high velocity impact with different configuration of the target. Zhang and Stronge [1], conducted study on impact response steel tube impacted

N. Khaire (✉) · G. Tiwari
Department of Mechanical Engineering, Visvesvaraya National Institute of Technology, Nagpur 440010, India
e-mail: nikhilkhaire16@gmail.com

H. Kumar and P. K. Jain (eds.), *Recent Advances in Mechanical Engineering*,
Lecture Notes in Mechanical Engineering,
https://doi.org/10.1007/978-981-15-1071-7_41

against blunt projectiles at various angle of incidence and its effect on local and global deformation and the rupture has studied. Global deformation was more at the velocity closed to ballistic limit and then diminishes with further increase in the velocity whereas diameter to thickness ratio has significant influence on the local deformation. Zhang et al. [2] presented experimental study on effect of angle of obliquity (30°–60°). on the thin mile steel tube impacted by flat-nose projectile at high angle of obliquity. Result revealed that impact speed required to rupture the tube depends on the angle of obliquity moreover with increased angle of incidence and rupture speed decreased rupture speed.

The spherical thin shell under the projectile impact is relatively unstable and prone to buckling. Permanent irreversible deformation resulting from localized missile impact is the combination of elastic buckling and plastic deformation. Palomby and Strange [3] have reported a study on effect velocity and nose radius of blunt projectile on thin plates and spherical shell structure and based on the result, they concluded that the projectile velocity and nosed radius has significant influence on the ballistic limit, deformation and failure mode. Similar study was done by Ning et al. [4] which present the effect of shell thickness, curvature and velocity of the projectile on global deformation of hemispherical shell. Global deformation of the shell impacted by the blunt-nose projectile depends upon the shell thickness and shell curvature, moreover with increase in the shell curvature, global deformation was also increased and vice versa, however, with increase in the shell thickness, global deformation diminished. Tiwari et al. [5, 6] have studied the effect of target span and thickness on the ballistic performance of the hemispherical shell and found that with increase in the span and thickness, resistance of the target increased. Further study compared both thin plate and hemispherical shell and found that the hemispherical shell performed better than the plate due to the large global deformation. Zhong and Ruiz [7] reported that spherical shell struck by cylindrical blunt-nose projectile target deforms by polyhedral dimple shape.

There also a few literature reported the energy-dispersed characteristic of the target such as plates and shell, Iqbal et al. [8], and found that the kinetical energy of the projectile absorbed in the inertial effect, friction and plastic work. Moreover, the energy dispersed was found to be maximum at the velocity closed to ballistic limit where total kinetical energy of the projectile converted into the plastic work of the target. The deformation behaviour of hemispherical shell is merely complex than the cylindrical shell due to the doubly curvature. On the other hand, very few studies are available on both the type of shell under the dynamic impact loading though it has important application on defence, aerospace, armoured vehicle, automotive industry and also used in the design of helmet, boiler dome, cylindrical pressure vessel and space rocket. Also comparative study of both the shell structure has not been carried out in the literature in depth. This paper presents a finite element investigation to

explore the performance of the 1-mm-thick aluminium alloy hemispherical shell and cylindrical target struck by ogive-nosed projectile. Span diameter (200 mm), thickness (0.7 mm, 1 mm) and mass of hemispherical and cylindrical shells are kept constant for direct comparison. Ogive-nosed projectiles of 19 mm diameter, 50.8 mm length and 52 mass were impacted at tip of the both shells target. Finite element modelling was carried out by using Abaqus explicit solver. Numerical result of cylindrical shell was elucidated against experimental result of hemispherical shell. Result shows that the hemispherical layered outperforms the monolithic shell of equivalent thickness. centre of the target. The response of both the target was compare in terms of radius of discing, residual velocity, ballistic limit, failure mode and energy dispersed in permanent plastic deformation.

2 Finite Element Modelling

The 3D numerical analysis has been completed using Abaqus (Version 6.13-Research) [9] explicit code for aluminium 1100-h12 spherical and cylindrical shells of 1 mm thickness with complete geometry. Both the cylindrical and hemispherical shells were considered as deformable body and ogive-nosed projectile as rigid body. The spatial discretization was carried out using 3D four-node solid (for higher accuracy and to capture proper failure mode) finite (C38DR) with reduced integration to mesh both the target. Both targets were divided into two sets: inner set and outer set. Inner set is the target and projectile contacting area and outer set is the non-contacting area. To capture the proper behaviour of the target under the high impact loading, the mesh region at contacting area was kept very fine of size 0.16 * 0.16 * 0.16 mm^3 and aspect ratio was maintained closed to the unity. The element size was selected based on previous mesh convergence study, Iqbal et al. [8]. For the target with 1 mm thickness six element layers were used across thickness and for 0.7 mm thickness four element layers were used. To provide interaction between target and projectile, Kinematic frictionless algorithm was used. Explicit surface to surface contact algorithm was used between the target and projectile by considering target as slave surface and projectile outer surface as master surface. All the degree of freedom of the node located at the target edge was restrained in all six directions. Also, the numerical model further extends to calculate the energy absorption in plastic deformation in polar, elevation, radial and tangential direction by using programme code written in Python language through Abaqus output.

Total energy obtained by multiplying the strain energy and volume of element.

$$E_{\text{plastic}} = E_{\text{radial}} + E_{\text{polar}} + E_{\text{elevation}} + E_{\text{shear}} \tag{1}$$

$$E_{\text{radial}} = (\sigma_{\text{r}}) \times (\varepsilon_{\text{r}})_{\text{plastic}} \times V_{\text{e}} \tag{2}$$

$$E_{\text{polar}} = (\sigma_{\theta}) \times (\varepsilon_{\theta})_{\text{plastic}} \times V_{\text{e}} \tag{3}$$

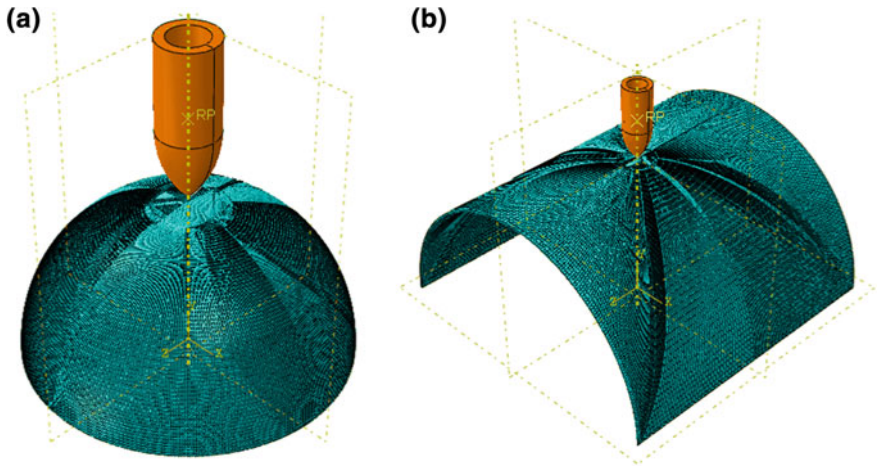

Fig. 1 Finite element modelling. **a** Hemispherical shell, **b** cylindrical shell

$$E_{\text{elevation}} = (\sigma_{\varnothing}) \times (\varepsilon_{\varnothing})_{\text{plastic}} \times V_{\text{e}} \tag{4}$$

$$E_{\text{shear}} = \left[\left\{(\tau_{r\theta}) \times (\gamma_{r\theta})_{\text{plastic}}\right\} + \left\{(\tau_{r\theta}) \times (\gamma_{r\theta})_{\text{plastic}}\right\} + \left\{(\tau_{r\theta}) \times (\gamma_{r\theta})_{\text{plastic}}\right\}\right] \times V_{\text{e}} \tag{5}$$

E_{Plastic}, E_{radial}, E_{polar}, $E_{\text{elevation}}$ and E_{tang} = energy dispersed in radial, polar, elevation and tangential direction. Parameters are the stress and strain in the respective direction and volume of the element (Fig. 1).

3 Constitutive Modelling

Impacts are considered as highly nonlinear complex phenomenon due to simultaneous occurrence of high strain rate, short duration, negative triaxiality, large plastic deformation and thermal softening phenomenon. The high strain rate phenomenon is considered when the strain rate value is 10^3 s^{-1} and beyond, in such a condition thermal effects and strain rate are foremost and need to be studied. To define the behaviour of the metal under the high loading condition, Johnson cook [9, 10] material model is given as

$$\overline{\sigma}\left(\overline{\varepsilon}^{\text{pl}}, \dot{\overline{\varepsilon}}^{\text{pl}}, \widehat{T}\right) = \left[A + B(\overline{\varepsilon}^{\text{pl}})^n\right]\left[1 + C \ln\left(\frac{\dot{\overline{\varepsilon}}^{\text{pl}}}{\dot{\varepsilon}_0}\right)\right]\left[1 - \widehat{T}^m\right] \tag{6}$$

A, B, C, n are material constant and calculated by experimentally. $\bar{\varepsilon}^{\mathrm{pl}}$ and , $\dot{\bar{\varepsilon}}^{\mathrm{pl}}$ are equivalent plastic strain and plastic strain rate, $\bar{\sigma}$ von mises stress, $\widehat{T}$ is dimensionless temperature and it expressed as

$$\widehat{T} = (T - T_0)/(T_{\mathrm{melt}} - T_0) \quad T_0 \leq T \leq T_{\mathrm{melt}} \tag{7}$$

When damage parameter D value exceeds the unity, failure of the material occurred.

$$D\left(\bar{\varepsilon}^{\mathrm{P}}, \dot{\bar{\varepsilon}}^{\mathrm{P}}, T, \sigma^*\right) = \sum \frac{\Delta\bar{\varepsilon}^{\mathrm{P}}}{\bar{\varepsilon}_{\mathrm{f}}^{\mathrm{P}}(\dot{\bar{\varepsilon}}^{\mathrm{P}}, T, \sigma^*)} \tag{8}$$

The fracture model [11] proposed by Johnson and Cook define the equivalent plastic fracture strain $\bar{\varepsilon}_{\mathrm{f}}^{\mathrm{pl}}$ expressed as (Table 1),

$$\bar{\varepsilon}_{\mathrm{f}}^{\mathrm{pl}}\left(\frac{\sigma_{\mathrm{m}}}{\bar{\sigma}}, \dot{\bar{\varepsilon}}^{\mathrm{pl}}, \widehat{T}\right) = \left[D_1 + D_2 \exp\left(D_3 \frac{\sigma_{\mathrm{m}}}{\bar{\sigma}}\right)\right]\left[1 + D_4 \ln\left(\frac{\dot{\bar{\varepsilon}}^{\mathrm{pl}}}{\dot{\varepsilon}_0}\right)\right]\left[1 + D_5 \widehat{T}\right] \tag{9}$$

Table 1 Material property of the aluminium target [8]

Modulus of elasticity, E (N/mm^2)	65,762
Poison's ratio, ν	0.3
Density (kg/m^3)	2700
Yield stress (N/mm^2)	148.361
B	345.513
N	0.183
Reference strain rate	1.0
C	0.001
M	0.859
T_{melt} (K)	893
T_0 (K)	293
Specific heat C_{p} (J/Kg-K)	920
Inelastic heat fraction	0.9
D_1	0.071
D_2	1.248
D_3	1.142
D_4	0.147
D_5	0.0

4 Result and Discussion

The present numerical study was conducted to find out the effectiveness of the cylindrical and hemispherical shells when impacted by ogive-nosed shape projectile at different velocity. Tables 2 and 3 show the residual velocity of cylindrical and hemispherical shells for diameter 200 mm and thickness 0.7 mm and 1 mm which is graphically shown in Fig. 2. From both figures, it is cleared that at higher impact velocity, the velocity drop of cylindrical and hemispherical shells was found to be

Table 2 Numerical result of hemispherical shell target for 200 mm diameter [6, 8]

Thickness	Impact velocity (m/s)	Experimental result (m/s) [8]	Numerical result (m/s)
	99.08	90.07	86.19
1 mm	84.06	75.66	66.04
	64.66	45.03	34.6
	53.5	0	14.19
	50	0	0
	105.08	97.05	98.38
	95.27	84.07	87.06
0.7 mm	55.45	37.52	37.63
	48	25.88	26.7
	42	0	15.67
	40	0	0

Table 3 Numerical result of residual velocity of the cylindrical target for 200 mm diameter

Thickness	Impact velocity (m/s)	Numerical result (m/s)
	99.08	85.23
	84.06	60.12
1 mm	64.66	25.23
	53.5	0
	50	0
	105.08	96.25
	95.27	83.56
0.7 mm	55.45	30.26
	48	18.27
	42	0
	40	0

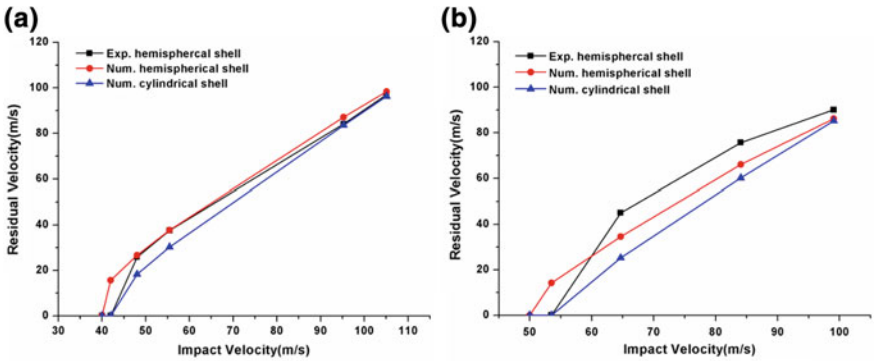

Fig. 2 Residual velocity. **a** 0.7 mm, **b** 1 mm for 200 mm diameter

almost same for each thickness. However, as the projectile velocity decreased, the difference in the velocity drop was increased and this velocity drop was more in cylindrical shell compare hemispherical shell. Similarly, Table 4 and Fig. 3 show variation in the ballistic limit for both the targets. Figure 3 shows that the ballistic limit of the target is increased with increase in the thickness of the targets. For hemispherical shell, ballistic limit increased by 26.9% and for cylindrical shell it was

Table 4 Ballistic limit of the cylindrical and spherical shells target for 200 mm diameter [6]

Target	Thickness (mm)	Ballistic limit (m/s)	
		Experimental result	Numerical result
Hemispherical shell	0.7	43.8	40.8
	1	54.8	51.8
Cylindrical shell	0.7	–	46.2
	1	–	58.5

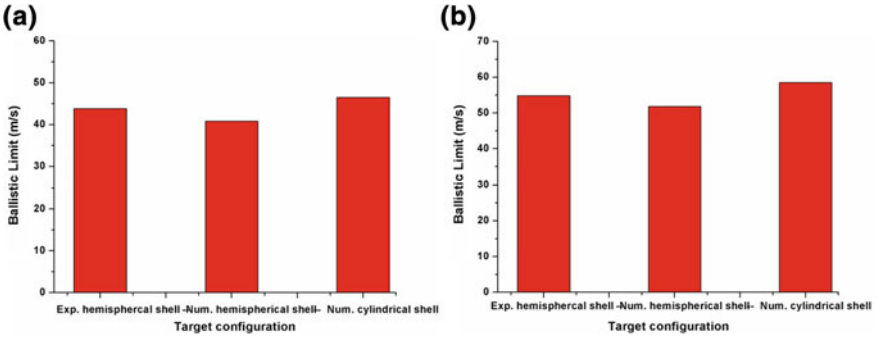

Fig. 3 Ballistic limit. **a** 0.7 mm, **b** 1 mm for 200 mm diameter

increased by 26.62% when thickness increased from 0.7 to 1 mm. Resistance of the target increased due to increase in stiffness. Also result shows that the cylindrical shell offered more resistance compared to the spherical shell. For 0.7 mm thickness, ballistic limit of the cylindrical shell is 13.23% more and for 1 mm thickness, the ballistic limit was 12.9% more compared to hemispherical shell. It was due to the reason that the global deformation and local of the cylindrical shell were higher than the spherical shell which lead to the higher absorbtion of the kinetic energy of the projectile.

5 Failure Mechanism

Analysis of failure mechanism is an important aspect which revealed the difference in the capability of target of different shape and configuration. Failure mode of cylindrical shell and hemispherical shell was similar and failed by dishing, hole enlargement with petal formation. Figure 5 shows the failure mode of the cylindrical and spherical shells. When a ogive-nosed projectile impacted at the top of the target shell, the nose of projectile pressed the target surface in the downward direction which convert the compressive loading into tensile loading and generate tensile stress .This tensile stress generate the crack at the top which propagates an lead the formation of the crack. Four number of petals were formed for both target for 0.7 and 1 mm thickness. Figure 4 shows the global deformation and global deformation of cylindrical shell was found to be more than spherical shell for 0.7 and 1 mm thickness global deformation of cylindrical shell 13.23 and 12.93% more than hemispherical shell of 0.7 and 1 mm thickness.

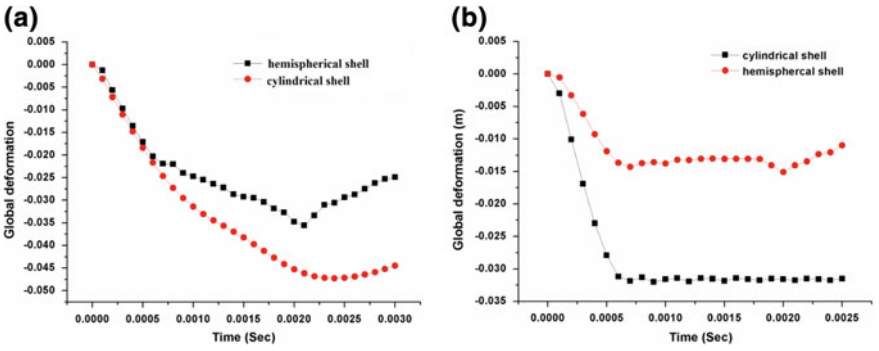

Fig. 4 Global deformation. **a** 0.7 mm, **b** 1 mm for 200 mm diameter

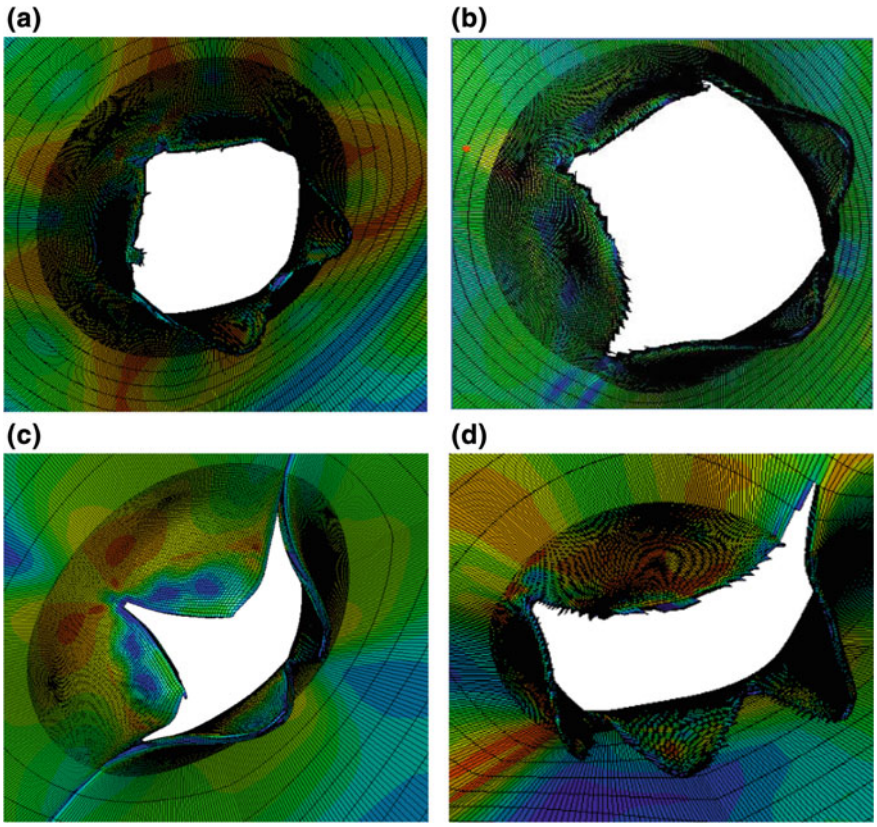

Fig. 5 Failure mode, spherical shell. **a** 0.7 mm, **b** 1 mm, cylindrical shell, **c** 0.7 mm, **d** 1 mm

6 Energy Dispersion Characteristic

The projectile kinetical energy is dispersed into vibrations near support, local permanent deformation and global permanent deformation, some of energy of the projectile was lost into projectile deformation and different failure mechanism such as plug formation and petal formation. The energy dispersed due to vibration at support region was assumed to be negligible and hence, neglected in present study. Also in the present study, the projectile is assumed to be rigid and hence, the energy dispersed due to projectile deformation also neglected. To relate the energy dispersed in permanent deformation of the cylindrical and hemispherical shells, the impact velocity closed to the ballistic limit of the projectile was selected because velocity near to ballistic limit the complete projectile energy converted into the permanent plastic deformation.

Figures 6 and 7 show energy dispersed in plastic deformation of cylindrical shell and hemispherical shell. Energy absorption is found to be more in the cylindrical shell

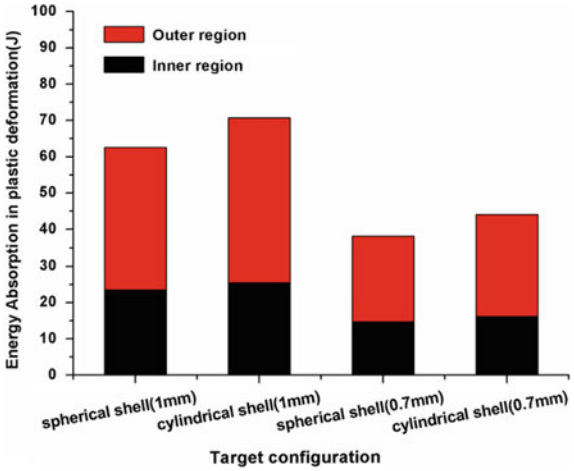

Fig. 6 Energy dispersed in plastic deformation in contact and non-contact region

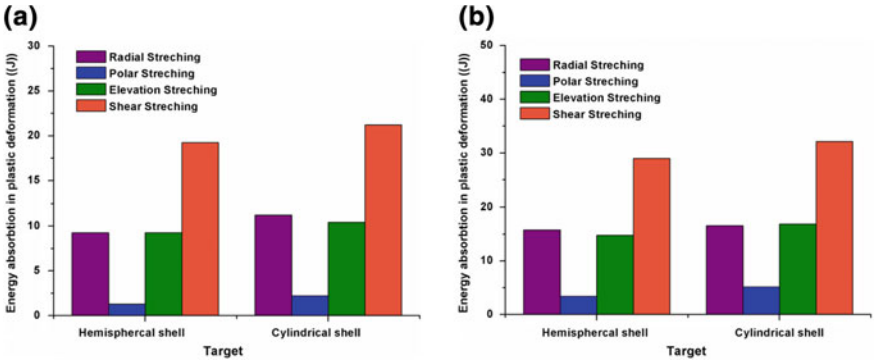

Fig. 7 Energy dispersed in plastic deformation in four different directions. **a** 0.7 mm, **b** 1 mm

than spherical shell due to larger global deformation in cylindrical shell compared to the spherical shell. Total energy absorbed in plastic deformation for of cylindrical shell was 45.13 J and 70.7 J and for spherical shell 38.12 J and 63.3 J for 0.7 mm and 1 mm, respectively. Figure 6 shows the kinetical energy of the projectile dispersed in permanent local and global deformation. As mentioned in finite element modelling to calculate the energy absorption in local plastic deformation and global plastic deformation inner set and outer set. In both the cylindrical and spherical shells, the energy absorption in local permanent deformation was found to be more than the permanent deformation in global deformation.

Figure 7 shows the plastic energy deformation in four different directions for cylindrical and hemispherical shells. For 0.7 and 1 mm the energy dispersed in polar direction for cylindrical shell was found to be 76.15 and 50.5% more than the

spherical shell. On the other hand for 0.7 and 1 mm, the energy dispersed in shear direction for cylindrical shell was found to be 10.34 and 10.94% increased than spherical shell. The energy dispersed in elevation direction for cylindrical shell was 21.07 and 8.25% less than spherical shell for 0.7 and 1 mm. The energy dispersed in axial direction for spherical shell was 25.37 and 14.09% less than cylindrical shell for 0.7 and 1 mm.

7 Conclusion

The objective of study was to carry out the numerical simulation to compare the ballistic resistance failure mode and energy-dispersed characteristic of Al-H1100 thin hemispherical shell and cylindrical shell. Span diameter (200 mm), thickness (0.7 mm, 1 mm) and mass of hemispherical and cylindrical shells kept constant for direct comparison. The response of cylindrical shell and spherical shell was compared in terms of global plastic deformation, residual velocity, ballistic limit, failure mode and total energy dispersed in permanent plastic deformation. Following conclusions can be drawn from the result

- Resistance offered by the cylindrical shell was higher than the spherical shell that the ballistic limit of the target is increased with increase in the thickness of the targets. For hemispherical shell, ballistic limit increased by 10% and for cylindrical shell it was increased by 20% when thickness increased from 0.7 to 1 mm.
- Failure mode for both the cylindrical and spherical shells was found to be same, moreover, both the target failed through hole enlargement along with petal formation struck the ogive-nosed projectile.
- Energy dispersed in plastic deformation was found to be highest in shear direction and lowest in polar direction. Energy dispersed in the axial and polar was nearly equal.

Acknowledgements This research was fully supported by SERB/DST under project number DST/SERB ECR/2016/001440 for providing resources for numerical simulations and experimentation. We thank our colleagues from Visvesvaraya National Institute of Technology, Nagpur who provided insight and expertise that greatly assisted the research.

References

1. Zhang T, Stronge W (1996) Theory for ballistic limit of thin ductile tubes hit by blunt missiles. Int J Impact Eng 18:735–752
2. Zhang TZ (1998) Rupture of thin ductile tubes by oblique impact of blunt missile: analysis. Int J Impact Eng 21:571–587
3. Palomby C, Stronge W (1988) Blunt missile perforation of thin plates and shells by discing. Int J Impact Eng 7:85–100

4. Ning J, Song W, Yang G (2006) Failure analysis of plastic spherical shells impacted by a projectile. Int J Impact Eng 32:1464–1484
5. Tiwari G, Iqbal M, Gupta P (2016) Energy absorption characteristics of thin aluminium plate against hemispherical nosed projectile impact. Thin-Walled Struct 126:246–257
6. Tiwari G, Iqbal M, Gupta P (2018) Impact response of thin aluminium plates and hemispherical shells. Int J Crashworthiness 1–16
7. Zhong H, Ruiz C (1990) Assessment of damage resulting from missile impact on a spherical shell. Int J Impact Eng 9:223–236
8. Iqbal M, Tiwari G, Gupta P (2016) Energy dispersed in thin metallic shells under projectile impact. Eur J Mech A/Solids 59:37–57
9. Hibbitt K, Sorensen Inc (2005) ABAQUS/explicit user's manual, version 6.5. 1, Rhode Island, New York
10. Johnson GR (1983) A constitutive model and data for materials subjected to large strains, high strain rates, and high temperatures. In: Proceedings of 7th international symposium on ballistics, pp 541–547
11. Johnson GR, Cook WH (1985) Fracture characteristics of three metals subjected to various strains, strain rates, temperatures and pressures. Eng Fract Mech 21:31–48

Experimental Study on PCM-Based External Wall Cladding for Energy Efficient Buildings

Kolli Sravani, R. Parameshwaran and V. Vinayaka Ram

Abstract The present work reports the experimental investigation of the phase change material (PCM) incorporated into the external wall claddings for achieving energy conservation in building through a passive cooling application. Three types of wall claddings of size 458 mm × 458 mm (1.5 ft × 1.5 ft) in dimension were developed in this experimental study. Lauric acid was utilized as the PCM to be incorporated into the wall claddings. Experimental results suggest that the lauric acid exhibited good latent heat potential, congruent phase change processes, and was thermally stable within operating temperature ranges. Furthermore, it was concluded that out of three cladding types being tested, the percentage drop of air temperature was more in composite wall cladding and the percentage drop of heat flux was more in aluminum box cladding with PCM and coarse aggregate. In total, the cladding incorporated with the PCM was found to be the potential candidate for the enhancement of energy efficiency in building through passive thermal storage and cooling load reduction.

Keywords Energy efficiency · Phase change material · Wall cladding · Thermal energy storage · Thermal properties

1 Introduction

As the demand for comfort in buildings is increasing these days, energy consumption is also increasing substantially. Buildings are one of the major sectors which consume energy because of high heating and cooling load needs. Buildings account for 40% of global energy consumption as presented in Table 1 and contribute 40% of CO_2

K. Sravani · R. Parameshwaran (✉) · V. Vinayaka Ram
Birla Institute of Technology and Science-Pilani (BITS-Pilani) Hyderabad Campus, Hyderabad, Telangana 500078, India
e-mail: parameshwaranr@hyderabad.bits-pilani.ac.in

K. Sravani
e-mail: Kollisravani94@gmail.com

V. Vinayaka Ram
e-mail: vinayak@hyderabad.bits-pilani.ac.in

H. Kumar and P. K. Jain (eds.), *Recent Advances in Mechanical Engineering*,
Lecture Notes in Mechanical Engineering,
https://doi.org/10.1007/978-981-15-1071-7_42

Table 1 Annual energy consumption in buildings [2]

Building energy consumption (%)	Commercial	Residential	Total
USA	18	22	40
UK	11	28	39
World	7	16	24

emissions. Residential sector consumes 27% of energy and contributes 17% of CO_2 emissions [1].

According to Energy Information Administration, International Energy Outlook 2017 Reference case, the average annual energy consumption in buildings is expected to increase by 2.7% in India between 2015 and 2040 as depicted in Fig. 1.

For now, building's energy demand is met by active systems to ensure indoor thermal comfort which leads to greenhouse gas emissions. In this era of energy crisis and environmental concerns, there is a great potential for the development of energy-saving and cost-effective technologies. One of the prominent technologies available in hand is the latent thermal energy storage (LTES), which uses the phase change material (PCM). The PCM while undergoing melting process would discharge the stored thermal energy when the surrounding temperature is high and would store the heat energy when the surrounding temperature is low and thereby, it solidifies. Melting and solidification occur at nearly isothermal conditions.

Most effective way of using LTES is by embedding PCM's into the passive components of the buildings such as walls, windows, ceiling, floor, bricks, tiles, etc., [3–10]. This results in a reduction of heat transfer and indoor temperature fluctuations leading to reduction in energy consumption and CO_2 emissions associated with heating and cooling [11–15]. Based on the literature review, there have been

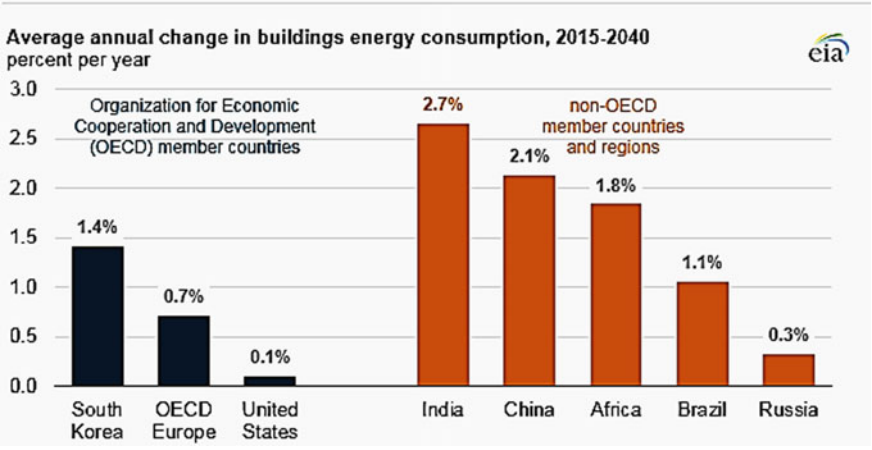

Fig. 1 Average annual change in buildings energy consumption, 2015–2040. *Source* The US Energy Information Administration, International Energy Outlook 2017 Reference case

no studies reported so far on PCM being embedded in external wall claddings. This had driven the authors to perform this research study on different cladding materials suitable for external walls where PCM can be embedded for energy efficiency in buildings.

Cladding materials are the panels used to cover exterior or interior wall surfaces in order to protect the wall from environment and to ensure energy efficiency of the buildings [16]. There are diverse ranges of cladding materials available in the market which are evolving as an attractive option for commercial and residential sectors pertaining to their easy application, economical, and esthetic advantage. They are available in different shapes and sizes.

Claddings are needed to stop wind and rain from penetrating into walls, to provide acoustic and thermal insulation, to provide fire resistance, and to make the building opaque [17]. Halawa et al. [18] proposed two types of cladding materials namely opaque and glazed. While glazed ones are made up of transparent material, opaque ones include materials like stone, bricks, wood, metal, etc.

With a view to enhance the thermal comfort inside the building, the present investigation was targeted at developing an innovative cladding option and to check its efficacy with respect to its performance. Two cladding options, incorporated with PCM and one option without PCM, were being developed and were subjected to investigations with indigenously fabricated test setup to check the efficacy of the cladding options in providing the thermal comfort inside the building. The drop in temperature and heat flux due to the provision of cladding material was investigated with the test setup and the details of which are presented in the following sections.

2 Experimental Details

2.1 Materials and Methods

Three alternate wall cladding options were developed and tested during the current investigations. Details of each of these options are presented below.

2.1.1 Cement Concrete with Perlite as Cladding Option

As per the IS 10262-2009 guidelines on concrete mix proportioning, perlite concrete mix design process has been carried out with different proportions of mix ingredients. Target strength of M35 was chosen, suiting the cladding application. Final mix design was arrived at by optimizing with respect to the characteristic compressive strength of standard 15 cm × 15 cm × 15 cm cube specimens after 28 days of curing in water. The final mix design details are presented below for ready reference.

- Cementitious and powder content: 548 kg/m^3 with 50% cement, 45% GGBS, and 5% Perlite
- Coarse aggregate: 480 kg/m^3
- Fine aggregate: 1120 kg/m^3
- Water/Cement ratio: 0.475

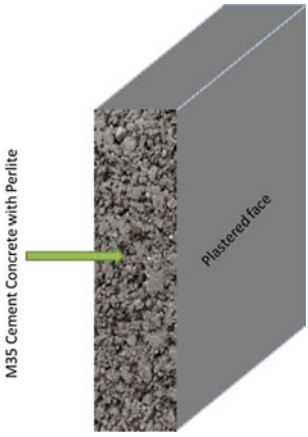

Fig. 2 Schematic representation of perlite concrete cladding block [458 mm (L) × 458 mm (B) × 12 mm (T)]

- Polycarboxylate ether based sperplasticizer: 0.5% by weight of cement
- Seven-day cube characteristic compressive strength: 26.81 MPa
- 28-day cube characteristic compressive strength: 45.57 MPa

With these optimized proportions, perlite concrete cladding blocks with dimensions of 458 mm (L) × 458 mm (B) × 12 mm (T) were prepared and cured for 28 days with a view to ensure the target strength of 35 MPa. A schematic of the block is presented in Fig. 2.

2.1.2 Aluminum Encased Loose Aggregate Plus PCM-Based Cladding Option

An aluminum sheet of 1.5 mm thickness was used to make an aluminum box cladding of 20.8 mm thickness with 17.8 mm hollow space in the interior of the box as depicted in Fig. 3. Lauric acid—$C_{12}H_{24}O_2$—(PCM) and black granite coarse aggregate passing through 10 mm and retained on 6.3 mm sieve were filled into the hollow space of box as shown in Fig. 4.

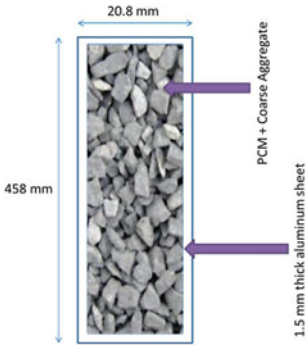

Fig. 3 C/S view of aluminum box cladding containing PCM and coarse aggregate

Fig. 4 PCM and coarse aggregate filled in aluminum box cladding (photo top view)

The volume of aluminum box was found to be 4.3896 L. For every 1000 ml, volume of box 1.5 kg of coarse aggregate was filled based on the porosity calculations, 43% of volume of aluminum box is filled with lauric acid (PCM). After filling the materials into the box, the top side of the box was sealed by welding and checked for leakages.

2.1.3 Composite Wall Cladding Option

A composite wall cladding was developed by combining cement concrete with perlite (as discussed in Sect. 2.1.1) and aluminum encased loose aggregate plus PCM (as discussed in Sect. 2.1.2) and the same is depicted in the schematic presented in Fig. 5.

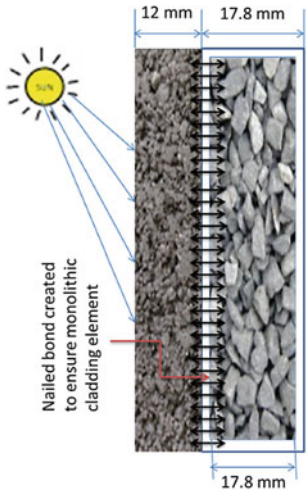

Fig. 5 Cross-sectional view of composite wall cladding

The procedure of fabricating both the elements in this composite cladding is the same as that explained in the respective sections.

2.2 Characterization Techniques

Thermal properties such as the latent heat of fusion (ΔH_{fusion}) and melting onset temperature (T_{onset}) were measured using the differential scanning calorimeter (DSC-60, SHIMADZU), wherein the PCM was sealed in aluminum pan and heated between 0 and 100 °C at a rate of 10 °C/min and cooled from 100 to 0 °C at the same rate. The experiment was carried out in the presence of a nitrogen gas atmosphere flowing at a rate of 50 mL/min. Thermogravimetric analysis (TGA) was performed in the range of ambient temperature to 500 °C in the presence of nitrogen stream to analyze the thermal stability of PCM.

2.3 Wooden Experimental Setup

A wooden setup of dimensions 1510 mm × 700 mm × 700 mm was developed to test the three types of claddings as described above. The wooden setup was partitioned into zone-1 and zone-2. Zone-1 contains six bulbs referring to the region or space "before cladding," which would otherwise represent the exterior conditions of the test building as shown in Fig. 6. Zone-2 refers to the region or space "after cladding" which would otherwise represent the interior conditions of the test building. A slit of 70 mm was used to hold intact the cladding to be tested, which separates the zone-1 from zone-2. The gap present in between the cladding and wooden slit was filled with adequate insulation material as shown in Fig. 7 to prevent infiltration of air from zone-1 to zone-2 and any heat losses as well.

The bulbs in zone-1 represent the heat source to resemble the external environmental conditions. Six bulbs of 60 W, six bulbs of 100 W, six bulbs of 200 W were used in sets one after the other to test the three claddings for air temperature drop and heat flux drop. Two thermocouples as shown in Fig. 8 were placed 350 mm before cladding to measure the average air temperature in zone-1. Two thermocouples as shown in Fig. 9 were placed 350 mm after the cladding to measure the average air temperature in zone-2. Six thermocouples (three on each side) were placed on the cladding surfaces to monitor the average surface temperature.

Heat flux meter was placed in the wooden setup to measure the heat flux in zone-1 and in zone-2 as shown in Fig. 10. The cladding which has to be tested was placed in the slit and the top of the wooden box was closed as shown in Fig. 11. The entire test setup was connected to a data logger to measure the required temperatures.

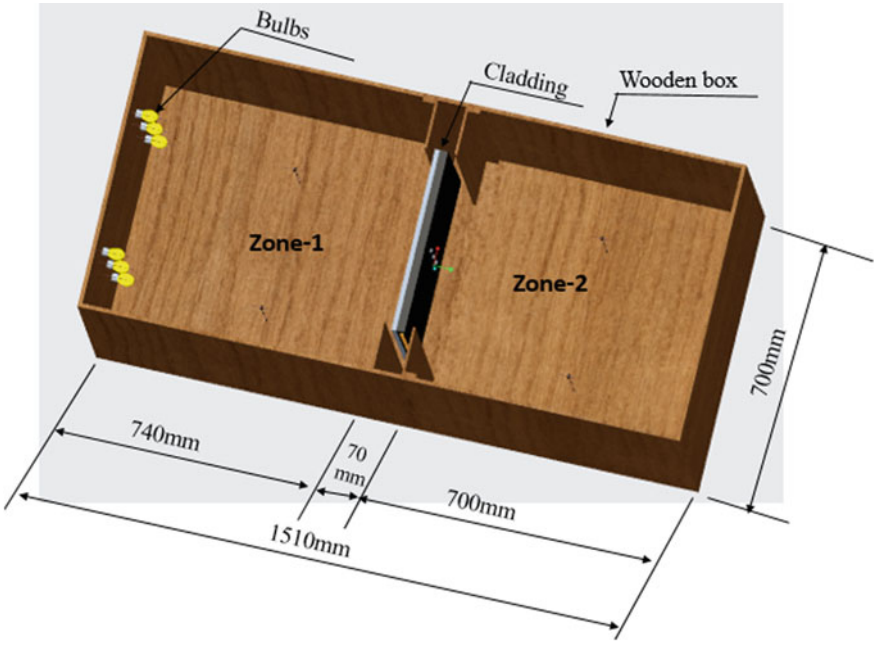

Fig. 6 Top view of wooden experimental setup

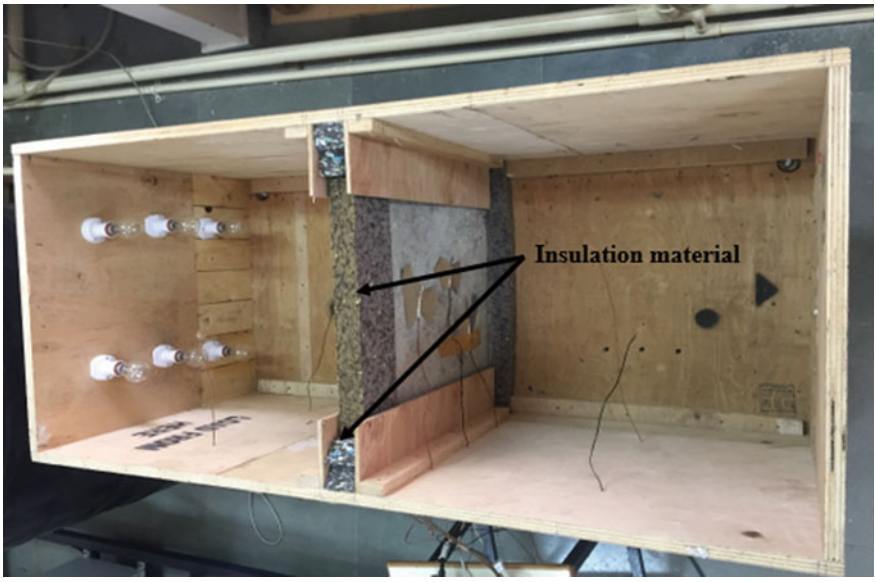

Fig. 7 Pictorial representation of the wooden setup with insulation material around cladding placed in the slit

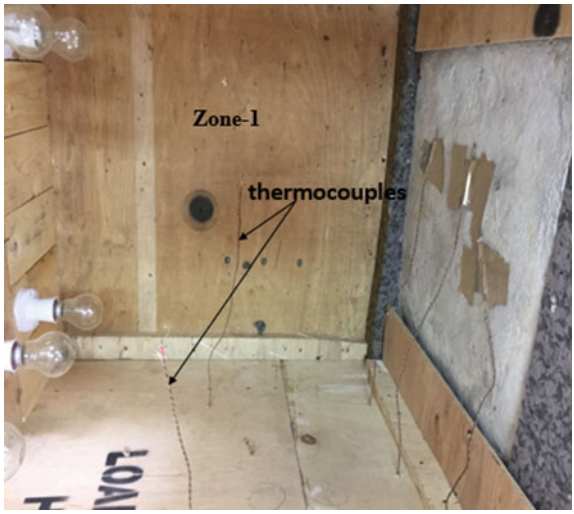

Fig. 8 Location of thermocouples in zone-1 of wooden experimental setup

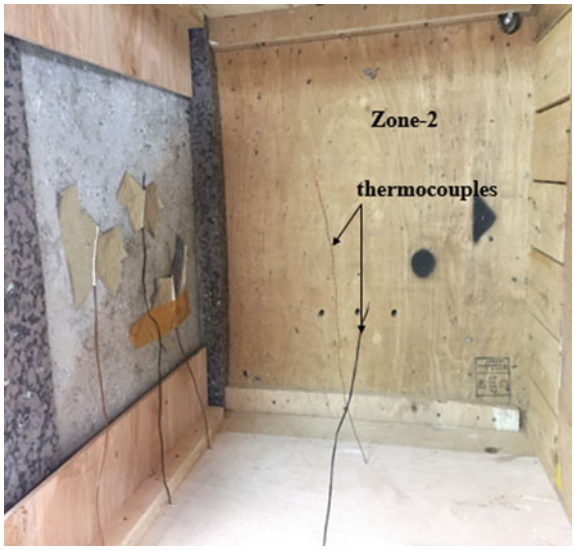

Fig. 9 Location of thermocouples in zone-2 of wooden experimental setup

3 Results and Discussions

Results obtained from the experiments being performed on the cladding materials are discussed below in terms of thermophysical properties of the PCM, percentage drop in the air temperature, and the heat flux after placing the cladding panels.

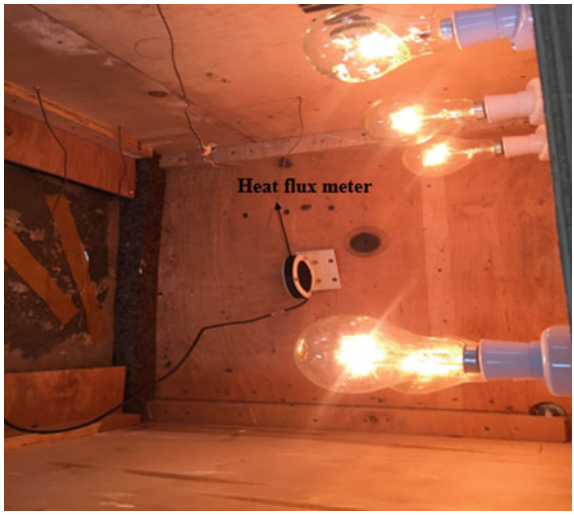

Fig. 10 Heat flux meter inserted in wooden setup

Fig. 11 Wooden experimental setup connected to data logger

3.1 DSC Analysis for Thermal Energy Storage Properties of Lauric Acid

The DSC result pertaining to the melting and freezing curves of the lauric acid (PCM) is shown in Fig. 12. The phase change temperature and the latent heat enthalpy for the melting process were measured to be 42.7 °C and 186.58 kJ/kg, respectively, whereas for the freezing process, it was found to be 40.47 °C and 183.49 J/g, respectively. The absence of any solid-solid secondary peaks in the DSC results suggests that the lauric acid has undergone congruent phase transition processes [19–21]. These

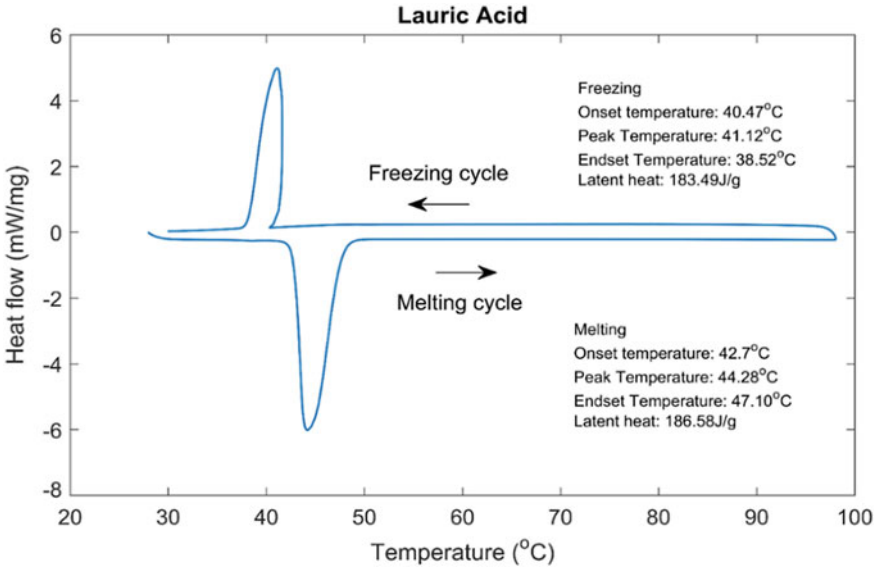

Fig. 12 Melting and freezing DSC curves for lauric acid

characteristics in turn were attributed to the good thermal storage properties which enabled the lauric acid to be possibly considered as a potential candidate for this exterior wall cladding application in test building.

3.2 TGA Analysis of Lauric Acid

The thermogravimetric analysis result as illustrated in Fig. 13 infers that the dominant mass loss of the lauric acid occurred through a continuous single-step process

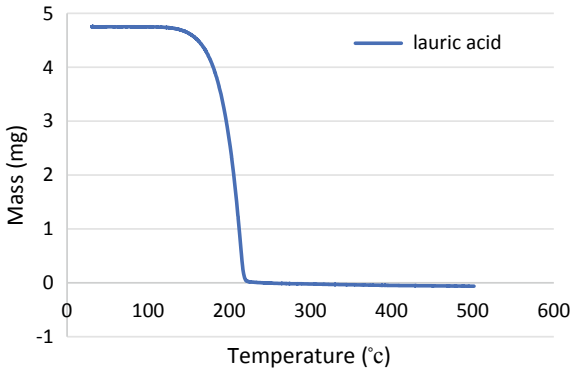

Fig. 13 TGA curve for lauric acid

between 140 and 210 °C [22]. This mass loss was ascribed to the complete decomposition and evaporation of the organic compounds of the PCM. This analysis shows that the lauric acid was thermally stable up to 140 °C which was much on the higher side, while compared to the actual operating temperature range for the present exterior wall cladding application.

3.3 Percentage Drop in Air Temperature

The thermocouples connected to the data logger were used to measure the air temperature before and after the cladding regions for the three different claddings, which were tested as mentioned in Table 2. As the air temperature before the cladding was increased by using high wattage bulbs, drop in the temperature of the air after cladding was also increased [13].

The test results reveal that for the concrete with perlite cladding, the percentage drop of air temperature in "after-cladding region" when compared to the "before-cladding region" was accomplished to be 7.26%, 14.65%, and 17.64%, with 60 W, 100 W, and 200 W heat source, respectively. Likewise, for the aluminum box cladding, it was 3.20%, 11.02%, and 14.89% and for the composite wall cladding, it was 8.54%, 20.96%, and 20.76%, respectively.

Table 2 Air temperature measurement in wooden setup

Location of air temperature	Type of cladding	Air temperature with 60 W bulb (°C)	Air temperature with 100 W bulb (°C)	Air temperature with 200 W bulb (°C)
Before-cladding region (zone-1)	–	35.26	39.12	41.38
After-cladding region (zone-2)	Concrete with perlite cladding	32.70	33.39	34.08
After-cladding region (zone-2)	Aluminum box cladding with PCM and coarse aggregate	34.13	34.81	35.22
After-cladding region (zone-2)	Composite wall cladding	32.25	30.92	32.79
Drop in air temperature (%)	Concrete with perlite cladding	7.26	14.65	17.64
Drop in air temperature (%)	Aluminum box cladding with PCM and coarse aggregate	3.20	11.02	14.89
Drop in air temperature (%)	Composite wall cladding	8.54	20.96	20.76

Thus, the experimental measurements justified that when the composite wall cladding was utilized, the temperature drop of air was more on the building interior side. This clearly validated the heat storage effectiveness of the composite wall cladding material in terms of reducing the heat being transferred from the exterior (zone-1) to the indoor space (zone-2) of the test building.

3.4 Percentage Drop in Heat Flux

Heat flux meter was used to measure the heat flux in "before cladding" and "after cladding" regions for the as-developed three claddings as depicted in Table 3. For the concrete with perlite cladding, the percentage drop of the heat flux in the "after-cladding region" when compared to the "before-cladding region" was achieved to be 88.89%, 91.67%, and 97.17%, with 60 W, 100 W, and 200 W heat source, respectively. Likewise, for the aluminum box cladding, it was 98.61%, 98.61%, and 96.70% and for the composite wall cladding, it was 94.44%, 88.19%, and 94.81%, respectively. Hence, it was observed from the experimental results that the percentage drop in the heat flux was more when aluminum box cladding containing PCM and coarse aggregate was used.

Table 3 Heat flux measurement in wooden setup

Location of heat flux measurement	Type of cladding	Heat flux with 60 W bulb (W/m^2)	Heat flux with 100 W bulb (W/m^2)	Heat flux with 200 W bulb (W/m^2)
Before-cladding region (zone-1)		72	144	212
After-cladding region (zone-2)	Concrete with perlite cladding	8	12	6
After -cladding region (zone-2)	Aluminum box cladding with PCM and coarse aggregate	1	2	7
After-cladding region (zone-2)	Composite wall cladding	4	17	11
Drop in heat flux (%)	Concrete with perlite cladding	88.89	91.67	97.17
Drop in heat flux (%)	Aluminum box cladding with PCM and coarse aggregate	98.61	98.61	96.70
Drop in heat flux (%)	Composite wall cladding	94.44	88.19	94.81

4 Conclusions

In this research work, the phase change material (PCM) incorporated into the external wall claddings for achieving energy conservation in building through passive cooling application was experimentally investigated. In this study, one cladding material without PCM and the two other cladding materials with the PCM were developed, wherein the lauric acid was utilized as the PCM. In order for this PCM not to settle down at the bottom of the aluminum box, coarse aggregate was first filled in the aluminum box of second, third cladding and later melted PCM was poured into the box.

Based on the DSC test result, it was observed that the latent heat potential and the melting point of the PCM were found to be 186.58 J/g and 42.7 °C, respectively, which make the PCM suitable for this exterior wall cladding application in building. In addition, the TGA results also confirmed that the PCM was quite thermally stable within the operating temperature ranges. The as-developed claddings were then tested in a wooden experimental setup simulating the external and internal environmental conditions of a building.

The percentage drop in air temperature was found to be more in the composite wall cladding followed by concrete with perlite cladding and aluminum box cladding. Likewise, the percentage drop in the heat flux was found to be more in the case of the aluminum box cladding. Since there is a chance of aluminum box getting affected by corrosion when it is exposed to the environment, it is suggested to prefer composite wall cladding due to its ability to reduce the indoor air temperature and reduce heat flux as comparable to the aluminum box cladding.

In summary, the composite wall cladding incorporated with the PCM was found to be the potential candidate for the enhancement of energy efficiency through cooling load reduction and passive thermal storage in building. The feasibility and the energy-cost analysis for the as-developed claddings are essentially required in order to realize their utilization potential for the real-time application in buildings, and which are included into the scope of future work.

Acknowledgements The authors gratefully acknowledge DST, New Delhi, and BITS-Pilani, Hyderabad for providing financial support to carry out this research work under DST SERB Sanction No. ECR/2017/001146. The authors express their sincere thanks to the Editor and the anonymous reviewers for their constructive suggestions which helped to improve the manuscript. The authors also thank Mr. G. V. N. Trivedi and Mr. R. Naresh, BITS-Pilani, Hyderabad Campus for their support during experimentation.

References

1. Soares N, Costa JJ, Gaspar AR, Santos P (2013) Review of passive PCM latent heat thermal energy storage systems towards buildings' energy efficiency. Energy Build 59:82–103. https://doi.org/10.1016/j.enbuild.2012.12.042
2. Pérez-Lombard L, Ortiz J, Pout C (2008) A review on buildings energy consumption information. Energy Build 40:394–398. https://doi.org/10.1016/j.enbuild.2007.03.007

3. Guarino F, Athienitis A, Cellura M, Bastien D (2017) PCM thermal storage design in buildings: experimental studies and applications to solaria in cold climates. Appl Energy 185:95–106. https://doi.org/10.1016/j.apenergy.2016.10.046
4. Chen C, Guo H, Liu Y, Yue H, Wang C (2008) A new kind of phase change material (PCM) for energy-storing wallboard. Energy Build 40:882–890. https://doi.org/10.1016/j.enbuild.2007.07.002
5. Frederic K, Virgone J (2009) Experimental investigation of wallboard containing phase change material: data for validation of numerical modelling. Energy Build 41:561–570. https://doi.org/10.1016/j.enbuild.2008.11.022
6. Xu X, Zhang Y, Lin K, Di H, Yang R (2005) Modeling and simulation on the thermal performance of shape-stabilized phase change material floor used in passive solar buildings. Energy Build 37:1084–1091. https://doi.org/10.1016/j.enbuild.2004.12.016
7. Arkar C, Suzana D, Medved S (2018) Lightweight composite timber façade wall with improved thermal response. Sustain Cities Soc 38:325–332. https://doi.org/10.1016/j.scs.2018.01.011
8. Pasupathy A, Velraj R (2008) Effect of double layer phase change material in building roof for year round thermal management. Energy Build 40:193–203. https://doi.org/10.1016/j.enbuild.2007.02.016
9. Karthik P, Kumaresan V, Velraj R (2017) Passive cooling potential in buildings under various climatic conditions in India. Renew Sustain Energy Rev 78:1236–1252
10. Kant K, Shukla A, Sharma A (2017) Heat transfer studies of building brick containing phase change materials. Sol Energy 155:1233–1242
11. Ismail KAR, Castro JNC (1997) PCM thermal insulation in buildings. Int J Energy Res 21:1281–1296. https://doi.org/10.1002/(SICI)1099-114X(199711)21:14%3c1281
12. Lee KO, Medina MA, Raith E, Sun X (2015) Assessing the integration of a thin phase change material (PCM) layer in a residential building wall for heat transfer reduction and management. Appl Energy 137:699–706. https://doi.org/10.1016/j.apenergy.2014.09.003
13. Jin X, Medina MA, Zhang X (2014) On the placement of a phase change material thermal shield within the cavity of buildings walls for heat transfer rate reduction. Energy 73:780–786. https://doi.org/10.1016/j.energy.2014.06.079
14. Roth K, Westphalen D, Brodrick J (2007) PCM technology for building materials. ASHRAE J 49(7):129–131
15. Hasan MI, Basher HO, Shdhan AO (2018) Experimental investigation of phase change materials for insulation of residential buildings. Sustain Cities Soc 36:42–58. https://doi.org/10.1016/j.scs.2017.10.009
16. Latha PK, Darshana Y, Venugopal V (2015) Role of building material in thermal comfort in tropical climates—a review. J Build Eng 3:104–113. https://doi.org/10.1016/j.jobe.2015.06.003
17. Llorens J (ed) (2015) Fabric structures in architecture. Elsevier, Amsterdam
18. Halawa E, Ghaffarianhoseini A, Ghaffarianhoseini A, Trombley J, Hassan N, Baig M, Yusoff SY, Ismail MA (2018) A review on energy conscious designs of building façades in hot and humid climates: lessons for (and from) Kuala Lumpur and Darwin. Renew Sustain Energy Rev 82:2147–2161. https://doi.org/10.1016/j.rser.2017.08.061
19. Harish S, Orejon D, Takata Y, Kohno M (2015) Thermal conductivity enhancement of lauric acid phase change nanocomposite with graphene nanoplatelets. Appl Therm Eng 80:205–211. https://doi.org/10.1016/j.applthermaleng.2015.01.056
20. Jiesheng L, Yuanyuan Y, Xiang H (2016) Research on the preparation and properties of lauric acid/expanded perlite phase change materials. Energy Build 110:108–111. https://doi.org/10.1016/j.enbuild.2015.10.043
21. Suresh Kumar KR, Parameshwaran R, Kalaiselvam S (2017) Preparation and characterization of hybrid nanocomposite embedded organic methyl ester as phase change material. Sol Energy Mat Sol Cell 171:148–160. https://doi.org/10.1016/j.solmat.2017.06.031
22. Chen Z, Shan F, Cao L, Fang G (2012) Synthesis and thermal properties of shape-stabilized lauric acid/activated carbon composites as phase change materials for thermal energy storage. Sol Energy Mat Sol Cell 102:131–136. https://doi.org/10.1016/j.solmat.2012.03.013

The Machining Characteristics of the Al7075-B_4C Nanocomposites Developed Using Ultrasonic Liquid Processor

Surender Kumar and P. K. Sood

Abstract The nanocomposites discover many applications in various manufacturing sectors due to their noticeable improvement in the mechanical strength compared to the parent alloy. The present research work was concentrated on the machining of the boron carbide (B_4C)-filled nanocomposites. The ultrasonic liquid processor along with stir casting machine is used for the development of the nanocomposites. The microstructure of the developed composites is studied under the microscope and the scanning electron microscopy (SEM). The CNC turning center is used to machining behavior of the nanocomposite material. The turning experiments are performed by varying cutting speed, depth of cut, feed rate, and fillers percentage (%). The cutting force and surface roughness are the output responses. Taguchi L9 orthogonal is used for finding the optimum combinations of variables. The machining tests are carried out in dry conditions at cutting speed (100, 150 and 200 m/min), feed rate (0.05, 0.10 and 0.15 mm/rev), depth of cut (0.15, 0.35 and 0.55), and percentage reinforcement (0.75, 1.50 and 2.25). The optimal parametric combination for responses is found to be A3-B1-C1-D1.

Keywords Aluminum matrix nanocomposites · Machining · Roughness · Cutting force

1 Introduction

Aluminum is one of the lightest metals. The high strength-to-weight ratio and its compatibility with the ceramics material like silicon carbide (SiC), aluminum oxide (Al_2O_3), and boron carbide (B_4C) are some important factors, which make aluminum excellent matrix material. The aluminum matrix nanocomposites (AMNCs) have found application in various sectors of automobile and aerospace industries [1]. The AMNCs have found more improved properties in comparison with micro-particulates reinforced composites, but problems associated with the development

S. Kumar (✉) · P. K. Sood
Mechanical Engineering Department, NIT Hamirpur, Hamirpur, H.P., India
e-mail: surender.nith@gmail.com

H. Kumar and P. K. Jain (eds.), *Recent Advances in Mechanical Engineering*,
Lecture Notes in Mechanical Engineering,
https://doi.org/10.1007/978-981-15-1071-7_43

of nanocomposites hinder their applications. The key problem is agglomeration of particles in between the matrix phase which deteriorates the overall properties of fabricated composites. The problems like agglomeration and clustering of particulates of nanoparticles are resolved by ultrasonic agitator and by creating the inert environment for casting [2, 3]. The ultrasonic vibrations in the melt break the clusters of the particles and the inert gas environment protects the melt from atmospheric gases.

The cast composite material needs some finishing operations to use it in specific applications. So, fabricated composites have to be machined to use it for particular applications. Kumar et al.[4]studied the turning of Al356-SiCp-filled aluminum matrix composites (AMCs). The polycrystalline diamond (PCD) inserts are used for machining of Al356-SiCp. The effects of input parameters (feed rate, cutting speed, and depth of cut) are studied on the surface roughness. Sahoo and Pradhan [5] used uncoated tungsten carbide insert for dry machining of Al-SiCp AMC. The tool wear and surface roughness of machined surface are analyzed; the abrasion and adhesion are the two tool wear mechanisms observed from the tool wear images. Also, the built-up-edge (BUE) is observed at low cutting speed and at higher feed rate combinations while surface roughness affected inversely [5]. Kumaran and Uthayakumar [6] studied the turning of Al635-SiC-B_4C hybrid AMC. The surface roughness, material removal rate (MRR), and power consumption are the selected output parameters. The enhancement in the MRR is observed with an increase in depth of cut and feed rate. The power consumption is directly proportional to cutting speed. The surface quality of machined surface deteriorated with increase in feed rate and depth of cut [6]. Kumar and Chauhan [7] studied the turning of Al7075/SiC AMC and Al7075/SiC/Gr hybrid AMC. The results indicated that the surface roughness of hybrid composites is better compared to unhybrid composites [7]. Shoba et al. [8] studied the machining of rice husk ash (RHA) and SiCp hybrid-filled AMCs. The results showed that the cutting force is inversely proportional to reinforce percentage [8]. Priyadarshi and Sharma [9]worked on the turning of hybrid AMNCs materials. The cutting force and surface roughness were the selected output parameters. The results of machining revealed that feed rate and depth of cut have maximum effect on both the responses. Most of the research works are related to machining of the composite material uses the micro-particulates-filled composites. The present investigation aimed to study machining behavior of B_4Cp reinforced nanocomposites for the optimum combination of input parameters. The ultrasonic cavitation assisted casting technique is used for the fabrication of nanocomposites.

2 Experimental Details

Al7075 is used as matrix phase in this research, and the B_4C nanoparticles are used as the reinforcement phase. The average size of B_4C particles used in this research is 80 nm. The fabrication of nanocomposites is carried out at Swam Equip, Chennai, with the help of an ultrasonic liquid processor and stir casting machine. In the beginning, the stir casting technique is used for nanoparticles distribution

Table 1 L9 Taguchi orthogonal array

Parameters	Notation	Level 1	Level 2	Level 3
Cutting speed (m/min)	A	100	150	200
Feed rate (mm/rev)	B	0.05	0.10	0.15
Depth of cut (mm)	C	0.15	0.35	0.55
Reinforcement (%)	D	0.75	1.50	2.25

afterward ultrasonic vibrator has been introduced in the melt for complete dispersion of nanoparticles. The ultrasonic processing of the melt has been carried out for half an hour. In the present research, the coated carbide cutting tool is used for the marching of composites due to the applicability of these tool materials with composite materials [5]. The computer numerical control (CNC) turning center is used for turning of developed nanocomposites. The cutting force is measured using dynamometer, TeLC DKM, Germany. The cutting force throughout the experiments is recorded in the PC with the help of XKM software. The lathe dynamometer is connected to CNC machine with the fixture. The acquisition card connects the dynamometer with the PC in which software is installed. After each experiment, the surface quality of machined sample is measured by the roughness tester SJ-301, Make: Mitutoyo. The diamond tip of the roughness tester moves on the machined surface in which the digital value of the roughness comes out in the digital readout system. The full factorial design increases the number of experiment according to the number of variables and their levels. The usage of full factorial increases the time and cost of overall experiments. In order to minimize the cost and the time-consuming, Dr. Genichi Taguchi introduced a special orthogonal array to study the entire parameters with the minimum number of experiments [10]. This methodology saves time and cost, and so in present research work the experiments were designed according to Taguchi L9 orthogonal array with four input parameters (A, B, C, and D) and three levels as shown in Table 1. The cutting force and surface roughness are the selected output parameters.

3 Results and Discussion

3.1 Microstructural Studies

The SEM images and micrographs of the fabricated nanocomposites are shown in Figs. 1 and 2. The optical microscope is used to check the microstructure of fabricated nanocomposites. The scanning electron microscopy (SEM) is used to scan the developed composites at 50 μm scale. The presence of the boron carbide particulates can be seen in the SEM images. The refined grained structure is seen in Fig. 2b as compared to Fig. 2a at 2.25 wt. The refined grain structure of the nanocomposites also advantages to enhance the mechanical strength of the composites.

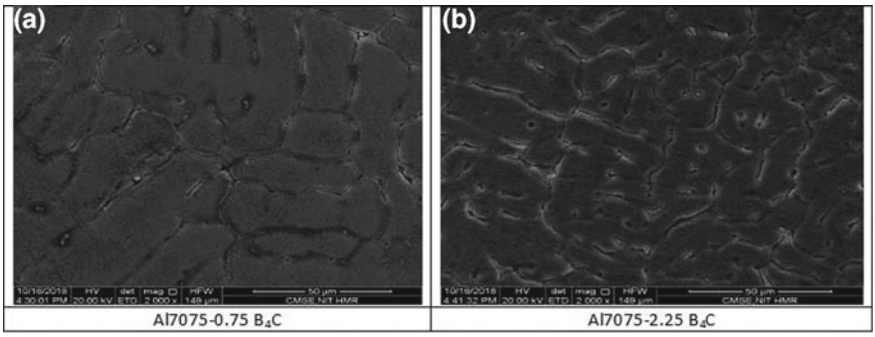

Fig. 1 SEM of fabricated composites filled with B_4C. **a** 0.75%, **b** 2.25%

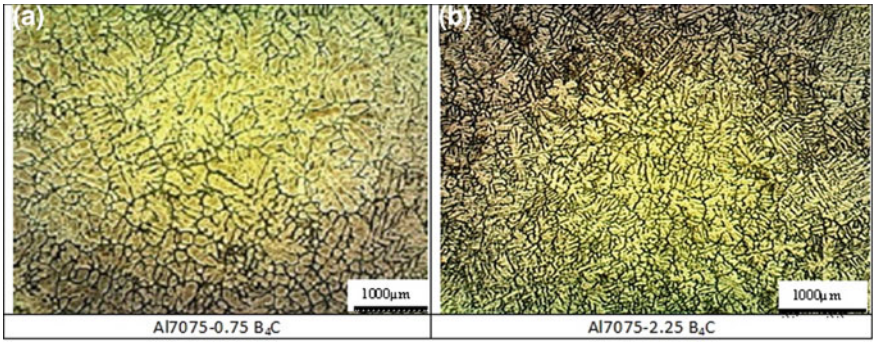

Fig. 2 Fabricated composites grains structures. **a** 0.75% B_4C, **b** 2.25% B_4C

3.2 Optimization of Machining Input Parameters for Minimizing Cutting Force

The combination of experiments with respect to Taguchi L9 orthogonal array has been demonstrated in Table 2. The cutting force has been detected during each experiment with the help of lathe tool dynamometer. The dynamometer is connected to computer with the support of acquisition card to access value of cutting force at the tip of insert. The XKM software installed in the computer is used as medium to convert the force at tool tip into the digital form.

Figure 3 shows the main effect plot for signal/noise ratio; it can be concluded from Fig. 3 that the combination of factors A3, B1, C1, and D1 will give the minimum cutting force. This implies that optimum parameters levels to minimize the cutting force are cutting speed 200 m/min, feed rate 0.05 mm/rev, depth of cut 0.15 mm, and 0.75 parentage reinforcement.

Table 2 Experimental design using L9 array for cutting force (F_c)

Ex. No.	Cutting speed (m/min) A	Feed rate (mm/rev) B	Depth of cut (mm) C	Reinforcement (%) D	Cutting force (N)	*S/N* ratio
1.	100	0.05	0.15	0.75	55	−34.80
2.	100	0.1	0.35	1.5	66	−36.39
3.	100	0.15	0.55	2.25	80	−38.16
4.	150	0.05	0.35	2.25	66	−36.39
5.	150	0.1	0.55	0.75	68	−36.65
6.	150	0.15	0.15	1.5	65	−36.25
7.	200	0.05	0.55	1.5	64	−36.12
8.	200	0.1	0.15	2.25	60	−35.56
9.	200	0.15	0.35	0.75	69	−36.77

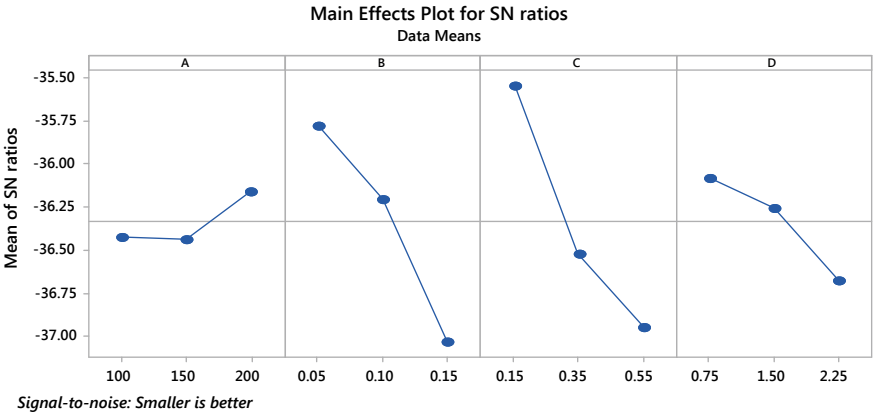

Fig. 3 Effect of control factors on cutting force

Table 3 ANOVA for cutting force

Source	DF	Seq SS	Adj SS	Adj MS	P (%)	
A	2	11.55	11.55	5.77	3.11	
B	2	146.88	146.88	73.44	39.60	Significant
C	2	176.22	176.22	88.11	47.51	Significant
D	2	36.22	36.22	18.11	9.76	
Residual error	0					
Total	8	370.88			100	

Table 3 shows the analysis of variance (ANOVA) table for cutting force. From Table 3, it can be concluded that factor depth of cut (C) has the highest contribution of 47.51% on cutting force followed by feed rate (B) 39.60%. The cutting speed and percentage reinforcement have least influence on the cutting force. During the experiments when value of the depth of cut increased from 0.15 to 0.55 mm, more tool penetration occurred in the work material resists the tool motion due to the availability of the boron carbide particles. The increase in the feed means tool moves at faster rate linearly with respect to the axis of the chuck. At the higher feed rate, the tool has to face the number of hard particles at a faster rate; these particles obstruct machining process and result in higher cutting force.

3.3 Optimization of Machining Input Parameters for Minimizing Surface Roughness

The combination of experiments and the results of surface roughness have been presented in Table 4 based on Taguchi L9 orthogonal array. The surface quality of the turned surface is calculated at the end of each cut.

From the main effect plot for *S*/*N* ratios Fig. 4, it can be concluded that the combination of factors A3, B1, C1, and D1 gives the minimum value of the surface roughness. This implies that optimal parametric combinations for minimum surface roughness are cutting speed 200 m/min, depth of cut 0.15 mm, feed rate 0.05 mm/rev, and 0.75% reinforcement. Table 5 shows the ANOVA for surface roughness. From Table 4, it can be concluded that factor feed rate (B) has the highest contribution of 80.69% on surface roughness followed by depth of cut (C) 11%. At the higher feed rate, the tool moved quickly on the composite surface and results in feed marks

Table 4 Experimental design using L9 array for surface roughness (R_a)

Ex. No.	Cutting speed (m/min) A	Feed rate (mm/rev) B	Depth of cut (mm) C	Reinforcement (%) D	Surface roughness (μm)	*S*/*N* ratio
1.	100	0.05	0.15	0.75	0.78	2.1581
2.	100	0.1	0.35	1.5	0.91	0.8191
3.	100	0.15	0.55	2.25	1.07	−0.5876
4.	150	0.05	0.35	2.25	0.80	1.9382
5.	150	0.1	0.55	0.75	0.95	0.4455
6.	150	0.15	0.15	1.5	0.99	0.0873
7.	200	0.05	0.55	1.5	0.81	1.8303
8.	200	0.1	0.15	2.25	0.86	1.3100
9.	200	0.15	0.35	0.75	0.93	0.6303

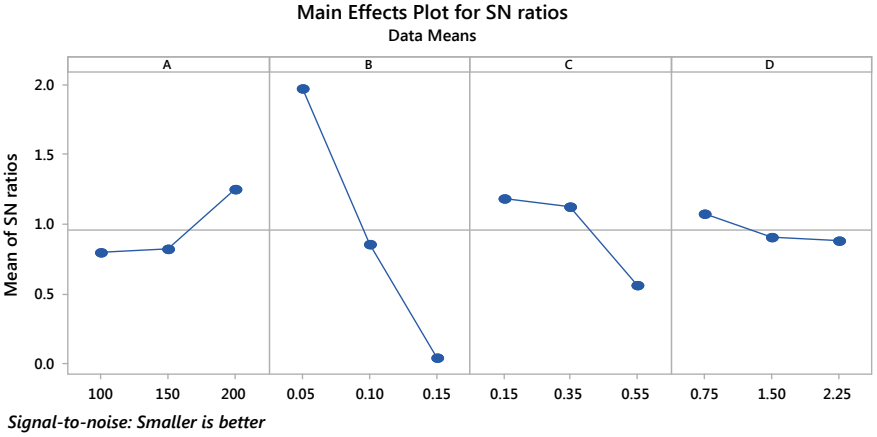

Fig. 4 Effect of control factor on surface roughness

Table 5 ANOVA for surface roughness

Source	DF	Seq SS	Adj SS	Adj MS	P (%)	
A	2	0.005067	0.005067	0.002533	6.79	
B	2	0.060200	0.060200	0.030100	80.69	Significant
C	2	0.008467	0.008467	0.004233	11.34	Significant
D	2	0.000867	0.000867	0.000433	1.16	
Residual error	0					
Total	8	0.074600			100	

on surface results in poor surface roughness. The percentage reinforcement (D) and cutting speed (A) have least influence on the surface roughness.

3.4 Confirmation Tests

The final step of Taguchi method is confirmation test. The results of this test show the variation of the experiment from predicted values. The predicted and experimented values are computed taking into consideration the main effect plot of *S*/*N* ratio and ANOVA results. The results are shown in Table 6.

4 Conclusions

The following conclusions can be drawn from present research.

Table 6 Results of conformation tests for cutting force and surface roughness

Response	Optimum levels of parameters	Optimal process parameters prediction	Optimal process parameters experimental	Error (%)
Cutting force	A3-B1-C1-D1	52.33	55	5.10
Surface roughness	A3-B1-C1-D1	0.72	0.75	4.16

- Taguchi method used for present research work revealed the same optimal combination of parameters for both surface roughness and cutting force.
- The microstructure and SEM images show the uniform distribution of boron carbide particles and improvement in the grain of the aluminum matrix with the increase in filler content.
- The cutting force decreased and surface quality improved with the enhancement of cutting speed while in case of other input parameters both surface roughness and cutting force enhanced with enhancement in depth of cut, feed rate, and percentage reinforcement.
- It can be concluded from the confirmation tests that errors are less than 10; hence, results are significant for both responses.
- For minimum cutting force and surface roughness, the combination of parameters is 200 m/min cutting speed, 0.05 mm/rev feed rate, 0.15 m depth of cut, and 0.75 parentage reinforcement.
- The Al7075 filled with boron carbide (B_4C) was studied in this research. In the future, the nanofillers can replace with the other nanomaterials like tungsten carbide (WC) alumina (Al_2O), titanium oxide, etc.

References

1. Kumar G, Rao C, Selvaraj N, Bhagyashekar M (2010) Studies on Al6061-SiC and Al7075 Al_2O_3 metal matrix composites. J Miner Mater Charact Eng 09(01):43–55
2. Poovazhagan L, Kalaichelvan, Sornakumar T (2015) Processing and performance characteristics of aluminum-nano boron carbide metal matrix nanocomposites. Mater Manuf Process 31(10):1275–1285
3. Kumar S, Sood PK (2019) A comparative study of dry sliding wear characterization of nano SiC and nano B_4C filled Al7075 nanocomposites under high temperature environment. Mater Res Express 6(5)
4. Palanikumar K, Muthukrishnan N, Hariprasad K (2008) Surface roughness parameters optimization in machining A356/SiC/20p metal matrix composites by PCD tool using response surface methodology and desirability function. Mach sci Technol 12(4):529–545
5. Sahoo A, Pradhan S (2013) Modeling and optimization of Al/SiCp MMC machining using Taguchi approach. Measurement 46(9):3064–3072
6. Kumaran S, Uthayakumar M (2014) Investigation on the machining studies of AA6351-SiC-B4C hybrid metal matrix composites. Int J Mach Mach Mater 15(34):174
7. Kumar R, Chauhan S (2015) Study on surface roughness measurement for turning of Al 7075/10/SiCp and Al 7075 hybrid composites by using response surface methodology (RSM) and artificial neural networking (ANN). Measurement 65:166–180

8. Shoba C, Ramanaiah N, Rao D (2015) Optimizing the machining parameters for minimum surface roughness in turning Al/6% SiC/6%RHA hybrid composites. Procedia Mater Sci 10:220–229
9. Priyadarshi D, Sharma R (2016) Optimization for turning of Al-6061-SiC-Gr hybrid nanocomposites using response surface methodologies. Mater Manuf Process 31(10):1342–1350
10. Sahoo A, Pradhan S, Rout A (2013) Development and machinability assessment in turning Al/SiCp-metal matrix composite with multilayer coated carbide insert using Taguchi and statistical techniques. Arch Civ Mech Eng 13(1):27–35

Influence of Alloying Compositions on the Properties of Nickel-Based Superalloys: A Review

Dileep Kumar Ganji and G. Rajyalakshmi

Abstract Superalloys were initially intended to take care of the demand in the materials execution prerequisites of space vehicles, turbo chargers, supplies of heat treatments, turbine motors of aircrafts and numerous others. Among the iron, nickel and cobalt-based superalloys, Ni as primary constituent is gaining lot of significance because of the presence of good mechanical properties including oxidation resistance at high temperatures, and also resistance to creep with precipitation strengthening. Nickel-based alloys also offer repetitivity to strengthen the phases either by solid solutioning or by hardening precipitated phase which enhances strength at peak temperatures. Also, the nature of solid solutions, pressures and environments, phase stability at different temperatures, grain shape, size and distribution are the important parameters for the study of superalloys based on nickel. The performance of these will largely depend on the composition of the elements used for alloying. To impart all the required characteristics for a particular application, alloying elements should be considered in appropriate proportions. With this review, future research endeavour might focus on the modelling and development of nickel-based superalloys for high-temperature applications along with the characterization studies of these superalloys with optimum composition of the constituent elements for better performance.

Keywords Elemental compositions · Oxide formers · Carbide formers · Selection of superalloys

1 Introduction

In the identification of an alloy for turbine blades, including the mechanical properties, environmental corrosion resistance also should be considered as one of the major aspects. When alloys are used at elevated temperatures, they are undergoing

D. K. Ganji · G. Rajyalakshmi (✉)
School of Mechanical Engineering, Vellore Institute of Technology, Vellore, India
e-mail: rajyalakshmi@vit.ac.in

D. K. Ganji
e-mail: dileep.309@gmail.com

H. Kumar and P. K. Jain (eds.), *Recent Advances in Mechanical Engineering*,
Lecture Notes in Mechanical Engineering,
https://doi.org/10.1007/978-981-15-1071-7_44

inevitable oxidation and in some cases, the formed oxide is protective so that further degradation of the material will be stopped or slowed down. However, if the working environment is too aggressive for the material, the corrosion will take place. Of course, designers in industry would prefer if corrosion could be completely avoided and a lot of efforts have been put to improve corrosion properties, in different ways. The morphologies and types of oxides or corrosion products are greatly influenced by the environment. Commonly, in industrial gas turbine blades, sulphides form due to the very oxidizing hot exhaust gases and this also carries some impurities. Thus, understanding of the corrosion mechanisms in different environments will help to reduce the occurrence of corrosion. A detailed review was made in the present paper on the influence of alloying compositions on the nickel-based superalloys. This effort can further be used to develop new materials through computational techniques which may rule out long lead times in designing novel materials together with the products, instead of compromising with the products besides the shortcomings of pre-existing materials.

In the last 60 years, many efforts were put for the development of materials applied in gas turbines by improving the processing methods and optimizing the chemical compositions. The nickel-based superalloys that can exploit in hot components of gas turbines always contain a certain amount of Al and Cr, which can form protective oxides of Al_2O_3 and Cr_2O_3 preventing further removal of the material in the aggressive environments. However, during long-term exposure, the depletion of the oxide layers or evaporation of Cr_2O_3 may lead to further depletion of the alloying elements. This finally causes material degradation and will eventually influence the mechanical properties of the alloys.

2 Characteristics of Superalloys

Superalloys has a wide application in aircraft gas turbines (disks, casings, combustion chambers, exhaust systems, thrust reversers, vanes, cases, blades, bolts and shafts), steam turbine power plants (blades, stack gas re-heaters), nuclear power systems (valve stems, springs and control rod drive mechanisms), metal processing (casting dies, hot-work tools and dies), reciprocating engines (turbochargers, hot plugs and exhaust valves), space vehicles (aerodynamically heated skins and ducting rocket engine parts), medical applications (prosthetic devices and dentistry uses), heat-treating equipment (furnace mufflers, conveyor belts, trays, fixtures and fans), petrochemical and chemical industries (bolts, fans, reaction vessels, valves, piping and pumps) and in many others. Due to its exceptional importance in aircraft and gas turbine engines, lot of research is being done on the elemental composition of the nickel-based alloys which will impart the desired properties for the specific high-temperature applications. Even after long exposure times above 650 °C (1200 °F), the superalloys have the ability to maintain their strength to the highest extent leading to many applications [1].

Superalloys constitute the major alloying elements like Fe, Ni, Co, Cr and are based on Group VIIIB elements and usually consists smaller amounts of W, Mo, Ta, Nb, Ti and Al. The heat-resistant superalloys are broadly classified into nickel-based, iron-based and cobalt-based.

Superalloys constitute face-centred cubic nickel as the primary constituent and may be up to a weight per cent of 40 and additions of five to ten other elements. In nickel-based heat-resistant alloys, the nickel weight per cent may be in the range of 37–80. Superalloys can also be manufactured through cast and in powder metallurgy forms. Cast alloys are rather used in aero engines due to better creep properties with the presence of large grains and accordingly suit them as one of the exceptional alloys for stress rupture limitations in typical applications. Table 1 shows the general composition of alloying elements in three different categories [2].

Most notable characteristic of alloys based on Ni is its usage in the load-bearing applications at temperatures of 80% of their melting temperatures, which is superior to all other alloys used in engineering. These alloys become stronger at high-temperatures, provide good corrosion and oxidation resistance, also have good resistance to rupture and creep. Even these will be best suited to the components of gas turbines such as turbine wheels and blades, and also turbine disks which will be affected by long-term rotational stresses at higher temperatures, i.e. superalloys exhibit good fatigue behaviour at very higher temperatures [3]. These also should maintain excellent chemical and mechanical properties at these temperatures besides withstanding the mechanical forces. Rotating hundreds of times per second in addition to the higher loads in the blades of modern jet engine is one of the most extreme environments, which is very difficult for any of the engineering materials to work, but this has been possible with the advent of Ni-based superalloys.

Table 1 Weight per cent of alloying elements in Fe-Ni, Co- and Ni-based superalloys

Fe-Ni-based										
Element	Ni	Fe	Cr	Ti	Al	Mo	Nb	Co	W	C
Weight %	9–44	29–67	0–25	0–3	0.3–1	0–3	0–5	0–20	0–2.5	<0.35
Co-based										
Element	Co	Ni	Cr	Ti	Al	Mo	Nb	Fe	W	C
Weight %	40–62	0–35	19–30	0–3	0–0.2	0–10	0–4	0–21	0–15	0–1
Ni-based										
Element	Ni	Ti	Cr	Co	Al	Mo	Nb	W	C	
Weight %	37–79.5	0–5	5–22	0–20	0–6	0–28	0–5.1	0–15	<0.30	

Also, minor proportions of Zr, Mn, La, Cu, Si, Mg, B, Ce, Hf, V and Ta can be included

3 Selection of Superalloys

Alloy selection is generally directed at optimizing the properties like creep strength, tensile strength, low- and high-cycle fatigue responses, fracture toughness, creep rupture behaviour and cyclic rupture behaviour [4].

Commonly controlled alloy elements could be as many as 14 or so in some alloys. Nickel and cobalt as well as chromium, tungsten, molybdenum, rhenium, hafnium and other elements used in superalloys are often expensive [2]. Steels will be affected with higher corrosion at elevated temperature applications. Ordinary steels and titanium alloys are not suitable when temperatures go above about 1000 °F (540 °C). To achieve highest temperatures with strength as the major consideration, nickel-based superalloys will be the best choice. Most wrought superalloys have considerable amounts of chromium in order to provide corrosion resistance. The oxidation resistance of nickel superalloys enhanced with the decrease in chromium content and increase in aluminium content. In the nickel-based superalloys, aluminium content increases with the reduction in chromium to keep the oxidation resistance similar to that of original levels or can be even increased. Refractory metals possess high melting points than superalloys, but they do not exhibit similar characteristics as that of superalloys [5]. Figure 1 shows the recent applications of Ni-based superalloys.

The main reason for the usage of superalloys aerospace gas turbine engine parts is because of high yield and ultimate tensile strength, good resistance to corrosion and oxidation in addition to excellent creep resistance at peak temperatures as these are exposed to high-service temperatures.

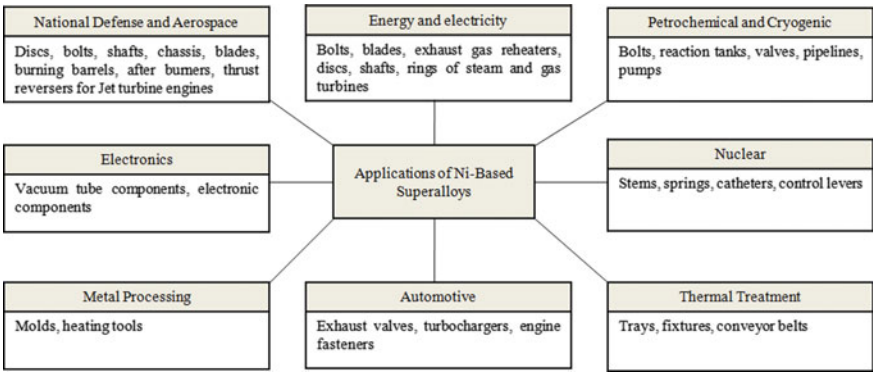

Fig. 1 Applications of Ni-based superalloys

4 Properties of Nickel-Based Alloys

Ni-based superalloys are principally utilized for the production of turbine blades used in turbine engines owing to their exceptional performance of mechanical properties at peak temperatures. Nickel-based superalloys are also capturing a lot of significance, with their applications in marine, chemical industries, boilers, aerospace and nuclear reactors. Many characteristics together with superior mechanical and chemical properties at higher temperatures, high melting point, high toughness and ductility, resistance to corrosion, resistance to thermal shocks, thermal fatigue are primarily liable for wide spectra of applications. These alloys are applicable in industrial chamber applications like muffles/liners in extreme temperature kilns, ball bearings, bearing races, springs, heart valves, etc. Some of the physical properties of nickel are represented in Table 2 [2].

The properties of the Ni-based superalloys can be adapted for specific applications by the addition of exotic materials like metals, metalloids and non-metals. In general, aluminium, niobium, chromium, cobalt, tantalum, molybdenum, iron, tungsten, zirconium, titanium, rhenium, vanadium, yttrium, boron, carbon or hafnium are used. These additions in proper proportions will optimize the properties required for high-temperature applications [6].

Titanium, aluminium and steel alloys loose their specific strength at higher temperatures and will be more ductile in nature. But nickel-based alloys exhibit better

Table 2 Physical properties of nickel

Property	Value
Atomic weight	58.71
Crystal structure	FCC
Lattice constant at 25 °C (nm)	0.35238
Density at 20 °C (g cm^{-3})	8.908
Melting temperature (°C)	1453
Specific heat at 20 °C (kJ kg^{-1} K^{-1})	0.44
Thermal conductivity (Wm^{-1} K^{-1})	
at 100 °C	82.8
at 300 °C	63.6
at 500 °C	61.9
Electrical resistivity at 20 °C (μΩ cm)	6.97
Coercive force (Am^{-1})	239
Saturation magnetization (T)	0.617
Curie temperature (°C)	353
Residual magnetization (T)	0.300
Modulus of elasticity (GPa) in tension	206.0
Shear modulus (GPa)	73.6
Poisson's ratio	0.30

specific strength with the raise in temperature and can withstand up to 0.8 times of its melting point temperature, and hence 40% of the aircraft engine is being manufactured with nickel-based alloys [7].

5 Effects of Alloying Elements in Nickel Alloys

For superalloys, nickel, chromium, iron and molybdenum are considered to be the primary alloying elements. Also, elements such as aluminium, tungsten, copper, carbon, titanium and sulphur in small proportions will also impact some of the characteristics of the material to be alloyed. Nickel in general enhances strength at higher temperatures, resistance to carburization, oxidation, nitridation and halogenation. It provides metallurgical stability too and improves stress corrosion and cracking at elevated temperatures. Alloying with chromium enhances the resistance to higher temperature oxidizing and sulphidation. The presence of molybdenum considerably enhances the resistance to non-oxidizing acids, like hydrochloric (HCl), hydrofluoric acid (HF) and phosphorous acid (H_3PO_4). Iron controls thermal expansion and improves resistance to carburization. Tungsten additionally provides resistance to localized corrosion, imparts strength and weldability. Carbon will hamper corrosion resistance however adds strength at higher temperatures. Aluminium as an alloying element forms aluminium oxide scale at higher temperature and provides resistance to attack by oxidization, chlorination and carburization. Along with Ti, it upholds age hardening in certain alloys. The susceptibility to intergranular corrosion can be reduced by adding Ti with C, as it forms chromium carbide after heat treatment [8, 9]. The resistance to sulphidation and carburization by the addition of Co due to the solubility of carbon in nickel-based alloys [10]. A consolidated list of materials that provide the basic mechanical properties like hardenability, strength, toughness and machinability when alloyed with different metals is shown in Table 3 [3].

Minor amounts of the rare-earth metals like yttrium improves the resistance to oxidation either the alloys based on nickel or cobalt. Yttrium provides the alloy with comprehensively persistent aluminium oxide film. This film provides resistance from oxidation, carburization and chlorine attack through 2200 °F (1205 °C). Because of the γ' nature of the alloy, it has excellent strength properties through 1700 °F (925 °C) [11].

Main requirements in materials for gas turbines and related high-temperature applications are high melting point, micro-structural stability at high temperature, high-temperature performance, good oxidation/corrosion behaviour, low density, high stiffness and easy to process. Table 4 gives the information pertaining to the properties that can be imparted by adding alloying elements with nickel in superalloys [12, 13].

In most of the materials, with the increase in temperature, there may be a fall in the yield stress, as the metal becomes softer at higher temperatures. As observed in Al-Ni-based superalloys, the yield stress will be constant initially and then increases gradually to a temperature of about 700 °C, providing for its use in high-temperature applications.

Table 3 Materials that impart different mechanical properties

Hardenability	Strength	Toughness	Machinability
Molybdenum	Chromium	Calcium	Lead
Carbon	Cobalt	Cerium	Manganese
Titanium	Manganese	Chromium	Phosphorus
Manganese	Molybdenum	Magnesium	Selenium
Chromium	Copper	Molybdenum	Sulphur
Boron	Carbon	Nickel	Tellurium
Phosphorus	Nickel	Niobium	
	Niobium	Tantalum	
	Phosphorus	Tellurium	
	Silicon	Vanadium	
	Tantalum	Zirconium	
	Tungsten		
	Vanadium		

Table 4 Properties imparted by addition of alloy elements in Ni

Nickel when alloyed with	Provides
Chromium, Molybdenum, Iron, Tantalum, Tungsten	Higher strength
Boron, Zirconium, Carbon	Creep resistance
Chromium, Aluminium, Tantalum	Oxidation resistance
Aluminium, Titanium	High temperature strength
Hafnium	Ductile at intermediate temperatures, Prevents oxides flaking

Oxidation and hot corrosion are because of the alloy degradation modes that relate with atmosphere and comparatively tough to manage. Dangerous high-temperature corrosion (hot corrosion) is because of the contaminants in environment like sulphur, sodium, halides and vanadium. Owing to the catastrophic failure of the components, this hot corrosion will reduce rapidly and enhance the load-carrying capability of the material. Vast studies have been made by the researchers to study the phenomena of hot corrosion, particularly in aircraft turbine engines [14–16].

Due to the unique presence of the combined mechanical and physical properties, nickel-based alloys are considered to be the maximum composition as structural materials in the turbine engines. In Table 5, the properties of superalloys are listed. In the development of nickel-based superalloys, optimization of the tensile properties, fatigue, creep and cyclic growth is of paramount importance [17, 18].

With a FCC matrix stabilizer, the elements like chromium, molybdenum, tungsten, cobalt, iron, tantalum, tungsten and rare-earth metal like rhenium will act as solution strengtheners in solid phase. Carbide formers in nickel-based alloys are tantalum,

Table 5 Physical properties of nickel-based superalloys

Properties	Typical ranges and values
Density	7.7–9.1 g/cm^3
Melting point	1320–1450 °C
Elastic modulus	Room temperature: 210 MPa
	800 °C: 160 MPa
Thermal expansion coefficient	8–18 × 10^{-6}/°C
Thermal conductivity	Room temperature: 11 W/mK
	800 °C: 22 W/mK

tungsten, molybdenum, niobium, titanium and hafnium. The elements that can be used for the raise in solvus temperature of precipitate hardening and intermetallic compounds are cobalt, titanium, aluminium and niobium. Oxidation resistance can be imparted with the elements like chromium, aluminium, yttrium, lanthanum and cerium. To refine the grain boundaries, boron, zirconium, carbon and hafnium can be utilized. Boron and tantalum can be used to impart creep properties, whereas cobalt, chromium and silicon can provide sulphidation resistance. As the components manufacture using nickel-based superalloy can withstand callous environments, they are the idyllic materials in various applications like valves, heat processing equipments, marine assemblies, processing of the chemicals, pumps, aerospace, military, oil and gas industries [19]. Superalloys are the only materials that can exhibit the desired mechanical properties with increase in temperature. There is a gradual increase within the rotary engine entry temperatures, and this phenomenon is anticipated to continue. Therefore, there is a need to develop superalloys to withstand average temperatures of 1050 °C and as high as 1200 °C. This may be nearly equal to 80% of the melting point temperature of the material.

5.1 Strengthening of Solid Solution

Chromium and aluminium are vital as they provide oxidation resistance. Minute amount of yttrium facilitates the oxide scale for sticking to the substrate. The higher creep strength and ductility are due to the reduction of grain boundary changes and the mechanism of failure is because of grain decohesion. Also, the carbide formers like W, Mo, Cr, Co, Nb, C, Ti, Ta and Hf will have their presence in these alloys. The slippery at grain boundary is due to the formation of precipitates of carbides at the grain boundaries. Cobalt, niobium, iron, tungsten, chromium, tantalum, aluminium, vanadium, molybdenum and titanium also are solid solution strengtheners, both in γ and γ' [20].

High percentage of disordered solid solution elements like Cr, Mo, Co and W were present in the γ-phase with a continuous matrix of face-centred cubic phase [21]. This is soft in nature. In γ' phase, the principal strengthening phase is Ni_3

(Al, Ti), which is considered as a precipitating phase in which the crystal planes of the precipitate are in accordance with the γ matrix. This is represented in Fig. 2. The phase precipitates homogeneously all through the matrix and have long-time stability due to its nearness in matrix/precipitate lattice parameter (~ 0–1%) besides the chemical compatability. The γ′-phase is somewhat hard in nature [22].

At high temperatures, solid solution strengthening is mainly due to elastic (misfit) and modulus interactions between matrix and foreign atoms, while other contributions can be ignored [21], interstitials usually have a stronger strengthening effect than substituted atoms (relative per unit concentration), due to the tendency to produce non-spherical distortion in the lattice.

In Table 6, a few elements typically found in superalloys are listed together with their atomic radii and elastic properties. In a Ni-30Cr matrix, best candidates based on differences in size and moduli are primarily Re, W and also Nb, Mo and Ta [23–25]. Each increment of 10 wt% of tungsten and molybdenum decreases the rate of creep

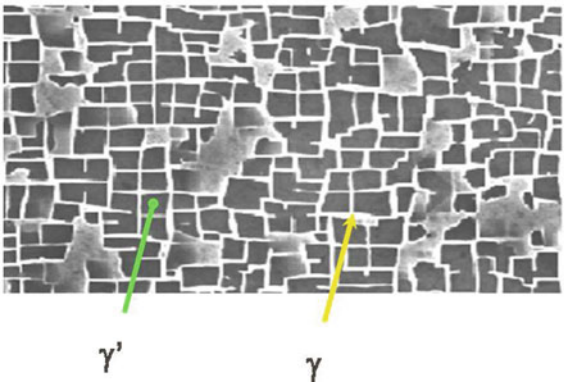

Fig. 2 γ-phase and γ′-phase [22]

Table 6 Relevant properties of some elements for solid solution strengthening

Element	Atomic radius (Å)	Young's modulus (GPa)	Shear modulus (GPa)
Ni	1.62	207	76
N	0.75	–	–
Co	1.67	211	83
Fe	1.72	200	81
Al	1.82	68	25
Cr	1.85	279	115
Re	1.97	469	176
Mo	2.01	330	120
W	2.02	400	175
Ta	2.09	185	69
Nb	2.09	103	37

such that tungsten strengthens to a fairly greater extent than molybdenum does [26], which is probably due to the difference in their elastic properties. Re has also been studied extensively as solid solution strengthener in nickel-bases alloys, and it is also found to dramatically slow down diffusion at high temperatures [25]. Ta and Nb are often alloyed in order to precipitate intermetallic precipitates. If these elements are to be used as solid solution strengtheners, then it is also important to consider the relative stability of their nitrides. Ta and Nb form very stable nitrides. Even though, Mo and W form stable carbides, they are not very strong nitride formers. In case of Ta, for instance, in a Ni30Cr alloy containing nitrogen, the matrix will be depleted because of the precipitation of nitrides [27].

Nickel forms a primary solid solution with copper and can be soluble completely with iron. 35% Cr, 20% each of W and Mo, and 5–10% each of manganese, titanium, aluminium and vanadium can be used to dissolve the same. The tough, ductile face centred cubic lattice matrix will dissolve the elements is varied combinations to form solution hardening along with improved oxidation and corrosion. The relation between the difference of atomic size and between the nickel and its alloying elements and the degree of solution hardening decides the ability of solute to hamper with the motion of dislocation [28].

The elements from Groups II, III and IV, like boron and carbon, tend to form borides and carbides and segregate at grain boundaries. It should be emphasized here that the grain boundary strengthening elements are favoured in polycrystalline alloys, but they are suppressed in single-crystalline materials [29].

γ-phase exhibits FCC structure, and in general, it forms a continuous matrix phase with other phases residing inside it. The elements consisting of γ matrix like iron, cobalt, chromium and some refractory metals like molybdenum and tungsten belongs to Group V, VI and VII. The γ' forms as a precipitate phase with FCC structure and is observed as spherical or cuboidal particles. The elements partitioning to γ' mainly belong to Group III, IV and V such as Al, Ti, Nb and Ta. The γ' precipitates are coherent with matrix and contribute to the strength of the precipitation hardened alloys [30].

The alloys might be improved by adjusting their composition; however, they can also be improved by innovations in processing, such as directional solidification or single crystal technology [31]. Unlike the polycrystalline alloys, the single-crystalline alloys are free from grain boundaries. The lack of grain boundaries leads to an increase in the incipient melting temperature, and therefore, it helps to get fine-scale precipitation of γ' when heat treated at 1240–1330 °C. In the applications for gas turbine blades, the lack of grain boundaries improves the creep and fatigue performance in service [32].

5.2 Carbides

Even though nickel is not carbide former, it can dissolve many elements enabling it to form carbides in the nickel constituent alloys (MC, M_6C, M_7C_3, $M_{23}C_6$ in which

M stands for alloying element). W, Ta, Ti, Mo, Nb forms MC carbides which are typically large and undesirable. Mo and W form M_6C carbides which can precipitate as small platelets in the grain boundaries. Cr forms M_7C_3 and can be useful when precipitated as discrete particles. Cr, Mo and W form $M_{23}C_6$ which can enhance creep rupture properties [33].

Ni-based superalloys are basically preferable when used at 760–890 °C, whereas Fe–Ni superalloys at the lower temperatures of 650–815 °C. Due to the absence of γ'-phase, cobalt-based alloys have still lower strength characteristics than Ni superalloys at medium and lower temperatures [34]. The relationship of creep strength for Fe-, Ni- and Co-based superalloys is shown in Fig. 3 with different types of strengthening [35].

Also, the stress rupture strength of the superalloys based on nickel are outstanding when compared with other materials used in the structures of aircraft like Mg, Ti and Al alloys as shown in Fig. 4 [36]. Rapid creep is observed in Mg, Al and Ti alloys above 100, 150 and 350 °C, whereas Ni-based alloys can resist even when it is used at a temperature of 850 °C.

Attributable to their splendid properties, like thermal stability, corrosion resistance, strength to fatigue under adverse environments, aero engines are made up of Ni-based superalloys by a weight per cent of 50 when compared to other materials [37–42]. Nonetheless, these materials represent a significant test for machining

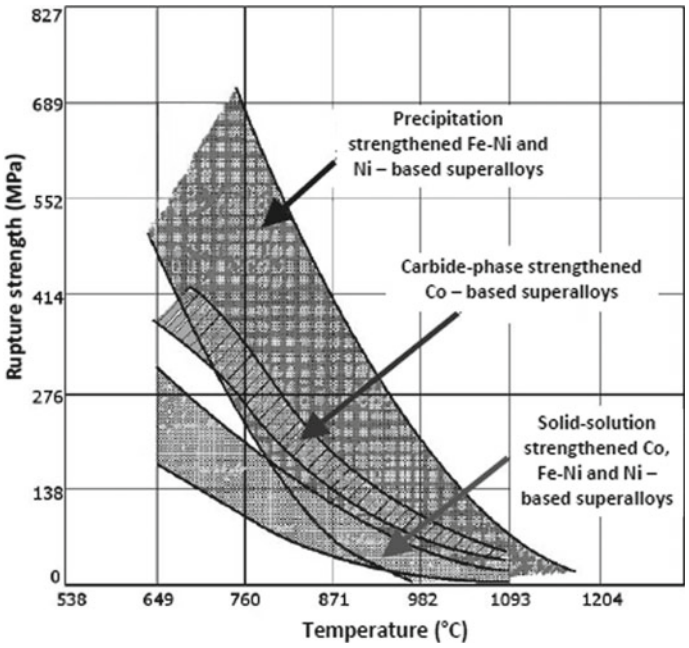

Fig. 3 Stress rupture of wrought Ni, Fe–Ni and Co-based superalloys with the strengthening mechanism [35]

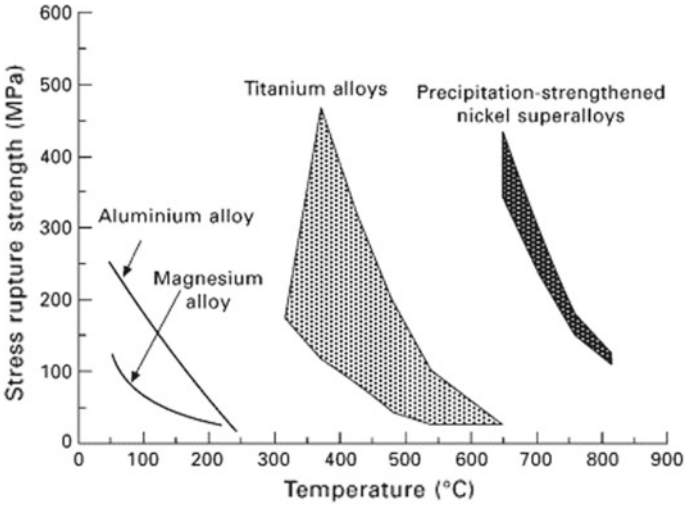

Fig. 4 Stress rupture characteristics of Mg, Ti, Al alloys and Ni-based superalloys [36]

because of its low thermal conductivity, hot hardness, tendency to work harden, existence of carbide particles in the microstructure, tool material chemical affinity [43–47]. Hence, noteworthy research consideration is drawn towards the manufacture of air craft engines and some other critical parts where safety is a prime consideration. Due to the formation of carbides in the microstructure of nickel-based alloys, it is difficult to machine [48]. The major components of gas turbine like compressor, combustor and turbine are manufactured through precision casting and then excess material can be removed through grinding, thereby desired surface finish can be obtained. Other machining processes may include turning, milling, drilling, boring and shaping of the spline couplings [49–51]. At present, electrical discharge machining, laser machining and electrochemical machining are being employed in many industries for hole-making processes besides twist drilling [52].

5.3 Oxidation Behaviour

The properties of Ni-based superalloys are often tailored to an explicit extent through the addition of the many different elements. Table 7 shows the effect of adding different alloying elements to nickel [53]. Alloying will improve the oxidation resistance of pure metals. With 10–30% chromium in nickel, iron or cobalt, the ensuing oxidation resistance is adequate at temperatures of use. An inclusion of 15% aluminium to iron additionally improves its oxidation resistance. Additions of Mo, V, Hf, W, Ti, Zr and S have considerably improved the oxidation resistance by forming a lot of stable complicated oxides [54]. Additions of yttrium in about less than 1% to chromium, scale back nitrogen penetration. Alloying will enhance the oxidation resistance of

Table 7 Alloying elements for various effects

Effect	Alloying elements
Strengtheners of solid solution	Mo, Cr
Stabilizers of FCC matrix	W, C, Ni
Carbide formers	Cr, Ti, Mo
γ' Ni_3 (Al, Ti) formers	Ti, Al, Ni
Hexagonal η (Ni_3Ti) formers	Zr, Al
Sulfidation resistance	Cr
Precipitate hardeners	Nb, Al, Ti
Rupture ductility	B
Corrosion resistance	La, Y
Oxidation resistance	Cr

metals that develop low-melting volatile oxides (rhenium, tungsten, molybdenum and vanadium) [55].

Figure 5 shows the composition of alloying elements in some of the commercially available nickel-based superalloys.

The variation of ultimate tensile strength (MPa), 0.2% yield strength (MPa), elongation and stress rupture at 1000 h (MPa) characteristics with change in temperature for Haynes-556, Haynes HR-120, Hastelloy X and Haynes-230 are shown in Fig. 6.

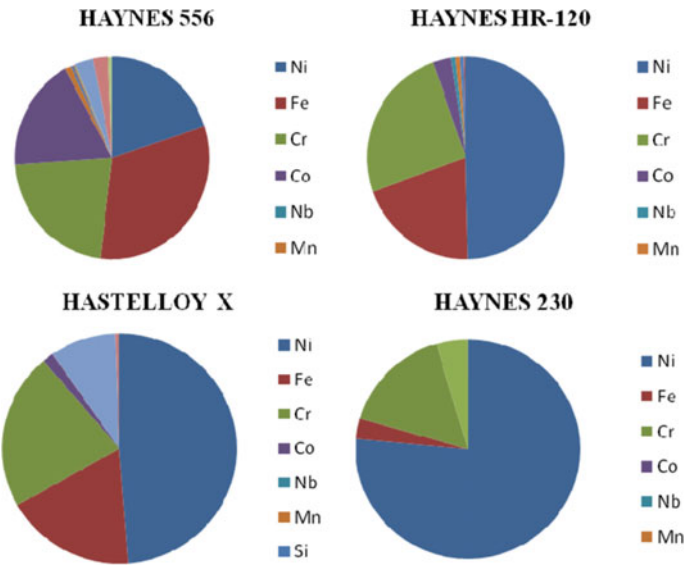

Fig. 5 Composition of various Ni-based superalloys

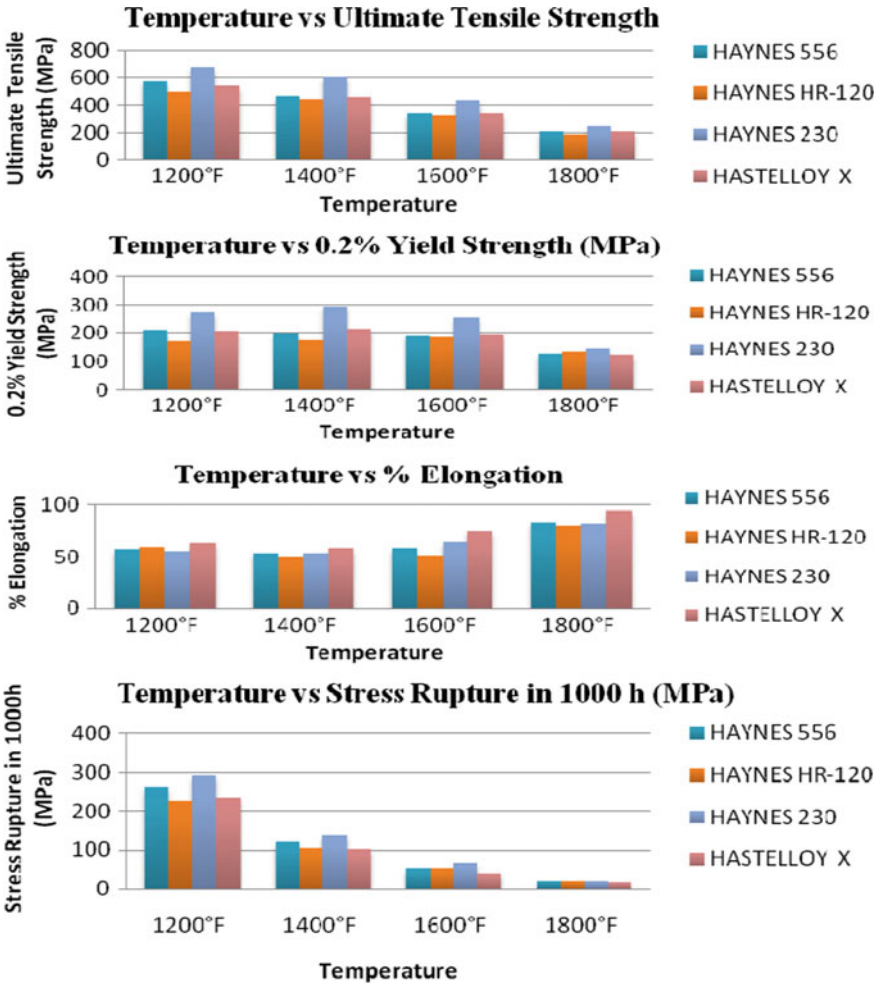

Fig. 6 Composition of various Ni-based superalloys

The Ni alloy with maximum composition of Fe, Cr and Co gives better mechanical properties when compared to other alloys even at higher temperatures.

At present, ruthenium was also being alloyed with nickel-based superalloys to forestall the formation of harmful topologically close-packed phases. Also, Ru can strengthen γ-phase and γ'-phase in comparison with Re due to a weaker partitioning of the γ matrix [39, 40, 56]. Table 8 presents the composition of the alloying elements for the formation of carbides and oxide layers.

The grain growth and mechanical deformation are closely related to surface roughness. This also will cause strain hardening and induce residual stresses [35, 57]. Shape parameters, fatigue durability and surface textures of nickel-based superalloy also need to be addressed through further investigations [52]. 0.05–0.2% carbon content

Table 8 Element compositions

Alloying elements	Composition range	Effect on properties
Mo	0–12	Due to the formation of carbides, these elements will enhance the mechanical strength of base alloy. Generally, these elements are at substitutional positions for solution strengthening
Ta	0–12	
W	0–12	
Nb	0–5	
Ti	0–6	
Si	0–5	Forms oxide scale on the surface of the alloys to protect surface
Al	0–6	
Cr	5–25	

can be added along with the refractory and reactive elements like tantalum, titanium, and hafnium, this forms carbides such as TaC, TiC or HfC. These carbides will decompose during heat processes and leads to lower carbides which will generate grain boundaries [17].

6 Future Work

The necessity of materials to work in the hot gas regions of gas turbines, like the blades/vanes, is very demanding. They need to be competent to operate at peak temperatures under both high and fluctuating stresses, and at the same time withstand severe operating environments. Due to the poor quality of fuels often used in industrial gas turbines, the turbine blades are exposed to hot combustion gases containing contaminants such as a mixture of inlet gases, combustion fuel, sulphur containing species, water vapour etc. As a result, the gas turbine materials will not only be oxidized, but could also suffer the more deleterious hot corrosion [58].

The plan and improvement of newer materials to cater very high-temperature needs is constantly a challenge between accomplishing better oxidation resistance and also creep strength and keeping up sufficient pliability and strength at both low and high temperatures. Many of the constituent elements can dissolve in Ni-based superalloys and maintain a high degree of structural stability. Further, this review can be used to focus on the development of Ni-based superalloys, by tailoring the composition, morphology and volume fraction of the major phases to obtain an optimum balance of tolerance to low and high temperatures along with considerable creep and oxidation resistance.

The machined surface integrity of these superalloys is a significant as it persuades the performance of material. As these materials metallurgically designed to have significant strength at peak temperatures, the stresses induced during machining are also high. Also, these will work harden easily leading to rise in diffusion wear, and may lead to formation of heavy burrs. Compositional changes can be made to overcome these challenges.

Artificial intelligence tools can be employed to develop new Ni-based superalloys for turbine applications, which may presumably satisfy all target properties at the same time [59]. The aim is to predict the composition and process variables that may provide a material satisfying the multi-criteria target specification. Initially, a predictive model is to be constructed for every property as a function of the composition. Then, the probability that a supposed composition suits the desired specification will be computed from the space search of the composition.

7 Conclusion

Tantalum, aluminium and titanium provide strength to the alloy, as they form γ'-phase. The resistance to creep can be enhanced by strengthening the solid solution of γ-phase with the addition of minor amounts of Re, W and Mo. Re increases the creep properties. Also, Cr, Co, W, Ta also does the same by addition of small amounts, else leads to microstructure instability. The fraction of Re can improve the hardness of the γ-phase. Al, Cr and Co can be added to improve resistance to oxidation, sulphidation and corrosion. Zr, Hf, B and C form borides and carbides at the grain boundaries in poly-crystal superalloys for strengthening of grain boundary. As the grain boundaries are not present in the single-crystal superalloys, the fractions Zr, Hf, B and C are lower, or not present in the single-crystal superalloys. In most of the materials, with the increase in temperature, there may be a fall in the yield stress, as the metal becomes softer at higher temperatures. But, nickel-based superalloys consisting γ'-phase has an intermetallic compound Ni_3 (Al,Ti) and are temperature resistant. If there is a need for higher strengths at lower temperatures, such as in turbine disk applications, γ''-phase can be used to strengthen the alloys by adding Nb or V forming Ni_3Nb or Ni_3V. The melting point of the Ni-based superalloys can be improved with the simplified alloy chemistry. So, alloys can be developed through varying compositions of the elements through modelling to cater the needs of modern high-temperature applications.

References

1. Nowotnik A (2016) Nickel-based superalloys. Reference module in materials science and materials engineering. https://doi.org/10.1016/b978-0-12-803581-8.02574-1
2. Donachie MJ, Donachie SJ (2002) Superalloys. A technical guide, 2nd edn. ASM International, Cleveland
3. Nunes R UFRGS, Adams JH Eagle-Picher Industries, Inc., Ammons M Martin Marietta Energy Systems (1990) Metals handbook, vol 2, 10th edn. ASM International, Cleveland
4. Singh S (2016) Super alloys technical report. ResearchGate Publications. https://doi.org/10.13140/rg.2.1.2385.0009
5. Palakudtewar RK, Gaikwad SV (2014) Dry machining of superalloys: difficulties and remedies. Int J Sci Res 3(7):277–282

6. Reed RC, Rae CMF (2014) Physical metallurgy of the nickel-based superalloys. In: Physical metallurgy, 5th edn. pp 2215–2290. https://doi.org/10.1016/b978-0-444-53770-6.00022-8
7. Sims CT, Stoloff NS, Hagel WC (1987) Superalloys II: high-temperature materials for aerospace and industrial power. Wiley, Hoboken
8. Appa Rao G, Kumar M, Srinivas M, Sarma DS (2003) Effect of standard heat treatment on the microstructure and mechanical properties of hot isostatically pressed superalloy Inconel 718. Mater Sci Eng A 355(1–2):114–125. https://doi.org/10.1016/s0921-5093(03)00079-0
9. Monajati H, Jahazi M, Bahrami R, Yue S (2004) The influence of heat treatment conditions on γ' characteristics in Udimet 720. Mater Sci Eng A 373(1–2):286–293. https://doi.org/10.1016/j.msea.2004.01.027
10. Zhang ZJ, Zhang P, Li L, Zhang ZF (2012) Fatigue cracking at twin boundaries: effects of crystallographic orientation and stacking fault energy. Acta Mater 60:3113–3127. https://doi.org/10.1016/j.actamat.2012.02.016
11. Fedelich B, Epishin A, Link T (2012) Rafting during high temperature deformation in a single crystal superalloy: experiments and modeling. Superalloys. https://doi.org/10.1002/9781118516430.ch54
12. Chen Z (2014) Surface integrity of broached Inconel 718 and influence of thermal exposure. Linköping studies in science and technology thesis no. 1676
13. Thellaputta GR, Chandra PS, Rao CSP (2017) Machinability of nickel based superalloys: a review. Mater Today Proc 3712–3721. https://doi.org/10.1016/j.matpr.2017.02.266
14. Goward GW (1998) Progress in coatings for gas turbine airfoils. Surf Coat Technol 108–109. https://doi.org/10.1016/s0257-8972(98)00667-7
15. Stringer J (2016) High temperature corrosion of superalloys. Mater Sci Technol 3(7):482–493. https://doi.org/10.1080/02670836.1987.11782259
16. Rapp RA (1986) Chemistry and electrochemistry of the hot corrosion of metals. Whitney award lecture, pp 568–577. https://doi.org/10.5006/1.3583026
17. Satyanarayana DVV, Eswara Prasad N (2016) Nickel-based superalloys. In: Aerospace materials and material technologies. Springer, Berlin, pp 199–228
18. Pollock TM, Field RD (2002) Dislocations and high temperature plastic deformation of superalloy single crystals. In: Dislocations in solids, vol 11, pp 547–618. https://doi.org/10.1016/s1572-4859(02)80014-6
19. Reed RC (2006) The superalloys—fundamentals and applications, 1st edn. Cambridge University Press, Cambridge
20. Sarosi PM, Wang B, Simmons JP, Wang Y, Mills MJ (2007) Formation of multimodal size distributions of γ' in a nickel-base superalloy during interrupted continuous cooling. Scripta Mater 57(8):767–770. https://doi.org/10.1016/j.scriptamat.2007.06.014
21. Aba-Perea PE, Pirling T, Withers PJ, Kelleher J, Kabra S, Preuss M (2016) Determination of the high temperature elastic properties and diffraction elastic constants of Ni-base superalloys. Mater Des 89:856–863. https://doi.org/10.1016/j.matdes.2015.09.152
22. Benghersallah M, Boulanouar L, Lecoz G, Dudzinski D (2003) Dry high speed milling of nickel-based superalloy. Mechanika 19(2):223–228. https://doi.org/10.5755/j01.mech.19.2.4149
23. Kirka M (2014) Thermomechanical behavior of a directionally solidified nickel-base superalloys in the aged state. Georgia Tech theses and dissertations, Georgia Institute of Technology
24. Matsuo T, Ueki M, Takeyama M, Tanaka R (1987) Strengthening if nickel base superalloys for nuclear heat exchanger application. J Mater Sci 22:1901–1907. https://doi.org/10.1007/BF01132914
25. Ko HS, Paik KW, Park LJ, Kim YG, Tundermann JH (1998) Influence of rhenium on the microstructures and mechanical properties of a mechanically alloyed oxide dispersion-strengthened nickel base superalloy. J Mater Sci 33(13):3361–3370. https://doi.org/10.1023/A:1013293515482
26. Lin YC, Li L, He D-G, Chen M-S, Liu GQ (2017) Effects of pre-treatments on mechanical properties and fracture mechanism of a nickel-based superalloy. Mater Sci Eng A 679:401–409. https://doi.org/10.1016/j.msea.2016.10.058

27. Jiang T, Chen LB, Jiang F, Chai HP, Sun J (2016) Microstructural evolution and mechanical properties of a nickel-based superalloy through long-term service. Mater Sci Eng A 656. https://doi.org/10.1016/j.msea.2016.01.037
28. Long Z, Liu X, Yang W, Chang KM, Barbero E (2004) Thermodynamic assessment of liquid composition change during solidification and its effect on freckle formation in superalloys. Mater Sci Eng A 386:254–261. https://doi.org/10.1016/j.msea.2004.07.038
29. Chapman L (2004) Applications of high temperature DSC technique to nickel based superalloys. J Mater Sci 39(24):7229–7236. https://doi.org/10.1023/B:JMSC.0000048736.86794.12
30. Sato A, Moverare JJ, Hasselqvist M, Reed RC (2012) On the mechanical behavior of a new single crystal superalloy for industrial gas turbine applications. Metall Mater Trans 43(7):2302–2315. https://doi.org/10.1007/s11661-011-0995-2
31. Reed RC, Tao T, Warnken N (2009) Alloys-by-design: application to nickel-based single crystal superalloys. Acta Mater 57(19):5898–5913. https://doi.org/10.1016/j.actamat.2009.08.018
32. Zao X, Dang Y, Yin H, Lu J (2016) Effect of heat treatment on the microstructure of a Ni–Fe based superalloy for advanced ultra-supercritical power plant applications. Prog Nat Sci Mater Int 26(2):204–209. https://doi.org/10.1016/j.pnsc.2016.03.013
33. Clemens ML, Price A, Bellows RS (2003) Advanced solidification processing of an industrial gas turbine engine component. JOM 27–31. https://doi.org/10.1007/s11837-003-0156-1
34. Bhadeshia HKDH (1997) Recrystallisation of practical mechanically alloyed iron-base and nickel-base superalloys. Mater Sci Eng A 223(1–2):64–77. https://doi.org/10.1016/S0921-5093(96)10507-4
35. Dye D, Roder BA, Tin S, Rist MA, James JA, Daymond MR (2004) Modeling and measurement of residual stresses in a forged IN718 superalloy disc. Superalloys. TMS (The Minerals, Metals & Materials Society) 315–322. https://doi.org/10.7449/2004/superalloys_2004_315_322
36. Das N (2010) Advances in nickel-based cast superalloys. Trans Indian Inst Met 63:265–274. https://doi.org/10.1007/s12666-010-0036-7
37. Ulutan D, Ozel T (2010) Machining induced surface integrity in titanium and nickel alloys: a review. Int J Mach Tools Manuf 250–280. https://doi.org/10.1016/j.ijmachtools.2010.11.003
38. Miller S (1996) Advanced materials means advanced engines. Interdisc Sci Rev 21(2):117–129. https://doi.org/10.1179/isr.1996.21.2.117
39. Ezugwu EO, Bonney J, Yamane Y (2003) An overview of the machinability of aero engine alloys. J Mater Process Technol 134(2):233–253. https://doi.org/10.1016/S0924-0136(02)01042-7
40. Pervaiz S, Rashid A, Deiab I, Nicolescu M (2014) Influence of tool materials on machinability of titanium- and nickel-based alloys: a review. Mater J Mater Manuf Process 29(3):219–252. https://doi.org/10.1080/10426914.2014.880460
41. Ezugwu EO (2005) Key improvements in the machining of difficult-to-cut aerospace superalloys. Int J Mach Tools Manuf 45:1353–1367. https://doi.org/10.1016/j.ijmachtools.2005.02.003
42. M'Saoubi R, Axinte D, Soo SL, Nobel C, Attia H, Kappmeyer G, Engin S, Sim WM (2015) High performance cutting of advanced aerospace alloys and composite materials. CIRP Ann 64(2):557–580. https://doi.org/10.1016/j.cirp.2015.05.002
43. M'Saoubi R, Outeiro JC, Chandrasekaran H, Dillon OW Jr, Jawahir IS (2008) A review of surface integrity in machining and its impact on functional performance and life of machined products. Int J Sustain Manuf 1:203–236. https://doi.org/10.1504/IJSM.2008.019234
44. Guo YB, Li W, Jawahir IS (2009) Surface integrity characterization and prediction in machining of hardened and difficult-to-machine alloys; a state-of-the-art research review and analysis. Mach Sci Technol 13(4):437–470. https://doi.org/10.1080/10910340903454922
45. Wu Q (2007) Serrated chip formation and tool-edge wear in high-speed machining of advanced aerospace materials. Utah State University
46. Li ZY, Wei XT, Guo YB, Sealy MP (2015) State-of-art, challenges, and outlook on manufacturing of cooling holes for turbine blades. Mach Sci Technol 19(3):361–399. https://doi.org/10.1080/10910344.2015.1051543

47. Biermann D, Kersting P, Surmann T (2010) A general approach to simulating workpiece vibrations during five-axis milling of turbine blades. CIRP Ann 59(10):125–128. https://doi.org/10.1016/j.cirp.2010.03.057
48. Choudhury IA, El-Baradie MA (1998) Machinability of nickel base super alloys: a general review. J Mater Process Technol 77(1–3):278–284. https://doi.org/10.1016/S0924-0136(97)00429-9
49. Hood R, Soo SL, Aspinwall DK, Andrews P, Sage C (2011) Twist drilling of Haynes 282 superalloy. Procedia Eng 19:150–155. https://doi.org/10.1016/j.proeng.2011.11.094
50. Pollock T, Tin S (2006) Nickel-based superalloys for advanced turbine engines: chemistry, microstructure and properties. J Propul Power 22(2):361–374. https://doi.org/10.2514/1.18239
51. Chen Z, Peng RL, Avdovic P, Moverare J, Karlsson F, Zhou JM, Johansson S (2014) Analysis of thermal effect on the residual stresses of broached Inconel 718. Adv Mater Res 966:574–579. https://doi.org/10.4028/www.scientific.net/AMR.996.574
52. Thakur A, Gangopadhyay S (2016) State-of-the-art in surface integrity in machining of nickel-based super alloys. Int J Mach Tools Manuf 100:25–54. https://doi.org/10.1016/j.ijmachtools.2015.10.001
53. Huang W, Li S, Yang X, Shi D, Qi H (2018) Experimental investigation and modelling of microstructure degradation in a DS Ni-based superalloy using a quantitative cross-correlation analysis method. J Alloy Compd 762:488–499. https://doi.org/10.1016/j.jallcom.2018.05.131
54. Neumeier S, Pyczak F, Goken M (2011) Influence of rhenium and ruthenium on the local mechanical properties of the γ and γ' phase in nickel-base superalloys. Philos Mag A 91(33):1–13. https://doi.org/10.1080/14786435.2011.607139
55. Zhong Z, Gu Y, Yuan Y, Yokokawa T, Harada H (2012) Mechanical properties and fracture modes of an advanced Ni–Co-base disk superalloy at elevated temperatures. Mater Charact 67:101–111. https://doi.org/10.1016/j.matchar.2012.02.021
56. Chang L, Jin H, Sun W (2015) Solidification behavior of Ni-base superalloy udimet 720Li. J Alloy Compd 653:266–270. https://doi.org/10.1016/j.jallcom.2015.09.001
57. Rist MA, James JA, Tin S, Roder BA, Daymond MR (2006) Residual stresses in a quenched superalloy turbine disc: measurements and modeling. Metall Mater Trans A 37(2):459–467. https://doi.org/10.1007/s11661-006-0017-y
58. Yang ZG, Stevenson JW, Paxton DM, Singh P, Weil KS (2002) Materials properties database for selection of high-temperature alloys and concepts of alloy design for SOFC applications. Pacific Northwest National Laboratory Richland, Washington
59. Furrer DU, Shankar R, White C (2003) Optimizing the heat treatment of Ni-based superalloy turbine discs. JOM 55(3):32–34. https://doi.org/10.1007/s11837-003-0157-0

Patient Pulse Rate Monitoring System Using LabVIEW

A. R. Krishnan, S. Jayanth and R. Janani

Abstract In this article, the authors have attempted to design a LabVIEW-based health monitoring system, which measures the human body temperature and continuous pulse monitoring with the help of ECG electrodes. The LabVIEW helps to create a user-friendly GUI which can graphically show the continuous pulse or heartbeat rate. This system is suitable where the doctor will monitor the patient's condition without being present physically. This system also helps the doctor by producing medical test and previous records of the patient when the doctor is present physically. This system uses various sensors, like, temperature sensor, heartbeat rate, and ECG electrodes. This system allows the doctor to diagnose the patient's condition and allows the doctor to suggest suitable treatment. The sensors are interfaced in LabVIEW to provide a graphical user interface-based monitoring systems.

Keywords ECG electrodes · Body mass index · Temperature sensor · Health monitoring · LabVIEW

Abbreviation

ECG	Electrocardiogram
PMS	Pulse monitoring system
DAQ	Data acquisition
VI	Virtual Instruments
GUI	Graphical user interface
BPM	Beats per minute

A. R. Krishnan · S. Jayanth · R. Janani (✉)
Sri Chandrasekharendra Saraswathi Viswa Mahavidyalaya, Enathur, Kanchipuram, India
e-mail: janani.rajaraman@kanchiuniv.ac.in

H. Kumar and P. K. Jain (eds.), *Recent Advances in Mechanical Engineering*,
Lecture Notes in Mechanical Engineering,
https://doi.org/10.1007/978-981-15-1071-7_45

1 Introduction

In a developing country like India, the major concern in the field of medical sciences are lack of proper diagnosis and treatment facilities especially in remote villages, this is because of the doctor-to-patient ratio is very less. The main advantage of the presented system in this article is this method does not require the doctor all the time. Because of the vast development in the area of Biomedical Instrumentation, such monitoring system is made. In this method, the system measures the patient ECG, respiration, heart rate, and temperature of the body using sensors. The graphical user interface system developed with the help of LabVIEW will measure the biosignals from the patient health and display it on the screen. The details of the patient will be recorded individually and stored in the separate database [1].

Section 2 gives a brief summary LabVIEW Environment; Sect. 3 describes on ECG measurement and its components. The block diagram of the presented system is in Sect. 4. Results are discussed in Sect. 5, followed by conclusion.

2 LabVIEW Environment

Laboratory Virtual Instrument Engineering Workbench is a graphical programming language used as analysis software system in various fields of engineering such as biomedical, image processing, control engineering, and wireless technologies. LabVIEW uses G language to create programs called Virtual Instruments which is in the form of block diagram and front panel thereby eliminating a lot of the syntactical errors produced in the other text-based programming. Each VI consists of user interface like knobs, push buttons as input control numerical, and graphical indicators as outputs, and all these inputs and outputs are grouped under front panel controls. Inputs can be digital data or real-time interface data. All these controls in front panel will have its corresponding terminals in the block diagram. The block diagram has lower level, built-in VI functions. The blocks can be connected using wires to indicate the dataflow [2].

3 ECG Biosignals in LabVIEW

LabVIEW with its processing abilities will provide the user robust and efficient environment for resolving ECG signal processing. ECG is a pictorial representation of the heartbeat. It is primary way to deduct the pulse and functionality of heart. A human heart consists of four chambers, two auricles and two ventricles. The heart sends the oxygenated blood to the other parts of the body by ventricles and it receives the deoxygenated blood from the other parts of the body by auricles. An ECG pulse as shown in Fig. 1 is representing the functionality of this auricles and ventricles. The portion (PQ) from the waveform represents the action of arteries, and portion (QRS) represents the function of ventricles. The (ST) portion of the waveform shows the normalization of the heartbeat [3] (Table 1).

Fig. 1 ECG waveform

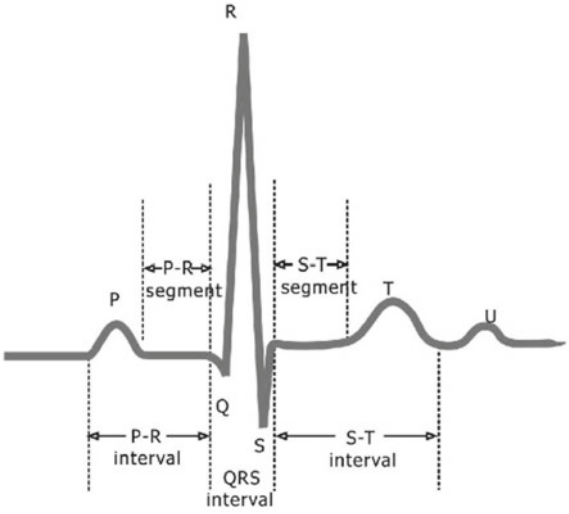

Table 1 Normal ECG waveform

Parameters	Range
P-portion	≤0.11 s
PR interval	min 0.12 s–max 0.21 s
QRS portion	≤0.12 s
QRS peak voltage	2.5–5 mv
QT interval	0.40–0.44 s

3.1 Temperature Measurement

Temperature of the body should be continuously monitored for a patient in an ICU. This individual body temperature depends on the ager, infection, and activity level, state of consciousness and emotional state. It should be maintained within the range by thermos regulation. The normal body temperature of the human is 37 °C or 98.6°. The temperature sensor used here is LM35, and it measures the temperature of the patient continuously [4] (Fig. 2).

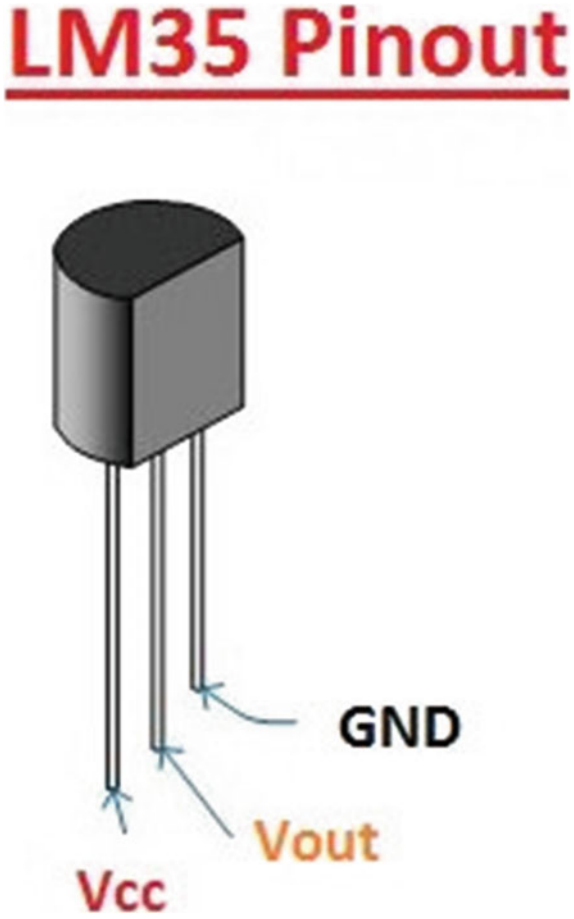

Fig. 2 Temperature sensor

4 Block Diagram of Patient Monitoring System

The functional block diagram of the patient monitoring system (PMS) is shown in Fig. 3. The major components are the temperature sensor, ECG electrodes, and National Instruments DAQ card. The temperature of the patient is measured and given to the LabVIEW interface through DAQ system in LabVIEW.

The biosignals from the patient health is also measured and given to the LabVIEW biosignal simulator, which generates the ECG waveform and this can be viewed by waveform monitor; ECG feature extractor module imports the ECG signal from a DAQ device and integrates robust extraction algorithms to detect ECG features, such

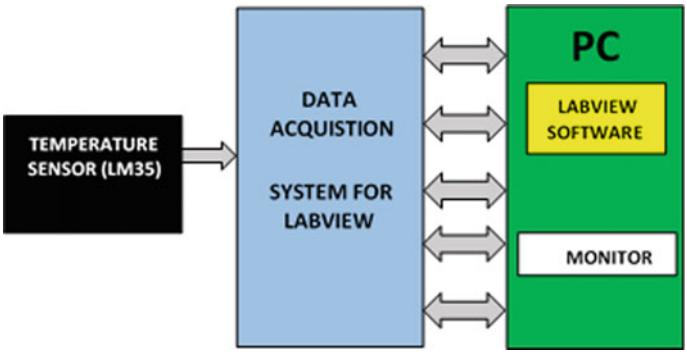

Fig. 3 Block diagram of PMS

as QRS complex, P interval, and T wave, and this also transfers the RR interval data to heart rate variability analysis application. This module also allows the user to take a printout form of patient ECG [5].

5 Results and Discussion

Figure 4 and Figure 5 shows the biosignal measure and the feature extractor, respectively. Figure 6 shows the real-time implementation of monitoring the patient's body temperature. The values of body parameters can be saved in spreadsheet file for future reference as shown in LabVIEW block diagram Fig. 7.

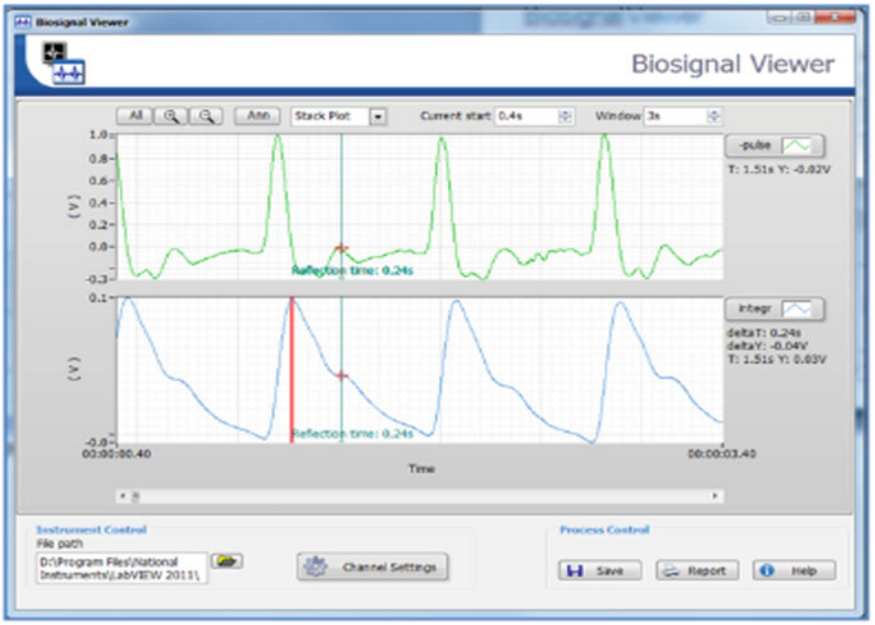

Fig. 4 Biosignal viewer

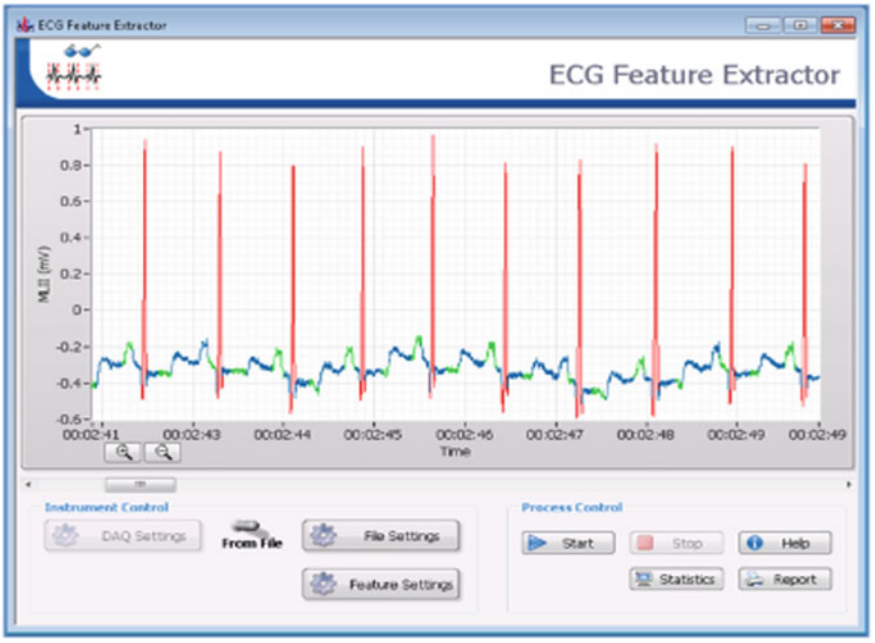

Fig. 5 ECG feature extractor

Fig. 6 Real-time experimental set-up for temperature monitoring

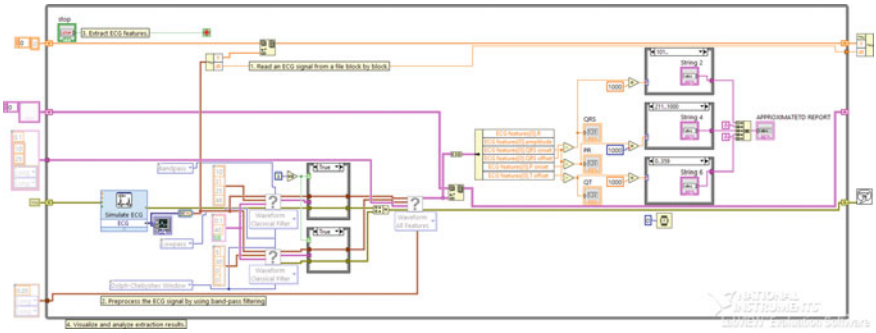

Fig. 7 Block diagram of ECG feature extraction in LabVIEW

6 Conclusion

The presented system when employed in all the medical centers will be a great impact as well as this will be much useful in the village sector where the ratio of doctor to the patient is less. This method have less cost and can be employed in rural and urban areas. In this article, LabVIEW platform provides an efficient environment and keeps track of patient's body temperature, ECG, and pulse rate in real time.

References

1. Mohanraj T, Keshore Raj SN (2017) Patient monitoring system using LabVIEW. IJETCS 4:67–71
2. Janani R (2017) Image processing application using LABVIEW. IJIACS 12:432–437
3. Natarajan N, Aparna S, Sam Jeba Kumar J (2016) Patient monitoring system based on e-health sensors and web services. In: ECAI 2016—international conference, 8th edn., July 2016
4. Subramanya K, Bhat VV, Kamath S, A wearable device for monitoring galvanic skin response to accurately predict changes in blood pressure indexes and cardiovascular dynamics. In: IEEE Annual IEEE India conference (INDICON)
5. Thomas SS, Sensing heart beat and body temperature digitally using Arduino. SS—AAICSP—10-01
6. www.ni.com/product-documentation/9037

War Field Spy and Fighter Robot

Manisha Bharti and Ayush Kumar Agrawal

Abstract Knowing the forthcoming generation is all about the Internet so why it can not be used for decreasing the casualties in the war field. Keeping in mind the value of an individual in the war field this latest trend Internet of things (IoT) will be the gift for the Indian army. As this idea is very much helpful for spying in war field and as further development is possible that the author thinks to make this robot as a clone of humans which can fight in the war field without any casualties and injuries.

Keywords War robot · Spy robot · Terror attack · IoT-based robot · Raspberry Pi

1 Introduction

Being developed much in robotics and even these days where the artificial intelligent robots like 'PEPPER' a robot by Softbank and Aldebaran can be seen, but to control a bot using Internet will be more valuable for spying or for in war field, so that the work will be done by robot, but the mind will be of human.

The main objective for this is to decrease the civilian fatality in an arsonist attack like 26/11 (mumbai attack). The fighter robot is designed to handle such a bad arsonist attack. This robot is mobile, which can be controlled as similar as controlling a remote-controlled car [1]. With a camera is on it (which will work as eyes for the robot), to monitor the enemies remotely and controlled wirelessly. It can secretly get into the rival's area and give you all the data which is required and works as a spy using its eyes present in the form of camera embedded in it. This kind of robots can be beneficial in war fields, hotel service, malls, etc. Where there will be a menace from arsonist or any intruders, this robot will be useful. As the life of a human is

M. Bharti · A. K. Agrawal (✉)
National Institute of Technology Delhi, New Delhi, Delhi 110040, India
e-mail: ayush6295@gmail.com

M. Bharti
e-mail: manishabharti@nitdelhi.ac.in

H. Kumar and P. K. Jain (eds.), *Recent Advances in Mechanical Engineering*,
Lecture Notes in Mechanical Engineering,
https://doi.org/10.1007/978-981-15-1071-7_46

very important and valuable, these killer robots will replace the combatant who fights with the terrorists in war fields. In a war field as if any casualties take place, which is not good for the army as well as not for the soldier.

This will be reduced by that of from this project where the robot will cost not more than 10,000, which has no comparison with that of anyone's life. The use of the Internet of things is done to control the robot which is having all the types of sensors attached to the controller's body so that in real time the robot will work as similar to as that of the controller is opting to do.

2 Theoretical Background

US Mechatronics developed an automatic watcher of the gun and is now working on it for general use and as a combatant [2]. The mule bot made by the US Army which is shown in Fig. 1. MIDARS, which have multiple cameras with four wheels and also with a fire mechanism which from itself from its own does the patrols in a pre-programmed way where it is being used like a war filed or any governmental or non-governmental facilities.

It gives a warning in the human monitor on detection of any kind of mishappenings in the areas where going is unapproved and different required conditions. The controller will have the full control so that the robot can be remotely controlled in a better way and which will also help to get the proper view with the help of the camera installed as eyes in the bot. This bot can also be able to verify the radio frequency identification (RFID) which was pasted in the inventories when it is passed so that any missing or improper objects can be checked. Autonomous Combatant Tactical Units (TACs), which were described in the Project study which is being named as "Unmanned Effects: Bringing People Out of the Loop" [3].

Fig. 1 Mule

This automatic special sniper system is one of the weapon systems in an robot which is being created by military of US during 2005–2006 [4–6]. It is embedded with remote-controlled rifles, which is connected to an automatic drones or air vehicles. The tests were done in 2009 summers and which was done successfully. In the context of knowing the people, who plan future operations and to implement them, and as to rely on "having ours"; principle regardless of battlefield size (space in the form of real time or imaginary, this special defense system or "Internet-based" defense technique, etc.). The enemy can not be decided by the type of resources, strategy, preparation, and qualifications available.

To have the influence for designing, with installing and operating this technique and also to prepare the soldiers in the war field. With the development of the training and such chance and abilities in the mind of the maker's are nicely thought and at the bottom of these steps can be taken. For which, it is to be crystal clear as the next generation is not limited to how the author solves this problem from any location, whereas it is an opportunity to increase their understanding [7–9].

The automatic bot software program for the research was inaugurated by Pentagon on December of 2003, and more 14 plus segways are bought for more high efficient bots. Which was that time is in the group of 1, 85, 28, 30, 200 Pentagon program for developing the softwares for automatic systems.

3 Development of a Prototype

Developing a vehicle using Raspberry Pi as a remote-operated robot which can be wirelessly monitored with the camera embedded in it is the authors first target. The bot with the help of the camera will weightlessly send live video which is also having night vision camera. These types of robots will be really good in war fields and also can be used as a spy.

The movement of the bot can be controlled using the IoT instructions, which is being sent to the receiving end. And at the receiver end, the motors are interfaced to be used for the motion of this robot. The mobile/laptop acts as a controller, a camera which is embedded on the eye of the robot is used for spying purpose, and again the idea can be better with the use of the IoT, which is the technology that helps the robot to be controlled by using a cell phone. Which has an profit than that of long-distance communication technology used in day to day life.

The Internet of things (IoT) refers to a system of interconnected computing devices may be electrical or mechanical devices, objects, etc. That is featured by some specific properties called unique identifiers (UIDs) and they possess the capability of transferring information/data over a prescribed network without any human to human or human to device interaction. The Internet of things offers a number of advantages to the organizations using this technology and enabling them to enhance employee productivity, save money, and time and to generate more revenue. As known, the forthcoming generation is all about the Internet and there are a number of real-world

applications of the Internet of things including the automotive, telecom industry, energy, and many more.

In this, an attempt has been made to use the Internet of things (IoT) for decreasing the casualties in the war field. Knowing the value of an individual in the war field and keeping it in mind with the help of the latest trend IoT, this can be a gift for the Indian army. As this is very much helpful for spying in war field and as further development is possible by making this robot as a clone of humans which can fight in the war field.

3.1 Hardware Specifications of Raspberry Pi

The Raspberry Pi (Fig. 2) is a type of one board computers, which is made in UK by foundation of Raspberry Pi specially to enhance some small computer education in all of the developing country institutes [10–12], and to sell beyond its main market like robotics and automation. It does not include chip parts and external boxes or covers. But, some parts are in many sets as in like for official or nonofficial. And its specifications are as follows:

- Broadcom of SoC with BCM2835 (DSP, GPU, CPU, SDRAM)
- 700 MHz CPU with ARM1176JZF-S core (which is from family of ARM11)
- Memory of RAM is 512 MB
- GPU of Broadcom VideoCore IV with OpenGL ES 2.0 and 1080p30 h.264/MPEG-4 AVC
- Video outputs of Composite RCA, HDMI

Fig. 2 Raspberry Pi—B3

– Onboard storage of MMC, SD and card slot of SDIO
– Audio outputs of 3.5 mm jack, HDMI
– Onboard network of 10/100 Ethernet RJ45
– Wi-Fi can be used with dongle which can be USB operated
– More than one USB port
– Power of the 1 mA at 5 V (can be operated with normal mobile charger).

3.2 Software Codes and Process

The software part is divided into two parts, where the one is for the control of the robot and the other is to collect the data that of the robot with live streaming and real-time values. While developing this, the main problem seen is with the real-time streaming with that of from the server. As for the data transfer, one of the best server found is ThingSpeak but this cannot be used because this server provides the data with the delay of 10 s, which is possible for controlling a robot. For now, in the prototype, the author used the clone server of that of the ThingSpeak but for real-time development of this idea, the satellite communication is being needed, which will make the robot more secure.

1. FOR ROBOT MOTION AND CONTROL (in python):

- Calling and cleaning up the pins
  importRPi.GPIO as GPIO
  GPIO.cleanup()
- GPIO pin setup
  GPIO.setmode(GPIO.BOARD)
  GPIO.setup(XX,GPIO.OUT)
  GPIO.setup(XX,GPIO.OUT)
- Channel server calling
  import requests
  from channel import channel
- Collecting data from the channel
  c = channel(1)
  while True:
  a = int(c.getLatestEntry("SSZVCNYQEZOOPEGN"))
- Motion of robot
  if a == 1:
  GPIO.output(xx,y)
  GPIO.output(xx,0)
  GPIO.output(xx,0)
  GPIO.output(xx,0)
  GPIO.output(xx,0)
  GPIO.output(xx,y)

```
    GPIO.output(xx,0)
    GPIO.output(xx,0)
    GPIO.output(xx,0)
    print "right"
elif a == 2:
    GPIO.output(11,0)
    …….. ##### ……
```

2. For LIVE Streaming:

- Calling
  daemon = off/on
  norm = X
  input = Y
- Setting levels
  auto_brightness = off/on
  framerate = XXX
  height = XXX
  width = XXX
  jpeg_filename = motion/%Y%m%d/%v-%H%M%S-%q
  noise_tune = off/on
  output_all = off/on
  output_motion = off/on
  output_normal = off/on
  quality = XXXX
  snapshot_interval = XXX
  text_left = (c) Author
  text_right = %d %b %Y\n%k:%M:%S
  threshold = XXX
  v4l2_palette = X
- Defining ports
  videodevice = /dev/video0
  webcam_localhost = off/on
  webcam_maxrate = XX
  webcam_port = XXXX
  wecam_quality = XXX

3.3 Prototype

For the development first, the small spy and fighter robot prototype are made and after the proper use of it, the further robot is made after this prototype stage, which is shown in Fig. 3.

Fig. 3 Prototype model

3.4 Working of the System

The working is basically divided into two parts which consist of the real-time data exchange as well as the controlling of the robot.

I. Data exchange from the controller to the robot.
   Where the controller equipped with the sensors sends the data to the server, and the robot with the receiver receives the data to go for further action which is being sent by the controller as shown in Fig. 4.
II. Working of server for live streaming.
   In this, as vice versa process takes place for the controlling is seen as shown in Fig. 5.

4 Results and Discussions

In these days, it can be seen that remotes are made to instruct the movement direction of the bot or any models for multiple modes. Which can be said as manual controlled mode and automatic mode, where the controller can control in the manual mode type remotes and it will be automatically controlled in automatic mode. The bot will move in the path or area and will work as per the environment in the automatic mode. To recognize the objects, the infrared sensors are embedded (left sensor and

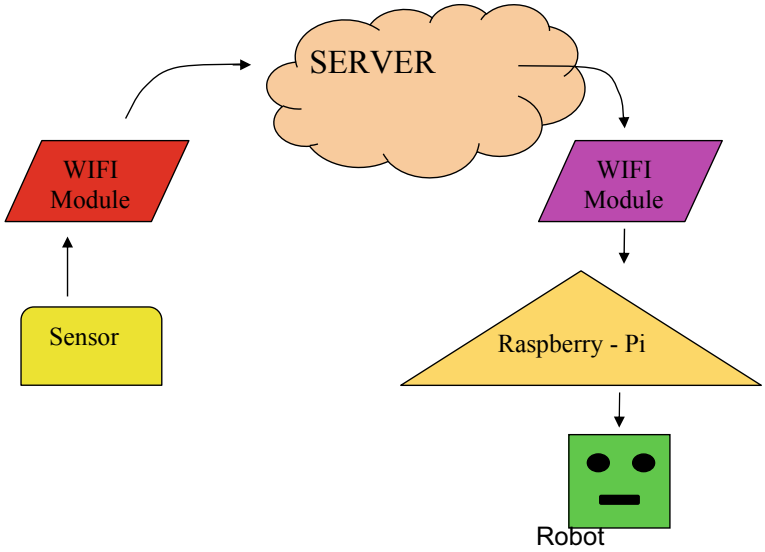

Fig. 4 Controlling of the robot

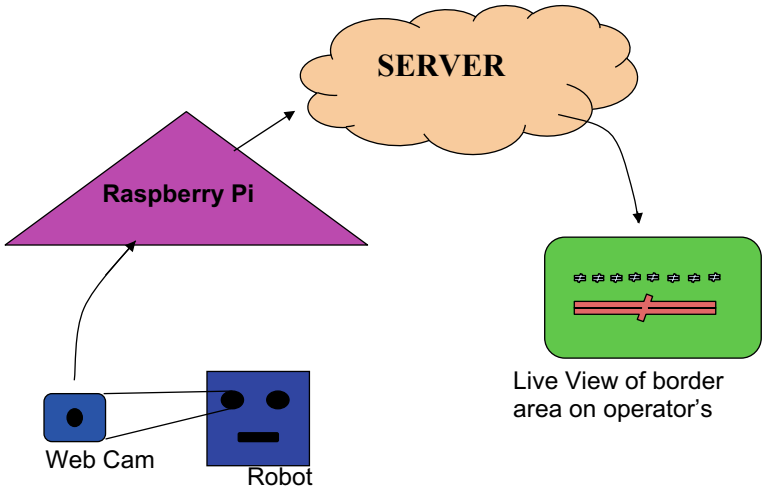

Fig. 5 Real-time video streaming

right sensor) in the front portion of the robot. While moving on the surface, when the sensor detects anything then the bot takes back for a second and then turns right. And if the right sensor is detected, robot gets back and turns left.

This robot works basically with the user-controlled mode where the controller have all the controls of the robot sitting 1000 miles away, According to the author

it can be specified as the army soldier is fighting in the war field and may be in the place which may be too much poisonous or in the place where human body is not capable of going, sitting 1000 miles away from the above areas.

This can be a fully automated robot also but artificial intelligence is not that good which can replace the human brain, the thinking capability of it and the working of it with decision-making. Which is going to be very much beneficial as in the soldier will be present in the war field but without his physical presence.

5 Conclusion

As, now a days we can hear a lot about the attacks, explosions of the bombs, etc., with many unethical things. And to decrease such type of illegal activities and all with ease, technological power must be greater than the human power.

As life of and human is very important, It is our onus to take a step forward to design a model of an bot using technologies which can meet combatant needs. So to avoid this suspicious illegal things, and to confidently get more security at the important areas such as borders/government organizations we can use this robot. It is good to have a world-class technology which can be used in army according to the needs of defense services. And each and every country wants their self designed protocols and technologies for army, which will help in their integrity and security. In such a way, making of these type bots will help in the country's name, fame worldwide.

6 Future Scope

In this prototype as Internet of things is being used and it is not as secure as compared to that of the private connection which can be done using satellite communication in this robot for interconnection of the robot and the controller.

References

1. Khamis A, Pérez Vernet M, Schilling K (2002) A remote experiment on motor control of mobile robots. In: 10th mediterranean conference on control and automation—MED2002
2. Szegedi P, Koronváry P, Békési B (2017) The use of robots in military operations. In: Scientific research and education in the air force—AFASES2017 221
3. Miles P, Carroll T (2002) Build your own combat robot
4. Fu KS, Gonzalez RC, Lee CSG, Tutorials robotics
5. Asaro P, How just could a robot war be? Front Artif Intell Appl 75:50–64
6. Harmon SY, Gage DW, Current technical research issues of autonomous robots employed in combat. In: 17th annual electronics and aerospace conference

7. Merrill B (2016) Is the future of war autonomous? (online) http://www.makeuseof.com/tag/future-warautonomous/ (2016.02.06)
8. Weapons systems Introduced Since Desert Storm (1991) that are available now (2003) (online) http://www.iwar.org.uk/military/resources/ndu/systems-for-iraq.pdf (2016.04.08)
9. Szegedi P, Tircsi H (2017) Nanotechnológia a katonai vezetés új kihívása? Hadtudományi Szemle, 2017. X. évfolyam, 1. szám (2017.04.06), pp 491–505
10. Cellan-Jones R (2011) A£15 computer to inspire young programmers. BBC News, 5 May 2011
11. Price P (2011) Can a £15 computer solve the programming gap?. BBC Click, 3 June 2011. Retrieved 2 July 2011
12. Bush S (2011) Dongle computer lets kids discover programming on a TV. Electronics Weekly, 25 May 2011. Retrieved 11 July 2011

Erosive Wear Study of Nitrogen-Containing 23-8-N Austenitic Stainless Steel and Bead on Plate Weld Using ER2209 Stainless Steel Filler Wire

Naveen Kumar, Navneet Arora and S. K. Goel

Abstract Jet-type slurry erosion testing of the nitrogen-containing austenitic stainless steel 23-8-N in as-received, heat-treated (950 °C and 1150 °C temperatures) and bead on plate weld have been carried out with less than 500 μm size of erodent silica sand. The bead on plate weld is performed with ER2209 filler wire with gas metal arc welding. Erosion resistance of base metal increases at higher heat treatment temperature but there is no effect on weld bead erosion resistance. Weld has higher cumulative weight loss as compared to base metal.

Keywords 23-8-N nitronic steel · Welding · Overlays · Slurry erosion · Cabides

1 Introduction

Every nation has its limitations for the present non-renewable energy resources, so dependency on the renewable resources is increasing. Hydropower energy is one of the main renewable energy resources in the world. But the hydropower generation faces a lot of problems like silt erosion, cavitation of propellers or hydraulic turbine parts during working. It reduces the life span of the hydro-turbine and the overall efficiency of the plant [1]. The other industries like oil processing, shipbuilding where the components have direct contact with flowing liquids [2, 3] are also facing the same problems. Slurry erosion wear of underwater parts of hydro-turbine is a complex phenomenon which depends on the various parameters like (a) shape, size, hardness and concentration of eroding particle (b) chemistry, surface morphology and elastic properties (c) operating conditions, impingement angle and the impact [4–6]. The nitrogen in the steels improves its mechanical properties like higher work hardening ability, higher strength and fatigue life at the little reduction of ductility

N. Kumar (✉) · N. Arora
Indian Institute of Technology Roorkee, Roorkee 247667, India
e-mail: nkumar3@me.iitr.ac.in

S. K. Goel
Star Wire (India) Ltd., Ballabgarh, Haryana 121004, India

H. Kumar and P. K. Jain (eds.), *Recent Advances in Mechanical Engineering*,
Lecture Notes in Mechanical Engineering,
https://doi.org/10.1007/978-981-15-1071-7_47

and toughness. [7]. Manganese is added to the steel to increase the solubility of nitrogen as nickel reduces the solubility of nitrogen [8].

The martensitic stainless steel containing 13% Cr and 4% Ni (also known as CA6NMsteel or 13/4 steel) has mostly applications in the fabrication of hydro-turbine underwater parts. The martensite quantity and high hardness cause the poor weldability to this steel which is a major problem for the repair of the eroded or damaged parts of the turbine. The nitrogen-containing austenitic stainless steels are widely preferred by industries for specific applications due to its improved mechanical, metallurgical and corrosion properties. The austenitic stainless steels have good weldability [9].

The erosion in underwater parts cannot be eliminated completely but can be minimized by developing more erosion resistant materials, optimization of operating parameters and more suitable maintenance provided to the turbine components. The erosion and cavitation studies on 23-8-N nitronic steel have been carried out by the researchers [10–12] but their weldability and erosion of bead on plate have not been found in the literature. The major objective of this work is to examine the effect of heat treatment on erosion resistant. Bead on plate weld has been deposited on 23-8-N nitronic steel and slurry erosion testing of these welds has been carried out. The characterization of base and weld metals has been studied.

2 Experimental Procedure

2.1 Base Metal and Welding Process

Base metal was provided by the M/s Star Wire India Pvt. Ltd. Faridabad, Haryana India in the form of billets of size 100 mm × 100 mm × 13 mm. The chemical composition of base metal and filler is presented in Table 1. Base metal was heat-treated at 950 °C and 1150 °C for 120 min followed by water quenching. The bead on plate welds is made using gas metal arc welding (GMAW) process with ER2209 filler wire on as-received and heat-treated base metal. The welding parameters are shown in Table 2.

Table 1 Chemical composition (wt%) of base and filler metal used

Elements	C	Cr	Ni	Mn	N	Si	Mo	Fe
Base 23-8-N steel	0.30	22.60	7.55	2.12	0.29	0.5	0.20	Bal
Filler metal ER2209	0.03	22.51	8.53	1.71	0.16	0.52	3.34	Bal

Table 2 Optimum welding parameters for bead on plate welding

Welding current (A)	132
Voltage (V)	22
Filler wire diameter mm	1.2
Filler wire speed (m/min)	3.5
Gas flow of Ar (L/min)	10
Welding speed (mm/min)	160

2.2 Hardness and Impact Toughness

The hardness of the samples was measured on Vickers microhardness tester (make; Omnitech Model: S Auto) on a difference of 0.5 mm between two consecutive indents. The eroded samples were cleaned using acetone and dried properly before taking the hardness. The Charpy impact test was performed according to ASTM E23-12c standard.

2.3 Jet-Type Slurry Erosion Test

The slurry erosion test was performed on the test rig [13] at an angle of 90° for a total time of 90 min. The samples were exposed to a slurry-jet consisting of water and silica sand particles. For weight loss calculations during erosion test, the samples were cleaned, dried using hot air and weighted again with the help of weighing machine. This process is repeated after a 30 min of time interval. The microstructure of base and weld metal was taken using an optical microscope (Make: Leica). The micrographs of the eroded surfaces were taken using field emission scanning electron microscopy (FESEM, Make: Carl Zeiss).

3 Results and Discussions

3.1 Base Metal Microstructure

The microstructures of base metal in as-received and heat-treated conditions are shown in Fig. 1a–c. It is observed that the microstructure is heterogeneous and contains austenite (bright phase) and clusters of carbides (dark phase). The carbides are present at grain boundaries and also within the grains. The XRD and EDS analysis shows that the 23-8-N nitronic steel has mainly two types of carbides (M_7C_3 and $M_{23}C_6$) due to high C:Cr ratio, where M is Cr [10]. A continuous network of lamellar morphology is formed due to the higher carbide precipitation [14]. On the other hand,

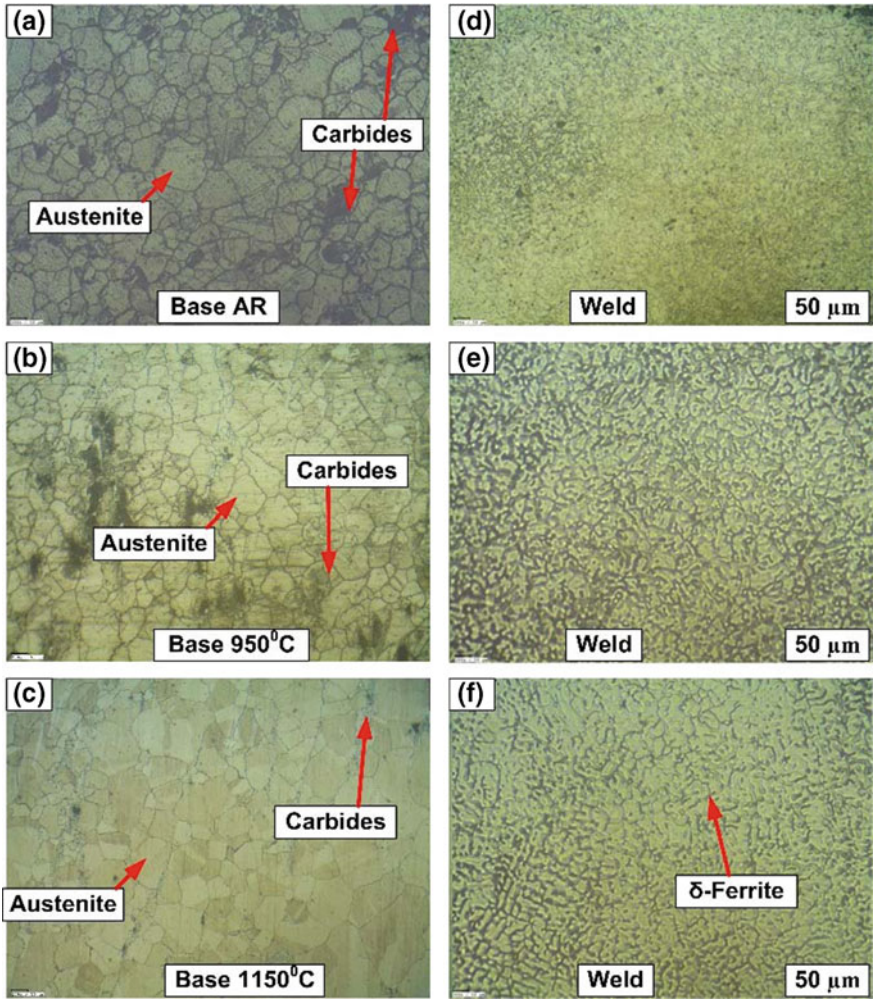

Fig. 1 Optical microstructures of: **a** as received, **b** annealed at 950 °C and **c** annealed at 1150 °C for base and **d**–**f** for weld (bead on plate), respectively

$M_{23}C_6$ types of carbides are mainly predicated at grain boundaries. During carbide precipitation, interstitial carbon can diffuse rapidly to the grain boundaries.

The volume of the carbides decreases as a result of solution treatment due to its dissolution into the matrix. The solution treatment at a higher temperature (1150 °C) causes larger grain size and amount of residual carbides is low as compared to 950 °C solution treatment. The grain boundaries are clear and larger with the fine carbides distribution in it and within the grains.

3.2 Weld Metal Microstructure

Optical micrographs of weld bead deposited with ER2209 duplex stainless steel filler wire are shown in Fig. 1d–f. It contains carbides (dark face) in the matrix of austenite (light phase). The chances of hard carbides formation are less due to lower C content of filler but, carbon diffusion takes place at the interface boundary. Nitrogen (being a good austenite former) reduces the δ-ferrite content. The $M_{23}C_6$ (where M=Cr) types of carbides were mainly precipitated at the grain boundaries in the weld.

As per WRC-1992 [15]

$$Cr_{eq} = Cr + M_0 + 0.7Nb \tag{1}$$

$$Ni_{eq} = Ni + 35C + 20N + 0.25Cu \tag{2}$$

The WRC-1992 diagram (Fig. 2) is used to predict the weld microstructures (Eqs. 1 and 2). Cr-equivalent and Ni-equivalents for base and filler metals are calculated. For 23-8-N Cr_{eq} and Ni_{eq} are 22.8 and 23.85. Filler ER2209 has Cr_{eq} and Ni_{eq} as 25.84 and 12.85, respectively. Considering a 30% dilution the weld shows Cr_{eq} (24.92)

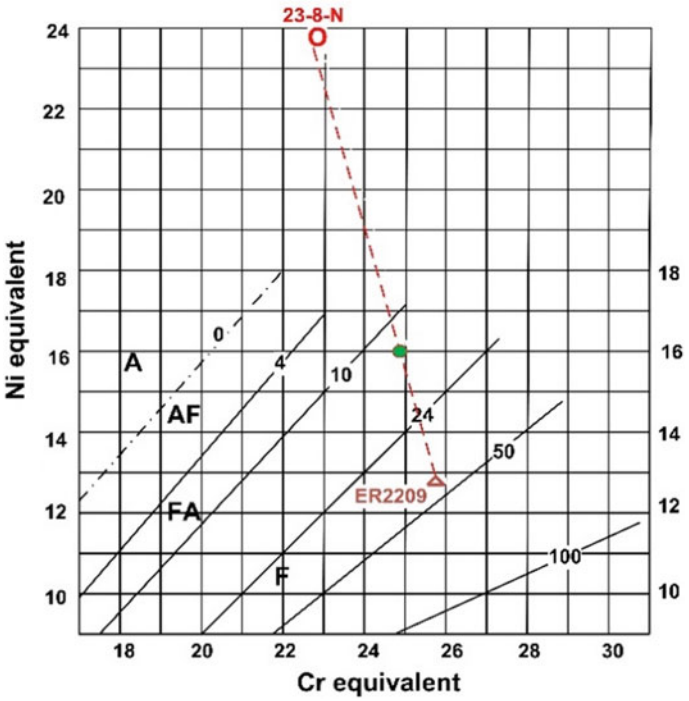

Fig. 2 WRC-1992 diagram [15]

Table 3 Cr_{eq} and Ni_{eq} of base metal, filler and weld metals as per WRC-1992 diagram

Type	Cr_{eq}	Ni_{eq}	Cr_{eq}/Ni_{eq}
23-8-N	22.8	23.85	0.956
ER2209	25.84	12.85	2.01
Weld	24.92	16.15	1.54

and Ni_{eq} (16.15). ER2209 weld showed higher Cr_{eq}/Ni_{eq} ratio (Table 3) than that of base metal. The microstructures evolved are indicated in Fig. 1. According to the WRC-1992, the weld microstructures solidify primarily as ferrite-austenite (FA) mode [9].

3.3 Hardness and Impact Strength

The hardness of the base metal depends on the various factors i. e., (1) formation and distribution of carbides (2) heat treatment temperature and (3) pointing of the indenter. For large clusters of carbide present in AR-base metal average hardness is higher (Fig. 3). As the heat treatment temperature increases, the hardness values decrease due to the dissolution of carbides and nitrides into the matrix which leads to the more homogenous microstructure. Hardness also depends on whether the tip of the indenter is on carbide or austenite. The hardness of weld is dependent on the individual phases of austenite and ferrite which are present in weld microstructure

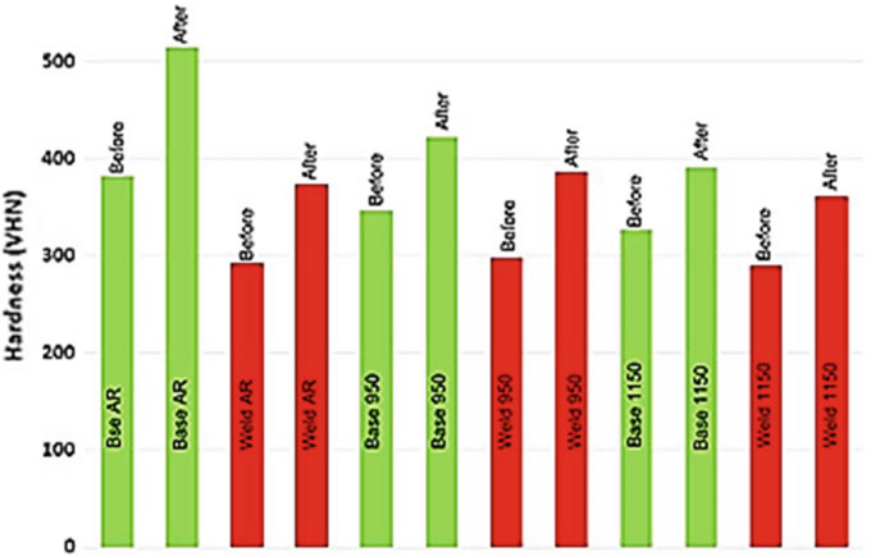

Fig. 3 Microhardness before and after erosion test

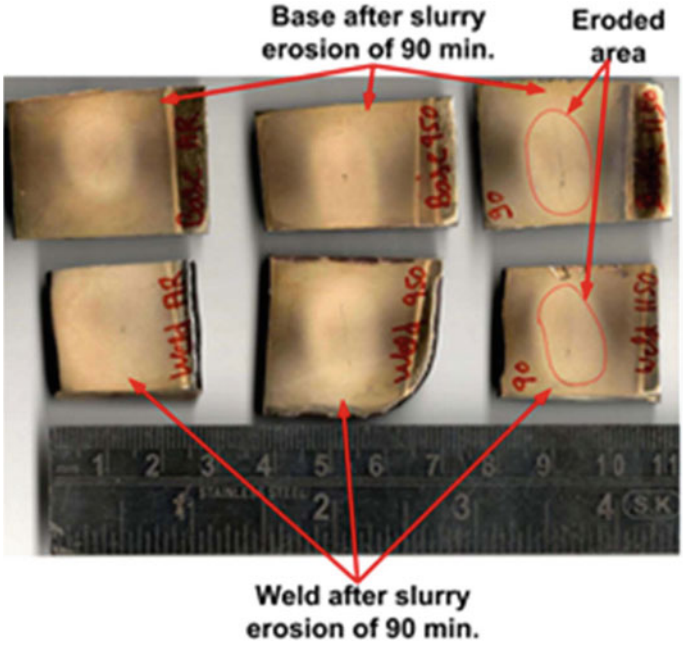

Fig. 4 Eroded samples after 90 min

as shown in Fig. 1. The AR-base metal exhibits the maximum hardness and welds in each case have approximately same hardness. The hardness before and after the slurry erosion test is shown in Fig. 3 and the picture of eroded samples in Fig. 4. The hardness of both base and weld increases with erosion testing in every condition due to the strain hardening effect of steel. Lower carbon and nitrogen content reduce the strain hardening ability of weld which leads to lower variation in hardness for before and after erosion test. Although, rapid weld solidification, weld thermal cycle, and the formation of residual stress in the weld, increases its hardness.

3.4 Slurry Erosive Wear

The cumulative weight loss of AR (as received) and solution treated (950 °C and 1150 °C) for base and weld metal is shown in Fig. 5. The cumulative weight loss during test was measured for a time interval of 30 min. This new grade of nitrogen-containing austenitic stainless steel 23-8-N shows more resistant to slurry erosion up to certain extent due to the presence of chromium carbides and nitrides in the matrix. Generally, the carbides present in a material degrade its mechanical properties like strength, impact toughness, ductility and work hardening capability. In the present

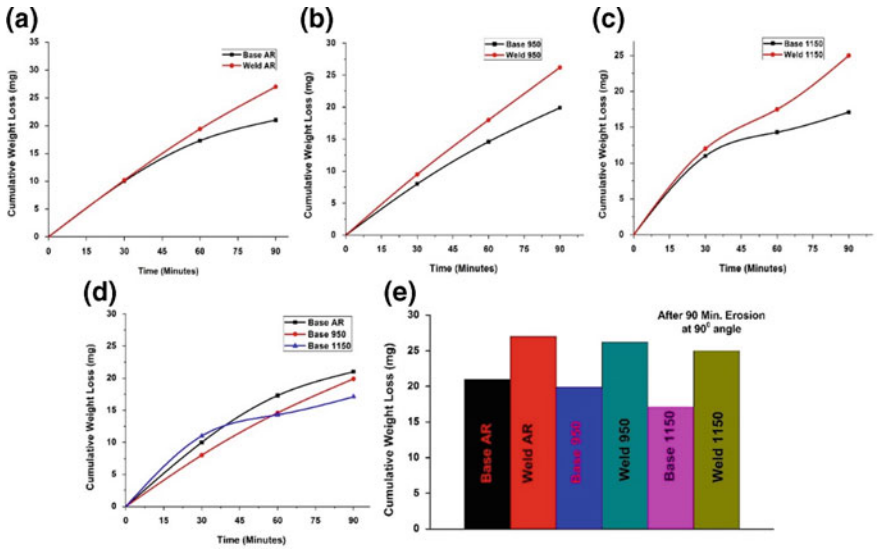

Fig. 5 Cumulative weight loss of base and weld metals with different time durations

study, the role of carbides present in the AR-base (maximum carbides) and heat-treated (comparatively lower carbides) conditions along with bead on plate weld has been studied. It is found from the study that heat treatment of base metal increases its slurry erosion resistance as the available clusters of carbide are dissolved (up to some extent) and significant improvement in impact strength as shown in Table 4. The strain hardening during the erosion test also supports higher resistance to erosion [10]. The materials with high toughness can absorb more energy transferred by the impacting sand particles and this absorbed energy can be used for plastic deformation which leads to the longer life span to the target material. Hardness also plays an important role in the erosion resistance property of a material [16]. The finer hard carbides are still present in the matrix and oppose the penetration to the sand particles into the target which further leads to lower erosion rate of the target material. The parameters for erosion test are shown in Table 5.

FE-SEM fractographs of the base metal are shown in Fig. 6a–c. From the fractographs of eroded samples, craters observed in AR condition are more and reduces in 950 °C and 1150 °C, respectively. It results that the higher heat treatment temperatures increase the erosion resistance of 23-8-N steel. In base metal after 950 °C and 1150 °C heat treatment for 120 min, the formation of small craters may be probably

Table 4 Impact test values of base metal in as received and heat-treated conditions

Material	Base metal condition		
Impact energy (J)	AR	950 °C	1150 °C
	9	16	55

Table 5 Parameters for erosion test

Parameter	Value
Erodent material and size (μm)	Silica sand, 500
Particle velocity (m/s)	18.5
Impact angle (°)	90
Slurry concentration (wt%)	10
Nozzle diameter (mm)	6
Nozzle to test surface distance (mm)	10
Test interval and total test time (min)	30, 90

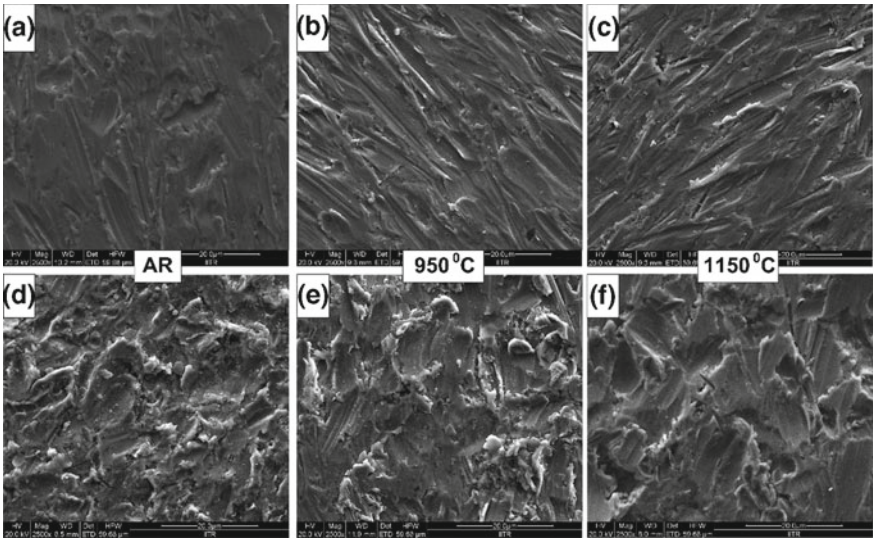

Fig. 6 FE-SEM micrographs of **a** as received, **b** annealed at 950 °C and **c** annealed at 1150 °C of the base and **d–f** for weld (bead on plate), respectively, after 90 min of test at 90° angles

due to the dissolution of carbides resulting in enhancement of mechanical properties [10].

The lower hardness of weld bead results in higher erosion rate. The weld overlay has different chemical composition (lower carbon and nitrogen), which leads to lower strength and hardness. Also, the carbides formation in the weld is minimum and mainly $M_{23}C_6$ types of carbides are formed on the grain boundaries. Thus, the lower hardness and lesser volume of carbides are the main reason for lower erosion resistant of the weld as compared to the base metal. The weld overlay contains δ- ferrite, which has lower hardness than carbides and results in its lower rate of erosion resistance. Figure 6d–f reveals the maximum erosion on the weld bead of as-received base metal, it decreases toward the weld bead deposited on the heat-treated conditions.

4 Conclusions

The following conclusions can be drawn from this study:

(1) Heat treatment at higher temperature caused lower erosion rate due to the dissolution of carbides and higher strain hardening ability of the base metal.
(2) Hardness decreases with higher heat treatment temperature with grain coarsening.
(3) Weld solidifies with approximately 5–8% of delta ferrite which reduces the possibility of weld solidification cracking.
(4) Weld has lower resistant to erosion to the base metal in each case due to lower hardness and the chemical compositional difference between base metal and weld.
(5) Welds are also showing the same trend (decrease in cumulative weight loss) like base metal for erosion resistant for different heat treatment conditions.

Acknowledgements Authors are grateful and obliged to Dr. D. B. Goel, former professor at Indian Institute of Technology Roorkee, for sharing his technical knowledge and also thankful to Star Wire (India) Pvt. Ltd. for supplying the material for the research.

References

1. Goel DB (2008) Metallurgy of erosion of underwater parts in hydroelectric projects. In: Proceedings of the 3rd international conference on silting problems in hydropower projects, pp 1–10
2. Mendez PF et al (2014) Welding processes for wear resistant overlays. J Manuf Process 4–25
3. Gou WJ (2016) Study on welding repair process of turbine blade. In: Chen (ed) Material science and environmental engineering, London, pp 497–500
4. Naidu BSK (2004) Silting problem in hydro power plant & their possible solutions. NPTI, India
5. Chaudhary CS (1999) Impact of high sediment on hydraulic equipment of Marsyangdi hydropower plant. In: Proceedings of the international seminar on sediment handling technique, NHA, Kathmandu
6. Singh RP (2009) Silt damage control measures for underwater parts—Nathpa Jhakri Hydro power station—case study of a success story Satluj Jal Vidyut Nigam Ltd., India, p 66
7. Gavriljuk V, Berns H (1999) High nitrogen steels: structure, properties, manufacture, applications, 1st edn. Springer, New York
8. Gavriljuk V, Razumov O, Petrov Y, Surzhenko I, Berns H (2017) High strength stainless austenitic CrMnCN steels—Part II: structural changes by repeated impacts. Steel Res Int 78:720–723
9. Chauhan AK, Goel DB, Prakash S (2008) Erosion behaviour of hydro turbine steels. Bull Mater Sci 31:115–120
10. Kumar A, Sharma A, Goel SK (2015) Effect of heat treatment on microstructure, mechanical properties and erosion resistance of cast 23-8-N nitronic steel. Mater Sci Eng A 637:56–62
11. Aniruddha AG (2011) Characterization study of steels for erosion resistant applications. Ph.D. thesis, MNIT, Jaipur, India

12. Kumar A, Sharma A, Goel SK (2016) Erosion behaviour of WC–10Co–4Cr coating on 23-8-N nitronic steel by HVOF thermal spraying. Appl Surf Sci 370:418–426
13. Thakur L (2014) An investigation on thermal spray wear resistant coating. Ph.D. thesis, IIT Roorkee, India
14. Padilha AF, Rios PR (2002) Decomposition of austenite in austenitic stainless steels. ISIJ Int 42:325–327
15. Kotecki DJ, Siewert TA (1992) WRC-1992 constitution diagram for stainless steel weld metals: a modification of the WRC-1988 diagram. Weld Res Suppl 171–178
16. Desale GR, Gandhi BK, Jain SC (2005) Improvement in the design of a pot tester to simulate erosion wear due to solid-liquid mixture. Wear 259:196–202

Calcium Fluoride a Potential Solid Lubricant for Green Tribology and Sustainability

Sanjay Mohan, Ankush Anand, Mir Irfan Ul Haq, Ankush Raina and Rajiv Kumar

Abstract Development of materials has been of great concern for scientists and researchers since ancient times. Lubrication is one such area where lot of work has been carried out by many researchers, especially in the area of solid lubrication. The emergence of solid lubricants has increased the lubrication potential of liquid lubricants many fold times. The term self-lubricating composites have been coined due to the association of solid lubricants with many base materials such as ceramics and metals. Various solid lubricants such as graphite, molybdenum disulphide and boron nitride have been tried by researchers, and amongst these lubricants, fluorides hold an important place. This paper presents a brief overview of solid lubricants along with a detailed description of calcium fluoride and their usage as solid lubricants in various materials, especially in metals and ceramics.

Keywords Wear · Friction · CaF_2 · Solid lubricant

1 Introduction

In the growing environmental concerns, energy demands have led to the development of green tribology. Green tribology, an emerging field in the area of tribology, deals with environmental aspects of tribology [1]. Out of the various principles of green tribology as proposed by Nasonovskyi and Bhushan [2], self-lubrication or elimination of liquid lubricants is an important one. There is widespread involvement of lubrication in various sliding applications, and without lubrication, the life of the contact materials decreases to larger extents. The science of contact surfaces, i.e. tribology would not have been originated without lubrication. Improper lubrication has led to huge energy consumption. It has been reported by scientists and researchers that wear and friction at the contact surfaces resulted in 23% of total energy consumption. Out of this, 20% is consumed to overcome friction and rest 3% for remanufacturing. Globally, saving in this regard amounts to 1.4% of the GDP on annual basis [1].

S. Mohan (✉) · A. Anand · M. I. U. Haq · A. Raina · R. Kumar
School of Mechanical Engineering, Shri Mata Vaishno Devi University, Katra 182320, India
e-mail: sanjay.mohan@smvdu.ac.in

H. Kumar and P. K. Jain (eds.), *Recent Advances in Mechanical Engineering*,
Lecture Notes in Mechanical Engineering,
https://doi.org/10.1007/978-981-15-1071-7_48

The researchers have explored that the parts of passenger cars, e.g. brakes, engine, etc. consume one-third of the energy from fuel to overcome friction. As reported by researchers, 21.5% of the fuel energy is utilized in causing the motion of the vehicle excluding friction due to brakes. With the advent of new ways and means of lubrication, losses due to friction in passenger cars can be reduced by 18% in the short term and by 61% in the long term [2]. Moreover, in case of paper mills, the consumption of energy to overcome friction in moving parts amounts to 15–25%, and the new technological advancements in the area of lubrication will result in reducing friction losses up to 11 and 23.6% in short term and long term, respectively. Similarly, in case of heavy-duty vehicles, energy utilized to overcome friction is around 26% of the fuel energy, which can be reduced to 14% by using technological innovations [3–5]. These statistics show that lubrication is inevitable due to the continuous use of sliding parts. In view of the above discussion, it is evident that there is a need is to explore better methods of lubrication.

This paper summarizes the role of solid lubricants in minimizing frictional properties and brings forth the role of fluorides as a solid lubricant. The paper focuses on the work carried out by researchers where they have used calcium fluoride as a solid lubricant and have obtained good results.

2 Solid Lubricants

Contrary to liquid lubricants, solid lubricants are solid materials that have been used to decrease the tribological properties at the contact surfaces of the sliding parts by preventing direct contact between the materials. These lubricants can be categorized as greases, free-flowing powders, additives in various oils/coatings, etc. [6]. The contact surfaces have many asperities with peaks and valleys which cause friction and wear. These peaks and valleys are levelled by the solid lubricants resulting in reduced friction and wear. Moreover, the type of lubrication offered by solid lubricants is boundary lubrication. While comparing with liquid lubrication, solid lubrication results in least contamination, corrosion resistance, dry lubrication, etc. In addition, solid lubricants can also survive in different temperatures and in typical conditions. Contrary to liquid lubrication, solid lubrication is sustainable, as it does not require changing of the lubricant, thereby having little impact on the environment as the lubricant spilled to the environment poses serious threats. These factors have given impetus to the use of solid lubricants. Dry and clean lubrication, resistance to contamination, protection against corrosion, lubrication at various conditions and temperatures, etc. are some of the significant characteristics of solid lubricants due to which such lubrication is frequently being adopted [7]. Solid lubricants are generally classified as lamellar solids, soft metals, oxides, halides, sulphides, alkali earth metals, organic materials, etc. [8].

Various techniques have been used for incorporating solid lubricants into other materials such as stir casting, powder metallurgy, pulse laser deposition, magnetron sputtering, ion-beam mixing and ion-beam-assisted deposition [9–12].

3 Fluorides

High-temperature lubrication has been of great concern for scientists and researchers. Various lubricants could not perform at high temperatures such as graphite and molybdenum disulphide. Researchers have always looked for lubricants, which could perform at both room and high temperature. Fluorides such as calcium fluoride (CaF_2) and barium fluoride (BaF_2) have played an important role, especially for high-temperature applications, i.e. for temperatures above 500 °C (1000 °F). Amongst fluorides, CaF_2 has been used extensively and still is being explored either alone as a solid lubricant or with other lubricants/fluorides. The adhesiveness of CaF_2 has made it a suitable candidate for solid lubrication [13, 14]. The thermal stability of various fluorides of calcium, barium, magnesium, aluminium, etc. has been studied at temperatures ranging from 100 to 1000 °C. The purpose of the study was to explore the possibilities of using fluorides as solid lubricant at different temperatures. The experiments carried out in air and hydrogen atmosphere have revealed that the thermal stability of zinc sulphide at temperatures from 500 to 1000 °C is higher than that of barium, calcium and magnesium fluorides. It has also been observed that sulphides of zinc decompose fully in air at 500 °C and in hydrogen and water vapour at 900 °C [15]. The hardness of fluorides of barium and calcium (CaF_2 and BaF_2) has been studied by researchers at temperatures ranging from 25 to 670 °C. The findings have shown fluoride eutectic as a good lubricant for high temperatures as it undergoes brittle to ductile transition at about 400–500 °C [16].

CaF_2 has a strong chemical, physical and microstructural influence on the tribological behaviour of contact surfaces. The structure of CaF_2 is same as that of graphite, molybdenum disulphide, i.e. it has a lamellar structure with hexagonal pattern in every plane, and these planes are connected by weak forces that shear easily at certain temperatures and thus lubricates. The efficacy of liquid lubricants in certain applications involving high temperatures or vacuum environments becomes very low, and thus, in those applications high-temperature solid lubricants like CaF_2 play an important role [17].

The low solubility of CaF_2 in water and its capability to resist radiations have placed it amongst the safe materials to be used in radiation exposure also. CaF_2 has shown good compatibility and enhanced tribological properties with many matrices. However, researchers have also reported decrease in mechanical properties, and some have confirmed increased hardness due to addition of CaF_2 [18–20].

The improvement in tribological properties against decrease in mechanical properties had made study of CaF_2 of great significance. CaF_2, being high-temperature solid lubricant, has also performed even at room temperature. This makes study of these materials most important as researchers are trying hard to find solid lubricants which could perform both at room as well as at high-temperature applications [21]. There is not much work being carried out with CaF_2 as solid lubricant. The succeeding section presents the research carried out using CaF_2 as solid lubricant with metals and ceramics.

4 CaF_2-Reinforced Metal Matrix Composites

Researchers have investigated many composites with metals as base matrix and CaF_2 as solid lubricant. The results were interesting due to the improvement in tribological properties. Wear and friction characteristics of sintered steels reinforced with titanium carbide, manganese sulphide and calcium fluoride have been investigated at high temperature. The results have shown improved lubricating characteristics with CaF_2 [22]. Fe–W–CaF_2 composites were fabricated using powder metallurgy, and their mechanical and tribological properties were investigated. Grain refinement resulting due to addition of CaF_2 along with intermetallic formations led to increased hardness. The wear and friction testing carried out at high temperature revealed decreased wear rate with increase friction at high speeds. The increase in friction at high speeds is due to the dominance of hard iron oxides over CaF_2 [23]. Researchers have developed iron base composite with molybdenum (15 wt%) and CaF_2 (6 and 9 wt%) as solid lubricant using powder metallurgy and have found that at high temperatures, there is an increase in mechanical properties such as hardness, impact strength and rupture strength, which is due to the high concentration of CaF_2 [24]. Using compaction and sintering, Fe-based composites were fabricated with FeS, ZnS, BaF_2, CaF_2 and BN as solid lubricants. Amongst all these developed composites, CaF_2 reinforced composite have shown low coefficient of friction and wear rate which is attributed to the decreasing shear strength of CaF_2 at high temperatures [25]. Sintered Fe-Mo-based composites were developed using CaF_2 as a solid lubricant, and the composites were subjected to mechanical and tribological testing at room and high temperature of 600 °C. The weight percentage of Mo and CaF_2 was varied and different composites were prepared. From the results, it was observed that reinforcing CaF_2 in Fe-10Mo matrix has enhanced mechanical as well as tribological properties. Composite with Fe–10Mo–8CaF_2 has shown raised mechanical along with tribological properties at both room and high temperature [26]. Composites with Fe–Cu–C as base and CaF_2 as solid lubricant have also been developed by the researchers and have been evaluated at room and high temperatures. Interestingly, the results have revealed that CaF_2 can offer increased tribological properties at room as well as high temperatures. However, a slight decrease in some physical and mechanical properties was observed with the increase in CaF_2 contents such as density and compression strength [27, 28]. Moreover, the wear and friction of the Fe–Cu–C as base matrix have been enhanced using CaF_2 as a solid lubricant [29]. The authors have evaluated the composites at high speeds, and improvement in the tribological properties have been reported. Fe-based impregnated diamond bit matrix was reinforced with CaF_2 and hBN, high-temperature solid lubricants. The composites were fabricated by powder metallurgy route and the volume percentage of the lubricants used was 2, 4, 6, 8 and 10. The objective was to study mechanical and tribological properties of the developed composites and draw a comparison between the usages of both high-temperature lubricants. Findings have shown that in general, increasing the lubricant content degrades the mechanical properties; however, the impact of CaF_2 in decreasing mechanical behaviour is less significant as compared

to hBN. A slight decrease in hardness was observed in CaF_2-added composite to that of hBN-added composite. Similarly, the wear loss of hBN-added composites was more than that of CaF_2-added ones. Moreover, the worn surface of CaF_2-added composite was better than that of hBN-added composite [30]. The mechanical and tribological properties of nickel base bearings developed using hot isostatic pressing have also been studied. Bearings were fabricated with nickel alone and nickel with CaF_2. CaF_2 was used in these bearings as a solid lubricant. The bearings were developed for high-speed printing machines, and the results have shown interesting outcomes. Intense friction films were observed for bearings made from nickel and CaF_2. These films formed at the contact surface resulted in low friction and enhanced wear resistance, 3.2–6 times more as compared to the bearings with nickel only [31].

5 CaF_2-Reinforced Ceramic Composites

Ceramics have been explored by many researchers in various applications and have obtained good results [32–34]. In order to obtain high tribological performance at elevated temperature of Titanium–Aluminium (TiAl) intermetallic alloy, CaF_2 was mixed with NiCr–Cr_3C_2, and finally, coatings of NiCr–Cr_3C_2–CaF_2 were fabricated on TiAl alloy using laser cladding process. From the wear and friction studies, it was found that the coating with NiCr–Cr_3C_2–40CaF_2 has shown low friction and wear rate [35]. The authors have developed coatings of cobalt alloy, titanium carbide (TiC) and CaF_2 on the copper specimen. The ratio of the coating material was fixed as Co alloy alone and variations in the proportions of Co alloy with TiC and CaF_2 powders. The coatings were fabricated on Cu specimen using laser cladding. It was observed that fine spherical particles of TiC along with spherical particles of CaF_2 dispersed uniformly in the Co matrix. The tribological tests revealed that introduction of CaF_2 and TiC in the coating resulted in reduced friction and wear rate of the fabricated composites [36]. A wear-resistant composite was fabricated using Al_2O_3 and CaF_2 using laser cladding. Al_2O_3 alone and Al_2O_3–30 wt% CaF_2 were tested for wear resistance at room temperature, and Al_2O_3–CaF_2 composite was found to exhibit better wear resistance than monolithic Al_2O_3. A unique microstructure comprising of isolated spherical CaF_2 particles in plate-like framework of Al_2O_3 was developed, and uniform distribution of the solid lubricant was observed in the inter-framework regions [37]. There was a need to develop silicon carbide-based self-lubricating composites which should operate up to a temperature of 900 °C. The researchers have developed two composites, with SiC alone and with combination of SiC and CaF_2. These composites were investigated for tribological properties and results showed raised friction and wear rate in SiC-based composites, whereas composites fabricated with SiC and CaF_2 have shown reduced friction and wear rate. This reduction in friction and wear of SiC+ CaF_2 up to 700 °C are due to the smearing of calcium fluoride on the contacting surfaces, and at 900 °C, CaF_2 reacted with silica, and thus, improvement in wear behaviour was observed [38]. CaF_2 has been tried with various ceramics to enhance their tribological properties. CaF_2 has

been reinforced in Al_2O_3/TiC composites in 5, 10 and 15 vol% using powder metallurgy route. The results have shown that addition of CaF_2 has resulted in decrease of the flexural strength, fracture toughness and hardness as compared to the base matrix. Coefficient of friction also decreased with the increase in CaF_2; however, the wear rate was observed to decrease up to 10 vol% CaF_2, and beyond 10 vol%, wear rate increases rapidly [39]. Due to the capability of enhancing wear and friction, CaF_2 was again tried by researchers with Al_2O_3 and TiC, but this time, the processing was slightly changed. Al_2O_3/TiC composites were prepared using cold pressing and sintering, and one more composite was prepared using CaF_2. Layered structure was developed by cold pressing, i.e. between the layers of Al_2O_3/TiC, there was introduced a layer of Al_2O_3/TiC/CaF_2. The friction and wear testing of these composites revealed low coefficient of friction and high wear resistance of the prepared Al_2O_3/TiC/CaF_2–Al_2O_3/TiC laminated composite as compared to that of Al_2O_3/TiC ceramic. The worn surface of the Al_2O_3/TiC/CaF_2–Al_2O_3/TiC laminated composites was found to improve and thus resulted in enhanced wear resistance. During the study, Al_2O_3/TiC/CaF_2 layer in the laminated composite was also observed to be more compact than Al_2O_3/TiC [40]. BaF_2/CaF_2 was used with Ag and Ti_3SiC_2 in a TiAl matrix and the composites were prepared using Spark Plasma Sintering at 1100 °C under a pressure of 40 MPa in pure Ar atmosphere. The proportions of BaF_2, CaF_2, Ag and Ti_3SiC_2 were varied in the composites. The objective was to investigate the tribological behaviour against Si_3Ni_4 over a temperature range from room temperature to 600 °C. The investigation depicted enhanced wear and friction behaviour which was ascribed to the synergetic effect of Ag, Ti_3SiC_2 and BaF_2/CaF_2 lubricants [41]. The lubricating potential of combined CaF_2 and BaF_2 has been investigated by fabricating a composite coating. The coating consists of base matrix as WC-Co, and copper along with both fluorides reinforced using powder metallurgy process. The weight percentage of CaF_2 and BaF_2 was kept constant at the rate of 19 wt% and 31 wt%, respectively. The findings have revealed that coatings with CaF_2 and BaF_2 exhibited raised compactness, low coefficient of friction and low wear loss. The study also reflected the capability of these solid lubricants to prevent decarburization and decomposition of the composite [42]. On the same lines, BaF_2/CaF_2 has been tried with NiCr–Cr_2O_3–Ag–CaF_2/BaF_2 coatings, and good results were obtained [43]. Ceramics such as ZrO_2 (Y_2O_3) were tried with 10 wt% of MoS_2 and 10 wt% of CaF_2 using powder metallurgy. The results of the study have shown the usefulness of such composites at both room as well as high temperatures, e.g. at room/low temperature, MoS_2 has shown good tribological behaviour, whereas at high temperatures, an intermetallic $CaMoO_4$ was formed which acted as an effective solid lubricant [44]. Table 1 summarizes various compositions, which have been discussed in this chapter.

Table 1 Compositions

S. No.	Details of the composite	Year	Reference
1	Fe–FeS/ZnS/BaF_2/CaF_2/BN	1968	[25]
2	Fe–Mo–CaF_2	1976	[24]
3	SiC–CaF_2	2001	[38]
4	CaF_2/Al_2O_3	2002	[37]
5	Fe–CaF_2/MnS/TiC	2004	[22]
6	NiCr–Cr_2O_3–Ag–CaF_2/BaF2	2005	[43]
7	Al_2O_3–TiC–CaF_2	2006	[39]
8	Fe–Mo/CaF_2	2009	[26]
9	Al_4C_3–TiC–CaF_2	2009	[35]
10	WC–Co–Cu–BaF_2/CaF_2	2010	[42]
11	Fe–W–CaF_2	2012	[23]
12	Co-based alloy–TiC–CaF_2	2013	[36]
13	Al_2O_3/TiC/CaF_2–Al_2O_3/TiC	2013	[40]
14	ZrO_2 (Y_2O_3)–MoS_2–CaF_2	2013	[44]
15	Ni–CaF_2	2014	[31]
16	Ti_3SiC_2–BaF_2/CaF_2	2014	[41]
17	Fe–Cu–C	2017, 2018	[27–29]
18	Fe–hBN/CaF_2	2018	[30]

6 Conclusion and Future Scope

The expenditure of energy in overcoming friction and the importance of solid lubricants have been discussed in the present work. Solid lubricants play a vital role in minimizing friction in the regimes where liquid lubrication is not suitable. Apart from this, solid lubricants have also been used to enhance the lubrication capability of the liquid lubricants. The paper also focuses upon the importance of fluorides especially CaF_2 as a high-temperature solid lubricant, which has also proved its worth at room temperature. Since there is not much work carried out with CaF_2 as solid lubricant, the usage of CaF_2 in combination with other low- and high-temperature lubricants has also not been explored much. Thus, there is a scope for further research where more materials with CaF_2 can be explored. This gives a space for researchers to develop more composites with combined lubricants. In fact, CaF_2 can also be tried with liquid lubricants and nano-CaF_2 powders with different matrices.

Acknowledgements Authors acknowledge assistance from colleagues and the staff for their continuous support throughout the work.

References

1. Zhang SW (2013) Green tribology: fundamentals and future development. Friction 1(2):186–194
2. Nosonovsky M, Bhushan B (eds) (2012) Green tribology: biomimetics, energy conservation and sustainability. Springer, New York
3. Holmberg K, Erdemir A (2017) Influence of tribology on global energy consumption, costs and emissions. Friction 5(3):263–284
4. Holmberg K, Andersson P, Nylund NO, Mäkelä K, Erdemir A (2014) Global energy consumption due to friction in trucks and buses. Tribol Int 78:94–114
5. Holmberg K, Siilasto R, Laitinen T, Andersson P, Jäsberg A (2013) Global energy consumption due to friction in paper machines. Tribology International 62:58–77
6. Sharma SM, Anand A (2016) Solid lubrication in iron based materials–a review. Tribol Ind 38(3)
7. Vasil'ev YN, Kolyaev IA (2011) On the friction mechanism of solid lubricants. J Fric Wear 32(5):324
8. Menezes PL, Nosonovsky M, Kailas SV, Lovell MR (2013) Friction and Wear. Tribology for Scientists and Engineers: from basics to advanced concepts. Springer, New York, pp. 43–91
9. Holmberg K, Ronkainen H, Matthews A (2000) Tribology of thin coatings. Ceram Int 26(7):787–795
10. Anand A, Haq MIU, Vohra K, Raina A, Wani MF (2017) Role of green tribology in sustainability of mechanical systems: a state of the art survey. Materi Today Proc 4(2):3659–3665
11. Singh N, Mir IUH, Raina A, Anand A, Kumar V, Sharma SM (2018) Synthesis and tribological investigation of Al-SiC based nano hybrid composite. Alexandria Eng J 57(3):1323–1330
12. Haq MIU, Anand A (2018) Dry sliding friction and wear behaviour of Hybrid AA7075/Si3N4/Gr self lubricating composites. Mat Res Expr
13. Milojević S, Pešić R, Taranović D (2015) Tribological Principles of constructing the reciprocating machines. Tribol Ind 37(1)
14. Kostornov AG, Fushchich OI, Chevychelova TM, Kostenko AD, Karpets MV (2014) Tribological characteristics of the iron-based composite at 500 °C. Powder Metall Metal Ceram 53(7–8):411–416
15. Miroshnikov VN, Shevchuk YF (1973) Choice of solid lubricants. Powder Metall Metal Ceram 12(10):844–847
16. Deadmore DL, Sliney HE (1987) Hardness of CaF_2 and BaF_2 solid lubricants at 25–670 °C. National Aeronautics and Space Administration, Lewis Research Center
17. Sliney HE (1991) Solid lubricants
18. Bolton JD, Gant AJ (1993) Phase reactions and chemical stability of ceramic carbide and solid lubricant particulate additions within sintered high speed steel matrix. Powder Metall 36(4):267–274
19. Muthuraja A, Senthilvelan S (2015) Abrasive wear performance of tungsten carbide based self-lubricant cutting tool material. Int J Refract Metals Hard Mater 51:91–101
20. Sliney HE (1973) High temperature solid lubricants: when and where to use them
21. Vadiraj A, Kamaraj M, Sreenivasan VS (2011) Wear and friction behaviour of alloyed gray cast iron with solid lubricants under boundary lubrication. Tribol Int 44(10):1168–1173
22. Zuomin L, Childs THC (2004) The study of wear characteristics of sintered high speed steels containing CaF_2, MnS and TiC additives at elevated temperature. Wear 257(3–4):435–440
23. Kostornov AG, Fushchich OI, Gorban VF, Chevychelova TM, Kostenko OD (2012) Effect of dry friction parameters on the tribosynthesis of secondary structures on composite antifriction iron-based material. Powder Metall Metal Ceram 51(7–8):412–419
24. Fedorchenko IM, Shevchuk YF, Miroshnikov VN, Borisenko VA (1976) Elevated-temperature mechanical properties of sintered iron-base materials containing calcium fluoride additions. Soviet Powder Metall Metal Ceram 15(3):238–242
25. Shevchuk YF, Zozulya VD, Khrienko AF (1968) Friction of materials with additions of substances acting as solid lubricants. Powder Metall Metal Ceram 7(12):985–988

26. Han J, Jia J, Lu J, Wang J (2009) High temperature tribological characteristics of Fe–Mo-based self-lubricating composites. Tribology letters 34(3):193–200
27. Sharma SM, Anand A (2017) Friction and wear behaviour of Fe–Cu–C based self lubricating material with CaF_2 as solid lubricant. Ind Lubric Tribol 69(5):715–722
28. Anand A, Sharma SM (2017) High temperature friction and wear characteristics of Fe–Cu–C based self-lubricating material. Trans Indian Inst Metals 70(10):2641–2650
29. Sharma SM, Anand A (2018) Effect of speed on the tribological behaviour of Fe–Cu–C based self lubricating composite. Trans Indian Inst Metals 71(4):883–891
30. Li C, Duan L, Tan S, Zhang W, Pan B (2018) Effect of CaF_2 and hBN on the mechanical and tribological properties of Fe-based impregnated diamond bit matrix. Int J Refrac Metals Hard Mater 75:118–125
31. Roik T, Gavrish A, Kyrychok P, Vitsuk Y, Askerov M (2014) Physical, mechanical and tribotechnical properties of new composite bearings for printing equipment. Zeszyty Naukowe/Wyższa Szkoła Oficerska Wojsk Lądowych im. gen. T, Kościuszki
32. Singh RP, Singhal S (2017) Rotary ultrasonic machining of macro ceramic: an experimental investigation and microstructure analysis. Mater Manuf Process 32(9):927–939
33. Kataria R, Singh RP, Kumar J (2016) An experimental study on ultrasonic machining of tungsten carbide-cobalt composite materials. AIMS Mater Sci 3(4):1391–1409
34. Singh RP, Singhal S (2018) Experimental study on rotary ultrasonic machining of alumina ceramic: microstructure analysis and multi-response optimization. Procee Inst Mech Eng Part L: J Mater Design Appl 232(12):967–986
35. Liu XB, Shi SH, Guo J, Fu GY, Wang MD (2009) Microstructure and wear behaviour of $\gamma/Al_4C_3/TiC/CaF_2$ composite coating on γ-TiAl intermetallic alloy prepared by Nd: YAG laser cladding. Appl Surf Sci 255(11):5662–5668
36. Yan H, Zhang J, Zhang P, Yu Z, Li C, Xu P, Lu Y (2013) Laser cladding of Co-based alloy/TiC/CaF_2 self-lubricating composite coatings on copper for continuous casting mold. Surf Coat Technol 232:362–369
37. Wang HM, Yu YL, Li SQ (2002) Microstructure and tribological properties of laser clad CaF_2/Al_2O_3 self-lubrication wear-resistant ceramic matrix composite coatings. Scripta Materialia 47(1):57–61
38. Shuaib M, Davies TJ (2001) Wear behaviour of a REFEL SiC containing fluorides up to 900 °C. Wear 249(1–2):20–30
39. Jianxin D, Tongkun C, Zeliang D, Jianhua L, Junlong S, Jinlong Z (2006) Tribological behaviours of hot-pressed Al_2O_3/TiC ceramic composites with the additions of CaF_2 solid lubricants. J Eur Ceram Soc 26(8):1317–1323
40. Yang X, Cheng J, Song P, Wang S, Yang L, Wang Y, Mao K (2013) Wear behaviour of cold pressed and sintered Al_2O_3/TiC/CaF 2–Al_2O_3/TiC laminated ceramic composite. Acta Metallurgica Sinica (English Letters) 26(2):157–166
41. Shi X, Yao J, Xu Z, Zhai W, Song S, Wang M, Zhang Q (2014) Tribological performance of TiAl matrix self-lubricating composites containing Ag, Ti_3SiC_2 and BaF_2/CaF_2 tested from room temperature to 600 °C. Mater Des 53:620–633
42. Yuan J, Zhu Y, Ji H, Zheng X, Ruan Q, Niu Y, Zeng Y (2010) Microstructures and tribological properties of plasma sprayed WC–Co–Cu–BaF_2/CaF_2 self-lubricating wear resistant coatings. Appl Surf Sci 256(16):4938–4944
43. Kim G, Choi H, Han C, Uhm S, Lee C (2005) Characterization of atmospheric plasma spray NiCr–Cr2O3–Ag–CaF2/BaF2 coatings. Surf Coat Technol 195(1):107–115
44. Kong L, Bi Q, Niu M, Zhu S, Yang J, Liu W (2013) ZrO_2 (Y_2O_3)–MoS_2–CaF_2 self-lubricating composite coupled with different ceramics from 20 to 1000 °C. Tribol Int 64:53–62

Friction and Wear Behaviour of AA2024/ZrO_2 Composites: Effect of Graphite

Smridh Slathia, Rahul Anand, Mir Irfan Ul Haq, Ankush Raina, Sanjay Mohan, Rajiv Kumar and Ankush Anand

Abstract The aim of the paper was to study the tribological behaviour of a novel self-lubricating AA2024–ZrO_2–Gr hybrid composite. A hybrid composite AA2024–ZrO_2–Gr is fabricated with 6 wt% zirconia (ZrO_2) reinforcement and varying the percentage from 0 to 4.5% by weight of graphite powder. Unidirectional friction/wear tests were carried out on a tribometer using pin-on-disc configuration. The results revealed that composites with 4.5 wt% of graphite exhibited minimum coefficient of friction (COF), whereas the composite with 3 wt% graphite showed minimum wear loss.

Keywords AA2024 · Friction · Wear · Self-lubricating composite · Tribofilm

1 Introduction

Modern engineering applications require materials that are light in weight [1], less expensive and have a vast spectrum of mechanical properties [2–6]. It becomes arduous for a monolithic material system to accommodate all the properties required in various engineering applications [7]. Aluminium and its alloys play an important role in automobile and aerospace sectors by reason of their high strength-to-weight ratio, better mechanical behaviour and corrosion resistance [8–11]. However, the problem of less resistance to abrasive wear with aluminium inhibits their use in most of the sliding applications [12]. In order to enhance the frictional and wear behaviour of aluminium alloys, they were associated with ceramic reinforcements which improved hardness and compression strength [4, 13] whereas degraded frictional properties which paved a way for the addition of solid lubricants as particulate in composites [14, 15]. These composites exhibit low thermal expansion, low friction and wear, high damping capacity, and reduced wear at contact zone with reduced temperature. Previous research reports that addition of 5% WS_2 and nano-alumina in

S. Slathia · R. Anand · M. Irfan Ul Haq (✉) · A. Raina · S. Mohan · R. Kumar · A. Anand
School of Mechanical Engineering, Shri Mata Vaishno Devi University,
Katra, Jammu 182320, India
e-mail: haqmechanical@gmail.com

H. Kumar and P. K. Jain (eds.), *Recent Advances in Mechanical Engineering*,
Lecture Notes in Mechanical Engineering,
https://doi.org/10.1007/978-981-15-1071-7_49

Al–SiC–nAl_2O_3 results in the reduction of wear and the coefficient of friction [12]. Baradeswaran et al. [16] in their study established increase in wear resistance with the addition of 10 and 5 wt% of B_4C and Gr. In another research, it was concluded that the addition of Gr as solid lubricant decreases wear with the rise in sliding speed and reported 5 wt% graphite as the optimum concentration [17]. Radhika et al. [18] in their research confirm the reduction in wear rate of reinforced composite (Al–9%Al_2O_3–3%Gr) in comparison with the base alloy. The self-lubricating Al–Gr composite develops a protective tribolayer of solid lubricant on the tribosurface, and its lamellar structure of graphite reduces shear stress at the surface of composite material [19–21]. This tribofilm formation prevents contact between metal surfaces and hence governs the wear behaviour of the material. In the present work, there is an attempt to evaluate the influence of graphite on wear and frictional properties of AA2024–ZrO_2 composite.

2 Methodology and Materials

The material details and the process used for fabrication of the composites have been discussed in previous work [22]. The wear and friction testing was carried out using a pin-on-disc (POD) Tribomachine. The testing was carried in accordance with ASTM D99. Proper procedure as per metallographic standards was adopted for sample preparation. All the testing was carried out at room temperature under dry conditions.

3 Results and Discussion

3.1 Effect of Graphite and Load on Wear Behaviour

The tribotesting was conducted for different samples, and weight of the pins was observed before as well as after the wear. Hence, wear loss for each sample is calculated and recorded against the different loads. Figure 1 represents the wear loss at constant loads for different specimens. The wear losses increase with the increasing loads. The increase in the mass loss with the rise in the applied load is in accordance with wear law given by Archard [23]. The wear/mass loss is a function of two parameters (a) the decrease in hardness due to graphite addition and (b) the protective tribofilm formation capability of graphite [24, 25]. Due to tribofilim formation by graphite, the contact shifts to composite tribolayer thereby reducing the wear [26]. It can be concluded that the film formation factor dominates the decrease in hardness due to graphite addition till 3 wt% graphite and afterwards the latter factor dominates the former.

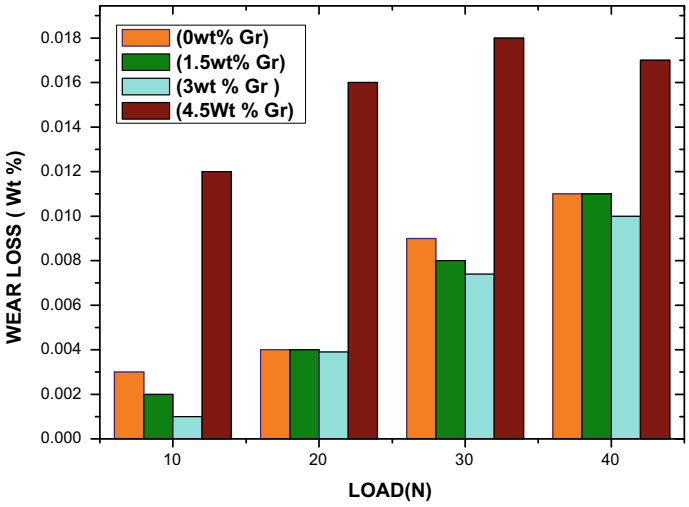

Fig. 1 Wear loss at constant loads

3.2 Effect of Load and Graphite on the Frictional Coefficient

Figure 2 depicts the friction coefficient for all the samples tested at 10, 20, 30, and 40 N, respectively. It is found that at lower loads, the decrease in frictional coefficient is not substantial in comparison with decrease at higher loads. This behaviour attributes to delay in the formation of stable tribolayer due to less quantity of graphite particles in wear debris at lower load conditions (10 N). It can also be observed from

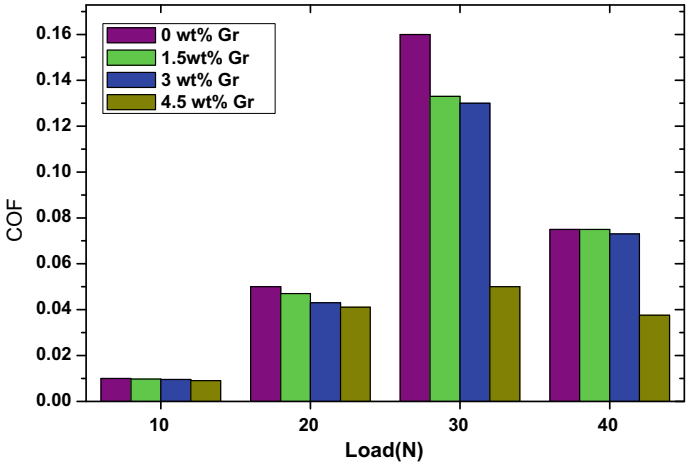

Fig. 2 Effect of graphite content on COF

the figure that with the increment in normal load (10 N–30 N), friction coefficient increases which is due to the increased asperity to asperity contact at higher loads which in turn increases the contact area prone to sliding [27]. Also, the value of COF decreases with an increasing percentage of graphite powder as reinforcement at constant loads. It shows shear characteristics [28] of graphite under wear conditions forming a graphite tribolayer restraining contact between metals in contact and lowers the friction coefficient. This is due to the increase in the quantity of graphite released and smeared on the wear surface. Contrary to this, at higher load conditions (40 N) the softening factor becomes dominant as high temperature due to heat generated at the interfacial contacts and thus leading to the layer softening of the composite leading to decrease in COF.

4 Conclusions

A novel composite comprising of AA2024 as the base and ZrO_2 as the reinforcement and four different concentrations (0, 1.5, 3, 4.5) wt% of solid lubricant (graphite) was developed using stir casting method. In this study, it has been observed that the addition of graphite has enhanced the frictional and wear behaviour of the base alloy up to a certain concentration as discussed below:

(a) Wear rate deteriorates with the rise in the graphite addition up to 3 wt% due to tribofilim formation; afterwards, there is surge in wear rate at higher concentration due to decrease in hardness of the material.
(b) The COF exhibits increasing trend with increase in normal load up to 30 N; after that, it decreases as surface layer softens due to rise in temperature at higher loading conditions. At constant load conditions, COF decreases with increase in Gr %.

Results obtained suggest that this hybrid composite has the potential to withstand as a strong contender for various industrial applications.

References

1. Anand A, Irfan Ul Haq M, Vohra K, Raina A, Wani MF (2017) Role of green tribology in sustainability of mechanical systems: a state of the art survey. Mater Today Proc 4
2. Singh RP, Singhal S (2016) Rotary ultrasonic machining: a review. Mater Manuf Process 31:1795–1824
3. Shafi WK, Raina A, Ul Haq MI (2018) Friction and wear characteristics of vegetable oils using nanoparticles for sustainable lubrication. Tribol Mater Surf Int 12
4. Ul Haq MI, Anand A (2018) Friction and wear behavior of AA 7075-Si_3N_4 composites under dry conditions: effect of sliding speed. Silicon
5. Dursun T, Soutis C (2014) Recent developments in advanced aircraft aluminium alloys. Mater Des 56:862–871

6. Wang DZ, Peng HX, Liu J, Yao CK (1995) Wear behaviour and microstructural changes of SiCw-Al composite under unlubricated sliding friction. Wear 184:187–192
7. Rino JJ, Chandramohan D, Sucitharan KS, Jebin VD (2012) An overview on development of aluminium metal matrix composites with hybrid reinforcement. IJSR, India online, ISSN 2319-7064
8. Singh RP, Singhal S (2018) Experimental study on rotary ultrasonic machining of alumina ceramic: microstructure analysis and multi-response optimization. Proc Inst Mech Eng Part LJ Mater Des Appl 232:967–986
9. Singh RP, Kumar J, Kataria R, Singhal S (2015) Investigation of the machinability of commercially pure titanium in ultrasonic machining using graph theory and matrix method. J Eng Res 3
10. Irfan Ul Haq M, Raina A, Vohra K, Kumar R, Anand A (2018) An assessment of tribological characteristics of different materials under sea water environment. Mater Today Proc 5
11. Harris SJ (1988) Cast metal matrix composites. Mater Sci Technol 4:231–239
12. Singh N, Mir IUH, Raina A, Anand A, Kumar V, Sharma SM (2018) Synthesis and tribological investigation of Al–SiC based nano hybrid composite. Alexandria Eng J 57:1323–1330
13. Haq MIU, Anand A (2018) Dry sliding friction and wear behavior of AA7075–Si_3N_4. Compos Silicon 10:1–11
14. Singh J (2016) Fabrication characteristics and tribological behavior of Al/SiC/Gr hybrid aluminum matrix composites: a review. Friction 4:191–207
15. Saravanan C, Subramanian K, Krishnan VA, Narayanan RS (2015) Effect of particulate reinforced aluminium metal matrix composite–a review. Mech Mech Eng 19:23–30
16. Baradeswaran A, Vettivel SC, Perumal AE, Selvakumar N, Issac RF (2014) Experimental investigation on mechanical behaviour, modelling and optimization of wear parameters of B_4C and graphite reinforced aluminium hybrid composites. Mater Des 63:620–632
17. Baradeswaran A, Perumal AE (2014) Wear and mechanical characteristics of Al 7075/graphite composites. Compos Part B Eng 56:472–476
18. Radhika N, Subramanian R, Venkat Prasat S, Anandavel B (2012) Dry sliding wear behaviour of aluminium/alumina/graphite hybrid metal matrix composites. Ind Lubr Tribol 64:359–366
19. Ames W, Alpas AT (1995) Wear mechanisms in hybrid composites of graphite-20 Pct SiC in A356 aluminum alloy (Al-7 Pct Si-0.3 Pct Mg). Metall Mater Trans A 26:85–98
20. Basavarajappa S, Chandramohan G, Mahadevan A, Thangavelu M, Subramanian R, Gopalakrishnan P (2007) Influence of sliding speed on the dry sliding wear behaviour and the subsurface deformation on hybrid metal matrix composite. Wear 262:1007–1012
21. Yang JB, Lin CB, Wang TC, Chu HY (2004) The tribological characteristics of A356. 2Al alloy/Gr(p) composites. Wear 257:941–952
22. Slathia S, Haq MIU, Raina A (2018) Fabrication and mechanical characterization of AA2024–ZrO_2–Gr hybrid composite. AIP Conf Proc 2006:30047
23. Archard J (1953) Contact and rubbing of flat surfaces. J Appl Phys 24:981–988
24. Ul Haq MI, Anand A (2018) Dry sliding friction and wear behaviour of hybrid AA7075/Si_3N_4/Gr self lubricating composites. Mater Res Express 5:66544
25. Jinfeng L, Longtao J, Gaohui W, Shoufu T, Guoqin C (2009) Effect of graphite particle reinforcement on dry sliding wear of SiC/Gr/Al composites. Rare Met Mater Eng 38:1894–1898
26. Suresha S, Sridhara BK (2010) Effect of addition of graphite particulates on the wear behaviour in aluminium-silicon carbide-graphite composites. Mater Des 31:1804–1812
27. Carbone G, Bottiglione F (2008) Asperity contact theories: do they predict linearity between contact area and load? J Mech Phys Solids 56:2555–2572
28. Mohan S, Pathak JP, Gupta RC, Srivastava S (2002) Wear behaviour of graphitic aluminium composite sliding under dry conditions. Zeitschrift für Met. 93:1245–1251

A Fractographic Study of PE, PP Self-reinforced Composites in Quasi-static Loading Conditions

M. Sharan Chandran and K. Padmanabhan

Abstract This study is an attempt to fill the gap in the fractographic studies conducted in various quasi-static mechanical tests to recognize the failure mechanisms and their correlation with its properties of self-reinforced polymer composite materials (SRC). SRCs are the class of composite materials developed by combining the same family of materials as constituent matrix and reinforcement. Thermoplastic linear aliphatic olefins like polyethylene (PE) and polypropylene (PP) are the systems analysed here for the purpose of deep understanding of their microstructural properties and correlations with the structural properties. Tension, in-plane shear and flexural parameters are tested, evaluated and correlated with corresponding fractographic features revealed under scanning electron microscopy (SEM). Selecting three different systems for this analysis also assisted in comparative study of various failure mechanisms and variations in fractographic features of SRCs with different chemical structure under quasi-static loading conditions. Fractography revealed failure mechanisms like matrix cracking, categories of fibre failures under different types of loading, effect of interface in bonding as well as fracture, shear flow patterns of matrix, phenomena like brooming, effect of coating in interface and fracture under quasi-static loading and behaviour matrix and reinforcement under various quasi-static loading.

Keywords Fractography · PE · PP · Quasi-static · SEM

1 Introduction

Polymer composite materials are alternative to metals in many applications with advantages of strength-to-weight ratio and strength-to-stiffness ratio. Aerospace and automobile applications are greatly inclined towards such researches to improve the

M. Sharan Chandran · K. Padmanabhan (✉)
School of Mechanical Engineering, VIT, Vellore 632014, India
e-mail: padmanabhan.k@vit.ac.in

M. Sharan Chandran
e-mail: Sharanchandran.m@vit.ac.in

H. Kumar and P. K. Jain (eds.), *Recent Advances in Mechanical Engineering*,
Lecture Notes in Mechanical Engineering,
https://doi.org/10.1007/978-981-15-1071-7_50

fuel efficiency [1–3]. Recycling the polymer materials is one of the greatest challenges in the development of these composites. Interfacial adhesion of matrix and the reinforcement is major factor in mechanical properties and overall performance of composite materials. Self-reinforced composites (SRC) constituting matrix and reinforcement from the same family of polymers offer better interface, recyclability and commendable strength-to-weight ratio and rigidity-to-weight ratio if the constituent components are selected properly [4, 5]. Polyethylene, polypropylene, polyamide, polyethylene terephthalate, poly vinyl chloride and poly lactic acid are the mostly selected polymers for different analysis so far [6, 7]. Most of the self-reinforced polymeric composites are made up of hot compaction method by utilizing the availability of a family of different polymers with wide range of melting points based on their different crystallinity. In this study also hot compaction method is adopted for the fabrication of laminates with matrix and reinforcement possesses a comfortable thermal processing window. Under the thermal treatment, matrix is expected to melt and the fibre is expected to be intact [8, 9].

Fractographic analysis reveals the microstructural reasons of failure and flashes light into the deep understanding of failure mechanisms. A recent study was carried out on knitted-reinforced SRCs prepared from polyamide 6 through powder coating and compression moulding techniques by Shafagh et al. They reported that the fractographic studies revealed a homogeneous distribution of polyamide 6 monofilaments in the knitted reinforcements without any damage during compression moulding [10]. Fractographic analysis of aerospace grade unidirectional carbon fibre-reinforced plastics and unidirectional glass fibre-reinforced plastics subjected to tensile loads are carried out by M. Suresh Kumar et al. and identified various events in fracture like crack initiation, propagation and cause of fracture with the help of SEM images [11]. Fractographic features of carbon/epoxy laminate composites are studied by J. Bieniaś et al. subjected to static and dynamic loads under elevated temperature. They emphasized the role interface in the occurence of crack and its subsequent propagation during mechanical loading and figured out some of the characteristic failure areas [12]. C. V. Opelt et al. analysed fractographic features with scanning electron microscope (SEM) on the effects of hydrothermal conditioning on carbon/epoxy laminates subjected to axial compression. Fractographic studies revealed that the moisture exposure causes a plasticizing effect causing a reduction in stiffness [13]. One of the notable recent fractographic study on thermoplastics is carried out by F. S. Senatov et al. about the structure and boundaries of UHMWPE and UHMWPE based composites subjected to mechanical activation and hot pressing and recognized that the fillers in the matrix phase enhances the strength of the boundary only due to high melt-viscosity of UHMWPE [14]. Elementary study on quasi-static mechanical properties of thermoplastics PE and PP systems is conducted by our research group well before and stated that the close tensile and in-plane shear structural properties could be due to the strong interface of these SRCs [15]. In this context, the present study is to bridge the gap in analysis and comparison of fractographic features of quasi-static mechanical tests in two chemically different systems of thermoplastic polymer SRCs of PE and PP. Some of the researchers have reported various fractographic features that can be studied in composite mateirls [16–19].

2 Theoretical Considerations

2.1 Quasi-static Mechanical Tests

Tension, flexure and in-plane shear are the tests conducted on polymer composites laminates based on the following formulae. Ultimate tensile stress under quasi-static loading can be evaluated from the expression.

$$\sigma = \frac{P}{bd} \tag{1}$$

where P being the applied load in Newton, b and d are the breadth and depth in millimetres, respectively. Young's modulus is evaluated from the slope of stress–strain plot.

$$\sigma\,(\text{flexure}) = \frac{3FL}{2bd^2} \tag{2}$$

$$E\,(\text{flexure}) = \frac{d\sigma}{d \in} \tag{3}$$

is the expression used for calculating the ultimate bending stress where F is the maximum flexural load and the flexural modulus can be evaluated from the slope of stress–strain curve of quasi-static flexural loading.

$$\sigma\,(\text{in-plane shear}) = \frac{P(i)}{bw} \tag{4}$$

Ultimate in-plane shear stress is evaluated from Eq. (3) in which the $P(i)$ represents the maximum in-plane shear load and bw is the area subjected to shear. In-plane shear test is conducted on a notched specimen with notches on both the sides of a laminate samples prepared at equal distance from the centre up to the mid-plane such that when the tensile load applies, the middle plane will be subjected to in-plane shear failure.

2.2 Fractography with SEM

ZEISS EVO 18 scanning microscope is used for the fractography with a coupled assistance from smartSEM software. Electron beam generated from lanthanum hexaboride (LaB_6) gun is passed through gold-coated samples of PE and PP. With an accelerating voltage of 5 kV, various fracture features could be studied from the micrographs.

Table 1 Details of raw materials

Polyethylene: Matrix volume fraction 73.7%	**Sheet**: HDPE Density: 0.93–0.97 g/cc Melting temperature: 125 °C **Fabric**: PE/PET copolymer Density 0.95 g/cc Melting point: 270 °C
Polypropylene: matrix volume fraction 75.1%	**Sheet**: PPs Density: 0.92 g/cc Melting temperature: 171 °C **Fabric**: coated iPP fabric Density: 0.9 g/cc Melting temperature: 279 °C

Table 2 Dimensions of the test samples

Test method	Dimensions
Tension test	Length: 250 mm (gauge length 190 mm, thickness: 3–4 mm, width: 25 mm)
Flexure test	Length: 16 × thickness (thickness: 3–4 mm, width: 25 mm)
In-plane shear	Length: 250 mm (thickness: 3–4 mm, width: 25 mm distance between notches: 25 mm)

3 Experimental Details

3.1 Laminate Fabrication and Sample Preparation

Laminates were fabricated using film stacking technique and instrument utilized for the fabrication was hot air type industrial oven. Both sheets and fabric were cut into 500 * 500 mm square sheets, weighed separately using a sensitive weighing machine and cleaned thoroughly. 6-mm mild steel plates each with 12 kg weight covered with high quality, high melting point nylon sprayed with silicon-v-bond is used as side plates. The stacking of fibre and matrix is done between these plates. Clamps are used for applying uniform load and a pressure of 1 N/mm^2 (10 bar) and hold the plates together. The set-up is placed inside the oven and temperature is set and maintained at that temperature for 45–60 min. Processing temperature is selected from the melting point data obtained through differential scanning calorimetry (DSC) and thermogravimetric analysis (TGA) mentioned in a previous study of the authors. Processing window has to be selected in such a way that the matrix melts and the fabric remains intact [15]. Laminate is allowed to cool inside the oven for 12 h before it is removed. The composite layers are formed because of hot compaction which causes considerable shear in the matrix due to its lower melting point compared to the fibre (Fig. 1).

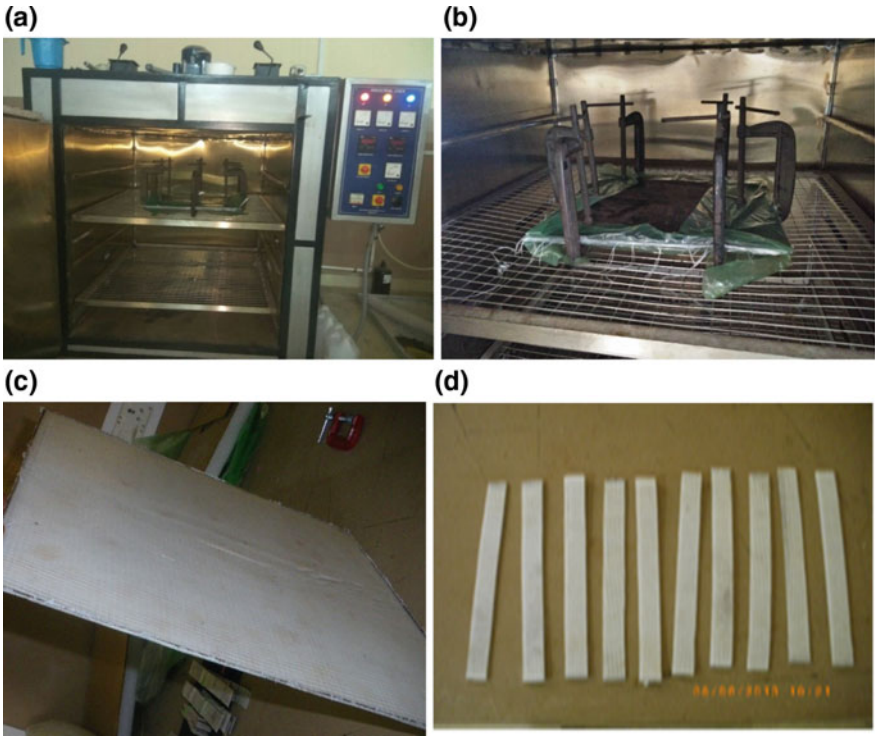

Fig. 1 Fabrication steps: **a** industrial oven, **b** assembly in the oven, **c** prepared laminate and **d** prepared samples

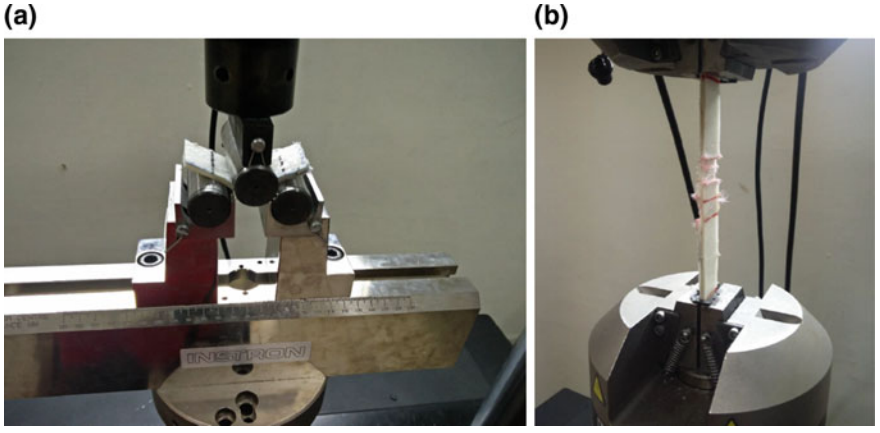

Fig. 2 **a** Flexure test, **b** in-plane shear test

3.2 Quasi-static Mechanical Tests

Tension, three-point bending and in-plane shear are the tests conducted on three different polymer composite materials in order to correlate their mechanical properties with the fractography. Instron 8801 up to ±100 kN axial force capacity and Patented Dyna cell load cell features with compensation for inertial loads caused by heavy grips and fixtures and with standard or extra-height frame options are used for the quasi-static mechanical tests. A standard of ASTM D3039/3039 M-95A is used for tension test and ASTM standard D790 M-03 is used for the flexural test. A crosshead speed of 5 mm/min was set for all the tests and tests were conducted at a temperature of 25 ± 2 °C. Same dimensions of the samples were maintained in order to compare the properties and fractography. Properties of the materials and the specimen dimensions are given in (Tables 1 and 2). Testing of the samples are shown in Fig. 2.

3.3 SEM Details of Fractography

Proper coating is required because the polymer samples are non-conducting. Samples are gold-coated initially for 90 s and loaded in the vacuum chamber of EVO 18 scanning electron microscope. An optimum coating time should be selected carefully in order to avoid charging of the samples which will lead to unclear images and strips in the images. Surface images were taken at 500× magnification and the details are captured by increasing the magnification.

4 Results and Discussions

4.1 Tensile, Flexural and In-Plane Shear Properties

Figures 3, 4 and 5 are the representative plots obtained directly from Instron from quasi-static tension, flexural and in-plane shear tests. Various parameters associated with these tests and evaluated properties are listed in Tables 3, 4, 5, 6, 7, and 8.

From the data, it could be noticed that average load-carrying capacity of SRCs made with PP > PE under quasi-static tensile loading while the load-carrying capacity of PP > PE under flexural loading and PP > PE for in-plane shear loading similar to tensile loading.

Average tensile modulus is PP > PE and average flexural modulus varies like PE > PP. shear modulus is also showing the similar trend of PE > PP under quasi-static in-plane shear test.

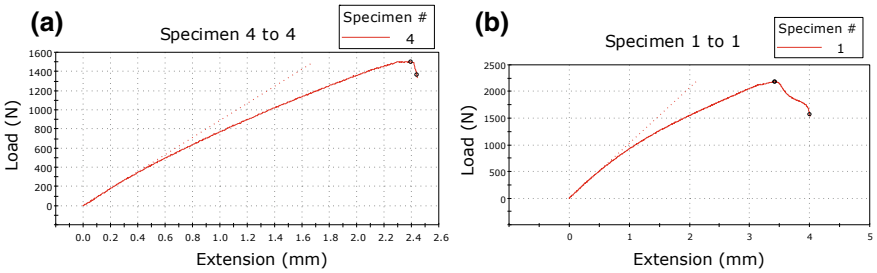

Fig. 3 Sample load deflection plot of **a** PE, **b** PP SRC tension test

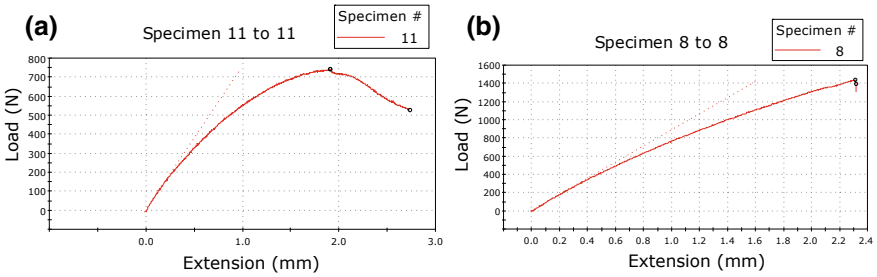

Fig. 4 Sample load deflection plot of **a** PE and **b** PP SRCs under in-plane test

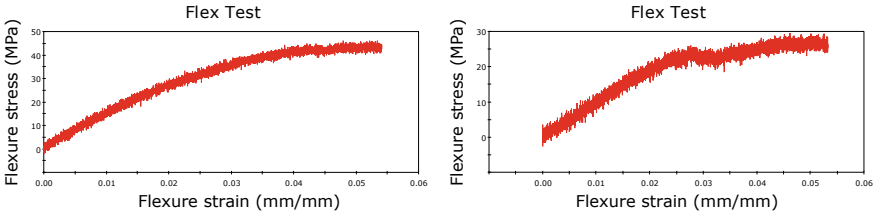

Fig. 5 Sample stress–strain plot of PE SRC under flexure test

Table 3 PE SRC (tension test data)

PE SRC (tension)	Maximum load (N)	Ultimate tensile stress (MPa)	Strain at maximum load (%)	Young's modulus (MPa)
Maximum	1505	20.043	2.822	2976.42
Average	1376.4	18.342	1.607	2764.99
Minimum	1260.6	17.564	0.975	2429.24
Standard deviation	122.73	1.543	1.05	294.01

Table 4 PE SRC (in-plane shear test data)

PE SRC (in-plane shear)	Maximum load (N)	Ultimate shear stress (MPa)	Shear strain at maximum load (%)	Shear modulus (MPa)
Maximum	1248.276	2.00	1.201	2731.38
Average	841.145	1.35	0.988	2479.486
Minimum	534.94	0.86	0.669	2191.238
Standard deviation	367.222	0.59	0.281	271.9

Table 5 PE SRC (flexural test data)

PE SRC (flexural)	Maximum load (N)	Ultimate flexural stress (MPa)	Flexural strain at maximum load (%)	Flexural modulus (MPa)
Maximum	147.58	51.93	5.1	6582.563
Average	140.05	41.5	5	5952.267
Minimum	130.58	37.2	4.9	5617.555
Standard deviation	6.57	6.13	0.07	431.274

Table 6 PP SRC (tension test data)

PP SRC (tension)	Maximum load (N)	Ultimate shear stress (MPa)	Shear strain at maximum load (%)	Young's modulus (MPa)
Maximum	2186.63	29.100	1.62	3451.69
Average	1905.23	26.200	1.53	2760.63
Minimum	1672.38	22.300	1.37	2610.5
Standard deviation	289.65	4.010	0.13	347.48

Table 7 PP SRC (in-plane shear test data)

PP SRC (in-plane shear)	Maximum load (N)	Ultimate shear stress (MPa)	Shear strain at maximum load (%)	Shear modulus (MPa)
Maximum	1730.32	2.77	0.4444	1998.892
Average	1392.24	2.23	0.28986	1750.905
Minimum	1101.09	1.76	0.1151	1551.101
Standard deviation	278.28	0.45	0.1603	167.54

Table 8 PP SRC (flexural test data)

PP SRC (flexural)	Maximum load (N)	Ultimate flexural stress (MPa)	Flexural strain at maximum load (%)	Flexural modulus (MPa)
Maximum	282.6	132.26	0.066	1328
Average	167.75	63.60	0.058	1249.92
Minimum	125.89	43.44	0.05	1154.53
Standard deviation	66.402	38.52	0.007	70.389

Average stress under tensile loading is PP > PE and flexural loading shows a trend of PE > PP while in-plane shear varies like PP > PE. Average tensile strain (%) is PE > PP. Similar trend can be observed from flexural and in-plane shear.

4.2 Fractographic

Fractography of tension test samples

Figures 6, 7, 8, 9, 10, and 11 are the fractographic images of PE and PP tested under quasi-static tension, in-plane shear and flexural loading. Figure 6a–c indicates failure pattern of PESRCs under quasi-static tensile loading. Clear matrix failure with fibre pull-out and interface failure is noted in the micrograph. Most of the fibres experienced an angled failure indicating a shear failure. Plastic deformation with stress whitening and layer formation was also noticed. Tensile failure in PE SRC is initiated through matrix failure followed by the fibre fracture. Matrix failure begins at the interface and propagates to the other regions. It could also be noticed that further yielding and pull-out of the fibres occurs and crack initiates at a location in the cross section of the fibre radiating in an angular direction inducing a catastrophic failure at some locations.

Figure 7a–c is the fractographic images of PPSRC subjected to tensile failure. Failure of the fibres is along the normal plane in brittle nature. Coating of the fibres remained intact in failure. Most of the interfaces remained intact indicating the strong interfacial strength and the failure was purely due to the brittle fracture of fibres followed by brittle fracture of matrix. Fibre corss sections revealed radial patterns indicating the direction of crack propagation and the failed surface were normal to the load direction.

Fractography of flexural test samples

Figure 8 shows the fractographic images of PE SRCs. Even though the samples got plastically deformed, none of the samples fractured and possessed moderate rigidity. Wrinkles were visible on the surface subjected to flexural compressive stresses.

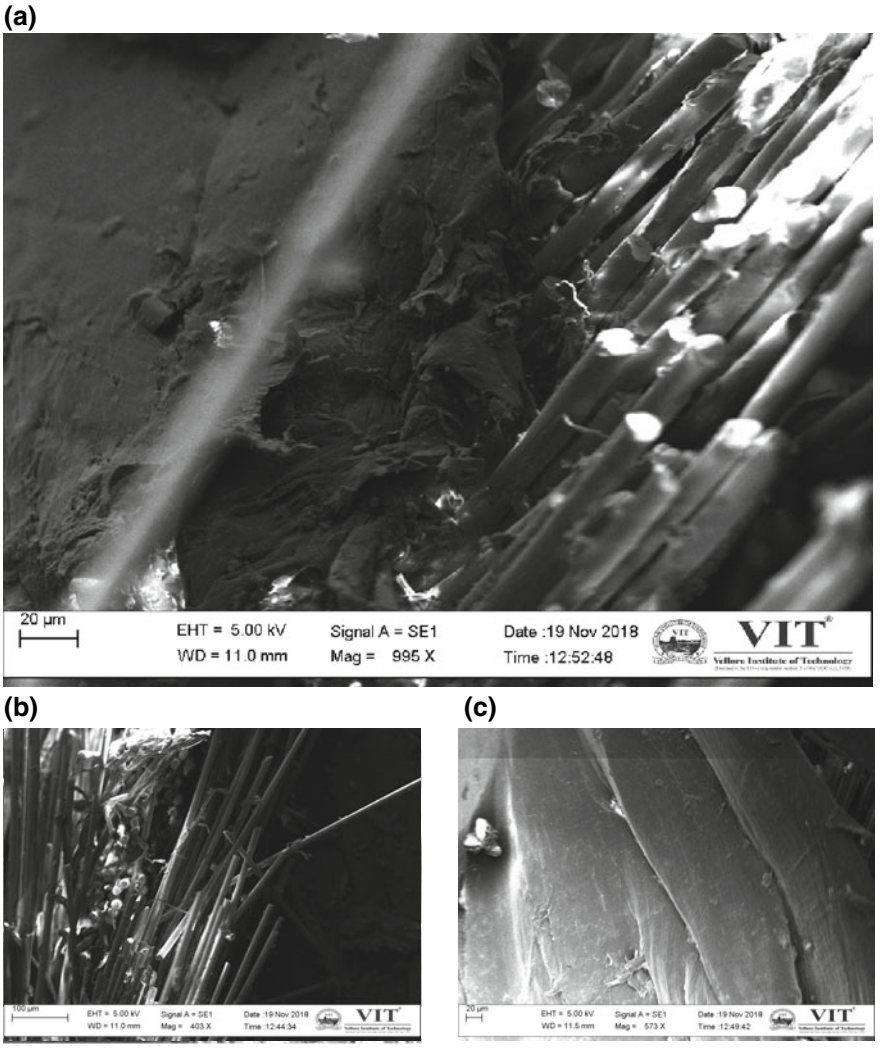

Fig. 6 Fractography of PE SRC subjected to tensile failure

Figure 9 explains the fracture features of PPSRCs subjected to flexural loading. Similar to PESRCs, PPSRCs also did not experience any visible fracture and experienced an excessive plastic deformation. Plastic deformation was visible with stress whitening on the surface of maximum flexural tensile stresses. Wrinkles due to compressive stresses were more clearly visible in PPSRCs.

In-plane shear

In-plane shear test conducted on notched samples of PESRCs experienced shear failure along the interface. SEM analysis revealed excessive shear flow of matrix

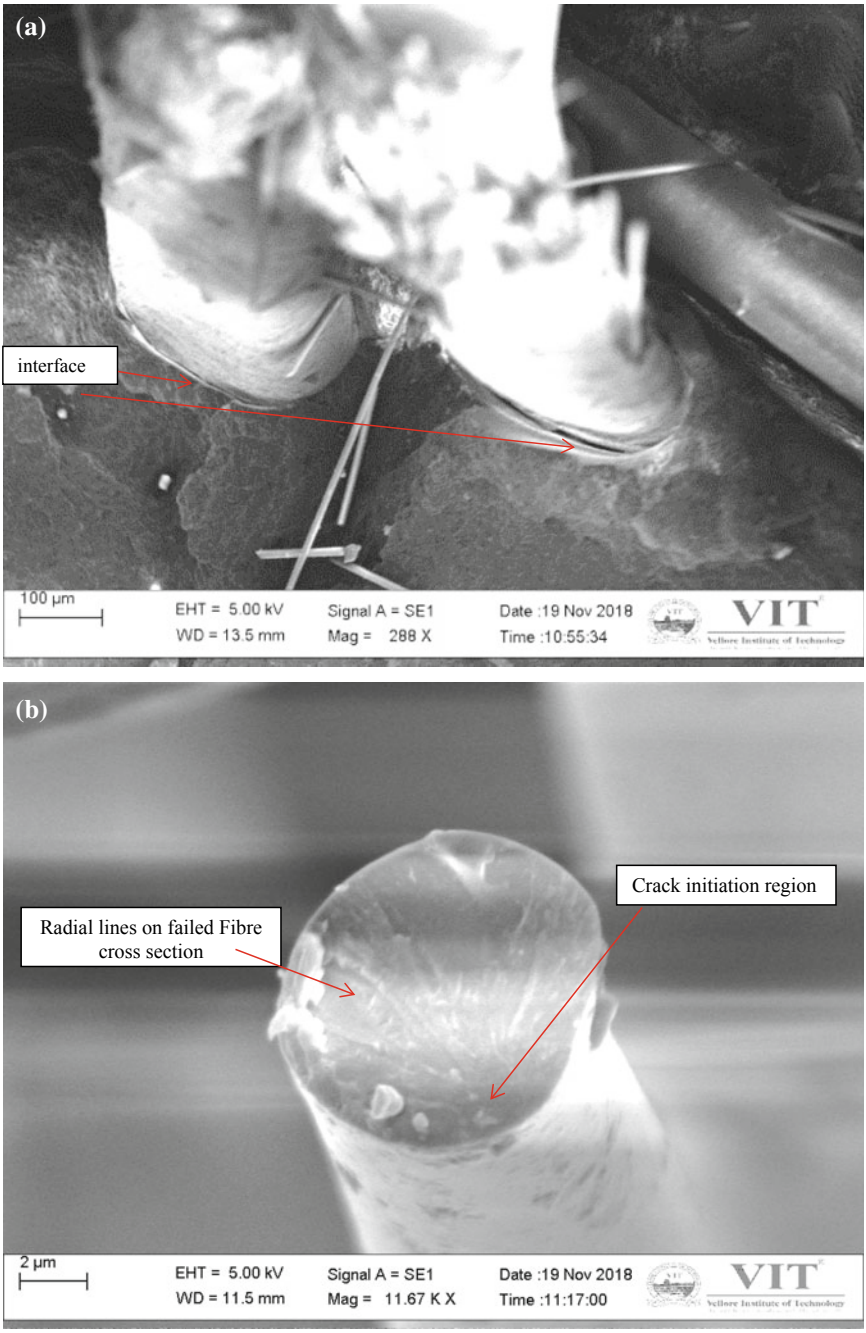

Fig. 7 Fractography of PP SRC subjected to tensile failure

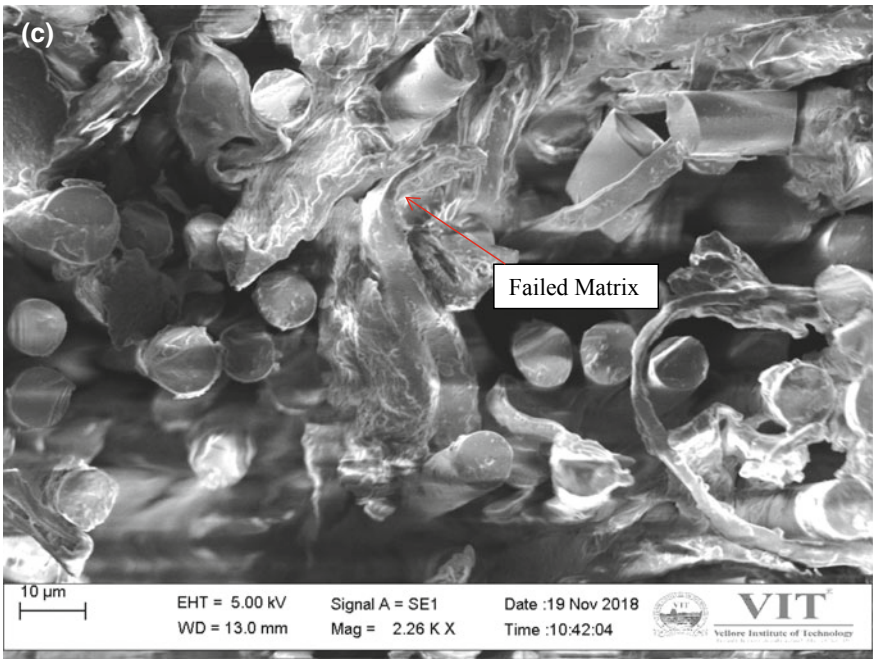

Fig. 7 (continued)

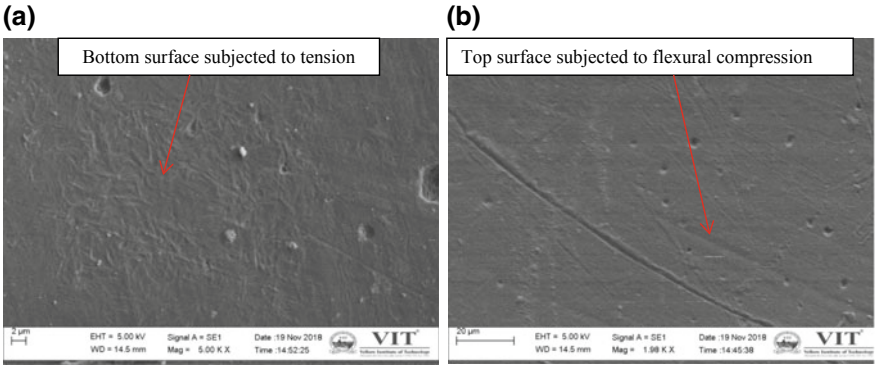

Fig. 8 Fractography of PE SRC subjected to flexural failure

(Fig. 10a). The region below the notch was failed by pure shear. Angled failure of the fibres was also visible (Fig. 10c). Crack propagation pattern was visible on the cross section.

PPSRCs also had undergone excessive shear failure under in-plane shear stress. Delamination, fibre pull-out and matrix shear flow were visible in the fractography (Fig. 11). Transverse fibres remain intact while the coating of the longitudinal

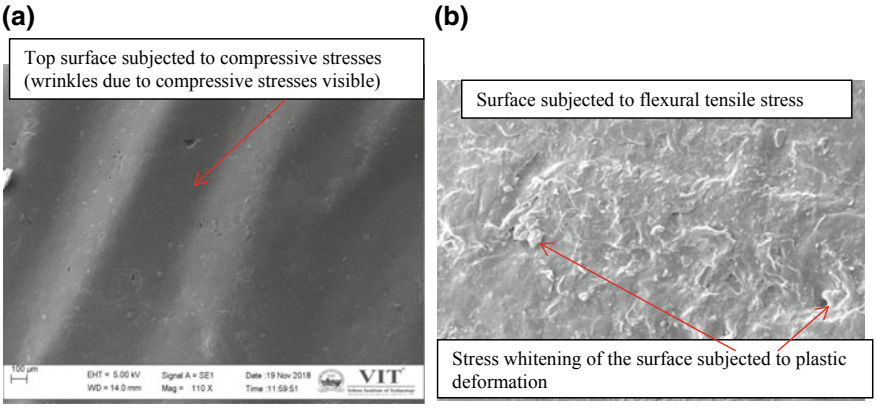

Fig. 9 Fractography of PP SRC subjected to flexural failure

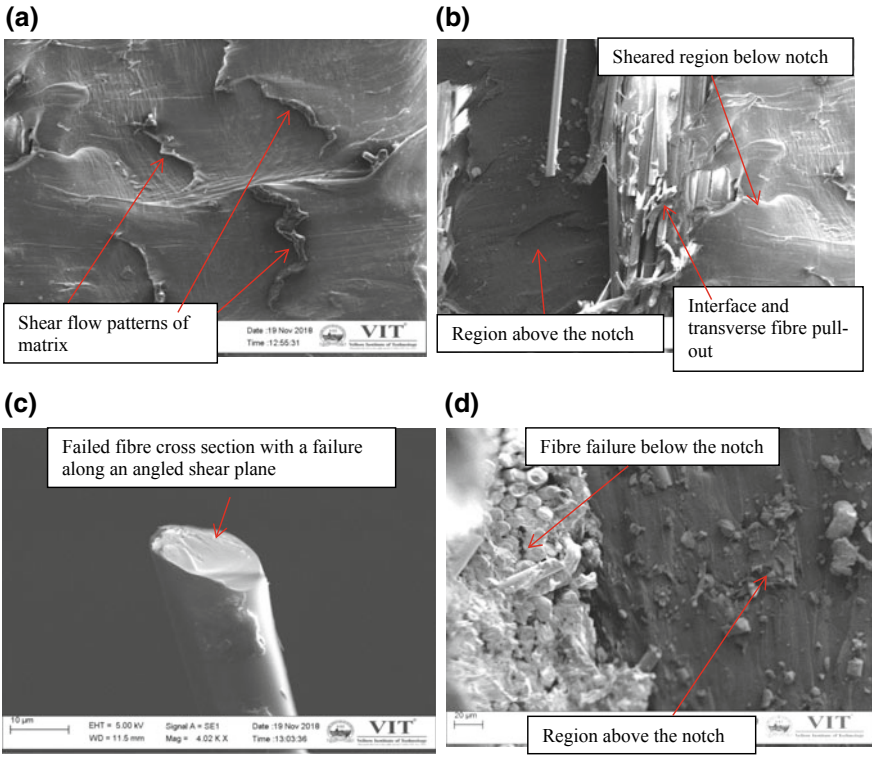

Fig. 10 Fractography of PE SRC subjected to in-plane shear failure

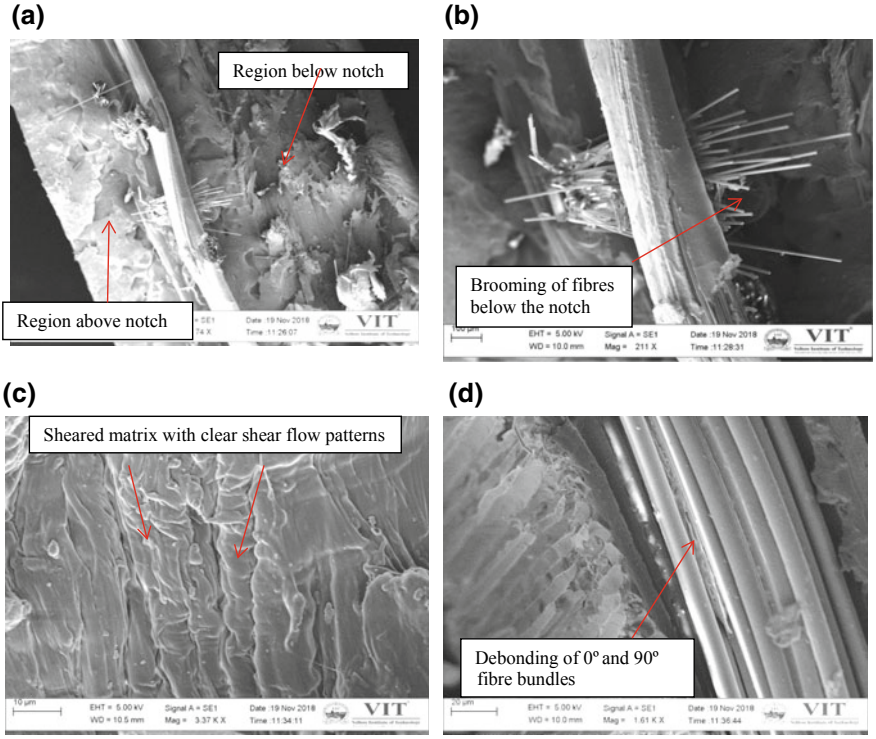

Fig. 11 Fractography of PP SRC subjected to in-plane shear failure

fibres sheared off the bundle and brooming was visible in the failed region. Interface debonding occurs because of the difference in rate of deformation of the fibre and the matrix. Here, though the fibre and matrix are of the same material, they have pseudo-structural differences. This can arise because of orientation, molecular weight or stereospecificity. PE is known to have a more lubricating surface than PP which explains its poorer bond strength even with itself. An unbalanced shear couple is formed at the interface which leads to interfacial debonding as a shear couple proceeds due to the application of forces. It should be further noticed that the PPSRC possess higher intrinsic bond strength (26 N) compared to that of PESRC (16 N) evaluated by microbond multiple fibre pull-out test [20].

As fractography plays a vital role in identifying the sources and cause of fracture, thereby providing a feedback for better material, design and process, the same was attempted here which would lead to design and development of better SRPCs.

5 Conclusions

Following points can be concluded from the fractographic analysis and test data.

- Fractography is an excellent tool to predict the failure nature and correlate it with test properties.
- Major fractographic features are qualitatively correlated with the quasi-static test data.
- Crack initiation, propagation and final fracture locations are used to predict the nature of failure.
- PESRC is more ductile compared to PPSRC and micrography revealed features of such fracture in all the tests.
- PPSRCs are exhibiting excellent interfacial strength compared to PESRC because of higher intrinsic bond strength of PPSRC compared to PESRC and PPSRC exhibited brooming type of phenomena under in-plane shear failure.
- Shear flow patterns were indications of the nature of fracture in matrix.
- Matrix cracking, interfacial debonding and fibre pull-out are the major cause of failure in PE and PP.

Acknowledgements Composites lab and SEM lab at VIT Vellore, M. Ramya are acknowledged for their assistance.

References

1. Matabola KP, De Vries AR, Moolman FS, Luyt AS (2009) Single polymer composites: a review. J Mater Sci 44(23):6213–6222
2. Morgan LM, Weager BM, Hare CM, Bishop GR (2009) Self reinforced polymer composites: coming of age. In: Proceeding of the 17th International Conference on Composite Materials, pp 12–15
3. Gao C, Yu L, Liu H, Chen L (2012) Development of self-reinforced polymer composites. Prog Polym Sci 37(6):767–780
4. Chen JC, Wu CM, Pu FC, Chiu CH (2011) Fabrication and mechanical properties of self-reinforced poly(ethylene terephthalate) composites. Express Polym Lett 5(3):228–237
5. Zhang JM, Peijs T (2010) Self-reinforced poly(ethylene terephthalate) composites by hot consolidation of Bi-component PET yarns. Compos Part A Appl Sci Manuf 41(8):964–972
6. Kuan HT, Cantwell W, Md Akil H (2009) The mechanical properties of hybrid composites based on self-reinforced polypropylene. Malaysian Polym J 4(2):71–80
7. Bilewicz M, Viana JC, Dobrzański LA (2007) Self reinforced polymer-polymer composites. J Achiev Mater Manuf Eng 24(2):43–46
8. Kmetty Á, Bárány T, Karger-Kocsis J (2010) Self-reinforced polymeric materials: a review. Prog Polym Sci 35(10):1288–1310
9. Alcock B (2004) Single polymer composites based on polypropylene: processing and properties, May 2004
10. Tohidi SD, Rocha AM, Dencheva NV, Denchev Z (2018) Single polymer laminate composites by compression molding of knitted textiles and microparticles of polyamide 6: preparation and structure-properties relationship. Compos Part A Appl Sci Manuf 109:171–183

11. Kumar MS, Raghavendra K, Venkataswamy MA, Ramachandra HV (2012) Fractographic analysis of tensile failures of aerospace grade composites. Mater. Res. 15(6):990–997
12. Bieniaś J, Ostapiuk M, Surowska B (2012) Fractography and damage analysis of carbon/epoxy composites under static and dynamic loads at elevated temperatures. Acta Mech Autom 6(1):17–20
13. Opelt CV, Paiva JMF, Cândido GM, Rezende MC (2017) A fractographic study on the effects of hygrothermal conditioning on carbon fiber/epoxy laminates submitted to axial compression. Eng Fail Anal 79:342–350
14. Senatov FS, Gorshenkov MV, Tcherdyntsev VV, Kaloshkin SD, Sudarchikov VA (2014) Fractographic analysis of composites based on ultra high molecular weight polyethylene. Compos Part B Eng 56:869–875
15. Sharan Chandran M, Padmanabhan K, Zilliox M, Tefouet KC (2014) Processing and mechanical characterization of self reinforced polymer composite systems. Int J Chem Tech Res 6(6):3310
16. Sacchetti F, Grouve WJB, Warnet LL, Villegas IF (2016) Woven fabric composites: can we peel it? Proced Struct Integr 2:245–252
17. Jollivet T, Peyrac C, Lefebvre F (2013) Damage of composite materials. Proced Eng 66:746–758
18. Shi H, Villegas IF, Bersee HEN (2013) Strength and failure modes in resistance welded thermoplastic composite joints: effect of fibre-matrix adhesion and fibre orientation. Compos Part A Appl Sci Manuf 55:1–10
19. Greenhalgh ES, Hiley MJ, Asp L, Gamstadt K (2008) Fractography of polymer composites: current status and future issues. In: 13th European Conference on Composition Materials
20. Sharan Chandran M, Kaushik Varma BNS, Padmanabhan K (2015) A novel microbond-fibre bundle pullout technique to evaluate the interfacial properties of self reinforced composites. In: ICNP Conference, MG University Kottayam, April 2015

Analysis of a Double-Stage Thermoelectric Refrigerator

Sudhanshu Sharma and Vijay Kumar Dwivedi

Abstract In the present work, a two-stage thermoelectric refrigerator that consists of 50 elements has been analyzed on the basis of the laws of thermodynamics. The elements are arranged as there are 49 elements on hotter side and only one element on colder side. A non-dimensional parameter 'x' has been considered that represents the ratio of number of elements on hot surface and that on cold surface. Refrigeration effect and coefficient of performance have been calculated to evaluate the operating performance of the double-stage thermoelectric refrigerator with $x = 49$. Refrigeration effect or rate of refrigeration and coefficient of performance both are the desirable performance measuring parameters of a refrigerating device. This work obtains the value of current input at which both the desirable parameters have the maximum value, therefore, the best performance of the device with this configuration.

Keywords Thermoelectric refrigerator · Laws of thermodynamics · Coefficient of performance · Rate of refrigeration

Nomenclature

COP	Coefficient of performance
TER	Thermoelectric refrigerator
A	Cross-sectional area of thermoelectric element
I	Input current of TER, A
T	Temperature
R	Electrical resistance of thermoelectric element, Ω
K	Thermal conductance of thermoelectric element, W/K
N	Number of thermoelectric elements

S. Sharma (✉) · V. K. Dwivedi
Department of Mechanical Engineering, Galgotias College of Engineering and Technology, Greater Noida, Uttar Pradesh 201306, India
e-mail: sudhanshu.shr@gmail.com

H. Kumar and P. K. Jain (eds.), *Recent Advances in Mechanical Engineering*, Lecture Notes in Mechanical Engineering,
https://doi.org/10.1007/978-981-15-1071-7_51

Q Cooling or heating capacity, W
x Ratio of thermoelectric elements in hooter and colder stages
L Length of thermoelectric element
W Power input in TER
j Ratio of current in hotter and colder stages

1 Introduction

Thermoelectric devices are pollution-free devices. A thermoelectric generator (TEG) can be used as heat engine (using Seebeck effect), and a thermoelectric refrigerator (TER) can be used as a refrigerator or heat pump (using Peltier effect). They possess encouraging potential in comparison with existing engines and refrigerators. As there is no moving component which increases durability, reduces maintenance cost, and improves span of system life. With change in direction of current, only the same device can be used as refrigerator as well as heat pump. The non-existence of refrigerant removes the hazards of leakages to the environment which are serious issues in vapor compression refrigeration systems. As there is no compressor used, it reduces the noise in the system. Nowadays, lots of new methods have been developed to make better-performing semiconductor materials; therefore, more and more applications and investigations to improve operating of thermoelectric devices are gaining importance. TERs are more appropriate in areas such as small electronic circuits, laser diodes, communication gadgets, medical, pharmaceutical, and defense operations where precise control of temperature is more important than other things. Thermoelectric refrigerators are better choice for the green environment as the ozone depleting working substances do not exist in the system. Due to these advantages, thermoelectric devices are being used in wide areas. The fundamental concepts of the thermoelectric technology and the bright likelihood of their applications have been studied by number of researchers and engineers [1]. As the gap between the energy consumption and finding energy sources in the world is widening day by day. The entire world is trying to face the challenges of discovering new energy sources to satisfy the spurt in energy consumption in day-to-day life along with degradation of the environment with pollution.

Thermoelectric devices are being viewed as alternatives systems which can utilize the waste heat for power generation. The low efficiency of nano-engineering thermoelectric device can be improved by decreasing the thermal conductivity of the materials, and they become a promising alternative for large-scale use because of their excellent performances [2]. A review of the research work to enhance the working of thermoelectric cooling systems was compiled. This work embraces the review of work related to enlist the new materials suitable for designing, making, and analyzing thermoelectric modules [3]. Thermoelectric refrigerators are found more appropriate for the applications where a regulation of temperature in limited space is required. A model was developed and studied to modify vapor content of

air using TEC channels. It was observed in this particular work that the model speculated the variation in the temperature of air along the channel with minor error. Numerous experimental and simulation-based analysis of the thermoelectric devices have been done to evaluate their performance in various applications related to power generation and refrigeration or air-conditioning [4, 5].

A thermo-economic optimization based on exergy analysis of a vapor compression and vapor absorption refrigeration systems has been carried out. Thermo-economic analysis in these systems plays a very important role to obtain feasible life-cycle cost. Many researchers have established thermodynamic and thermo-economic objective functions based on second law and thermo-economic principles [6–9]. Comparison of single-stage and double-stage thermoelectric cooler has been done for specific designs [10]. Exergo-economic analysis has also been done for a multistage thermoelectric cooler [11, 12]. A three-dimensional numerical simulations' investigation has been done to optimize the design of a thermoelectric cooler using finite element method [13]. A study to evaluate the effect of input parameters on exergy flow in a thermoelectric system was done to establish the optimum value of input parameters [14].

2 Two-Stage Thermoelectric Refrigerator

A double-stage thermoelectric refrigerator (TER) is an arrangement of *n* and *p* type elements in which two single-stage TERs are connected thermally in series. That means the total heat absorbed from first stage will be transferred to second stage. There may be equal or different number of elements in the two stages. Figure 1 shows a double-stage TER. The energy balance equation for a two-stage TER can

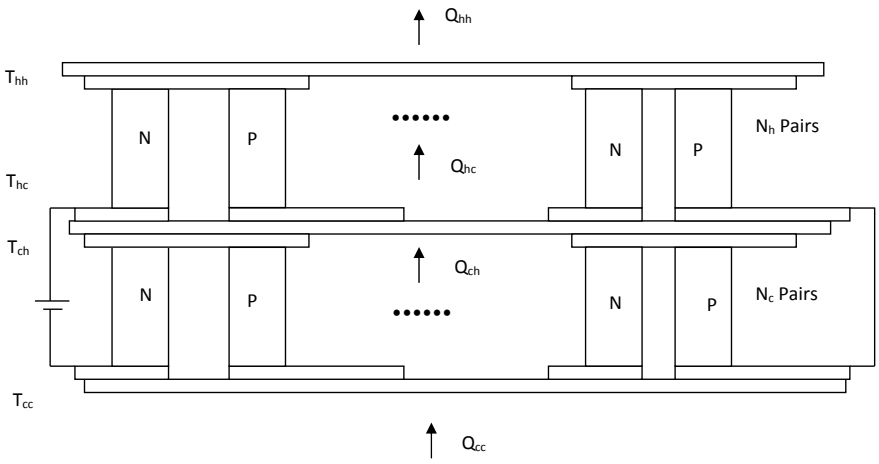

Fig. 1 Double-stage TER

be represented as:

$$Q_{cc} = \left[\alpha I_c T_{cc} - \frac{I_c^2 R}{2} - k(T_{ch} - T_{cc})\right] N_c \tag{1}$$

$$Q_{ch} = \left[\alpha I_c T_{ch} + \frac{I_c^2 R}{2} - k(T_{ch} - T_{cc})\right] N_c \tag{2}$$

$$Q_{hc} = \left[\alpha I_h T_{hc} - \frac{I_h^2 R}{2} - k(T_{hh} - T_{hc})\right] N_h \tag{3}$$

$$Q_{hh} = \left[\alpha I_h T_{hh} + \frac{I_h^2 R}{2} - k(T_{hh} - T_{hc})\right] N_h \tag{4}$$

where Q_{cc} is the heat absorbed at the cold side of the colder stage; Q_{ch} is the rate of heat rejected at the hot side of the colder stage; Q_{hc} is the heat absorbed at the colder side of the hotter stage; and Q_{hh} is the rate of rejected at the hotter side of the hotter stage. I_c is the current flow in colder side, and I_h is the current flow in hotter side of TER. In this analysis, the two stages are electrically is series, so the current I_c and I_h are equal. N_h and N_c are number of elements in colder and hotter sides of TER, respectively. For this analysis $N_h + N_c = 50$ has been considered. T_{cc} and T_{ch} represent the temperatures of the cold side and hot side of colder stage, and T_{hc} and T_{hh} represent the cold side and hot side temperature of hotter side. It can be assumed that there exists a junction temperature T_m which can be calculated by equating Q_{ch} and Q_{hc}. Since the two stages are thermally in series so the heat rejected from first stage will be transferred completely to second stage.

Hence $Q_{ch} = Q_{hc}$

$$T_m = \frac{k(T_{cc} + xT_{hh}) + \left(xj^2 + 1\right)\frac{1}{2} I_c^2 R}{k(x+1) + I_c \alpha (xj - 1)} \tag{5}$$

where $x = N_h/N_c$ and $j = I_h/I_c$.

The energy balance equations can be written as:

$$Q_{cc} = \left[\alpha I_c T_{cc} - \frac{I_c^2 R}{2} - k(T_m - T_{cc})\right] N_c \tag{6}$$

$$Q_{ch} = \left[\alpha I_c T_m + \frac{I_c^2 R}{2} - k(T_m - T_{cc})\right] N_c \tag{7}$$

$$Q_{hc} = \left[\alpha I_h T_m - \frac{I_h^2 R}{2} - k(T_{hh} - T_m)\right] N_h \tag{8}$$

$$Q_{hh} = \left[\alpha I_h T_{hh} + \frac{I_h^2 R}{2} - k(T_{hh} - T_m)\right] N_h \tag{9}$$

COP of double-stage TER:

$$(\mathrm{COP})_{\mathrm{act}} = \frac{Q_{\mathrm{cc}}}{W_{\mathrm{hh}} + W_{\mathrm{cc}}} = \frac{Q_{\mathrm{cc}}}{(Q_{\mathrm{hh}} - Q_{\mathrm{hc}}) + (Q_{\mathrm{ch}} - Q_{\mathrm{cc}})} = \frac{Q_{\mathrm{cc}}}{(Q_{\mathrm{hh}} - Q_{\mathrm{cc}})} \quad (10)$$

W_{hh} and W_{cc} are the work inputs in hot and cold sides, respectively. Since the two-stage TER is a combination of two single-stage TER's which are thermally in series, so the total work input would be equal to the sum of the work input to individual stages. But Q_{cc} would be the heat absorbed at the cold side plate only.

N_{h} and N_{c} are number of elements in hot and cold sides, respectively, and $N_{\mathrm{h}} + N_{\mathrm{c}} = 50$. There may be three possibilities to select N_{h} and N_{c} such that $N_{\mathrm{h}} > N_{\mathrm{c}}$, $N_{\mathrm{h}} < N_{\mathrm{c}}$, and $N_{\mathrm{h}} = N_{\mathrm{c}}$. A non-dimensional parameter 'x' has been used which is the ratio of number of elements in hot side and cold side in a double-stage TER.

The value of 'x' may vary from 0.0204 ($N_{\mathrm{h}} = 1$ and $N_{\mathrm{c}} = 49$) to 49 ($N_{\mathrm{h}} = 49$ and $N_{\mathrm{c}} = 1$). If the value of x is considered to be the maximum, i.e., 49, the performance of TER is as in Table 1.

Table 1 Variation in performance parameters of double-stage TER with I ($x = 49$)

I	T_{m}	Q_{cc}	Q_{ch}	Q_{hc}	Q_{hh}	COP
4	281.715	0.016	0.071	0.071	2.901	0.005
5	277.415	0.135	0.208	0.208	4.563	0.030
6	273.409	0.247	0.342	0.342	6.525	0.039
7	269.682	0.354	0.473	0.473	8.776	0.042
8	266.220	0.455	0.601	0.601	11.309	0.042
10	260.039	0.641	0.850	0.850	17.182	0.039
11	257.298	0.726	0.972	0.972	20.507	0.037
12	254.773	0.806	1.092	1.092	24.081	0.035
13	252.457	0.881	1.211	1.211	27.899	0.033
14	250.338	0.951	1.329	1.329	31.953	0.031
15	248.408	1.016	1.446	1.446	36.237	0.029
16	246.659	1.077	1.563	1.563	40.747	0.027
17	245.083	1.133	1.679	1.679	45.477	0.026
18	243.673	1.185	1.795	1.795	50.422	0.024
19	242.420	1.233	1.912	1.912	55.578	0.023
20	241.320	1.276	2.028	2.028	60.940	0.021
21	240.365	1.316	2.146	2.146	66.504	0.020
22	239.550	1.351	2.263	2.263	72.266	0.019
23	238.868	1.382	2.382	2.382	78.223	0.018
24	238.316	1.409	2.501	2.501	84.370	0.017

(continued)

Table 1 (continued)

I	T_m	Q_{cc}	Q_{ch}	Q_{hc}	Q_{hh}	COP
25	237.887	1.433	2.622	2.622	90.706	0.016
26	237.576	1.453	2.743	2.743	97.226	0.015
27	237.381	1.469	2.866	2.866	103.928	0.014
28	237.295	1.481	2.990	2.990	110.808	0.014
29	237.315	1.490	3.116	3.116	117.865	0.013
30	237.438	1.495	3.244	3.244	125.095	0.012
31	237.658	1.497	3.373	3.373	132.496	0.011
32	237.974	1.495	3.504	3.504	140.066	0.011
33	238.381	1.490	3.637	3.637	147.803	0.010
34	238.876	1.482	3.772	3.772	155.704	0.010
35	239.457	1.470	3.910	3.910	163.768	0.009
36	240.120	1.455	4.049	4.049	171.992	0.009
37	240.862	1.437	4.191	4.191	180.375	0.008
38	241.681	1.415	4.334	4.334	188.915	0.008
39	242.575	1.391	4.481	4.481	197.610	0.007
40	243.540	1.363	4.630	4.630	206.459	0.007
41	244.575	1.332	4.781	4.781	215.460	0.006
42	245.678	1.298	4.935	4.935	224.612	0.006
43	246.846	1.261	5.091	5.091	233.913	0.005
44	248.076	1.221	5.251	5.251	243.362	0.005
45	249.368	1.178	5.413	5.413	252.958	0.005
46	250.720	1.132	5.578	5.578	262.700	0.004
47	252.129	1.083	5.745	5.745	272.585	0.004
48	253.594	1.031	5.916	5.916	282.614	0.004
49	255.112	0.977	6.090	6.090	292.785	0.003
50	256.684	0.919	6.266	6.266	303.097	0.003
51	258.306	0.858	6.446	6.446	313.549	0.003
52	259.978	0.795	6.629	6.629	324.140	0.002
53	261.698	0.729	6.814	6.814	334.869	0.002
54	263.465	0.660	7.003	7.003	345.735	0.002
55	265.277	0.588	7.195	7.195	356.737	0.002
56	267.134	0.514	7.391	7.391	367.875	0.001
57	269.033	0.437	7.590	7.590	379.148	0.001
58	270.974	0.357	7.792	7.792	390.555	0.001
59	272.956	0.274	7.997	7.997	402.094	0.001
60	274.978	0.189	8.205	8.205	413.767	0.000

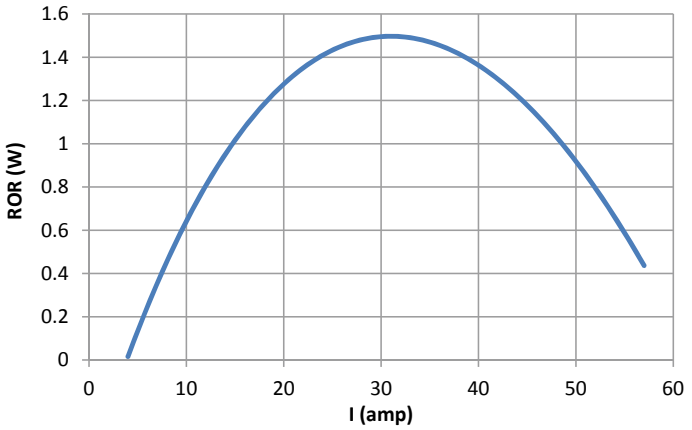

Fig. 2 ROR of double-stage TER with $x = 49$

Figure 2 shows the variation in ROR for a double-stage TER with $x = 49$ with current. The peak value of ROR is 1.49 at $I = 31$ Å.

Figure 3 shows the variation in COP for a double-stage TER with $x = 49$ with current. The peak value of COP is 0.042 at $I = 7$ Å.

The results represented in Table 2 show that COP is maximum with value 0.042 at current input as 7 Å with ROR as 0.354. The comparison of this result with the

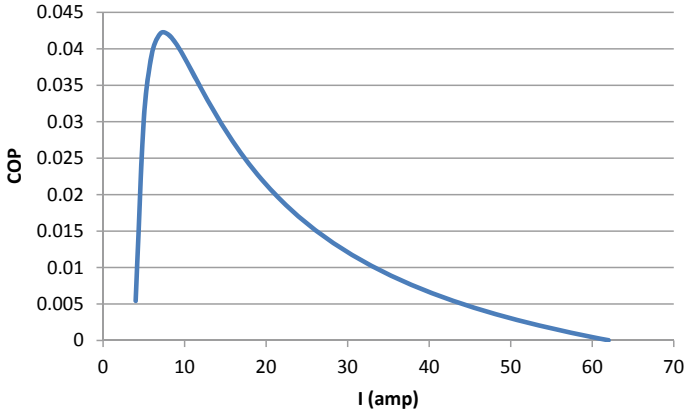

Fig. 3 COP of double-stage TER with $x = 49$

Table 2 Double-stage TER with $x = 49$ for COP and ROR

I (Å)	COP	ROR
07	0.042	0.354
31	0.011	1.49

results at 31 Å shows that the maximum ROR is obtained at 31 Å, i.e., 1.49 but with a loss in COP. There is a significant improvement in ROR at 31 Å. So these results show that the same device should be used at these different values of current to obtain the best performance according to the application and desired effect.

3 Conclusion

A two-stage thermoelectric refrigerator, with 49 elements on hotter side and only one element on colder side, has been analyzed. Rate of refrigeration and coefficient of performance have been calculated to measure the performance. As rate of refrigeration and coefficient of performance both are the desirable performance measuring parameters of a refrigerating device. This work shows the values of current input at which both the desirable parameters, rate of refrigeration and coefficient of performance have the maximum values, respectively. The results may be useful for a user to obtain the best performance according to the application and desired effect. Thermoelectric refrigerators are more useful in the applications where meticulous control of the temperature is needed. So this work may be extended to design a thermoelectric refrigerator for such applications.

References

1. Riffat SB, Ma X (2003) Thermoelectrics: a review of present and potential applications. Appl Therm Eng 23(8):913–935
2. Martín-González M, Caballero-Calero O, Díaz-Chao P (2013) Nanoengineering thermoelectrics for 21st century: energy harvesting and other trends in the field. Renew Sustain Energy Rev 24:288–305
3. Riffat SB, Ma X (2004) Improving the coefficient of performance of thermoelectric cooling systems: a review. Int J Energy Res 28(9):753–768
4. Jradi M, Ghaddar N, Ghali K (2012) Experimental and theoretical study of an integrated thermoelectric-photovoltaic system for air dehumidification and fresh water production. Int J Energy Res 36(9):963–974
5. Belanger S, Gosselin L (2012) Multi-objective genetic algorithm optimization of thermoelectric heat exchanger for waste heat recovery. Int J Energy Res 36(5):632–642
6. Lertsatitthanakorn C, Srisuwan W, Atthajariyakul S (2008) Experimantal performance of a thermoelectric ceiling cooling panel. Int J Energy Res 32(10):950–957
7. Kızılkan O, Şencan A, Kalogirou SA (2007) Thermoeconomic optimization of a LiBr absorption refrigeration system. Chem Eng Process 46(12):1376–1384
8. Ahmed JU, Saidur R, Masjuki HH (2011) A review on exergy analysis of vapor compression refrigeration system. Renew Sustain Energy Rev 15(3):1593–1600
9. Rezayan O, Behbahaninia A (2010) Thermoeconomic optimization and exergy analysis of CO_2/NH_3 cascade refrigeration system. Energy 36(2):888–895
10. Sharma S, Dwivedi VK, Pandit SN (2014) Exergy analysis of single-stage and multi stage thermoelectric coolers. Int J Energy Res 38:213–222
11. Sharma S, Dwivedi V, Pandit SN (2014) Thermoeconomic analysis of multi-stage thermoelectric coolers. Int J Therm Environ Eng 8(2):77–82

12. Sharma S, Dwivedi VK, Pandit SN (2016) Exergoeconomic analysis of two-stage thermoelectric cooler with genetic algorithm. Int J Adv Res Innov 4(1):24–28
13. Gong T, Gao L, Wu Y, Zhang L, Yin S, Li J, Ming T (2019) Numerical simulation on a compact thermoelectric cooler for the optimized design. Appl Therm Eng 146:815–825
14. Dizaji HS, Jafarmadar S, Khalilarya S, Pourhedayat S (2019) A comprehensive exergy analysis of a prototype Peltier air-cooler; experimental investigation. Renew Energy 131:308–317

A Review on Solar Energy-Based Smart Greenhouse

Padma Wangmo, Vinay Kumar Jadoun and Anshul Agarwal

Abstract Greenhouse farming system has so many advantages, such as the easiness to grow plants in cold climate and enhance the production, quality, and the overall output of the products. On the other hand, this arrangement requires additional input that increases the cost of production. The main function of a greenhouse is to trap the heat of the sunlight and provide additional energy for photosynthesis. In greenhouse growing, the stabilization of temperature swings is the primary challenge. This can be done by the people to adopt the conventional which can provide the additional energy via heating or cooling systems into the greenhouse. Solar energy is a very important source, directly connected to the greenhouse as a power supply. The smart and sustainable method to establish a stable greenhouse environment is to harness the additional surplus solar energy collected during the day time after that store that energy and then consume it during night or during unfavorable weather conditions.

Keywords Solar energy · Greenhouse · Sustainable energy

1 Introduction

To empower the farming sector, there is a need to approach farming with modern farming method. One way is to use a greenhouse as a farming system. A good and effective greenhouse aims to create the optimal weather conditions needed by the plants. Traditionally, this is done with the help of the greenhouse structure. Therefore, to trap the maximum heat, greenhouse should have a high light transmission, enough and efficient ventilation, a strong structure, a low operational cost and high quality. But to make the greenhouse really efficient, additional energy needs to be provided.

P. Wangmo · V. K. Jadoun · A. Agarwal (✉)
National Institute of Technology Delhi, New Delhi, Delhi 110040, India
e-mail: anshul@nitdelhi.ac.in

P. Wangmo
e-mail: piwang.wangmo@gmail.com

V. K. Jadoun
e-mail: vjadounmnit@gmail.com

H. Kumar and P. K. Jain (eds.), *Recent Advances in Mechanical Engineering*,
Lecture Notes in Mechanical Engineering,
https://doi.org/10.1007/978-981-15-1071-7_52

However, it requires a quite higher cost as compared to the conventional way. The utilization of the sustainable energy is one of the components that can reduce the production cost. The main purpose of this survey is to increase the efficiency of greenhouse by the using solar cells. Solar cells are used to supply the needs of the whole system, from watering, sensing the outdoor condition, opening and closing the roof, and many more.

In wintertime, the growth of summer growing crops is one of the essential requirements and it can be done by proper heating of greenhouse. There are two methods have been applied to heat up greenhouse, one is passive and other is active method. The passive heating method is carried out through water storage, rock bed storage, insulated walls, movable insulation, thermal curtain, etc. Active heating methods rely on an external energy source such as photovoltaic panels, ground collector, geothermal heat pump, and ground-coupled heat exchanger. Utilizing the active method for thermal heating has been investigated by many researchers [1–4].

The sun's energy can be harnessed as light or heat. Solar energy has been used in different ways for various purposes. Continuous research has resulted in innovations feasible in much colder and cloudy climates today, [5, 6]. Researches [7] have looked into solar water heaters to convert solar energy into thermal energy. Correspondingly, there are various methodologies present to properly tap the solar energy for multipurpose applications.

For cold and arid regions like Ladakh, the energy requirement for heating is very large. With the global threat of depleting fossil fuel, there is need for exploiting the sustainable energy. Based on the two aforementioned needs, Ladakh needs to use maximum solar energy and then transmit power to its smart greenhouse. The combination of high solar intensity due to altitude (3000–5000 m above mean sea level (amsl)) and latitude (32° N–35° N, 77° E–80° E) and cold and arid weather conditions makes the greenhouse technology a lucrative option in Ladakh.

This paper presents a survey of different ways to consume solar energy and used this solar energy as a multipurpose way in a greenhouse. This can increase and improve the efficiency, and it is also a clean and reliable energy source.

2 Literature Survey

2.1 The Smart Greenhouse

In every year, as the autumnal equinox passes us by, the length of a day dwindles to increasing degree. During wintertime, it becomes too cold and dark in many regions making it almost impossible to grow anything. During these periods, the cultivating period of cold and arid regions is restricted to an average four months with the land lying cold and barren for eight months. Through these eight months, the entire population is mostly dependent on external food supply along with the roads blocked by snow eventually leading to low quality and high price of the items. This can lead

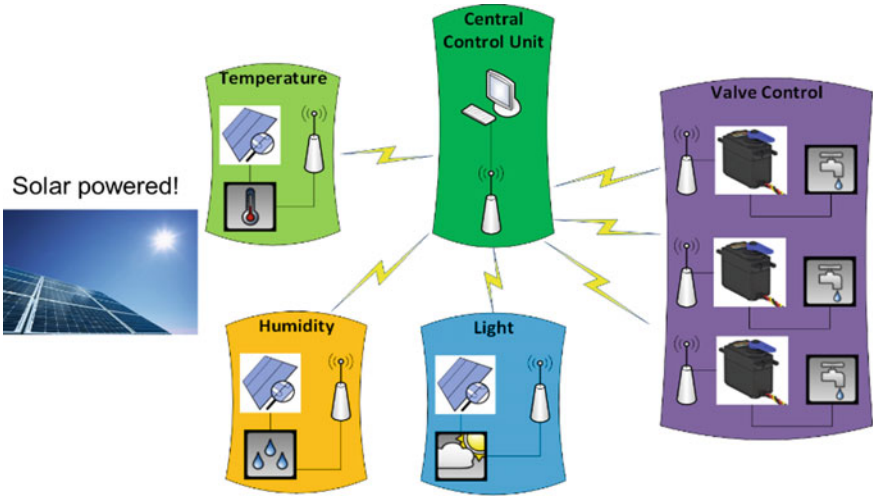

Fig. 1 Solar-powered smart greenhouse

to food insecurity in times of adverse situations. Therefore, setting up of greenhouse is the optimal solution to overcome agriculture challenges especially in such regions for extending the growing season.

Greenhouses provide a considerable control for the growing environment of the plants. The main factors which can be controlled are temperature, levels of light and shade, fertilizer application, atmospheric humidity, and irrigation. There are many different growing problems such as a short growing season, poor temperature, and different light levels occurred. This can be overcome by using greenhouses. Greenhouses can increase the production of food in marginal environments. Greenhouses are not just limited to cold regions only. Shade houses have been used in hot or dry climate regions to provide shade.

A better way to ensure the increase in productivity is smart greenhouses as seen in Fig. 1. Micro-climatic conditions are created with the aid of automation. Most widely used greenhouse automation are microcontroller (Arduino) based [8], ZigBee technology based [9], and Internet of Things (IOT) based [10].

2.2 Solar Energy

Nowadays, solar technologies are becoming popular and important in Ladakh. Passive solar heating and active solar heating are the most widely used technologies. Reference [11] have integrated both forms of heating to increase the overall efficiency and energy cost of a conventional greenhouse. For implementing this technology on a small to large scale for heating in greenhouse in the Ladakh, there is need to have knowledge regarding the amount of solar energy available in this region. Reference

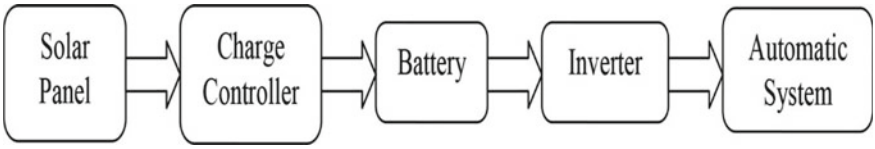

Fig. 2 Block diagram of a solar panel system

[12] had collected solar data in 1996–98 in some villages in the Ladakh region. The available annual global solar energy (average) on a horizontal plane for Leh during the period was 5530 Wh/m^2/day, and at a tilt of 35° south, the annual average energy was 6360 Wh/m^2/day. Moreover, according to ref. [13], Ladakh has solar radiation as one of the most abundant natural resources, with overall annual average solar radiation of 7–7.5 kWh/m^2/day. Based on the abovementioned solar data is can be analyzed that there is a sufficient amount of solar energy available in the Ladakh region. So, by evaluating the particular locations in this region, the solar energy can be successfully used in harvesting. The block diagram of a solar panel system is shown in Fig. 2.

Two of the main components required in the smart greenhouses are electrical and thermal energy. The sun's energy can be exploited and converted into both forms. Electrical energy solar panels systems are used worldwide to convert and store the solar energy. The entire system begins with the integrated solar cells. These solar cells are actually used to produce electricity. Reference [14] has tested solar energy to power office appliances. The output results showed a good performance of the system. The average solar power output obtained during the testing period was higher than the total load demand of office appliances. Similarly, the solar energy can be utilized to power the automation system such as ventilation system, fans, fertigation system, etc., and the excess energy can be stored to supply power to the greenhouse during nights and cloudy days. The efficiency of the photovoltaic system can also be increased [15] for maximum efficiency.

Thermal energy is being provided through solar water heating, solar space heating, and solar PVT system as investigated in [16]. These can be integrated to heat the greenhouse to maintain the ambient growing temperature. Such systems have been operated for indoor space heating [17]. Solar-assisted underfloor heating is another heating method. It was tested and it was concluded that the system was more suitable for cold climate [18].

A solar-assisted heat pump (SAHP) machine consists of a heat pump and thermal solar panels in a single system where thermal energy is used instead of light energy. Direct-expansion solar-assisted heat pump is a more advanced and efficient version of SAHP investigated by Chaturvedi et al. [19]. By using direct-expansion solar-assisted heat pump, the cost is reduced and performance is improved.

3 Conclusion

Solar energy is one of the many types of renewable energy source. It is a clean and pollution-free source. Solar energy can be used either as electric or thermal energy sources in the smart greenhouse system. This energy source is becoming new environmental technology. The key role of this technology is to influence the design and the quality of the environment to be greener and cooler.

The utilization of the smart greenhouse system supported by solar energy source helps in caring of plants such as fertigation, lighting, and maintenance of the temperature which is needed by the plants to grow in the cold climate. If all of these are combined and implemented on a large scale, it can be one of the best ways to reduce the global warming and green the environment.

The other renewable energy sources like wind, geothermal, biogas energy, etc. can be used in smart greenhouses in the different regions of India [20]. The development of technology and proper utilization of these energy sources according to the climatic conditions and accessibility of the particular regions can provide maximum output and minimum cost.

References

1. Connellan G (1986) Solar greenhouse using liquid collectors. In: Proceedings of solar energy society, Atlanta, GA
2. Santamouris M, Mihalakakou G, Balaras CA, Lewis JO, Vallindras M, Argiriou A (1996) Energy conservation in greenhouse with buried pipes. Solar Energy 52(5)
3. Bargach MN, Tadili R, Dahman AS, Boukallouch M (2000) Survey of thermal performances of a solar system used for the heating of agricultural greenhouses in Morocco. Renew Energy 20
4. Jain D, Tiwari GN (2003) Modeling and optimal design of ground air collector for heating in controlled environment greenhouse. Energy Conserv Manag 44(8)
5. Bennet T (2007) Solar thermal water heating, a simplified modeling approach
6. European Commission, Photovolatic solar energy—development and current research
7. Vinubhai TS, Jain Vishal R, Thakkar K (2014) A review: solar water heating systems. In: National Conference on Emerging Vista of Technology in 21st Century. Parul Institute of Technologi, Limda, Vadodara, India
8. Arif KI, Abbas HF (2015) Design and implementation of smart greenhouse. Int J Comput Sci Mob Comput (IJCSMC) 4:335–347
9. Gaikwad A, Ghatge A, Kumar H, Mudliar K (2016) Monitoring of smart greenhouse. Int Res J Eng Technol (IRJET) 3:573–575
10. Imam A, Gaur D (2018) Smart greenhouse monitoring using internet of things. Int J Adv Res Electron Commun Eng (IJARECE) 7:519–523
11. Ahamed MS, Guo H, Tanino K (2019) Energy saving techniques for reducing the heating cost of conventional greenhouses. Biosyst Eng 178:9–33
12. Jacobson A (2000) Solar energy measurements for Ladakh, India. In: Proceedings of the 24th national renewable energy convention 2000 of the solar energy society of India. Solar energy measurements for Ladakh, India
13. Santra P (2016) Scope of solar energy in cold arid region of India at Leh Ladakh. Ann Arid Zone 54(3–4):109–117

14. Adejuyigbe SB, Bolaji BO, Olanipekun MU, Adu MR (2013) Development of a solar photovoltaic power system to generate electricity for office appliances. Eng J 17(1):29–39
15. Lin C-L (2015) Case study of solar power producing efficiency from a photovoltaic system. Open J Energy Effic 4:45–52
16. Ge TS, Wang RZ, Xu ZY, Pan QW, Du S, Chen XM, Ma T, Wu XN, Sun XL, Chen JF (2018) Solar heating and cooling: present and future development. Renew Energy 126:1126–1140
17. Zhao D, Ji J, Yu H, Zhao X (2019) A study on thermal characteristic and sleeping comfort of a hybrid solar heating system applied in cold rural areas. Energy Build 182:242–250
18. Karimi MS, Fazelpour F, Rosen MA, Shams M (2019) Comparative study of solar-powered underfloor heating system performance in distinctive climates. Renew Energy 130:524–535
19. Chaturvedi SK, Chen DT, Kheireddine A (1998) Thermal performance of a variable capacity direct expansion solar-assisted heat pump. Energy Convers Manag 39(3–4):181–191
20. Lohan SK, Dixit J, Modasir S, Ishaq M (2012) Resource potential and scope of utilization of renewable energy in Jammu and Kashmir, India. Renew Energy 39(1):24–29

Analysis of Firm-Level Innovativeness Indicators

Sanjay Kumar, Abid Haleem, Sushil and Mohd. Asim Qadri

Abstract The article is aimed at developing a clearer understanding of the causal relationships among the major indicators of innovativeness in manufacturing firms. The key innovativeness indicators are identified from literature and are then validated by experts through structured questionnaire and follow up interview. The Decision-Making Trial and Evaluation Laboratory (DEMATEL) technique is then used to analyze the causal relationships among the indicators. The framework indicates that the 'cause group' factors viz. behavioral and strategic innovations are the most important factors for the innovativeness enhancement in manufacturing enterprises. The product, process, and marketing innovations fall under 'effect' group. The study provides a visual demonstration through Impact-Relations Map (IRM) which can be used by the decision-makers to plan and organize their own actions. The article provides useful insights into the interplay and dynamics of innovativeness indicators to the practitioners, researchers, and consultants.

Keywords Innovativeness · DEMATEL · Causal relationship · Impact-Relations Map

1 Introduction

Innovation, in today's fast-changing turbulent business environment, is the key to competitive advantage. It is a crucial driving force for ensuring sustained growth for individual firms, industry sectors, and economy as a whole. The business units that fail to appreciate the importance of innovativeness are unlikely to handle the looming

S. Kumar (✉) · A. Haleem
Jamia Milia Islamia, New Delhi 110025, India
e-mail: sanj_gcet@rediffmail.com

Sushil
IIT Delhi, New Delhi, India

Mohd. A. Qadri
Galgotias College of Engineering and Technology, Greater Noida, UP, India

H. Kumar and P. K. Jain (eds.), *Recent Advances in Mechanical Engineering*,
Lecture Notes in Mechanical Engineering,
https://doi.org/10.1007/978-981-15-1071-7_53

challenges and are doomed to struggle for survival in today's volatile environments. Zahra and Covin [1] very rightly considered innovation as the 'life blood' of corporate survival and growth.

The globalization of markets has put strong competitive pressure on the manufacturing firms. Due to rapid technological changes and ever-changing market conditions, the firms are challenged to continuously offer a portfolio of innovative products and services. Hutt and Speh [2] suggested that a firm has to be innovative in its approach if it wishes to ensure alignment of its products with the ongoing market changes, customer requirements and the product offerings of the competitors. In a nutshell, use of innovativeness as a competitive ploy is outstandingly important for a firm's long-term survival and growth. To improve the chances of successful implementation of innovativeness agenda, it becomes extremely important for a firm to identify and analyze the key factors contributing to innovativeness.

The qualitative analysis of inter-relationships in terms of the nature and intensity of interactions among the factors helps the practicing firms in focusing its efforts on the most important and productive activities. This can enable the firms to adopt a comprehensive approach in dealing with the issue. The DEMATEL technique has been employed for developing clearer understanding of the environment settings in which innovativeness improvement assignments are undertaken. The key innovativeness indicators are then categorized into cause and effect groups based on the total effects caused and received by each one of them.

The remainder of the paper is structured as follows: The following section explains the innovativeness dimensions in brief. Third section, then, explains the implementation procedure of the proposed DEMATEL method with the help of an illustrative example. The results are discussed and interpreted in the concluding section.

2 Innovativeness Dimensions

The various indicators of innovativeness identified from literature are as under:

Product innovativeness: Product innovativeness refers to designing and offering a considerably new or improved good or service in terms of its features and/or intended uses. Product innovativeness is very often measured in terms of the newness, originality, or uniqueness of the product in one or more aspects [3].

Process innovativeness: Process innovations have been defined as deliberate and new organizational attempts to change production and service processes [4]. Process innovativeness involves developments in processes, systems, and reengineering activities [5] and helps the firms exploit the hitherto untapped potential as regards the resources and capabilities.

Market innovativeness: Market innovativeness is devising and adopting a new marketing method with significant changes in the way a product is designed or packaged, placed, promoted, or priced. As market innovativeness is closely related to product innovativeness, it is sometimes also referred to as product–market innovativeness [6–8].

Strategic innovativeness: Strategic innovation is adopting a new method/system as regards the firm's business practices, workplace organization and conduct or in dealing with outside world. Markides [9] defined strategic innovation as '*a fundamental re-conceptualization of what the business is all about that, in turn, leads to a dramatically different way of playing the game in an existing business.*'
Behavioral innovativeness: Behavioral innovativeness is the willingness and cooperative mindset of the members of the organization to participate in innovativeness enhancement endeavors. It is demonstrated by the members at all levels viz. individual, group and organization [10].

3 DEMATEL Method

The DEMATEL method is often used to ascertain interrelations among various factors influencing a decision situation [11, 12]. The method has successfully been applied in various areas like formulation of marketing strategies, development of the competencies of global managers, and group decision-making processes [13]. In this method, firstly, a panel of experts is asked to compare the identified factors in a pair-wise manner and indicate the extent of direct influence each factor i leaves on every other factor j. Here, the scale 0–4 can be used to express the range of response from 'non-influence' to 'very high influence.' Each expert would make its assessments and produce an individual direct matrix. The average matrix $A = [a_{ij}]$ is then established by accommodating the opinion of all the experts (Table 1).

The average matrix $\boldsymbol{A}$ is then normalized to get the initial direct influence matrix, using the formula, $X = \lambda x A$, where,

Table 1 Average matrix

	Product innovativeness	Process innovativeness	Marketing innovativeness	Behavioral innovativeness	Strategic innovativeness	Total
Product innovativeness	**0.00**	3.00	2.40	2.00	1.40	8.80
Process innovativeness	3.00	**0.00**	0.80	1.40	1.20	6.40
Marketing innovativeness	1.60	0.40	**0.00**	1.40	0.80	4.20
Behavioral innovativeness	3.80	3.40	3.40	**0.00**	2.20	12.80
Strategic innovativeness	3.20	3.40	3.40	2.00	**0.00**	12.00
Total	11.60	10.20	10.00	6.80	5.60	

$$\lambda = \min\left[\frac{1}{\max\limits_{i}\sum_{j=1}^{n}|a_{ij}|}, \frac{1}{\max\limits_{j}\sum_{i=1}^{n}|a_{ij}|}\right] \tag{1}$$

n being the number of factors under consideration. The normalized matrix is provided in Table 2 below.

The full direct/indirect influence matrix is derived from initial direct influence matrix, $X = [x_{ij}]_{n\times n}$ using the formula (Table 3):

$$T = X(1 - X)^{-1} \tag{2}$$

The row totals (D_i) show the amount of influence factor i has on each of the other factors. The column totals (R_j), on the other hand, show the degree of permeability of factor j to other factors. The values of D_i and R_j are calculated using Eqs. (3–4) and are presented in Table 4:

Table 2 Normalized matrix

	Product innovativeness	Process innovativeness	Marketing innovativeness	Behavioral innovativeness	Strategic innovativeness
Product innovativeness	**0.00**	0.23	0.19	0.16	0.11
Process innovativeness	0.23	**0.00**	0.06	0.11	0.09
Marketing innovativeness	0.13	0.03	**0.00**	0.11	0.06
Behavioral innovativeness	0.30	0.27	0.27	**0.00**	0.17
Strategic innovativeness	0.25	0.27	0.27	0.16	**0.00**

Table 3 Resultant matrix

	Product innovativeness	Process innovativeness	Marketing innovativeness	Behavioral innovativeness	Strategic innovativeness
Product innovativeness	**1.00**	−0.23	−0.19	−0.16	−0.11
Process innovativeness	−0.23	**1.00**	−0.06	−0.11	−0.09
Marketing innovativeness	−0.13	−0.03	**1.00**	−0.11	−0.06
Behavioral innovativeness	−0.30	−0.27	−0.27	**1.00**	−0.17
Strategic innovativeness	−0.25	−0.27	−0.27	−0.16	**1.00**

Table 4 Total relation matrix

	Product innovativeness	Process innovativeness	Marketing innovativeness	Behavioral innovativeness	Strategic innovativeness	D_i	$D_i + R_j$	$D_i - R_j$
Product innovativeness	0.35	**0.50**	**0.46**	0.36	0.29	1.96	4.48	−0.56
Process innovativeness	**0.48**	0.26	0.31	0.28	0.24	1.57	3.80	−0.67
Marketing innovativeness	0.30	0.21	0.17	0.22	0.17	1.08	3.26	−1.10
Behavioral innovativeness	**0.72**	**0.65**	**0.63**	0.32	**0.41**	2.72	4.34	1.11
Strategic innovativeness	**0.66**	**0.62**	**0.61**	**0.43**	0.24	2.56	3.89	1.22
R_j	2.52	2.24	2.18	1.62	1.34			

Table 5 Ranking and grouping of innovativeness indicators

	D	R	Prominence effect ($D + R$)	Net effect ($D - R$)	Ranking	Group
Product innovativeness	1.96	2.52	4.48	−0.56	**1**	E
Process innovativeness	1.57	2.24	3.80	−0.67	**4**	E
Marketing innovativeness	1.08	2.18	3.26	−1.10	**5**	E
Behavioral innovativeness	2.72	1.62	4.34	1.11	**2**	C
Strategic innovativeness	2.56	1.34	3.89	1.22	**3**	C

$$D_i = \sum_{j=1}^{n} t_{ij} (i = 1, 2, \ldots, n) \tag{3}$$

$$R_j = \sum_{i=1}^{n} t_{ij} (i = 1, 2, \ldots, n) \tag{4}$$

The D_i and R_j are then used to compute the values of $(D_i - R_j)$ and $(D_i + R_j)$ for each innovativeness indicator. The values thus obtained are provided in Table 5. The sum of D_i and R_j represented by $(D_i + R_j)$ shows the total effect intensity and permeability of a factor on all other factors under consideration. The positive and negative values of $(D_i - R_j)$, on the other hand, let us know whether the factor causes effect or is permeable to effects caused by other factors. So, the innovativeness indicators can be classified into cause (C) and effect (E) groups based on their $(D_i + R_j)$ and $(D_i - R_j)$ values. As an extension of logic, a criterion is included in the cause category if the value of $(D_i - R_j)$ is positive and is ascribed to the effect category, otherwise.

IRM is constructed on a (X, Y) graph. It is a matter of common observation that an attempt to consider all the information contained in matrix $\boldsymbol{T}$ in totality, while developing the IRM, would render a high degree of complexity to the map. To deal with this concern, a threshold value, α, is set for the influence level with a view to filter out the minor effects. The factors having influence value greater than the set value of α would only be retained. The relation structure of the factors is thus isolated. The $(D_i + R_j)$ and $(D_i - R_j)$ values are plotted on the horizontal and the vertical axis, respectively. The coordinate $(D_i + R_j, D_i - R_j)$ represents the relative position of each innovativeness indicator on the graph in terms of overall effect caused and overall effect received by it. The Impact-Relations Map provides the decision-makers better understanding of the inter-relationships through graphic means. The IRM for the identified innovativeness indicators is depicted in Fig. 1.

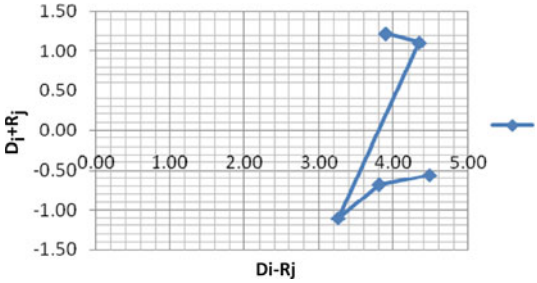

Fig. 1 Impact-Relations Map

4 Conclusion

Product innovativeness emerges as the most important innovativeness indicator having the $(D_i + R_j)$ value of 4.48. Marketing innovativeness, on the other hand, was found to be the least important indicator with $(D_i + R_j)$ value of only 3.26. Based on $(D_i + R_j)$ values, the order of the importance of five innovativeness indicators was as under: *Product Innovativeness* > *Behavioral Innovativeness* > *Strategic Innovativeness* > *Process Innovativeness* > *Marketing Innovativeness.*

A positive value of $(D_i - R_j)$ for an innovativeness indicator shows 'net cause' and suggests that the indicator should be classified into the cause group. The higher the $(D_i - R_j)$ value an innovativeness indicator has the more direct effect it produces on the other indicators. In this study, behavioral innovativeness and strategic innovativeness with $(D_i - R_j)$ values of 4.34 and 3.89, respectively, were classified in the cause group. The behavioral innovativeness is the most influencing factor.

The innovativeness indicators having negative $(D_i - R_j)$ values are treated as 'receivers' as these are largely influenced by other indicators. All such indicators fall under the effect group. In this study, three indicators—product innovativeness, process innovativeness, and marketing innovativeness, with $(D_i - R_j)$ values of -0.56, -0.67, and -1.10, respectively—constitute the effect group. Marketing innovativeness was the one affected the most by the cause group indicators viz. behavioral innovativeness and strategic innovativeness.

References

1. Zahra SA, Covin JG (1994) The financial implications of fit between competitive strategy and innovation types and sources. J High Technol Manage Res 5(2):183–211
2. Hutt MD, Speh TW (2012) Business marketing management: B2B. South-Western Cengage Learning, Australia
3. Henard DH, Szymanski DM (2001) Why some new products are more successful than others? J Mark Res 38(3):362–375
4. Barney JB (1991) Firm resources and sustained competitive advantage. J Manage 17(1):99–120
5. Khazanchi S, Lewis MW, Boyer K (2007) Innovation-supportive culture: the impact of organizational values on process innovation. J Oper Manage 25(4):871–884
6. Cooper AC (1973) Technical entrepreneurship: what do we know? Res Dev Manage 3(2):59–64

7. Miller D (1983) The correlates of entrepreneurship in three types of firms. Manage Sci 29(7):770–791
8. Schumpeter JA (1934) The theory of economic development: an inquiry into profits, capital, credit, interest and the business cycle. Oxford University Press, London
9. Markides C (1998) Strategic innovation in established companies. MIT Sloan Manage Rev 39(3):31–42
10. Wang CL, Ahmed PK (2004) The development and validation of the organisational innovativeness construct using confirmatory factor analysis. Eur J Innov Manage 7(4):303–313
11. Fontela E, Gabus A (1974) DEMATEL, innovative methods. Report no. 2, Structural analysis of the world problematique. Battelle Geneva Research Institute
12. Fontela E, Gabus A (1976) The DEMATEL observer: Battelle Institute. Geneva Research Center
13. Wu WW, Lee YT (2007) Developing global managers' competencies using the fuzzy Dematel method. Expert Syst Appl 32(2):499–507

Comparative Study of Basin Type Double Slope Active Solar Stills Based on Energy Metrics

Abhishek Sharma, Vijay Kumar Dwivedi and Desh Bandhu Singh

Abstract Water is one of the crucial components for the existence of life on our planet. This gift of nature has several usages and applications. One can see a clear implication of water availability on industries, civilization, livelihood, etc. Though a plethora of water is available, however, not all of it is of direct use; only 2.6% of total available water is freshwater and of that only 1% is in human reach. Unfortunately, that little amount is also prone to several impurities, mainly because of human activities. Indian ministry of water resources, United Nations, UNICEF and several other organizations reported on the ignorance of environmental norms pertaining to water discharge by many industries and organizations. All such ignorance somehow enhances water scarcity. The investigation of active solar desalination system working in dynamic mode is one of the best considerations to lessen the water scarcity problem. This work focuses on energy metrics scrutiny of basin type double slope active solar desalination systems, and these solar desalination systems have been judged against each other on the grounds of energy metrics.

Keywords Double slope active solar desalination systems · Energy metrics · Potable water

1 Introduction

The reducing figures for availability of water can be seen through the data regarding the parameter of annual per capita of water availability. A decrement of 6042–1545 m^3 within a time phase of 1947–2011 has been found; recent surveys show that this data will keep on decreasing and will approximately reach a figure of 1140 m^3 by the end of

A. Sharma (✉) · V. K. Dwivedi
Department of Mechanical Engineering, Galgotias College of Engineering and Technology, Plot No. 1, Knowledge Park II, Greater Noida, UP 201306, India

D. B. Singh
Department of Mechanical Engineering, Graphic Era Deemed to be University, Bell Road, Clement Town, Dehradun, Uttarakhand 248002, India
e-mail: Deshbandhusingh.me@geu.ac.in

H. Kumar and P. K. Jain (eds.), *Recent Advances in Mechanical Engineering*, Lecture Notes in Mechanical Engineering,
https://doi.org/10.1007/978-981-15-1071-7_54

year 2050 [1]. All these data suggest nothing but a huge threat of freshwater scarcity which our world will face in the upcoming years. So, to counter these problems, researchers have come across several technologies, but most of them are based on conventional sources of energy and are very energy intensive. Solar distillation is one of the best alternatives as it requires less energy and is based on renewable sources of energy which makes it eco-friendly. In order to make this system better and better and to enhance its performance, researchers have come up with several different designs. Zaki et al. [2] were the first ones to report on the dynamic behavior of the solar still under natural circulating conditions. Rai and Tiwari [3] and several other researchers have proved that by integrating several other external devices to the still in order to design an active still by manipulating the parameter of temperature difference between condensing glass and vapor. So, after coming across such several designs of solar stills, it is very crucial to have examining criteria so as to judge these different designs and compare them on different grounds. So, the aim of this paper is to compare double slope active state solar desalination system coupled with different collectors like flat plate collector (FPC), compound parabolic concentrator collector (CPC) and evacuated tubular collector (ETC) on the ground of energy matrices for generating an insight regarding comparative performance of various assemblies.

2 Active State Solar Still

In order to produce freshwater from brackish/saline water, a simple natural phenomenon of hydrological cycle (a basic principle working behind rainfall) is being used by several man-made desalination systems. Producing freshwater from saline water involves removal of salts and unwanted material from it which requires energy [4]. Heat as a form of energy is being supplied to a brackish or saline water in order to attain a phase change of that saline water so as to gain freshwater. Active state solar still is nothing but an idea to boost the performance of solar desalination system by supplying additional heat using collectors so that rate of evaporation can be enhanced and hence enhanced freshwater production. Under forced circulation, water is pumped by a DC motor assembled in the system so as to overcome the pressure drop and maintain an optimum flow. Thus, by maintaining the flow, the temperature of the water rises, and in turn, it gives rise to the difference in temperature between condensing glass cover and water surface. As temperature difference acts as a potential for heat flow, with the enhancement in temperature difference, heat transfer between water surface and glass cover rises which helps the assembly to generate distillate at a faster rate. In the case of active solar desalination system, collectors receive solar energy from sun and provide heat to the circulating water so as to enhance its temperature. Besides solar collectors, several other external sources could be utilized like heat exchangers, fins, nanoparticles, etc. Energy received by solar collectors could be utilized by PV module, if photovoltaic (PV) module gets mounted on the collectors. This PV module can in turn convert the energy obtained from solar intensity impinging on the surface into high-grade energy. Thus, direct

current (DC) motor rather than to take power from the grid could utilize this electrical energy generated from solar energy by PV module. This idea of PV module was first represented by Kern and Russel [5]. His idea helped this technology to attain a tag of self-sustained machine.

2.1 Active State Double Slope Solar Desalination Unit Attached with Series Connected N *Alike PVT-CPC Collectors (Case (i))*

CPC is a solar water collector which is integrated into the assembly of solar still in order to provide heat to the circulating water. Impure water present in the basin of the still is allowed to circulate throughout the assembly, by the virtue of DC motor in this case. When impure water enters CPC during circulation throughout the assembly, it gains some heat from the collector. Now, the end of the collector is connected to the entry of the basin, so after gaining the heat from collector, water again joins the basin and gives the effect of rise in the temperature of basin water. The design of the CPC water collectors was presented by Renold Winston and was further developed by Watter Welford by the 1970s. CPCs are able to focus a wider region of the sky on the surface of receiver and do not require much tracking and thus are enormously attractive in nature. Atheaya et al. [6] proposed the design of the integration of CPC with PV module. There are several ways to arrange PV module on the CPC collector; different arrangements are required for different requirements of operation. PV module can cover the surface of the collector either fully or partially. In partially covered arrangements, percentage coverage of PV module on the collector could also vary like 25, 50%, etc. An appreciable amount of work was done by Tripathi et al. in analyzing such arrangements and gave a conclusion that the water temperature can be increased by connecting the *N*-photovoltaic thermal (PVT) CPC in series [7]. The idea of coupling series connected *N*-PVT-CPCs with basin type double slope solar desalination unit shown in Fig. 1 was given by Singh and Tiwari [8]. The outlet of the solar desalination unit is connected to the inlet of the 1st PVT-CPC collector, so, by the virtue of DC motor driven by the PV module, water gets circulated and after leaving the basin, it first enters the 1st collector. There, it collects heat from collector and then leaves to enter the 2nd collector as the outlet of 1st collector is attached to the inlet of the 2nd collector. The inlet and outlet of the collectors are connected in this manner because the whole PVT-CPC collectors are arranged in series so as to maximize the basin water temperature. So after gaining heat from all the collectors of the series, water returns back to the basin with an increased temperature. When it joins the water present in the basin, then a thermal equilibrium gets created which in turn enhances basin water temperature. All the necessary measures are taken so as to minimize the heat loss and vapor loss. A layer of glass wool having 0.01 m thickness is applied at the bottom and side of the basin, absorbers are provided and pipes get insulated to ensure that heat loss must be minimized. To ensure the receiving of

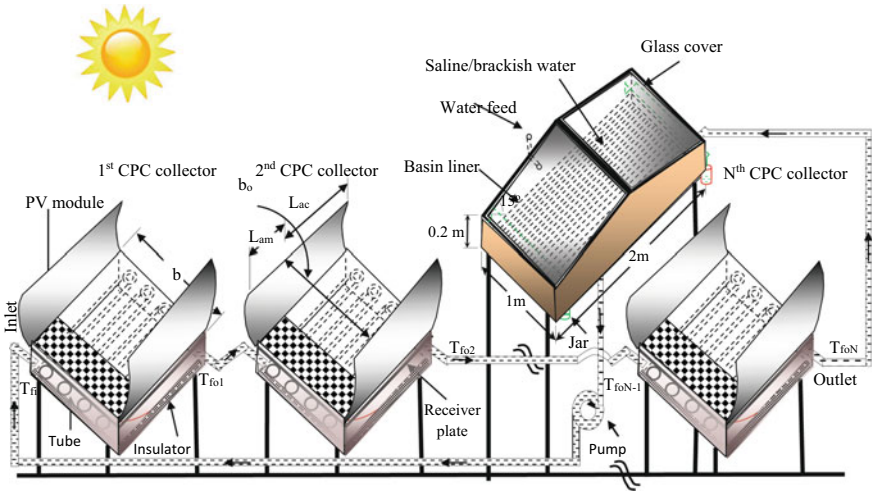

Fig. 1 Double slope solar desalination unit integrated with *N* alike PVT-CPCs [8]

maximum annual solar radiation, an inclination of 30° with the horizontal is provided to the PVT-CPC collectors. The transparent glass which acts as a condensation base and glazing for the still is also provided an inclination of 15° to maximize effective area. Receiver area of the collector is half the aperture area. Basin is also painted with black color so as to absorb the heat and then transfer the heat to water. A hole is also provided at the bottom of the still for cleaning the basin. So after gaining a maximum temperature, water gets evaporated and converted into vapor. This vapor then rises up and strikes the glass cover. Because of the temperature difference between vapor and glass cover, vapor gets condensed after releasing its latent heat. This condensate is now the potable water which we call distillate. This distillate then drops down to the container present on the sideline.

2.2 Active State Double Slope Solar Desalination Unit Attached with Series Connected N *Alike PVT Flat Plate Collectors (NPVTFPCs) (Case (ii))*

Just like CPC, FPC is also a solar water collector which is integrated into the solar still in order to provide heat to the circulating water. If parabolic surface is removed from CPC, the collector becomes FPC as shown in Fig. 2. There is not much of a difference between the still integrated with CPC and still integrated with FPC regarding the working. Usually, solar collectors are arranged in parallel to obtain higher amount of fluid per unit time at lower temperatures and are arranged in series to obtain low amount of fluid per unit time at high temperature. Here, the collectors are connected in series so as to gain low discharge at high temperature. All the specifications regarding

Fig. 2 Setup of double slope solar desalination unit integrated with two FPCs [9]

different components of the still and collector are encountered exhaustively in Singh et al. [9]. Just like in the still integrated with CPC, here also the water gathers the heat by circulating (by the virtue of DC motor driven by electrical energy from PV module) through the collectors which are connected in series and returns back to the basin to increase the temperature of the water. All boundaries and gaps are sealed; pipes were made insulated so as to minimize heat loss and vapor loss. Collectors are kept in such a way that it faces south, and an inclination of 30° is provided to them with respect to horizontal. Solar desalination unit is also kept in such a way that it is oriented along east–west. It is done to maximize the incident solar intensity. A layer of black paint is provided inside surface of the basin to absorb the heat and then transfer that heat to the water present in the basin so as to enhance its temperature. After all such efforts, water gets evaporated and its vapor then loses its latent heat to condense and form the distillate. This distillate then gets drops down in the container placed on the sidelines of the still. Singh et al. [9] studied experimentally double slope solar desalination system integrated with two collectors in which some portion of only one collector was covered with PV panel to generate self-sustainability in the system. This system is illustrated in Figs. 2 and 3.

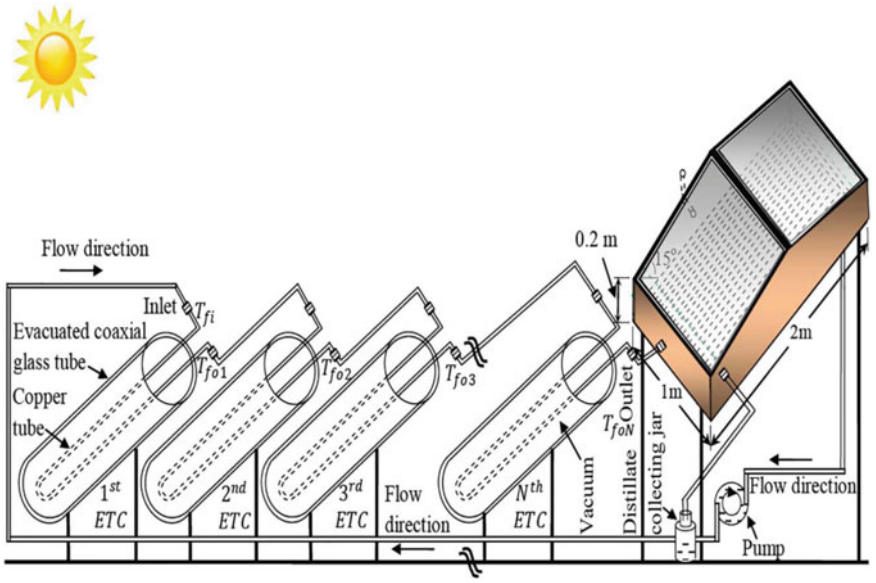

Fig. 3 Double slope solar desalination unit integrated with *N*-ETCs [10]

2.3 Active State Double Slope Solar Desalination Unit Integrated with Series Connected N*-ETCs (Case (iii))*

Here, in this assembly shown in Fig. 3, the proposed system has a solar desalination unit coupled to *N* alike ETCs arranged in series. A series assembly is preferred here so as to obtain high basin water temperature rather than a parallel assembly. Each ETC is comprised of an inner copper tube and an outer evacuated co-axial tube. The outer evacuated co-axial tube is comprised of two glass tubes, in between of which a vacuum space is created. This vacuum space is created just to drop down the ways of heat transfer to radiation only, as conduction and convection cannot take place without medium. Water flows through the inner tube of the ETC. All the specifications regarding different components of ETC and still are given by Singh and Al-Helal [10]. As these ETCs are connected in series, inlet of one ETC is connected to the outlet of its previous ETC in the series. Inlet of the first ETC of the series is connected with the outlet of the basin from where the water circulates to the whole system by virtue of a DC motor which could be powered by either the gird or the PV modules. Rest of the working is same as that of the previous stills discussed above.

3 Energy Metrics

Energy matrices are the analysis parameters to give us the performance of the technology and help us to judge the technology on the grounds of its uniqueness or its drawbacks etc. It is a very prudent aspect regarding all the technologies especially the one which is based on renewable energy. The technology is of no use if the amount of energy/exergy generated by that technology during its lifetime is less than that of its embodied energy (energy/exergy which is being used to develop that technology). Energy metrics consist of several analytical parameters like energy payback time (ET), energy production factor (EP) and life cycle conversion efficiency (LCCE). These factors represent nothing but a comparison between energy required for manufacturing the whole setup and energy produced by that setup, which in turn become the determining factor of the technological and economical success of that particular setup [11]. Embodied energy is the total (direct or indirect) energy which is consumed for generating an element or set up. As a better economic approach, whether the study is being on theoretical or experimental grounds, the embodied energy and payback time should be as low as possible. To keep this payback time low, PVT modules, water pumps, etc. are used for enhancing the performance by better heat transfer.

3.1 Energy Payback Time (ET)

This parameter is mathematically expressed as the ratio of the embodied energy (EBE) to annual energy output (AO), so as to compare both of them with respect to each other. This parameter represents the period of time required by the setup in order to return that much amount of energy which is being consumed to generate that setup (embodied energy). The net annual energy output is being represented by the addition of net thermal energy output and net thermal energy which is equivalent to the electrical energy output by PV module. Equation (1) represents the total energy output of distillation unit.

$$E_{\text{out}} = \frac{M_{ew} L}{3600} + \frac{P_m - P_u}{0.38} \tag{1}$$

here '$(P_m - P_u)$' represents the net annual electrical energy output by PV module. For converting this high-grade energy into low-grade energy, i.e., thermal energy, it is being divided by 0.38 [12]. Mathematically, Eq. (2) represents energy payback time with respect to energy ($ET_{(e)}$) and Eq. (3) represents (energy payback time with respect to exergy ($ET_{(ex)}$).

$$\mathrm{ET_e} = \frac{\mathrm{EBE}}{\mathrm{AO}} \tag{2}$$

$$\mathrm{ET_{ex}} = \frac{\mathrm{EBE}}{\mathrm{AXO}} \tag{3}$$

3.2 Energy Production Factor (EP)

The inclusive performance of a solar distillation system is being represented by the virtue of an energy metrics parameter, i.e., EP. Mathematically, EP is nothing but the reciprocal of ET. So, we can conclude that EP is inversely proportional to ET. As we have discussed, a better system has a lower ET. Thus, for a better performance of solar stills on both economic and technological ground the value of EP must be higher. Equations (4) and (5) represent EP on the basis of energy and exergy respectively for active solar distillation units [11].

$$\mathrm{EP_e} = \frac{\mathrm{AEO}}{\mathrm{EBE}} \tag{4}$$

$$\mathrm{EP_{ex}} = \frac{\mathrm{AXO}}{\mathrm{EBE}} \tag{5}$$

here AXO stands for the exergy output in a year.

3.3 Life Cycle Conversion Efficiency (LCCE)

This energy metrics parameter represents how efficient the system is in converting the input of solar energy into the net output energy throughout its lifetime period. Higher the efficiency of the system, higher will be the capability of the system to get maximum output energy from the input energy. Ideal LCCE value of the system should be unity, i.e., an ideal system possesses the capability to convert the total input energy into output energy. Idea of LCCE parameter was given by Tiwari and Mishra [11]. Mathematically, Eqs. (6) and (7) represent LCCE on the grounds of energy and exergy, respectively.

$$\mathrm{LCCE_e} = \frac{(\mathrm{AEO}) \times (n) - (\mathrm{EBE})}{\mathrm{AS} \times n} \tag{6}$$

$$\mathrm{LCCE_{ex}} = \frac{[(\mathrm{AXO}) \times (n)] - (\mathrm{EBE})}{\mathrm{AS} \times 0.93 \times n} \tag{7}$$

93% of the total annual solar energy represents annual solar exergy, and this concept was given by Petela [13]. Here, *n* stands for life of the system, and AS stands for solar energy in a year.

4 Discussions

The variation of energy metrics for different systems is shown in Fig. 4. From Fig. 4, it is seen that the energy payback time on the ground of energy as well as exergy is minimum for case (iii). The main reason its occurrence was found to be contributed by the lack of presence of convection loss in the case of ETC which in turn happens due to the presence of vacuum between tubes which result in higher energy as well as exergy output and hence lower ET. Life cycle conversion efficiency is far away dissimilar from the efficiency. The evaluation of LCCE takes into consideration the whole life of the solar desalination system under study. The value of LCCE on the basis of energy as well as exergy is highest for case (iii) due to the fact the lower losses occur in the case of ETC due to the absence of loss through convective heat transfer mode.

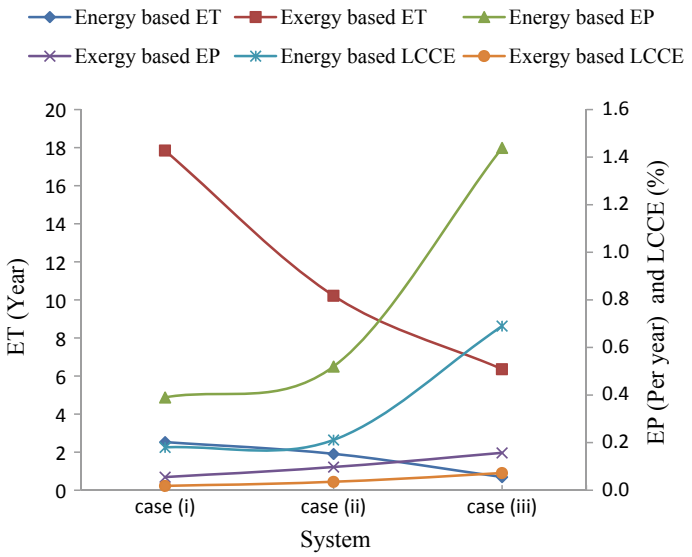

Fig. 4 Energy metrics for different systems

5 Conclusions

The comparative study of active double slope solar desalination systems has been conducted on the ground of energy metrics. From the present study, one can conclude that ET on the ground of exergy as well as energy is minimum for case (iii) followed by cases (ii) and (i) in succession. The life cycle conversion efficiency on the ground of energy as well as exergy is uppermost regarding case (iii) followed by cases (ii) and (i) in succession.

6 Recommendations

The theoretical scrutiny of double slope solar desalination system integrated with N alike collectors under optimized condition has been conducted. They have not been validated experimentally. So, one should validate the result experimentally before installing it on commercial level.

References

1. UNICEF-WHO (2015) Progress on sanitation and drinking water. Update and MDG assessment, pp 1–90
2. Zaki GM, Dali TEl, Shafie HEl (1983) Improved performance of solar still. In: Proceedings of the first Arab international solar energy conference, Kuwait, pp 331–335
3. Rai SN, Tiwari GN (1983) Single basin solar still coupled with flat plate collector. Energy Convers Manage 23(3):145–149
4. Mohameed QH, Fawzi B (2008) Solar thermal desalination technologies. Desalination 220:633–644
5. Kern EC, Russell MC (1978) Combined photovoltaic and thermal hybrid collector systems. In: Proceedings of the 13th IEEE photovoltaic specialists, 5–8 June 1978, Washington DC, USA, pp 1153–1157
6. Atheaya D, Tiwari A, Tiwari GN, Al-Helal IM (2015) Analytical characteristic equation for partially covered photovoltaic thermal (PVT) – compound parabolic concentrator (CPC). Sol Energy 111:176–185
7. Tripathi R, Tiwari GN, Al-Helal IM (2016) Thermal modelling of N partially covered photovoltaic thermal (PVT) - compound parabolic concentrator (CPC) collectors connected in series. Sol Energy 123:174–184
8. Singh DB, Tiwari GN (2016) Effect of energy matrices on life cycle cost analysis of partially covered photovoltaic compound parabolic concentrator collector active solar distillation system. Desalination 397:75–91
9. Singh G, Kumar S, Tiwari GN (2011) Design, fabrication and performance of a hybrid photovoltaic/thermal (PVT) double slope active solar still. Desalination 277:399–406
10. Singh DB, Al-Helal IM (2018) Energy metrics analysis of N identical evacuated tubular collectors integrated double slope solar still. Desalination 432:10–22

11. Tiwari GN, Mishra RK (2012) Advanced renewable energy sources. Royal Society of Chemistry Publishing House, UK. ISBN 978-1-84973-380-9
12. Huang BJ, Lin TH, Hung WC, Sun FS (2001) Performance evaluation of solar photovoltaic/thermal systems. Sol Energy 70(5):443–448
13. Petela R (2003) Exergy of undiluted thermal radiation. Sol Energy 86:241–247